

AD-A191 235

DTIC FILE COPY

②

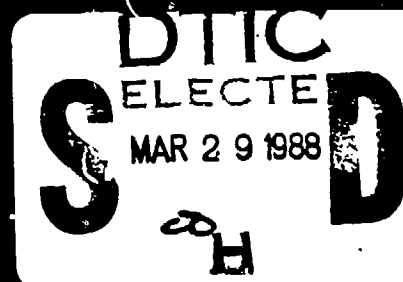
Travelling Wave Concepts for the Modeling
and Control of Space Structures.

Final Report for Contract F49620-36-C-0033

Dept. of Aeronautics & Astronautics
Massachusetts Institute of Technology

3/1/86-10/31/87

Conv 4



DISTRIBUTION STATEMENT A

Approved for public release;
Distribution Unlimited

②

Final Report of Research on

Travelling Wave Concepts for the Modelling and Control of Space Structures

performed at the

Massachusetts Institute of Technology,
Department of Aeronautics and Astronautics
Massachusetts Institute of Technology

for the

**Air Force Office of Scientific Research
(Contract F4 9620-86-C-0039)**

1 March 1986 - 31 October 1987

DTIC
ELECTE
MAR 29 1988

1. The information requested is
not available. File # 190-12.
2. Not available.
3. Not available.
4. Bureau of Information Division

DISTRIBUTION STATEMENT A

Approved for public release;
Distribution Unlimited

88 3 28 12 6

REPORT DOCUMENTATION PAGE

1a. REPORT SECURITY CLASSIFICATION Unclassified			1b. RESTRICTIVE MARKINGS		
2a. SECURITY CLASSIFICATION AUTHORITY			3. DISTRIBUTION / AVAILABILITY OF REPORT Approved for public release, distribution unlimited		
2b. DECLASSIFICATION / DOWNGRADING SCHEDULE					
4. PERFORMING ORGANIZATION REPORT NUMBER(S)			5. MONITORING ORGANIZATION REPORT NUMBER(S) AFOSR-TR- 88 - 0278		
6a. NAME OF PERFORMING ORGANIZATION Aeronautics and Astronautics Mass. Institute of Technology		6b. OFFICE SYMBOL (if applicable)	7a. NAME OF MONITORING ORGANIZATION Air Force Office of Scientific Research		
6c. ADDRESS (City, State, and ZIP Code) 77 Massachusetts Avenue Cambridge, MA 02139			7b. ADDRESS (City, State, and ZIP Code) AFOSR, Bldg 410 Bolling Air Force Base, DC 20332-6448		
8a. NAME OF FUNDING / SPONSORING ORGANIZATION Air Force Office of Scientific Research		8b. OFFICE SYMBOL (if applicable) AFOSR / NA	9. PROCUREMENT INSTRUMENT IDENTIFICATION NUMBER F49620-86-C-0039 and FQ8671-88-00398		
8c. ADDRESS (City, State, and ZIP Code) Building 410 Bolling Air Force Base, DC 20332-6448		10. SOURCE OF FUNDING NUMBERS			
		PROGRAM ELEMENT NO. 611057	PROJECT NO. 2302	TASK NO. B1	WORK UNIT ACCESSION NO.
11. TITLE (Include Security Classification) Travelling Wave Concepts for the Modeling and Control of Space Structures.					
12. PERSONAL AUTHOR(S) A.H. von Flotow, S.R. Hall					
13a. TYPE OF REPORT Final		13b. TIME COVERED FROM 3/1/86 TO 10/31/87		14. DATE OF REPORT (Year, Month, Day) January 31, 1988	
15. PAGE COUNT approx. 300					
16. SUPPLEMENTARY NOTATION					
17. COSATI CODES			18. SUBJECT TERMS (Continue on reverse if necessary and identify by block number)		
FIELD	GROUP	SUB-GROUP	Wave Propagation, Flexible Structures, Active Control, Localisation		
19. ABSTRACT (Continue on reverse if necessary and identify by block number) This report draws together several publications, summarizing research performed into wave propagation in, and control of, large flexible spacecraft structures. The topics of individual papers range from wave propagation modeling in periodic and disordered periodic structures, through active control of reflection and transmission at discrete points, and distributed hierarchic control architectures for flexible structures.					
20. DISTRIBUTION / AVAILABILITY OF ABSTRACT <input checked="" type="checkbox"/> UNCLASSIFIED/UNLIMITED <input checked="" type="checkbox"/> SAME AS RPT. <input checked="" type="checkbox"/> DTIC USERS			21. ABSTRACT SECURITY CLASSIFICATION Unclassified		
22a. NAME OF RESPONSIBLE INDIVIDUAL J.R. ARCS, NAEHOLAN			22b. TELEPHONE (Include Area Code) (202) 7107-4937		22c. OFFICE SYMBOL NA

Summary

This report summarizes 20 months of research into Travelling Wave Concepts for the Modelling and Control of Space Structures, performed at the Massachusetts Institute of Technology under the supervision of Professors von Flotow, Hall and Crawley. Major contributors to the work were graduate research assistants Miller, Signorelli, O'Donnel, and Kissel. Many undergraduate assistants also contributed.

The research has led to seven research papers which were published in the open literature or presented at conferences, and to two graduate theses and two undergraduate theses in MIT's Department of Aeronautics and Astronautics. These publications are presented in full in the Appendix.

In addition to these published papers, the past few months have witnessed other forms of dissemination of research results. Professor von Flotow has given invited lectures derived in part from this AFOSR sponsored research at the Office of Naval Research in September 1986, Yale University in May 1987, the Naval Underwater Systems Center in June 1987, Lockheed Palo Alto in August 1987, the University of Buffalo in October 1987, and at the meeting of the American Acoustical Society in Miami in November 1987. In addition, we have influenced research into the dynamics and control of space robotics at Martin Marietta Aerospace in Denver, by sending them requested computer software, and work in active control of structural acoustics at the Naval Underwater Systems Center in Newport, R.I.

This report consists of a brief executive summary highlighting the main results of the research publications collected in the Appendix.



on For	
A&I <input checked="" type="checkbox"/>	
DTIC TAB <input type="checkbox"/>	
Unannounced <input type="checkbox"/>	
Justification	
By	
Distribution/	
Availability Codes	
Dist	Avail and/or Special
A-1	

Modelling of Disturbance Propagation in Elastic Structures

A good portion of the research has focused upon the development of techniques for the modelling of structural response in terms of disturbance propagation. Such models are of interest for several reasons:

1. Understanding the mechanisms that govern the propagation of disturbances through an elastic structure is useful for building intuition, for structural design and for design of active control.
2. Disturbance propagation models have the potential for providing high-fidelity analysis capabilities in response regimes where other techniques are inapplicable. Of considerable interest to the researchers at MIT is the response of elastic spacecraft to disturbances with significant spectral content at frequencies including many (even hundreds) of the spacecraft natural modes of structural vibration.
3. Elastic disturbance propagation is a classic area of research in applied mechanics, having application in acoustics, seismology, microwave electronics, transducer design, biological fluid mechanics, design of mechanisms and machines, and many other areas.

The MIT research effort has made good progress in development of models for elastic disturbance propagation. This progress is summarized here with reference to specific papers written during the period of the contract and with its financial support.

Wave Propagation and Power Flow in Truss Structures

The MS thesis research of Joel Signorelli took a computational approach to investigating the wave propagation behaviour of simple beam-like truss structures. Although Joel began the work with the intention of investigating the behaviour of a very complex spacecraft truss beam, he found enough interesting effects in a simple situation, originally intended to serve only as a preliminary warm-up.

Joel introduced a modelling technique which takes explicit advantage of the spatial periodicity of the structure. This is similar to an approach developed by M.S. Anderson at NASA Langley Research Center in recent years, but unlike Anderson's approach, has no difficulty with the application of boundary conditions. Joel's approach begins with the spatial state transition matrix (also known as the transfer matrix) of a single bay. This transition matrix is formulated in the frequency domain, by any of a host of techniques, including exact solutions of the partial differential equations governing motion of the truss members internal to the bay. For purpose of comparison with a prior finite element solution of a segment of the truss, Joel chose to derive the transition matrix with the identical finite element discretization.

One approach to modelling the dynamics of a finite portion of a one-dimensional spatially periodic structure involves multiplication of a series of segment transition matrices. This is numerically not stable, since the transition matrix can, in general, have an extremely large range in the magnitudes of its eigenvalues. An alternative, transforming to the transition matrix eigenspace, is numerically superior, and has interpretation in terms of wave modes.

Much of Joel's work focused upon the frequency-dependence of wave propagation in a beam-like truss. From a numerical viewpoint, this is just a study of the eigenvalues and eigenvectors of the bay transition matrix, and of their dependence on frequency. Joel discovered a host of interesting effects:

1. The model exhibits as many wave modes in each direction as one chooses coupling coordinates between neighboring bays. The wave modes come in identical pairs, of each pair one wave travels in each direction.

2. Each wave mode travels independently of the others.
3. Each wave mode can be described by its dispersion behaviour (the frequency dependence of the propagation velocity), and by the corresponding deflection shape. Joel's thesis is full of plots of the deflection shape of a truss beam supporting a single travelling wave.
4. The dispersion characteristics of a truss beam are astoundingly complex. Each wave mode may be either:
 - a) propagating without attenuation (a traveling wave),
 - b) propagating with attenuation (a complex wave), or
 - c) not propagating (an evanescent wave). Joel found that each of the wave modes he studied exhibited all three types of behaviour, different behaviour in different frequency ranges. Such complex behaviour is unprecedented in the study of wave propagation in periodic structures.
5. Joel is among the first few analysts (perhaps the first) to clearly describe the complex traveling wave, a wave which both propagates and is attenuated. He demonstrates that simple, mono-coupled structures cannot support such behaviour, but that at least two coupling coordinates are required. Furthermore, he demonstrates that such wave motion does not propagate energy in isolation, but may in conjunction with other wave modes.
6. Joel investigates power flow in the truss beam due to these wave modes in isolation. He neglected to consider power flow due to wave-mode interaction, since at that time we did not yet know that such a thing could happen. Dave Miller's work discovered this a few months later.
7. Joel applied two types of boundary conditions to the truss beam and transformed these boundary conditions into a wave-mode description involving the boundary scattering matrix. This is a unique approach, which permits investigation of the causal behaviour at the boundary, the mechanism of reflection of incident disturbances.
8. Having transformed the analysis to wave mode coordinates, Joel was able to derive exact (to numerical precision) structural

transfer functions of the structure. The numerical difficulty of multiplication of a sequence of transfer matrices is thus avoided.

Full details of Joel's work are recorded in the appendix in the thesis, "Wave Propagation in Periodic Truss Structures," and the paper "Wave Propagation, Power Flow, and Resonance in a Truss Beam." This paper has been accepted for publication in the Journal of Sound and Vibration.

Power Flow in Structural Networks

In the fall of 1986 and winter of 1987 PhD candidate David Miller was grappling with control formalisms for structures whose dynamics are described in terms of wave propagation. One concept that surfaced was the desirability of influencing the power flow in such structures by active means, rather than to monitor and actively control the direct response. This consideration led to the development of a theory and computational procedure for calculating such power flow. This procedure is briefly mentioned in the paper, "Active Modification of Reflection Coefficients in Elastic Structures," presented by David Miller as an invited paper at the American Control Conference in Minneapolis, in June 1987, and included in the appendix of this report. David Miller and Prof. von Flotow are continuing to develop these concepts of power flow, and are preparing further papers for publication.

Waves in Spacecraft Tethers

Tethered spacecraft are envisioned which consist of two (or more) relatively compact bodies connected to one another by long, slender wires under very slight tension. The dynamics and control of such configurations is beginning to receive serious attention of analysts around the world. In the

summer of 1986, Prof. von Flotow considered the problem and proposed an engineering model which explicitly separates the motion into slow dynamics (comparable to orbital rate) and fast dynamics.

The fast dynamics, confined primarily to the tether, are governed by a system of partial differential equations. In the linear approximation, these equations are related to the well-known wave equations, differing significantly because the equilibrium shape of the tether is slightly curved. The analysis then investigates the dynamics of such a curved, elastic wire in terms of both travelling waves and in terms of exact frequency-domain solutions of the governing equations. The analyses are summarized in a paper, "Some Approximations for the Dynamics of Spacecraft Tethers," which is included in the appendix of this report, and which is to be published in the AIAA Journal of Guidance, Control and Dynamics.

In the winter and fall of 1987, two undergraduate students in MIT's Department of Aeronautics and Astronautics, Todd Barber and Earl Gregory, accepted the challenge to experimentally investigate the dynamics of an elastic catenary, and to verify (or disprove) the analysis proposed by Prof. von Flotow. Wave propagation speeds, transfer functions, and mode shapes were measured, and compared favourably with the analytically predicted values. The transition from the behaviour of an inelastic hanging chain to that of a taut elastic string was investigated. These results are summarized in Todd Barber's report, "Dynamic Cable Response: The Effect of Cable Sag," included in the appendix.

Wave Propagation and Localisation in Disordered Periodic Structures

Wave propagation in periodic structures has received the attention of dozens of investigators over the past century, beginning with Lord Rayleigh, who was interested in light transmission through crystals. Recent work has been motivated by interest in seismology, structure-borne sound, solid state physics, microwave electronics, and other applications. Our interest originates in the realization that many future large spacecraft structures will also be spatially periodic; i.e., truss structures.

Recent work at MIT and elsewhere has investigated the dynamics of structures which are slightly perturbed from perfect periodicity. Under the partial sponsorship of this contract, doctoral student Glen Kissel has in the past two years achieved a fundamental analysis of these effects in structural systems. He drew heavily on a large literature, primarily in solid state physics. Glen's writings on this subject (a paper "Localization in Disordered Periodic Structures," presented at the 28th AIAA Structures, Structural Dynamics and Materials Conference in Monterey in April 1986, and a PhD thesis at MIT in September 1987 with the same title, represent an elegant theoretical summary of a broad disjointed literature, and make significant new contributions to that literature. Glen also provides a computational procedure for evaluating the strength of the localization effect in structural systems. Glen Kissel now works at the Jet Propulsion Laboratories, and is writing two further papers for journal publication based on his PhD dissertation.

In the winter of 1987 two undergraduate students, Cathy Sybert and Tupper Hyde attempted an experimental verification of localization in a relatively complex structure, intentionally disordered. Their experiment was

not a glorious success, as is documented in the report by Tupper Hyde, "Mode/Wave Localization in Disordered Periodic Structures."

Active Control of Elastic Structures

The preceding section describes the research into structural dynamic modelling performed under the terms of this contract. We have also been active in research into active control of such structures as is summarized by the following paragraphs and by the four relevant papers in the appendix.

Hierarchic Control

An important consideration in the control of flexible structures is the computational architecture which is used to implement the control. Because of the large number of modes, sensors, and actuators in a typical flexible space structure, traditional control system architectures (such as a full state feedback controller cascaded with a full state estimator) are infeasible.

The approach that has been taken in this investigation is to develop a hierarchic control system architecture which can greatly reduce the amount of computation required, while at the same time allowing the processing to be distributed. This allows much of the control to be performed locally, so that the approach also reduces the need for transferring large amounts of data to and from a central processor.

In February 1987 the paper, "A Hierarchic Control Architecture for Intelligent Structures," was presented at the AIAA Rocky Mountain Guidance and Control Conference (see appendix). The general approach is to divide the structure into coarse and fine finite element models. The coarse FEM is used to control the lower modes of the structure through a central (or "global") processor. The local controllers then operate on the residual, which is the

difference between the global (or coarse) FEM and the fine FEM. Results presented in the paper demonstrate that the approach may be easily applied to test cases, and that under some circumstances, stability can be guaranteed.

Control-Motivated Tailoring of Structural Dynamics

The extensive research literature on control of structural dynamics has almost invariably taken the approach that the structural dynamics are difficult to control, and may not be modified to ease the task of the control engineer. Thus one often reads, for example, that the dynamics of large flexible spacecraft are characterised by many (even hundreds) of lightly damped modes (damping ratio less than one percent) spectrally closely spaced. Moreover, these modes are poorly known, both with respect to frequency and mode shapes.

An exception to this approach is the growing literature on simultaneous design of the control system and the structure. Unfortunately most of this literature attempts an "optimal" approach to this design problem, and the research quickly bogs down to research into computational techniques of minimizing a complex non-linear function of many parameters. The examples that have been thus treated are extremely simple, and it appears that the techniques are computationally limited to such simple examples. Furthermore, since one can only optimize over parameters which are modelled, and since modelling of passive damping is extremely difficult, this literature tends to have ignored this extremely important design freedom by assuming some given level of passive damping.

In August 1986 Prof. von Flotow presented the paper, "Control-Motivated Tailoring of Spacecraft Truss Structures," at the AIAA Guidance,

Dynamics and Control Conference in Williamsburg, VA. This paper (full text in the appendix) takes a very informal approach to:

1. Quantitatively estimating the benefits of passive damping to the problem of active control of structural dynamics.
2. Quantitatively estimating the mass penalties associated with various passive damping treatments.
3. Computationally demonstrating the possibilities for tailoring the dynamics of a truss beam for active control.

The Acoustic Limit of Active Control of Structural Dynamics

In the winter of 1987 Prof. von Flotow was invited to write a chapter for the Monograph, "Large Space Structures: Dynamics and Control," ed. S.N. Atluri, A.K. Amos, Springer Verlag, to appear, 1988. The invitation was accepted, and the result, entitled, "The Acoustic Limit of Active Control of Structural Dynamics," is included in the appendix. This paper is based on the relevant work done by Prof. von Flotow and partners over the past few years.

The main points of the paper are:

1. Modal analysis (or any global model of structural dynamics) becomes fatally unreliable in the acoustic limit, defined to be the frequencies above the natural frequency of perhaps the tenth mode.
2. Passive damping is an important vibration remedy to be used in this limit.
3. If active control must be used, then it must be based upon (local) acoustic models of the structural response.
4. Examples of such a control design procedure are given.

Appendix

A collection of papers, theses, and reports written under the terms of this research contract.

Contents

1. J. Signorelli, "Wave Propagation in Periodic Truss Structures," MS Thesis, Dept. of Aeronautics and Astronautics, MIT, Feb. 1987.
2. J. Signorelli, A.H. von Flotow, "Wave Propagation in Periodic Truss Structures," Proceedings of the AIAA Dynamics Specialists Conference, Monterey, CA, April 9-10, 1987, in press, Journal of Sound and Vibration.
3. D.W. Miller, A.H. von Flotow, S.R. Hall, "Active Modification of Wave Reflection and Transmission in Flexible Structures," Proceedings of the American Control Conference, Minneapolis, MN, June 1987, (invited paper).
4. A.H. von Flotow, "Some Approximations for the Dynamics of Spacecraft Tethers," in press, AIAA Journal of Guidance, Control and Dynamics.
5. T.J. Barber, "Dynamic Cable Response: The Effect of Cable Sag," internal report, Dept. of Aeronautics and Astronautics, Massachusetts Institute of Technology, December 1987.
6. G.J. Kissel, "Localization in Disordered Periodic Structures," Proceedings of the 28th AIAA Structures, Structural Dynamics and Materials Conference, Monterey, April 6-8, 1987.
7. G.J. Kissel, "Localization in Disordered Periodic Structures," PhD Thesis, Dept. of Aeronautics and Astronautics, Massachusetts Institute of Technology, September 1987.
8. T. Hyde, "Mode/Wave Localization in Disordered Periodic Structures," internal report, Dept. of Aeronautics and Astronautics, Massachusetts Institute of Technology, May 1987.
9. K.J. O'Donnell, E.F. Crawley, B.A. Ward, S.R. Hall, "A Hierarchic Control Architecture for Intelligent Structures," Proceedings of the Rocky Mountain Guidance and Control Conference, February 1987.
10. A.H. von Flotow, "Control-Motivated Dynamic Tailoring of Truss-Work Structures," Proceedings, AIAA Guidance and Control Conference, Williamsburg, VA, August 1986.

11. A.H. von Flotow, "The Acoustic Limit of Control of Structural Dynamics," Large Space Structures: Dynamics and Control, Springer Verlag, 1988, editors: S. Atluri, A. Amos.

11. A.H. von Flotow, "The Acoustic Limit of Control of Structural Dynamics," Large Space Structures: Dynamics and Control, Springer Verlag, 1988, editors: S. Atluri. A. Amos.

WAVE PROPAGATION IN PERIODIC TRUSS STRUCTURES

by

JOEL SIGNORELLI

B.S. Aeronautical & Astronautical Engineering, 1982

University of Illinois at Urbana-Champaign

SUBMITTED IN PARTIAL FULFILLMENT OF THE REQUIREMENTS

FOR THE DEGREE OF

MASTER OF SCIENCE IN

AERONAUTICS AND ASTRONAUTICS

at the

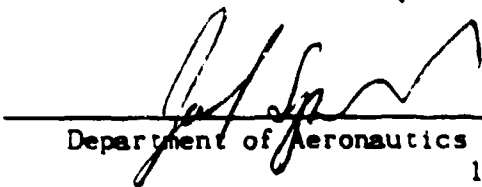
MASSACHUSETTS INSTITUTE OF TECHNOLOGY

February 1987

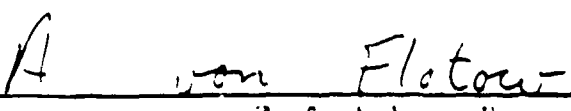
© Joel Signorelli, 1987

The author hereby grants to M.I.T. permission to reproduce and to distribute copies of this thesis document in whole or in part.

Signature of Author


Department of Aeronautics and Astronautics
15 December, 1986

Certified by


Prof. Andreas H. von Flotow
Thesis Supervisor

Accepted by


Prof. Harold Y. Wachman
Chairman, Department Graduate Committee

WAVE PROPAGATION IN PERIODIC TRUSS STRUCTURES

by

JOEL SIGNORELLI

ABSTRACT

Wave propagation in periodic truss-work beams was analytically investigated. Transfer matrix methods were applied to the analysis of two truss beams. The results of a truss with members modelled as pinned rods agree well with results obtained from equivalent continuum models of the same structure. Use of beam models for the truss members shows that the pinned rod truss model loses fidelity at the first resonant frequency of the lateral motion of the truss members.

The pinned beam truss exhibits complicated mechanical filtering properties. Each travelling wave mode experiences alternating stop, pass, and complex mode bands as a function of frequency. It was shown that complex modes cannot exist alone and must form in groups of four. Net power flow in right/left-going complex mode pairs is found to be zero.

Scattering matrices were determined for fixed and free boundary conditions. The phase closure principle was then used to determine natural frequencies of the truss. It was found that closely spaced resonant frequencies were not identified by this method. Computed results show subtle erroneous characteristics which are attributed to numerical effects.

Thesis Supervisor: Andreas H. von Flotow

Title: Assistant Professor of Aeronautics and Astronautics

Acknowledgements

First and foremost I would like to thank Prof Andy von Flotow for all the help and guidance he has given me over the last year. I have never come across a teacher who was so willing to give of his time and his talent to help a student out whenever help was needed. Without his prodding, insight, and leadership, this thesis would truly not have been possible.

Also many thanks to Dave Miller and Glen Kissel who showed interest in this work and were always willing to lend a hand or give a helpful suggestion. Thanks to Rich Mauer who helped me get this whole thing started a year ago with his software and 'Athena skills.' A special thanks to Greg Martin and Donald 'Mr Cow' Raines who taught me much about Unix and Athena and were always around to help me out of the computer quicksand. Thank you, Dr Alok Das, for encouraging me to pursue my education and for making me feel that it was possible.

And finally there's Rigel Kent. What can be said...

TABLE OF CONTENTS

Abstract	1
Acknowledgements	2
Table of Contents	3
List of Figures	5
1 Introduction	8
1.1 Background	8
1.2 Wave Propagation in the Literature	10
1.3 The Present Work	10
2 The Transfer Matrix Method	12
2.1 The State Vector	12
2.2 The Transfer Matrix	13
2.3 Derivation of the Transfer Matrix	15
2.4 Condensation of the Dynamic Stiffness Matrix	18
2.5 Truss Closure	19
2.6 Natural Frequencies of the Truss	21
3 Wave Propagation Analysis	23
3.1 Eigenvalues of the Transfer Matrix	23
3.2 Propagation Coefficient	25
3.3 Wave Propagation in a Uniform Two-Dimensional Pinned-Joint Truss with Rod Members	27
Dispersion Curves of the Four Right-Going Wave Modes	28
Eigenvectors of the Four Right-Going Wave Modes	32
Comparison to Continuum Models	34

3.4 Wave Propagation in a Uniform Two-Dimensional Pinned-Joint Truss with Beam Members	38
Eigenvalues and Eigenvectors of the Evanescent Wave Mode	40
Eigenvalues and Eigenvectors of the S Wave Mode	42
Eigenvalues and Eigenvectors of the PE Wave Mode	48
Eigenvalues and Eigenvectors of the CE Wave Mode	49
3.5 Complex Modes	54
4 Wave Mode Power Flow	57
4.1 Determination of Average Power Flow in a Wave Mode	57
4.2 Wave Mode Power Flow	59
4.3 Eigenvector Normalization	64
5 Wave Mode Boundary Conditions	67
5.1 Scattering Matrices	67
5.2 Derivation of the Scattering Matrices for a Pinned Beam Truss Attached to the Shuttle Orbiter	69
5.3 Natural Frequencies by Phase Closure	75
6 Conclusions	80
References	84
Appendix A: Propagation Coefficients for a Pinned Beam Truss	85
Appendix B: Scattering Matrices for a Pinned-Free Truss	88

List of Figures

1.1	NASA's 'Space Station	8
2.1	State Vectors Associated with One Bay of a Periodic Truss	12
2.2	State Vectors for a Seven Bay Truss	14
2.3	Force/Displacement Definitions for the Finite Element and Transfer Matrix Methods	16
2.4	Node Assignment for the Finite Element Analysis of a Bay	16
2.5	Truss with Closing End Member	19
2.6	A Truss Cantilevered to the Shuttle Orbiter	21
3.1	The ξ Plane	25
3.2	Example Propagation Coefficient Values as a Function of Damping and Frequency	26
3.3	State Vectors for One Bay of the Pinned Rod Truss	27
3.4	Dispersion Curves for the Evanescent and S Modes (Pinned Rod Truss)	30
3.5	Dispersion Curves for the PE and CE Modes (Pinned Rod Truss)	31
3.6	First Bay of the Evanescent Mode as a Function of Frequency (Pinned Rod Truss)	33
3.7	One Wavelength of the S Mode as a Function of Frequency (Pinned Rod Truss)	35
3.8	First Twenty-Four Bays of the PE Mode as a Function of Frequency (Pinned Rod Truss)	36
3.9	The CE Mode as a Function of Frequency (Pinned Rod Truss)	36
3.10	Member Slopes, Pinned Beam Case	39
3.11	Pinned-Pinned and Clamped-Clamped Bending Resonances for Truss Longerons and Diagonals	39
3.12	Dispersion Curves for the Evanescent Mode (Pinned Beam Case)	41
3.13	First Bay of the Evanescent Mode as a Function of Frequency (Pinned Beam Truss)	42
3.14	Dispersion Curves for the S Mode as a Function of Frequency (Pinned Beam Truss)	43

3.15	One Wavelength of the S Mode in the First Pass Band (Pinned Beam Truss)	44
3.16	First Ten Bays of the S Mode in the First Stop Band (Pinned Beam Truss)	45
3.17	One Wavelength of the Complex S Mode (Pinned Beam Truss)	46
3.18	One Wavelength of the S Mode in the Second Pass Band (Pinned Beam Truss)	47
3.19	Dispersion Curves for the PE Mode (Pinned Beam Truss)	48
3.20	First Ten Bays of the PE Mode in the First Stop Band (Pinned Beam Truss)	50
3.21	PE Mode in the First Pass Band (Pinned Beam Truss)	50
3.22	PE Mode in the Second Stop Band (Pinned Beam Truss)	51
3.23	One Wavelength of the PE Mode in the Second Pass Band (Pinned Beam Truss)	51
3.24	Dispersion Curves for the CE Mode (Pinned Beam Truss)	52
3.25	CE Mode in the First Pass Band (Pinned Beam Truss)	53
3.26	CE Mode in the Second Pass Band (Pinned Beam Truss)	53
3.27	Complex Mode Coupling Between the S and PE Modes	55
3.28	Complex Mode Coupling About 70 Hz	55
3.29	Eigenvalues of Four Complex Wave Modes in the ξ Plane	56
4.1	Power Flow in the Right-Going Wave Modes	60
4.2	Power Flow in the Left-Going Wave Modes	61
4.3	Magnitude of Power Flow in the Right-Going Wave Modes	62
4.4	Magnitude of Power Flow in the Left-Going Wave Modes	63
4.5	Power Flow in the S and PE Modes in a Complex Mode Region	64
4.6	Invariability of Wave Propagation Under a Coordinate Transform	65
4.7	Wave Mode Eigenvectors at 80 Hz	66
5.1	Representation of Arriving and Departing Wave Modes at Beam Boundaries	68
5.2	Scattering Matrix for Pinned End of Truss	71
5.3	Scattering Matrix for Free End of Truss	72

5.4	Reflection Coefficients for the S and CE Modes at Low Frequency	74
5.5	Enforcing the Zero Displacement Boundary Condition by Means of a Phantom Wave	75
5.6	Natural Frequencies Obtained By Phase Closure	78
5.7	Natural Frequencies Near 35 Hz From Phase Closure	79

Chapter 1 - Introduction

1.0 Background

Many future space structures will have physical characteristics radically different from those flying today. Among these will be large direct broadcast satellites, the space station, and numerous scientific and commercial satellites. Critical to the success of the Strategic Defense Initiative will be large space based radar and surveillance platforms. Since the size and weight of these systems greatly impact launch costs, these so-called large space structures (LSS) will be built largely of light and flexible aerospace materials. Because of their size and distributed flexibility, the structural vibration modes of these structures may well be within the bandwidth of the control system. It is therefore of great importance to be able to characterize the dynamics of these LSS through analysis and simulation. One method of analysis involves examining these structures in terms of wave propagation.

Many of these planned large space structures will be constructed, in part, by truss-work structures. Truss structures are favored because of their ease of packaging, transportation, fabrication, and space assembly. A current example of a large space structure that will be assembled in part by truss members is NASA's space station (Fig 1.1). Truss structures generally consist of an assemblage of identical elements and are thus

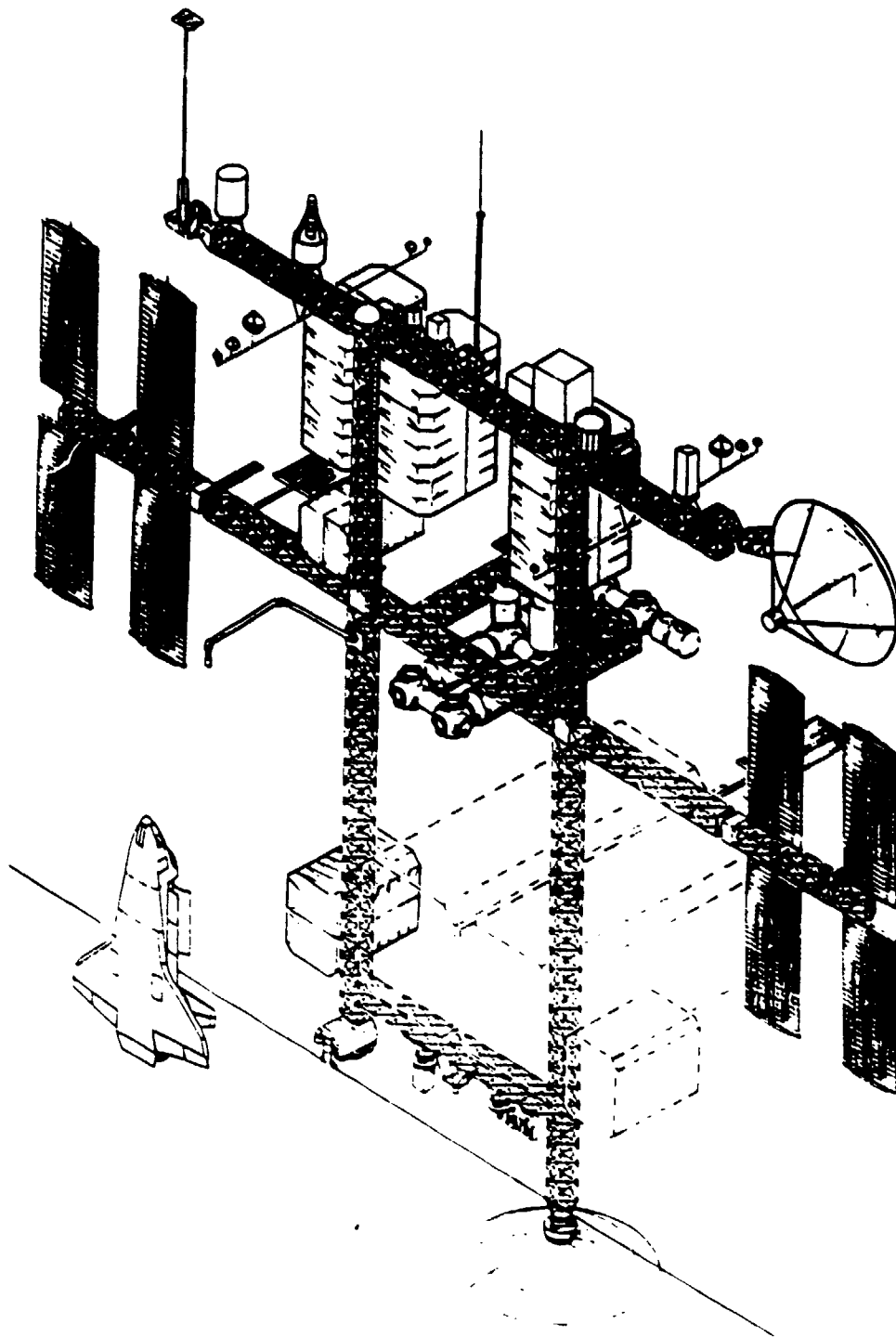


Figure 1.1 - NASA's Space Station

spatially periodic. Periodic structures have long been known to act as mechanical filters for travelling waves [B-1]. In order to gain more insight and understanding as to how wave propagation properties can be exploited in the dynamics and control of LSS, this thesis examines wave propagation in two-dimensional, periodic truss-work structures.

1.2 Wave Propagation in the Literature

The study of wave propagation in periodic structures began long ago in the field of solid state physics. Noteworthy among the early investigators is Brillouin who made a significant contribution to the study of wave propagation in crystals, transmission lines and atoms [B-1]. Cremer and Leilich studied flexural motion in periodic beams and showed that waves can propagate in certain frequency bands but not in others [C-1]. The notion of propagation coefficients was defined by Heckl in 1964 [H-1]. He investigated wave propagation in periodically supported, undamped grillages. Mead included damping effects in the wave propagation theory for periodic beams [M-1]. Mead and Eatwell theoretically described the so-called complex modes which have characteristics of propagating and attenuating waves [M-2] [E-1]. von Flotow introduced the use of scattering matrices to describe junctions in structural junctions. He also modelled members by transfer matrices and demonstrated the superiority of this approach over equivalent continuum models [V-1].

1.3 The Present Work

In this thesis, the methods of von Flotow and Mead will be

employed in the analysis of a two-dimensional periodic truss structure. Chapter 2 will introduce and develop the concept of the transfer matrix. Advantage is taken of the fact that truss structures are periodic by examining their dynamics in terms of the transfer matrix of a single bay of the truss. In Chapter 3 the eigenvalues and eigenvectors of the transfer matrix will be used to identify and characterize the wave modes present in the truss structure. By use of dispersion plots, the mechanical filtering properties of the truss will be demonstrated. Power flow in wave modes will be investigated in Chapter 4. And finally, by through the use of scattering matrices, Chapter 5 describes the interactions of the wave modes with truss boundaries. Natural resonant frequencies of an example truss will also be determined.

Chapter 2 - The Transfer Matrix Method

2.1 The State Vector

A periodic truss structure consists of several identical substructures called bays. At any station along the truss, a cross-sectional state vector, Y , which describes the force and displacement at that station, can be examined. Figure 2.1 shows one bay of a two-dimensional truss structure and the state vector associated with each side of the bay.

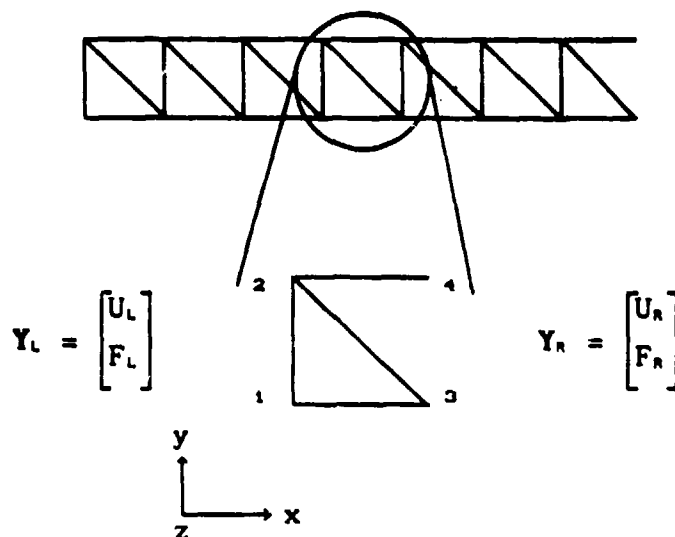


Figure 2.1 - State Vectors Associated with One Bay of a Periodic Truss

Each bay consists of four structural members. The state vector is chosen such that it describes the forces and displacements of the endpoints of the members. U_L and U_R describe the displacements of

the joints on the left and right sides of the bay respectively, while the forces on the joints are represented by F_L and F_R . If only joint translation in the X and Y directions, and rotation about the Z axis are modelled, the state vector on the left side of the bay, Y_L , will be,

$$U_L = \begin{bmatrix} U_1 \\ U_2 \end{bmatrix} \quad F_L = \begin{bmatrix} F_1 \\ F_2 \end{bmatrix} \quad (2.1)$$

$$\text{where } U_1 = \begin{bmatrix} U_{1x} \\ U_{1y} \\ \theta_{1z} \end{bmatrix} \quad F_1 = \begin{bmatrix} F_{1x} \\ F_{1y} \\ \tau_{1z} \end{bmatrix} \quad (2.2)$$

The state vector on the right hand side of the bay, Y_R , is similar and involves the state of joints 3 and 4.

2.2 The Transfer Matrix

The state at any two stations can be related by means of a transfer matrix, T.

$$Y_{i+1} = [T] Y_i \quad (2.3)$$

where Y_i is the state vector for the i-th station. The transfer matrix may be thought of as a spatial state transition matrix between two stations on the truss. The elements of the transfer matrix depend on the bay properties and, on frequency. Without damping the transfer matrix will be purely real.

Once the transfer matrix for a single bay has been determined, the transfer matrix for the entire structure can be assembled. For a seven bay truss (Fig. 2.2), we have,

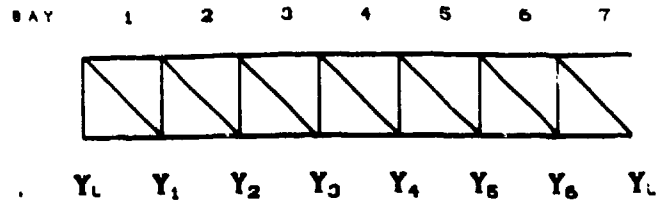


Figure 2.2 - State Vectors for a Seven Bay Truss

The states at the left and right sides of a bay are related by the bay transfer matrix,

$$\begin{aligned}
 Y_1 &= [T_1] Y_L \\
 Y_2 &= [T_2] Y_1 \\
 &\vdots \\
 Y_{i+1} &= [T_{i+1}] Y_i
 \end{aligned}
 \tag{2.4}$$

By multiplication of transfer matrices we obtain,

$$Y_n = [T_7] [T_6] [T_5] [T_4] [T_3] [T_2] [T_1] Y_L \tag{2.5}$$

But since the bays are considered to be identical, we have,

$$\begin{aligned}
 [T_1] &= [T_2] = [T_3] = \dots = [T_i] \\
 \text{so that,} \quad Y_n &= [T]^7 Y_L
 \end{aligned}
 \tag{2.6}$$

which relates the states at the right and left hand sides of a seven bay truss. T is referred to as the rearward transfer matrix of the structure [R-1]. The transfer matrix can also be expressed in terms of its eigenvalues and eigenvectors,

$$T_1 = v_1^{-1} \Lambda_1 v_1 \quad (2.7)$$

where v = the matrix of right eigenvectors of T

Λ = the diagonal matrix of eigenvalues of T

so that by Eqn 2.5, the states at opposing ends of the truss can be related by,

$$Y_n = [v^{-1} \Lambda^T v] Y_1 \quad (2.8)$$

2.3 Derivation of the Transfer Matrix

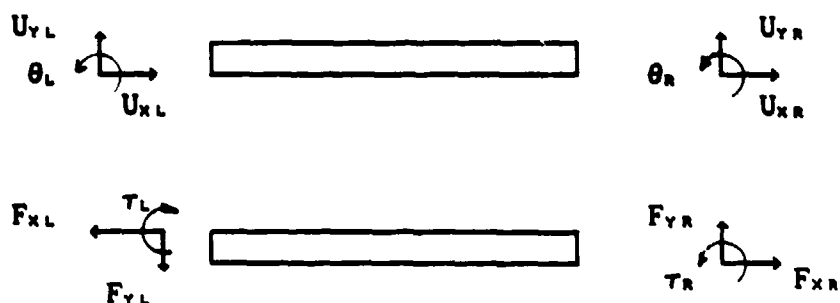
There are several methods to determine the transfer matrix of a structure. Among these are deriving the matrix from an n-th order differential equation, and deriving it from the system's mass and stiffness matrices [P-1]. The second method will be used throughout this work.

The mass matrix, M , and the stiffness matrix, K , for a bay can be determined by means of a finite element analysis of the bay. But first, care must be taken to ensure that differences in displacement and force coordinate definitions between the finite element analysis and those of the transfer matrix method are taken into account. For the transfer matrix method, the positive face of a cross-section of the truss is defined as the face whose outward normal points in the positive x direction. Positive displacements coincide with positive directions of the coordinate system, and forces are positive if, when acting on the positive face, their vectors are in the positive direction [P-1]. Fig 2.3 illustrates the force/displacement coordinate definitions for the two analyses. Note that in the transfer matrix method forces and

moments of adjacent elements are of opposite sign so that all internal forces in the structure are balanced.



Finite Element Force/Displacement Coordinate Definitions



Transfer Matrix Method Force/Displacement Coordinate Definitions

Figure 2.3 - Force/Displacement Definitions for the Finite Element and Transfer Matrix Methods

For the finite element analysis the bay was modelled with eight elements (Fig 2.4).

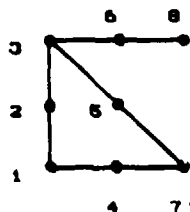


Figure 2.4 - Node Assignment for the Finite Element Analysis of a Bay

The nodes located at the member midpoints were included so as to

better model the bay's higher order modes. The 'left' coupling dof's between adjacent bays are identified by the subscript L, the 'internal' dof's by I, and the 'right' coupling dof's between bays by R. The finite element analysis produces matrices M and K such that,

$$[M] \begin{bmatrix} U_L \\ U_I \\ U_R \end{bmatrix} + [K] \begin{bmatrix} U_L \\ U_I \\ U_R \end{bmatrix} = \begin{bmatrix} F_L \\ F_I \\ F_R \end{bmatrix} \quad (2.9)$$

For a truss with only nodal displacements as coupling dof's this

$$\text{becomes, } U_L = \begin{bmatrix} U_1 \\ U_3 \end{bmatrix} \quad U_I = \begin{bmatrix} U_2 \\ U_4 \\ U_5 \\ U_6 \end{bmatrix} \quad U_R = \begin{bmatrix} U_7 \\ U_8 \end{bmatrix} \quad (2.10)$$

$$F_L = \begin{bmatrix} F_1 \\ F_3 \end{bmatrix} \quad F_I = \begin{bmatrix} F_2 \\ F_4 \\ F_5 \\ F_6 \end{bmatrix} \quad F_R = \begin{bmatrix} F_7 \\ F_8 \end{bmatrix} \quad (2.11)$$

with U_I and F_I given as in Eqn 2.2. After Fourier transformation, Eqn 2.9 becomes,

$$[K - \omega^2 M] \begin{bmatrix} U_L \\ U_I \\ U_R \end{bmatrix} = \begin{bmatrix} F_L \\ F_I \\ F_R \end{bmatrix} \quad (2.12)$$

If structural damping is modelled, the leading matrix becomes,

$$[K(1 - i\eta) - \omega^2 M] \quad (2.13)$$

where η is the structural damping coefficient (loss factor). Eqn 2.13 forms the dynamic stiffness matrix of the bay.

2.4 Condensation of the Dynamic Stiffness Matrix

In order to derive the transfer matrix between the left and right hand sides of a bay, it is necessary to condense the internal nodes into the dynamic stiffness matrix. We reject the option of static condensation because we wish to model the internal dynamics of the bay. The dynamic stiffness matrix may be partitioned as,

$$\begin{bmatrix} D_{LL} & D_{LI} & D_{LR} \\ D_{IL} & D_{II} & D_{IR} \\ D_{RL} & D_{RI} & D_{RR} \end{bmatrix} \begin{bmatrix} U_L \\ U_I \\ U_R \end{bmatrix} = \begin{bmatrix} F_L \\ F_I \\ F_R \end{bmatrix} \quad (2.14)$$

Since the internal forces, F_I , must be zero, the second row of the matrix gives,

$$U_I = -D_{II}^{-1} (D_{IL} U_L + D_{IR} U_R) \quad (2.15)$$

Eqn 2.15 is substituted into rows 1 and 3 of Eqn 2.14, and after some rearrangement we get,

$$\begin{bmatrix} D_{LL} - D_{LI} D_{II}^{-1} D_{IL} & -D_{LI} D_{II}^{-1} D_{IR} \\ -D_{RI} D_{II}^{-1} D_{IL} & -D_{RI} D_{II}^{-1} D_{IR} + D_{RR} \end{bmatrix} \begin{bmatrix} U_L \\ U_R \end{bmatrix} = \begin{bmatrix} F_L \\ F_R \end{bmatrix} \quad (2.16)$$

For simplification, this can now be written as,

$$\begin{bmatrix} A & B \\ C & D \end{bmatrix} \begin{bmatrix} U_L \\ U_R \end{bmatrix} = \begin{bmatrix} -F_L \\ F_R \end{bmatrix} \quad (2.17)$$

where negative values of F_L have been taken to ensure compatibility of the transfer matrix and finite element analyses force coordinate definitions. And finally, the transfer matrix is determined by,

$$\begin{bmatrix} U_R \\ F_R \end{bmatrix} = \begin{bmatrix} -B^{-1} A & -B^{-1} \\ C - DB^{-1} A & -DB^{-1} \end{bmatrix} \begin{bmatrix} U_L \\ F_L \end{bmatrix} \quad (2.18)$$

or equivalently,

$$Y_R = [T] Y_L \quad (2.19)$$

2.5 Truss Closure

Before the global or complete transfer matrix of the truss can be assembled, the transfer matrix for the member closing off the right end of the truss must be determined.

Consider the end member as shown below. Once again, the member is modeled as two elements.

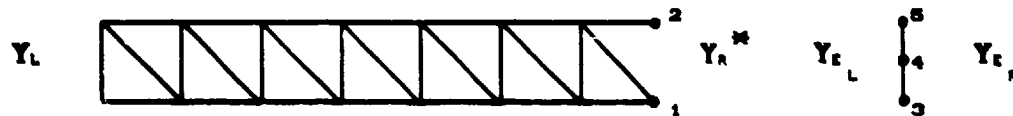


Figure 2.5 - Truss with Closing End Member

The displacements for the end members are,

$$U_{3R} = U_{3L} \quad U_{4R} = U_{4L} \quad U_{5R} = U_{5L} \quad (2.20)$$

while the forces acting on the nodes are,

$$F_3 = F_{3R} - F_{3L} \quad F_4 = 0 \quad F_5 = F_{5R} - F_{5L} \quad (2.21)$$

The end member's mass and stiffness matrices are obtained from a finite element analysis of the member. Following the same procedure as in section 2.4, we eliminate the internal degrees of freedom at node 4.

$$\left[\begin{array}{c|c} A & B \\ \hline C & D \end{array} \right] \begin{bmatrix} U_3 \\ U_6 \end{bmatrix} = \begin{bmatrix} F_3 \\ F_6 \end{bmatrix} \quad (2.22)$$

with A, B, C, and D as defined in Eqns 2.16 and 2.17. Substitution of Eqn 2.21 into Eqn 2.22 leads to,

$$\begin{bmatrix} F_{3n} \\ F_{6n} \end{bmatrix} = \left[\begin{array}{c|c} A & B \\ \hline C & D \end{array} \right] \begin{bmatrix} U_3 \\ U_6 \end{bmatrix} + \begin{bmatrix} F_{3L} \\ F_{6L} \end{bmatrix} \quad (2.23)$$

Combining this with Eqn 2.20 we get,

$$\begin{bmatrix} U_{3n} \\ U_{6n} \\ F_{3n} \\ F_{6n} \end{bmatrix} = \begin{bmatrix} [I] & 0 & 0 & 0 \\ 0 & [I] & 0 & 0 \\ [A] & [B] & [I] & 0 \\ [C] & [D] & 0 & [I] \end{bmatrix} \begin{bmatrix} U_{3L} \\ U_{6L} \\ F_{3L} \\ F_{6L} \end{bmatrix} \quad (2.24)$$

which defines the point transfer matrix across the end member as,

$$Y_{Ln} = [T_c] Y_{Ll} \quad (2.24)$$

or,

$$Y_n^* = [T_c] Y_n \quad (2.25)$$

So that for the whole truss we get,

$$Y_n = [T_c][T]^T Y_L \quad (2.26)$$

or,

$$Y_n = [T_o] Y_L \quad (2.27)$$

where T_o is the global transfer matrix for the entire truss.

2.6 Natural Frequencies of the Truss

Once the global transfer matrix for the structure has been determined, the system's natural frequencies can be determined. First, boundary conditions are applied to the truss. The boundary conditions will depend on how the truss is suspended in space. For example, a future on-orbit experiment will have a truss cantilevered to the shuttle orbiter as shown below.

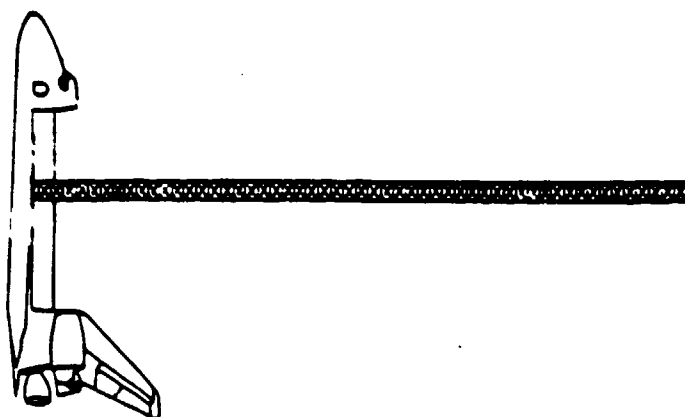


Figure 2.6 - A Truss Cantilevered to the Shuttle Orbiter

If the truss attach points are pinned, and the orbiter is assumed to be very stiff and massive, no displacements or torques can exist at those points. This leads to the boundary conditions,

$$U_L = \begin{bmatrix} U_{1x} \\ U_{1y} \\ \theta_1 \\ U_{3x} \\ U_{3y} \\ \theta_3 \end{bmatrix}_L = \begin{bmatrix} 0 \\ 0 \\ \theta_1 \\ 0 \\ 0 \\ \theta_3 \end{bmatrix}_L \quad F_L = \begin{bmatrix} F_{1x} \\ F_{1y} \\ T_1 \\ F_{3x} \\ F_{3y} \\ T_3 \end{bmatrix}_L = \begin{bmatrix} F_{1x} \\ F_{1y} \\ 0 \\ F_{3x} \\ F_{3y} \\ 0 \end{bmatrix}_L \quad (2.28)$$

The free end of the truss has the boundary condition $F_n = 0$. With this we obtain from Eqn 2.18,

$$\begin{bmatrix} U_R \\ 0 \end{bmatrix} = \begin{bmatrix} T_A \\ T_b \end{bmatrix} \begin{bmatrix} U_{1z} \\ U_{3z} \\ F_{1z} \\ F_{1y} \\ F_{3z} \\ F_{3y} \end{bmatrix} \quad (2.29)$$

where T_A and T_b are appropriately selected submatrices of the global transfer matrix T_0 . The bottom row of submatrices gives,

$$0 = [T_b] \begin{bmatrix} U_{1z} \\ U_{3z} \\ F_{1z} \\ F_{1y} \\ F_{3z} \\ F_{3y} \end{bmatrix} \quad (2.30)$$

The only non-trivial way this can be true is if

$$\det [T_b] = 0 \quad (2.31)$$

A plot of $|\det [T_b(\omega)]|$ as a function of frequency will indicate the system eigenvalues.

The determination of natural frequencies by this method may not always work. Some of the eigenvalues of the transfer matrix are quite large. The result of this is that when one attempts to determine the transfer matrix for n bays, the value of $[T]^n$ very quickly reaches the computational limit of the computer. A method will, however, be presented in Sections 5.3 which will enable the natural frequencies of the truss structure to be determined.

Chapter 3 - Wave Propagation Analysis

3.1 Eigenvalues of the Transfer Matrix

A wave propagating along a periodic structure can be characterized by,

$$Y_{i+1} = \xi Y_i \quad (3.1)$$

indicating that the state at station $i+1$ is the state at station i multiplied by a factor ξ . This, together with the basic transfer matrix relation

$$Y_{i+1} = [T] Y_i \quad (3.2)$$

forms an eigenvalue problem for ξ . The eigenvalues are generally complex and occur in ξ and $1/\xi$ pairs, corresponding to identical waves propagating in opposite directions [eigenvalues of a symplectic matrix occur in inverse pairs].

For each wave mode there are frequency regions in which the wave will propagate unattenuated (pass bands) and regions in which the wave is attenuated (stop bands). Complex modes (modes for which the eigenvalue is complex) are also considered to be in stop bands. The magnitude of an eigenvalue at a given frequency will indicate whether the wave is in a pass or stop band at that frequency. If the magnitude of the eigenvalue differs from unity, the frequency is in a stop band. For magnitudes equal to unity,

the frequency is in a pass band [R-2]. In a stop band, since $|\xi| < 1$, the cross-sectional state vector will eventually be diminished to zero.

$$\begin{aligned} |\xi| < 1 & \quad \text{stop band} \\ |\xi| > 1 & \quad \text{stop band} \\ |\xi| = 1 & \quad \text{pass band} \end{aligned} \quad (3.3)$$

Eigenvalue magnitudes greater than unity correspond to negative-going waves and those less than unity correspond to positive-going waves.

The relation between ξ and $1/\xi$ can be seen by constructing a plot of the ξ plane (Fig 3.1). For a given frequency, values of $|\xi|$ which lie on the unit circle are in a pass band. Those inside the unit circle are positive-going waves in a stop band while those reflected outside the circle are negative-going waves in a stop band. Values of $|\xi|$ which lie in the interior (exterior) of the circle, but not on the real axes, are complex modes. As a function of frequency, the eigenvalues move about the plane, continually changing magnitude and phase.

In the absence of damping, the transfer matrix, T , is real, thus its eigenvalues will be real or members of a complex conjugate pair. Complex modes thus occur only in groups of four--wave mode interaction is necessary. Mono-coupled systems (with 2×2 transfer matrices) cannot support complex wave modes. It is perhaps for this reason that complex wave modes have received scant attention in the literature, being mentioned in only two papers [E-1] [M-2].

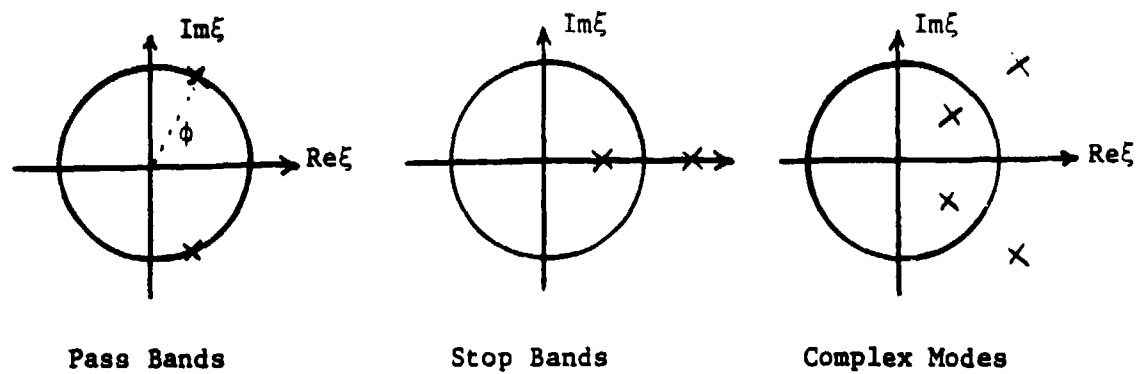


Figure 3.1 - The ξ Plane

3.2 Propagation Coefficient

The eigenvalues ξ are related to the propagation coefficient μ by

$$\xi = e^{\mu L} \quad (3.4)$$

where L is the bay length. μ is generally complex so that

$$\mu = \mu_r + \mu_i \quad (3.5)$$

$$\xi = e^{L\mu_r} e^{L\mu_i} \quad (3.6)$$

or
$$\xi = e^{L\mu_r} e^{i(kL + 2n\pi)} \quad (3.7)$$

where kL is the nondimensional wave number. The wave number is related to wavelength λ by

$$k = 2\pi / \lambda \quad (3.8)$$

μ_r (the attenuation constant) describes the exponential rate of decay of a wave as it passes through a bay, while μ_i (the phase

constant) describes the phase change a wave undergoes as it passes through a bay [M-2]. The propagation coefficients occur in +/- pairs, corresponding to negative and positive-going waves respectively.

Without damping, a wave is non-propagating whenever $\mu_r \neq 0$. The classic stop band behavior then has $\mu_i = 0$ implying no phase difference between motion in adjacent bays, and spatial exponential decay of amplitude. If $\mu_i \neq 0$, there is phase difference between the motion in adjacent bays and the wave now propagates, but transfers no energy along the length of the beam [M-2]. The spatial amplitude behavior of such a complex wave mode is an exponential decay of a sinusoidal envelope. These relations, including the effects of structural damping, are illustrated in Fig 3.2 [M-1].

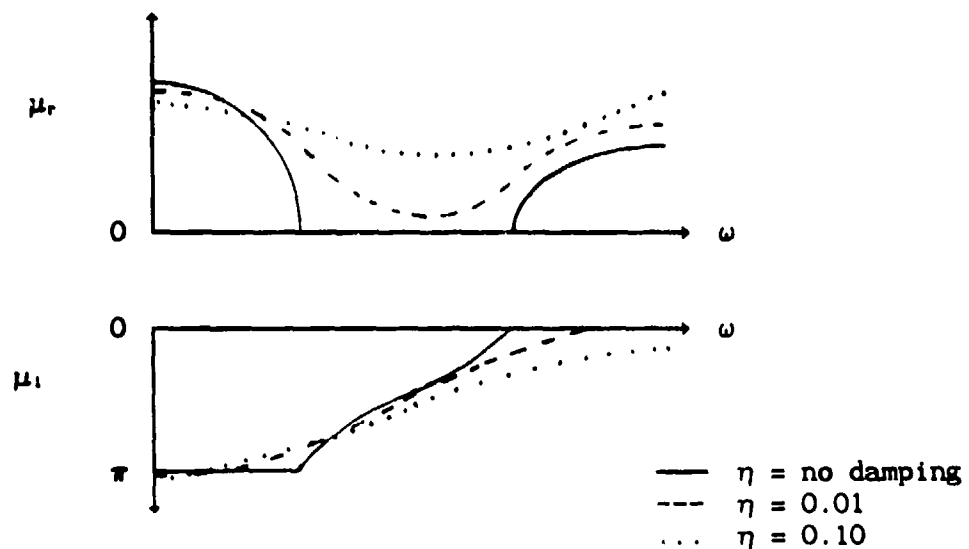


Figure 3.2 - Example Propagation Coefficient Values as a Function of Damping and Frequency

μ_r has alternating bands of positive and zero values. Positive values imply that the cross-sectional state variables decrease from bay to bay.

If structural damping is modelled, all the propagation coefficients are complex. This is necessary if energy is to flow from the source of vibration to the energy dissipating sinks in the truss. The presence of damping causes the wave to decay as it passes from bay to bay. If the damping is light, pass bands can still be seen in the plot of μ_r . μ_r is no longer zero in these bands but it is much smaller than in the adjacent attenuating bands.

3.3 Wave Propagation in a Uniform Two-Dimensional Pinned-Joint Truss with Rod Members

Wave propagation was studied in two different truss structures. The first truss to be analysed was a two-dimensional truss consisting of rod elements. Rod elements do not have bending stiffness and are only capable of carrying loads in tension and compression. The rod elements were joined by pinned joints, and the members were free to rotate about these joints. The cross-sectional state vector at each end of the bay consists of four joint translations and four joint forces (Fig 3.3).

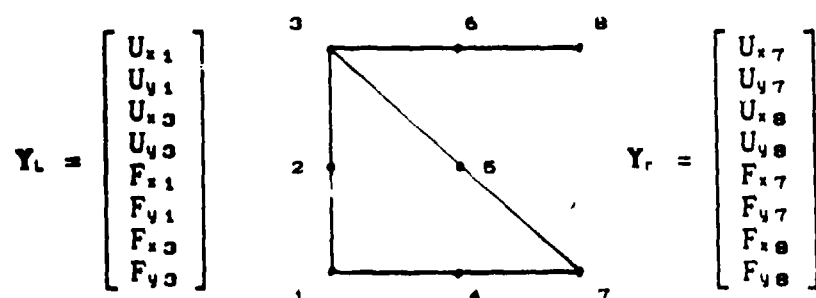


Figure 3.3 - State Vectors for One Bay of the Pinned Rod Truss

Each bay consisted of four members. Each of the members was modelled as two rod elements. There were a total of 16 degrees of freedom for each bay. Only four translational DOF and four forces couple adjacent bays. This leads to an $[8 \times 8]$ transfer matrix. The mass and stiffness matrices for the bay were obtained from a finite element analysis as described in Section 2.3. The physical properties of this truss were adapted from the Structural Assembly Demonstration Experiment (SADE) truss of [M-3]. In this model, it was assumed that there was no structural damping present, that the bay longerons were 55 inches long, and that the bay diagonals were $55\sqrt{2}$ inches long. The dynamic stiffness and transfer matrices were assembled as outlined in section 2.4.

The eigenvalues and eigenvectors of the transfer matrix were then determined as a function of frequency by a MATRIXx user defined command file [M-4]. Eight wave modes are present in the truss due to the four degrees of freedom present at each side of the bay. Four of these wave modes are positive-going and four are negative-going. Fig 3.4 and Fig 3.5 present values of the magnitude, $|\xi|$, and phase, φ , of the eigenvalues of the four positive-going wave modes.

Dispersion Curves for the Four Right-Going Waves

The magnitude and phase of the first mode over the frequency range 0 to 100 Hz are approximately zero (Fig 3.4). Because the magnitude of the eigenvalue is essentially zero, the cross-sectional state variables at the right side of the bay are also essentially zero ($Y_r = \xi Y_l$). This indicates that the wave dies out so quickly that it can be considered to be confined to a

single bay. This type of localized, quickly decaying near-field wave is also known as an evanescent wave. An evanescent wave will form only at the truss boundaries or at some discontinuity along the length of the beam. The zero phase of this wave also indicates that it does not propagate to the adjacent bay and that its wavelength approaches infinity. So throughout the given frequency range, this wave is in a stop band.

The magnitude of the eigenvalue of the second wave mode is approximately unity throughout the bandwidth (Fig 3.4), indicating that the wave does not attenuate throughout the frequency range. The non-zero phase indicates that the wave does propagate to the adjacent bays. For example, at 20 Hz the wave has a phase of -15° which indicates that the response of two adjacent bays in this mode at this frequency will be 15° out of phase. With this phase, Eqn 3.8 indicates that one wavelength of this wave mode will be 24 bays. As a function of frequency, the increasing phase value leads to decreasing wavelength.

The third mode is shown in Fig 3.5. Like the evanescent mode, this mode also has zero phase (non-propagating) and does have attenuation. However, the attenuation is not as pronounced as with the evanescent mode. In the frequency range shown, the lowest value of $|\xi|$ is about 0.8. After traversing many bays, this attenuation factor will eventually 'amortize' the wave, and as such, the wave is considered to be in a stop band.

As indicated by the $|\xi|$ value of unity, the fourth wave mode is in a pass band throughout the frequency range. Its small but increasing phase value implies the wavelength of this mode decreases with frequency.

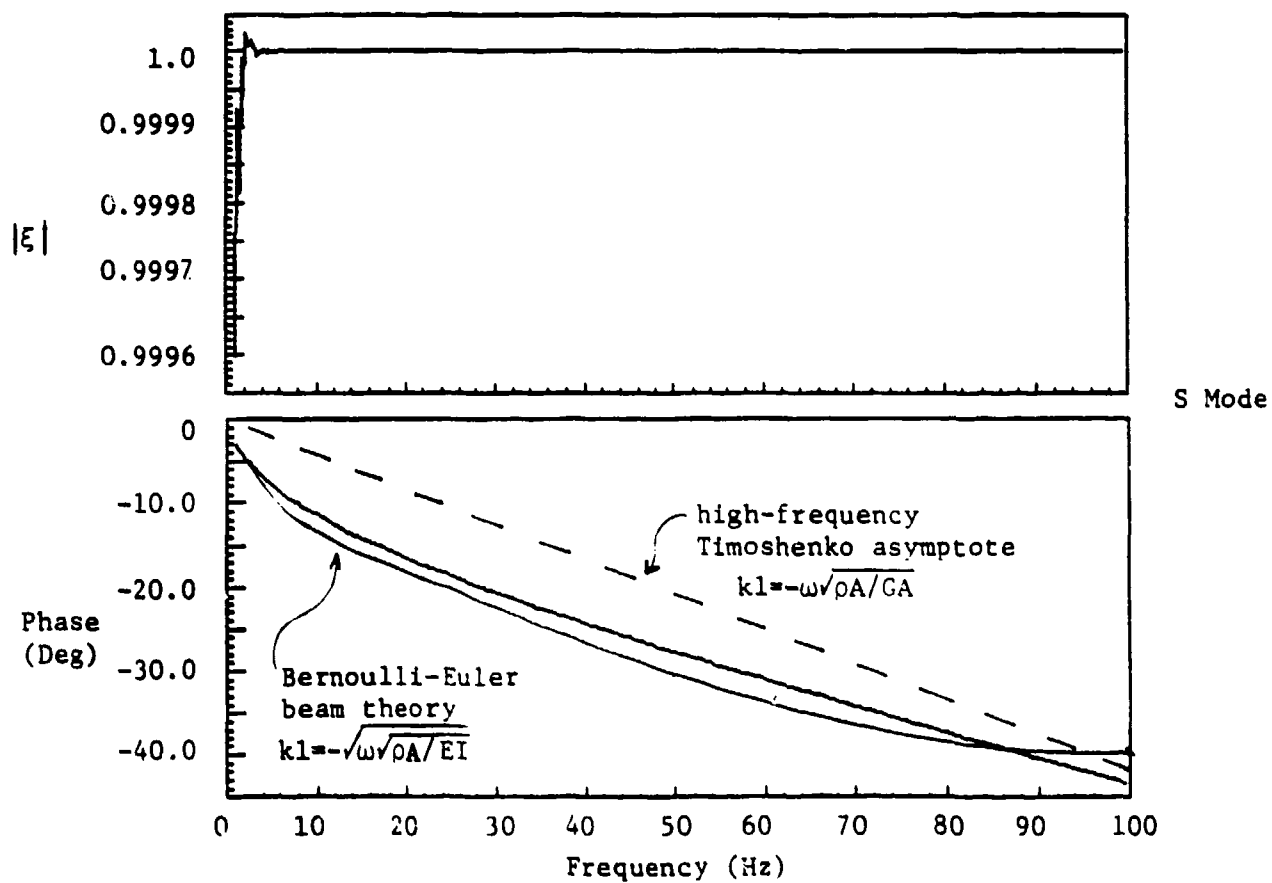
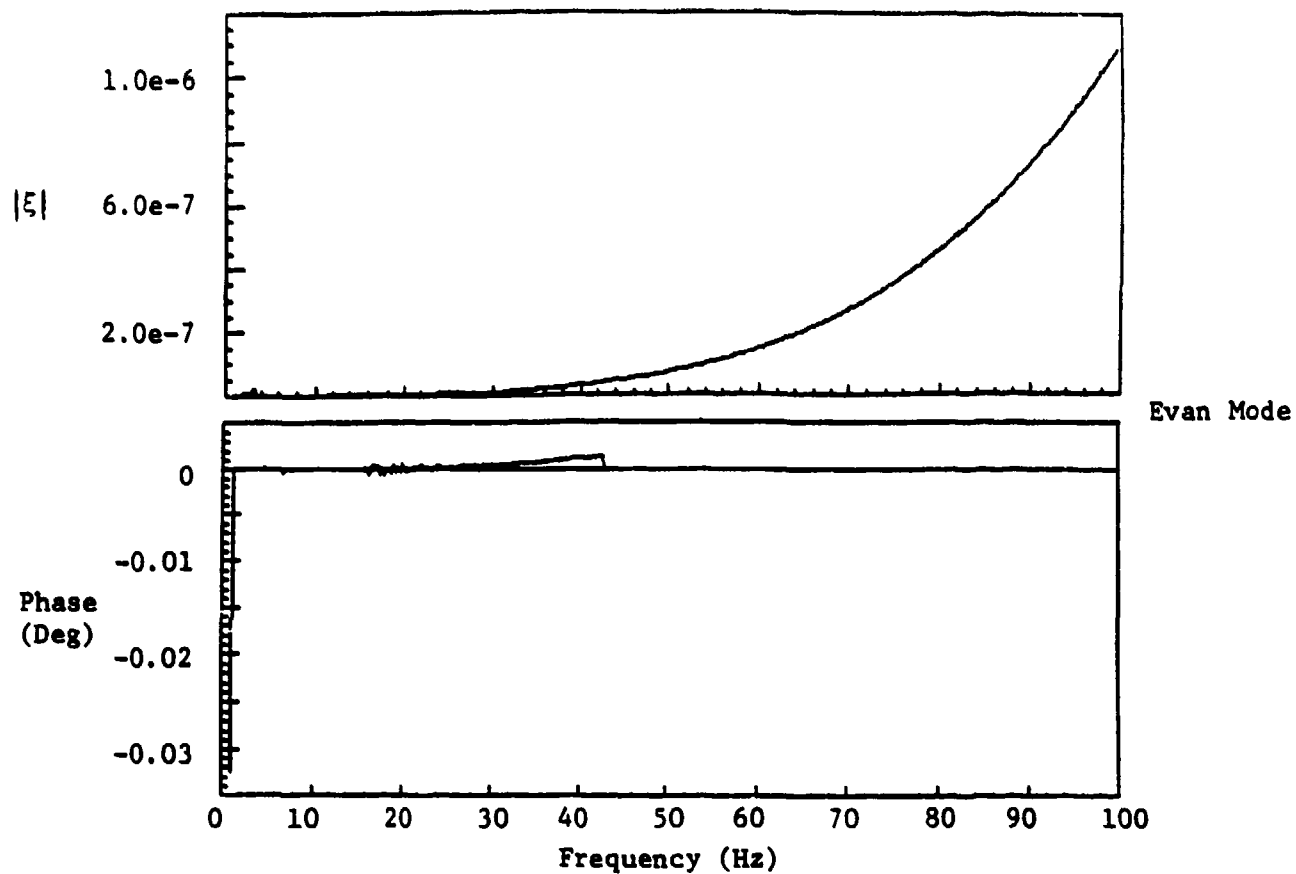
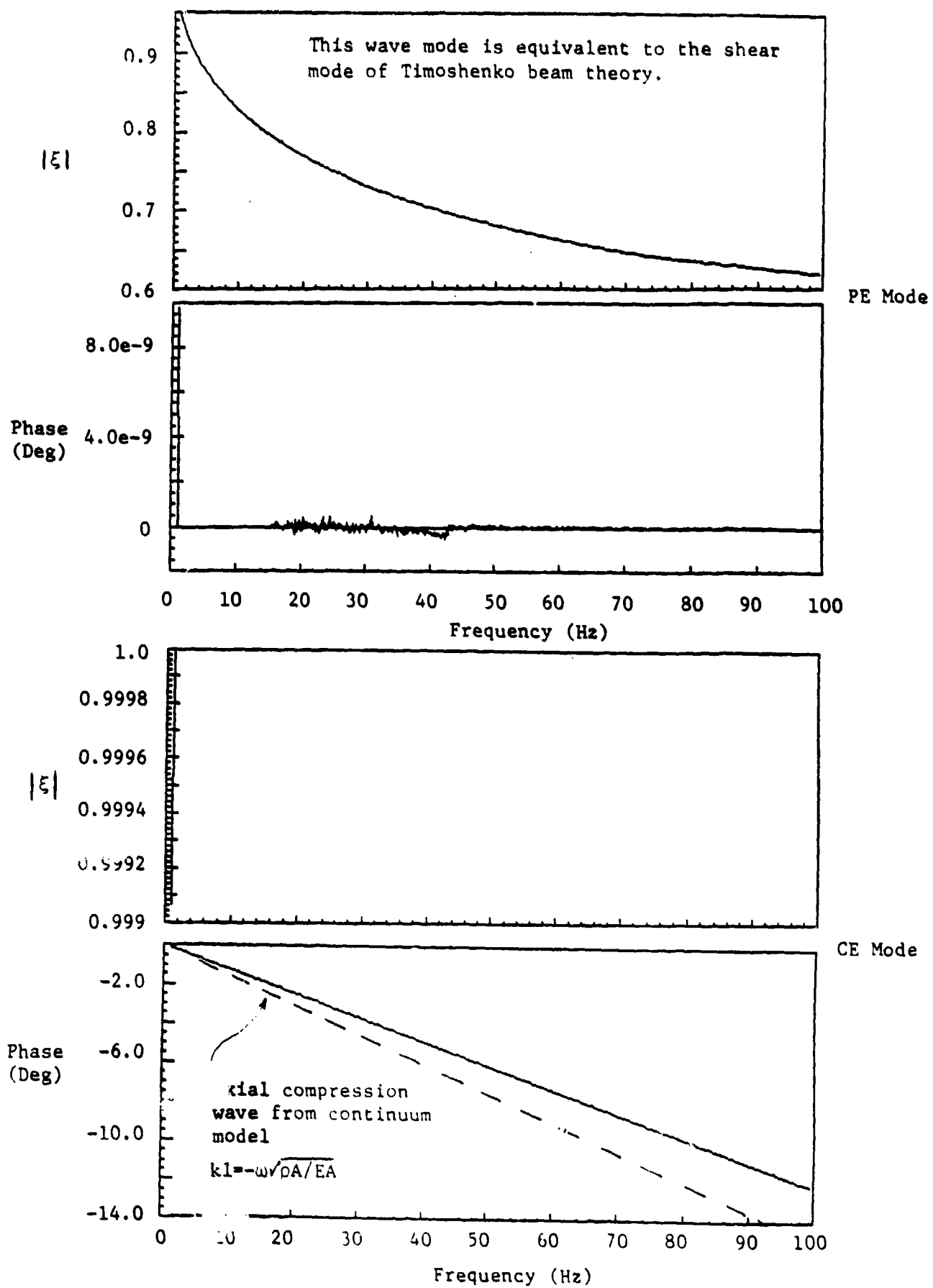


Figure 3.4 - Dispersion Curves for the Evanescent and S Modes (Pinned Rod Truss)



It should be noted that for any given frequency, the response of the truss is a superposition of all eight wave modes at that frequency.

Eigenvectors of the Four Right-Going Wave Modes

The eigenvectors, v , of the transfer matrix can be used to generate plots of the wave modes. For the $[8 \times 8]$ pinned rod truss, the eigenvector for a mode at a given frequency is a $[1 \times 8]$ matrix. This matrix contains values of deflection from the original node locations as well as the forces on these nodes.

$$v_r = \begin{bmatrix} U \\ \dots \\ F \end{bmatrix} \quad (3.8)$$

where

$$U = \begin{bmatrix} U_{1x} \\ U_{1y} \\ U_{2x} \\ U_{2y} \end{bmatrix} \quad F = \begin{bmatrix} F_{1x} \\ F_{1y} \\ F_{2x} \\ F_{2y} \end{bmatrix} \quad (3.9)$$

The response at the right side of any bay can be obtained by

$$v_{R_n} = \xi_i v_{L_{n-1}} \quad (3.10)$$

where n is the bay number and i is the number of the desired mode. Once the response of the right and left sides of the bay are known, the response of the internal nodes can be obtained by Egn (2.17)

$$U_i = -D_{ii}^{-1} (D_{iL} U_L + D_{iR} U_R) \quad (3.11)$$

The response of the right, left, and internal nodes of each bay were then 'propagated rightward' (by multiplication by ξ_i^n) and were obtained for as many bays as was needed to show one wavelength of a wave mode.

While plotting the wave modes, only the real component of the complex eigenvector was used. This corresponds to taking a 'snapshot' of the response.

Because only translational degrees of freedom were included in the finite element analysis, the deformed truss was plotted as simply linear connection of the deformed nodes. A scaling factor multiplied the eigenvectors in order to accentuate the displacement from the undeformed truss. Unless otherwise noted, the maximum displacement plotted was equivalent to 80% of the length of a longeron.

The response of the evanescent mode is effectively confined to only one bay. The motion consists primarily of extension and compression of the vertical member, and changes little with frequency (Fig 3.6).

Fig 3.7 displays one wavelength of the second mode for 10, 30, 40, 50, 70, and 90 Hz. At 10 Hz, one wavelength is 33 bays long, while at 90 Hz, this drops to 10. For all these frequencies, the global sinusoidal displacement dominates the mode. Thus it is labeled the 'S' mode. At 10 Hz the members exhibit very little extension or compression. But at 90 Hz, there

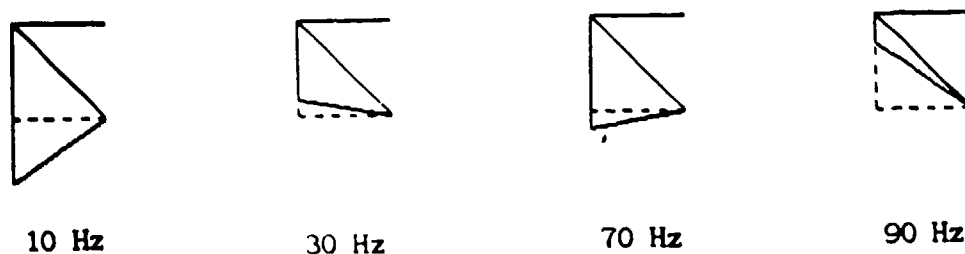


Figure 3.6 - First Bay of the Evanescent Mode as a Function of Frequency (Pinned Beam Truss)

is obvious extension and compression in the members do to the fact that the 's' shape must cycle in only 10 bays, while at 10 Hz, there are 33 bays in which to do so.

Mode three will be labeled the 'pseudo-evanescent' (PE mode) mode because, like the evanescent mode, mode three is attenuated and requires an almost infinite number of bays to exhibit one wavelength. The difference in these two modes, however, is that the PE mode exhibits far less attenuation than does the evanescent mode. In fact, the state vector is not completely diminished for several bays (Fig 3.8).

The most outstanding feature of the fourth mode is the compression/extension along the longitudinal direction of the truss at low frequencies. For this reason it has been dubbed the 'CE' mode. At 10 Hz, one wavelength requires 297 bays to observe. Fig 3.9 shows the first few bays of this mode as a function of frequency. Also shown is one complete wavelength of the CE mode at 90 Hz.

Comparison to Continuum Models

The eigenvectors of the S and CE modes exhibit displacements similar to a beam in bending and a rod in axial compression, respectively. These modes can thus be compared to results obtained from continuum models of the same truss. Mills in [M-3] has developed continuum models for the same truss as analysed in this work. Bending is modeled by Timoshenko beam theory, compression-extension by simple rod theory. Mills' equivalent values are: axial stiffness $EA = 8.7220 \times 10^6$ lb, bending stiffness $EI = 6.5960 \times 10^9$ lb-in², shear stiffness $GA =$

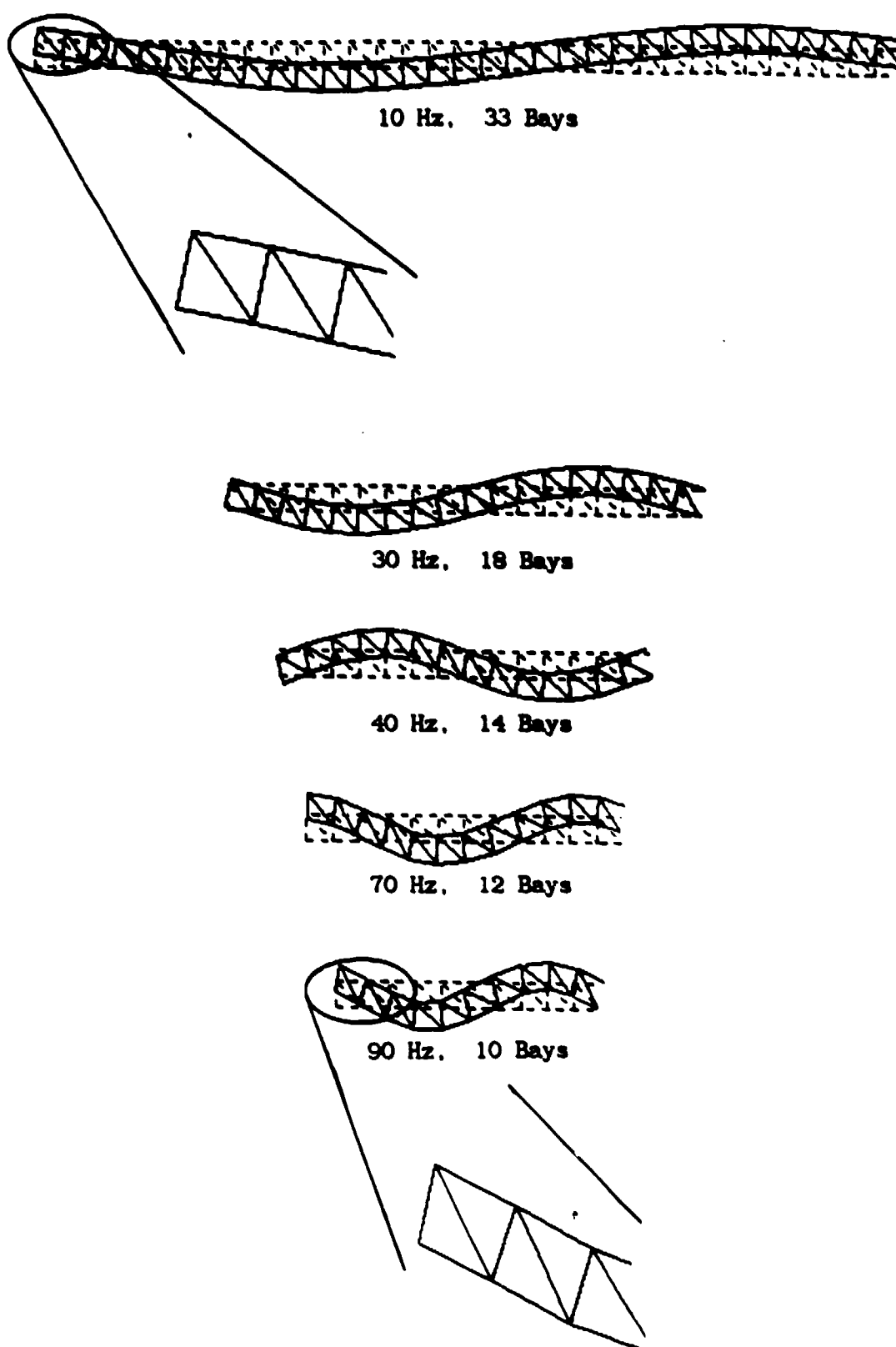


Figure 3.7 - One Wavelength of the S Mode as a Function of Frequency (Pinned Rod Truss)



10 Hz (24 of ∞ Bays)



40 Hz (24 of ∞ Bays)



90 Hz (24 of ∞ Bays)

Figure 3.8 - First Twenty-Four Bays of the PE Mode as a Function of Frequency (Pinned Rod Truss)



10 Hz, 24 of 297 Bays



40 Hz, 24 of 60 Bays



90 Hz, 34 of 34 Bays

Figure 3.9 - The CE Mode as a Function of Frequency (Pinned Beam Truss)

1.0693×10^6 lb, mass per length $\rho A = 4.8627 \times 10^{-4}$ lb-s²/in², and inertia per length $\rho I = 0.19438$ lb-s². Figure 3.4 shows a comparison of the computed results with the predictions of Bernoulli-Euler beam theory (valid for low frequencies), and the high-frequency asymptotic behavior of the bending model of Timoshenko beam theory. The CE mode of Fig 3.5 is compared to an axial compression wave from the continuum model. It can be seen that the results obtained from the transfer matrix method are in close agreement with those of continuum models of the same truss.

The PE mode (Fig 3.5) can be viewed as a Timoshenko shear mode. This wave mode will not propagate at frequencies below the cut-off frequency $\omega = \sqrt{GA/\rho I}$, in this case 365 Hz. The behavior of the PE mode is thus consistent with the Timoshenko shear mode.

The evanescent mode has no equivalent analogue in the continuum model, and appears to be entirely an artifact of the truss modeling approach.

3.4 Wave Propagation in a Uniform Two-Dimensional Pinned-Joint Truss with Beam Members

A more realistic representation of the high frequency dynamics of a truss structure can be made if the elements which comprise the structure are given bending stiffness. As such, the second truss structure studied was the same two-dimensional uniform beam truss as in Section 3.3, but with members modelled as beams. The beam elements were connected by pinned joints. A finite element program was developed to determine the mass and stiffness matrices of the bay. Each member of the truss now has two translational and one rotational DOF at each end. Care must be taken to ensure that differences in displacement and force coordinate definitions between the finite element analysis and those of the transfer matrix method are taken into account (Sect 2.3).

For the pinned beam truss, there are 16 translational DOF and 12 rotational DOF in each bay. This produces a $[28 \times 28]$ dynamic stiffness matrix for the bay. The transfer matrix is still $[8 \times 8]$, since there are still only four coupling coordinates between bays. Internal node displacements and beam rotations have been condensed into the transfer matrix (Section 2.4). Fig 3.10 defines the member rotations.

Because the members have bending stiffness, it is important to note the members' resonant bending frequencies. Fig 3.11 lists the first several natural frequencies of the longerons and diagonal truss members.

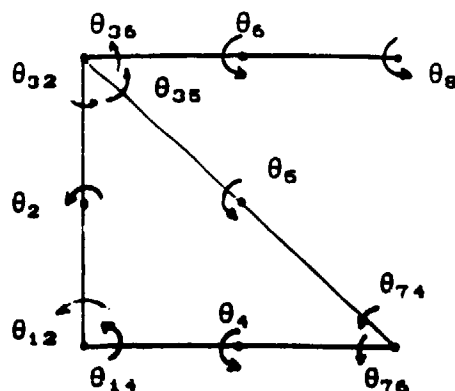


Figure 3.10 - Member Slopes, Pinned Beam Case

A MATRIXx user defined command file was used to produce the transfer matrix from the dynamic stiffness matrix and to extract its eigenvalues and eigenvectors. Fig 3.12-16 present dispersion curves for the four positive-going modes over a 0 - 170 Hz bandwidth. These figures can be directly compared to Fig 3-4 and 3-5 which are based upon a model which ignores member bending. Appendix A contains the propagation coefficient plots for these modes.

Longerons: $\omega_1 = 70.42 \text{ Hz}$ 1st pinned-pinned freq.
 $\omega_1 = 159.6 \text{ Hz}$ 1st clamped-clamped freq.

Diagonals: $\omega_1 = 35.2 \text{ Hz}$ 1st pinned-pinned freq
 $\omega_2 = 79.8 \text{ Hz}$ 1st clamped-clamped freq.
 $\omega_3 = 140.8 \text{ Hz}$ 2nd pinned-pinned freq.

with $EI = 2.0263E6 \text{ lb in}^2$ $L_{\text{LONG}} = 55.0 \text{ in}$
 $m = 1.016E-4 \text{ slug/in}$ $L_{\text{DIAG}} = 55.0 \sqrt{2} \text{ in}$

Figure 3.11 - Pinned-Pinned and Clamped-Clamped Bending Resonances for Truss Longerons and Diagonals

The wave modes were then plotted using a cubic spline routine. A scale factor was used to accentuate the displacements and rotations of the members in order to make the deformations visible. Unless otherwise noted, the scale factor was chosen such that the largest displacement was 80% of a longeron length or the largest slope (relative to the undeformed members) was 45° , whichever occurred first.

Eigenvalues and Eigenvectors of the Evanescent Wave Mode

The first mode examined was very similar to the evanescent mode of Section 3.3. The wave is in a stop band throughout almost all of the frequency range (Fig 3.12).

The difference between the rod truss and beam truss evanescent modes occurs in a sharp spike in $|\xi|$ and ϕ at approximately 70 Hz. At this frequency, the attenuation constant becomes non-zero, and there is a non-zero phase, indicating that the evanescent mode actually propagates. As noted in Fig 3.11, 70 Hz corresponds to the 1st pinned-pinned frequency of the longeron members. Fig 3.13 shows the first bay (of approximately infinite bays for a wavelength) of the evanescent wave mode as a function of frequency.

The difference between the beam truss and the rod truss eigenvector plots (Fig 3.6) is that in the beam truss case, the wave mode consists not only of extension and compression of the members but also bending of the internal members. Starting at 30 Hz, the diagonal member begins to show pinned-pinned motion. At 35 Hz, the lower longeron also starts to exhibit this motion, while the diagonal dies out. At 70 Hz, the propagating wave mode

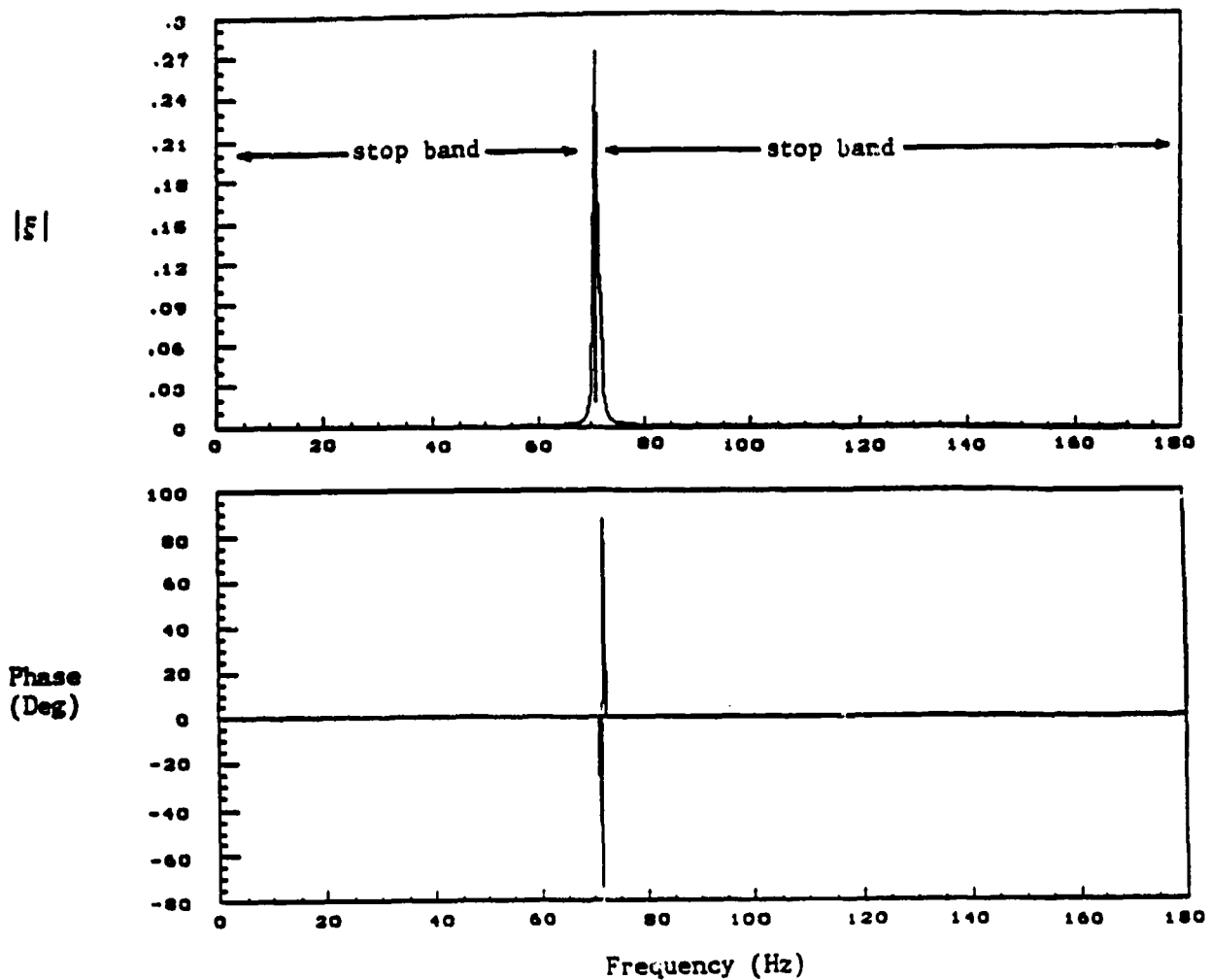


Figure 3.12 - Dispersion Curves for the Evanescent Mode
(Pinned Beam Truss)

involves pinned-pinned motion of the horizontal longerons. The evanescent mode starts to exhibit the second pinned-pinned motion together with lower longeron motion.

It is important to note that this internal motion was not present when the truss was modelled with rod members. Therefore, by using beam elements, the fidelity of the model has been increased.

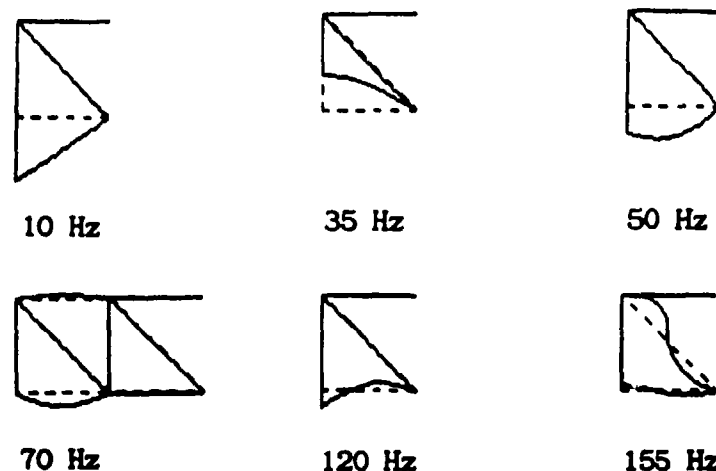


Figure 3.13 - One Bay of the Evanescent Mode as a Function of Frequency (Pinned Beam Truss)

Eigenvalues and Eigenvectors of the S Wave Mode

The magnitude and phase of the eigenvalues of the second wave mode are presented in Fig 3.14. This should be compared to Fig 3.4, which represents the same wave mode, but for the pinned rod truss.

The general trends in $|\xi|$ and φ are the same for both the rod and beam truss cases until 35 Hz. Because of this initial similarity, this mode will be referred to as the 'S' mode. Both waves are unattenuated and propagating.

The eigenvectors of the transfer matrix were determined as described in preceeding sections. Fig 3.15 depicts one wavelength of the S mode while it is in its initial pass band.

Like the S mode of the rod truss, the initial mode shape is that of a global 'S'. But whereas in the rod truss the global 'S' persisted as the frequency increased, in the beam truss the global 'S' dies out as the frequency is increased. At 10 Hz, one

|E|

Phase
(Deg)

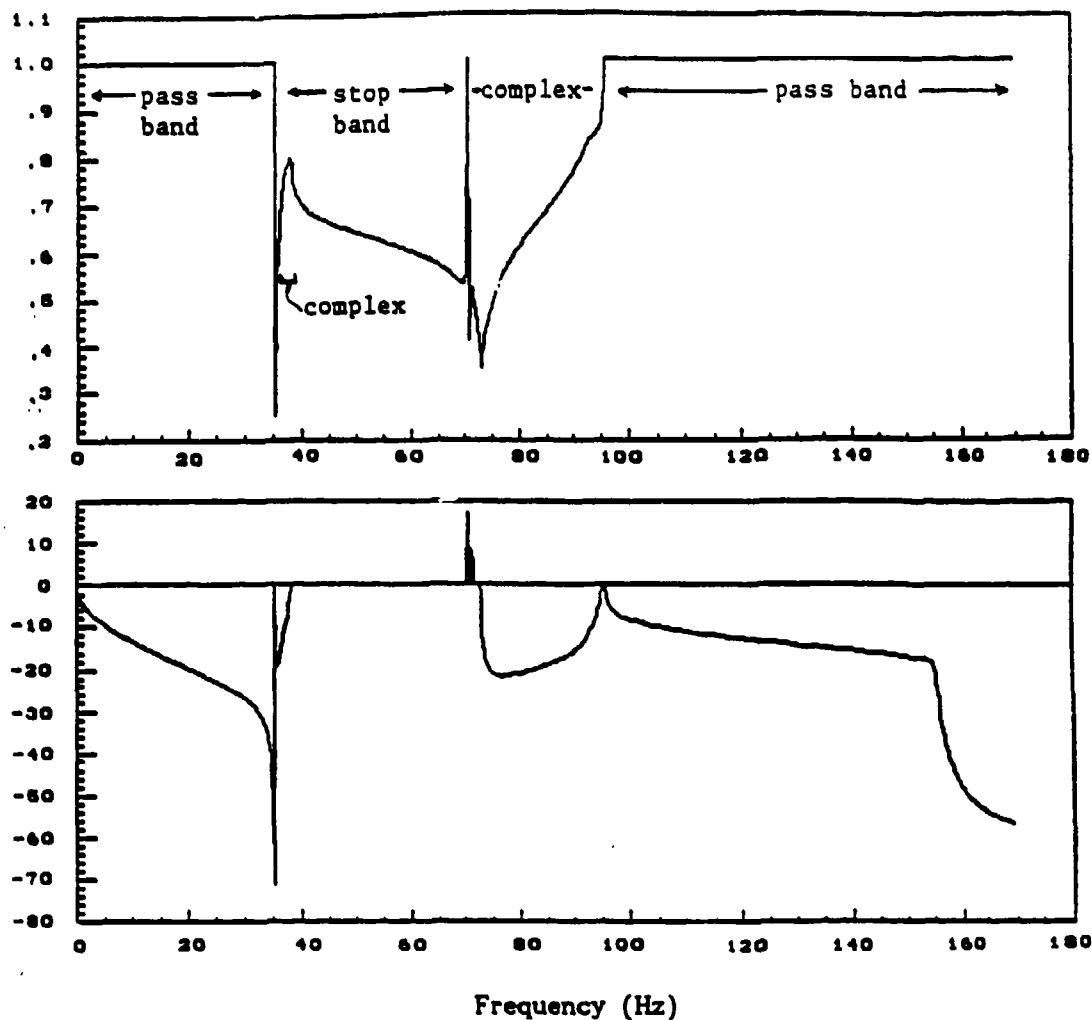


Figure 3.14 - Dispersion Curves for the S Mode as a Function of Frequency (Pinned Beam Truss)

wavelength simultaneously occupies 33 bays, and the members are essentially straight. But by 20 Hz, the diagonals start to exhibit their first pinned-pinned resonance, their deflection becoming maximum at 35 Hz. The direction of diagonal bending alternates every quarter wavelength at 20 Hz, while at 30 Hz, it alternates every half wavelength. By 35 Hz the global 'S' has essentially disappeared.

After 35 Hz, the rod and beam truss 'S' modes are not similar. At 35 Hz, the diagonal members of the truss are in their



10 Hz, 28 Bays



20 Hz, 19 Bays



30 Hz, 14 Bays



35 Hz, 8 Bays

Figure 3.15 - One Wavelength of the S Mode
in the First Pass Band
(Pinned Beam Truss)

1st pinned-pinned resonance, after which the wave enters a stop band at 40 Hz. Apparently when the diagonals resonate, energy becomes localized in this motion and does not propagate along the beam.

At 35 Hz the wave enters a region where it exhibits properties of a complex mode. In this region the wave both propagates and attenuates. The complex mode region ends at 39 Hz.

From 40 - 70 Hz the wave enters a classic stop band. Here the phase is near zero, implying that all the elements of adjacent bays move in phase causing the wavelength of the wave to approach infinity. The wave exists simultaneously in a near infinite number of bays and does not propagate. The state vector from one bay to

the next is however decreased. The first ten bays of the truss for 40, 50, 60, and 70 Hz are shown in Fig 3.16. As before, the diagonals dominate the dynamics for frequencies about 35 Hz, and give way to longeron movement about 70 Hz. Such modes, as with the evanescent modes, can only originate at the boundary of the structure or at some discontinuity along the length of the structure.

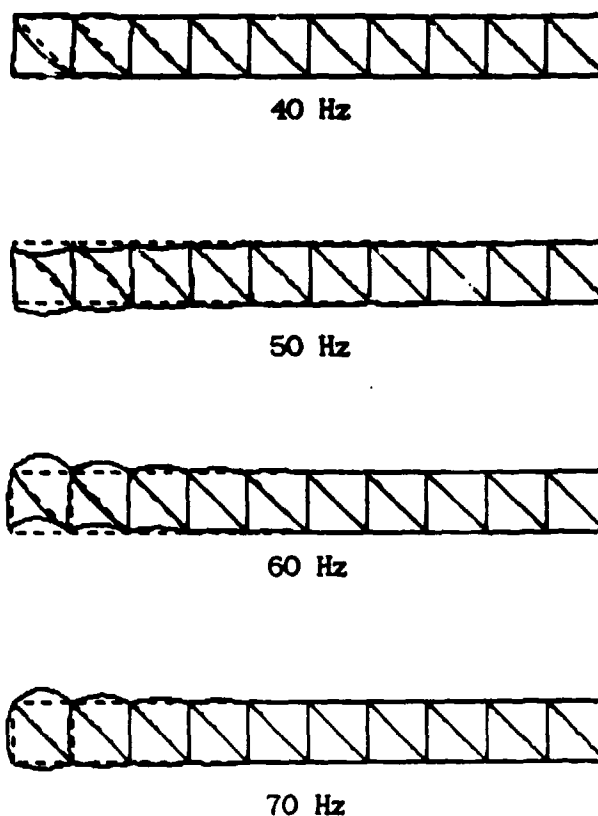


Figure 3.16 - First Ten Bays of the S Mode in the First Stop Band (Pinned Beam Truss)

As the 1st pinned-pinned frequency of the longerons is reached, the wave enters a spike-like pass band (70 Hz). From 75 - 90 Hz the mode is complex and is in a stop band. The mode shapes in this frequency range appear similar to those in the preceeding stop band. However, because of the non-zero phase

difference between bays in this region, a wavelength now occupies a finite number of bays. As can be seen in Fig 3.17 (the scaling has been increased to excentuate displacements), although the wavelength is finite, the mode does not appear to repeat after undergoing 360° of phase change. The mode does repeat--the state vector is attenuated to such an extent after one wavelength that the wave does not appear to repeat.

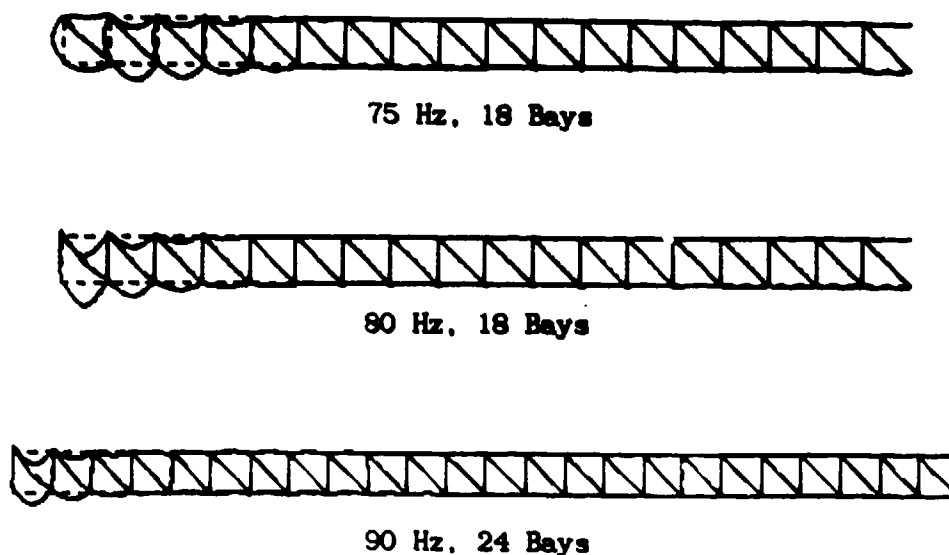


Figure 3.17 - One Wavelength of the Complex S Mode (Pinned Beam Truss)

The next pass band begins at 95 Hz and continues until the end of the bandwidth examined. One wavelength of the S mode for 100, 150, 155, and 165 Hz is shown in Fig 3.18. Global motion is not present. The second pinned-pinned resonance of the diagonal members starts to appear around 140 Hz. The wavelength drops off sharply near the first clamped-clamped resonance of the longerons (160 Hz). Although the first clamped-clamped frequency occurs at 160 Hz, the second diagonal pinned-pinned motion still dominates.

For the 0 - 165 Hz bandwidth, the S wave mode was in alternating pass and stop bands. Note that each of the pass and stop bands were separated by a complex mode region (complex modes are considered to be in stop bands).

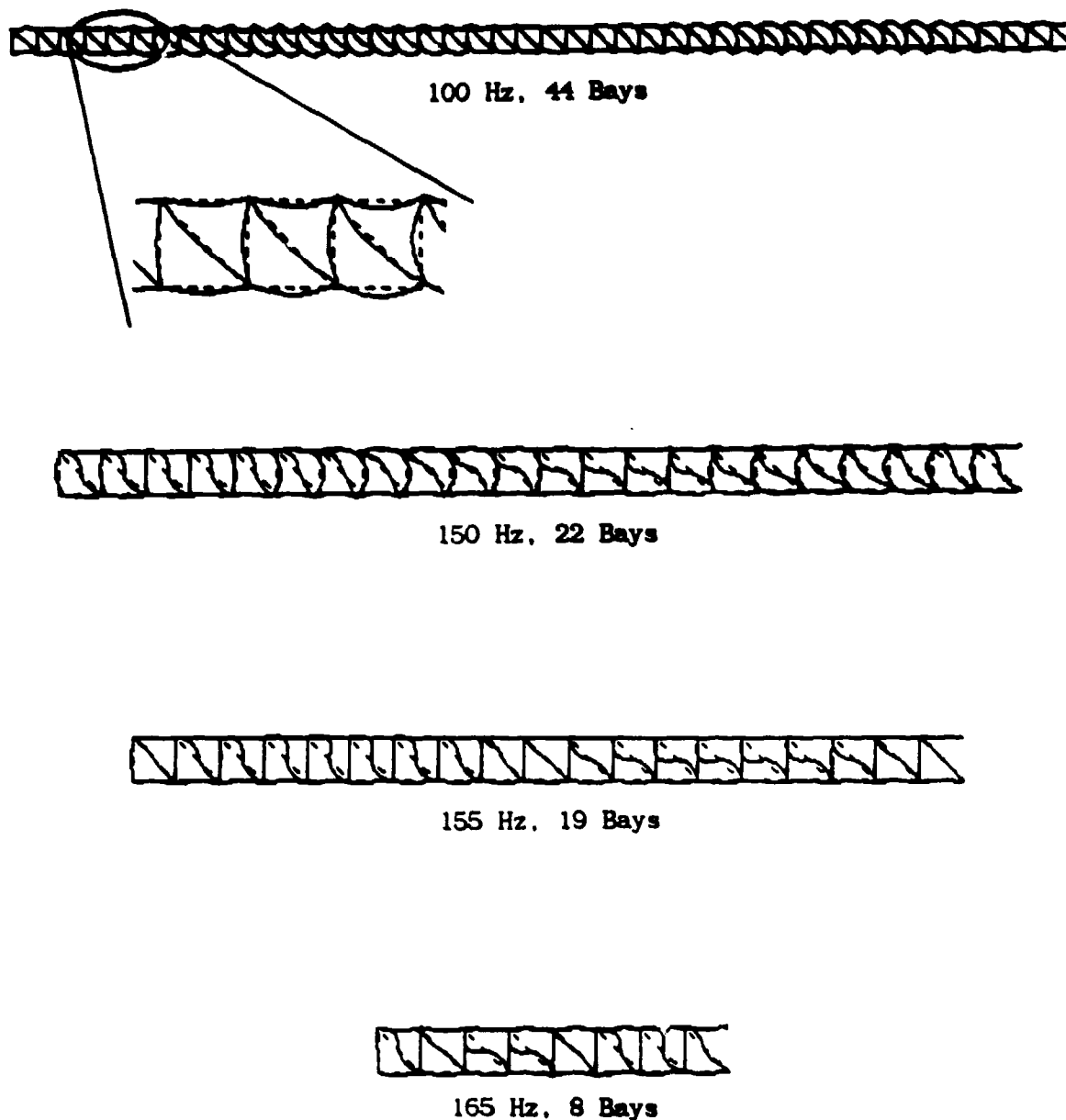


Figure 3.18 - One Wavelength of the S Mode in the Second Pass Band (Pinned Beam Truss)

Eigenvalues and Eigenvectors of the PE Wave Mode

Unlike the S mode which begins in a pass band, the third mode begins in a stop band (Fig 3.19). It has the same basic attenuation and phase as for the pinned rod truss PE mode (Fig 3.5) up to 35 Hz, the diagonals' first pinned-pinned resonance. Because of this initial similarity, this mode has been dubbed the PE mode. Like the S mode, the PE mode goes through alternating stop and pass bands, separated by stop bands in which the mode is complex. Until 35 Hz, the wavelength is approximately infinite.

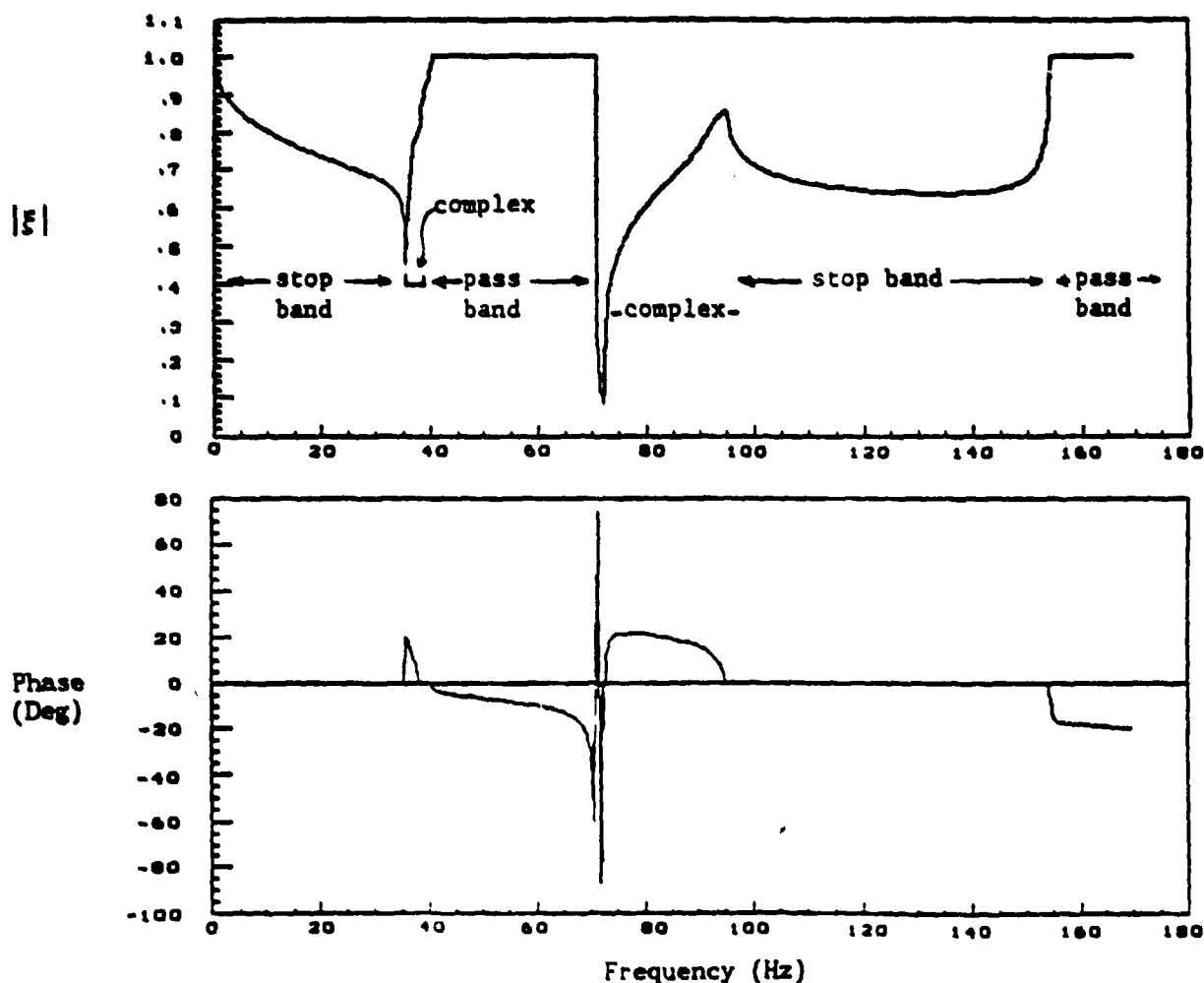


Figure 3.19 - Dispersion Curves for the PE Mode
(Pinned Beam Truss)

This mode, unlike the first stop band of the S mode, exhibits mostly global bending instead of local member bending (Fig 3.20). This should be expected being that global motion, not local member motion, dominates the dynamics of all modes at low frequencies.

The wave enters its first pass band at 40 Hz after becoming a complex mode for a range of 5 Hz. The first few bays of the PE mode are shown in Fig 3.21.

The complex mode shapes (range 75-95 Hz) are identical to those of the S mode, with the exception of phase angle sign. Complex modes are discussed more fully in Section 3.5.

At 95 Hz, the second stop band begins. As can be seen in Fig 3.22, the PE mode does not exhibit much global motion. Near 130 Hz the second pinned-pinned resonance of the diagonals appears in the truss plots.

The second pass band for the PE mode begins at 155 Hz. The PE mode of the second pass band is like that of the first except that now there is more movement in the horizontal longerons and the diagonals are in their second pinned-pinned resonance (Fig 3.23).

Eigenvalues and Eigenvectors of the CE Wave Mode

Once again, the $|\xi|$ and ϕ values for the rod truss and beam truss follow the same trend from 0-35 Hz (Fig 3.24). As with the CE mode in the pinned rod truss, the fourth mode in the pinned beam case also starts out with at low frequencies with the same compression/extension shape (Fig 3.25). It is therefore called the CE mode. But by 20 Hz, bending of the diagonals and vertical longerons can be seen. At 35 Hz, bending seems to be confined to



10 Hz. 10 of ∞ Bays



20 Hz. 10 of ∞ Bays



30 Hz. 10 of ∞ Bays



40 Hz. 10 of ∞ Bays

Figure 3.20 - First Ten Bays of the PE Mode in the First Stop Band (Pinned Beam Truss)



50 Hz. 15 of 53 Bays



65 Hz. 15 of 29 Bays

Figure 3.21 - PE Mode in the First Pass Band (Pinned Beam Truss)



100 Hz. 10 of ∞ Bays



130 Hz. 10 of ∞ Bays



150 Hz. 10 of ∞ Bays

Figure 3.22 - The PE Mode in the Second Stop Band
(Pinned Beam Truss)



155 Hz. 24 Bays



165 Hz. 20 Bays

Figure 3.23 - One Wavelength of the PE Mode in the
Second Pass Band (Pinned Beam Truss)

the diagonals. By 50 Hz, a global 's' shape appears as the horizontal longerons and diagonals are in bending. Only the horizontal longerons remain in bending by 65 Hz.

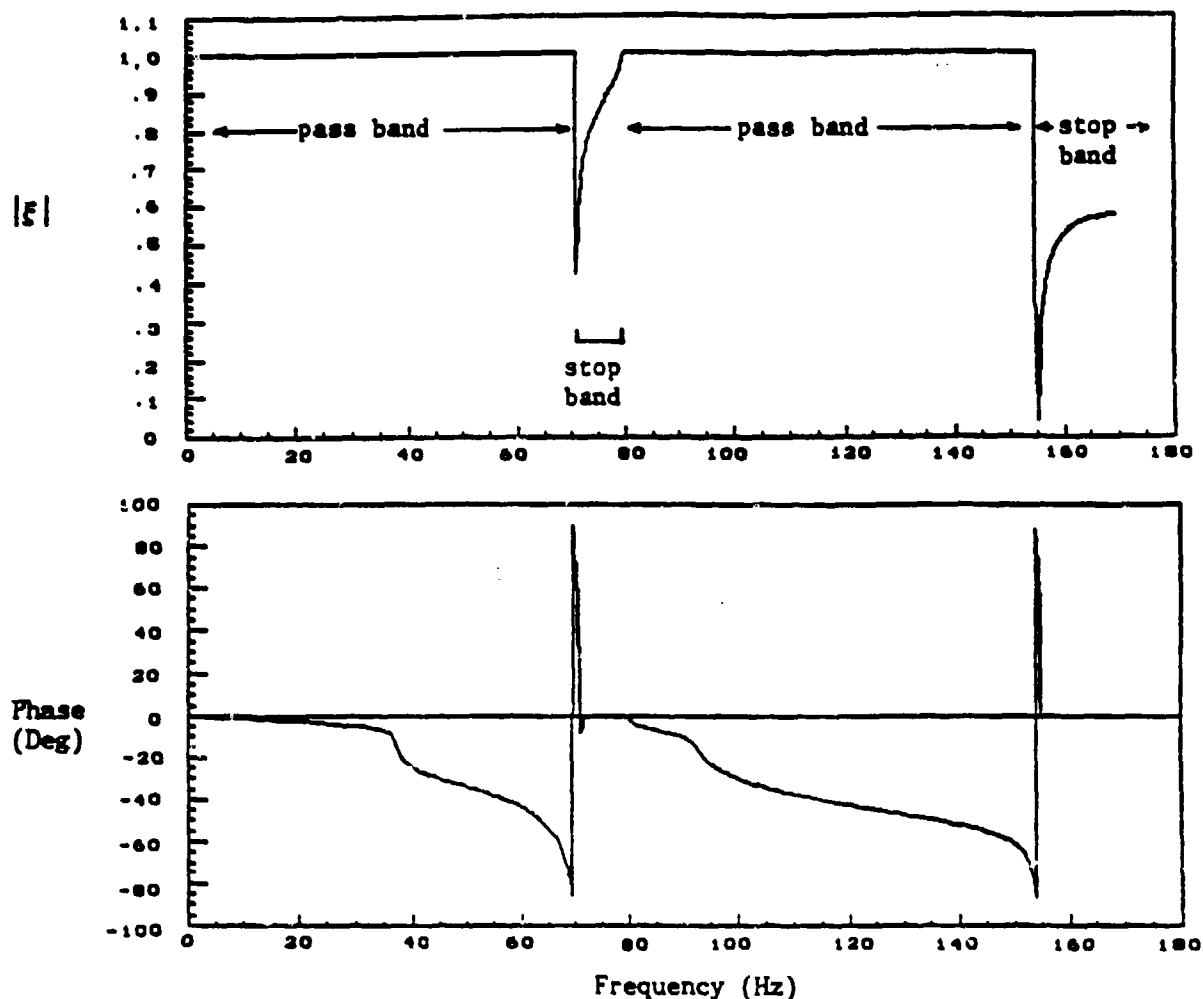


Figure 3.24 - Dispersion Curves for the CE Mode
(Pinned Beam Truss)

The CE mode is complex in a 1 Hz band starting at 70.8 Hz. and continues for 0.6Hz.

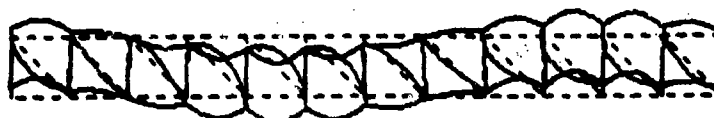
The first pass band is a small region between 72 and 80 Hz. Wavelengths in this region are of near infinite wavelength and their wave modes involve only motion of the vertical longerons.



20 Hz. 15 of 119 Bays



35 Hz. 15 of 50 Bays



50 Hz. 12 of 12 Bays



65 Hz. 8 of 8 Bays

Figure 3.25 - The CE Mode in the First Pass Band
(Pinned Beam Truss)



90 Hz. 15 of 35 Bays



120 Hz. 9 of 9 Bays



150 Hz. 7 of 7 Bays

Figure 3.26 - The CE Mode in the Second Pass Band
(Pinned Beam Truss)

The second pass band begins at 80 Hz and continues until 155 Hz. Initially the motion consists of longeron bending, but becomes second pinned-pinned diagonal bending by the end of the band (Fig 3.26).

And finally, the CE mode enters its second stop band at 155 Hz. The wavelengths in this band are near infinite and the motion consists of second pinned-pinned diagonal bending.

3.5 Complex Modes

For the pinned beam truss there were two frequency bands in which wave modes were complex--from 35 to 40 Hz and from 72 to 95 Hz. If the dispersion curves of the S and PE modes are plotted together, some interesting observations can be made (Fig 3.27).

Both modes are complex throughout the same bandwidths (35-40 Hz and 75-95 Hz). In addition, the magnitude of the eigenvalues are exactly the same. The two wave modes couple throughout these regions, producing the complex modes. The complex modes begin at the first pinned-pinned frequencies of the diagonals and longerons at a joining point. At the break-away points the modes once again take on separate character.

The frequency range between 70 and 85 Hz is full of complex modes (Fig 3.28). Within this range, there are three pairs of right-going complex modes. The S and CE modes couple for a very short band centered at 71.2 Hz. At 71 Hz even the evanescent mode forms a complex mode with the PE mode. But the longest coupling is between the S and PE modes. These two wave modes are complex from 72.5 to 95 Hz. Note that the coupling is triggered near the first pinned-pinned frequency of the longerons.

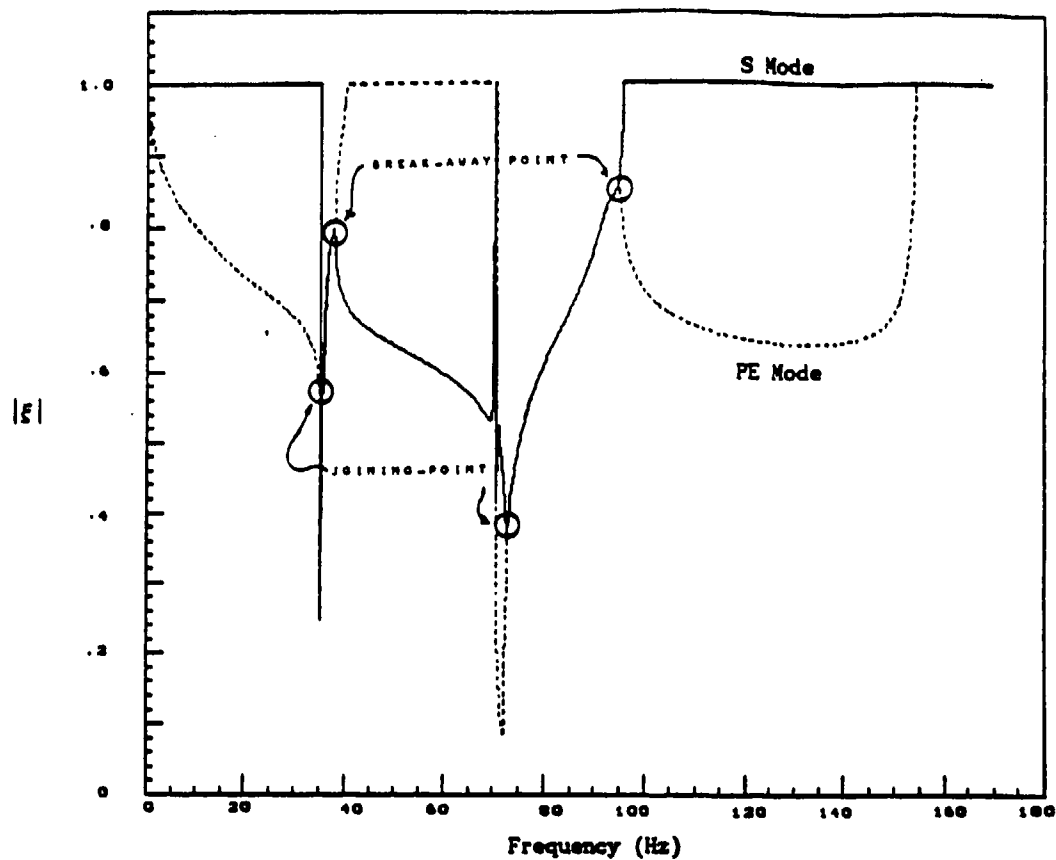


Figure 3.27 - Complex Mode Coupling Between the S and PE Modes

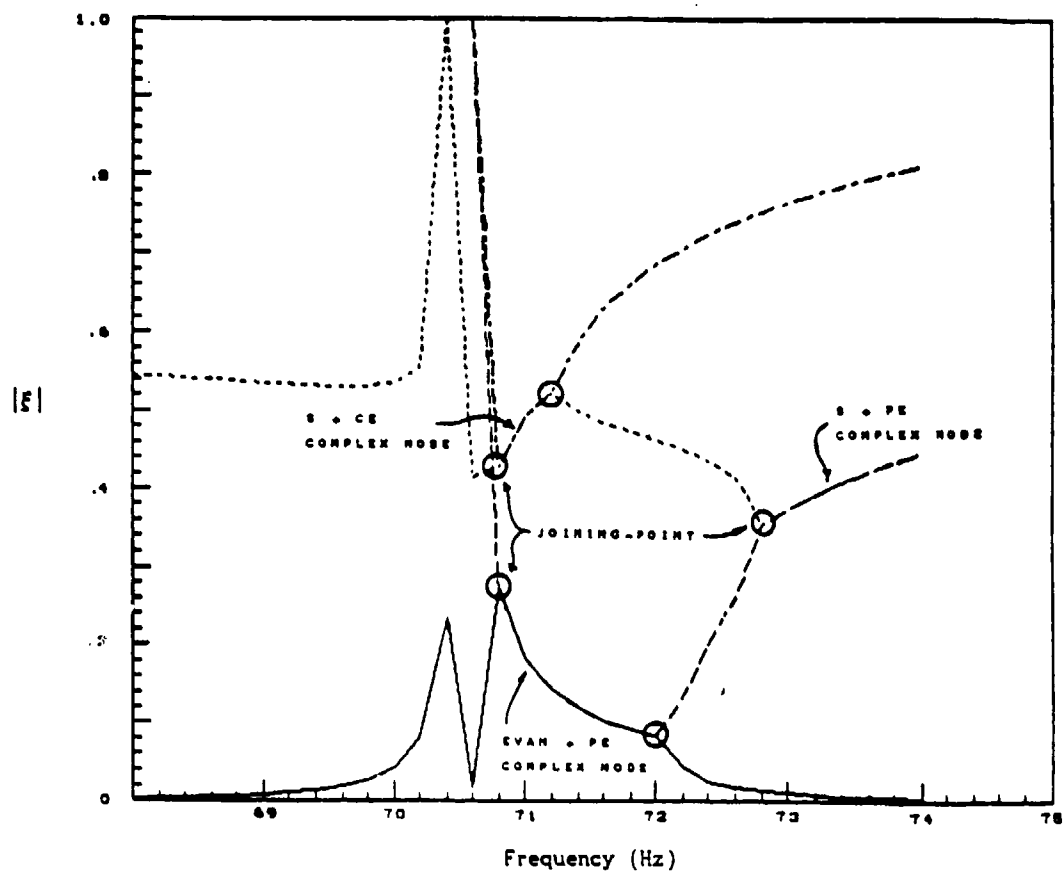


Figure 3.28 - Complex Mode Coupling About 70 Hz

It would appear then that a complex mode cannot exist alone. Complex modes are formed in pairs. In fact, when two wave modes couple to form complex modes, there also exist their left-going 'brother' modes, which are also complex. So when both right and left-going waves are considered, four (eight, twelve, etc.) complex modes must exist simultaneously in the truss. This can be visualized in the ξ -plane (Fig 3.29). For example, between 75 and 95 Hz the S and PE modes couple to form complex modes. The eigenvalues of the right-going complex modes (labeled with an 'r' subscript) are complex conjugate pairs as are their eigenvectors. The eigenvalues of the left-going complex modes ('l' subscript) lie outside the unit circle and also have complex conjugate eigenvalues and eigenvectors.

Discussion of power flow in complex modes as well as properties of their eigenvectors are presented in Sections 4.2 and 4.3.

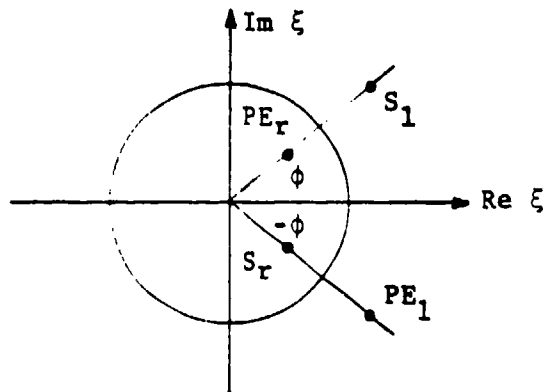


Figure 3.29 - Eigenvalues of Four Complex Wave Mode in the ξ Plane

Chapter 4 - Wave Mode Power Flow

4.1 Determination of Average Power Flow in a Wave Mode

In Chapter 3 it was shown that each wave mode has frequency bands in which there is propagation, bands in which there is no propagation, and bands in which there is both attenuation and propagation (the complex modes). Intuition might tell us that when a wave propagates, it transmits energy along the structure and when it does not propagate, it does not carry energy along the structure. But what about complex modes which share aspects of both propagating and attenuating waves? Do complex modes transmit energy along the structure? And if so, how is this possible if there is no damping in the system? Mead addressed this point in 1973 and found theoretically that there is no net power flow in these modes [M-2]. In order to gain some insight into this question, this chapter examines power flow in the wave modes of a pinned beam truss.

Instantaneous power is the product of the instantaneous velocity and force. While noting that these are vector quantities, this becomes,

$$P(t) = \mathbf{v}(t) \cdot \mathbf{f}(t) \quad (4.1)$$

where $\mathbf{v}(t) = V_M \cos(\omega t + \varphi_v) = \text{Re} (V e^{i\omega t}) \quad (4.2)$

$$V = V_M e^{i\varphi_v} \quad V_M = |V| \quad (4.3)$$

and, $f(t) = F_R \cos(\omega t + \varphi_r) = \text{Re} (F e^{i\omega t})$ (4.4)

$$F = F_R e^{i\varphi_r} \quad F_R = |F| \quad (4.5)$$

The instantaneous power flow can now be written as.

$$P(t) = \text{Re} (V e^{i\omega t}) \cdot \text{Re} (F e^{i\omega t}) \quad (4.6)$$

$$= \text{Re} (\dot{u} e^{i\omega t}) \cdot \text{Re} (F e^{i\omega t}) \quad (4.7)$$

$$= \text{Re} (i\omega u e^{i\omega t}) \cdot \text{Re} (F e^{i\omega t}) \quad (4.8)$$

which can be expanded to.

$$P(t) = \text{Re} [i\omega (u_R + iu_I) (\cos \omega t + i \sin \omega t)] \cdot \text{Re} [(F_R + iF_I) (\cos \omega t + i \sin \omega t)] \quad (4.9)$$

After multiplying and taking the dot product this becomes.

$$P(t) = \omega [-u_R \cdot F_R \sin \omega t \cos \omega t + u_R \cdot F_I \sin^2 \omega t + -u_I \cdot F_R \cos^2 \omega t + u_I \cdot F_I \sin \omega t \cos \omega t] \quad (4.10)$$

The average power flow over one period, $T=2\pi/\omega$, is defined as.

$$P_{AVG} = 1/T \int_0^T P(t) dt \quad (4.11)$$

After integrating Eqn 4.10 over one period we get.

$$P_{AVG} = 1/2 \omega (u_R \cdot F_I - u_I \cdot F_R) \quad (4.12)$$

This then gives us the average power flow for each wave mode. u and F are entries of the wave mode eigenvectors.

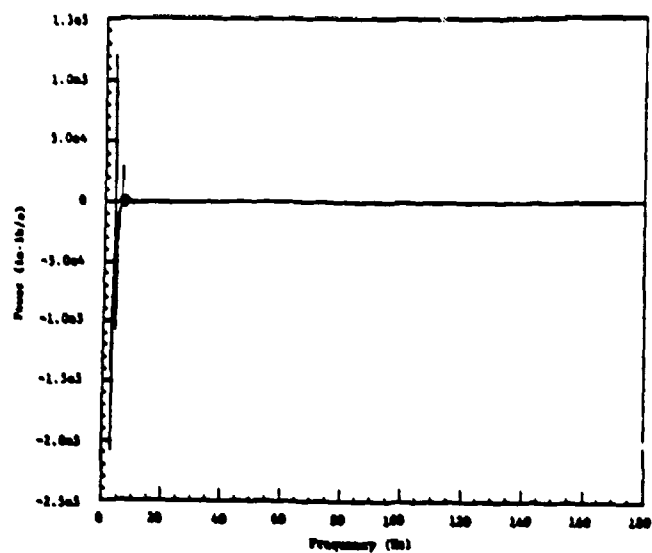
4.2 Wave Mode Power Flow

Power flow was calculated for the eight wave modes present in a pinned beam truss. The eigenvectors used in Eqn 4-12 were normalized so that the x-displacement of node one was unity.

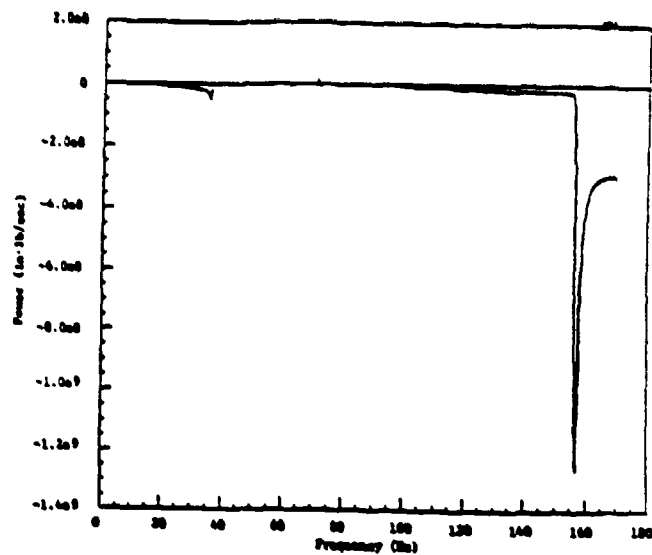
Figs 4.1 and 4.2 show plots of the power flow in the four right and left-going wave modes. The outstanding features of these curves are sharp spikes in power flow at member resonant frequencies. Notice that power flow in left and right-going 'brother' waves (i.e., PE left-going and PE right-going) is equal and opposite.

More detail can be seen when the magnitude of the power is plotted on a log scale (Figs 4.3 and 4.4). As expected, the S, PE, and CE modes show power flow in pass bands—power flow in each left and right-going brother wave pair being equal and opposite. No power flow occurs in stop bands. Complex mode regions of the S and PE modes show up as 'noisy' data on the plots. But as can be seen by data from the right-going complex mode pair in the 73-95 Hz bandwidth (Fig 4.5), the magnitude of the power flow in these complex modes is equal and opposite. Thus it would appear that the net power flow in a right-going (left-going) complex mode pair is zero. Mead, however, claims that the net power flow in a single complex mode is zero [M-2]. It is, therefore, uncertain whether the equal and opposite power flow shown in Fig 4.5 is actual or the result of numerical round-off.

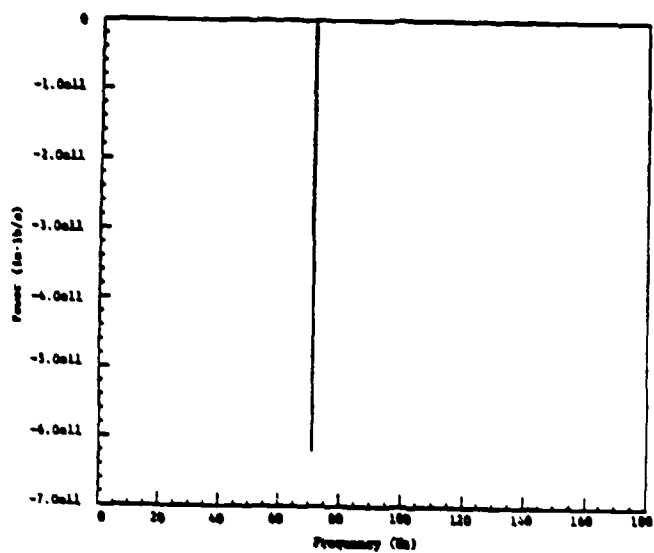
Power flow in the evanescent modes, however, is contrary to what one would expect. With the exception of a small pass band about 70 Hz, the evanescent modes are in a stop band throughout all of the bandwidth investigated. Because of this, one would



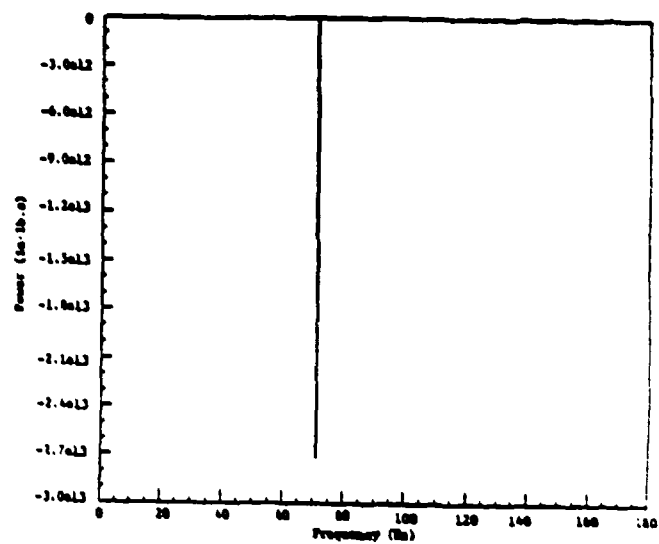
Evan Mode



S Mode

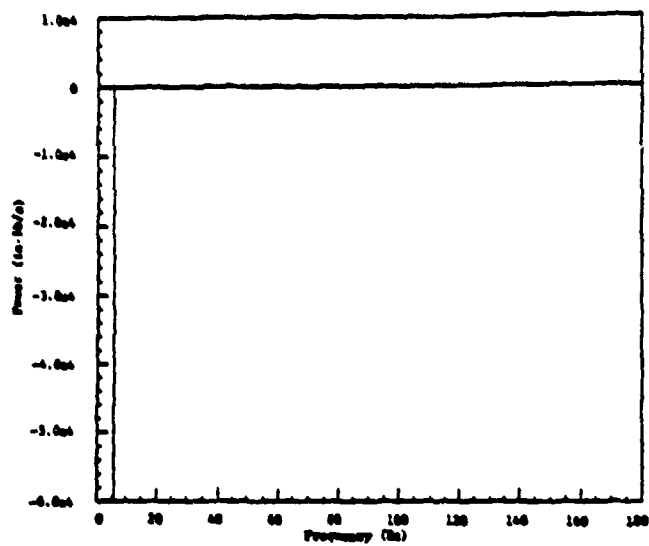


PE Mode

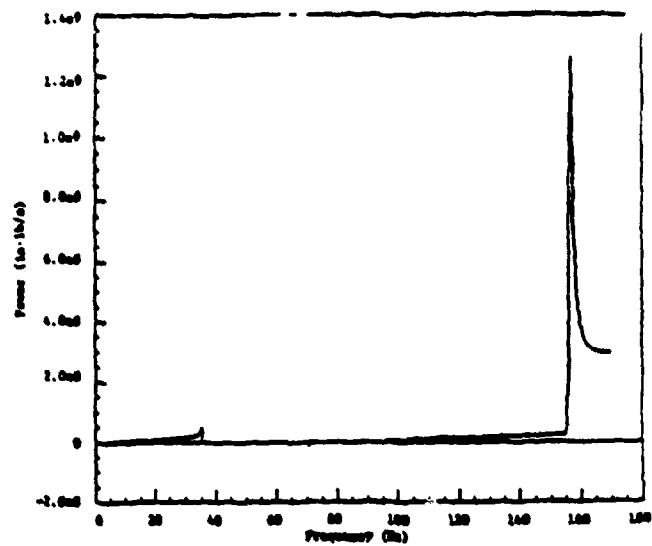


CE Mode

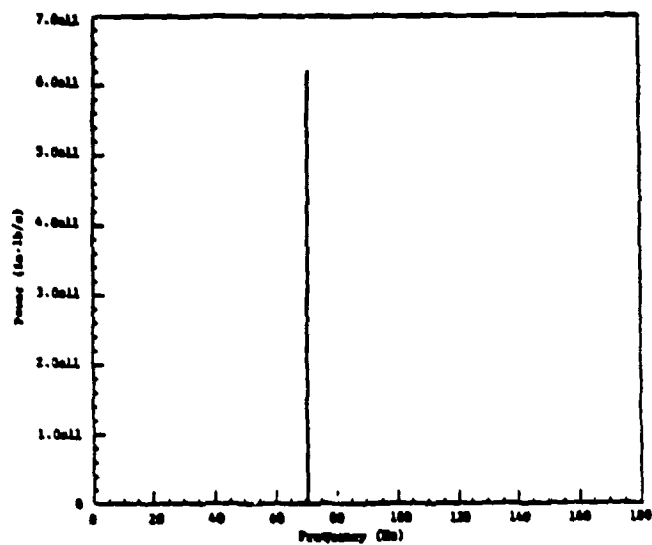
Figure 4.1 - Power Flow in the Right-Going Wave Modes



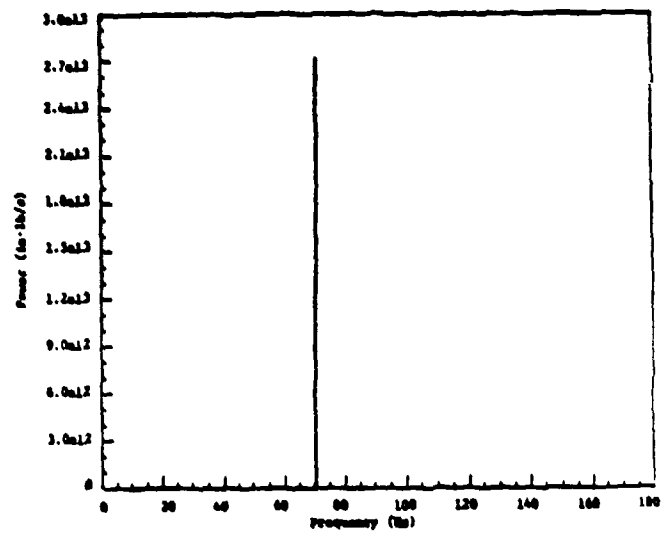
Even Mode



S Mode

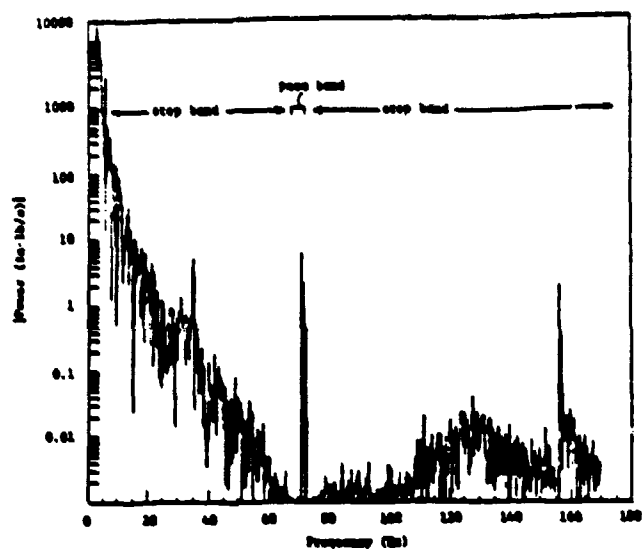


PE Mode

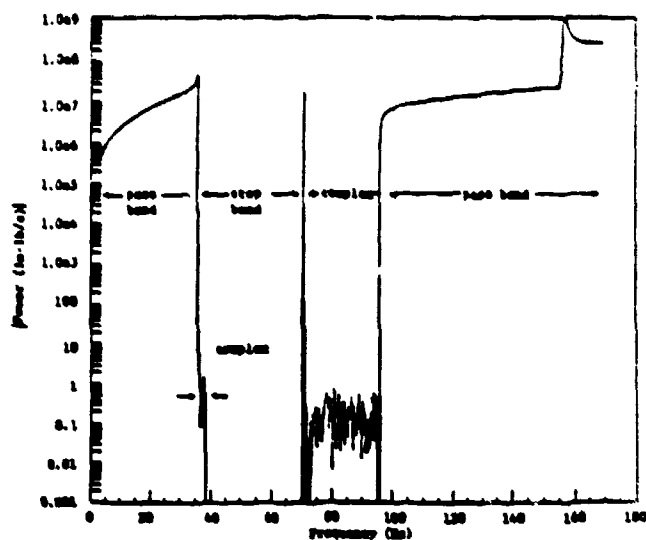


CE Mode

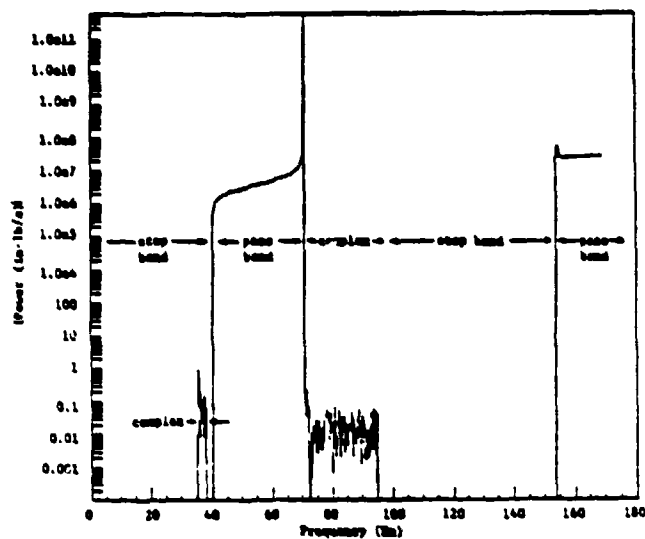
Figure 4.2 - Power Flow in the Left-Going Wave Modes



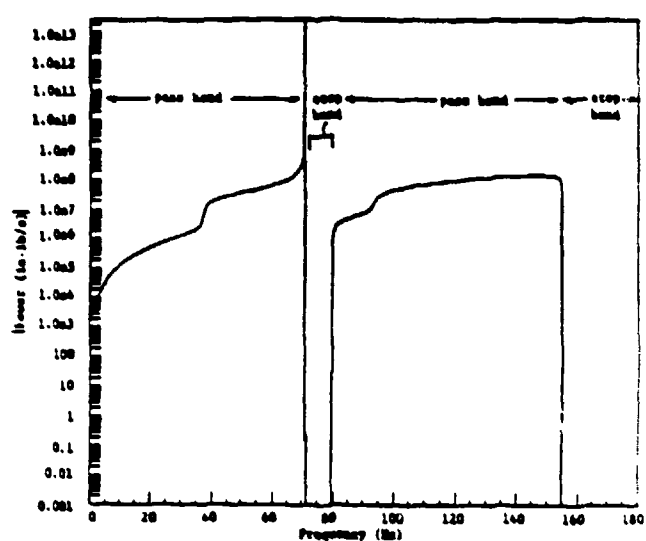
Evan Mode



S Mode

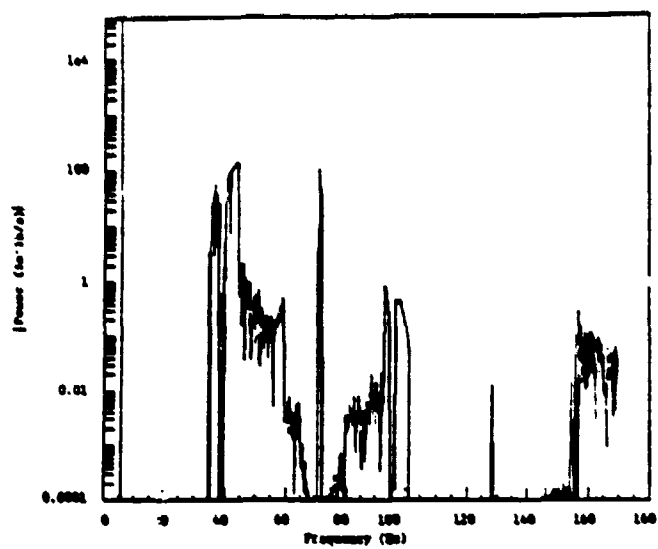


PE Mode

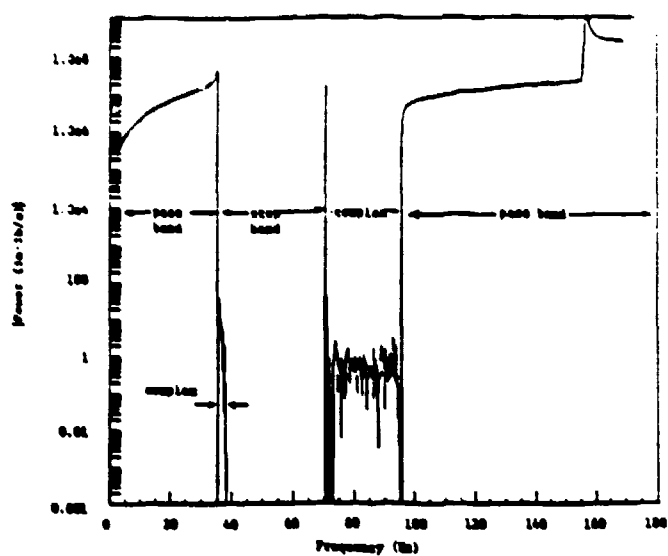


CE Mode

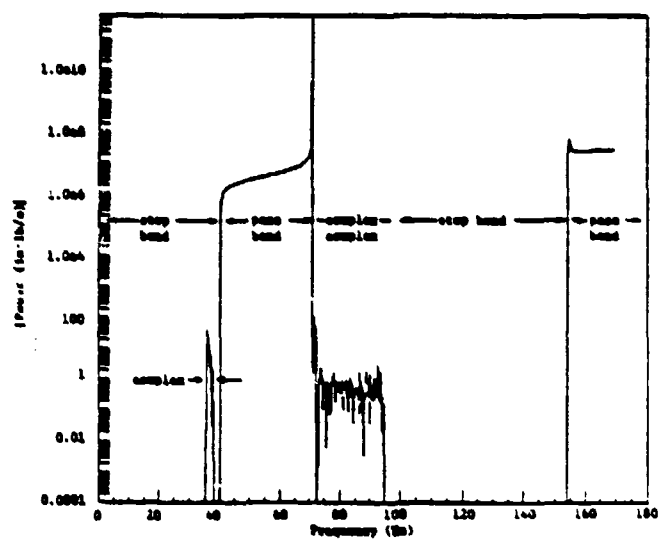
Figure 4.3 - Magnitude of Power Flow in the Right-Going Modes



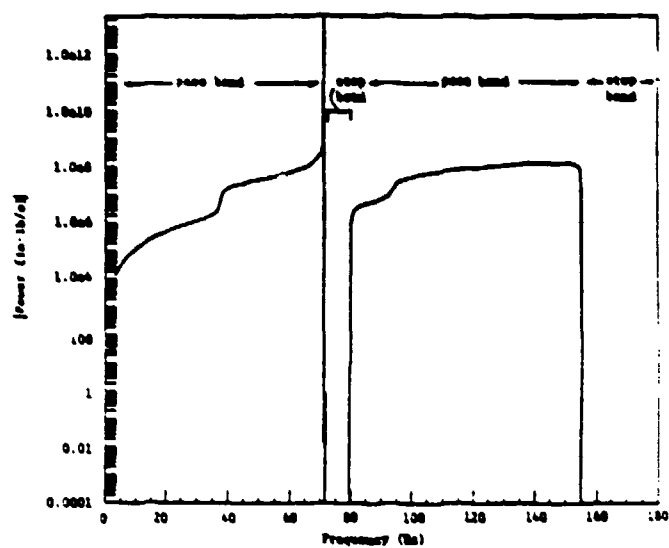
Evan Mode



S Mode



PE Mode



CE Mode

Figure 4.4 - Magnitude of Power Flow in the Left-Going Modes

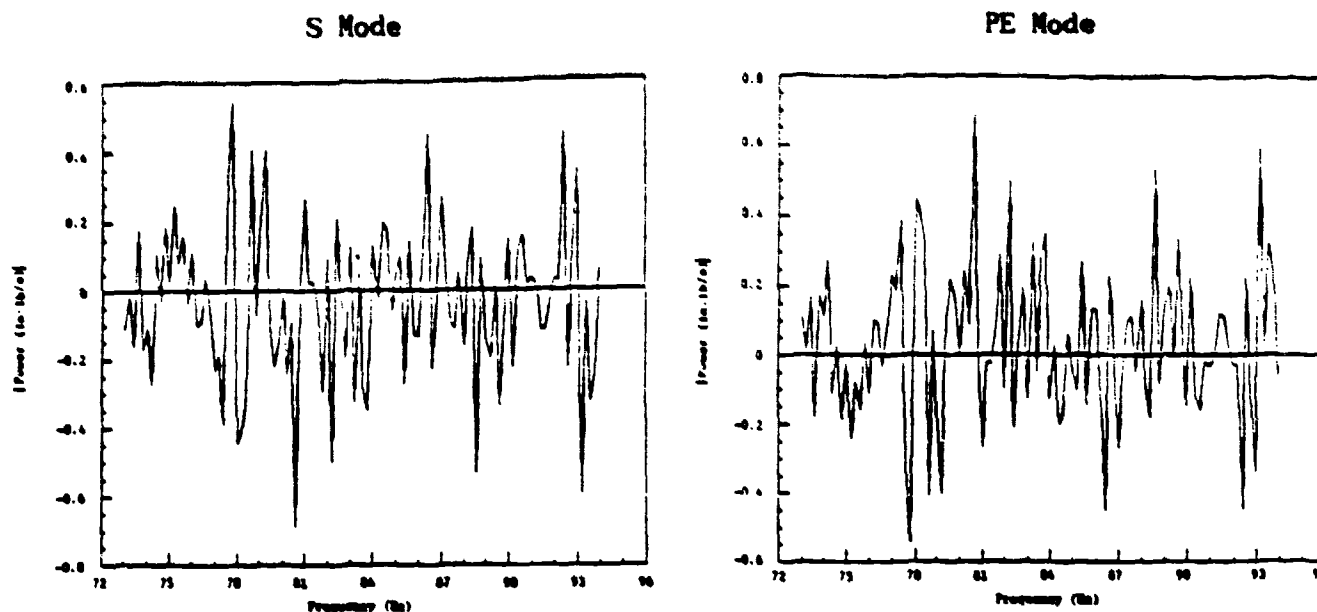


Figure 4.5 - Power Flow in the S and PE Modes
In a Complex Mode Region

expect there to be no net power flow in the right/left-going pair. But Figs 4.1-4.4 clearly show that there is power flow. By changing the eigenvector normalization, a check can be made on the validity of this result.

4.3 Eigenvector Normalization

The truss structure should 'appear the same' to a right-going wave as it does to a left-going wave. This can be seen by considering Fig 4.6. A right-going wave mode 'sees' the truss as in Fig 4.6(a). The eigenvector normalization used in the preceding analysis was to set the x-displacement of node one (u_1) to unity. To a left going wave, the truss would appear as in Fig 4.6(b). Bay (b) can be obtained from (a) by a simple rotation of (a). In order for the eigenvector normalizations to remain the same, the normalization for the left going wave should be made by setting u_3 to negative unity.

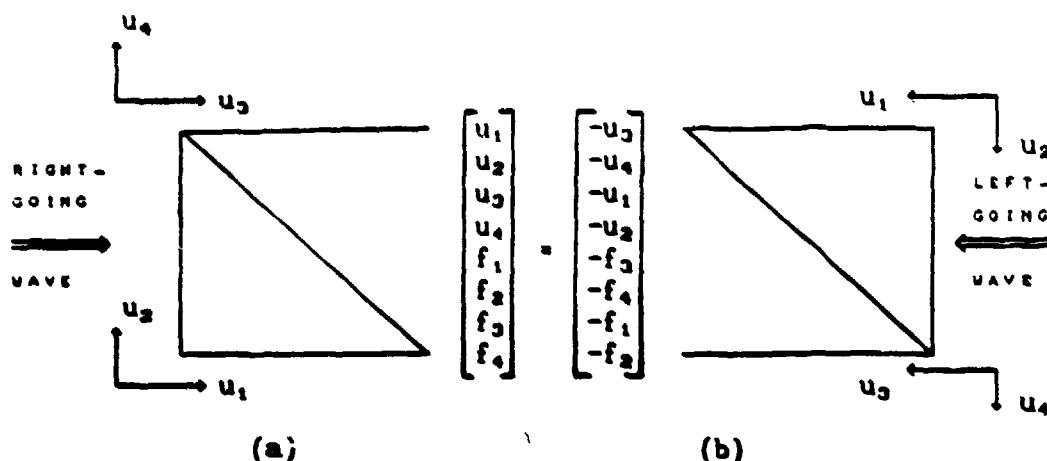


Figure 4.6 - Invariability of Wave Propagation Under a Coordinate Transform

With the original normalization, the eigenvectors of the left/right going brother waves in pass bands occurred in complex conjugate pairs. With the new normalization (left-going modes normalized to $u_3 = -1$), the eigenvectors had equal but reordered values (to correspond to the bay rotation). They were now 'physically' similar. The left and right-going waves both 'saw the same structure.'

A sample set of eigenvectors for 80 Hz. is shown in Fig 4.7. At 80 Hz there are four complex modes present (between the S and PE modes). Notice that the right-going complex modes (the PE and S) have complex conjugate eigenvectors (as do the left PE and S). Also notice that the eigenvectors of the left/right-going brothers have physically similar displacements and forces with the exception of the shear forces. The PE and Evan modes clearly show differences in the shear force terms. What this implies is that the results of the analysis depend on the frame of reference. A right-going wave sees a different truss than a left-going wave. This, however, cannot be true. It violates the principal of invariance under a coordinate transformation. This then leads to

u_1	1.0000d+00 +0. d+00i	6.3860d-04 -1.3325d-18i
u_2	6.5862d+01 +2.3498d-10i	-2.8461d+00 -1.6876d-17i
u_3	-6.3467d-04 +3.6498d-12i	-1.0000d+00 +1.6941d-21i
u_4	2.8461d+00 +7.3888d-12i	-6.5862d+01 -4.5753d-17i
u_5	-7.9606d-04 -2.8110d-07i	7.7927d+04 +9.9587d-14i
f_1	-5.0201d+06 -1.8117d-05i	-7.9757d+04 -9.0483d-14i
f_2	7.6782d+04 +2.7789d-07i	-7.9728d+04 -1.2024d-13i
f_3	4.9351d+06 +1.7834d-05i	-5.7902d+04 -9.2037d-14i
Evan Right		Evan Left
	1.0000d+00 +0. d+00i	4.8519d-01 -2.0160d-01i
	1.4958d-01 +2.5836d+00i	-1.3121d-02 -2.3309d+00i
	-4.8519d-01 +2.0159d-01i	-1.0000d+00 +0. d+00i
	1.3096d-02 +2.3309d+00i	-1.4960d-01 -2.5836d+00i
	-3.3916d+04 -1.7479d+04i	3.1204d+04 +1.4055d+04i
	-1.1613d+04 -2.2034d+04i	-1.2399d+04 -1.5726d+04i
	3.0484d+04 +1.3878d+04i	-3.3593d+04 -1.7248d+04i
	-1.5319d+03 +6.1601d+03i	-8.7070d+02 -3.9139d+03i
S Right		S Left
	1.0000d+00 +0. d+00i	4.8519d-01 +2.0160d-01i
	1.4958d-01 -2.5836d+00i	-1.3121d-02 +2.3309d+00i
	-4.8519d-01 -2.0159d-01i	-1.0000d+00 -6.9389d-18i
	1.3096d-02 -2.3309d+00i	-1.4960d-01 +2.5836d+00i
	-3.3916d+04 +1.7479d+04i	3.1204d+04 -1.4055d+04i
	-1.1613d+04 +2.2034d+04i	-1.2399d+04 +1.5726d+04i
	3.0484d+04 -1.3878d+04i	-3.3593d+04 +1.7248d+04i
	-1.5319d+03 -6.1601d+03i	-8.7070d+02 +3.9139d+03i
PE Right		PE Left
	1.0000d+00 +0. d+00i	-9.9838d-01 +5.6796d-02i
	-1.9834d-01 +5.9521d-03i	1.9835d-01 -5.3222d-03i
	9.9839d-01 -5.6796d-02i	-1.0000d+00 +0. d+00i
	-1.9835d-01 +5.3200d-03i	1.9833d-01 -5.9542d-03i
	-1.3367d+03 -3.5127d+03i	1.1350d+03 -3.5829d+03i
	2.4765d+02 -6.7984d+01i	-2.5111d+02 -5.3808d+01i
	-8.8809d+02 -3.5330d+03i	6.8599d+02 -3.5778d+03i
	-4.0156d+02 +5.4033d-01i	4.0094d+02 -2.2267d+01i
CE Right		CE Left

Figure 4.7 - Wave Mode Eigenvectors at 80 Hz

the conclusion that the power flow observed in the evanescent modes is a numerical effect, and cannot be believed.

One normalization that would prove useful in the next chapter is to normalize all the wave mode eigenvectors to imply unit power flow. If this were done, the scattering matrix (to be discussed in Chapter 5) will be unitary -- all columns and rows have unit magnitude [V-1]. But because power flow in some of the wave modes is zero, this type of normalization could not be used. If damping were added to the system, this normalization would be viable.

Chapter 5 - Wave Mode Boundary Conditions

5.1 Scattering Matrices

All of the analysis of Chapters 3 and 4 was performed without regard to truss boundary conditions. In order to consider wave mode propagation in a finite length truss, boundary conditions must be taken into account. The concept of a scattering matrix will be used to give the infinite truss closure.

The cross-sectional state vector, Y , may be transformed into wave mode coordinates by the transformation [V-1].

$$Y = v(\omega) W \quad (5.1)$$

where W is the cross-sectional state vector in wave mode coordinates, and v are the eigenvectors of the transfer matrix T .

The cross-sectional state vector W can be partitioned into components which represent right-going waves, w^+ , and left-going waves, w^- .

$$W = \begin{bmatrix} w^+ \\ w^- \end{bmatrix} \quad (5.2)$$

One can also consider wave modes which arrive at a member boundary, a , and those which depart a boundary, d . The relationship between the arriving and departing wave modes at beam boundaries is depicted in Fig 5.1.

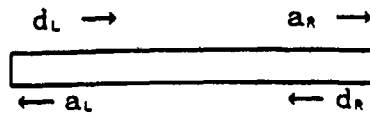


Figure 5.1 - Representation of Arriving and Departing Wave Modes at Beam Boundaries

a and d are related by the wave mode eigenvalues, ξ ,

$$a_R = \xi^n d_L \quad (5.3)$$

$$a_L = \xi^n d_R$$

where n is the number of bays

The boundary conditions at the ends of the truss may be written as,

$$[B(\omega)] Y = F_{EXT}(\omega) \quad (5.4)$$

where the boundary conditions, B , and external forces, F , may be functions of frequency. In wave mode coordinates this becomes

$$[B(\omega)] [v(\omega)] \begin{bmatrix} a \\ d \end{bmatrix} = F_{EXT}(\omega) \quad (5.5)$$

Partitioning the boundary conditions gives,

$$\left[\begin{array}{c|c} B_A(\omega) & B_D(\omega) \end{array} \right] \begin{bmatrix} a \\ d \end{bmatrix} = F_{EXT}(\omega) \quad (5.6)$$

After some manipulation, the departing wave modes may be expressed as,

$$d = -B_D^{-1}(\omega) B_A(\omega)a + B_D^{-1} F_{EXT} \quad (5.7)$$

$$\text{or,} \quad d = S(\omega)a + B_s^{-1} F_{ext} \quad (5.8)$$

where $S(\omega)$ is defined as the scattering matrix at the boundary. With no external forcing this becomes,

$$d = [S(\omega)] a \quad (5.9)$$

Components of the scattering matrix are complex, frequency dependent reflection coefficients for the boundary. The second term of Egn 5.8 is the wave mode generating matrix which indicates how external forces at the boundary generate outgoing wave modes [V-1]. The reflection coefficients indicate how an incoming wave mode contributes to generating outgoing wave modes.

5.2 Derivation of the Scattering Matrices for a Pinned Beam Truss Attached to the Shuttle Orbiter

Scattering matrices will now be determined for the case of a pinned beam truss attached to the shuttle orbiter. Consider the orbiter attached truss shown in Fig 2.6. The mass of the orbiter is assumed to be much greater than that of the truss, thus enabling the left side of the beam to be treated as being attached to a 'brick wall'. Therefore, the truss left boundary condition is zero displacement. This leads to writing the boundary conditions of Egn 5.5 as,

$$\begin{bmatrix} 1 & & & 0 \\ & 1 & & 0 \\ & & 1 & 0 \\ & & & 1 \end{bmatrix} \begin{bmatrix} Y_{\xi} > 1 & Y_{\xi} < 1 \end{bmatrix} \begin{bmatrix} a_i \\ d_i \end{bmatrix} = 0 \quad (5.10)$$

where $Y_{\xi} < 1$ and $Y_{\xi} > 1$ represent the eigenvectors of the

right-going and left-going wave modes, respectively.

As discussed in Section 2.5, the last bay on the free end of the truss must be closed by the addition of an end member. The dynamic stiffness matrix of this member is frequency dependent and so, therefore, is the boundary condition. This then leads to the frequency dependent free end boundary condition,

$$\begin{bmatrix} A & B \\ C & D \end{bmatrix} \begin{bmatrix} I \end{bmatrix} \begin{bmatrix} Y_F < 1 & Y_F > 1 \end{bmatrix} \begin{bmatrix} a_n \\ d_n \end{bmatrix} = 0 \quad (5.11)$$

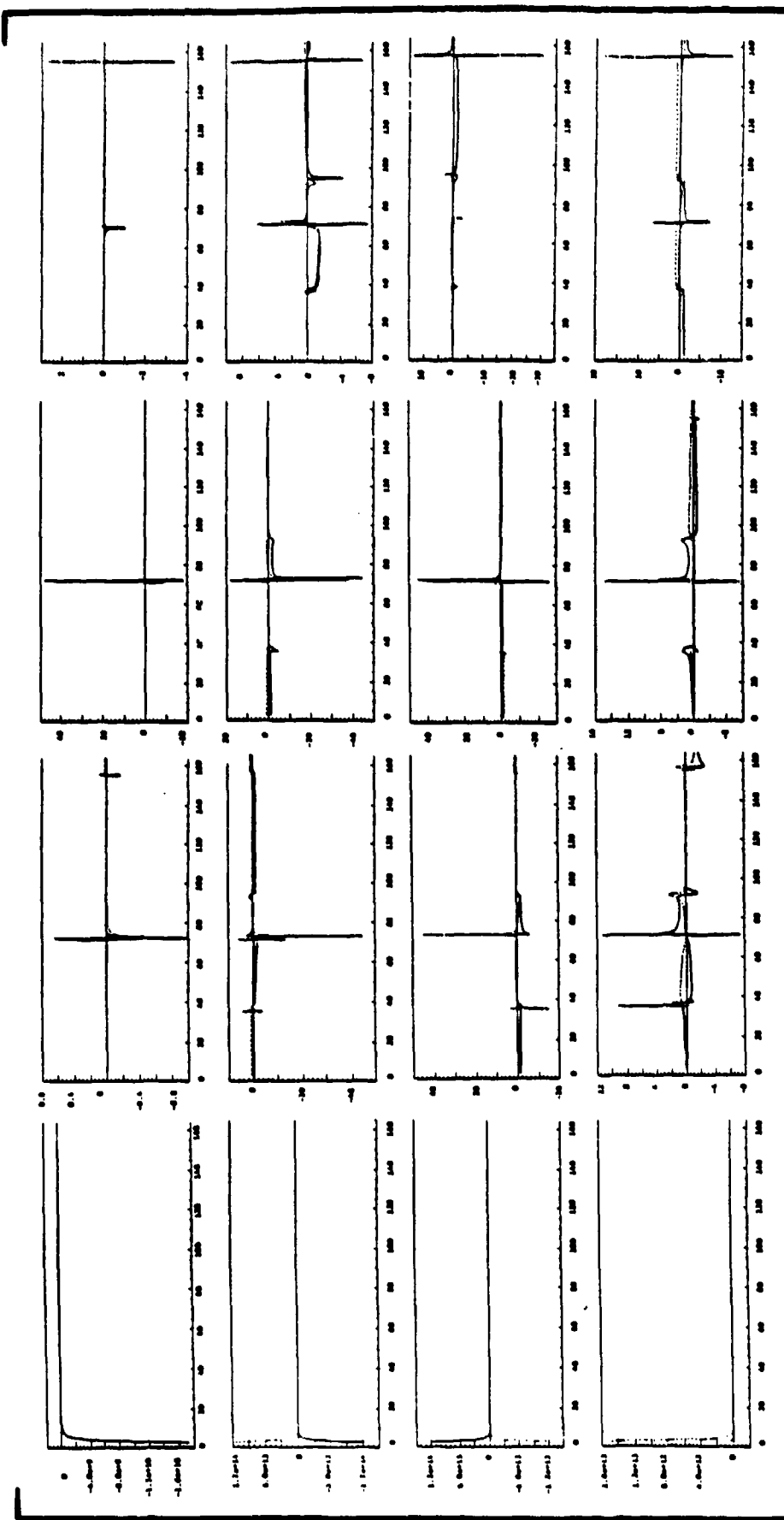
where A, B, C, D are elements of the dynamic stiffness matrix of the end member (Eqns 2.16,17).

In this example, the eigenvectors were normalized so that x-displacement of node one of each bay was unity (the same normalization used to determine the power flows of Chapter 4). The left and right scattering matrices were calculated from 0 to 170 Hz, in steps of 0.2 Hz. Figs. 5.2 and 5.3 depict the real and imaginary components of the scattering matrices as a function of frequency. More detailed plots of the elements of the scattering matrices are contained in Appendix B.

Each entry of the scattering matrices, S_{ij} , represents how much departing wave mode j is created by incoming wave mode i . For example, the first column of S_r and S_l indicates how the outgoing evanescent, S, PE, and CE wave modes are produced by the incoming evanescent wave mode.

Checks can be made on the validity of these reflection coefficients by examining limiting cases of these values. As noted in Chapter 3, at low frequencies the S mode resembles a beam

$$d_1 = [S_1(\omega)] a_1 \quad \text{where} \quad [S_1(\omega)] =$$

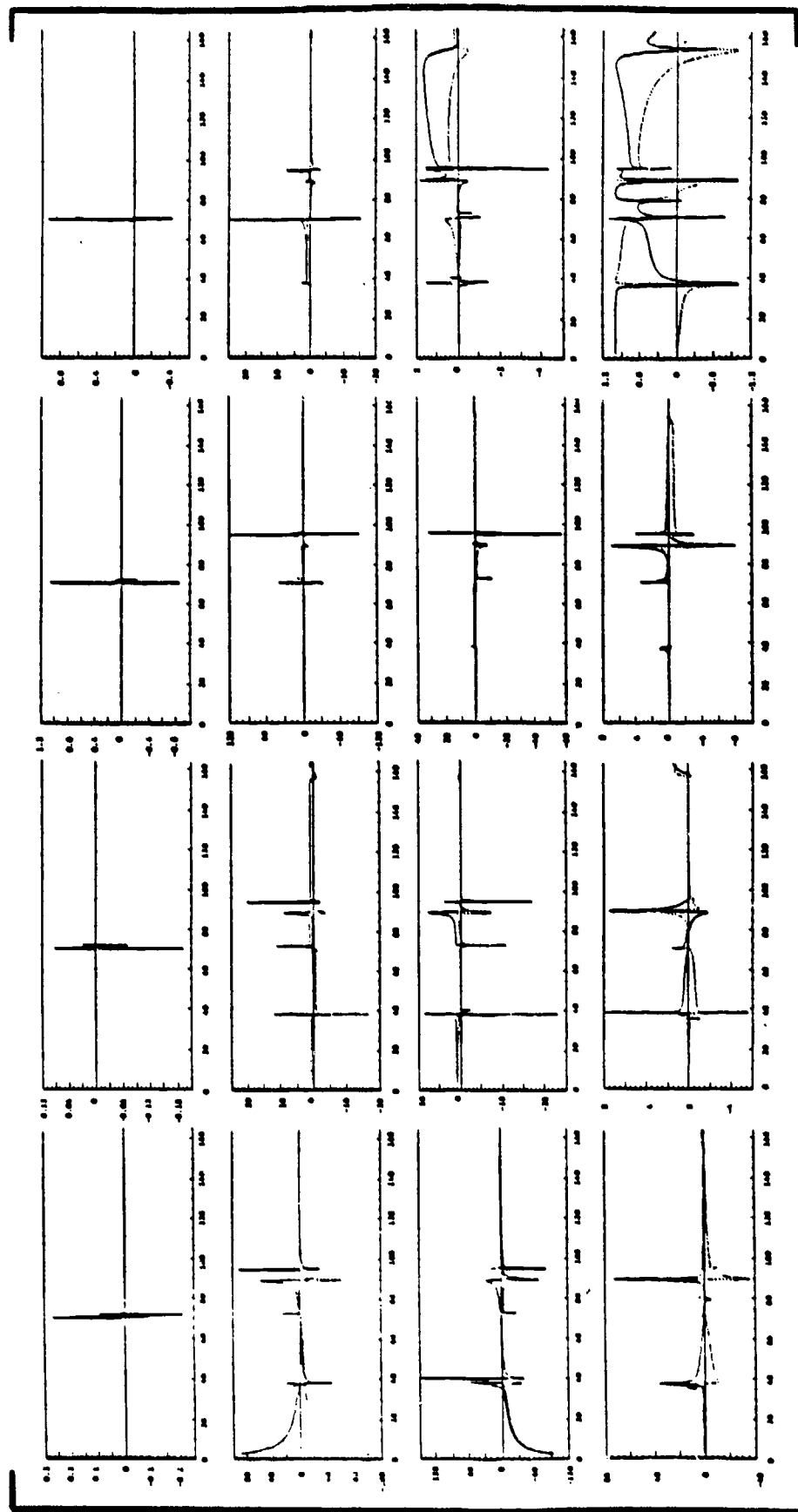


— = Real(S_1)

..... = Imag(S_1)

Figure 5.2 - Scattering Matrix for Pinned End of Truss

$$d_r = [S_r(\omega)] a_r \text{ where } [S_r(\omega)] =$$



— = Real(S_r)

..... = Imag(S_r)

Figure 5.3 - Scattering Matrix for Free End of Truss

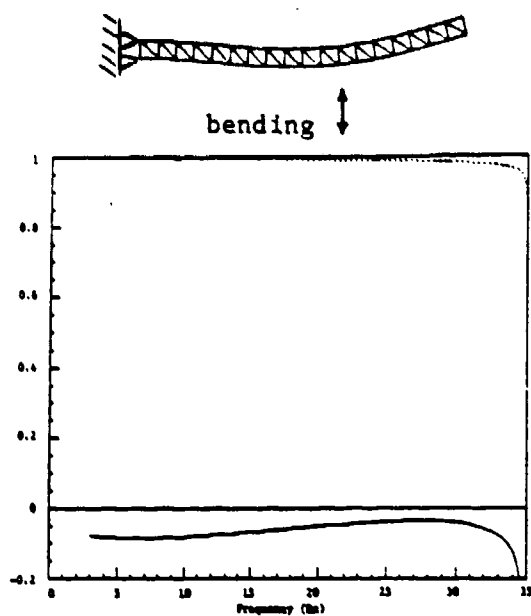
in bending, while the CE mode resembles a rod in tension/compression. Since the wave mode eigenvectors have been normalized with the x-deflection of the first node equal to unity, checks can be made on the reflection coefficients of the CE mode at both ends. Fig 5.4 shows selected terms of the left and right scattering matrices at low frequency. The $S_L(4,4)$ plot indicates that the reflection coefficient for the CE mode at the left boundary should be $-1.0 + i0$, while $1 + i0$ at the right.

The incoming CE wave mode must satisfy the zero displacement boundary condition on the left end of the truss. The reflection coefficient for this wave mode can be easily determined. Consider the arriving wave mode at the left boundary (Fig 5.5).

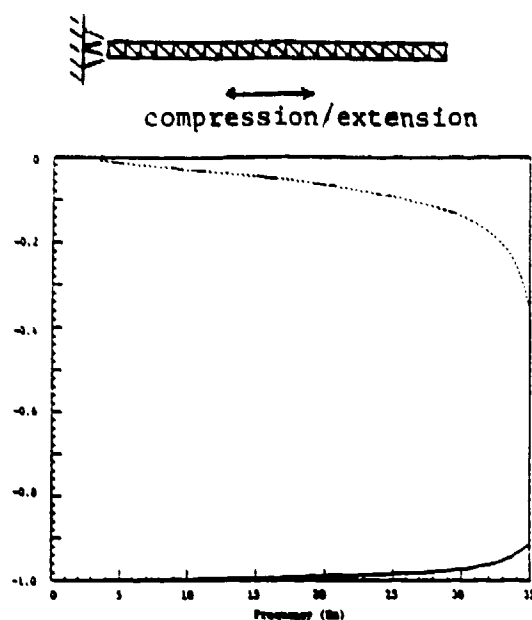
The zero displacement boundary condition can be met by visualizing a phantom wave, w_{ph} , being created behind the boundary and travelling to the right. The phantom wave has equal but opposite magnitude at the boundary as compared to the CE wave. This wave then, exactly cancels the displacement of the incoming CE wave, thereby insuring zero displacement at the boundary. The boundary amplitude of the phantom wave is π out of phase with the incoming CE wave. The reflection coefficient is then $-1 + i0$.

A check can be made of the $S_R(4,4)$ term by a similar process. The incoming CE wave mode must satisfy the zero slope boundary condition at the right end of the truss. In this case, the phantom wave will have the same magnitude as the incoming CE wave, and will be in phase. This leads to a reflection coefficient of $1 + i0$.

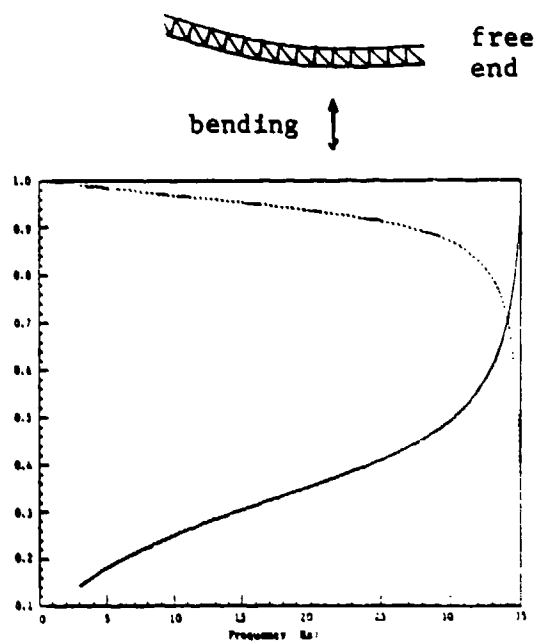
$S_L(2,2)$ and $S_R(2,2)$ can be verified by thinking of the S mode as a Bernoulli-Euler beam in bending. For this case, however,



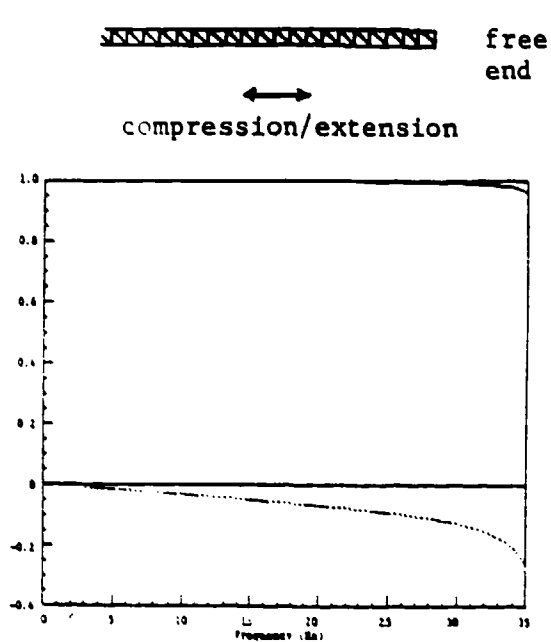
$S_L(2,2)$



$S_L(4,4)$



$S_R(2,2)$



$S_R(4,4)$

Figure 5.4 - Reflection Coefficients for the S and CE Modes at Low Frequency

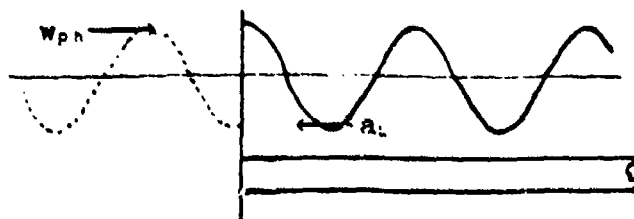


Figure 5.5 - Enforcing the Zero Displacement Boundary Condition by Means of a Phantom Wave

consideration must also be given to near-field effects. The reflection coefficients (at low frequency) for the pinned and free ends were found to be consistent with those determined in [C-1] [H-1].

5.3 Natural Frequencies by Phase Closure

Recall that in Section 2.6 a method was presented for determining the natural frequencies of a truss by using the global transfer matrix of the structure. It was pointed out that even for trusses consisting of a small number of bays, it may not be possible to determine the natural frequencies due to large eigenvalues of the transfer matrix (generally associated with the evanescent modes). By transforming the problem to wave mode coordinates and employing the phase closure principle this difficulty can be eliminated. The phase closure principle states that natural resonances occur at frequencies at which all wave modes complete a circumnavigation of the beam with a total phase change of $2n\pi$.

For the case of a seven bay truss Eqn 5.3 becomes,

$$\begin{aligned} a_R &= \xi^T d_L \\ a_L &= \xi^T d_R \end{aligned} \quad (5.12)$$

where ξ is a diagonal matrix of eigenvalues associated with the right-going wave modes. Eqn 5.9 can be written for both boundaries as,

$$\begin{aligned} d_L &= [S_L] a_L \\ d_R &= [S_R] a_L \end{aligned} \quad (5.13)$$

By repeated substitutions of Eqns 5.12 and 5.13, we obtain with a_R , after one circumnavigation of the beam,

$$a_R \leftarrow \xi^T S_L \xi^T S_R a_R \quad (5.14)$$

Resonance occurs when this relation is an equality;

$$[\xi^T S_L \xi^T S_R - I] a_R = 0 \quad (5.15)$$

The only non-trivial way this can be true is if the determinant of Eqn 5.15 is zero. Therefore,

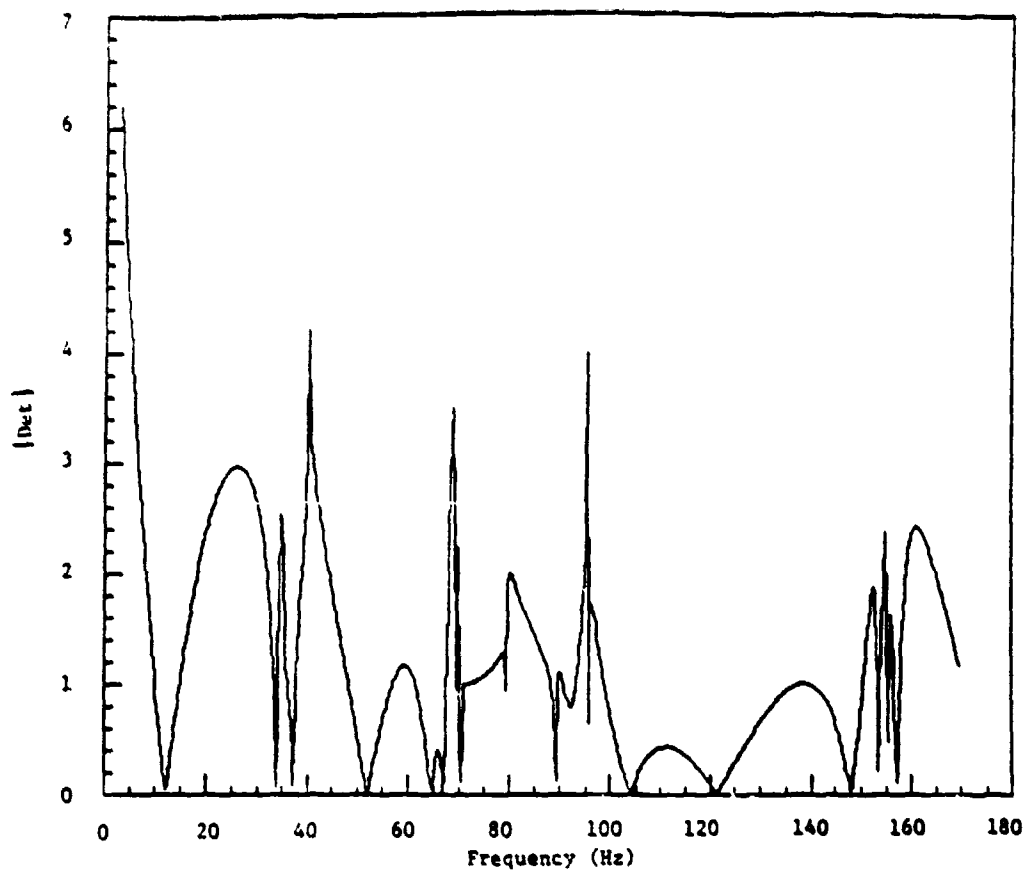
$$\det [\xi^T S_L \xi^T S_R - I] = 0 \quad (5.16)$$

is satisfied at a truss resonance.

Notice that, by replacing only one value in the formulation (the number of bays), the natural frequencies for a truss with an arbitrary number of bays can be determined "quick as a bunny." The order of the problem does not increase with increasing number of bays because the dimension of the transfer matrix is independent of the number of bays in the structure.

Fig 5.6 is a plot of the determinant of Eqn 5.16 for a seven bay, pinned beam truss with one free and one pinned end. The

natural frequencies of the truss can be identified whenever Eqn 5.16 tends to zero. Resonant frequencies determined by this phase closure method are listed in Fig 5.6. These frequencies reproduce those determined by a finite element analysis of the same truss except whenever the modes are closely spaced. The finite element analysis obtains five modes within the 35.13 - 35.31 Hz bandwidth while the phase closure method locates only two. This remains true even when frequency steps of 0.001 Hz are used in Eqn 5.16 (Fig 5.7). The same results also occur about 70 and 154 Hz. Because the isolated modes are so accurately determined, one may be tempted to attribute the phase closure method's failure on numerical round-off rather than the physics of the problem. This, however, remains to be shown.



<u>Present Analysis</u>	<u>Finite Elements</u>		
12.10	12.10	n/i	70.51
33.97	33.97	n/i	70.52
<u>35.13</u>	<u>35.13</u>	n/i	70.54
n/i	35.25	n/i	70.54
n/i	35.29	n/i	70.55
?	35.30	n/i	70.57
<u>n/i</u>	<u>35.31</u>	n/i	70.59
37.16	37.16	n/i	70.59
51.84	51.84	n/i	70.59
64.51	64.51	<u>n/i</u>	<u>70.59</u>
<u>67.00</u>	<u>67.00</u>	89.23	89.23
?	69.50	103.83	103.83
n/i	70.04	121.14	121.12
70.22	70.22	147.91	147.91
n/i	70.39	<u>153.45</u>	<u>153.45</u>
n/i	70.40	?	154.32
n/i	70.43	n/i	154.57
n/i	70.47	<u>n/i</u>	<u>154.69</u>
n/i	70.47	155.28	155.28
n/i	70.49	157.07	157.07

n/i = not identified

? = possible identification

Figure 5.6 - Natural Frequencies Obtained by Phase Closure

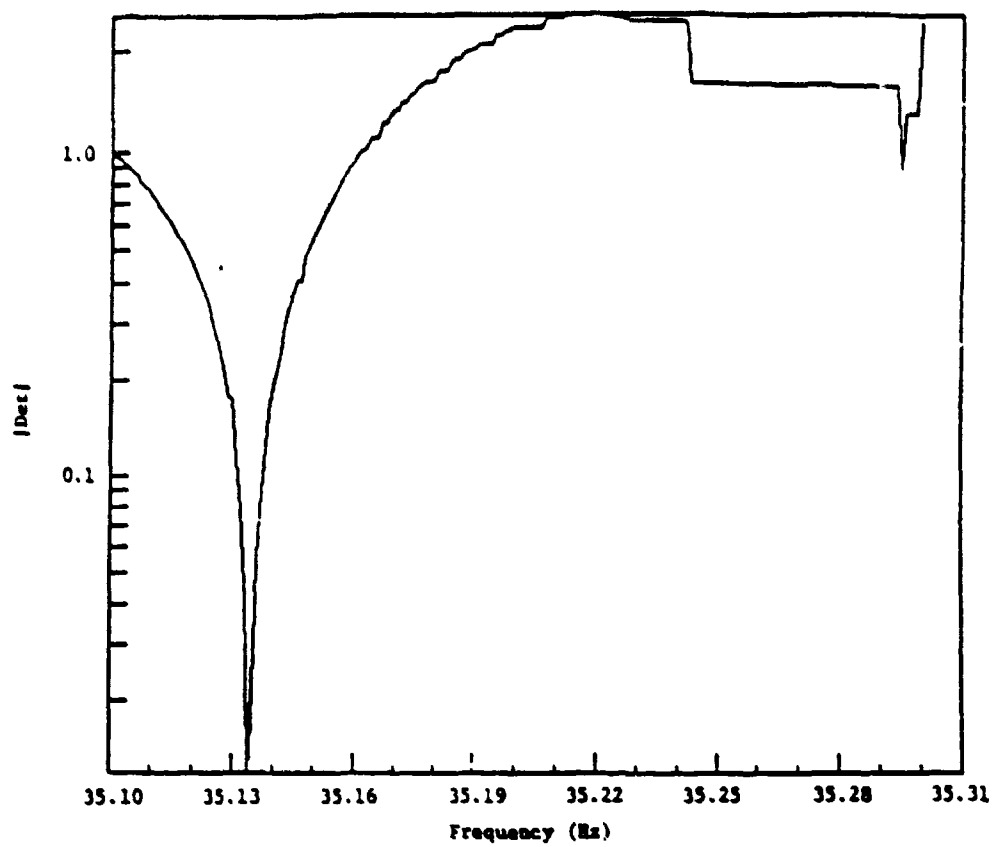


Figure 5.7 - Natural Frequencies Near 35 Hz From Phase Closure

Chapter 6 - Conclusions and Recommendations

This thesis computationally investigated wave mode propagation in two-dimensional, periodic truss structures. Some conclusions based on this research follow.

- 1) The transfer matrix technique proved useful in that the dynamics of a complete truss beam were determined by analysing only one of the periodic elements. Conventional analysis tools such as the finite element analysis become computationally cumbersome as the number of degrees of freedom needed to model the structure increases. In the transfer matrix method the order of the problem depends solely on the order of one of the periodic elements.
- 2) The method of obtaining natural frequencies of the truss by sequential multiplication of the transfer matrix and subsequent application of boundary conditions is only practical for cases in which the eigenvalues of the transfer matrix are not large.
- 3) The results obtained by examining a pinned rod truss by transfer matrices closely match the results obtained by continuum models of the same structure.

- 4) As with continuum models of the truss structure, the pinned rod truss loses its fidelity at the first resonant frequency of the truss members. The rod modelling masks all local member dynamics that would be present if member bending were modeled.
- 5) The pinned beam truss exhibits complicated mechanical filtering properties. As a function of frequency, there are bands in which certain wave modes will propagate and bands in which wave modes will not propagate.
- 6) At low frequencies, non-evanescent modes are characterized by predominantly global displacements whereas at higher frequencies this displacement becomes localized in the truss members.
- 7) Complex modes must form in pairs and cannot exist alone. Thus in a pinned beam truss, there must be at least four (eight, twelve etc.) or more complex modes present in order for any to exist at all. Mono-coupled systems cannot support complex wave modes.
- 8) Complex mode formation is initiated at member resonant frequencies. No explanation could be found for termination of complex mode coupling.
- 9) Net power flow in a right-going (left-going) complex mode pair is zero.

10) Several results were obtained that indicate there may be numerical round-off errors in this formulation.

a. Power flow was evident in the evanescent modes throughout much of the of the bandwidth examined.

b. Shear force terms in the eigenvectors of modes in stop bands are not invariant under a coordinate transformation.

c. Closely spaced natural frequencies of the truss are not detected when analysed by phase closure.

11) By using the phase closure principle and the eigenvectors of the transfer matrix in wave mode coordinates, the restriction imposed in 2) can be circumvented. In fact, by changing just one variable in the formulation, the natural frequencies for a truss consisting of an arbitrary number of bays can be determined. As stated in 10), however, this method will only locate isolated resonances.

Following are some suggestions for follow-on research.

1) Investigate wave propagation in a three dimensional periodic truss structure.

2) Identify and characterize wave modes experimentally.

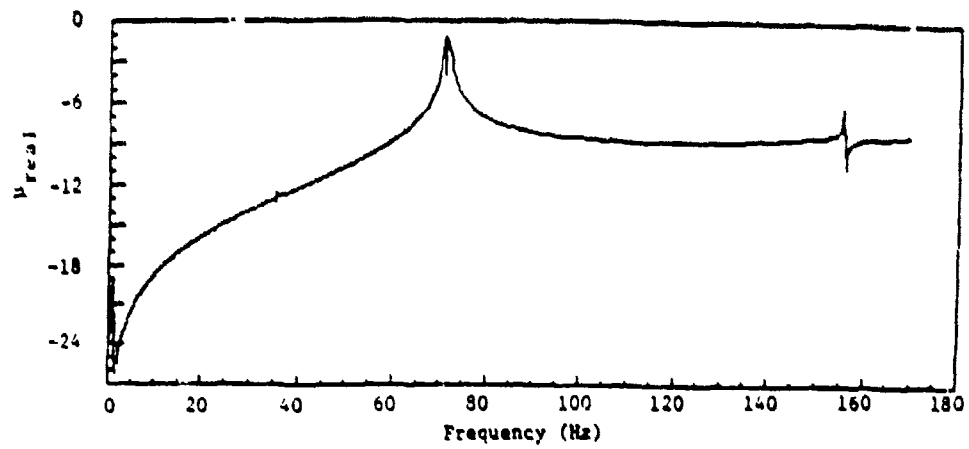
- 3) Develop vibration isolation and suppression schemes which exploit the filtering behavior of truss beams.
- 4) Investigate localization effects in random periodic structures.
- 5) Determine if issues of (10) are due to numerical round-off error or are inherent in the transfer matrix formulation.
- 6) Investigate when and why complex modes decouple.
- 7) Resolve the questions involved with power flow in complex modes. Is the net power flow in a single complex mode zero or equal and opposite to that of its coupled 'brother?'
- 8) And on a more practical and mundane level, determine a quick and reliable automated method to sort eigenvalues!

References

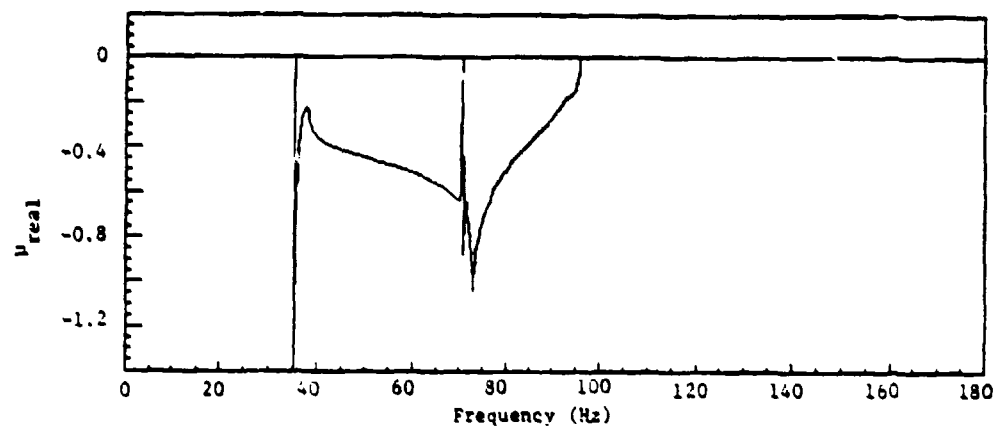
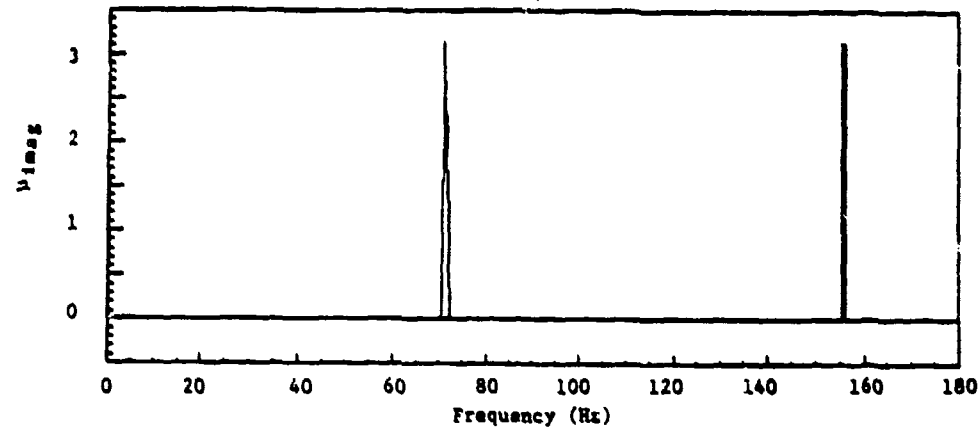
- [B-1] Brillouin L., "Wave Propagation in Periodic Structures," Dover Publications, Inc., New York, 1946
- [C-1] Cremer L., and Leilich H.O., "Zur Theorie der Biegekettenteiler," Archiv der Elektrischen Übertrag., 1953, 7, 261-270.
- [E-1] Eatwell G.P., "Free-Wave Propagation in an Irregularly Stiffened, Fluid-Loaded Plate," *Journal of Sound and Vibration*, 1983, 88(4), 507-522.
- [H-1] Heckl M.A., "Investigations on the Vibrations of Grillages and Other Simple Beam Structures," *Journal of the Acoustical Society of America*, 1964, 36, 1335-1343.
- [M-1] Mead D.J., "The Random Vibrations of a Multisupported Heavily Damped Beam," *Shock and Vibration Bulletin*, 1966, 35(3), 45-54.
- [M-2] Mead D.J., "A General Theory of Harmonic Wave Propagation in Linear Periodic Systems with Multiple Coupling," *Journal of Sound and Vibration*, 1973, 27(2), 235-260.
- [M-3] Mills R.A., "Natural Vibrations of Beam-Like Trusses," SM Thesis, Aeronautics and Astronautics, MIT, June 1985.
- [M-4] "Matrix," Integrated Systems Inc., 1982, Palo Alto Ca.
- [P-1] Pestel I.E., "Matrix Methods in Elastomechanics," McGraw-Hill, 1963.
- [R-1] Rubin S., "Transmission Matrices for Vibration and Their Relation to Admittance and Impedance," *Transactions of the ASME: Journal of Engineering for Industry*, Feb 1964.
- [R-2] Roy A.K., and Plunkett R., "Wave Attenuation in Periodic Structures," *Journal of Sound and Vibration*, 1986, 104(3), 395-410.
- [V-1] von Flotow A.H., "Disturbance Propagation in Structural Networks," *Journal of Sound and Vibration*, 1986, 106(3), 433-450.

Appendix A - Propagation Coefficients for a Pinned Beam Truss

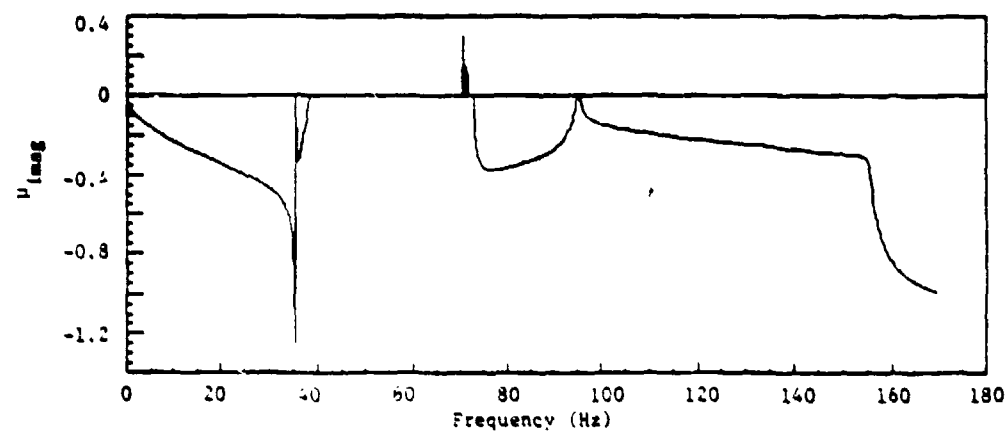
The next two pages contain the propagation coefficients, μ_r and μ_l , of the four right-going wave modes for the pinned beam truss. An explanation of these plots can be found in Section 3.2.

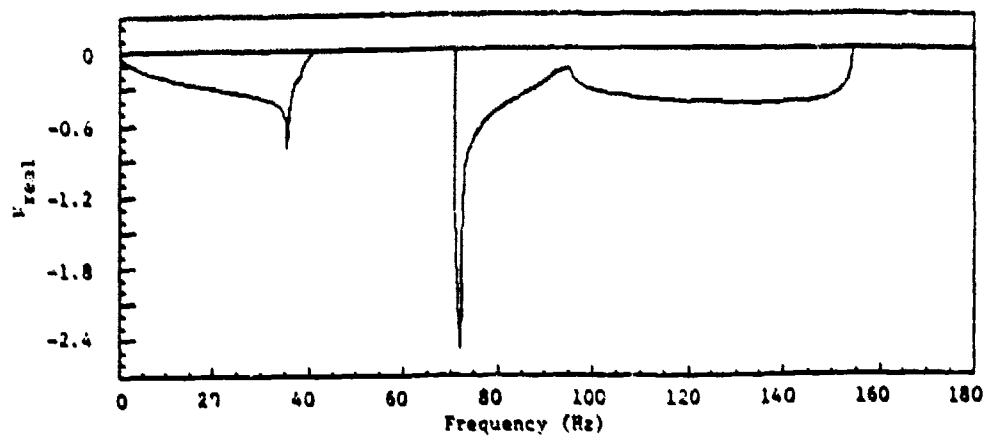


Evan Mode

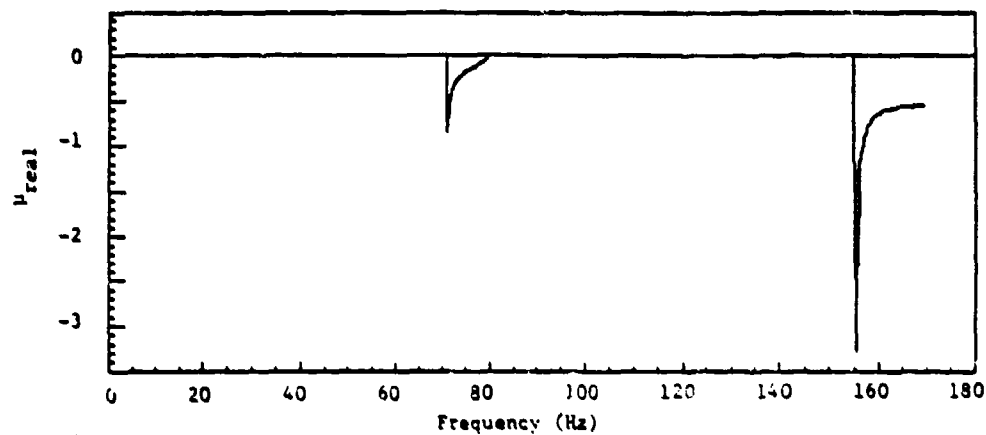
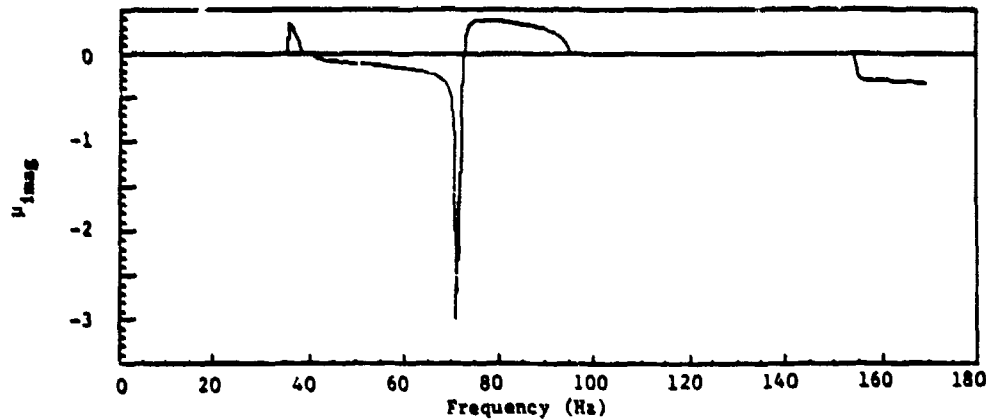


S Mode

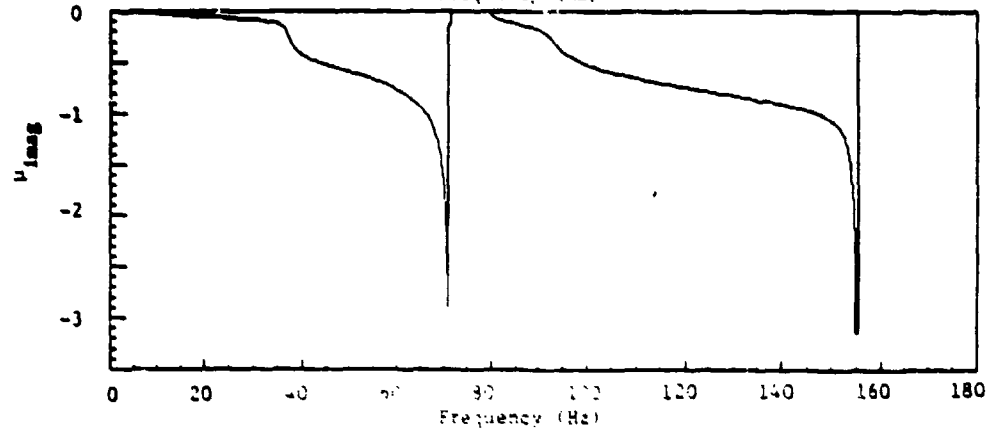




PE Mode

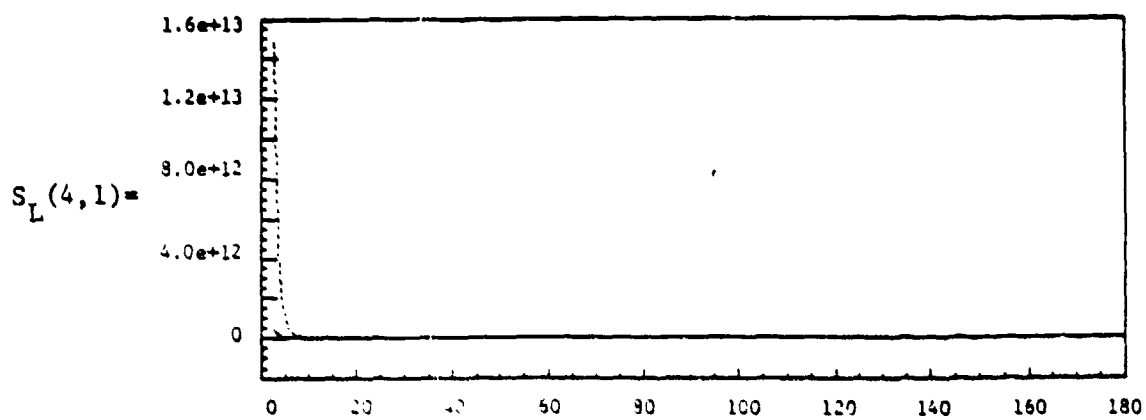
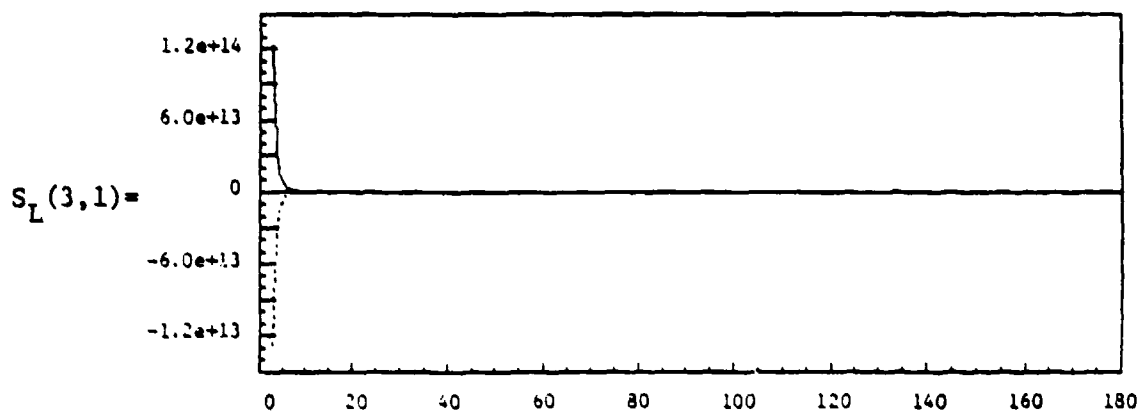
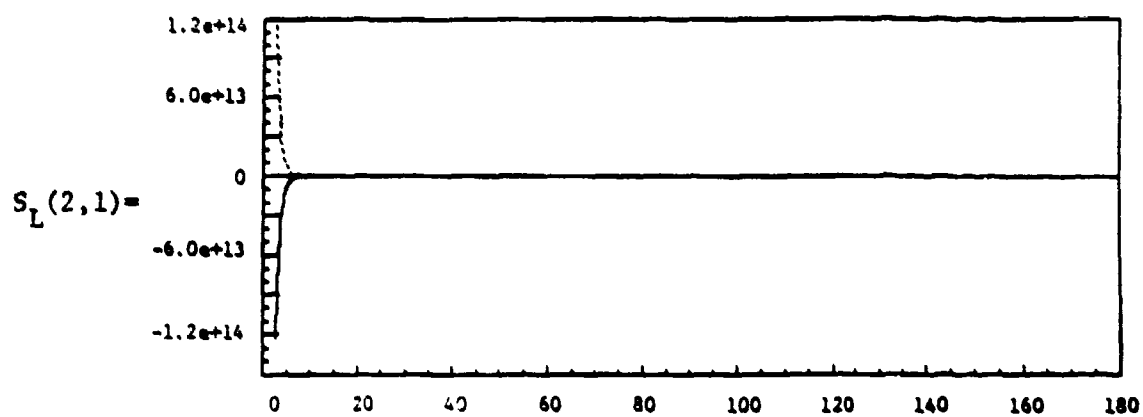
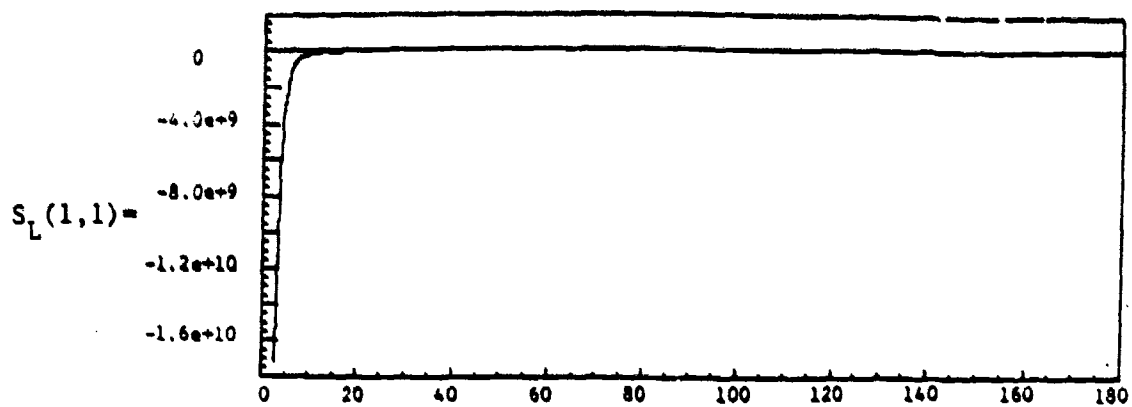


CE Mode

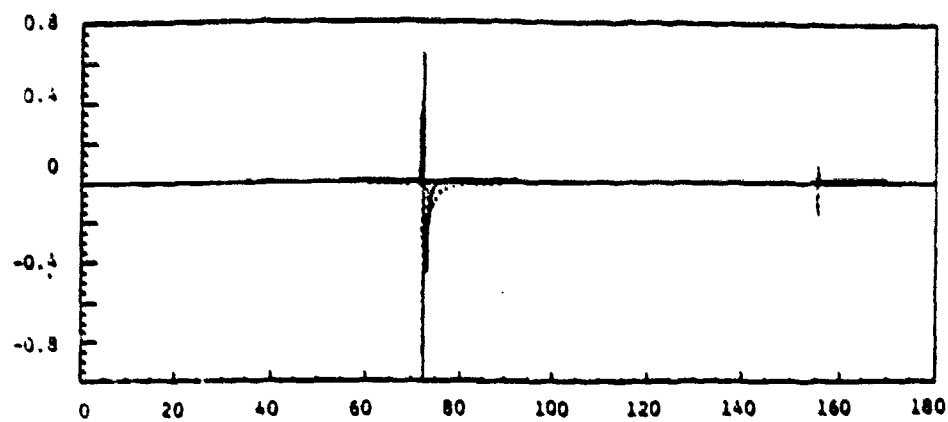


Appendix B - Scattering Matrices for a Pinned-Free Truss

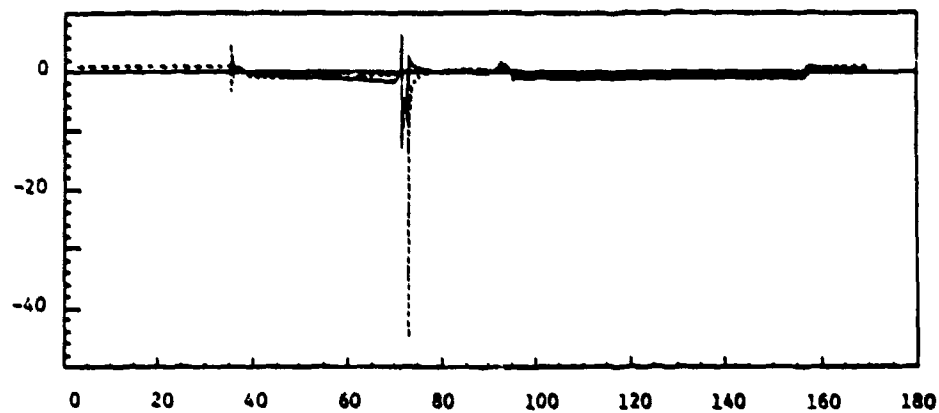
This appendix contains the left and right scattering matrices for a pinned-free truss. The elements of the scattering matrices are presented in more detail than possible in Figs 5.2 and 5.3. Each page represents a column of the given scattering matrix. For example, the first page presents the first column of the left scattering matrix -- how the arriving evanescent mode produces outgoing Evan, S, PE, and CE waves. The solid lines correspond to the real component of the reflection coefficient while the dotted lines correspond to the imaginary part of the reflection coefficient.



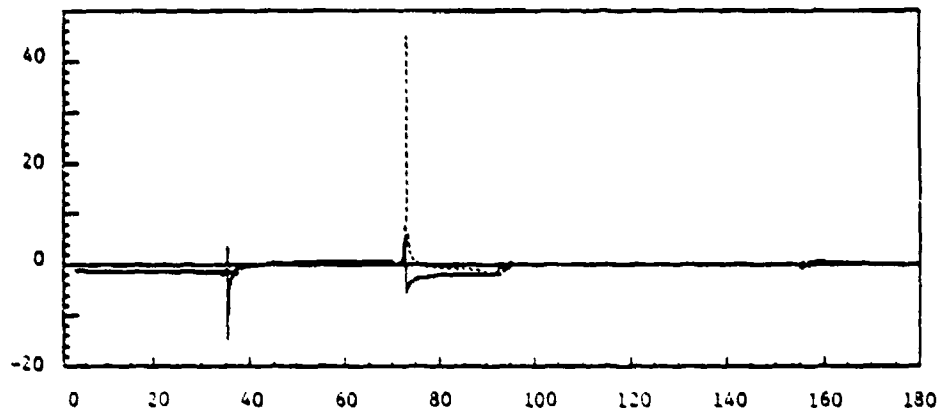
$S_L(1,2)=$



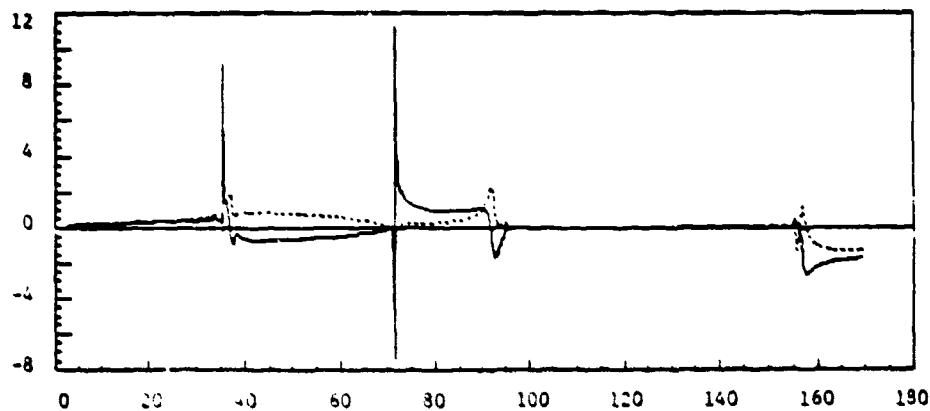
$S_L(2,2)=$



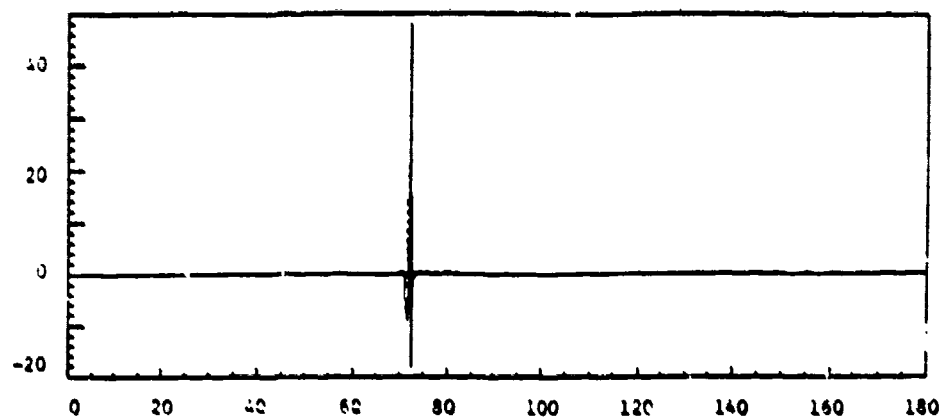
$S_L(3,2)=$



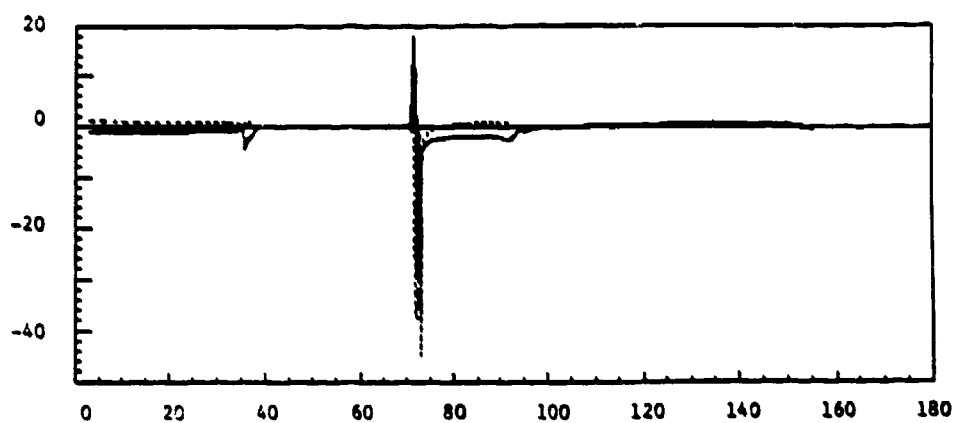
$S_L(4,2)=$



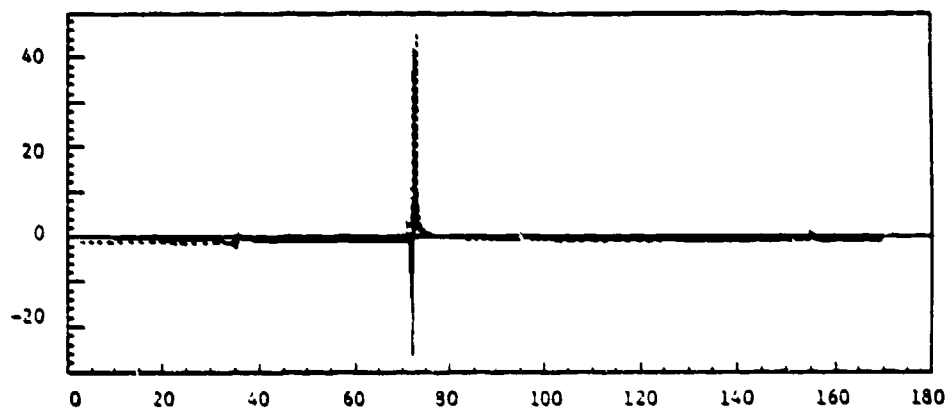
$S_L(1,3) =$



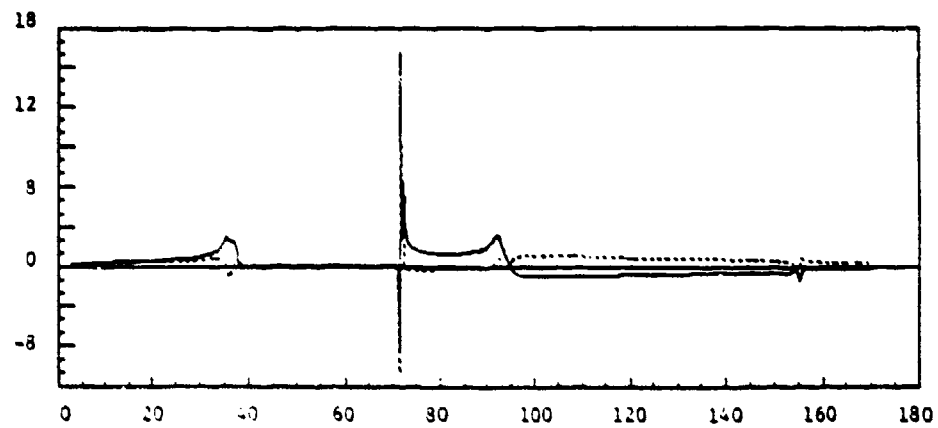
$S_L(2,3) =$



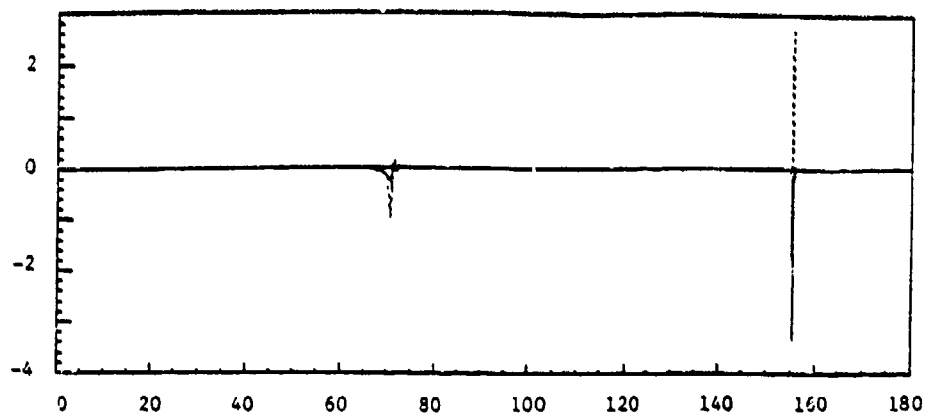
$S_L(3,3) =$



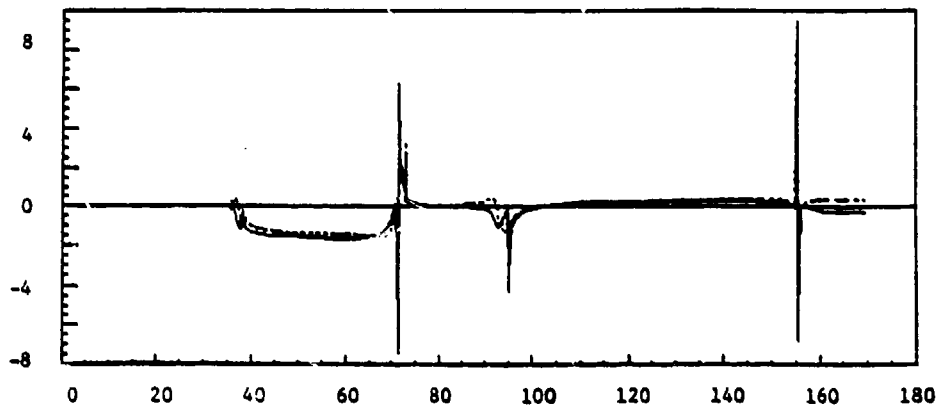
$S_L(4,3) =$



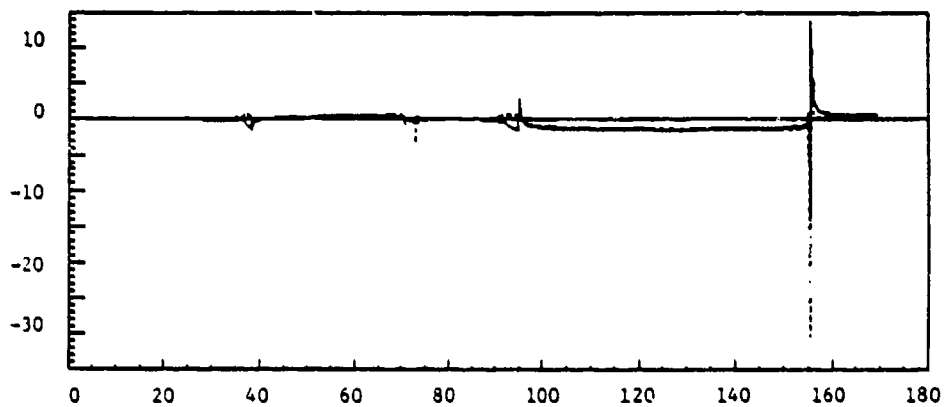
$S_L(1,4) =$



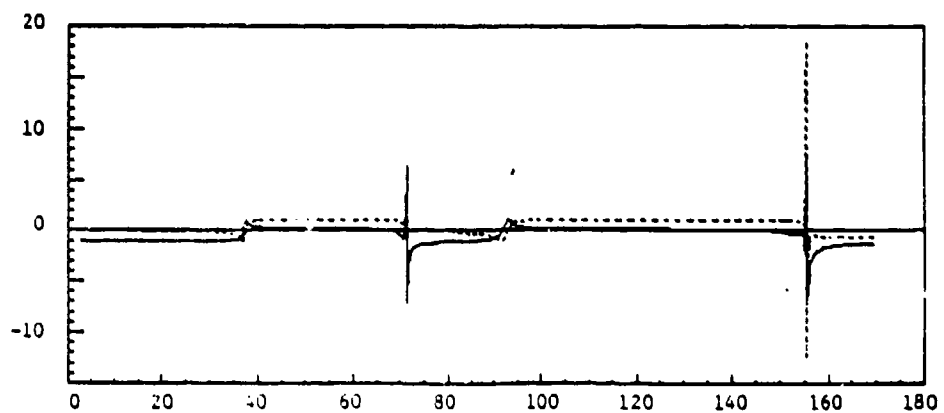
$S_L(2,4) =$



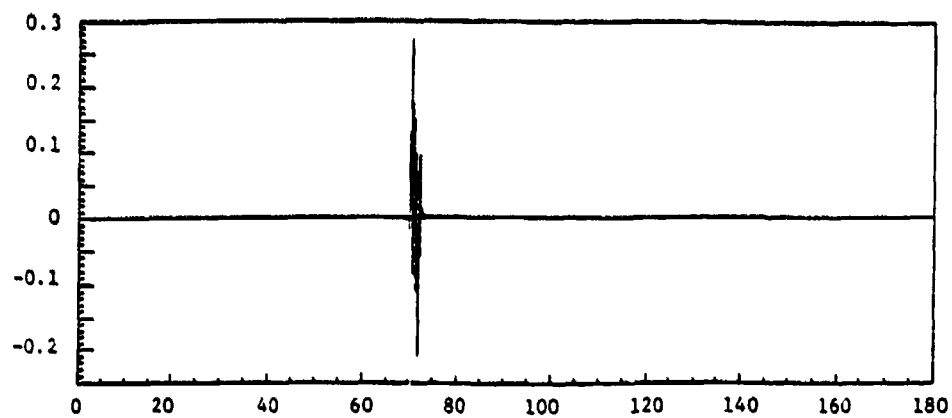
$S_L(3,4) =$



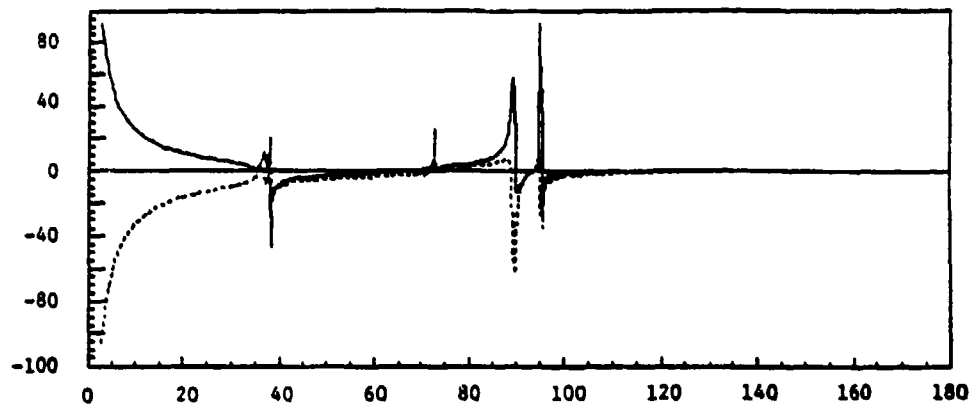
$S_L(4,4) =$



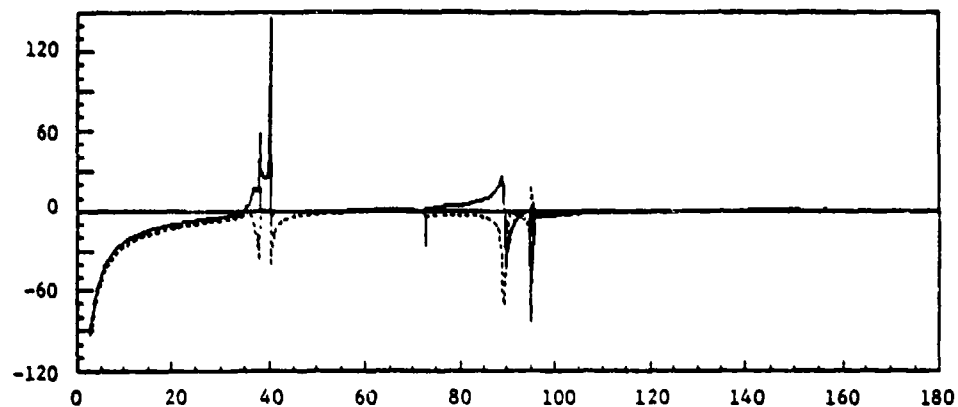
$S_R(1,1)=$



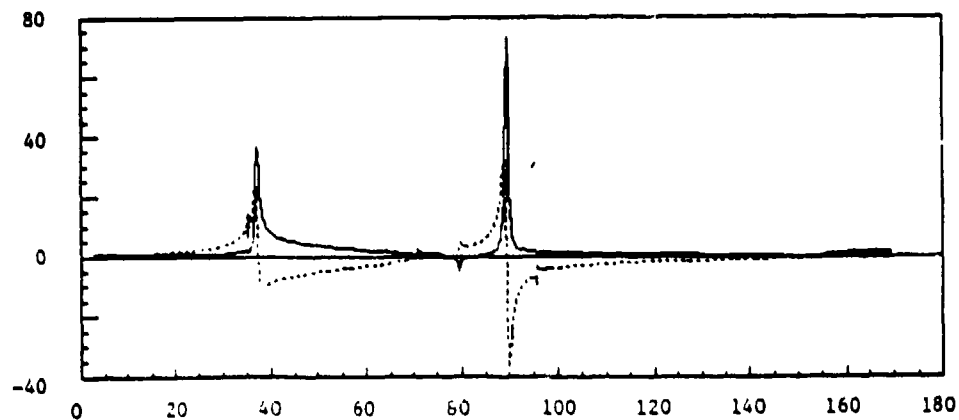
$S_R(2,1)=$



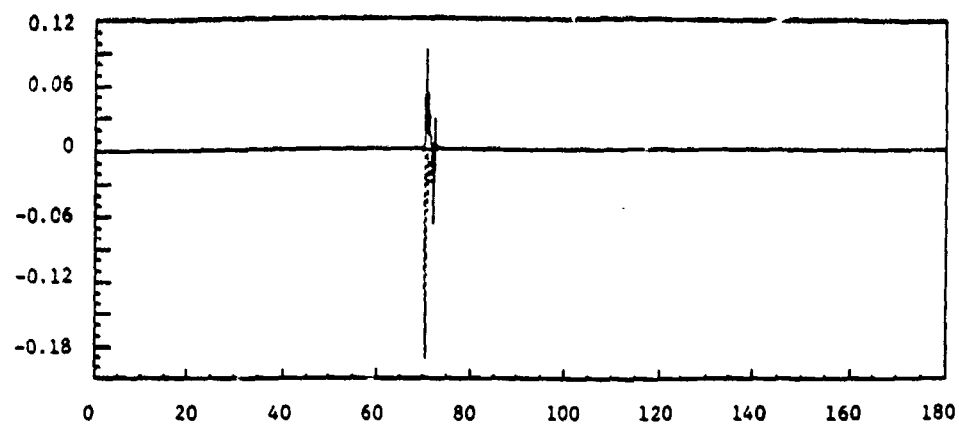
$S_R(3,1)=$



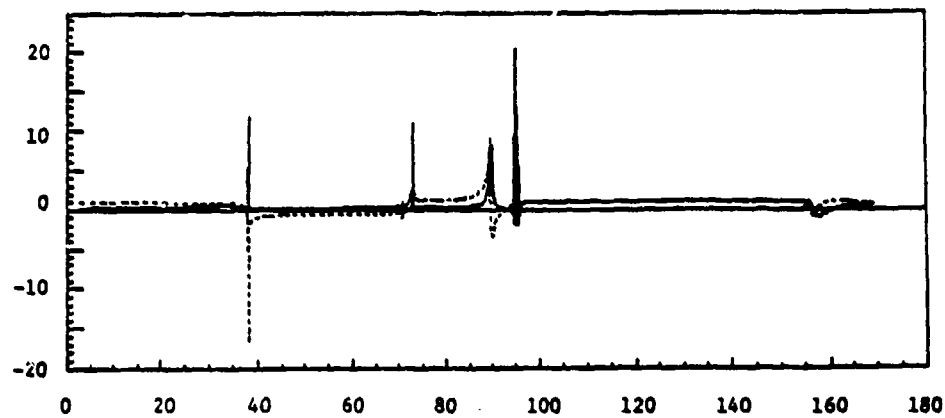
$S_R(4,1)=$



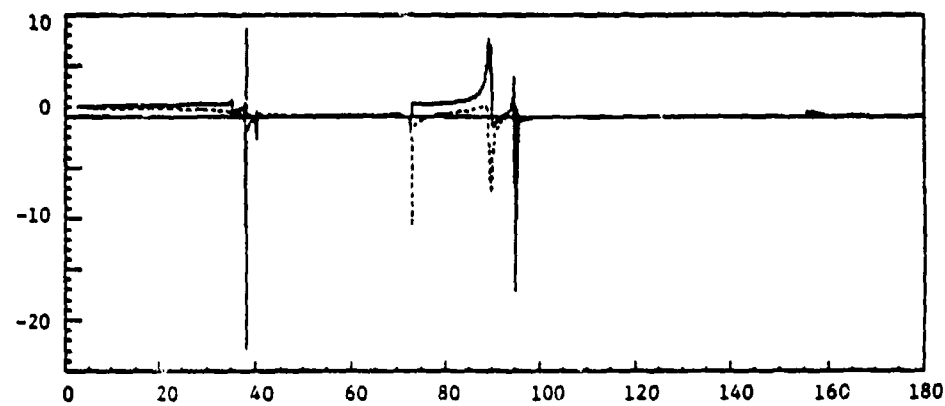
$S_R(:,2) =$



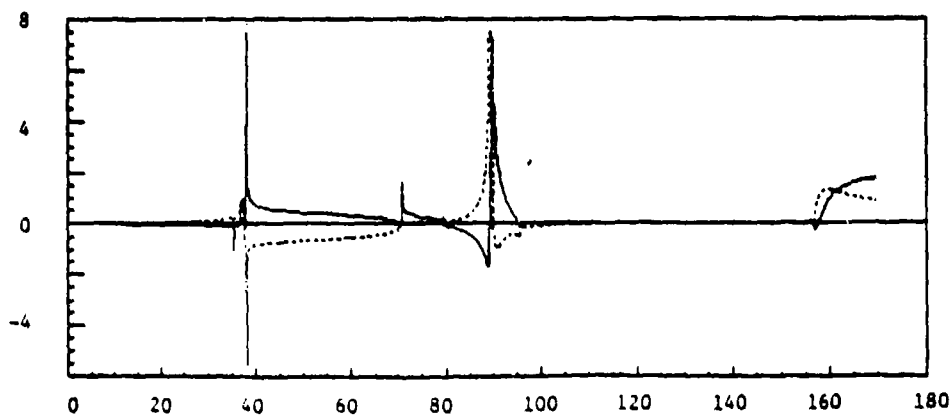
$S_R(2,2) =$

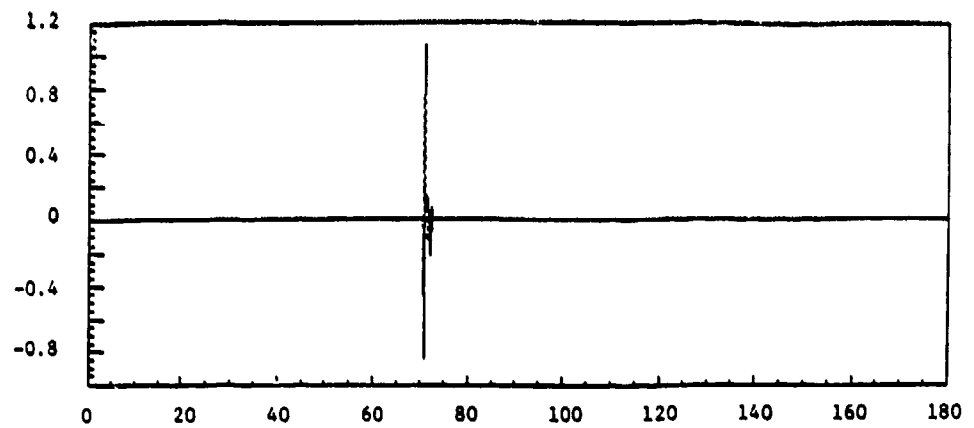
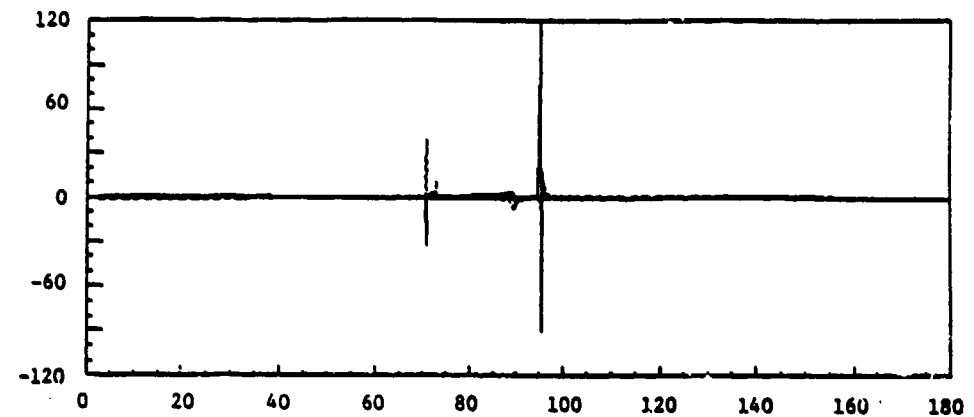
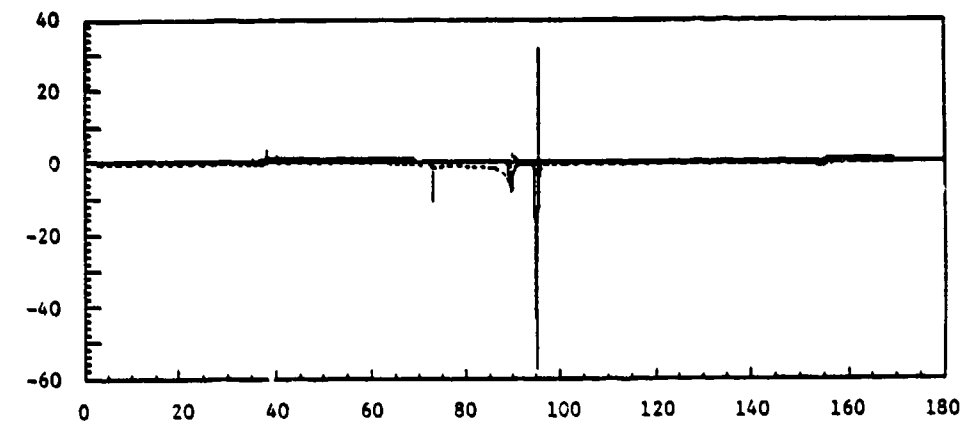
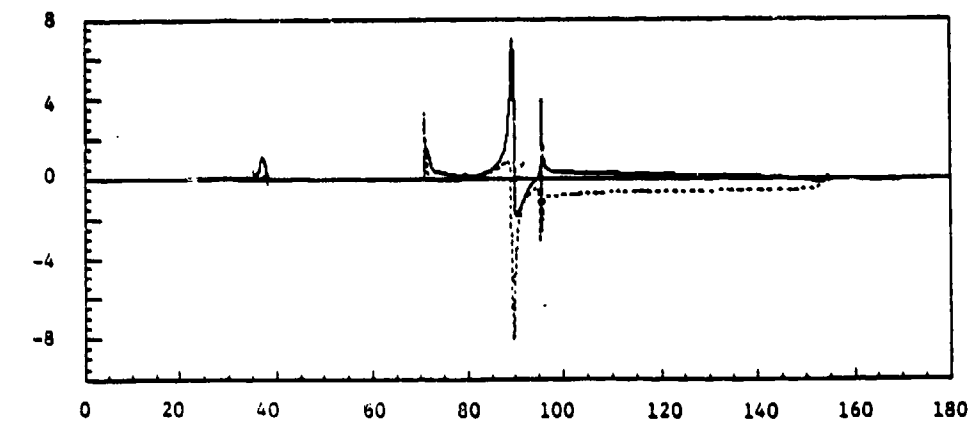


$S_R(3,2) =$

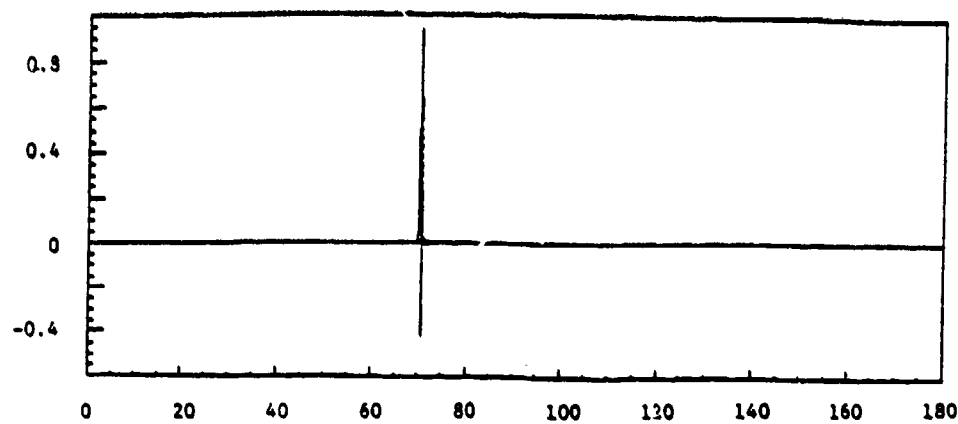


$S_R(4,2) =$

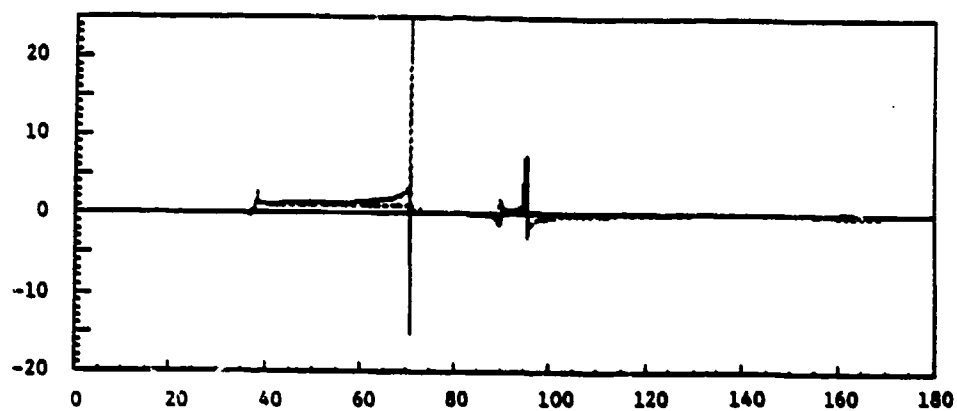


$S_R(1,3)=$

 $S_R(2,3)=$

 $S_R(3,3)=$

 $S_R(4,3)=$


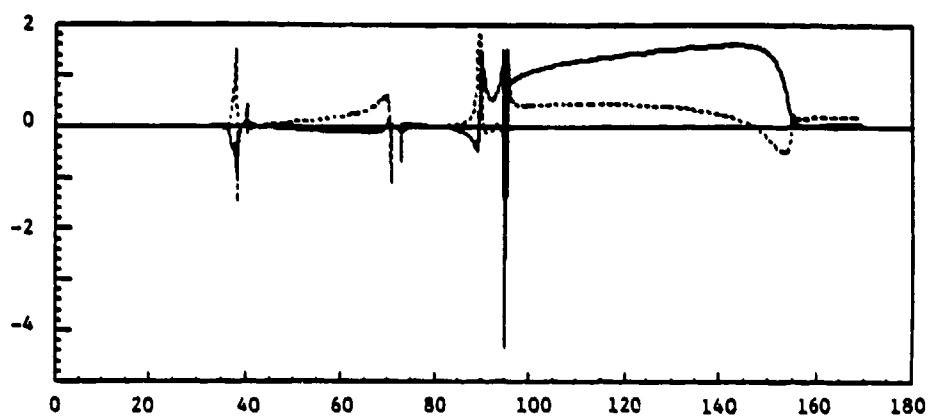
$S_R(1,4) =$



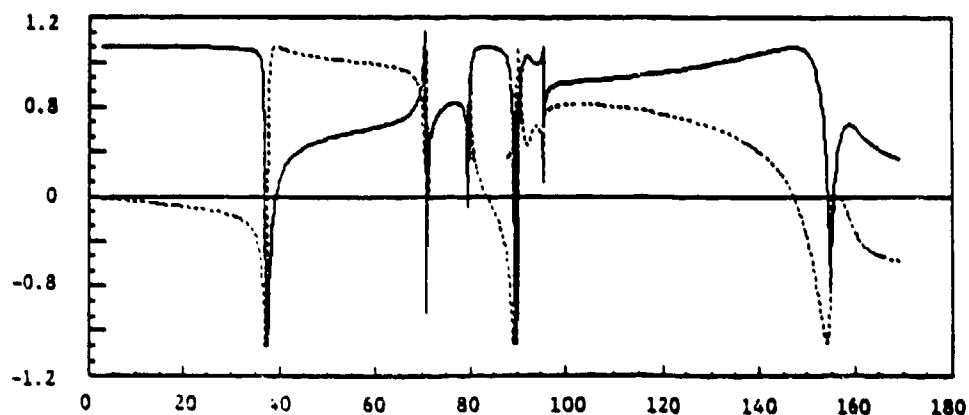
$S_R(2,4) =$



$S_R(3,4) =$



$S_R(4,4) =$



Joel Signorelli* and A.H. von Flotow†
Massachusetts Institute of Technology
Cambridge, Massachusetts

Abstract

Wave propagation in periodic truss-work structures is analytically investigated. Transfer matrix methods are applied to the analysis of a truss beam. The results, with members modeled as rods with pinned joints, agree well with results obtained from an equivalent continuum model of the same structure. Use of beam models for the members, including bending, shows that the pinned rod model loses fidelity above the first resonant frequency of lateral motion of the members. The truss, modeled with beam members exhibits complicated mechanical filtering properties. Fixed and free boundary conditions are converted to reflection matrices. The phase closure principle is invoked to predict natural frequencies of a fixed-free portion of the truss. It is found that closely spaced resonant frequencies are not identified by this method. Computed results show subtle erroneous characteristics which are attributed to numerical effects.

1. Background

Many large space structures will be constructed, in part, of truss-work components. A current example is NASA's space station. Truss structures generally consist of an assemblage of identical bays and are thus spatially periodic. Periodic structures have long been known to act as mechanical filters. In order to gain more insight and understanding as to how such filtering properties can be exploited in the dynamics and control of large space structures, this paper examines wave propagation in several mathematical models of a truss beam.

Any survey of the literature of wave propagation in periodic structures must mention the book by Brillouin¹. Since Brillouin's book, many papers have treated wave propagation in periodic structures, primarily mono-coupled systems (systems with one coupling coordinate linking neighboring bays). Models used include spring-mass², strings and rods³, and periodically constrained beams⁴. These works have all verified Brillouin's dictum paraphrased here: "A one-dimensional periodic waveguide supports as many travelling wave modes in each direction as the (minimum) number of coupling coordinates between bays. Each wave-mode exhibits alternating (possibly overlapping) frequency ranges of pass-band and stop-band behavior. The number of pass bands is equal to the number of degrees of freedom within each bay." Few works have dealt with multi-coupled periodic wave guides. Mead has approached the problem mathematically, both for general situations⁵, and for a specific model (Timoshenko beams with periodically attached inertias)⁶. Hodges, Powers and Woudhouse have reported theoretical and confirming experimental work on wave propagation in periodic, rib-stiffened cylindrical shells⁷. Eatwell⁸ has considered wave

propagation in periodic fluid loaded plates. In each study, the introduction of multiple coupling coordinates between bays has permitted a new type of travelling wave mode; the 'complex mode' which both travels and is spatially attenuated. Such modes were also discovered in this work, in which four coupling coordinates between adjacent truss bays were used.

A structural analysis is incomplete without consideration of boundary conditions. In this paper, conventional boundary conditions for truss beams (equations relating forces and deflections of boundary points) are converted to wave-mode coordinations. The result is a matrix of frequency dependent reflection coefficients at each boundary.

This paper then invokes the phase-closure principle to define and calculate natural frequencies: "Resonance occurs at those frequencies at which each propagation path closes on itself with total change of $2k\pi$ ($k=1,2,\dots$) after one circumnavigation." The truss is thus modeled as a multi-mode waveguide, terminated by reflection matrices, rather than an assemblage of lumped parameter member models.

2. Wave Modes; Definition and Derivation

A wave mode, on a one-dimensional waveguide is described by both a wave-mode eigen-shape, and by an associated propagation coefficient. The eigen-shape is that unique mix of cross-sectional variables which propagates with constant relative value and phase along the member. The associated propagation coefficient specifies the wavelength (or, equivalently, phase speed) with which propagation occurs. A tensioned cable, for example, can support (in the classic approximation) three wave modes in each direction; one axial with a velocity of $\sqrt{EA/\mu}$, the other two are lateral with velocity of $\sqrt{T/\mu}$. (EA is axial stiffness, T is tension, μ is linear mass density).

Note that, in agreement with Brillouin's quote given in the introduction, these three wave modes correspond to the three modeled deflection coordinates.

Wave modes in periodic structures can be analogously defined. We select any reference cross-section in each bay, introduce kinematic assumptions, and assign a number of deflection variables to define the deformation state of that cross-section. (Mead has shown that a wise choice for the reference cross-section is the one that minimizes the number of deflection variables required). A wave mode is then defined as that mix of cross-sectional variables which repeat with fixed relative amplitude and phase in each subsequent bay along the structure. A corresponding propagation coefficient per bay defines wavelength and propagation speed.

*Graduate Student
†Assistant Professor,
Aeronautics and Astronautics
Members AIAA

Wave Modes in a Truss Beam

This paper investigates the travelling wave modes supported by two models of a truss beam constrained to move in a plane. Fig 1 is a sketch of the beam and of the chosen repeating element.

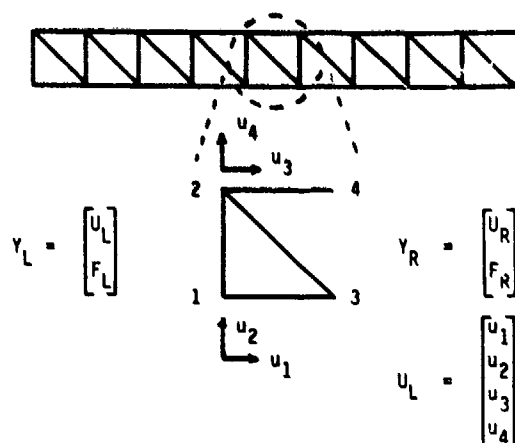


Fig 1 State Vectors Associated with One Bay of a Periodic Truss

The members are modeled as being pinned at the junctions, thus four deflections are required to define the deformation of the coupling cross-section. If one introduces the corresponding four coupling forces, and groups the coupling deflections and forces into a "cross-sectional state vector", then the dynamics of the bay can be described by a transfer matrix relation;

$$Y_R = [T] Y_L \quad (1)$$

This bay transfer matrix is square, with dimension 8.

This transfer matrix can be obtained in many ways. In this analysis, for purposes of direct comparison with a conventional finite element analysis, we derive $T(\omega)$ by exact numerical dynamic condensation of a finite element model of the bay.

Two bay models are used, each based upon a particular finite element discretization. Each model yields a mass and stiffness matrix;

$$[K - \omega^2 M] \begin{bmatrix} U_L \\ U_I \\ U_R \end{bmatrix} = \begin{bmatrix} F_L \\ F_I \\ F_R \end{bmatrix} \quad (2)$$

which is then partitioned into left, right and internal degrees of freedom and manipulated to yield the transfer matrix:

$$\begin{bmatrix} D_{LL} & D_{LI} & D_{LR} \\ D_{IL} & D_{II} & D_{IR} \\ D_{RL} & D_{RI} & D_{RR} \end{bmatrix} \begin{bmatrix} U_L \\ U_I \\ U_R \end{bmatrix} = \begin{bmatrix} F_L \\ F_I \\ F_R \end{bmatrix} \quad (3)$$

$$\begin{bmatrix} D_{LL} - D_{LI} D_{II}^{-1} D_{IL} & -D_{LI} D_{II}^{-1} D_{IR} \\ -D_{RI} D_{II}^{-1} D_{IL} & -D_{RI} D_{II}^{-1} D_{IR} + D_{RR} \end{bmatrix} \begin{bmatrix} U_L \\ U_R \end{bmatrix} = \begin{bmatrix} F_L \\ F_R \end{bmatrix} \quad (4)$$

$$\begin{bmatrix} A & B \\ C & D \end{bmatrix} \begin{bmatrix} U_L \\ U_R \end{bmatrix} = \begin{bmatrix} -F_L \\ F_R \end{bmatrix} \quad (5)$$

(Negative values of F_L have been taken for compatibility of the transfer matrix and finite element analysis force coordinate definitions.)

$$\begin{bmatrix} U_R \\ F_R \end{bmatrix} = \begin{bmatrix} -B^{-1} A & -B^{-1} \\ C - DB^{-1} A & -DB^{-1} \end{bmatrix} \begin{bmatrix} U_L \\ F_L \end{bmatrix} \quad (6)$$

$$Y_R = [T] Y_L \quad (7)$$

The first bay model uses 4 pinned-rod elements and yields 8 by 8 mass and stiffness matrices. Thus, no internal degrees of freedom need be eliminated. The second bay model includes member bending effects. Eight beam elements are used, as sketched in Figure 2.

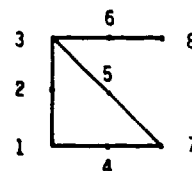


Fig 2 Finite Element Model of Bay used to Include Member Bending Effects

Nodes 2,4,5 and 6 are clamped, nodes 1,3,7 and 8 are pinned. The resulting 28-degree-of-freedom finite element model thus includes 20 internal degrees of freedom. Note that only the linear deflections of modes 1,3,7 and 8 are external degrees of freedom; the resulting transfer matrix is again 8 by 8.

Wave Modes Properties Inferred from The Transfer Matrix

A wave propagating along a periodic structure can be characterized by,

$$Y_{i+1} = \xi Y_i \quad (8)$$

indicating that the state at station $i+1$ is the state at station i multiplied by a factor ξ . This, together with the transfer matrix relation

$$Y_{i+1} = [T] Y_i \quad (9)$$

forms an eigenvalue problem for ξ . The eigenvalues are generally complex and occur in ξ and $1/\xi$ pairs, corresponding to identical waves propagating in opposite directions [Eigenvalues of a symplectic matrix occur in inverse pairs].

For each wave mode there are frequency regions in which the wave will propagate without attenuation ($|\xi| = 1$ (pass bands) and regions in which the wave is attenuated ($|\xi| < 1$ (stop bands).

The relation between ξ and $1/\xi$ can be seen by constructing a plot of the ξ plane (Fig 3).

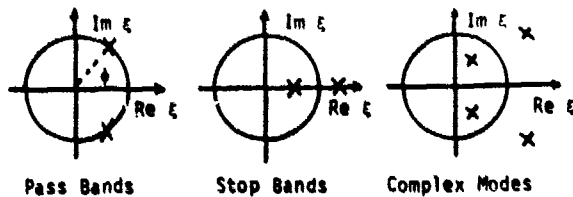


Fig 3 The ξ Plane

For a given frequency, values of $|\xi|$ which lie on the unit circle are in a pass band. Those inside the unit circle are positive-going waves in a stop band while those reflected outside the circle are negative-going waves in a stop band. Values of $|\xi|$ which lie in the interior (exterior) of the circle, but not on the real axes, are termed complex wave modes. As a function of frequency, the eigenvalues move about the plane, continually changing magnitude and phase.

In the absence of damping, the transfer matrix, T , is real, thus its eigenvalues will be real or members of a complex conjugate pair. Complex modes thus occur only in groups of four; wave mode interaction is necessary. Mono-coupled systems (with 2 by 2 transfer matrices) cannot support complex wave modes.

Particular results were calculated for a truss beam used in prior studies^{1,10}. The bay members were assumed to have no structural damping, a bending stiffness $EI = 2.8263e6$ lb-in², mass per length $m = 1.18163e-4$ slug/in, an axial stiffness of $EA = 4.361e6$ lb and longeron and batten length of 55.8 in. Mills' developed continuum models for this truss, a Timoshenko beam model for bending, and a rod model for extension. Mills' equivalent values for the truss are: axial stiffness $EA = 8.722E6$ lb, bending stiffness $EI = 6.5968e9$ lb-in², shear stiffness $GA = 1.8693e6$ lb, mass per length $m = 4.852e-4$ lb-s²/in² and inertia per length $\rho I = 7.19438$ lb-s².

Figures 4-8 present dispersion curves and wave mode shapes for the four right-going wave modes. Comparison with predictions of the continuum model is provided. Wave mode shapes were derived from the transfer matrix eigenvectors. One wavelength of a wave mode is shown at a given frequency.

At low frequencies the first wave mode shape exhibits a global sinusoidal response and is thus labeled as the bending mode. The dispersion curves for the bending mode indicate complicated mechanical filtering of this mode as a function of frequency. At low frequencies the mode is in a pass band (propagation with no attenuation). The mode shape shows mostly global response. As the first resonant frequency of the bay diagonals approaches, the response now becomes more localized in the bay diagonals. At 35 Hz (the diagonal members' first pinned-pinned resonant bending frequency) the mode becomes complex for a narrow bandwidth, both propagating and attenuating. At 40 Hz the mode enters a stop band, a region in which the wave mode will not propagate. The sharp spike at 70 Hz corresponds to the first pinned-pinned resonance of the bay longerons. The mode once again becomes complex after this resonant frequency. For higher

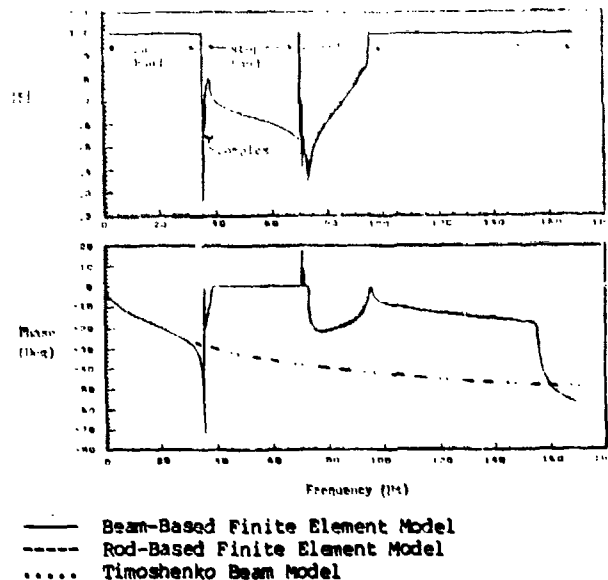
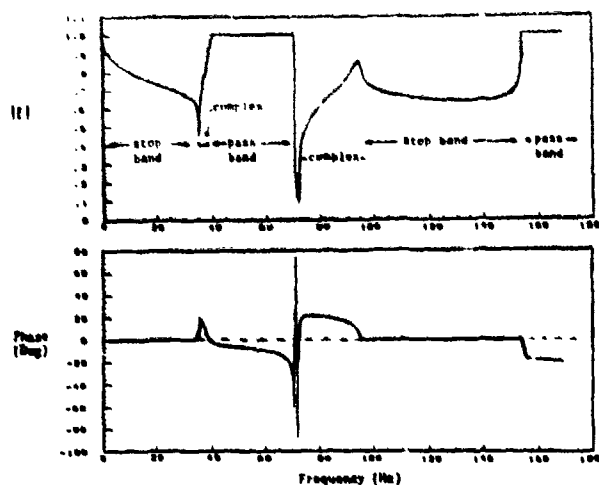


Fig 4 Dispersion Curves and Wave Mode Shapes for the Bending Mode

frequencies, the truss response is no longer global, but becomes localized in the truss members.

Predictions based on Timoshenko beam theory, and results of the analysis with pinned rod members compare almost exactly, but diverge from those of the more complete model at higher frequencies. Internal resonances completely dominate the motion at these frequencies.



— Beam-Based Finite Element Model
 - - - Rod-Based Finite Element Model

Wave mode shapes calculated from the beam-based finite element model:

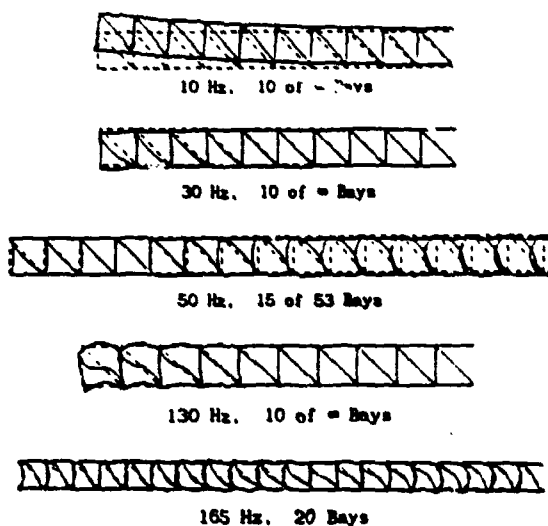
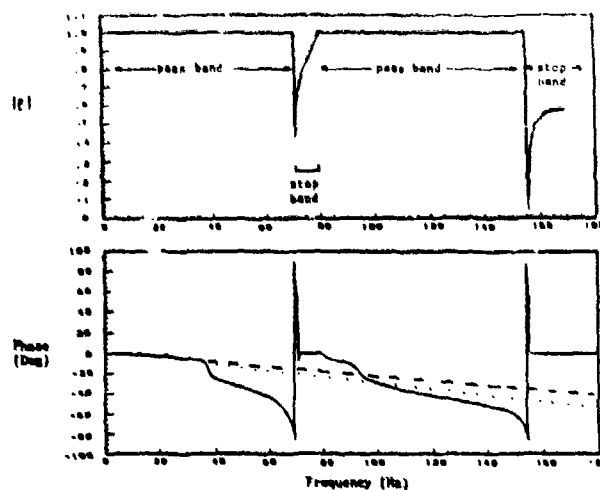


Fig 5 Dispersion Curves and Wave Mode Shapes for the Shear Mode

Unlike the bending mode which begins in a pass band, the second mode examined begins in a stop band. This mode initially has zero phase (non-propagating) and does attenuate. These properties are similar to those of the Timoshenko beam shear mode, which is a near field below $\omega = \sqrt{GA/\rho I} = 368$ Hz. Because of this initial similarity, this mode is labelled the shear mode. Like the bending mode, the shear mode goes through alternating stop and pass bands, separated by bands in which the mode is complex. Below 35 Hz, the wavelength is infinite. The complex mode shapes (range 75-95 Hz) are identical to those of the bending mode, since these modes couple to create the complex modes in this frequency range. Near 130 Hz, the second pinned-pinned resonance of the diagonals appears in the mode shape plots.



— Beam-Based Finite Element Model
 - - - Rod-Based Finite Element Model
 Timoshenko Beam Model

Wave mode shapes calculated from the beam based finite element model:

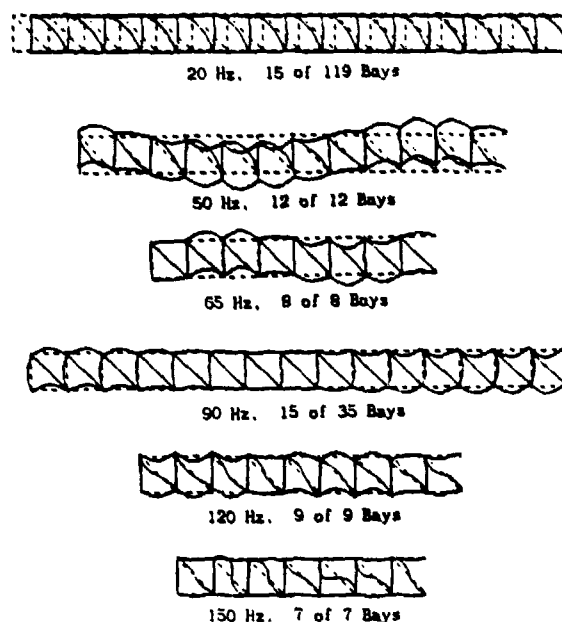
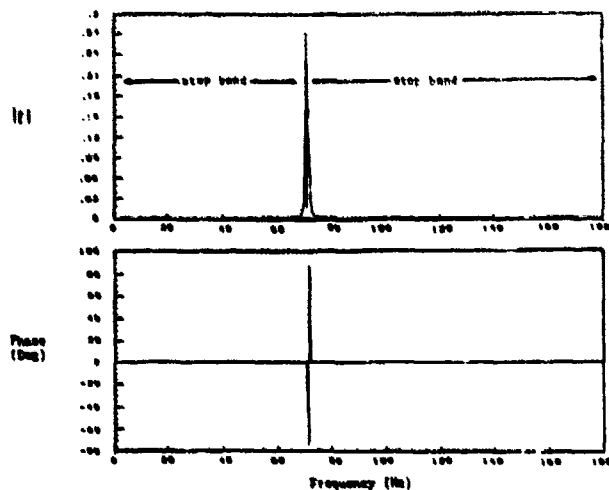


Fig 6 Dispersion Curves and Wave Mode Shapes for the Compression Mode

The low-frequency behavior of this wave mode is essentially just compression-extension and all models predict similar response. This mode is characterized by quite large pass bands separated by narrow stop bands. Complex mode formation for this mode only occurs between 70.8 and 71.3 Hz. Near 50 Hz, the compression/extension response is suppressed by quite active longeron and diagonal response. Only the horizontal longerons remain in bending by 65 Hz. Near 150 Hz, the response is confined to the second pinned-pinned resonance of the diagonals.



Wave mode shapes calculated from the beam-based finite element model:

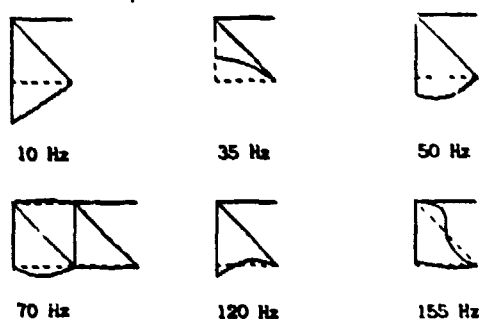


Fig 7 Dispersion Curves and Wave Mode Shapes for the Evanescent Mode

The magnitude and phase of the fourth mode over the frequency range investigated is essentially zero. This indicates that the mode 'dies out quickly' so that the response can be considered to be confined to a single bay. With the exception of a very narrow pass band at 72 Hz (the first pinned-pinned diagonal resonance of the diagonals), this mode is always in a stop band. The response of the first bay as a function of frequency is shown above. Between 71 and 72 Hz, the evanescent mode is complex. There is no analogous wave mode in the continuum model.

Complex Mode

Complex wave modes have not received much attention in the structural dynamics literature, and appear to have been mentioned in only three published papers^{6,7,8}. The pinned-beam truss model reveals two frequency bands in which wave modes are complex--from 35 to 40 Hz and from 72 to 95 Hz. If the dispersion curves of the bending and shear modes are plotted together, some interesting observations can be made (Fig 8).

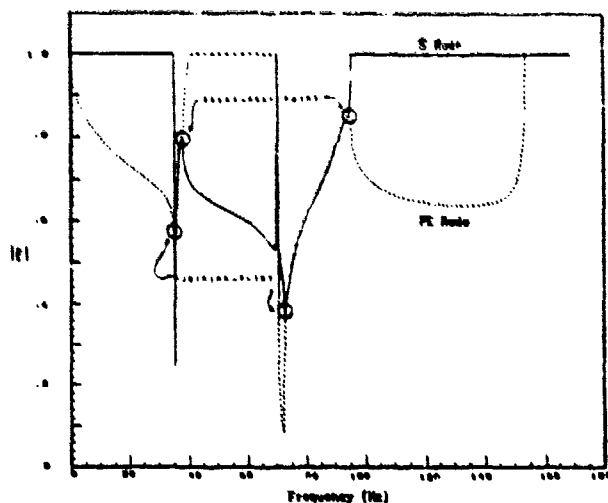


Fig 8 A Complex Mode Coupling Between the Bending and Shear Modes

Both modes are complex throughout the same bandwidths (35-40 Hz and 75-95 Hz). In addition, the magnitude of the eigenvalues are exactly the same. The two wave modes couple throughout these regions, producing the complex modes. The complex modes begin at the first pinned-pinned frequencies of the diagonals and longerons at a joining point. At the break-away points the modes once again take on separate character.

The frequency range between 70 and 85 Hz is full of complex modes (Fig 9). Within this range, there are three pairs of right-going complex modes. The bending and compression modes couple for a very short band centered at 71.2 Hz. At 71 Hz even the evanescent mode forms a complex mode with the shear mode. But the longest coupling is between the bending and shear modes between 72.5 and 95 Hz. Note that the coupling is triggered near the first pinned-pinned frequency of the longerons.

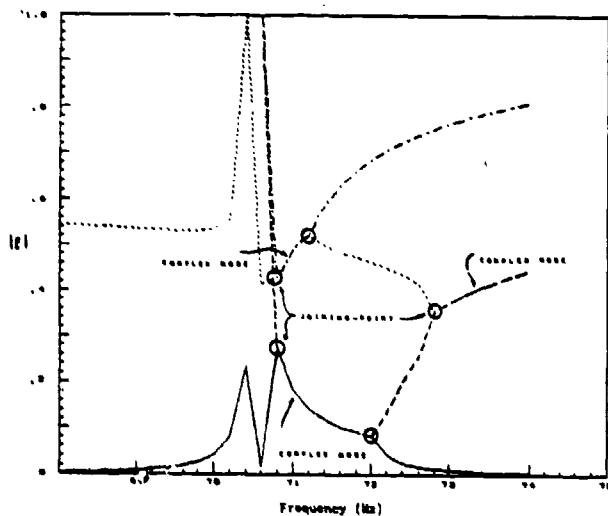


Fig 9 Complex Mode Coupling About 70 Hz

Wave Mode Power Flow

The preceding figures show that each wave mode has frequency bands in which there is propagation, bands in which there is no propagation, and bands in which there is both attenuation and propagation (the complex modes). Intuition might tell us that when a wave propagates, it transmits energy along the structure and when it does not propagate, energy cannot move. But what about complex modes which share aspects of both propagating and attenuating waves? Do complex modes transmit energy along the structure? And if so, how is this possible if there is no damping in the system? Mead addressed this point in 1973 and found theoretically that there is no net power flow in these modes.

Instantaneous power is the product of the instantaneous velocity and force. While noting that these are vector quantities, this becomes,

$$\begin{aligned} P(t) &= \text{Re}(V e^{i\omega t}) \cdot \text{Re}(F e^{i\omega t}) \\ &= \text{Re}(i\omega u e^{i\omega t}) \cdot \text{Re}(F e^{i\omega t}) \\ &= \text{Re}(i\omega u e^{i\omega t}) \cdot \text{Re}(F e^{i\omega t}) \end{aligned} \quad (10)$$

which can be expanded to

$$\begin{aligned} P(t) &= \text{Re}(i\omega(u_R + iu_I)(\cos\omega t + i\sin\omega t)) \cdot \\ &\quad \text{Re}((F_R + iF_I)(\cos\omega t + i\sin\omega t)) \end{aligned} \quad (11)$$

The average power flow over one period, $T = 2\pi/\omega$, is defined as,

$$P_{\text{avg}} = 1/T \int_0^T P(t) dt \quad (12)$$

After integrating over one period we get,

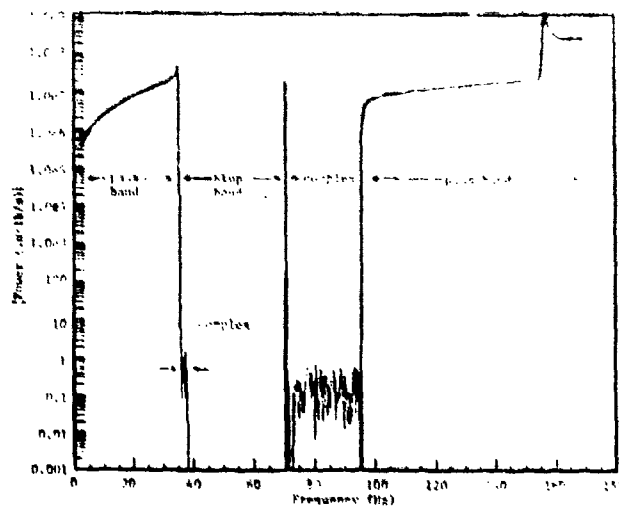
$$P_{\text{avg}} = 1/2 \omega(u_R \cdot F_I - u_I \cdot F_R) \quad (13)$$

This then gives us the average power flow for each wave mode, were it alone present in the structure. Interaction between wave modes, creating other forms of power flow, is also possible.

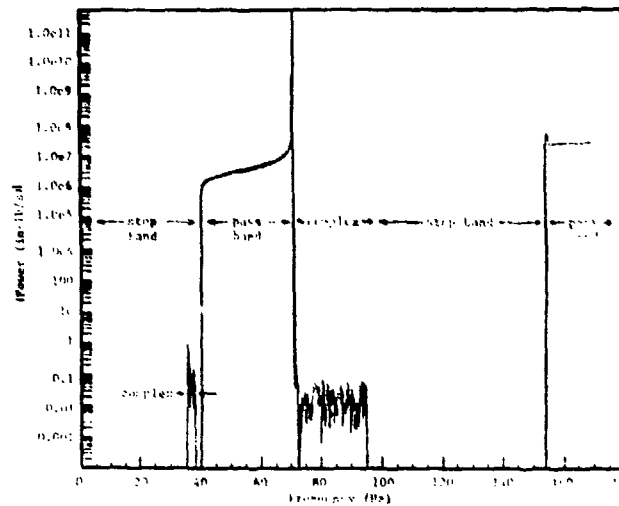
Power flow was calculated for the eight wave modes present in a pinned beam truss. The eigenvectors used in Eqn 13 were normalized so that the axial-displacement of node one was unity (see Figure 1).

Figs 10 shows plots of the log of the magnitude of power flow in the four left-going wave modes.

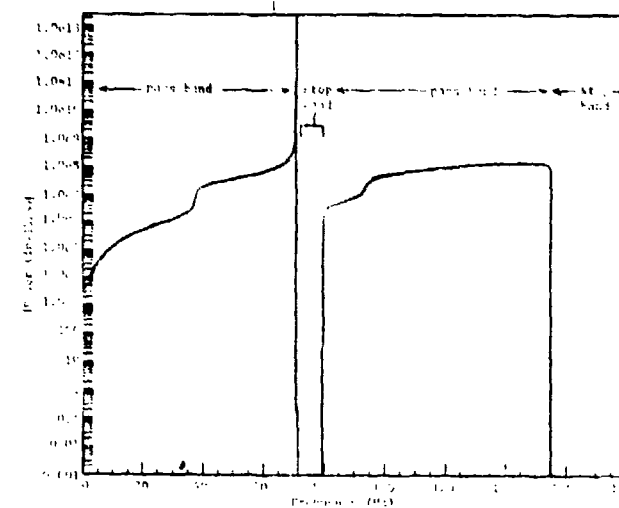
As expected, the bending, shear, and compression modes show power flow in pass bands—power flow in each left and right-going brother wave pair being equal and opposite. No power flow occurs in stop bands. Complex mode regions of the bending and shear modes show up as 'noisy' data on the plots. But the magnitude of the power flow in these complex modes is equal and opposite. Thus it would appear that the net power flow in a right-going (left-going) complex mode pair is zero. Mead, however, claims that the net power flow in a single complex mode is zero. It is as yet, uncertain whether the equal and opposite power flow is actual or the result of numerical round-off.



Bending Mode



Shear Mode



Compression Mode

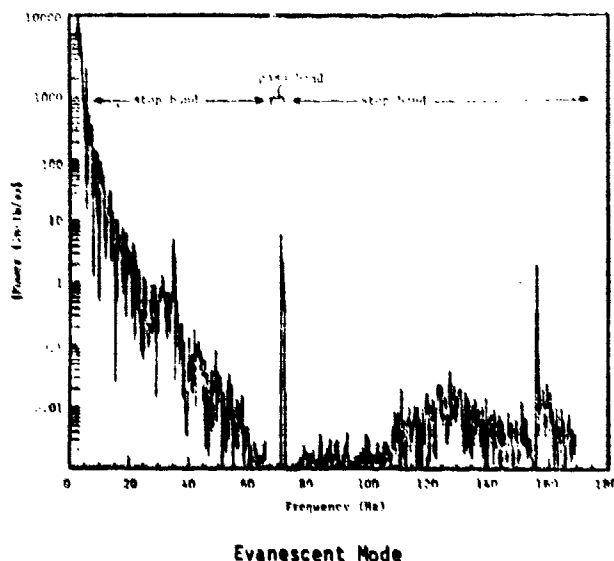


Fig 10 Magnitude of Power Flow in the Left-Going Modes

Power flow in the evanescent mode is also contrary to expectation. With the exception of a small pass band about 70 Hz, the evanescent modes are in a stop band throughout all of the bandwidth investigated. Because of this, one would expect there to be no net power flow. Since Figure 10 suggests that power is flowing, numerical effects are suspected, and are presently being investigated.

3. Wave Mode Boundary Conditions

All of the analysis of Chapters 3 and 4 was performed without regard to truss boundary conditions. In order to consider wave mode propagation in a finite length truss, boundary conditions must be taken into account. The concept of a scattering matrix will be used to give the infinite truss closure.

The cross-sectional state vector, Y , may be transformed into wave mode coordinates by the transformation

$$Y = v(\omega) W \quad (14)$$

where W is the cross-sectional state vector in wave mode coordinates, and v are the eigenvectors of the transfer matrix T .

The cross-sectional state vector W can be partitioned into components which represent right-going waves, w^+ , and left-going waves, w^- .

$$W = \begin{bmatrix} w^+ \\ w^- \end{bmatrix} \quad (15)$$

We also label wave modes which arrive at a member boundary, a , and those which depart a boundary, d . The relationship between the arriving and departing wave modes at beam boundaries is depicted in Fig 11.



Fig 11 - Representation of Arriving and Departing Wave Modes at Beam Boundaries

a and d are related by the wave mode eigenvalues,

$$\begin{aligned} a_R &= \epsilon^n d_L \\ a_L &= \epsilon^n d_R \end{aligned} \quad (16)$$

where n is the number of bays

The boundary conditions at the ends of the truss may be written as,

$$[B(\omega)] Y = F_{\text{ext}}(\omega) \quad (17)$$

there the boundary conditions, B , and external forces, F , may be functions of frequency. In wave mode coordinates this becomes

$$\begin{bmatrix} B_a(\omega) & B_d(\omega) \end{bmatrix} \begin{bmatrix} a \\ d \end{bmatrix} = F_{\text{ext}}(\omega) \quad (18)$$

A partial inversion yields the boundary condition in casual form,

$$d = -B_b^{-1}(\omega) B_a(\omega) a + B_b^{-1} F_{\text{ext}} \quad (19)$$

$$\text{or,} \quad d = S(\omega) a + B_b^{-1} F_{\text{ext}} \quad (20)$$

where $S(\omega)$ is termed the scattering matrix at the boundary. With no external forcing this becomes,

$$d = [S(\omega)] a \quad (21)$$

Components of the scattering matrix are complex, frequency dependent reflection coefficients. The second term of Eqn 20 is the wave mode generating matrix which indicates how external forces at the boundary generate outgoing wave modes.

Derivation of the Scattering Matrices for a Pinned-Free Truss Beam

The boundary conditions for the pinned end of our truss (taken to be the left end) are

$$\begin{bmatrix} 1 & 0 \\ 1 & 0 \\ 1 & 0 \\ 1 & 0 \end{bmatrix} \begin{bmatrix} a \\ d \end{bmatrix} = 0 \quad (22)$$

Following the preceding derivation, we obtain the scattering matrix given in Figure 12. More detailed plots of the individual entries are available in reference 11.

Application of the free boundary conditions at the right end requires a bit more care. These

$$d_r = [S_r(\omega)] a_r \text{ where } [S_r(\omega)] =$$

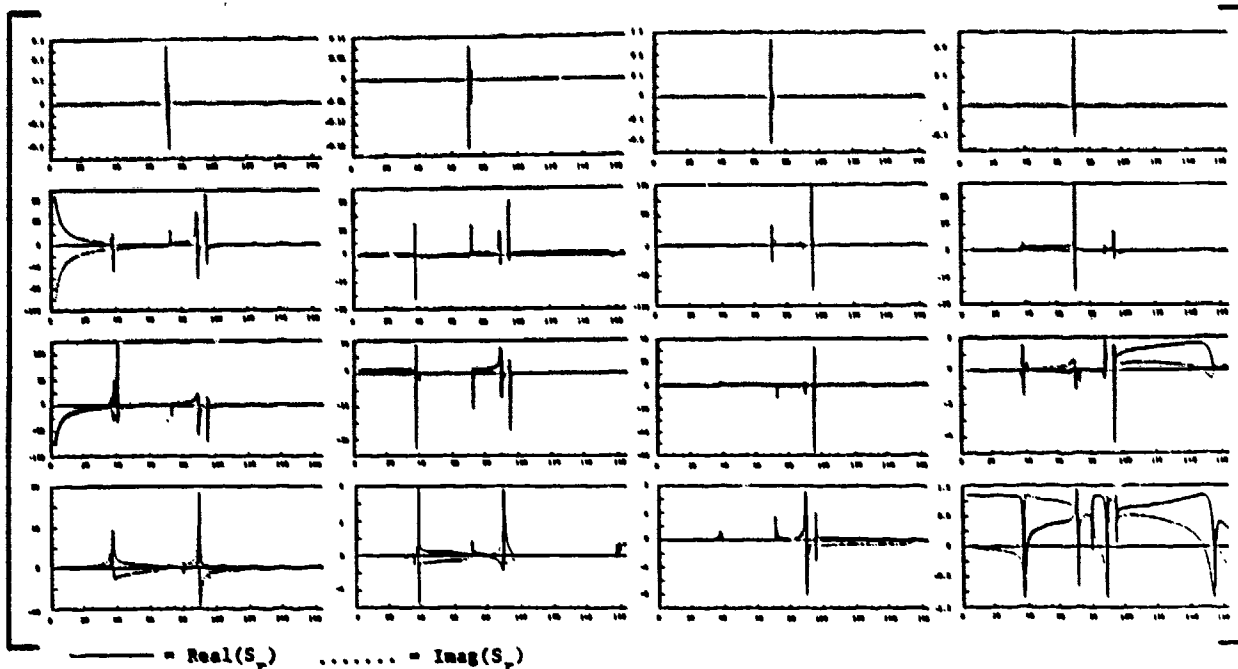
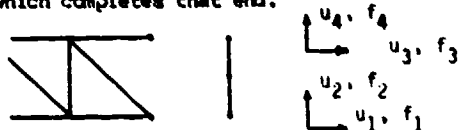


Fig 12 Reflection Coefficients for Free End of Truss

boundary conditions must include the effect of the member which completes that end.



This member has a force-deflection relation

$$\begin{bmatrix} A & B \\ C & D \end{bmatrix} \begin{bmatrix} u_L \\ u_R \end{bmatrix} = \begin{bmatrix} f_L \\ f_R \end{bmatrix} \quad (23)$$

Where $[A \ B; C \ D]$ can be obtained from dynamic condensation of a finite element model of that member.

In this analysis, the member was modeled by 2 beam elements, thus the 9 dimensional finite element model must be reduced to the form equation by dynamic condensation of five internal degrees of freedom.

Checks can be made on the validity of these reflection coefficients by examining limiting cases of these values. At low frequencies the bending mode resembles a beam in bending, while the compression mode resembles a rod in tension/compression. Since the wave mode eigenvectors have been normalized with the axial deflection of the first node equal to unity, checks can be made on the reflection coefficients of the compression mode at both ends. The deflection-normalized reflection coefficient of a

compression wave is well known to be 1 for a free-end and -1 for a fixed end. The $S(4,4)$ plot of Figure 12 indicates that the reflection coefficient for the compression mode at the fixed boundary tends to -1.0, while $S(4,4)$ at the free end tends to 1.0. The low-frequency limiting behavior of these two terms is thus correct.

4. Natural Frequencies by Phase Closure

The phase closure principle states that natural frequencies occur when all wave modes complete a circumnavigation of the structure with a total phase change of $2K\pi$. For the case of an n-bay truss, the wave modes arriving and departing the two ends are related by (Fig 11)

$$\begin{aligned} a_r &= \xi^n d_L \\ a_L &= \xi^n d_R \end{aligned} \quad (24)$$

where ξ is a diagonal matrix of eigenvalues associated with the right-going wave modes. Eqn 21 can be written for both boundaries as,

$$\begin{aligned} d_L &= [S_L] a_L \\ d_R &= [S_R] a_L \end{aligned} \quad (25)$$

By repeated substitutions of Eqns 24 and 25, we obtain a_R after one circumnavigation of the beam,

$$a_R = \xi^n S_L \xi^n S_R a_R \quad (26)$$

Resonance occurs when this relation is an equality;

$$[\xi^n S_L \xi^n S_R - I] = 0 \quad (27)$$

The only non-trivial way this can be true is if the determinant of Eqn 27 is zero. Therefore,

$$\det [\zeta^N S_L \zeta^N S_R - I] = 0 \quad (28)$$

is satisfied at a truss resonance.

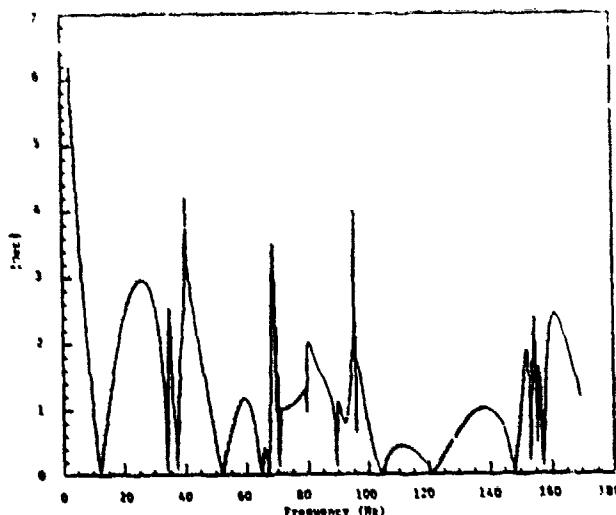
Notice that, by replacing only one value in the formulation (the number of bays), the natural frequencies for a truss with an arbitrary number of bays can be determined "quick as a bunny." The order of the problem does not increase with increasing number of bays, but remains that of the transfer matrix.

Fig 13 is a plot of the determinant of Eqn 28 for a seven bay, pinned beam truss with one free and one pinned end. The natural frequencies of the truss can be identified whenever Eqn 28 tends to zero. Resonant frequencies determined by this phase closure method are listed in Fig 13. These frequencies reproduce those determined by a finite element analysis of the same truss except whenever the modes are closely spaced. The finite element analysis obtains five modes within the 35.13 - 35.31 Hz bandwidth while the phase closure method locates only two. This remains true even when frequency steps of 0.001 Hz are used in Eqn 28. The same results also occur about 70 and 154 Hz. Because the isolated modes are so accurately determined, one may be tempted to attribute the phase closure method's failure on numerical round-off. This, however, remains to be shown.

5. Unmodeled Effects

Linear behavior has been assumed. An actual spacecraft truss may exhibit significant non-linearities, particularly if it is deployable and thus has relatively loose joints. The effects of such joint non-linearities upon the results presented here are not known. It seems plausible that the situation would become even more complex, and that the pattern of stop and pass bands, at any given response amplitude, would suffer some sort of blurring.

Even were an actual truss linear, it would not be perfectly periodic. Small, unintentional variations from perfect periodicity would be present. The statistical effect on wave propagation of such random variations in bay properties is the subject of reference¹². This reference shows that the first-order effect is that all wave modes at all frequencies will be spatially attenuated. The degree of attenuation is proportional to the "randomness" and inversely proportional to the "coupling strength" between bays. (Suitable non-dimensional measures of randomness and coupling strength must be introduced). The physical exploration for such localization is that the coherent wave is scattered into incoherence; the vibrational energy is transferred into a spatially localized response. We thus anticipate that an actual truss (as compared to its idealized mathematical model) will exhibit the characteristics described by this paper only approximately. Real-world effects (non-linearity, disorder, and others) will tend to modify this response (especially at higher frequencies) to be more of an ill-defined local rattle that slowly appears and disappears in local portions of the structure.



Present Analysis	Finite Elements		
12.10	12.10	n/i	70.51
33.97	33.97	n/i	70.52
35.13	35.13	n/i	70.54
n/i	35.25	n/i	70.54
n/i	35.29	n/i	70.55
?	35.30	n/i	70.57
n/i	35.31	n/i	70.59
37.16	37.16	n/i	70.59
51.04	51.04	n/i	70.59
64.51	64.51	89.23	89.23
67.00	67.00	103.83	103.89
?	69.50	121.14	121.12
n/i	70.04	147.91	147.91
70.22	70.22	153.45	153.45
n/i	70.39	?	154.32
n/i	70.40	n/i	154.57
n/i	70.43	n/i	154.69
n/i	70.47	155.28	155.28
n/i	70.47	157.07	157.07
n/i	70.49		

n/i = not identified

? = possible identification

Figure 13 - Natural Frequencies Obtained by Phase Closure

6. Conclusions

This research computationally investigated wave mode propagation in two-dimensional, periodic truss structures. Some conclusions based on this research follow.

1) The transfer matrix technique proved useful in that the dynamics of a complete truss beam were determined by analysing only one of the periodic elements. Conventional analysis tools such as the finite element analysis become computationally cumbersome as the number of degrees of freedom

needed to model the structure increases. In the transfer matrix method the order of the problem depends only on the order of one of the cross-sectional state vector.

2) The method of obtaining natural frequencies of the truss by sequential multiplication of the transfer matrix and subsequent application of boundary conditions is only practical for cases in which the eigenvalues of the transfer matrix are not large.

3) The results obtained by examining a pinned rod truss by transfer matrices closely match the results obtained by continuum models of the same structure.

4) As with continuum models of the truss structure, the pinned rod truss loses its fidelity at the first resonant frequency of the truss members. The rod modelling masks all local member dynamics that would be present if member bending were modeled.

5) The pinned beam truss exhibits complicated mechanical filtering properties.

6) Complex modes must form in pairs and cannot exist alone. Thus in a pinned beam truss, there must be at least four (eight, twelve etc.) or more complex modes present in order for any to exist at all. Mono-coupled systems cannot support complex wave modes.

7) Complex mode formation is initiated at member resonant frequencies. No explanation could be found for termination of complex mode coupling.

8) Net power flow in a right-going (left-going) complex mode pair is zero.

9) Several results were obtained that indicate there may be numerical round-off errors in this formulation.

a. Power flow was evident in the evanescent modes throughout much of the bandwidth examined.

b. Shear force terms in the eigenvectors of modes in stop bands are not invariant under a coordinate transformation.

c. Closely spaced natural frequencies of the truss are not detected when analysed by phase closure.

10) By using the phases closure principle and the eigenvectors of the transfer matrix in wave mode coordinates, the restriction imposed in 2) can be circumvented. In fact, by changing just one variable in the formulation, the natural frequencies for a truss consisting of an arbitrary number of bays can be determined. As stated in 10), however, this method may only locate isolated resonances.

References

1. Brillouin L., "Wave Propagation in Periodic Structures," Dover Publications, Inc., New York, 1946.
2. Johnson, R.A., "Mechanical Filters in Electronics," John Wiley Sons, 1983.
3. von Flotow A.H., "Disturbance Propagation in Structural Networks," Journal of Sound and Vibration, 1986, 106(3).
4. Miles, J.W., "Vibration of Beams on Many Supports," ASCE Journal, Jan 1986, 1-9.
5. Mead D.J., "A General Theory of Harmonic Wave Propagation in Linear Periodic Systems with Multiple Coupling," Journal of Sound and Vibration, 1973, 27(2), 235-268.
6. Mead, D.J., "A New Method of Analyzing Wave Propagation in Periodic Structures: Applications to Periodic Timoshenko Beams and Stiffened Plates," Journal of Sound and Vibration, 1986, 104(1), 9-27.
7. Hodges, C.H., Power, J., Woodhouse, J., "The Low Frequency Vibration of a Ribbed Cylinder," Journal of Sound and Vibration, 1985, 101(2) 219-256.
8. Eatwell, G.P., "Free-Wave Propagation in an Irregularly Stiffened, Fluid-Loaded Plate," Journal of Sound and Vibration, 1983, 88(4) 507-522.
9. Mills, R.A., "Natural Vibrations of Beam-Like Trusses," SM Thesis, Department of Aeronautics and Astronautics, MIT, June 1985.
10. von Flotow, A.H., "Control Motivated Dynamic Tailoring of Spacecraft Truss Structures," Proceedings of the AIAA Guidance and Control Conference, Williamsburg, VA, Aug 17 and 18, 1986.
11. Signorelli, J., "Wave Propagation in Periodic Truss Structures," SM Thesis, Department of Aeronautics and Astronautics, MIT, Dec 1986.
12. Kissel, G., "Wave Localization in Disordered Periodic Structures," Proceedings of the AIAA Dynamic Specialist's Conference, Monterey, CA, April 1987.

ACTIVE MODIFICATION OF WAVE REFLECTION AND TRANSMISSION IN FLEXIBLE STRUCTURES

David W. Miller¹, Andreas von Flotow², Steven R. Hall²

Space Systems Laboratory, Department of Aeronautics and Astronautics
Massachusetts Institute of Technology
Cambridge, Massachusetts

ABSTRACT

A theory for active control of elastic wave propagation in structures is developed. Attention is focused on active modification of the scattering behavior of discrete locations in a structural network. The wave mode input/output relation at a structural junction containing control actuators can be altered in two ways. First, the closed loop reflection and transmission coefficients can be specified, and the necessary feedback to achieve these coefficients determined. Second, an optimal wave controller can be formulated which maximizes the average power dissipation at a junction. If the open loop structure is stable, then the optimal control guarantees stability, since energy is actively dissipated at the junction. Sample controllers are derived and simulated for a free-free beam to demonstrate the techniques and indicate the achievable performance.

INTRODUCTION

Modal analysis of structural dynamics is a powerful and widely applied technique. The technique, however, is limited to systems with a relatively sparse spectrum, since the modal parameters, particularly eigenshapes, are otherwise known to be extremely sensitive to small parameter perturbations of the structure (1). Since modal density increases with mode number, this sensitivity has prompted one analyst to suggest (2) that it is possible to make the modal model too complex (of too large a dimension). Analyses (3,4) for some future space missions show that hundreds of modes of an elastic spacecraft can contribute significantly to performance degradation. Many of these modes are considerably beyond the range where they may be confidently modelled. Thus, one faces the problem of controlling structural dynamics which are well beyond the frequency range in which modal analysis is applicable.

One alternative is the achievement of significant levels of damping by passive or by active means. Direct velocity feedback between dual (colocated and of like type) sensors and actuators has been shown (5) to be unconditionally stabilizing if the matrix of feedback gains is positive definite. This concept has been formalized in a two level control architecture, known as HAC/LAC (6). Although the feedback gain matrix may, in principle, be full, experience has

shown (7) that a restriction to local velocity feedback (a diagonal gain matrix) results in negligible degradation in performance.

This paper develops an alternative to direct velocity feedback for active damping. Feedback compensators, based on spatially local models, actively modify wave transmission and reflection characteristics of the structure. Such reflection and transmission coefficients are relatively insensitive to modelling errors, depending only to first order upon local parameter perturbations.

Prior work (8,9) has shown that, in special cases, compensators designed for active absorption of travelling waves can be very similar to direct velocity feedback. In general they can be quite different.

TRAVELLING WAVE DYNAMICS

Modelling wave propagation through structures of arbitrary complexity can become impractical. However it is invariably possible to find many components in any structure for which a wave propagation viewpoint is feasible.

This paper considers one such component: a junction of an arbitrary number of slender one-dimensional elastic members (Fig. 1). The members are viewed as waveguides along which a set of discrete decoupled travelling wave modes may propagate. These travelling wave modes are coupled to one another at the junction, the dynamics of which are described by frequency dependent reflection and transmission coefficients. Since the remainder of this paper builds upon the travelling wave description of junction dynamics, we provide a brief summary (10).

Junction Dynamics Formulation.

This section makes reference to Fig. 1 which shows an arbitrary junction of several members, and may include a flexible body. The boundary conditions, which may be a function of frequency ω , describe how boundary motions interact with member forces and externally exerted influences. Such a relation has, the general form

$$B(\omega) y(\omega) = [B_u(\omega) \ B_f(\omega)] \begin{bmatrix} u(\omega) \\ f(\omega) \end{bmatrix} = Q(\omega) \quad (1)$$

where the vector u contains the boundary motions and f contains the member forces at the boundary. The square matrices B_u and B_f contain the homogeneous dynamics of the boundary while Q is a

¹ Research Assistant, Member AIAA

² Assistant Professor

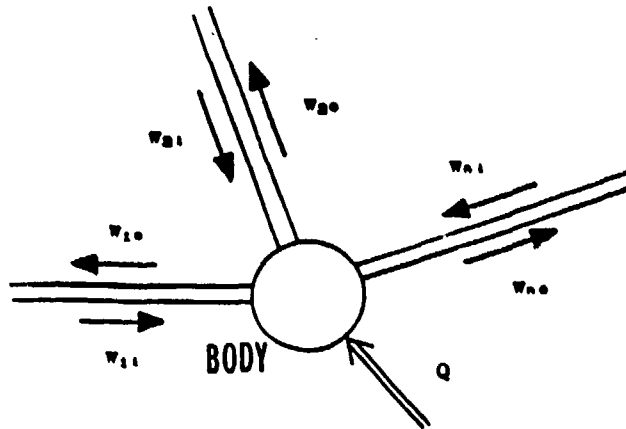


Figure 1 The generic junction. The junction can include a flexible body and can be connected to many members. Each member supports incoming w_i and outgoing w_o wave modes. External influences Q may also be applied.

vector of external influences (forces and relative deflections) acting on the boundary.

This boundary relation can be transformed into a relation governing the local wave behavior. A full rank transformation is made from physical variables u and f to wave mode coordinates w , as follows:

$$y(\omega) = \begin{bmatrix} u \\ f \end{bmatrix} = \begin{bmatrix} Y_{u,i} & Y_{u,o} \\ Y_{f,i} & Y_{f,o} \end{bmatrix} \begin{bmatrix} w_i \\ w_o \end{bmatrix} = Y(\omega) w(\omega) \quad (2)$$

where the transformation Y has been partitioned into square submatrices and the vector of wave mode amplitudes has been partitioned into incoming and outgoing wave mode amplitudes w_i and w_o . This transformation is a characteristic of the members attached to the junction. Each wave mode propagates along one of the members, independently of the remainder of the member response. Associated with each wave mode is a frequency dependent mix of member deflections and forces (each column of $Y(\omega)$ in Eq. 2). Substituting Eq. 2 into the boundary relation (Eq. 1) gives

$$\begin{bmatrix} B_u & B_f \end{bmatrix} \begin{bmatrix} Y_{u,i} & Y_{u,o} \\ Y_{f,i} & Y_{f,o} \end{bmatrix} \begin{bmatrix} w_i \\ w_o \end{bmatrix} = Q, \quad (3)$$

which is an expression of the boundary conditions in wave mode coordinates.

Equation 3 can be rearranged to give the input/output relation governing a junction with outgoing waves resulting from the scattering of incoming waves and generation by external forcing:

$$w_o = S w_i + \psi Q \quad (4)$$

where

$$S = -[B_u Y_{u,o} + B_f Y_{f,o}]^{-1} [B_u Y_{u,i} + B_f Y_{f,i}] \quad (5)$$

$$\psi = [B_u Y_{u,o} + B_f Y_{f,o}]^{-1} \quad (6)$$

In this junction description, the matrices S and ψ represent homogeneous and nonhomogeneous wave behavior and are called the scattering and generation matrices, respectively. Both may be complex and frequency dependent. This description contains only local junction and structural dynamics and does not contain information about other portions of the structure.

The scattering behavior of this junction description can be altered actively through exertion of external influences, such as commanded motions or applied generalized forces, which depend upon incoming wave motion at the junction. Before doing so, methods are required to help determine the performance and stability of such active control.

Average Junction Power Flow

Travelling waves can move elastic and kinetic energy through a structure. The net power flow out of the junction is a quantity of interest and can be used for control design. The power flow out of a junction is given by

$$\text{Power} = \frac{\partial u^T}{\partial t} \cdot f(t) \quad (7)$$

It is necessary that care be taken to ensure that the entries in u and f are ordered such that their dot product represents power flow out of the junction with positive net power flow indicating that more power flows out of the junction than into the junction (an example of this is given later). Note that power flow is a time dependent quantity, which is a bilinear function of the boundary forces and velocities. Hence, the average power flow is not simply the sum of the power flow of the individual wave modes. However, the total average power flow is equal to the sum of the average power flow at each frequency, due to the orthogonality of sines and cosines at different frequencies. Therefore we consider the average power flow at each frequency ω independently.

The time average power flow over one cycle is

$$P_{\text{ave}}(\omega) = \frac{1}{2} w(\omega)^H P(\omega) w(\omega) \quad (8)$$

where w is the vector of wave mode amplitudes, and the superscript H denotes the complex conjugate transpose. The matrix P is given by

$$P = \frac{1}{2} \omega \left[\begin{bmatrix} Y_{u,i}^H Y_{f,i} & Y_{u,i}^H Y_{f,o} \\ Y_{u,o}^H Y_{f,i} & Y_{u,o}^H Y_{f,o} \end{bmatrix} - \begin{bmatrix} Y_{f,i}^H Y_{u,i} & Y_{f,i}^H Y_{u,o} \\ Y_{f,o}^H Y_{u,i} & Y_{f,o}^H Y_{u,o} \end{bmatrix} \right] \quad (9)$$

P_{ave} is real for any mix of wave modes in w since P is hermitian. A passive, nondissipative junction will have zero net power flow ($P_{\text{ave}} = 0$).

CONTROL DESIGN

Two methods for wave control derivation are presented in this section. In the first method, the closed loop scattering matrix is fully or partially specified, and the control which achieves this behavior is derived. In the second method, the control is derived such that it minimizes a

cost based upon the sum of junction power flow plus the control effort expended. Finally, the performance achieved by both methods is discussed.

Scattering Matrix Specification

If the externally applied influence Q is given by a linear combination of the incoming wave mode amplitudes

$$Q = F w_i \quad (10)$$

then the junction relation will have the form

$$w_o = [S + \psi F] w_i = S_{cl} w_i \quad (11)$$

If the control designer specifies the entries needed in the closed loop scattering matrix S_{cl} , then the frequency dependent gains can be found (10). For example, all outgoing waves can be eliminated by setting the closed loop scattering matrix equal to the null matrix using the gain

$$F = -\psi^{-1}S \quad (12)$$

Since wave modes may be difficult to measure, Eqs. 1 and 2 can be used to derive equivalent feedback using physical deflections u .

Optimal Wave Control

Optimal control is defined by the minimization of some cost, typically based upon the response of the system and the effort expended in control. For the wave control problem, with a goal of active damping, net power flow out of a junction is an obvious quantity to minimize since that increases the energy dissipation at that junction.

Using Eq. 8, a possible cost functional has the form

$$J = \frac{1}{2} \int_{-\infty}^{\infty} (w^H P w + Q^H R Q) dw \quad (13)$$

where R penalizes control effort. Since the wave mode amplitudes are affected by the control action, the w vector is a function of the incoming wave modes and the control, so that

$$w = \begin{bmatrix} w_i \\ S w_i + \psi Q \end{bmatrix} \quad (14)$$

Then the integrand of Eq. 13 is given by

$$\begin{aligned} & w_i^H P_{11} w_i + w_i^H P_{10} (S w_i + \psi Q) \\ & + (S w_i + \psi Q)^H P_{01} w_i \\ & + (S w_i + \psi Q)^H P_{00} (S w_i + \psi Q) \end{aligned} \quad (15)$$

where the P matrix has been partitioned as

$$P = \begin{bmatrix} P_{11} & P_{10} \\ P_{01} & P_{00} \end{bmatrix} \quad (16)$$

This cost functional can be minimized by minimizing the integrand at every frequency. The integrand is minimized with respect to the control Q when

$$Q = -[\psi^H P_{00} \psi + R]^{-1} \psi^H [P_{01} + P_{00} S] w_i = F w_i \quad (17)$$

This gives control exertion which is proportional to the incoming wave mode amplitudes. Again, these wave mode amplitudes can be transformed to give proportional feedback of physical deflections at the junction using Eqs. 1 and 2.

The second derivative of the integrand of Eq. 13 (Eq. 15) with respect to Q is

$$\psi^H P_{00} \psi + R \quad (18)$$

P_{00} is hermitian and positive semidefinite, since outgoing waves propagate energy away from the junction. (In fact, this condition defines outgoing wave modes.) If R is chosen to be positive definite, then Eq. 18 is positive definite and the control in Eq. 17 minimizes the cost functional in Eq. 13.

Several properties of Eq. 17 can be readily seen. For conservative systems that support only propagating waves, energy is carried independently by each wave. This causes P_{00} to be of full rank and P_{01} to be the zero matrix. This allows a control to be derived using Eq. 17 with R equal to the zero matrix. In other words, if ψ is square (all actuator types used) then there exists a minimum achievable cost and it corresponds to the control derived using Eq. 12.

For systems with evanescent waves, P_{00} will not be of full rank and R must not be nonzero in order to prevent inversion of a singular matrix. In this case, actuator restrictions such as saturation limit the achievable performance. If only a subset of possible controls is available, there are situations in which the product $\psi^H P_{00} \psi$ will result in a matrix of full rank and R can be set equal to the zero matrix to obtain minimum cost with the available actuators. Note that with $R = 0$, the resulting closed loop scattering matrix will be nonzero. This is because the outgoing evanescent wave can combine with the incoming evanescent wave to dissipate energy at the junction.

Since P_{00} is never positive for an uncontrolled junction and the control in Eq. 17 is chosen to minimize the quadratic in Eq. 13, the optimal feedback guarantees dissipation in the active junction independent of the incoming wave mode mix.

FREE-FREE BEAM EXAMPLE

The derivation and properties of wave control can be best demonstrated using an example. A free-free beam is chosen for the example structure because such a beam exists in our laboratory (Table 1) allowing designs to be experimentally demonstrated. The Bernoulli-Euler beam model supports one evanescent and one propagating wave mode in each direction.

Beam End Dynamics Formulation

The first step is to derive the boundary conditions for each beam end. The free-free beam and externally applied influences are shown in Fig. 2. The boundary condition relations for the left and right ends are

Table 1 Free-Free beam and actuator specifications

Beam Properties:	
Material	Brass
Length	$l = 7.3152 \text{ m}$
Bending Stiffness	$EI = 31.1 \text{ Nt/m}^2$
Mass per Unit Length	$\rho A = 2.8523 \text{ kg/m}$
Actuator Properties:	
$B_s = \begin{bmatrix} -0.051 & 0.0039 \\ 1.576 & -0.1109 \end{bmatrix} \omega^s$; $B_r = \begin{bmatrix} 1 & 0.038 \\ 0 & 1 \end{bmatrix}$	

$$\begin{bmatrix} 0 & 0 & 1 & 0 \\ 0 & 0 & 0 & 1 \end{bmatrix} \begin{bmatrix} v \\ v' \\ -EI v'' \\ EI v''' \end{bmatrix}_{L,R} = \begin{bmatrix} F \\ M \end{bmatrix}_{L,R} \quad (19)$$

where the primes denote spatial partial derivatives of the transverse beam displacement v .

The four wave solutions to the Bernoulli-Euler beam equation are

$$v = w_{rp} e^{-ikx+i\omega t} + w_{re} e^{ikx+i\omega t} + w_{lp} e^{ikx+i\omega t} + w_{le} e^{-ikx+i\omega t} \quad (20)$$

where the wave number

$$k = (\rho A / EI)^{1/4} \omega^{1/2} \quad (21)$$

is a positive, real quantity and the subscripts and constants are defined as

rp: rightward propagating
re: right end evanescent
lp: leftward propagating
le: left end evanescent
 ρ : mass density
 A : cross-sectional area
 E : modulus of elasticity
 I : cross-sectional moment of inertia

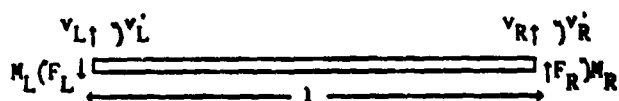


Figure 2 Schematic of free-free beam. Orientation of external influences Q and beam deflections, v and v' , are shown.

For the left end of the beam in Fig. 2, where the active junction control will be performed, the incoming and outgoing wave mode amplitudes are defined as

$$\begin{bmatrix} w_i \\ w_o \end{bmatrix} = \begin{bmatrix} w_{rp} \\ w_{re} \\ w_{lp} \\ w_{le} \end{bmatrix} \quad (22)$$

For the remainder of this example, only the left junction will be dealt with explicitly.

Evaluating the entries in the transformation matrix of Eq. 2, using Eq. 20, gives

$$\begin{bmatrix} v \\ v' \\ -EI v'' \\ EI v''' \end{bmatrix} = \begin{bmatrix} 1 & 1 & 1 & 1 \\ ik & k & -ik & -k \\ iEI k^3 & -EI k^3 & -iEI k^3 & EI k^3 \\ -EI k^3 & EI k^3 & -EI k^3 & EI k^3 \end{bmatrix} \begin{bmatrix} w_{rp} \\ w_{re} \\ w_{lp} \\ w_{le} \end{bmatrix} \quad (23)$$

with $x = 0$ at the boundary position. Substituting Eqs. 22 and 23 into Eq. 19 and solving for the scattering and wave generation matrices as defined by Eqs. 5 and 6, respectively, gives

$$S_L = \begin{bmatrix} -1 & 1+i \\ 1-i & 1 \end{bmatrix} \quad (24)$$

$$\psi_L = \frac{1+i}{2EI k^3} \begin{bmatrix} 1 & -k \\ i & -ik \end{bmatrix} \quad (25)$$

The transfer function from an external force applied to the right end of the beam to the transverse displacement at the same end can be expressed as

$$v_R = [1 \ 0 \ 0 \ 0] Y \begin{bmatrix} 1 \\ S_R \end{bmatrix} (I - FS_L FS_R)^{-1} FS_L \psi_R \begin{bmatrix} 1 \\ 0 \end{bmatrix} F \quad (26)$$

where

$$F = \begin{bmatrix} e^{-i(1+i)} & 0 \\ 0 & e^{-i(1+i)} \end{bmatrix} \quad (27)$$

and l is the length of the beam. This is an exact solution of the governing equation and boundary conditions.

The next step is to derive the net power matrix P at any beam cross section. This is done by substituting the square submatrices of Eq. 23 into Eq. 9. The resulting matrix, using the definition of wave number in Eq. 21, is

$$P = 2 \omega^2 k (\rho A EI)^{1/2} \begin{bmatrix} -1 & 0 & 0 & 0 \\ 0 & 0 & 0 & 1 \\ 0 & 0 & 1 & 0 \\ 0 & -1 & 0 & 0 \end{bmatrix} \quad (28)$$

Since the wave mode amplitude vector is defined by Eq. 22, the (1,1) and (3,3) entries in Eq. 28 represent the power flow associated with propagating waves. The imaginary (4,2) and (2,4) entries represent power propagated by the interaction between the two evanescent modes. Note that the evanescent modes do not propagate power by themselves.

Wave Absorbers for the Beam

Now that the junction dynamics and power relations have been derived, junction control compensation can be formulated. First, the closed loop (1,1) scattering matrix entry will be set to zero assuming that only one physical deflection

measurement is available. This results in no outgoing propagating wave being created by an incoming propagating wave. Since the characteristic attenuation length of the evanescent modes is inversely proportional to the square root of frequency (Eq. 15), the importance of this (1,1) entry becomes more obvious at higher frequencies. Second, optimal feedback of physical deflection measurements will be derived. Performance of the two designs will then be evaluated. In the following discussion, the F and G matrices denote incoming wave mode and physical deflection feedback gains, respectively.

Feedback of a physical deflection can be achieved by setting $Q = G u$ in Eq. 4 and substituting for u from the top half of Eq. 23. The gain for which the closed loop (1,1) scattering matrix entry is zero can be extracted in closed form or numerically at various values of frequency.

If a transverse displacement measurement is chosen in conjunction with torque actuation, giving feedback of the form

$$M(\omega) = G(\omega) u(\omega) = g(\omega) v(\omega) \quad (29)$$

then the closed loop scattering matrix has the form

$$S_{cl} = \frac{1}{1+\tau(1+i)} \begin{bmatrix} -1-\tau(1-i) & 1+i-2\tau \\ 1-i-2i\tau & 1+\tau(1-i) \end{bmatrix} \quad (30)$$

where

$$\tau = \frac{(1+i)R}{2EI k^3} \quad (31)$$

Setting the (1,1) term to zero and using the definition from Eq. 21 gives

$$\tau = \frac{-1}{1-i} \quad \text{or} \quad g(\omega) = -1 (\rho AEI)^{1/2} \omega \quad (32)$$

This corresponds to feedback of transverse velocity to torque through a gain equal to $-(\rho AEI)^{1/2}$. The resulting closed loop scattering matrix is

$$S_{cl} = \begin{bmatrix} 0 & 1 \\ -1 & 0 \end{bmatrix} \quad (33)$$

The power flowing out of the closed loop junction, at each frequency, can be found by substituting Eqs. 33 and 11 into Eq. 8 to get

$$P_{ave} = \frac{1}{2} w_1^* \begin{bmatrix} -1 & 1 \\ 1 & 1 \end{bmatrix} w_1 = \frac{1}{2} w_1^* P_{cl} w_1 \quad (34)$$

This quadratic yields a real value for average power. The eigenvalues of the closed loop power matrix are 1.414 and -1.414. This means that P_{cl} is an indefinite matrix and may amplify certain incoming wave mode mixes. Therefore, junction dissipation depends on the mix of incoming wave modes, and therefore on the dynamics of the remainder of the beam.

Optimal feedback can be derived using Eq. 17 with R equal to the zero matrix since only torque actuation is being used. This results in incoming

wave mode feedback of

$$F = EI k^3 \begin{bmatrix} (-1-i) & (1+i) \end{bmatrix} \quad (35)$$

or, equivalently, feedback of deflection and rotation with

$$G = 0.5 (EI)^{3/4} (\rho A)^{1/4} \begin{bmatrix} 0 & (-1+i) \omega^{1/2} \end{bmatrix} \quad (36)$$

This only calls for rotation feedback and does so through what can be termed a half differentiator since it provides a frequency dependence of $\omega^{1/2}$ and a forty-five degree phase lead. This results in a closed loop scattering matrix of

$$S_{cl} = \begin{bmatrix} 0 & 1 \\ -1 & 1+i \end{bmatrix} \quad (37)$$

The resulting net power is

$$P_{ave} = \frac{1}{2} w_1^* \begin{bmatrix} -1 & 1 \\ 1 & -1 \end{bmatrix} w_1 = \frac{1}{2} w_1^* P_{cl} w_1 \quad (38)$$

This closed loop power matrix has eigenvalues equal to 0 and -2. Therefore, the matrix is negative semidefinite and energy is never generated at the junction.

Fig. 3 compares the closed loop responses with the open loop responses, found using Eq. 26, using the feedbacks given in Eqs. 32 and 36. The open loop system is provided with about 0.5X damping through the addition of a linear dashpot at the right junction. Note that the feedback in both cases result in 135 degrees phase lag and a logarithmic magnitude rolloff slope of -3/2 above 1 rad/sec. This matches the receptance from force to displacement at the right end of a semi-infinite beam. In other words, at high frequencies (above 1 rad/sec in Fig. 3), where evanescent modes become insignificant, the beam behaves as if it were semi-infinite. Fig. 4 illustrates that the corresponding power flow out of the left junction is negative for all frequencies. Noting Fig. 3, the performance is slightly better at low frequencies for the optimal feedback, since evanescent waves are being exploited to increase junction power dissipation.

Fig. 5 compares the closed loop transfer functions to the open loop transfer function with the dynamics of a torque wheel actuator included (Table 1). The actuator dynamics were ignored during control design, but need not be. Note that the controller derived by setting $S_{cl}(1,1) = 0$ results in an instability at 72 rad/sec. This instability was verified using a finite element model and is seen in Fig. 6 where the power flow out of the junction becomes a positive quantity near 67 rad/sec. An interesting feature can be seen by comparing Fig. 3 with 5 and Fig. 4 with 6. Note that when the compensator is derived based upon the correct model, resonant behavior appears to vanish. When not based upon the exact model, resonant behavior still exists, because wave cancelling is not exact, and instability occurs for the compensator in Eq. 32.

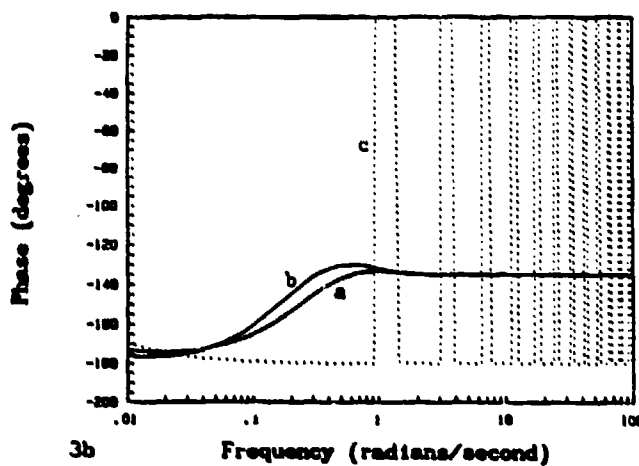
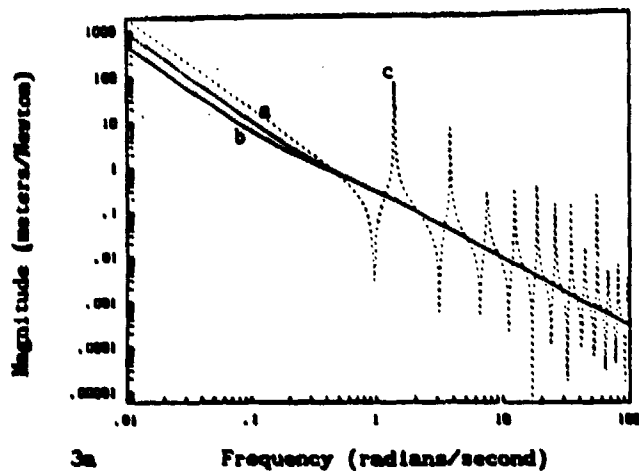


Figure 3 Magnitude (a) and phase (b) of beam transfer function from unit forcing at the right end to colocated transverse displacement for a) $S_{c1}(1,1)=0$ control, b) optimal control, and c) open loop. Actuator dynamics are not included.

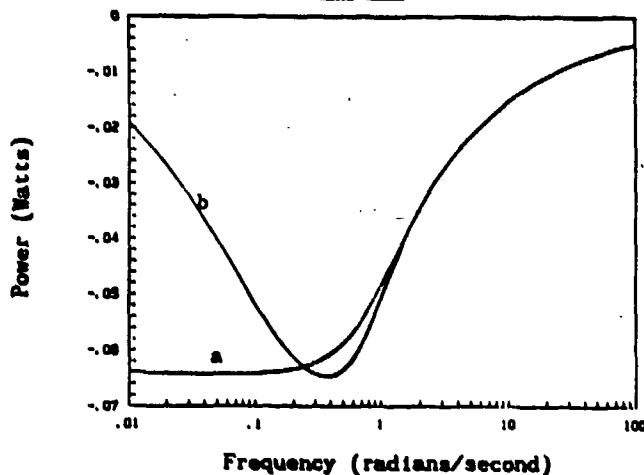


Figure 4 Net power flowing out of the left junction for unit amplitude forcing at the right end and for a) $S_{c1}(1,1)=0$ control and b) optimal control. Actuator dynamics are not included.

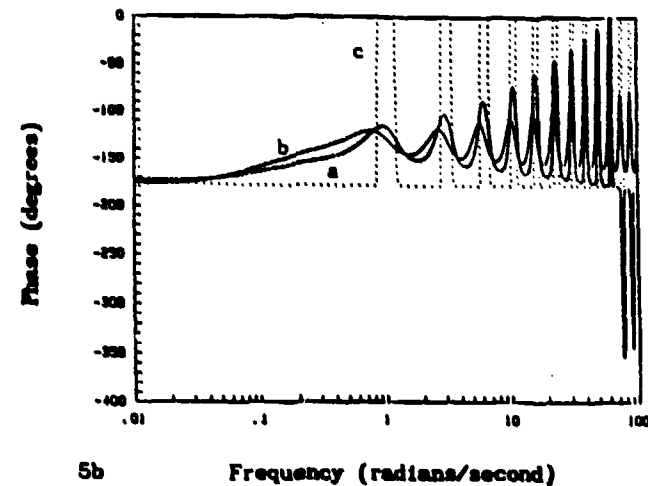
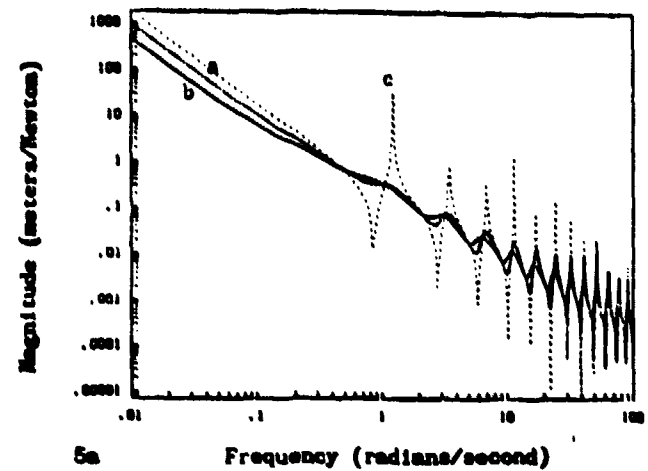


Figure 5 Magnitude (a) and phase (b) of beam transfer function from unit forcing at the right end to colocated transverse displacement for a) $S_{c1}(1,1)=0$ control, b) optimal control, and c) open loop. Actuator dynamics are included.

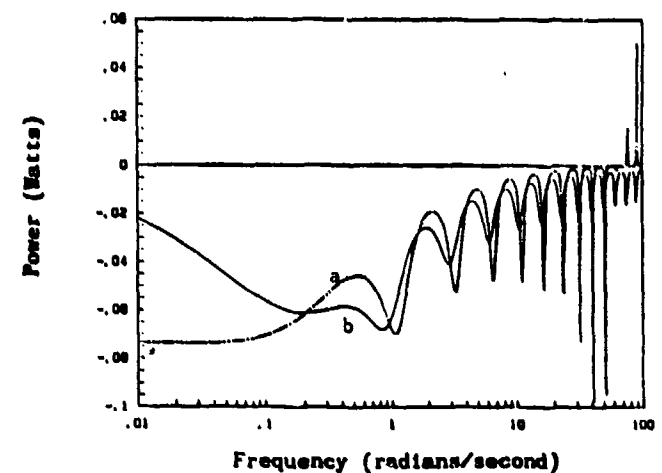


Figure 6 Net power flowing out of the left junction for unit amplitude forcing at the right end and for a) $S_{c1}(1,1)=0$ control and b) optimal control. Actuator dynamics are included.

CONCLUSIONS

Wave junction control takes advantage of combining the robustness of collocated feedback with the high performance of feedback gains optimized at every frequency. The performance and dissipation of the junction control can be determined without knowledge of global structural behavior. Since the design depends only upon local dynamics, it cannot be sensitive to modelling errors in distant portions of the structure. By maximizing junction dissipation at all frequencies, high performance vibration suppression is achieved, perhaps even to the extent of eliminating resonant behavior in the structure. It was shown that designing compensators without regard to actuator dynamics causes a degradation in performance. But, the actuator dynamics may be included in the boundary conditions to prevent this.

Several disadvantages must also be faced in using this scheme. The compensators are typically complex functions of frequency. These can be difficult to implement, and may become more difficult when actuator dynamics are modelled.

Many extensions to this theory of active control of wave propagation are possible. One might, for example, attempt to adapt such controllers by observation of their performance. One might attempt dynamic estimation of incoming wave modes, using partial measurements and theory yet to be developed. One might make these measurements some distance "upstream" from the actuator to provide for actuation and sensing dynamics, and thus make the theoretical compensators easier to implement. This promises to be an interesting area for research.

REFERENCES

- (1) Courant, R., Hilbert, D., Methods of Mathematical Physics, Vol. 1, Interscience Publishers, Inc., New York, 1953.
- (2) Skelton, R. E., "Algorithm Development for the Control Design of Flexible Structures," NASA CP 2258, Modeling, Analysis, and Optimization Issues for Large Space Structures.
- (3) Kissel, G. J., Hogg, D. R., "Stability Enhancement for Control of Flexible Space Structures," IEEE Control Systems Magazine, Vol. 6, No. 3, June 1986, pp. 19-26.
- (4) Bernstein, D. S., Greeley, S. W., "Robust Controller Synthesis Using the Maximum Entropy Design Equations," IEEE Transactions Automatic Control, Vol. AC-31, 1986, pp. 362-364.
- (5) Balas, M. J., "Direct Velocity Feedback Control of Large Space Structures," Journal of Guidance, Control, and Dynamics, Vol. 2, no. 3, May-June 1979.
- (6) Aubrun, J-N., "Theory of the Control of Structures by Low-Authority Controllers," Journal of Guidance, Control and Dynamics, Vol. 3, No. 5, Sept.-Oct. 1980, pp. 444-451.
- (7) Miller, D. W., "Experimental Investigations into Passive and Active Control Using Space-Realizable Techniques," Damping 1986, Vol. 1, Flight Dynamics Laboratory AFWAL, Las Vegas, April 1986.
- (8) von Flotow, A. H., "Disturbance Propagation in Structural Networks," Journal of Sound and Vibration, (1986) 106(3), pp. 433-450.
- (9) von Flotow, A. H., "Traveling Wave Control for Large Spacecraft Structures," Journal of Guidance, Control, and Dynamics, Vol. 2, No. 4, July-Aug 1986, p. 462.
- (10) von Flotow, A. H., Schafer, B., "Wave-Absorbing Controllers for a Flexible Beam," Journal of Guidance, Control, and Dynamics, Vol. 2, no. 6, Nov-Dec 1986, p. 673.

A. H. van Flotow
Massachusetts Institute of Technology

INTRODUCTION

Past analyses of the dynamics of spacecraft tethers have generally been of two types; either quite simple models were used, typically with the tether assumed to be straight and inextensible, or comprehensive simulations [1,2,3] were prepared for computer implementation. General agreement on the importance of various physical effects does not seem to have been reached. Each analyst has individually made the choice of which effects to model, sometimes quite arbitrarily. Reference 2 is a broad summary of work published to date, and includes 97 citations.

The work reported in this paper was motivated by the philosophy that the appropriate approach to developing an engineering model of a physical system is to include no more than the bare minimum of effects required to reproduce the behaviour of interest. Since this is necessarily an iterative procedure, this paper builds upon insights gleaned from the results of previous analyses. Spectral separation is invoked to reduce the dynamics to a relatively fast vibrational motion, decoupled from and superimposed upon the slow roll/yaw librations of the system. It is suggested (with experimental evidence) that, because of the low tensions experienced by spacecraft tethers, non-linear extensional stress-strain behaviour will be important.

Infinitesimal perturbations of the tether from its slowly varying quasi-equilibrium are described by a system of linear partial differential equations, in which longitudinal and lateral motion are coupled by slight curvature of the equilibrium shape. These equations are non-dimensionalised and investigated with respect to wave propagation, revealing that for wave lengths much smaller than equilibrium radius of curvature, lateral and longitudinal motions effectively decouple. Assumption of point-mass dynamics for the end bodies leads to an eigen-analysis which yields eigen-frequencies and shapes, the first few of which can be quite different from those of the classic cable approximation. Effects of tether stiffness, curvature, tension, length, retrieval rate, etc. are illuminated in terms of non-dimensional parameters.

The intent of this paper is to provide simple conceptual models of the motion of tethered satellites, both to guide development of future simulations, and to provide a basis against which to compare simulation results.

APPROPRIATE MODELS OF TETHER ELASTICITY

To date, models of tether elasticity have ranged from that of an inextensible chain, to that of a beam with non-symmetric cross-section and with torsional strain energy. It is easy to show that the "bending length," l_B , beyond which the effects of bending stiffness, EI , are negligible compared to those of tension, T , is given by $l_B \approx \sqrt{EI/T}$. With tether diameter on the order of one millimeter, and tether tension on the order of a few Newtons, this bending characteristic length is on the order of a few centimeters. Thus, for such tethers, with lengths of many meters or kilometers, bending stiffness does not contribute significantly to global restoring forces, and a beam model is inappropriate.

Bending stiffness does, however, contribute non-linearly to the extensional stress-strain behaviour of such tethers. The natural form of a real wire is not straight. Residual stresses of unspecified origin, and a spiral shape due to deployment from a reel will both be present. The

characteristic length of these imperfections may very well be comparable to the bending length. Figure 1, adapted from reference 4, presents relevant experimental results.

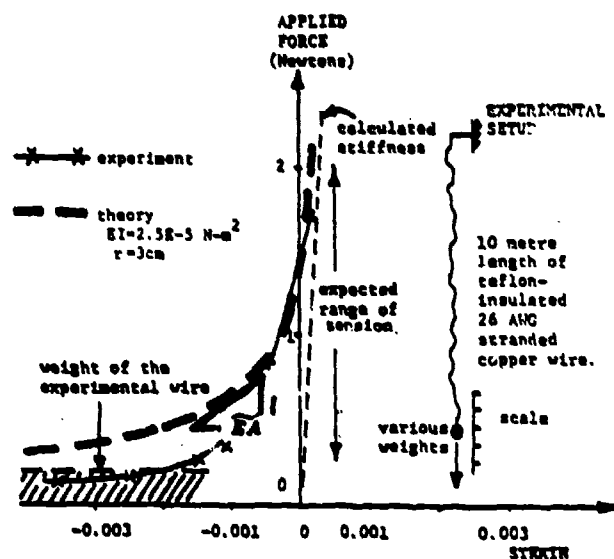


FIGURE 1 A wire exhibits a non-linear stress-strain relation due to straightening. This figure compares the results of one experiment with an analysis based upon the assumption that the unstressed wire shape is to be wound on a reel of radius r .

Non-Linear Extensional Stiffness of a Wire

Spacecraft tethers will often operate under very low tension, even as low as a few Newtons for end masses of many hundreds of kilograms. We are thus interested in the extensional stress/strain behaviour as tension approaches zero. The most common assumption has been bilinear; linear elastic for extensional strain, and zero tension for compressive strain. The experimental results of Figure 1 show the behaviour to be more complex.

Two approximate analyses of the force/deflection behaviour of a wire with initial curviness can be offered. Both predict a similar non-linear stress/strain behaviour:

$$\epsilon = -\left(\frac{\kappa}{T}\right)^2 + \frac{T}{EA} \quad (1)$$

(valid for small strain, approximately $-0.05 < \epsilon < 0.01$). The strain, ϵ , is thus seen to be the sum of two contributions, a linear elastic extension proportional to the tension, T , and inversely proportional to the axial stiffness EA , and a non-linear shortening due to the wire's tendency to return to its unstressed shape as $T \rightarrow 0$. The value of κ depends on the assumptions made in the derivations.

If an inextensible wire's unstressed shape is assumed to be a helix of radius r , pitch angle $\alpha \approx 0$, and arclength L (the wire is tightly wound on a reel of radius r), then the tension, T , required to extend the wire to a length A (while preventing untwisting) is given by [5]

$$T = \frac{GJ}{\pi^2 L} - \frac{EI}{\pi^2 L} \left(1 - \frac{1}{\sqrt{1 - (h/L)^2}}\right) \quad (2)$$

where EI is the bending and GJ the torsional stiffness. If we define the strain with respect to the wire's arclength, $\epsilon = (h - L)/L$, and limit $|\epsilon| \ll 1$, then expression (2) reduces to

$$T = \frac{GJ}{\pi^2} - \frac{EI}{\pi^2} \frac{1}{\sqrt{1 - \epsilon}} \quad (3)$$

which, since $GJ \approx EI$, becomes

$$\epsilon = -\left(\frac{\pi}{2}\right)^2 \quad ; \quad \kappa = EI/\sqrt{2}r^2 \quad (4)$$

An alternative derivation attempts to model a slightly wrinkled unstressed shape by introduction of a sinusoidal planar wrinkle with amplitude Δ and wavelength Λ . It is not difficult to show that under this assumption, the tension/strain behaviour of the axially inextensible wire becomes

$$\epsilon = -\left(\frac{\pi}{2}\right)^2 \quad ; \quad \kappa = 32\sqrt{6}E\Delta/\Lambda^2 \quad (5)$$

as $\Lambda \rightarrow L$. Equation (1) is then the sum of the non-linear shortening of equation (4) or (5), and the linear elastic extension $T/E\Lambda$.

The experimental curve of Figure 1 was measured for a length of teton-insulated stranded copper wire sold on a small plastic reel. This wire was under consideration for use as a spacecraft tether[4]. Plausible values have been inserted into expressions (1) and (4) to calculate the theoretical curve in Figure 1.

It would be interesting to speculate about (or to measure) the low-tension stress/strain behaviour of other candidate tethers. Effects of braiding, stranding, twist and other tether details would potentially add to the non-linearity introduced by residual stresses. The results summarized by Figure 1 suggest that such non-linear behaviour will be much more important than many of the other non-linear effects included in past analyses. For the mission studied in reference 4, the non-linear flexibility, $\bar{EA}(\epsilon)$, can be greater than the linear flexibility by a factor of up to one thousand!

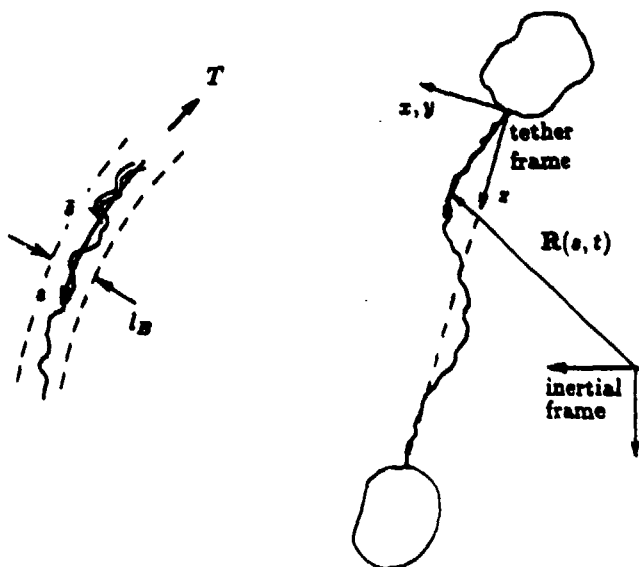


FIGURE 2 It is proposed to forgo detailed modeling of the tether "wrinkles" in favour of modeling only the approximate position and using a non-linear stress-strain relation. The tether position would then be modeled with a resolution of approximately $l_B \approx \sqrt{EI/T}$.

In principle it is possible to model this subtle effect of tether bending stiffness by using a beam model for the tether and resolving the details of the tether shape. The resolution demanded would be on the order of a few centimeters (the bending length); thus would lead to a hopelessly large computer simulation for tethers of several kilometers length. The approach introduced in the preceding paragraphs would be to use an elastic cable model, with a non-linear stress-strain behaviour as in equation (1). Figure 2 indicates that the tether position would then be modeled to a precision on the order of the bending length, adequate for most purposes.

REFERENCE FRAMES AND EQUATIONS OF MOTION

The equations of motion of an elastic cable (no bending or torsional stiffness) have long been known[5], and are concisely expressed in vector notation;

$$\mu \frac{\partial^2 \mathbf{R}}{\partial s^2} = \frac{\partial}{\partial s} \left(T \frac{\partial \mathbf{R}}{\partial s} \right) + \mathbf{F} \quad (6)$$

where μ is the mass per unit strained length of the tether, $\mathbf{R}(s, t)$ is the vector position of the tether as a function of time, t , and strained arclength, s . The arclength is conveniently measured from one end of the tether, say within and body A . External forces per unit length are indicated by vector \mathbf{F} . The tension, T , is given as a function of ϵ , where $\epsilon = \|\partial \mathbf{R}/\partial s\| - 1$, by equation (1). If the tether is to be modeled as constant length, equation (1) is replaced by the constraint $\|\partial \mathbf{R}/\partial s\| = 1$. (The issue of when an in-elastic model of the tether is appropriate is discussed in a subsequent section.)

The boundary conditions required to complete equations (6) will depend on the dynamics of the end bodies of the tethered satellite system. The force exerted by the tether on the end body A (at $s = s_A$) is just

$$\mathbf{F}_A = \left[\left(T - \mu \left(\frac{\partial s_A}{\partial t} \right)^2 \right) \frac{\partial \mathbf{R}}{\partial s} \right]_{s=s_A} \quad (7)$$

Note the appearance of the (normally negligible) thrusting term due to tether deployment.

Reference 3 reports the development of a simulation based upon a finite difference discretization of equation (6), and boundary conditions built upon equation (7) and the assumption of suitable models for the end bodies. The reference frame chosen is earth-centered inertial, thus relative motion must be resolved as the small difference of two large numbers. In this reference frame, equations (6) and (7) are highly non-linear in the three components of \mathbf{R} .

A more common approach has been to introduce a tether reference frame[1,2], and to express tether motion with respect to this frame. This tether frame has historically been chosen with one axis defined by the tether attachment points on the two bodies and the other axis defined via their orientation with respect to the orbital plane (see Figure 2). If tether deflections are expressed with respect to this frame, then the rotational motions of the reference frame add coriolis, centripetal and angular acceleration terms to the time derivatives of equations (6) and (7), and the equations describing tether deflection are coupled to those describing system attitude. Since the angular velocity of the tether reference frame is defined by end body motion, which depends (in part) upon tether forces, the equations of motion governing system attitude are also coupled to the partial differential equations governing tether deflections.

The approach of reference [1] has been to numerically simulate this system of equations. The tether shape is discretized by the introduction of shape functions or by a lumped mass model. The resulting ordinary differential equations can then be integrated forward in time. Experience with these simulations has revealed the system to be "stiff"; some motions occur much faster than others, and the integration time step must be chosen to be a very small fraction of the orbital period.

THE APPROXIMATION OF SPECTRAL SEPARATION

An alternative approach to extracting information from a stiff system of ordinary differential equations is to introduce the approximation of spectral separation. This approximation is based upon the realization that the effect of coupling between fast and slow dynamics of a system is well approximated by the introduction of two assumptions:

- 1 The slow dynamics define a quasi-equilibrium from the point of view of the fast dynamics.
- 2 The fast dynamics modify the slow dynamics quasi-statically, that is, they participate in the slow dynamics at their instantaneous equilibrium levels.

The best reference for the theory and practice of spectral separation, with application to many examples, is perhaps an unpublished book draft.[9]

Table 1 is a summary of estimates of the eigen-frequencies of a tethered system, both in symbolic and numerical form. The numbers used are representative of the Italian/American shuttle tethered satellite system. Note that the numerical estimates for this specific system indicate that most internal motions will be much faster than pitch and roll of the entire system. The one exception to this spectral separation is the pendular attitude oscillation of the orbiter due to tether tension acting at the end of the tether deployment boom.

TABLE 1 Estimates of Periods of Vibration of a Tethered Satellite System

Description	Symbolic	Numerical ¹
System Pitch	$\frac{2\pi}{\omega_p}$	3100 seconds
System Roll	$\frac{\pi}{\omega_r}$	2700 seconds
Elastic Bounce	$2\pi\sqrt{\frac{L\mu A E}{T(m_A + m_B)}}$	61 seconds ²
Tether Modes:		
First Lateral	$2L\sqrt{\frac{T}{EI}}$	440 seconds
First Longitudinal	$2L\sqrt{\frac{T}{EA}}$	9 seconds ²
End Body Attitude	$2\pi\sqrt{\frac{I_B}{T}}$	orbiter: 1000 seconds sub-satellite: 13 seconds

¹ Numerical values used are: orbital rate $\omega_o = 1.16 \times 10^{-3}$ per second, (low earth orbit), axial stiffness $EA = 10^8 N$, orbiter mass $m_A = 10^3 kg$, sub-satellite mass $m_B = 500 kg$, tether length $L = 20 km$, tension $T = 40 N$, tether mass density $\mu = 5 \times 10^{-3} kg/m$, orbiter inertia $I_o = 10^7 kg - m^2$, orbiter attach point offset $d = 10 m$, sub-satellite inertia $I_s = 125 kg - m^2$, sub-satellite attach point offset $d = 0.75 m$.

²

This period is based on a linear elastic model for tether axial stiffness. The non-linear stress-strain behaviour of the tether to be used for the Italian/American mission is not available.

THE QUASI-EQUILIBRIUM TETHER SHAPE

The attitude motion of a general rigid body in orbit, responding to environmental torques, is well understood.[12] The motion of a general flexible body in orbit, and its interaction with the gravitational field is less well understood. Initial studies have shown that the rigid body motion is essentially unperturbed by flexible deformations as long as these deformations remain small relative to system dimensions,[10] and their natural frequencies remain perhaps a factor of ten[11] larger than than the orbital rate ω_o . Review of Table 1 reveals that, with the exception of orbiter attitude motion, the natural frequencies of the internal motion of the tethered system are indeed much faster than orbital rate. If slow end-body attitude motion can be ignored or is actively controlled, the attitude librations of the tethered system will occur much like those of a rigid body, as long as internal deformations remain small compared to tether length.

References 13 and 14 have considered the equilibrium longitudinal strain and tension distributions in a tether, subject to the assumptions of linear elasticity and a constant gravitational gradient acting along the axis of a straight tether. These studies have mathematically confirmed the validity of a simple approximation, exact for infinitesimal tether strain; tether tension is effectively constant if both end masses are much greater than tether mass, and spatially parabolic if tether mass is significant.

The quasi-equilibrium shape of a tether is not necessarily straight. Lateral forces due to aerodynamic drag, gravity gradient, electrodynamic interaction with the earth's magnetic field and coriolis effects due to retrieval or deployment of the tether from a massive end body will all deflect the tether laterally against tensile restoring forces. Each of these forces will vary with time and space, both in magnitude and direction, with much of the variation occurring at frequencies comparable to orbital rate. Order-of-magnitude estimates of these lateral forces are:

Aerodynamic Drag (atmospheric density 10^{-14} to $10^{-13} g/cm^3$)	10^{-4} to $10^{-3} N/m$
Electrodynamic (earth's magnetic field in low earth orbit)	$2 \times 10^{-5} N/m/Ampere$
Gravity Gradient (v is lateral deflection in meters)	$v \times 10^{-3} N/m$
Coriolis (\dot{L} is retrieval or deployment rate, in m/s)	$\dot{L} \times 10^{-3} N/m$

Numerical values given in Table 1 have been used where needed.

The approximation of spectral separation permits calculation of an instantaneous tether shape by insisting upon static equilibrium with these lateral forces. If one assumes that the tether experiences a linear force density, F , uniform in direction and magnitude along the wire, then the equilibrium curve is planar, and is given by the solution of

$$\frac{\partial}{\partial s} \left(T \frac{\partial \mathbf{R}}{\partial s} \right) + \mathbf{F} = 0 \quad (8)$$

together with an appropriate stress/strain relation. Since this curve will be very shallow, we will assume it to be a portion of a circular arc of radius, R , $R \gg L$, and will assume tension, T , to be independent of s . Basic equilibrium analysis then yields $R = T/F_{\perp}$, (F_{\perp} is the

component of F perpendicular to the line connecting the tether attach points) and mid point sag of $\delta = L^2/8R$. Using a tension of $T = 60\text{ N}$, and a lateral force density of $2 \times 10^{-3}\text{ N/m}$, yields a radius of curvature of $R = 2000\text{ km}$ and a mid point sag of $\delta = 36\text{ meters}$ for a tether length of 30 km . These values become $R = 200\text{ km}$, and $\delta = 2.5\text{ m}$ for a tether length of 3 km and a tension of 4 N . The non-dimensional equilibrium radius of curvature, $\bar{R} = R/L$, is thus seen to be very large (approximately 100), and independent of length.

References 10 and 11 define the libration of a flexible system in terms of the attitude of a reference frame which origin remains at the deformed system mass center, and which attitude is defined by orthogonality of the system flexible and rigid body motion. The tether frame satisfies this definition of attitude only approximately, even when the end bodies are modeled as point masses. Since the equilibrium slope of the tether with respect to the line connecting the two attach points is very small (approximately $1/2\bar{R}$), the curved tether will couple the two end bodies much as a straight tether would, and system libration is essentially the same as the libration of the tether frame. Reference 11 comes to a similar conclusion.

The slowly varying equilibrium shape we will consider can thus be summarized as follows: A global pitch and roll libration of the system creates a spatially near uniform tension in the tether, which varies slowly in time. The equilibrium tether shape is nearly straight, with a shallow planar sag which slowly changes amplitude and swings about the line connecting the two tether attachment points. This equilibrium is static when observed on the time scale of internal tether modes.

FAST TETHER MOTIONS

Fast tether motions are of interest for several reasons;

- 1 Simulations have shown[2] that such tether motions may grow during retrieval.
- 2 For maneuvers involving intermittent thrusting of the end bodies,[2,15] such fast tether motions will be excited directly.
- 3 The performance of kinetic isolation and sub-satellite attitude control systems based upon remote tethering of a sensitive payload to a noisy space station,[16] depends strongly on these tether dynamics.

Prior studies[7] of the dynamics of slightly curved elastic cables have concluded that even very slight equilibrium curvature can have a great influence upon perturbational motion. The fundamental symmetric mode of a pinned-pinned wire was shown to change character when a non-dimensional parameter, $\lambda^2 = (L/R)^2 EA/T$, exceeded a critical value. The value of this parameter defines whether the tether behaves extensibly ($\lambda < 2\pi$) or inextensibly ($\lambda > 2\pi$) as it is perturbed from the equilibrium shape. The values of Table 1, together with the estimate of $R/L = 100$, yield a value of $\lambda = 2$, very near the critical value. Since these values are only estimates, and since the boundary conditions on spacecraft tethers are very different from those treated in reference 7, an analysis is appropriate.

This section derives the equations of motion governing infinitesimal perturbations of a slightly curved tether. The equilibrium curve is taken to be planar, and the perturbations are defined within this tether equilibrium plane, and normal to it. The effects of small coupling due to the slow (order ω_0) angular velocities of the reference frame are ignored, consistent with the approximation of spectral separation.

Figure 3 defines the small perturbations $u(s,t)$, $v(s,t)$, $w(s,t)$, $\xi(s,t)$ and $\eta(s,t)$ of the tether with respect to its equilibrium shape, defined by $x(s)$ and $y(s)$ where s is the equilibrium arclength. This equilibrium arclength differs slightly from the natural arclength, z ,

(see Figure 3) depending upon the equilibrium tension. The tension is taken to be the sum of the equilibrium value, $T(s)$, and a perturbation $r(s,t)$. Under the assumptions justified in the preceding paragraphs, and using the equilibrium defined by equation (8), equations (9) can be expanded to:

In plane of tether equilibrium:

Axial:

$$\frac{\partial}{\partial s} \left(T \frac{\partial u}{\partial s} + r \frac{dx}{ds} \right) = \mu \dot{u} \quad (9)$$

Lateral:

$$\frac{\partial}{\partial s} \left(T \frac{\partial v}{\partial s} + r \frac{dy}{ds} \right) = \mu \dot{v} \quad (10)$$

Normal to the plane of tether equilibrium:

$$\frac{\partial}{\partial s} \left(T \frac{\partial w}{\partial s} \right) = \mu \dot{w} \quad (11)$$

where terms of second and higher order in perturbational quantities have been dropped. The perturbational tension is given by

$$r = \bar{EA} \left(\frac{dx}{ds} \frac{\partial u}{\partial s} + \frac{dy}{ds} \frac{\partial v}{\partial s} \right) \quad (12)$$

where \bar{EA} is the effective extensional stiffness of the tether at the equilibrium strain (see Figure 1).

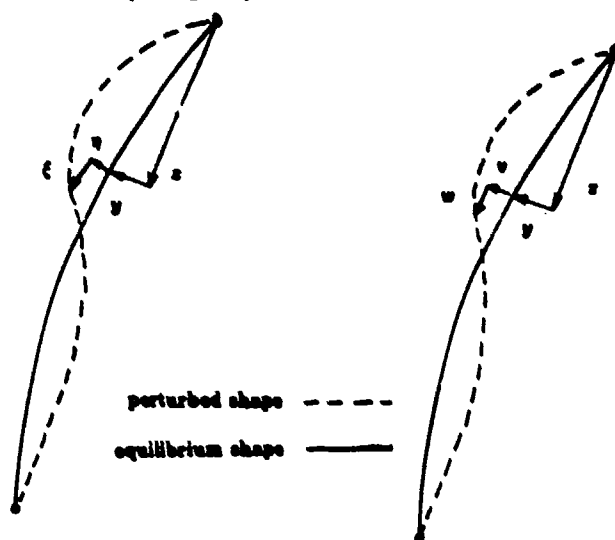


FIGURE 3 The equations of motion governing infinitesimal tether deflections from the equilibrium curve can be expressed in several different coordinate systems. Curvilinear coordinates are useful for exposing the high frequency wave-propagation limiting behaviour, and can be used for an eigen-analysis.

Reference 7 makes further approximations, valid for very shallow pinned-pinned catenaries, to manipulate equations (9), (10) and (12) into a single second order partial differential for $w(s,t)$. We prefer the approach of reference 17, in which cable deflections are expressed in terms of components tangential and perpendicular to the equilibrium curve (see Figure 3). Equations (9), (10) and (12) can be transformed, using the transformation

$$w = \xi \frac{dz}{ds} - \eta \frac{dy}{ds} \quad (13)$$

$$v = \xi \frac{dy}{ds} + \eta \frac{dz}{ds} \quad (14)$$

into an equivalent system;

In plane of tether equilibrium:
Parallel to equilibrium tether

$$\frac{\partial}{\partial s} \left(EA \frac{\partial \xi}{\partial s} \right) - \mu \frac{\partial^2 \xi}{\partial s^2} = -\frac{T}{R} \left(\frac{\partial \eta}{\partial s} - \xi \frac{1}{R} \right) - \frac{\partial}{\partial s} \left(\frac{EA}{R} \eta \right) \quad (15)$$

Perpendicular to equilibrium tether

$$\frac{\partial}{\partial s} \left(T \frac{\partial \eta}{\partial s} \right) - \mu \frac{\partial^2 \eta}{\partial s^2} = \frac{EA}{R} \left(\frac{\partial \xi}{\partial s} + \eta \frac{1}{R} \right) + \frac{\partial}{\partial s} \left(\frac{T}{R} \xi \right) \quad (16)$$

where $R = (dy/ds^2 x/ds^2 - dx/ds^2 y/ds^2)^{-1}$ is the equilibrium radius of curvature of the tether. Equation (11) remains unchanged.

Equations (11), (15) and (16) now describe the perturbational motion of an elastic cable from its planar equilibrium curve. The curve need not be shallow, nor need the radius of curvature, R , be constant with s . It is clear that curvature couples the two components of the planar motion; equations (15) and (16) are coupled by terms involving $1/R$. As $R \rightarrow \infty$, the coupling disappears, and the equations reduce to the familiar decoupled wave equations for axial and lateral motion of an elastic cable. Motion normal to the equilibrium plane remains unaffected by curvature.

Wave Propagation Along the Tether

Equations (15) and (16) are suitable for investigation of the intuition that high frequency tether motion is effectively described by propagation of decoupled lateral and tangential waves. We assume a solution of the form

$$\begin{pmatrix} \xi \\ \eta \end{pmatrix} = \begin{pmatrix} \xi_0 \\ \eta_0 \end{pmatrix} e^{\gamma(\omega, s) + i\omega t} \quad (17)$$

where $\gamma(\omega, s) = \alpha(\omega, s) + i\beta(\omega, s)$ is known as the propagation coefficient. Substitution of equations (17) into (15) and (16) yields a pair of coupled second order polynomials in γ and ω . These polynomials are satisfied along the lines sketched in Figure 4. We see that wave propagation becomes non-dispersive for $hR \gg 1$, that is, when the wavelength becomes small relative to the radius of curvature. Since the frequency has been non-dimensionalized with respect lateral wave speed, $\sqrt{T/\mu}$, three values of T/EA (both assumed constant with s) give three different values of non-dimensional tangential wave speed. Investigation of the corresponding wave-mode eigen-vector, $(\xi_0, \eta_0)^T$, reveals that the response consists of pure extensional $(\xi_0, \eta_0) = (1, 0)$, or pure lateral $(\xi_0, \eta_0) = (0, 1)$ motion for $hR \gg 1$. An order-of-magnitude analysis of the terms of equations (15) and (16), as $|hR| \rightarrow \infty$ will yield a similar insight.

Natural and Forced Motions of the Tethered System

Irvine and Caughey[7] report an approximate eigen-analysis of equations (9), (10) and (12) for pinned-pinned boundary conditions and shallow parabolic catenaries. They conclude that the only mode strongly affected by slight curvature of an elastic cable is the first symmetric lateral mode. For analysis of a tethered spacecraft system, we are interested in different boundary conditions. A general end body of such a tethered system can provide a complex boundary condition, including effects of end body flexibility and attitude motion. We formulate the eigen-analysis for arbitrary boundary conditions, and show representative solutions for the simplest; one end effectively pinned by attachment to a very massive body, the other end connected to a point mass only several times more massive than the tether.

Introduction of the non-dimensional cross-sectional vector

$$\Gamma = (\xi/L, EA/T \frac{\partial \xi}{\partial s}, \eta/L, \frac{\partial \eta}{\partial s})^T \quad (18)$$

permits writing (Fourier transformed) equations (15) and (16) as

$$\Gamma' = \begin{pmatrix} 0 & 0 & 0 & 0 \\ -\omega^2 + 1/R^2 & 0 & 0 & -1/R \\ 0 & 0 & 0 & 1/R \\ 0 & 1/R & -\omega^2 + 1/R^2 & 0 \end{pmatrix} \Gamma \quad (19)$$

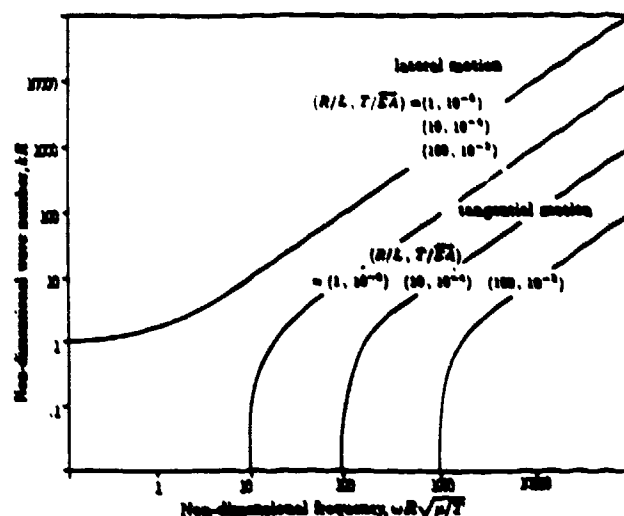


FIGURE 4 Dispersion curves of lateral and tangential waves propagating along a tether with uniform equilibrium tension and radius of curvature.

where $\epsilon = T/EA$, $R = R/L$, $\omega = \omega L \sqrt{\mu/T}$, and the spatial derivative is taken with respect to a non-dimensional distance, $\Gamma' = L \partial \Gamma / \partial s$.

Boundary conditions on either end of the tether are conventionally expressed as a matrix equation;

$$B(\omega) \Gamma = f \quad (20)$$

where f is the vector of applied forces or enforced displacements, as appropriate. To define a pinned end at $s = 0$ equation (20) would employ

$$B = \begin{pmatrix} 1 & 0 & 0 & 0 \\ 0 & 0 & 1 & 0 \end{pmatrix} ; \quad f_0 = \begin{pmatrix} \xi/L \\ \eta/L \end{pmatrix}_{s=0}$$

and f_0 is an enforced displacement. A point mass, m , at $s = L$ is described by

$$B = \begin{pmatrix} -\frac{\mu}{L} \omega^2 & 1 & 0 & 0 \\ 0 & 0 & -\frac{\mu}{L} \omega^2 & 1 \end{pmatrix} ; \quad f_1 = \begin{pmatrix} f_{\xi}/T \\ f_{\eta}/T \end{pmatrix}_{s=L}$$

The general form of the solution of equation (19) is

$$\Gamma(s, \omega) = (\Gamma_1 e^{\gamma_1 s/L} \quad \Gamma_2 e^{\gamma_2 s/L} \quad \Gamma_3 e^{\gamma_3 s/L} \quad \Gamma_4 e^{\gamma_4 s/L}) \begin{pmatrix} C_1 \\ C_2 \\ C_3 \\ C_4 \end{pmatrix} \quad (21)$$

where Γ_i is the i^{th} eigenvector of the matrix in equation (19), and $\gamma_i(\omega)$ is the corresponding eigenvalue. Application of boundary conditions at the two ends, each in the form of equation (20) permits evaluation of the constants C_i , $i = 1, 2, 3, 4$ in terms of the force vector $(f_0, f_1)^T$. The response anywhere along the tether can then be expressed in terms of a matrix of transfer functions;

$$\Gamma(s, \omega) = H(s, \omega) \begin{pmatrix} f_0 \\ f_1 \end{pmatrix} \quad (22)$$

These 16 transfer functions can be evaluated for any value of $s, 0 < s < L$, and any value of Ω , and relate the response along the tether to the excitation at the two ends.

Transfer Functions

The transfer functions of equation (23) will vary slowly with time, since they depend upon the current equilibrium condition. This equilibrium establishes values of tension, T , radius of curvature, R , and defines the directions of ξ , η and u . (Note that deflections normal to the plane of tether equilibrium, u , decouple from ξ and η . The relevant transfer functions can be derived from equation (11) and suitable boundary conditions.)

Figure 5 gives a plot of $H_{1,5}(L, \Omega)$, parameterized with three non-dimensional groups; $R = R/L$, $\epsilon = T/\bar{EA}$ and $m/\mu L$. This transfer function shows the tangential acceleration of the far end of the tether ($s = 1$) being excited by a unit lateral acceleration at the near end ($s = 0$). If the equilibrium tether shape were straight, this response would be zero. Figure 5a shows, for a fixed equilibrium ϵ/\bar{EA} , and a fixed sub-satellite mass ratio, $m/\mu L$, the ratio of $\xi(s = L)$ and $\eta(s = 0)$ as a function of frequency. As expected, the low frequency response tends towards zero as the tether becomes straight, $R/L \rightarrow \infty$ as it is clear that even slight tether curvature will couple these two motions, particularly at resonance.

Figure 5b shows the same curves for an increased value of T/\bar{EA} . The low frequency limiting behavior remains unchanged, however the non-dimensional frequencies of the first few resonances are strongly affected.

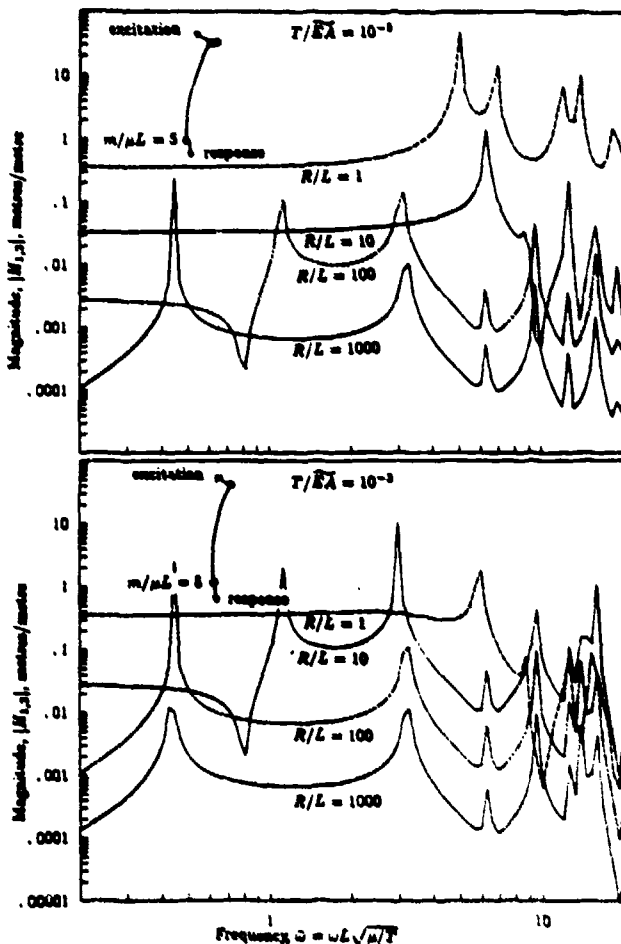


FIGURE 5 Transfer functions of the tangential response at one end of the tether to a lateral excitation at the other end

Tether Modes

Figures 5a and 5b yield little insight into the character of the underlying vibration. Figures 6 show the evolution of the first few natural frequencies and mode shapes as a function of two non-dimensional parameters, R/L and T/\bar{EA} . R/L is held fixed at two values, $R/L = 10, 100$ while T/\bar{EA} is varied. Strong modal coupling is predicted between the two lowest lateral modes whenever $\lambda^2 > 10$. At $\lambda^2 \approx 30$ (very close to the value predicted by reference 7) these mode shapes become identical, and their contribution disappears from all transfer functions. Further study is required to understand this behavior. The lateral and longitudinal modes can also couple strongly. Figure 6b shows such coupling between the first few lateral modes and the longitudinal bounce mode.

EFFECT OF DEPLOYMENT OR RETRIEVAL

The preceding analysis has ignored effects of deployment and retrieval on the first tether dynamics, both the coriolis coupling due to a tangential velocity of the tether, and the gradual length change.

Effect of Tether Translational Velocity

Retrieval of the tether to a massive end body will result in an equilibrium translational velocity of the tether along its equilibrium curve. This translational velocity will add coriolis coupling terms to equations (15) and (16). Reference 6 has shown that such translational velocity will have a negligible effect upon the perturbational motion of an elastic catenary as long as this velocity is much less than the classic lateral wave speed $\sqrt{T/\mu}$. Retrieval speed of spacecraft tethers is limited by attitude stability considerations to $\dot{L}/L \ll \omega_n$, which, on the basis of the spectral separation assumed implies $\dot{L} \ll \sqrt{T/\mu}$. Ignoring the effect of this coriolis coupling is then consistent with the assumption of spectral separation upon which the preceding analysis is based.

Effect of Gradual Length Changes

The preceding paragraph argues that relative tether length changes will be small over the period of even the fundamental tether mode. When this is satisfied, tether mode shapes will be effectively those of the constant length system, but their amplitude will vary slowly with the length. An approximate expression for this dependence can be derived by assuming a given mode shape, of amplitude a and geometrically independent of length, and insisting upon conservation of strain energy. This leads to the conclusion that $\bar{EA}a^2/L$ remain constant if the mode is primarily tangential, and that Ta^2/L remain constant if the mode is primarily lateral. Since T is approximately proportional to length, lateral deflection amplitudes should be approximately independent of length. This agrees with the simulation results reported in reference 2. The dependence of \bar{EA} on length is more difficult to approximate. If the non-linear effects can be neglected, then $\bar{EA} = EA$ is independent of length, and tangential tether vibrations should decrease during retrieval according to $a \sim \sqrt{L}$. If the tether mode is coupled lateral and axial, then its dependence on length should be some weighted average of the individual dependencies.

MODELING LIMITATIONS

The insights gained in these analyses were achieved only at the cost of rather severe assumptions. Interest was restricted to tethered systems involving one tether and two end bodies, with a spectrum permitting the approximation of spectral separation. The results of Figures 5 and 6 show that for some choices of parameters, the assumption of spectral separation will be violated. The conclusions reached will

not be applicable to very different systems such as tethers with negligible end masses, massive tapered tethers, multiple tethers, rapidly spinning tethers, and many others.

The eigen-analysis presented is based upon the assumption of small deflections. References 18 and 19 have considered larger amplitude motion of cables. Reference 18 shows that the quadratic terms in the strain energy expression of a shallow catenary remain dominant only as long as deflections remain small compared to the equilibrium sag.

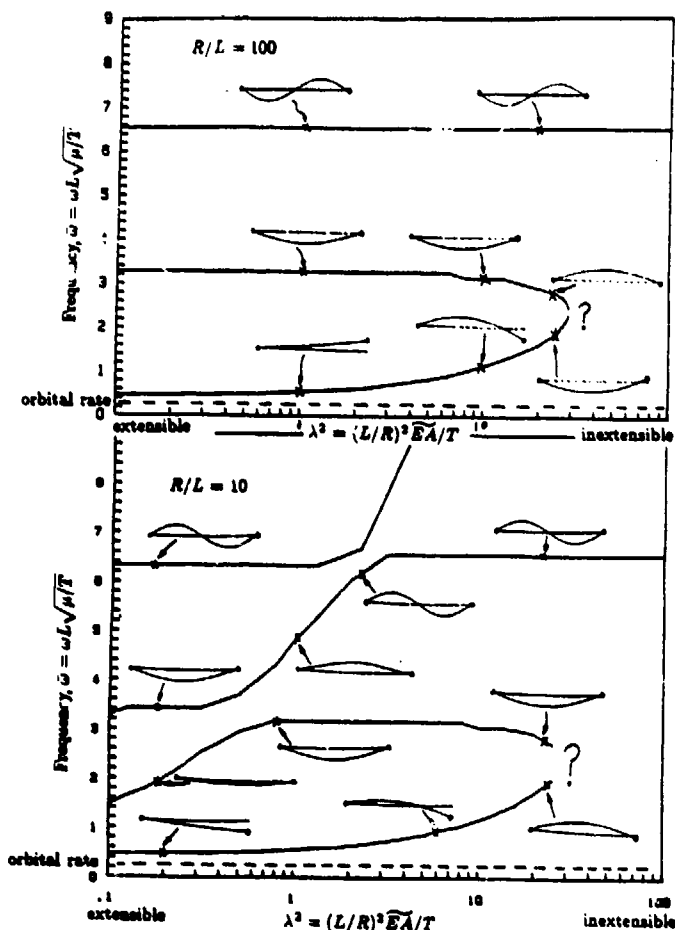


FIGURE 6 Trends of the first few natural frequencies and mode shapes of a tethered system with slight equilibrium curvature. One end mass is effectively infinite, the other has five times the tether mass, $m/\mu L = 5$.

Equations (15) and (16) are thus only valid for very small deflections, less than $\delta = L/8R \approx 0.001L$. Reference 19 derives the equations of motion of a sequence of assumed deflection modes of a spacecraft tether, where the reference state is taken to be straight, and axially unstrained. This work shows that non-linear effects will couple axial and both lateral deflection modes, and by integration of the equations of motion, shows this coupling to be significant when deflections become as large as $0.1L$.

Unmodeled effects which threaten to be important are end body attitude motion and flexibility. Very slow end body attitude motion would still permit spectral separation, simply redefining the reference equilibrium. Fast end body attitude motion, and end body flexibility will potentially couple strongly to the tether modes. Table 1 estimates the sub-satellite pendular motion to have a period of 13 seconds. One should expect strong coupling of this motion with the bounce mode, and with several (perhaps the 40th) lateral tether modes. The introduction

of fast end body attitude dynamics would require the use of at least two more non-dimensional parameters, perhaps d/L and $d\sqrt{m/I_0}$, where d is the offset between the tether attach point and the end body mass center, m its mass, and I_0 its inertia. A study of the effects of this coupling is left as a topic of future research.

SUMMARY

This paper has investigated the dynamics of typical tethered spacecraft systems in an expository approximate way. The motion is shown to occur at two time scales, one comparable to orbital rate, the other much faster. Spectral separation is invoked to approximately decouple this motion.

Fast tether vibrations occur with respect to a slowly varying quasi-equilibrium. The equilibrium shape of the tether is estimated to be slightly sagged from a straight line, and the small perturbations from this equilibrium are described by a system of linear partial differential equations. Non-dimensional parameter groups are identified which govern the character of the fast tether vibrations.

ACKNOWLEDGEMENTS

The work summarized by this paper was begun during the summer of 1986 during a research visit at the German Aerospace Research Establishment, DFVLR Oberpfaffenhofen. The visit was made possible by the hospitality of the DFVLR, in particular Dr. Konrad Reinelt, and by the generosity of the Alexander von Humboldt Foundation. The work was continued at the Massachusetts Institute of Technology under the sponsorship of the U. S. Air Force Office of Scientific Research with Dr. Anthony Amos as monitor. Computations were performed by Jeff Morse as part of MIT's Undergraduate Research Opportunities Program.

REFERENCES

1. D. Lang, "TOSS (Tethered Object System Simulation) Reference Manual", Version C, May 1985
2. A. K. Misra, V. J. Modi, "A Survey on the Dynamics and Control of Tethered Satellite Systems", *NASA/AIAA/PSN International Conference on Tethers in Space*, Arlington, VA, September 1986
3. P. Kohler, W. Meag, R. Wehrli, R. Weber, H. Brauchli, "Dynamics of a System of two Satellites Connected by a Deployable and Extensible Tether of Finite Mass", Vol. 1 and 2, ESA Contract Report, Contract No. 2922/76/NL/AN(SC), October 1978
4. A. H. Flotow, P. R. Williamson, "Deployment of a Tethered Plasma Diagnostics Satellite into Low Earth Orbit", *J. Astronautical Sciences*, Vol. 34, No. 1, Jan-March 1986, p 65
5. A. E. H. Love, *A Treatise on the Mathematical Theory of Elasticity*, Doyer, 1944
6. V. V. Beletskii, E. M. Levin, "Dynamics of the Orbital Cable System", *Acta Astronautica*, Vol. 12, No. 5, pp. 235-291, 1985
7. H. M. Irvine, T. K. Caughey, "The Linear Theory of the Free Vibration of a Suspended Cable", *Proc. R. Soc. Lond., A* 341, 299-315 (1974)
8. A. Simpson, "On the Oscillating Motions of Translating Elastic Cables", *J. Sound and Vibration*, (1972), 20(2), 177-189

- 9 A. E. Bryson, *Control of Spacecraft and Aircraft*, Stanford University lecture notes, draft of September 1985
- 10 C. M. Diarra, P. M. Bainum, "On the Accuracy of Modeling the Dynamics of Large Space Structures", *Proceedings of IAF'85, 36th Congress of the International Astronautical Federation*, Stockholm, Sweden, October 1985
- 11 H. Ashley "Observations on the Dynamic Behaviour of Large Flexible Bodies in Orbit", *AIAA Journal*, Vol. 5, No. 3, 1967, p. 460-469
- 12 P. C. Hughes, *Spacecraft Attitude Dynamics*, Wiley, 1986
- 13 J. Storch, S. Gates, "The Dynamics of a Uniform Tether with a Tip Mass Subject to Gravitational Body Forces", CSDL-R-1791, Internal Report of the Charles Stark Draper Lab, June 1985
- 14 A. K. Misra, V. J. Modi, "Frequencies of Longitudinal Oscillations of Tethered Satellite Systems", *AIAA/AAS Astrodynamics Conference*, Williamsburg, VA, August 1986, Paper 86-2274
- 15 D. M. Xu, "Dynamics and Control of Shuttle Supported Tethered Satellite Systems", Ph.D. Thesis, Dept. of Mechanical Engineering, McGill University, Montreal, Canada, 1984
- 16 L. G. Lemke, J. D. Powell, Xiaohua He, "Attitude Control of Tethered Spacecraft", *NASA/AIAA/PSN International Conference on Tethers in Space*, Arlington, VA, September 1986
- 17 D. S. Saxon, A. S. Cahn, "Modes of Vibration of a Suspended Chain", *Quart. Journ. Mech. and Applied Math.*, Vol. VI, Pt. 3(1953)
- 18 P. Hagedorn, B. Schäfer, "On Non-Linear Vibrations of an Elastic Cable", *Int. J. Non-Linear Mechanics*, Vol. 15, pp. 333-340, 1980
- 19 A. K. Misra, D. M. Xu, V. J. Modi, "On Vibrations of Orbiting Tethers", *Acta Astronautica*, Vol. 13, No. 10, pp 587-597, 1986

DEL 11 E 300

DYNAMIC CABLE RESPONSE:

THE EFFECT OF CABLE SAG

Final Report

16.622

Author: Todd J. Barber

Advisor: Prof. A.H. von Flotow

Partner: Earl M. Gregory

December 11, 1987

Abstract

A cable pinned on both ends was excited by a variable frequency shaker and various aspects of its dynamic response were measured, including cable wave propagation speeds, resonant frequencies, and resonant mode shapes. Cable tangential velocity at a point was determined by using electromagnets to create a magnetic field that the cable oscillated in, thus giving rise to an induced voltage in a small filament wrapped around the cable at that point. This voltage produced made it possible to experimentally determine cable wave propagation speeds and resonant frequencies. Resonant mode shapes were determined photographically. Results were compared to a new theoretical model that used the midspan deflection of the cable as a running parameter. All experiments were performed at three different sag levels to test the validity of the model. The results of the experiment presented a limited proof that the model proposed accurately describes actual behavior. It was concluded that certain non-modeled effects, particularly three dimensional cable oscillations, were significant in the actual experiments and recommendation has been made to incorporate these effects into the theoretical model.

Table of Contents

1. Introduction	1
2. Theoretical Background	3
3. Experimental Apparatus	7
3.1 General Setup	7
3.2 Wave Speed Propagation	8
3.3 Resonant Frequencies	8
3.4 Mode Shapes	8
4. Experimental Procedures	13
4.1 Wave Speed Propagation	13
4.2 Resonant Frequencies	13
4.3 Mode Shapes	14
5. Results and Discussion	15
5.1 Wave Propagation Speed	15
5.2 Resonant Frequencies	15
5.2.1 Low Sag ($\delta = 0.035$ m)	17
5.2.2 High Sag ($\delta = 0.200$ m)	17
5.2.3 Intermediate Sag ($\delta = 0.140$ m)	22
5.3 Resonant Mode Shapes	22
5.3.1 Low Sag ($\delta = 0.035$ m)	25
5.3.2 High Sag ($\delta = 0.200$ m)	25
5.3.3 Intermediate Sag ($\delta = 0.140$ m)	25
6. Conclusion	32
I. Transfer Function Plot Programs	33
II. Mode Shape Data Programs	34
III. Mode Shape Data	35

1. Introduction

A curved cable sustaining driving oscillations exhibits a complex dynamic response that is largely a function of how much the cable is sagged. A cable with a small degree of sag (with the term "small" defined more quantitatively later) behaves in a well known manner. This behavior is predicted analytically by the so-called "string equation", which is the linear differential equation that predicts the completely familiar normal string vibration modes. A cable with a large degree of sag behaves in a somewhat different way; however, its analytical solution is completely determined by solving a different linear differential equation. This classic "hanging chain" equation, as well as the string equation, have been known for centuries.

As one might expect, the dynamic response of a sagged cable with an intermediate sag should exhibit a dynamic response intermediate between the results obtained for the string and the hanging chain. However, an analytical model of the behavior was not formulated until recently. In a paper¹ entitled Some Approximations for the Dynamics of Spacecraft Tethers, Prof. A.H. von Flotow proposed a model to explain the intermediate behavior for the intermediate sag case. His model predicts that there are two coupled differential equations which are functions of sag describing the tangential and lateral motion of a driven cable. My partner and I have attempted to verify the validity of Prof. Flotow's model by driving a pinned-pinned cable with a variable frequency shaker and measuring its dynamic response. We have chosen three figures of merit to determine experimentally: wave propagation speed along the cable, resonant frequencies, and resonant mode shapes. We performed our experiment at three different sag levels: a shallow sag representing string behavior, a large sag representing hanging chain behavior, and an intermediate sag representing the interesting intermediate behavior. By using an eigenvalue solution technique, solutions to Prof. von Flotow's equations of motion can be solved and theoretical results for wave propagation speeds, resonant frequencies, and resonant mode shapes can be ascertained for all three experimental sag levels. Clearly, then, the results from theory and the results from the experiment can be directly compared and the validity of Prof von Flotow's model (barring large experimental errors) can be established.

In addition to possibly verifying a previously untested hypothesis, a further motivation for our experimental study is the real-world application to spacecraft tethers. In a situation when the only link between an astronaut and the mother ship is a spacecraft tether, the very safety of the astronaut depends on the dynamic response of the spacecraft tether. Unfortunately, my partner

and I were unable to simulate the pinned-free boundary conditions of a zero gravity environment. However, a reworking of Prof. von Flotow's analysis with our pinned-pinned boundary conditions was done and thus good experimental verification of the pinned-pinned case with our pinned-pinned analysis will represent a verification of Prof. von Flotow's general model.

The methods used to experimentally determine wave propagation speed, resonant frequencies, and resonant mode shapes are quite complicated and I will explain the basic principles here. Basically, a way was needed to measure the tangential cable velocity at a point along the cable. After much brainstorming, a reasonable solution was proposed. If the tangential velocity of the cable at a point could be converted into a voltage, we would have a quantitative measure of the cable's tangential velocity at that point. However, this can be accomplished relatively simply by remembering simple electromagnetic theory. A wire moving through a magnetic field develops a voltage proportional to its velocity through the magnetic field. Therefore, by wrapping a small copper filament around the cable at a point and allowing this point of the cable to shake through a magnetic field, a voltage could be generated in the filament which could be sent to an amplifier and then to a signal recorder. Indeed, this was done in order to measure wave propagation speed and a cable velocity (tangential) vs driving frequency, resulting in a transfer function plot, which exhibits peaks at the resonant frequencies. The experimental determination of mode shapes has a much simpler solution. After experimentally varying the frequency until a normal mode occurs, a time exposure photograph could be made at that frequency. A "washed-out" picture of this mode shape could thus be obtained. All of these experimental results can be compared graphically to theoretical results, which is a much clearer method to compare experimental and hypothetical results than comparing numerical data.

2. Theoretical Background

An attempt will be made in this section to point out the main points in Prof. von Flotow's theoretical model derivation and to explain how our theoretical results (to which our experimental results were compared) were obtained. To begin, we must review the dynamics of a hanging cable (refer to Figure 1). An equation can be derived for the radius of curvature R in terms of the length of the cable L and the midspan deflection, or sag, δ by considering simple geometry. We obtain the following result:

$$R = L^2 / 8\delta \quad (1)$$

By considering force equilibrium on the cable, an equation relating the tension in the cable T to the sag δ can be formulated:

$$T = mgR = \frac{mgL^2}{8\delta} \quad (2)$$

where m is the mass per unit length of the cable and g is the acceleration due to gravity.

From Prof. von Flotow's paper (Ref. 1), the following non-dimensional parameter may be a convenient way to reduce data and make it more general. This non-dimensional parameter λ is defined as follows:

$$\lambda^2 = \left(\frac{L}{R}\right)^2 \frac{EA}{T} \quad (3)$$

where E is the Young's modulus of the cable and A is the cable cross-sectional area. In this paper, it was discovered that for $\lambda^2 \approx 1$, δ was small enough for the cable to be treated as a string. Similarly, for $\lambda^2 \approx 15$, δ was large enough for the cable to be treated as a hanging chain. However, for $\lambda^2 \approx 30$, δ was at the interesting intermediate case described in the introduction section. Knowing this, it only remained for my partner and I to determine the value of sag needed to give us the desired value for λ .

However, this can be done simply by substituting in equations 1 and 2 into equation 3 for R and T , respectively. The result of this substitution:

$$\lambda^2 = \frac{512EA\delta^3}{mgL^4} \quad (4)$$

4.

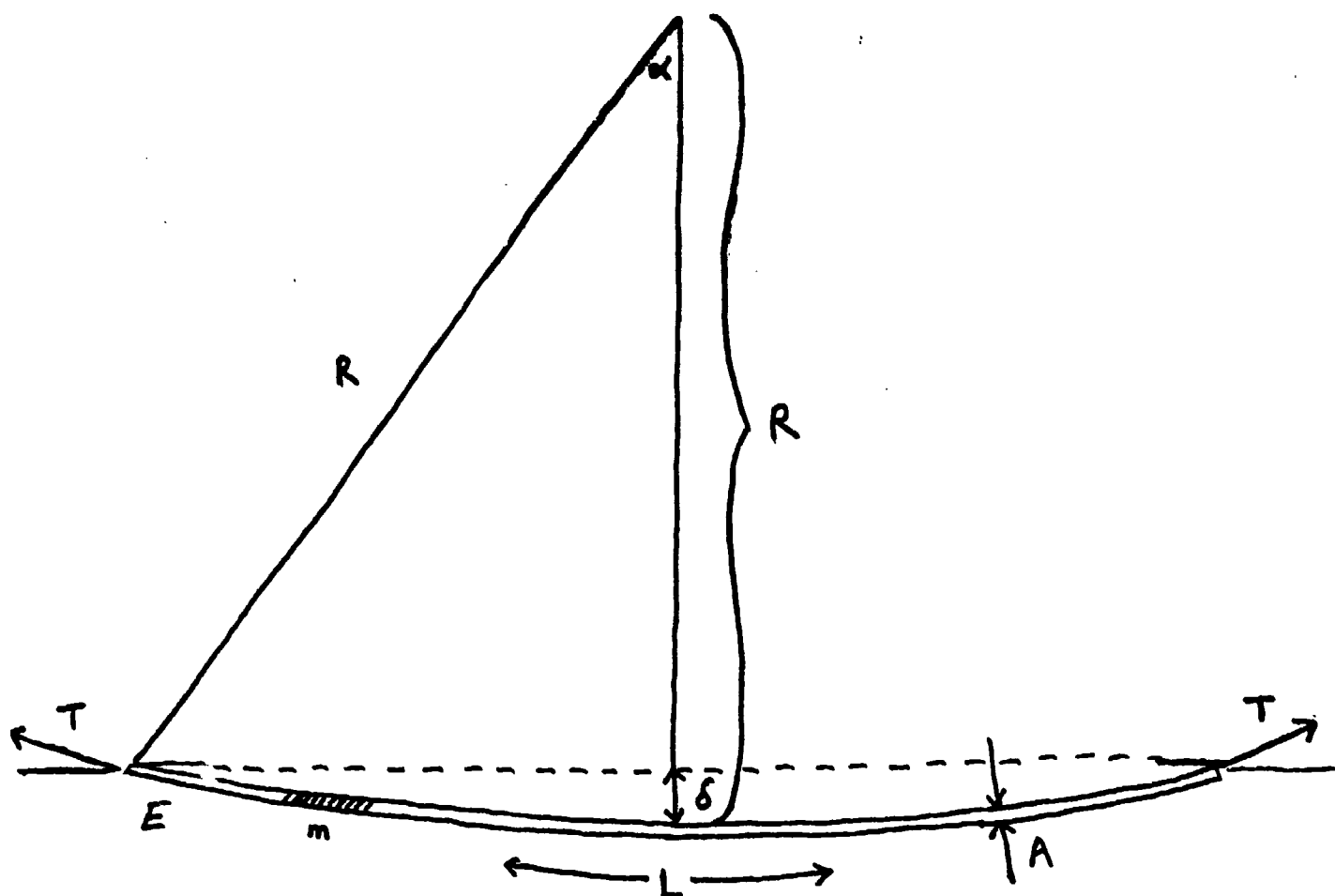


FIGURE 1: GEOMETRY OF A HANGING CABLE

R = Radius of curvature of cable

δ = Midspan deflection of cable

L = Length of cable

α = Angle subtended at center of radius of curvature from midspan to one cable end

T = Tension supporting cable

A = Cross-sectional area of cable

E = Young's Modulus of cable

m = mass per unit length of cable

Therefore, since all quantities except for δ and λ can be experimentally measured (and indeed were measured), for a given value of λ^2 , the value needed for δ is completely determined. Plugging in the numbers, we arrived at the following settings for δ : for the low sag case ($\lambda^2 \approx 1$), $\delta=0.0350$ meters; for the high sag case ($\lambda^2 \approx 75$), $\delta=0.200$ meters; and for the intermediate sag case ($\lambda^2 \approx 30$), $\delta=0.140$ meters.

I won't attempt to rigorously develop the analytical model used in Prof. von Flotow's paper, as the mathematics are quite abstract and complicated. Basically, linear partial coupled differential equations were formulated and solved by using an eigen-analysis solution technique. The resulting solutions were similar to a set of solutions prepared by a UROP student of Prof von Flotow's a year ago, with one modification. Our analysis used pinned-pinned boundary conditions while the boundary conditions discussed in Prof. von Flotow's paper were pinned-free boundary conditions. Because of the large amount of matrix algebra involved in this solution technique, the problem was solved on a computer using the programming language MATRIX, which has fantastic matrix manipulation techniques. The code was written to predict theoretical mode shapes and transfer function plots of cable tangential deflection at a point vs. driving frequency. Refer to Appendix A for a copy of the program used to predict the transfer function plots and a page explaining the variables and constants used in the program. The output of this program was three plots of cable tangential deflection vs. driving frequency for the three different sag cases mentioned above. These graphs can be seen in the results section of this report. Appendix B contains the programs used to generate mode shape data at the given resonant frequencies. These resonances were determined by locating the peaks of the transfer function plots. Again, a sheet is included to define the variables used in the computer program. Appendix C contains the data obtained from executing this program. This data, which represents cable tangential deflection vs. non-dimensional cable length, can be plotted on top of given plots of the cable in the equilibrium position to obtain the deflected shape of the cable at the resonant frequencies. Hence, these plots can be directly compared to plots made by taking data from actual time exposure photographs. Again, these plots will appear in the results section next to their theoretical counterparts.

The analytical model for determining the wave propagation speed down the cable is to use the classic formula known for centuries:

$$c = \sqrt{T/m} \quad (5)$$

where T is the tension supporting the cable at the ends and m is the mass per unit length of the cable. The value for T can be obtained from equation 2 and a numerical value can be obtained for the wave propagation speed for each of the three sag levels. Again, these numbers will be presented in the results section in a table comparing theoretical and experimental wave propagation speeds.

One important result that should be stated at this point is that theory predicts mode coupling for the intermediate sag case. Mode coupling occurs when two different resonances mode shapes are excited at closer and closer frequencies. In fact, as the resonant frequencies merge into the same frequency, a mode shape with mixed characteristics of the two parent modes is seen. This mode shape coupling, as predicted by Prof. von Flotow's model, actually was observed when the theoretical plots of the first four mode shapes were printed out for the intermediate sag case. If nothing else, this helps to confirm that our number-crunching truly represents the solution (for our boundary conditions) of Prof. von Flotow's previously untested theory.

3. Experimental Apparatus

3.1 General Setup

A section of the strong back in lab was procured and our apparatus was setup. Subsequently we attached a twelve foot long nylon cable to the strong back with one vertical and one horizontal cable clamp. The horizontal cable clamp was found in lab and simply bolted rigidly into the vertical strong back wall. We found the base of the vertical cable clamp in the lab as well. Using a lathe, we machined threads into the vertical aluminum rod that the cable attaches to and screwed it into the rigid bolted-down base. With this design, it would appear that our assumption of pinned-pinned boundary conditions is a valid one. This base could be moved horizontally and bolted again -- thus, this offered us a way to vary the midspan deflection.

A variable frequency shaker was mounted near one end of the cable. Either a wave-tech generator or a frequency spectrum analyzer was used to drive the shaker (after passing through an amplifier) at a fixed frequency or as a white noise, respectively. The choice of the driving mechanism depended on which of the experimental variables we were trying to measure (mode shapes or resonant frequencies, respectively).

As mentioned in the introduction, a magnetic field is needed to measure tangential velocity. This quantity was needed for the resonant frequency and wave propagation speed phases of the experiment. From theoretical considerations, a practical minimum for the required magnetic field strength was found to be about 10,000 Gauss. It is difficult to obtain magnetic field strengths of this magnitude in the lab; therefore, my partner and I decided to construct electromagnets that would give us the required magnetic field strength. This proved to be a demanding task. Indeed, the construction of these magnets took up the majority of our machining time. Please refer to Figure 2 for a diagram showing our magnet construction scheme. The cable, when driven, moves vertically in the air gap of the electromagnet. A small copper filament wrapped around the cable at this point will achieve a voltage when passing through this magnetic field. The necessary number of turns of wire around the magnet core was determined to be approximately 2500. The wire was wrapped around the core by using a lathe.

3.2 Wave Speed Propagation

In this phase of our experiment, both magnets were used. The small copper filaments wrapped around the cable were connected to leads that lead to a two-channel oscilloscope with memory. In the experimental procedures section, the method of obtaining the wave propagation speed will be explained. Please see Figure 3 for the experimental setup for the wave speed propagation phase of the experiment.

3.3 Resonant Frequencies

For this part of our experiment only one magnet was needed. A frequency spectrum analyzer drove our variable frequency shaker(via an amplifier) with white noise, The induced voltage in the coil was then sampled by the input channel to the frequency spectrum analyzer. Please see Figure 4 for the experimental setup for this phase of the experiment.

3.4 Mode Shapes

In the final phase of our experiment, all magnets were removed. A manually controlled wavetech generator was used to drive the shaker at a fixed frequency. A construction paper background was painted black and used as a backdrop for our photographs. We used a 750W spotlight to illuminate the cable so it would register on a time exposure photograph. A 35mm camera with a wide angle lens was used to photographically record black and white pictures of the mode shapes. Please refer to Figure 5 for the experimental setup for the resonant mode shapes of the experiment.

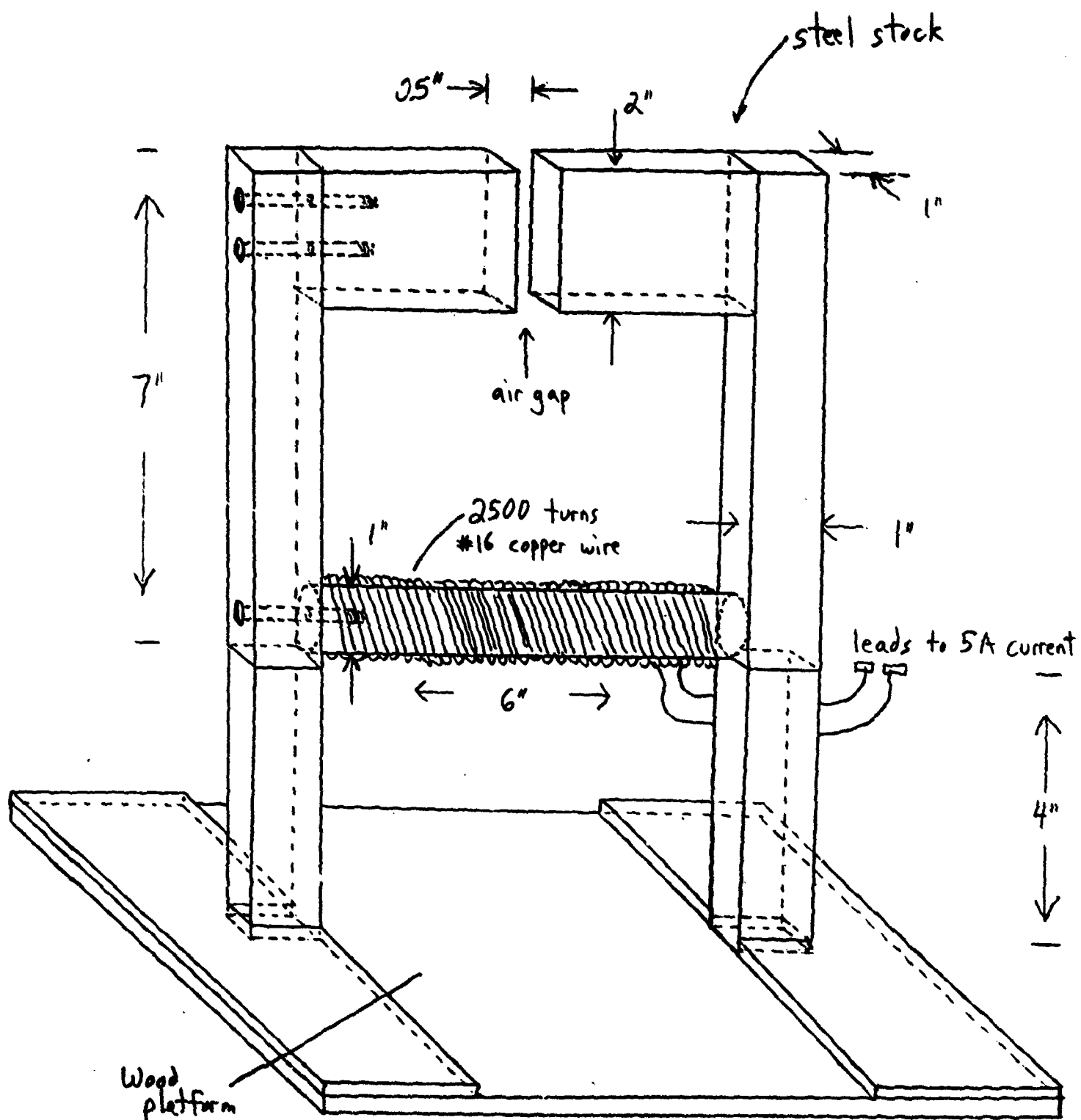


FIGURE 2: Electromagnet design

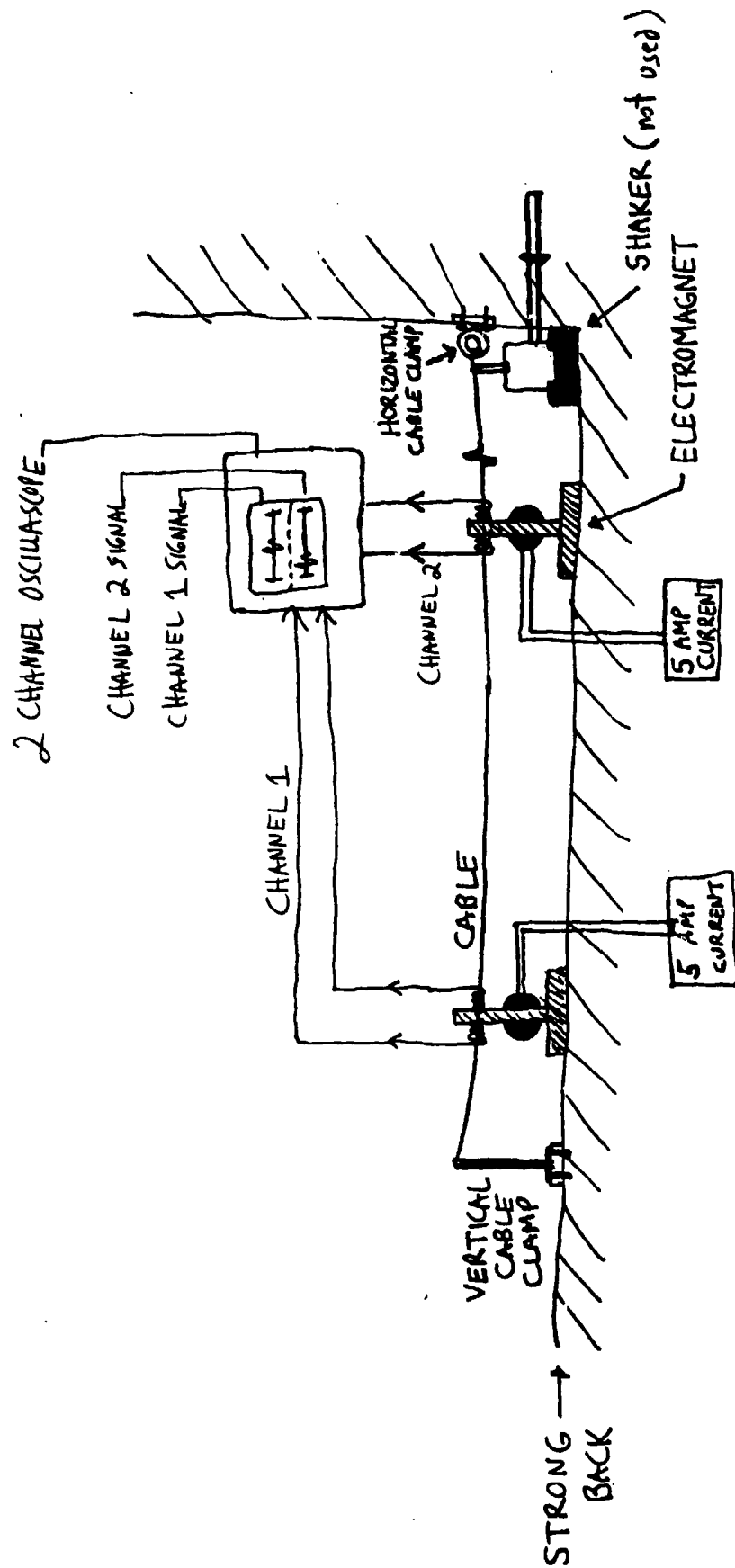


FIGURE 3: Wave speed propagation experimental

setup.

11.

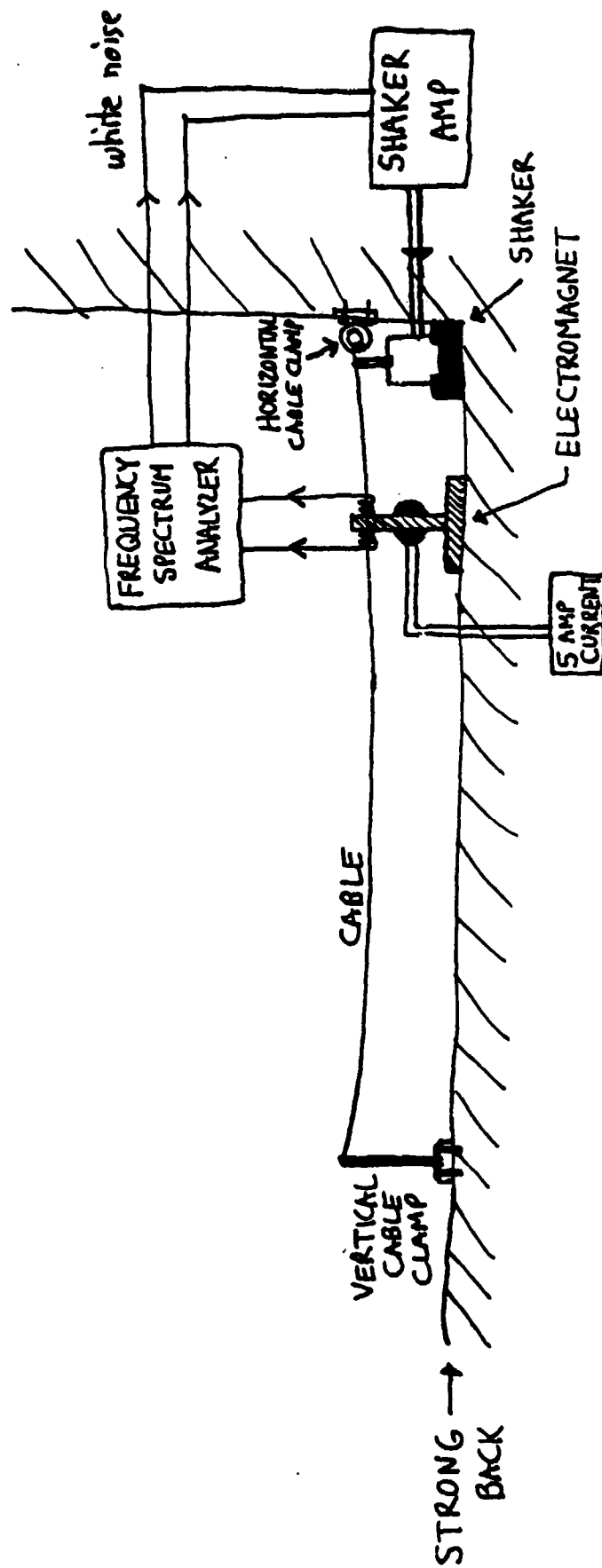


FIGURE 4: Resonant frequency experimental setup

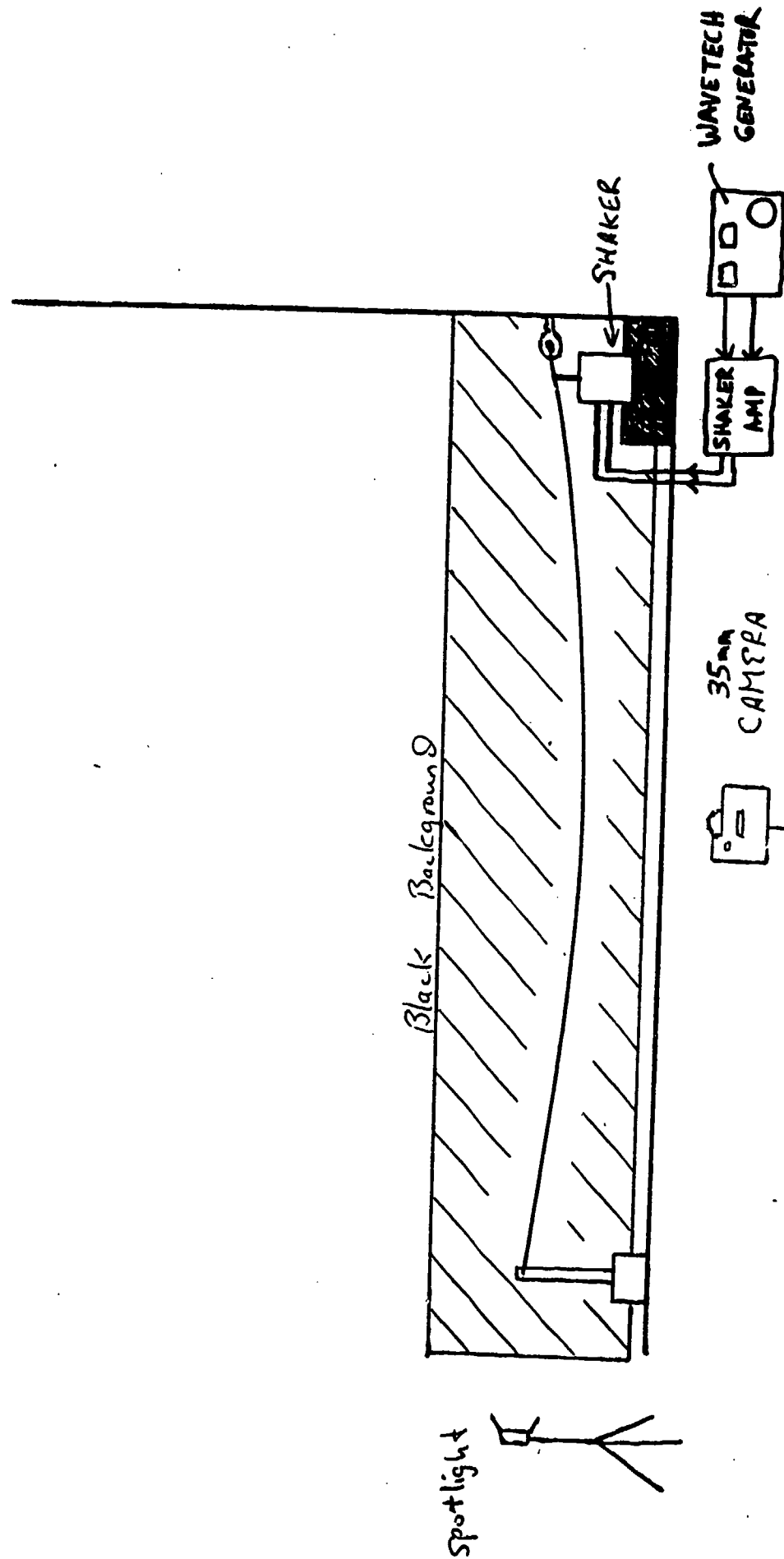


FIGURE 5:

Resonant mode shape experimental setup

4. Experimental Procedures

4.1 Wave Speed Propagation

The experimental procedure in this case was particularly simple. We tweaked the cable at a point to the right of the right magnet. This tweaking motion was accomplished by applying a sharp pulse to the cable with one finger. When the transverse wave had propagated along the cable to the point where the right magnet was located, the sudden displacement of the cable at this point triggered our two-channel oscilloscope to begin a time sweep on both channels. It took a small but measurable time for the transverse wave to propagate down the cable to the second magnet. When the wave reached this point the first non-zero signal was generated on the left magnet channel. By comparing the two channels on the oscilloscope, it was observed that the channels registered a very similar signal separated by a time delay. By knowing the distance between the two magnets, we then calculated the wave propagation speed along the cable by simply dividing the distance by the time delay. This experiment was performed five times at each of the three sag levels. The average of the five trials was calculated and is displayed in the subsequent results section, compared with the theoretical value of the wave speed for each case.

One source of error in this experiment is certainly the setting of cable sag. Especially for the case of small sag, a small error in setting the midspan deflection can cause a large change in the experimentally measured wave speed. Therefore, we would expect a better correlation between theory and experiment for the case of higher sag.

4.2 Resonant Frequencies

Performing this experiment was the most difficult in terms of the actual implementation. A position was selected for the magnet near the right end of the cable. For each of the three midspan deflection levels, a total of ten trials were used and an average was taken. For each trial, the frequency spectrum analyzer outputted a white noise signal. This was fed through the shaker amplifier to the shaker. The measured cable response at the magnet location due to this white noise was amplified and fed back to the frequency spectrum analyzer. The frequency spectrum analyzer then Fourier analyzed the incoming data to obtain a transfer function of voltage in the coil vs. the driving frequency. Since the voltage in the coil is proportional to the tangential

velocity at this point, the frequency spectrum analyzer actually had data for the cable velocity vs. frequency transfer function. This transfer function data was plotted by the spectrum analyzer and saved on floppy diskette. Later, hardcopies of these transfer function plots were printed out. Since, at a point, the tangential cable velocity is maximized at the resonant frequencies of the vibrating cable, the graphs of the (plotted) transfer function should have maximums at the resonant frequencies. Therefore, the resonant frequencies can be read directly from the transfer function plots.

The sources of experimental error in this phase of our experiment are numerous due to the complexity of the data taking process. Circuit noise appears to be the primary source of error, especially in the low frequency range.

4.3 Mode Shapes

In this phase of our experiment, the lab was darkened as much as possible and the data was taken at night. A spotlight was shined down the length of the cable in order to create a white washed-out picture of the desired mode shapes against the black background. We varied the frequency on the wavetech generator until we had visual confirmation that we had indeed excited a pure mode of the system. Once this frequency was set, three one-second time exposures were made: one at the optimal f-stop (read from a lightmeter installed in the camera) , and one at the next higher and next lower f-stops. We obtained these three pictures for the first four measurable mode shapes for each of the three sag settings.

Sources of error were numerous here too. The most pronounced effect was the existence of three-dimensional whirling modes, which were neglected in the analytical model provided by Prof. von Flotow. Therefore, a washed-out photographic mode shape might appear two-dimensional even if in actuality it was a whirling three-dimensional mode.

5. Results and Discussion

5.1 Wave Propagation Speed

The results of the experimental wave propagation speed are compared directly to the theoretical results for each of the three different sag levels of .035 meters, .14 meters, and .20 meters in Table 1. As mentioned before, we expect a better correlation between theory and experiment in the higher sag cases. Clearly, this is exhibited in the data, with experimental results from the two higher sag cases actually quite consistent with the theoretical results.

There are many possible sources of error in this experiment, and below I mention ones I feel to be the most significant.

1. Error in setting midspan deflection
2. Error in generating a consistent impulse by hand for different data trials.
3. Error in the value for the Young's modulus of the cable. (This changes the theoretical value of the wave propagation speed)

Even with these errors, I feel the results are significant and offer reasonable proof that the theoretical model actually predicts the experimental behavior in the two higher sag cases. The lowest sag case will probably need to be confirmed with a more elaborate experimental setup to minimize the errors mentioned above. Overall, I would say that experiment and theory match reasonably and our results show some degree of validity.

5.2 Resonant Frequencies

As mentioned above, we will compare data graphically in this phase of the experiment. The results and discussion are presented below for each of the three sag levels. It should be noted that the actual value read from the theoretical vs. experimental graphs cannot be compared because the experimental graphs represent cable tangential velocity vs. driving frequency while the theoretical graphs represent cable tangential deflection vs. driving frequency. However, since the velocity and deflection scale with each other (with a phase delay), the general shapes (and therefore the resonant frequencies, which are where the peaks of each graph occur) can be compared.

TABLE 1: Experimental and theoretical values for wave propagation speed along cable for 3 different sag levels

δ Sag (m)	C_{theory} (Wave speed) theory (m/s)	C_{exp} (Wave speed) exp (m/s)
0.035 (Low)	20.9	36.0
0.200 (High)	8.77	7.92
0.140 (Intermediate)	10.5	11.3

5.2.1 Low Sag ($\delta = 0.035$ m)

Please compare the theoretical transfer function plot Figure 6 to the experimental transfer function plot Figure 7. It can be seen from Figure 6 that values for the first four resonant frequencies are 3.1 Hz, 5.9 Hz, 8.9 Hz, and 11.8 Hz. Looking at Figure 7, we find a clear second, third and fourth mode at 6.1 Hz, 9.4 Hz, and 12.4 Hz, respectively. However, the resonant peak at the first mode is obscured by low frequency noise in the circuit. The results for modes two through four are encouraging. It appears that the experimentally determined resonant frequencies are only slightly higher than their predicted counterparts. This good correlation helps to validate Prof. von Flotow's dynamic model in the low sag case.

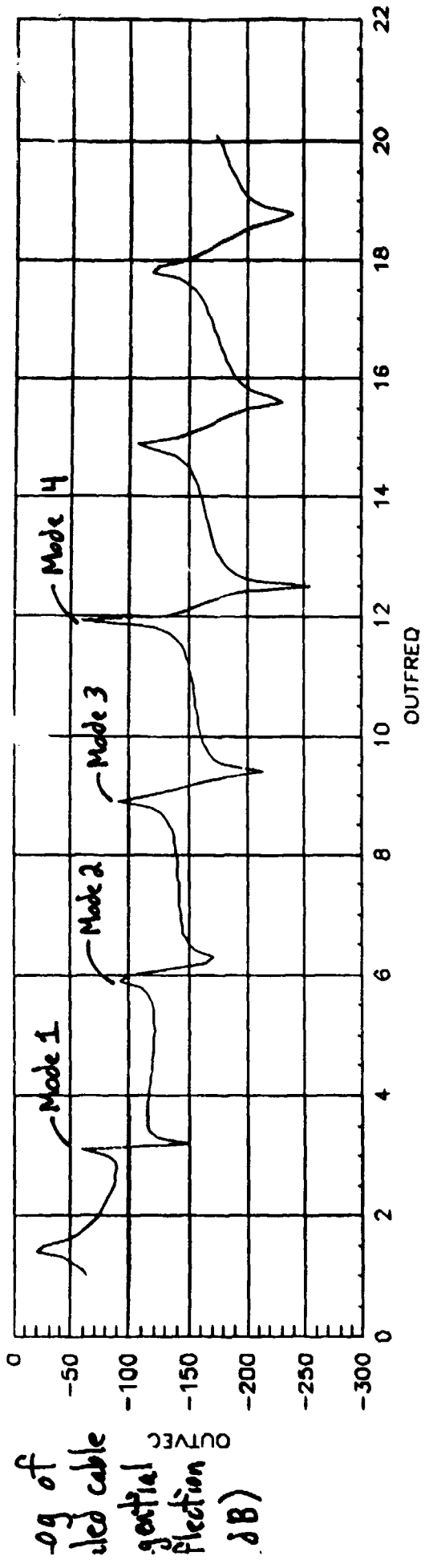
Again, in this situation, the sources of error were numerous. Clearly the low frequency noise in our circuit is a major source of error, as an entire resonant peak was obliterated by its presence. Attempts were made to reduce the noise; indeed a good deal of noise was rejected by reducing the antenna effect of the wires in our circuit. Unfortunately, time did not permit any further modification to eliminate undesired signal noise. The inaccuracy in setting cable sag could easily account for the fact that our experimental data was (consistently) slightly higher than the predicted results.

5.2.2 High Sag ($\delta = 0.200$ m)

The theoretical transfer function plot Figure 8 can similarly be compared to the experimental transfer function plot Figure 9. From Figure 8, the first four resonances are found to be at 2.5 Hz, 3.0 Hz, 4.1 Hz, and 4.9 Hz, respectively. Again, low frequency noise appears to have affected our results in the experimental case, but I believe I can discern the first four resonant frequencies at 2.6 Hz, 3.6 Hz, 4.6 Hz, and 5.3 Hz. These results are fairly consistent, but not quite as close as the low sag case. Again, the experimental values are seen to be slightly higher than their theoretical counterparts.

Possible sources of error in the high sag case include circuit noise at low frequencies (as before), incorrect values for the Young's modulus of the cable and particularly three dimensional vibrating effects not incorporated into our model. In this case, the noise was more pronounced than in the low sag case, thus rendering the experimental transfer function plot more difficult to read.

18.



Driving frequency \sim Hz.

FIGURE 6: Theoretical Transfer Function Plot for Low Sag

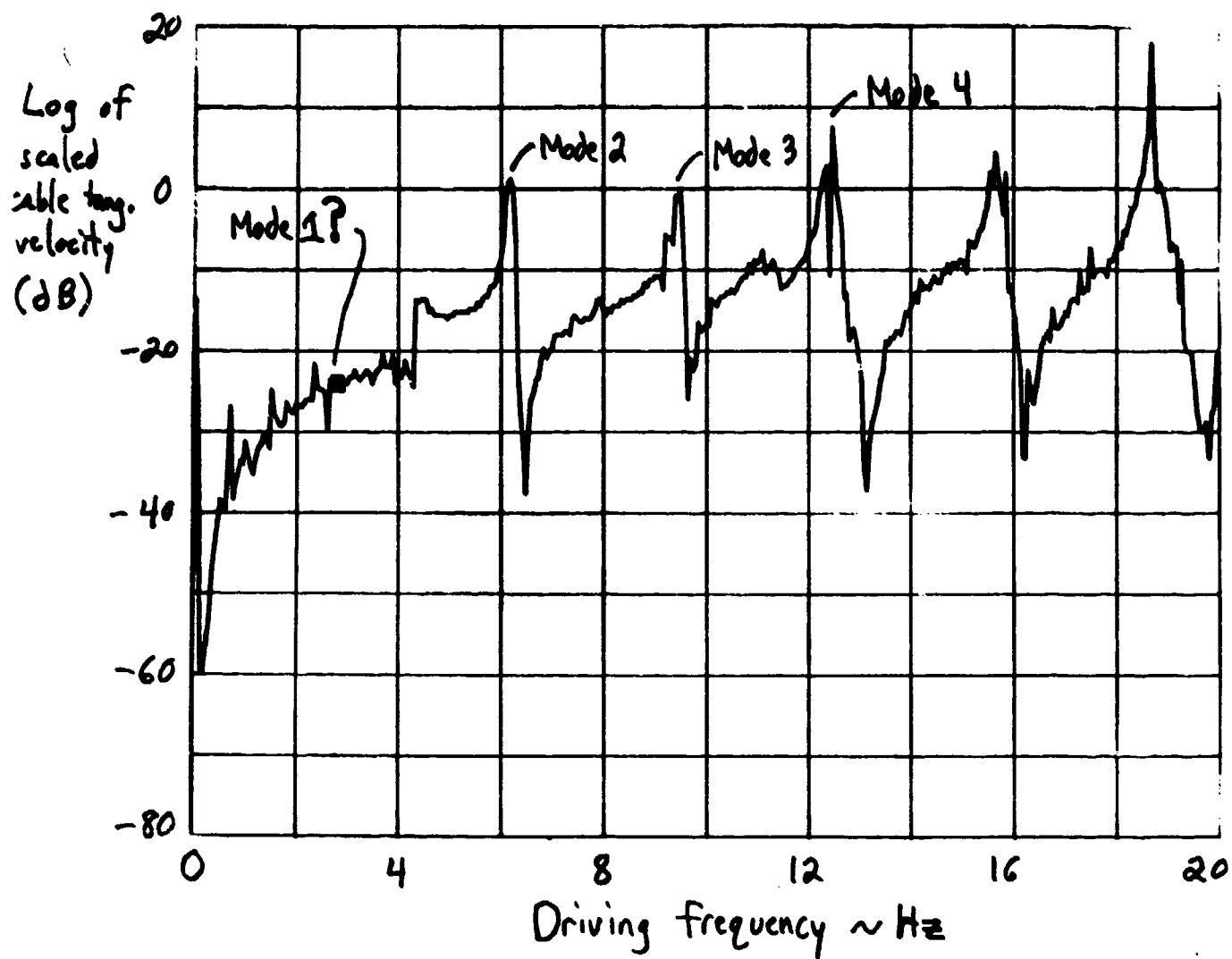
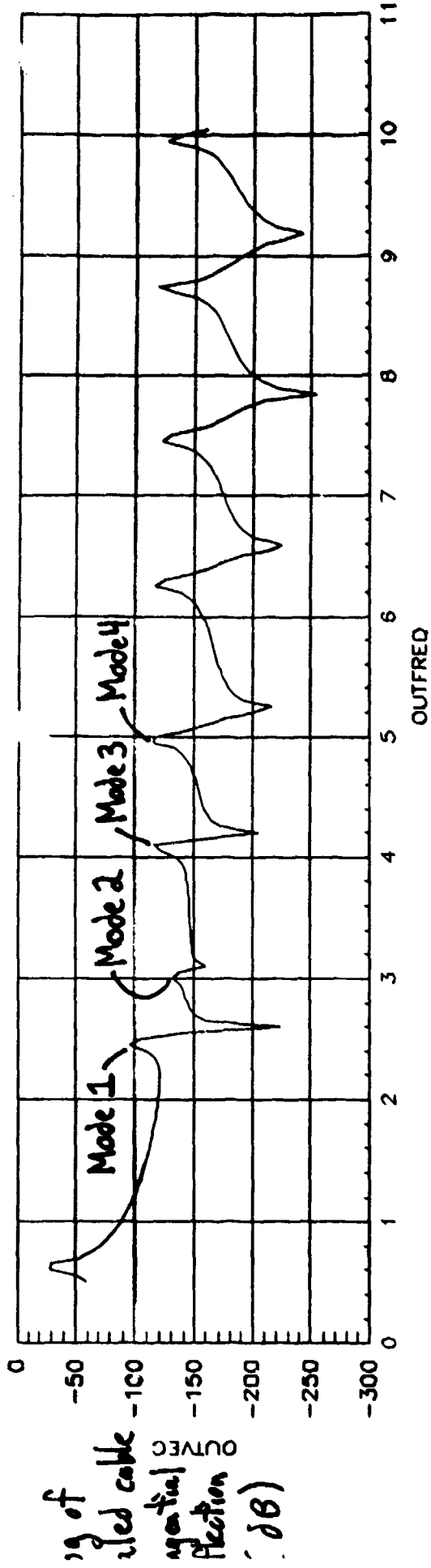


FIGURE 7: Experimental Transfer Function Plot for Low Sag

20.



Driving frequency ~ Hz.

FIGURE 8: Theoretical Transfer Function Plot for High Sag

21.

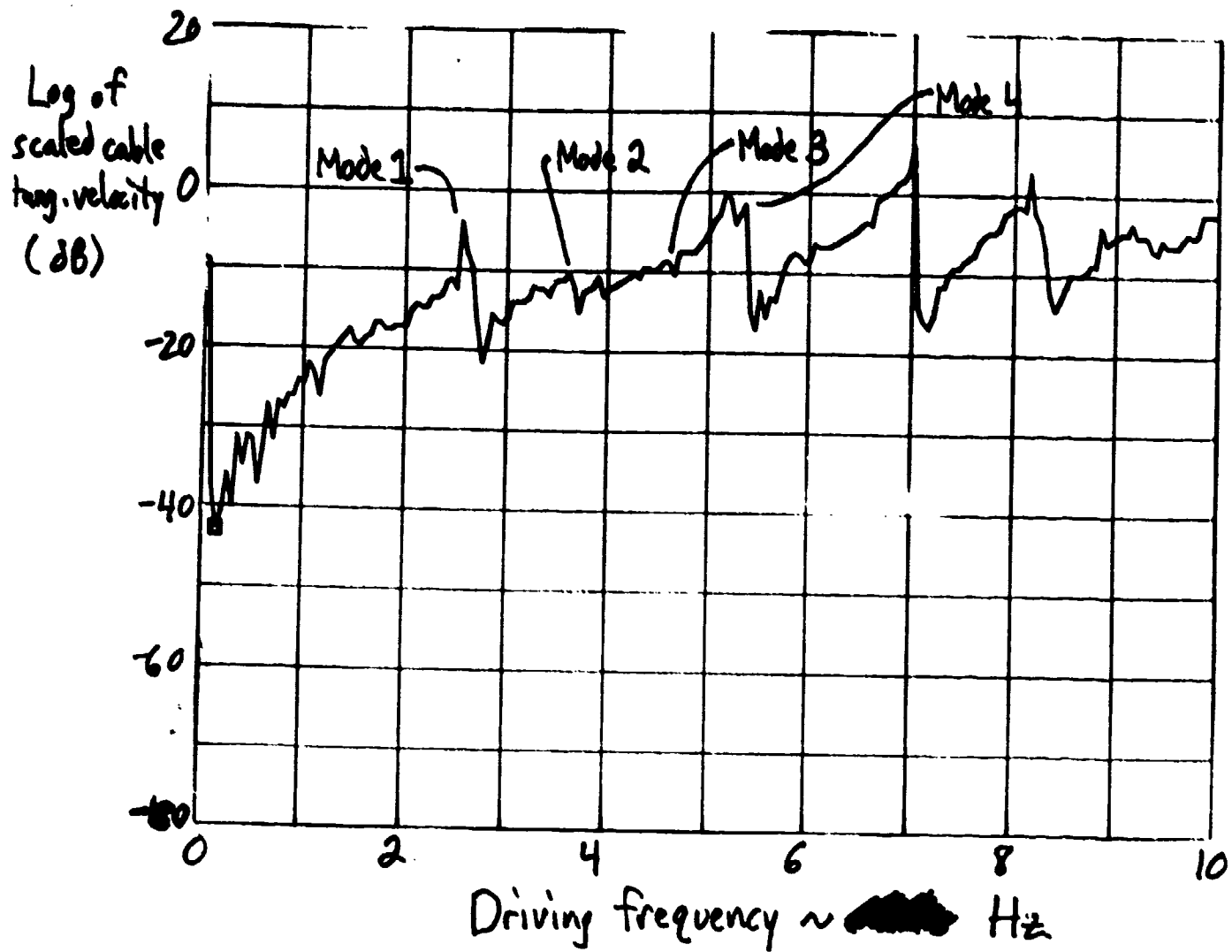


FIGURE 9: Experimental Transfer Function Plot for High Sag

5.2.3 Intermediate Sag ($\delta = 0.140$ m)

Please compare the theoretical transfer function plot Figure 10 to the experimental transfer function plot Figure 11. From Figure 10, the first four theoretical resonant frequencies can be seen to be 3.0 Hz, 4.5 Hz, 5.9 Hz, and 7.4 Hz. Reading the values of the first four experimental resonant frequencies from Figure 11, I find the peaks to occur at 3.1 Hz, 4.2 Hz, 6.3 Hz, and 8.1 Hz. These results are promising, as well, and the correlation is pretty good. This is encouraging, for the case of the intermediate sag levels represents the little-known hybrid case between the well known string and hanging chain behaviors and is the important case that we originally set out to analyze.

In this intermediate case, possible sources of error include any of the sources present in either the high sag or low sag case, although probably to an intermediate extent. For example, inaccuracies in measuring the cable sag would be more significant than in the high sag case and less significant than in the low sag case. In general, the most pronounced effect was again the presence of three-dimensional vibration modes, with a mixture of vertical oscillations and horizontal oscillations of the cable. Remember that we neglected the horizontal oscillations of the cable in using Prof. von Flotow's two-dimensional model.

5.3 Resonant Mode Shapes

Slides were obtained from the photographs that were taken of the experimental resonant mode shapes. These slides were then projected on a wall and adjusted until the subsequent washed-out mode shape could be traced on graph paper taped to the wall. We needed to do this in order that the experimentally obtained mode shapes would be the same size as the theoretical mode shape plots. Only then can a reasonable comparison be made.

As it turned out, our pictures were too underexposed to allow for sharp mode shape photographs (that is, the washed-out pictures of the cable were not bright enough). However, using the method described above, feasible results were obtained with minimal effort.

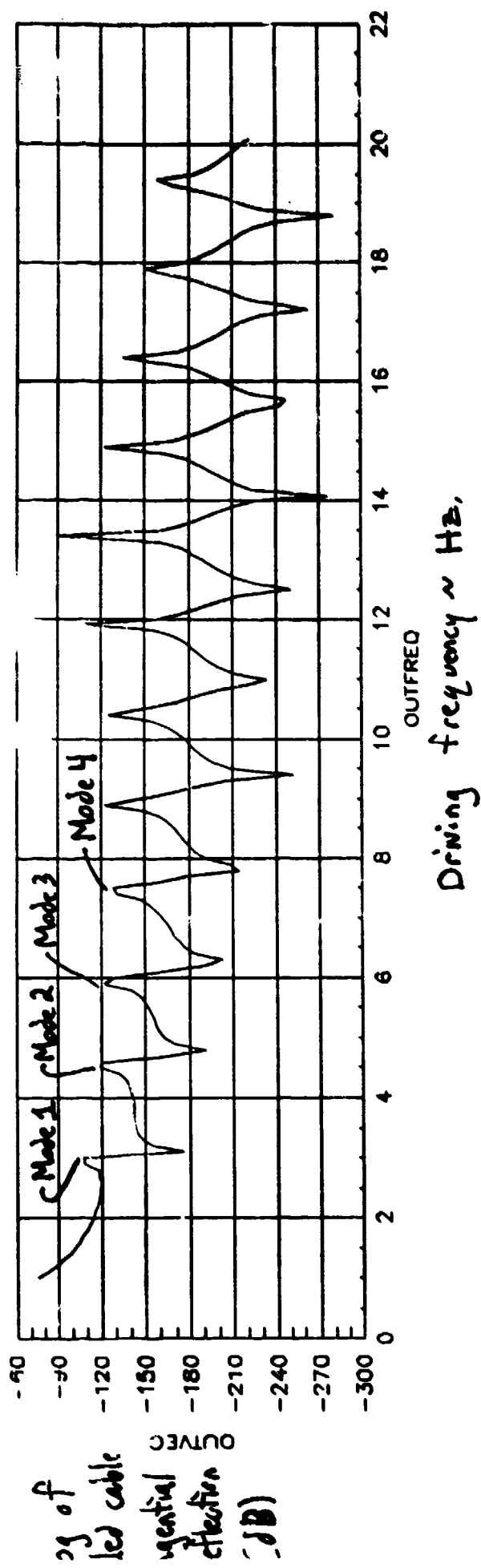


FIGURE 10: Theoretical Transfer
Function Plot for Intermediate Sag

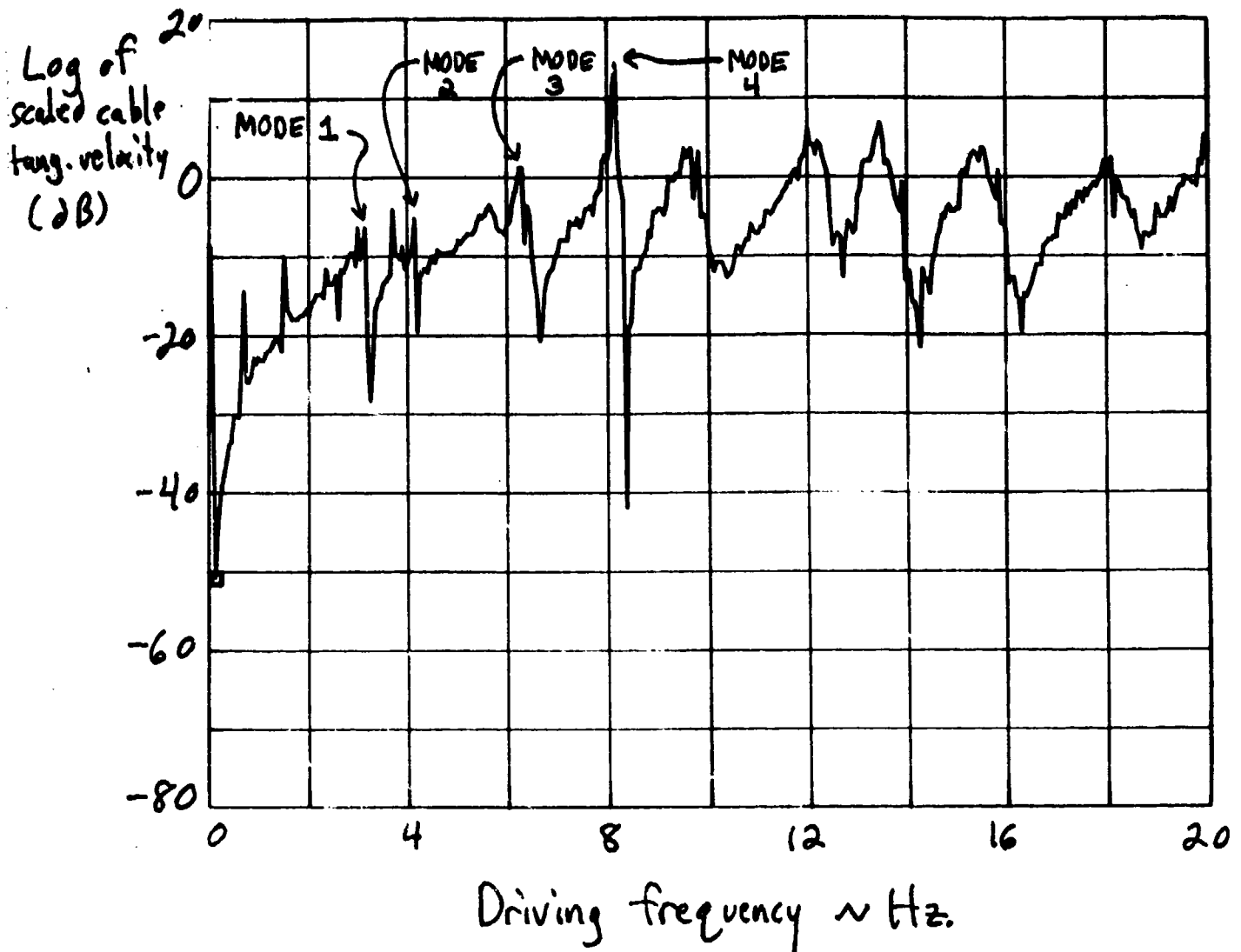


FIGURE 11: Experimental Transfer Function Plot for Intermediate Sag

5.3.1 Low Sag ($\delta = 0.035$ m)

In this classic string case, the first four mode shapes corresponded perfectly. See Figure 12 and 13 for the first four theoretical and experimental mode shapes, respectively. Little more can be said about these results -- they were expected to be quite consistent and they are.

5.3.2 High Sag ($\delta = 0.200$ m)

For this sag setting, the experimental and theoretical results were similar, but not exact. See Figure 14 for the first four theoretical mode shapes and Figure 15 for the corresponding experimental mode shapes. The first and second mode shapes seemed to correspond very well. The third theoretical mode shape showed two nodes (points where the cable is stationary) near the middle of the cable, while third experimental mode shapes had only one node at the center. This is due to the fact that it is difficult to experimentally excite certain mode shapes for some reason (proximity to other resonances, presence of whirling modes, etc.). Therefore, in this third mode case, the true third mode was not experimentally excited at all. A similar phenomenon occurred at the fourth resonance -- the experimental case had one node at the center and two nodes closer than halfway to the center while the theoretical case had one node at the center and two nodes halfway to the center. However, the general shape in each is approximately the same.

5.3.3 Intermediate Sag ($\delta = 0.140$ m)

In this case, results were a little more bizarre. Please compare the theoretical mode shapes plot (Figure 16) with the experimental mode shapes plot (Figure 17). For the first mode, the coupling between the traditional first and second string vibration modes as predicted by theory was seen in the experimental case. Modes three and four also matched well when we compared theory and experiment, giving a symmetric three node and four node result, respectively. However, the results for the second mode were not consistent. Theory predicted a symmetric two-node scenario, whereas our experimental results showed another coupled mode with no nodes. Again, this was probably due to the problem of trying to experimentally excite the correct mode. Notice, also, that the resonant frequencies in this case (4.5 Hz theoretically vs. 5.2 Hz experimentally) are sizeably different. This clearly points to the possibility that an experimental mode shape was bypassed.

26.

(1" = 0.3537 m)

$\delta = 0.035$ m

$\omega = 3.1$ Hz

MODE 1

$\omega = 5.9$ Hz

MODE 2

$\omega = 8.9$ Hz

MODE 3

$\omega = 11.8$ Hz

MODE 4

FIGURE 12:

TRANSVERSE MODE SHAPES FOR BRIDGE

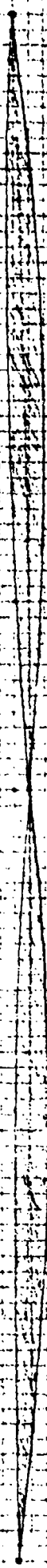
$$(I'' = 0.3531 \text{ in})$$

$$\delta = 0.035 \text{ in}$$



$$\omega = 4.0 \text{ Hz}$$

MODE 1



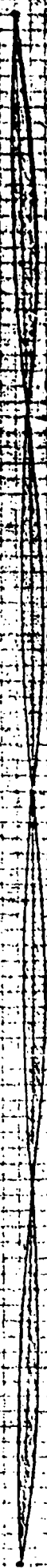
$$\omega = 7.2 \text{ Hz}$$

MODE 2



$$\omega = 11.3 \text{ Hz}$$

MODE 3



$$\omega = 14.8 \text{ Hz}$$

MODE 4

FIGURE 3:

Experimental mode shapes for low sag

1" = 0.3537 m

$\delta = 0.20$ m

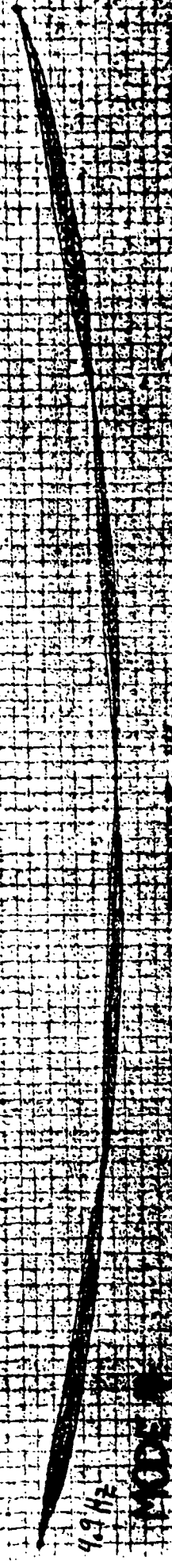
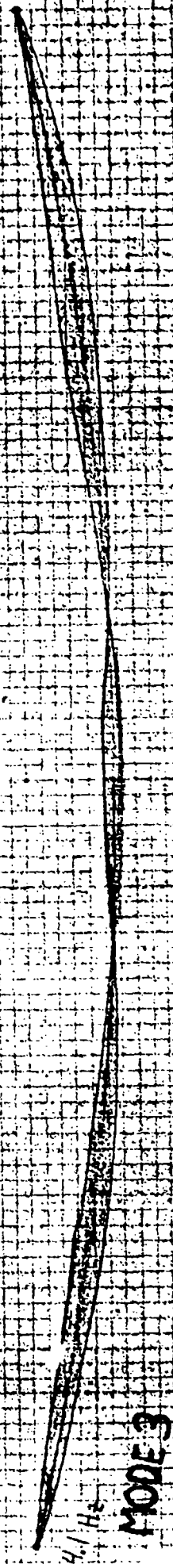
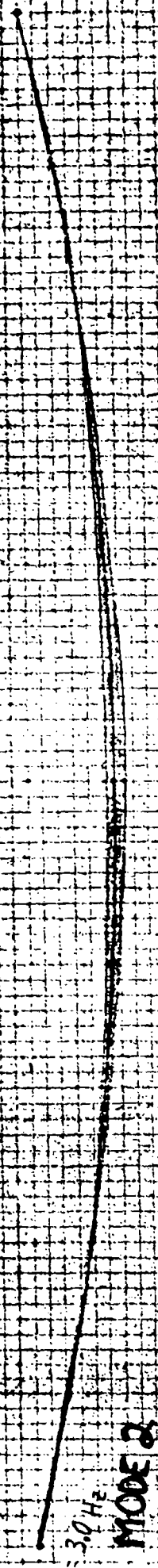


FIGURE 14

THEORETICAL MODE SHAPES FOR EIGENVALUE

28.

$$\delta = 0.200 \text{ m}$$

$$1'' = 0.3537 \text{ m}$$

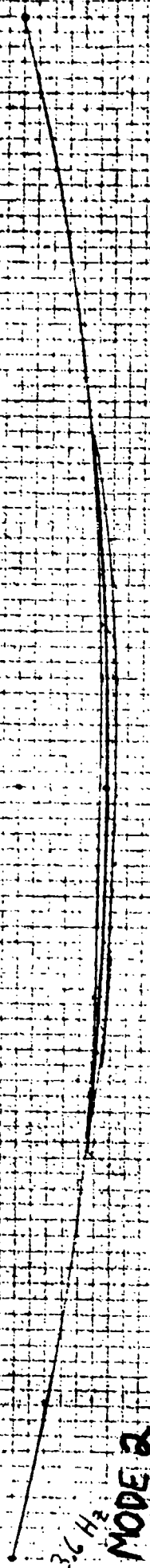
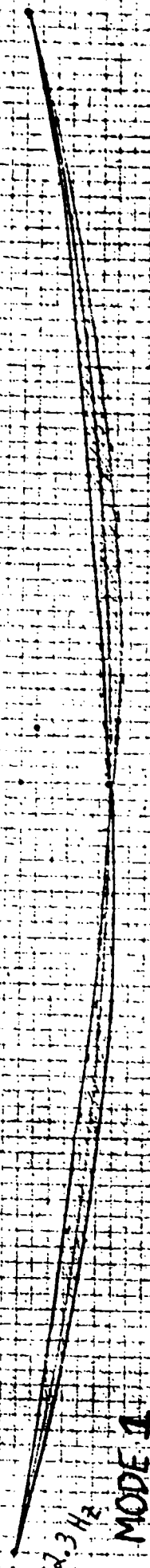


FIGURE 15:
Experimental Mode Shapes for High Bay

$\lambda = 0.3537 \text{ m}$

3d.

$\delta = 0.140 \text{ m}$

$\nu = 30 \text{ Hz}$

MODE 1

$\nu = 4.5 \text{ Hz}$

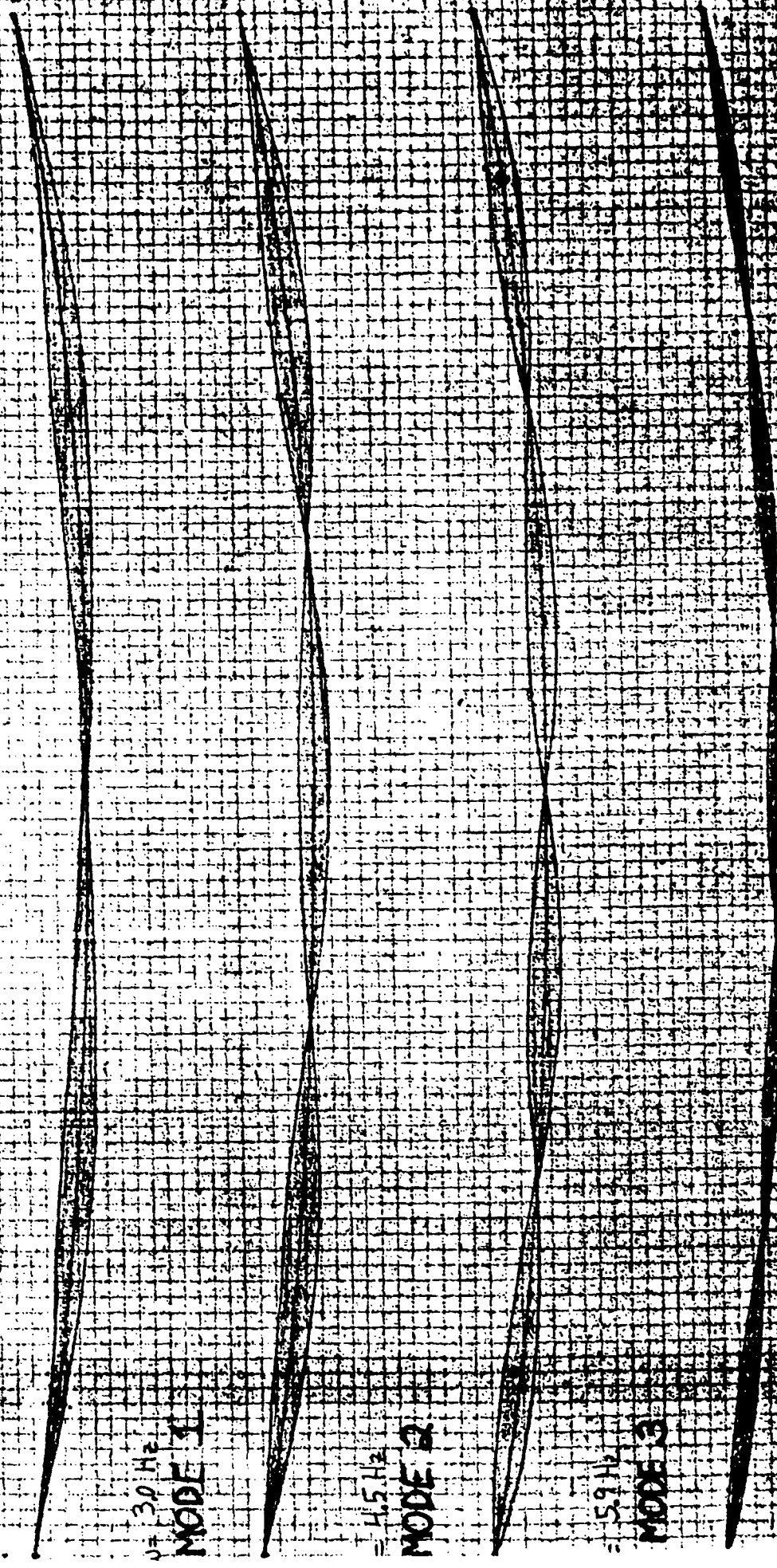
MODE 2

$\nu = 5.9 \text{ Hz}$

MODE 3

$\nu = 7.4 \text{ Hz}$

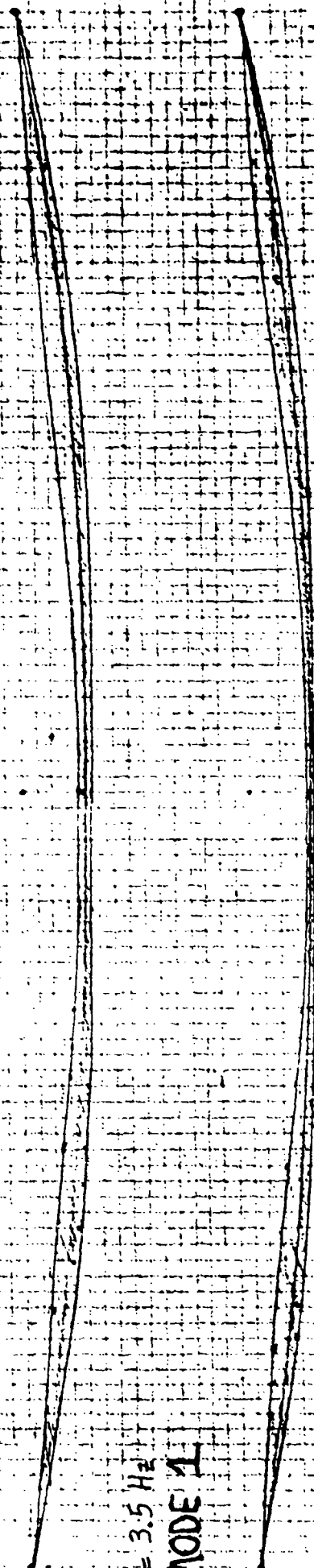
MODE 4



36

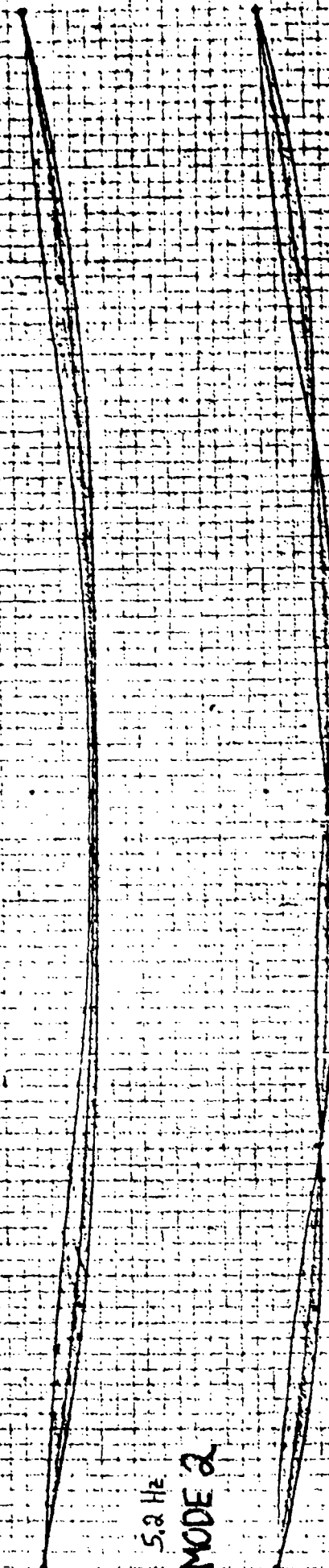
$$\delta = 0.10 \text{ m}$$

$$(I^0 = 0.3537 \text{ m})$$



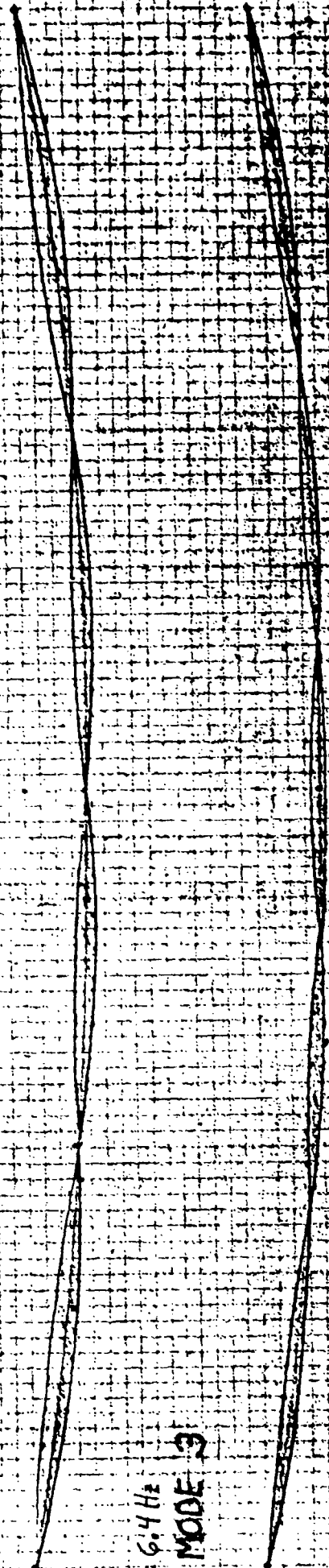
$$\omega = 3.5 \text{ Hz}$$

MODE 1



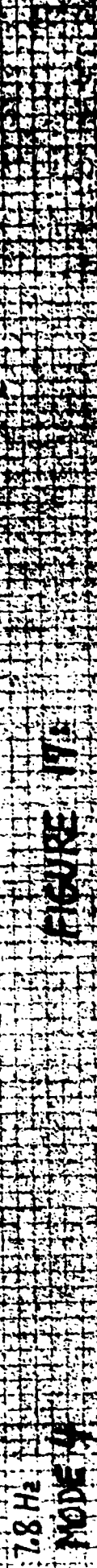
$$\omega = 5.2 \text{ Hz}$$

MODE 2



$$\omega = 6.4 \text{ Hz}$$

MODE 3



$$\omega = 7.8 \text{ Hz}$$

MODE 4

FIGURE 17:

Experimental Mode Shapes for Experimental No. 100

6. Conclusion

It appears that no absolute statement concerning the validity of Prof. von Flotow's model can be made with our crude experimental results and sizable experimental errors. However, in all three phases of the experiment, it appears that our results suggest that Prof. von Flotow's model is a valid one and experimental results can be predicted by his theories.

The mode shape coupling seen in the intermediate sag case was predicted to occur as it did. Since spacecraft tethers operate in the intermediate sag case, this mode coupling probably would manifest itself in the pinned-free boundary conditions of space. Of course, the normal modes are different for this case of pinned-free boundary conditions -- it is the coupling of these new normal modes that we predict. Perhaps this may someday be tested in a zero-gravity environment to further validate Prof. von Flotow's model.

Finally, we would like to recommend that the horizontal dimension be taken into account in a more advanced theoretical model. The horizontal motions of our cable were simply too large to ignore. In fact, whirling modes were occasionally set up where the horizontal motion was the same magnitude as the vertical motion. Clearly, in this situation, the assumption of a two-dimensional model is no longer valid. However, adding a third dimension would significantly complicate the theoretical model, so tradeoffs would be involved.

I. Transfer Function Plot Programs

APPENDIX A

Transfer function plot programs with explanation
of program symbols

```

n=191;
delta=0.035;
l=3.537;
t=.666;
e='1600000;
a= 0000143;
mu=.00152;
epsbar=t/(e*a);
rbar=1/(8*delta);
frerat=1*sqrt(mu/t);
sfix=.951;
fext=1;
fextb=fext/t;
j=1;
wmin=6.283185307;
wmax=125.6637061;
abar=.0233;
mass=.09935;
mbar=mass/(mu*l);
for i=0:n,...

```

Case 1: $\delta = 0.035m$

~~LOW~~ LOW SAG

```

    wbar=frerat*(wmin+((wmax-wmin)/n)*i);...
    b0=[1,0,0,0;0,0,1,0];...
    b1=[1,0,0,0;0,0,1/abar-mbar*(wbar)**2,1];...
    amat=[0,epsbar,0,0;1/(rbar**2)-(wbar)**2,0,0,...
    -1/(rbar*epsbar);0,0,0,1;0,1/rbar,1 /((rbar)*...
    *2*epsbar)-(wbar)**2,0];...
    [evec,eval]= eig(amat);...
    y0=evec;...
    compex1=exp(eval(1,1));...
    compex2=exp(eval(2,2));...
    compex3=exp(eval(3,3));...
    compex4=exp(eval(4,4));...
    -evec*diagonal([compex1,compex2,compex3,compex4]);...
    dmatu=[1,0;0,1;0,0;0,0]*(b0*y0);...
    dmatl=[0,0;0,0;1,0;0,1]*(b1*y1);...
    dmat=dmatu+dmatl;...
    commag1=exp(eval(1,1)*sfix);...
    commag2=exp(eval(2,2)*sfix);...
    commag3=exp(eval(3,3)*sfix);...
    commag4=exp(eval(4,4)*sfix);...
    ymat=evec*diagonal([commag1,commag2,commag3,commag4]);...
    hmat=ymat*inv(dmat);...
    outvec(j)=20*log(abs(hmat(3,4)));...
    outfreq(j)=.9+(j/10);...
    j= j+1;...

```

```

nd
return

```

Case 2: $\delta = 0.20m$

HIGH SAG

```
n=191;
delta=0.20;
l=3.537;
t=.117;
e=.00000000;
a=.0000143;
mu=.00152;
epsbar=t/(e*a);
rbar=1/(8*delta);
frerat=1*sqrt(mu/t);
sfix=.951;
fext=1;
fextb=fext/t;
j=1;
wmin=6.283185307/2;
wmax=125.6637061/2;
abar=.0233;
mass=.09935;
mbar=mass/(mu*l);
for i=0:n,...
    wbar=frerat*(wmin+((wmax-wmin)/n)*i);...
    b0=[1,0,0,0;0,0,1,0];...
    b1=[1,0,0,0;0,0,1/abar-mbar*(wbar)**2,1];...
    amat=[0,epsbar,0,0;1/(rbar**2)-(wbar)**2,0,0,...
    -1/(rbar*epsbar);0,0,0,1;0,1/rbar,1 /((rbar)*...
    *2*epsbar)-(wbar)**2,0];...
    [evec,eval]= eig(amat);...
    y0=evec;...
    compex1=exp(eval(1,1));...
    compex2=exp(eval(2,2));...
    compex3=exp(eval(3,3));...
    compex4=exp(eval(4,4));...
    evec=diag([compex1,compex2,compex3,compex4]);...
    dmatu=[1,0;0,1;0,0;0,0]*(b0*y0);...
    dmatl=[0,0;0,0;1,0;0,1]*(b1*y1);...
    dmat=dmatu+dmatl;...
    commag1=exp(eval(1,1)*sfix);...
    commag2=exp(eval(2,2)*sfix);...
    commag3=exp(eval(3,3)*sfix);...
    commag4=exp(eval(4,4)*sfix);...
    ymat=evec*diag([commag1,commag2,commag3,commag4]);...
    hmat=ymat*inv(dmat);...
    outvec(j)=20*log(abs(hmat(3,4)));...
    outfreq(j)=.45+(j/20);...
    j= j+1;...
end
return
```

Case 3 : $\delta = 0.14 \text{ m}$

INTERMEDIATE SAG

```
n=191;
delta=0.14;
l=3.537;
t=.167;
e=.0000000;
a=.0000143;
mu=.00152;
epsbar=t/(e*a);
rbar=1/(8*delta);
frerat=1*sqrt(mu/t);
sfix=.951;
fext=1;
fextb=fext/t;
j=1;
wmin=6.283185307;
wmax=125.6637061;
abar=.0233;
mass=.09935;
mbar=mass/(mu*l);
for i=0:n,...
    wbar=frerat*(wmin+((wmax-wmin)/n)*i);...
    b0=[1,0,0,0;0,0,1,0];...
    b1=[1,0,0,0;0,0,1/abar-mbar*(wbar)**2,1];...
    amat=[0,epsbar,0,0;1/(rbar**2)-(wbar)**2,0,0,...
    -1/(rbar*epsbar);0,0,0,1;0,1/rbar,1 /((rbar)*...
    *2*epsbar)-(wbar)**2,0];...
    [evec,eval]= eig(amat);...
    y0=evec;...
    compex1=exp(eval(1,1));...
    compex2=exp(eval(2,2));...
    compex3=exp(eval(3,3));...
    compex4=exp(eval(4,4));...
    y1=evec*diagonal([compex1,compex2,compex3,compex4]);...
    dmatu=[1,0;0,1;0,0;0,0]*(b0*y0);...
    dmatl=[0,0;0,0;1,0;0,1]*(b1*y1);...
    dmat=dmatu+dmatl;...
    commag1=exp(eval(1,1)*sfix);...
    commag2=exp(eval(2,2)*sfix);...
    commag3=exp(eval(3,3)*sfix);...
    commag4=exp(eval(4,4)*sfix);...
    ymat=evec*diagonal([commag1,commag2,commag3,commag4]);...
    hmat=ymat*inv(dmat);...
    outvec(j)=20*log(abs(hmat(3,4)));...
    outfreq(j)=.9+(j/10);...
    j= j+1;...

end
return
```

EXPLANATION OF PROGRAM SYMBOLS

n = # of data pts.
 $\delta_{\text{elva}} = \delta$, midspan deflection (m)
 $l = L$, cable length (m)
 $t = T$, cable tension (N)
 $e = E$, cable Young's modulus (N/m²)
 $q = A$, cable X-S area (m²)
 $\mu = \mu$, mass/unit length of cable (kg/m)
 $\bar{\epsilon} = \bar{\epsilon}$, non-dimensional force ratio
 $\bar{r} = \bar{R}$, non-dimensional radius of curvature
 $\bar{\omega} = \bar{\omega}$, normalized frequency ratio (s)
 $\bar{s} = \bar{s}$, non-dimensional distance of magnet location along cable
 $f = f$, normalized external force (N)
 $\bar{f} = \bar{f}$, non-dimensional external force
 i = loop variable
 $\omega_{\text{min}} = \omega_{\text{min}}$, minimum value of frequency (rad/s)
 $\omega_{\text{max}} = \omega_{\text{max}}$, maximum " " " "
 $\bar{a} = \bar{a}$, non-dimensional distance of shaker position to wall.
 $m = m$, shaker mass (kg)
 $\bar{m} = \bar{m}$, non-dimensional mass ratio
 $\bar{U}, \bar{B}_0, \bar{B}_1, \bar{g}$ boundary conditions, matrices
 $A = A$, state vector matrix
 $H = H$, output matrix
 $\text{mat}(3,4) = H_{3,4}$ = cable tangential deflection = outvec
 $\omega = \omega$ = driving frequency (Hz)

Plots are of $\text{Log}[H_{3,4}]$ vs. ω

II. Mode Shape Data Programs

APPENDIX B

Mode shape data programs with explanation
of program symbols

```

n=50;
delta=.035;
l=3.537;
t=.666;
e=61600000;
a=.000143;
mu=.00152;
epsbar=t/(e*a);
rbar=1/(8*delta);
frerat=1*sqrt(mu/t);
fext=1;
fextb=fext/t;
abar=.0233;
mass=.09935;
mbar=mass/(mu*l);

```

Case 1: $\delta = 0.035\text{m}$
LOW SAG

```

inquire w 'Enter frequency (rad/s)'
wbar=frerat*w;
b0=[1,0,0,0;0,0,1,0];
b1=[1,0,0,0;0,0,1/abar-mbar*(wbar)**2,1];
amat=[0,epsbar,0,0;1/(rbar**2)-(wbar)**2,0,0,-1/(rbar*epsbar);...
0,0,0,1;0,1/rbar,1/((rbar)**2*epsbar)-(wbar)**2,0];
[evect,eval]=eig(amat);
y0=evect;
compex1=exp(eval(1,1));
compex2=exp(eval(2,2));
compex3=exp(eval(3,3));
compex4=exp(eval(4,4));
y1=evect*diagonal([compex1,compex2,compex3,compex4]);
dmatu=[1,0;0,1;0,0;0,0]*(b0*y0);
dmatl=[0,0;0,0;1,0;0,1]*(b1*y1);
dmat=dmatu+dmatl;
dir inv(dmat);

for i=0:n,...
    commag1=exp(eval(1,1)*(i/n));...
    commag2=exp(eval(2,2)*(i/n));...
    commag3=exp(eval(3,3)*(i/n));...
    commag4=exp(eval(4,4)*(i/n));...
    ymat=evect*diagonal([commag1,commag2,commag3,commag4]);...
    hmat=ymat*dinv;...
    outmod(i+1)=abs(hmat(3,4));...
    length(i+1)=i/n;...

end
return

```

```

n=50;
delta=.200;
l=3.537;
t=.117;
e=30000000;
a= 000143;
mu=.0152;
epsbar=t/(e*a);
rbar=1/(8*delta);
frerat=1*sqrt(mu/t);
fext=1;
fextb=fext/t;
abar=.0233;
mass=.09935;
mbar=mass/(mu*l);

```

Case 2: $\delta = 0.200\text{m}$

HIGH SAG

```

inquire w 'Enter frequency (rad/s)'
wbar=frerat*w;
b0=[1,0,0,0;0,0,1,0];
b1=[1,0,0,0;0,0,1/abar-mbar*(wbar)**2,1];
amat=[0,epsbar,0,0;1/(rbar**2)-(wbar)**2,0,0,-1/(rbar*epsbar);...
0,0,0,1;0,1/rbar,1/((rbar)**2*epsbar)-(wbar)**2,0];
[vec,eval]=eig(amat);
y0=vec;
compex1=exp(eval(1,1));
compex2=exp(eval(2,2));
compex3=exp(eval(3,3));
compex4=exp(eval(4,4));
y1=vec*diagonal([compex1,compex2,compex3,compex4]);
dmatu=[1,0;0,1;0,0;0,0]*(b0*y0);
dmatl=[0,0;0,0;1,0;0,1]*(b1*y1);
dmat=dmatu+dmatl;
di=inv(dmat);

for i=0:n,...
    commag1=exp(eval(1,1)*(i/n));...
    commag2=exp(eval(2,2)*(i/n));...
    commag3=exp(eval(3,3)*(i/n));...
    commag4=exp(eval(4,4)*(i/n));...
    ymat=vec*diagonal([commag1,commag2,commag3,commag4]);...
    hmat=ymat*dinv;...
    outmod(i+1)=abs(hmat(3,4));...
    length(i+1)=i/n;...

end
return

```

```

n=50;
delta=.140;
l=3.537;
t=.167;
e=36000000;
a= 0000143;
mu .00152;
epsbar=t/(e*a);
rbar=1/(8*delta);
frerat=1*sqrt(mu/t);
fext=1;
fextb=fext/t;
abar=.0233;
mass=.09935;
mbar=mass/(mu*1);

```

CASE 3: $\delta = 0.14_m$

INTERMEDIATE SAG

```

inquire w 'Enter frequency (rad/s)'
wbar=frerat*w;
b0=[1,0,0,0;0,0,1,0];
b1=[1,0,0,0;0,0,1/abar-mbar*(wbar)**2,1];
amat=[0,epsbar,0,0;1/(rbar**2)-(wbar)**2,0,0,-1/(rbar*epsbar);...
0,0,0,1;0,1/rbar,1/((rbar)**2*epsbar)-(wbar)**2,0];
[evect,eval]=eig(amat);
y0=evect;
compex1=exp(eval(1,1));
compex2=exp(eval(2,2));
compex3=exp(eval(3,3));
compex4=exp(eval(4,4));
y1=evect*diagonal([compex1,compex2,compex3,compex4]);
dmatu=[1,0;0,1;0,0;0,0]*(b0*y0);
dmatl=[0,0;0,0;1,0;0,1]*(b1*y1);
dmat=dmatu+dmatl;
dinv=inv(dmat);

for i=0:n,...
    commag1=exp(eval(1,1)*(i/n));...
    commag2=exp(eval(2,2)*(i/n));...
    commag3=exp(eval(3,3)*(i/n));...
    commag4=exp(eval(4,4)*(i/n));...
    ymat=evect*diagonal([commag1,commag2,commag3,commag4]);...
    hmat=ymat*dinv;...
    outmod(i+1)=abs(hmat(3,4));...
    length(i+1)=i/n;...

end
return

```

EXPLANATION OF (NEW) PROGRAM SYMBOLS

ω = resonant frequency (rad/s)
outmod = cable tangential deflection
length = non-dimensional cable length

Data is in the form of equally spaced length ratios assumed and only the cable tangential deflection printout. (See Appendix C)

III. Mode Shape Data

APPENDIX C

Mode shape data for first four mode shapes
for three different sag levels

<> outmod

OUTMOD

= tangential
cable deflection

$$\delta = 0.035 \text{ m}$$

$$\omega = 19.2 \text{ rad/s} = \text{MODE 1}$$

LOW SAG

①

increasing
cable length

midpoint

0.0000
0.0179
0.0358
0.0536
0.0712
0.0886
0.1056
0.1223
0.1386
0.1543
0.1694
0.1839
0.1977
0.2106
0.2228
0.2341
0.2445
0.2539
0.2623
0.2696
0.2759
0.2810
0.2851
0.2880
0.2898
~~0.2904~~
0.2898
0.2881
0.2852
0.2812
0.2761
0.2699
0.2626
0.2542
0.2449
0.2345
0.2233
0.2111
0.1982
0.1844
0.1700
0.1549
0.1392
0.1230
0.1063
0.0892
0.0719
0.0543
0.0365
0.0186
0.0007

>

>

> diary (0)

<> outmod

OUTMOD

- tangential cable
de flection

$$\delta = 0.035 \text{ m}$$

$$\omega = 37.2 \text{ rad/s} = \text{MODE 2}$$

(2)

LOW SAG

increasing
cable length

midpoint

0.0000
0.0368
0.0729
0.1080
0.1413
0.1724
0.2007
0.2259
0.2476
0.2653
0.2788
0.2879
0.2925
0.2925
0.2878
0.2786
0.2650
0.2472
0.2255
0.2003
0.1718
0.1407
0.1074
0.0723
0.0361
0.0006
- 0.0374
- 0.0735
- 0.1085
- 0.1418
- 0.1728
- 0.2012
- 0.2263
- 0.2479
- 0.2655
- 0.2790
- 0.2880
- 0.2925
- 0.2924
- 0.2877
- 0.2784
- 0.2647
- 0.2469
- 0.2251
- 0.1998
- 0.1714
- 0.1402
- 0.1068
- 0.0718
- 0.0355
- 0.0012

<> diary(0)

<> outmod

OUTMOD

= tangential cable
deflection

$$\delta = 0.035 \text{ m}$$

$$\omega = 55.8 \text{ rad/s} = \text{MODE 3}$$

(3)

LOW SAG

increasing
cable length

0.0000
0.0216
0.0425
0.0619
0.0791
0.0935
0.1046
0.1119
0.1154
0.1147
0.1100
0.1014
0.0892
0.0739
0.0559
0.0360
0.0148
-0.0070
-0.0284
-0.0489
-0.0676
-0.0839
-0.0972
-0.1070
-0.1131
-0.1151

midpoint

0.1131
0.1070
0.0971
0.0838
0.0675
0.0488
0.0284
0.0069
0.0148
0.0360
0.0559
0.0739
0.0892
0.1014
0.1100
0.1147
0.1154
0.1119
0.1045
0.0934
0.0790
0.0618
0.0425
0.0216
0.0001

<> diary(0)

<> outmod

OUTMOD

- tangential cable
deflection

$$\delta = 0.035 \text{ m}$$

$$\omega = 74.4 \text{ rad/s} = \text{MODE } 4$$

(4)

increasing
cable length

LOW SAG

0.0000

0.0498

0.0965

0.1371

0.1690

0.1904

0.1998

0.1965

0.1810

0.1540

0.1174

0.0734

0.0247

-0.0255

-0.0741

-0.1180

-0.1545

-0.1813

-0.1967

-0.1998

-0.1902

-0.1687

-0.1366

-0.0959

-0.0492

+0.0006

midpoint

0.0504

0.0970

0.1375

0.1694

0.1906

0.1998

0.1965

0.1808

0.1537

0.1170

0.0729

0.0242

0.0260

0.0745

0.1184

0.1548

0.1815

0.1968

0.1997

0.1900

0.1684

0.1362

0.0954

0.0486

0.0012

<> diary(0)

<> outmod

OUTMOD

0.0000
0.0229
0.0454
0.0671
0.0878
0.1071
0.1247
0.1403
0.1536
0.1645
0.1728
0.1784
0.1811
0.1810
0.1780
0.1722
0.1637
0.1525
0.1390
0.1232
0.1055
0.0862
0.0654
0.0437
0.0212
~~0.0016~~
0.0243
0.0467
0.0684
0.0889
0.1081
0.1255
0.1410
0.1542
0.1650
0.1732
0.1786
0.1812
0.1809
0.1778
0.1719
0.1632
0.1519
0.1383
0.1224
0.1046
0.0851
0.0642
0.0423
0.0198
0.0031

- tangential cable
deflection



increasing
cable length

$$\delta = 0.140 \text{ m}$$

$$w = 18.6 \text{ rad/s} = \text{MODE 1}$$

(5)

INTERMEDIATE SAG

MIDPOINT

<> diary(0)

<> outmod

OUTMOD

= tangential cable
deflection

$$\delta = 0.140 \text{ m}$$

$$w = 28.5 \text{ rad/s} = \text{MODE 2}$$

INTERMEDIATE SAG

⑥

0.0000
0.0082
0.0163
0.0239
0.0308
0.0368
0.0415
0.0449
0.0467
0.0471
0.0458
0.0430
0.0388
0.0333
0.0268
0.0194
0.0115
0.0033
-0.0048
-0.0126
-0.0198
-0.0260
-0.0312
-0.0350
-0.0374
~~-0.0382~~
0.0374
0.0351
0.0314
0.0263
0.0201
0.0129
0.0052
0.0030
0.0112
0.0191
0.0265
0.0331
0.0386
0.0429
0.0457
0.0470
0.0468
0.0450
0.0417
0.0370
0.0311
0.0242
0.0166
0.0086
0.0004

increasing cable
length

midpoint

<> diary (0)

<> outmod

OUTMOD

= tangential cable
deflection

$$S = 0.140 \text{ m}$$

$$w = 37.1 \text{ rad/s} = \text{MODE 3}$$

⑦

INTERMEDIATE SAG



increasing cable
length

0.0000
0.0154
0.0299
0.0425
0.0524
0.0590
0.0618
0.0608
0.0560
0.0476
0.0363
0.0226
0.0075
- 0.0080
- 0.0231
- 0.0367
- 0.0480
- 0.0563
- 0.0611
- 0.0621
- 0.0592
- 0.0525
- 0.0426
- 0.0300
- 0.0155
- 0.0000

midpoint

0.0154
0.0299
0.0425
0.0525
0.0591
0.0621
0.0611
0.0564
0.0481
0.0368
0.0232
0.0081
0.0075
0.0225
0.0362
0.0476
0.0560
0.0608
0.0618
0.0590
0.0524
0.0425
0.0300
0.0155
0.0001

<> diary (0)

<> outmod

OUTMOD

0.0000
0.0042
0.0081
0.0112
0.0132
0.0139
0.0133
0.0114
0.0084
0.0046
0.0003
- 0.0039
- 0.0077
- 0.0108
- 0.0127
- 0.0134
- 0.0127
- 0.0108
- 0.0077
- 0.0039
+ 0.0003
+ 0.0045
+ 0.0083
+ 0.0113
+ 0.0133
+ 0.0139
0.0132
0.0112
0.0081
0.0043
0.0000
0.0042
0.0080
0.0109
0.0128
0.0134
0.0126
0.0106
0.0075
0.0036
0.0006
0.0048
0.0086
0.0115
0.0133
0.0139
0.0131
0.0110
0.0079
0.0040
0.0003

= tangential cable
deflection

$$\delta = 0.140 \text{ m}$$

$$\omega = 46.7 \text{ rad/s} = \text{MODE 4}$$

INTERMEDIATE SAG

increasing
cable length

midpoint

⑤

<> diary(0)

<> outmod

OUTMOD

= tangential cable deflection $\delta = 0.20 \text{ m}$

$\omega = 15.5 \text{ rad/s} = \text{MODE 1}$

HIGH SAG

(9)

0.0000

0.0387

0.0766

0.1133

0.1482

0.1806

0.2102

0.2364

0.2589

0.2772

0.2912

0.3005

0.3051

0.3048

0.2998

0.2900

0.2756

0.2569

0.2341

0.2076

0.1779

0.1453

0.1105

0.0739

0.0362

~~0.0021~~

0.0404

0.0781

0.1145

0.1491

0.1813

0.2107

0.2368

0.2592

0.2774

0.2913

0.3006

0.3051

0.3048

0.2997

0.2898

0.2754

0.2566

0.2337

0.2071

0.1771

0.1444

0.1093

0.0724

0.0344

0.0043

↓ increasing
cable length

midpoint

<> diary (0)

<> outmod

OUTMOD

= tangential cable
deflection

$$\delta = 0.20 \text{ m}$$

$$\omega = 19.0 \text{ rad/s} = \text{MODE 2}$$

(10)

increasing
cable length

HIGH SAG

0.0000
0.0204
0.0361
0.0467
0.0521
0.0521
0.0467
0.0360
0.0202
-0.0002
-0.0247
-0.0529
-0.0839
-0.1172
-0.1519
-0.1872
-0.2223
-0.2563
-0.2885
-0.3180
-0.3443
-0.3666
-0.3845
-0.3975
-0.4053
-0.4077

0.4048
0.3965
0.3830
0.3648
0.3421
0.3155
0.2857
0.2533
0.2192
0.1841
0.1488
0.1142
0.0811
0.0502
0.0224
0.0018
0.0218
0.0371
0.0473
0.0523
0.0518
0.0460
0.0348
0.0187
0.0021

<> diary (0)

<> outmod

OUTMOD

0.0000
0.0035
0.0072
0.0110
0.0146
0.0179
0.0208
0.0232
0.0249
0.0259
0.0261
0.0256
0.0243
0.0223
0.0197
0.0167
0.0132
0.0095
0.0058
0.0022
-0.0013
-0.0043
-0.0068
-0.0087
-0.0098
-0.0103
0.0099
0.0089
0.0071
0.0046
0.0017
0.0017
0.0053
0.0091
0.0128
0.0162
0.0194
0.0220
0.0241
0.0254
0.0261
0.0259
0.0250
0.0234
0.0211
0.0183
0.0150
0.0115
0.0077
0.0040
0.0004

- tangential cable
deflection

increasing
cable length

midpoint

$$\delta = 0.20 \text{ m}$$

$$w = 25.5 \text{ rad/s} = \text{MODE 3}$$

HIGH SAG

(11)

<> diary (0)

<> outmod

OUTMOD

- tangential cable
deflection

$$\delta = 0.20 \text{ m}$$

$$\omega = 31.1 \text{ rad/s} = \text{MOPF } 4$$

(12)

HIGH SAG

increasing
cable length

0.0000

0.0108

0.0209

0.0296

0.0365

0.0411

0.0431

0.0423

0.0389

0.0331

0.0252

0.0156

0.0051

- 0.0057

- 0.0163

- 0.0257

- 0.0336

- 0.0394

- 0.0428

- 0.0434

- 0.0414

- 0.0367

- 0.0298

- 0.0210

- 0.0109

- 0.0001

midpoint

0.0107

0.0208

0.0297

0.0366

0.0413

0.0434

0.0428

0.0395

0.0337

0.0259

0.0164

0.0059

0.0049

0.0155

0.0250

0.0330

0.0389

0.0423

0.0431

0.0411

0.0366

0.0297

0.0210

0.0109

0.0002

<> diary (0)

Notes

¹Some Approximations for the Dynamics of Spacecraft Tethers by A. H. von Flotow , April 1987

Localization in Disordered Periodic Structures

Glen J. Kissel*
Massachusetts Institute of Technology
Cambridge, MA 02139

Abstract

Disorder in periodic structures is known to cause spatial localization of normal modes and attenuation of waves in all frequency bands. This paper uses a wave perspective to investigate these effects on one-dimensional periodic structures of interest to the engineer. Relevant work in the fields of solid state physics and mathematics is reviewed. A limit theorem for products of random matrices is exploited to calculate localization effects as a function of frequency. Localization is studied on two disordered periodic systems using both theoretical calculations and Monte Carlo simulations. The problem of localization in multiwave systems is briefly discussed.

Nomenclature

a	element of Cayley matrix
A	cross-sectional area of rod
$A_{R(L)}$	amplitude of left traveling wave at right(left) end of bay
b	element of Cayley matrix
$B_{R(L)}$	amplitude of right traveling wave at right(left) end of bay
C	Cayley matrix
E	Young's modulus
H	(superscript) hermitian transpose
\bar{H}	nondimensional transfer function
i	$i^2 = -1$
k	wave number
k_s	spring constant

\bar{k}_s	nondimensional spring constant
m_j	random mass of jth bay
\bar{m}	average mass, mass of perfectly periodic structure
N	number of bays
\bar{N}_j	nondimensional internal force, jth point
$o(*)$	terms of order greater than the argument
$p(*)$	probability density function
r_j	reflection coefficient of jth bay
r_N	reflection coefficient of N bays
t_j	transmission coefficient of jth bay
t_N	transmission coefficient of N bays
T	(superscript) matrix transpose
\mathbf{T}	transfer matrix
\mathbf{T}_j	random transfer matrix, jth bay
$\mathbf{T}(\alpha)$	transfer matrix, function of random variable α
u_j	displacement of jth mass
\bar{U}_j	nondimensional longitudinal displacement, jth point
\mathbf{W}_j	wave transmission matrix, jth bay
\mathbf{x}	a state vector
$\hat{\mathbf{x}}$	normalized state vector or direction of state vector
\mathbf{X}	eigenvector matrix
α	random variable
γ	localization factor
μ_j	nondimensional jth mass
ρ	mass density per unit volume

*graduate student, Department of Aeronautics and Astronautics, student member AIAA

σ_a^2	variance of random variable a
ω	radian frequency
$\bar{\omega}$	nondimensional frequency
$*$	(superscript) complex conjugate
$\langle \rangle$	average of a random variable
$1_A(\cdot)$	indicator function, its value is one when the argument lies on A and 0 otherwise

1 Introduction

This paper describes some of the consequences of disorder in what are normally perfectly periodic structures. The periodic structures of interest are those having repetitive bays along one linear dimension and include the skin-stringer panels found in airplane fuselages and truss beams that will form the support structure of the space station. See Figure 1. The dynamics of periodic systems are characterized by frequency bands that alternately pass and stop traveling waves (assuming no damping) with the frequencies of the structure lying within the passbands.

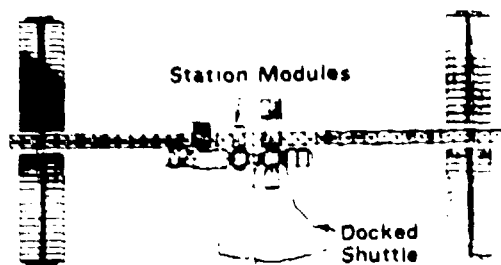


Figure 1. Truss beam extending the length of the space station, from [1].

Because of manufacturing or assembly defects, no structure will be perfectly periodic. Disorder can occur in the length of bays and in the material and mass properties of the structure. The disorder is assumed to be distributed among all the bays and not confined to just a few. Recently, Hodges and Woodhouse [2,3] demonstrated with simple examples that this disorder in periodicity can have some amazing consequences. Disruption in the periodicity will lead to attenuation of waves in all frequency bands independent of any dissipation in the system! Equivalently, each normal mode, whose amplitude is equally predominant along the length of a perfectly periodic structure, will have its amplitude spatially localized in the disordered counterpart. See Figure 2.

This localized behavior of the mode shapes, or equivalently the attenuation of all the traveling waves, means that energy injected into one end of a disordered structure will not be able to propagate, but will be confined to the region near the input. Because such behavior can impact

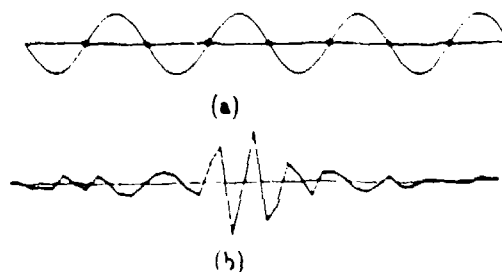


Figure 2.

(a) Mode of a perfectly periodic structure, from [3].

(b) Localized mode of a disordered structure, from [4].

disturbance propagation in and control of structures, as well as complicate schemes to identify the actual damping of a system, engineers should be aware of the localization phenomenon.

Localization effects have been studied extensively by solid state physicists but only recently by engineers. This is the first paper to calculate frequency dependent localization factors for disordered periodic systems of interest to the structural dynamicist.

In Section 2 the literature relevant to the study of localization, including works by physicists, mathematicians and engineers is surveyed. The modeling of periodic and disordered periodic systems carrying one pair of waves is discussed in Section 3. Section 4 explains how the theory of products of random matrices is used to calculate frequency dependent localization factors when one parameter in each bay is disordered. In Section 5 localization effects are investigated for a chain of springs and disordered masses. Section 6 includes an examination of a rod in longitudinal compression with periodically attached disordered resonators. Section 7 includes a brief discussion of the localization phenomenon in multiwave systems. Concluding remarks are made in Section 8.

2 Survey of Localization Literature

The study of localization has a colorful history spanning three decades with contributions from researchers around the world. In this section we survey some of the relevant contributions to localization studies by solid state physicists and mathematicians and discuss the handful of engineering papers that have recently appeared on the subject.

The localization phenomenon was first explained in 1958 by Philip Anderson [5] in the context of electron transport in disordered crystals. As a result of his original contribution, the phenomenon is occasionally referred to as Anderson localization. Anderson was cited in part for his work on localization when he was awarded the Nobel

Prize for Physics in 1977. Despite a Nobel Prize, some fundamental questions arose about even the existence of localization. As a result, localization in one-dimensional systems received a fresh look in the early 1980's [6,7].

In 1963 Furstenberg [8] published an important limit theorem on products of random matrices. Because a disordered periodic structure can be modeled via a product of random transfer matrices, with each matrix modeling one bay, Furstenberg's theorem is obviously relevant to the study of such systems. In 1968 the Russian mathematician Oseledets [9] proved another limit theorem for products of random matrices relevant to multiwave one-dimensional systems. Mathematicians have taken renewed interest in the theory of products of random matrices as indicated by two recent publications [10,11].

The Japanese physicists Matsuda and Ishii [12] pointed out the importance of Furstenberg's work to one-dimensional disordered systems. However, theorems on products of random matrices have generally received scant attention from physicists working on localization, because they have relied on their own heuristic techniques, and because they have been more interested in two- and three-dimensional systems which cannot be as easily handled with transfer matrices.

Hodges [2] was the first to exploit the analogy between localization work on periodic systems of importance to the solid state physicist and some simple periodic models of interest to the structural dynamicist. Hodges and Woodhouse [3] also demonstrated the phenomenon experimentally. More recently Bendiksen [13] has examined mode localization in closed disordered periodic structures, like a compressor rotor and a dish antenna. These closed systems are not mathematically equivalent to the linear one-dimensional structures under consideration here. Pierre, Tang and Dowell [14] also examined localization, but only with the aid of a deterministically disordered beam on three supports. None of these engineering papers provided analytical calculations for localization effects over a wide frequency range.

The most rigorous examination of localization in an acoustical setting has been that by Baluni and Willemssen [15]. They effectively used Furstenberg's work to find frequency dependent localization factors (defined below); however, their application was for layers of sandstone and shale with random slicknesses.

In this paper localization effects as a function of frequency will be calculated for simple periodic structures of interest to the structural dynamicist. These calculations are greatly facilitated by making use of a traveling wave description of the structures.

3 Models of Periodic and Disordered Periodic Structures

Before discussing the calculation of localization effects we will show in this section how periodic and disordered periodic structures can be modeled. The discussion will be confined to systems described by 2×2 transfer matrices.

A periodic structure in one linear dimension consists of identical substructures connected in identical ways. When each substructure can be modeled with a 2×2 transfer matrix the system is called a mono-coupled periodic structure. Each transfer matrix relates a 2×1 state vector x_i to the succeeding state vector x_{i+1} along the length of the structure. The formulation of the transfer matrix assumes a sinusoidal time dependence, and no damping is included in the models so that the effects of disorder can later be highlighted.

Because each substructure or bay is identical, (as in [16]) it is assumed that the boundary conditions are such that the transfer matrices at the ends of the structure are the same as those modeling the rest of the structure) the state vector at the end of the structure is simply related to that at the beginning by

$$x_N = T^N x_0$$

Because we are raising a transfer matrix to the N th power, we only need to examine the transfer matrix T to understand the dynamic properties of the periodic structure.

Briefly, a periodic system is characterized by alternating frequency bands known as passbands and stopbands. In the passbands waves travel according to $e^{\pm ik}$, where k is the real wave number and the positive sign indicates negative-going waves and the negative sign positive-going waves. The wave number k refers to the phase difference of motions in adjacent bays. In the stopbands, waves travel according to the $e^{\pm \alpha}$ or $e^{\pm(\alpha + i\pi)}$. The real exponent α implies nontraveling or attenuating waves. The $\alpha + i\pi$ exponent implies adjacent bays vibrating out of phase with each other in addition to wave attenuation. Only in the passbands can energy be transmitted along the structure.

This underlying wave structure becomes apparent when the transfer matrix T and T^N are diagonalized. Diagonalizing T^N we get in the passbands:

$$\begin{bmatrix} e^{+iNk} & \\ & e^{-iNk} \end{bmatrix} \quad (1)$$

and in the stopbands we get:

$$\begin{bmatrix} e^{+N\alpha} & \\ & e^{-N\alpha} \end{bmatrix} \quad (2)$$

Note that α and k are functions of frequency.

The natural frequencies of the periodic structure lie within the passbands. In particular N natural frequencies lie in each passband of an N bay structure. (This is only strictly true when each bay has symmetry of mass

and stiffness about its midpoint. If the bay is unsymmetric, one frequency will occur in a stopband. See [17] for details.) For a periodic structure the mode shapes have equal amplitude along the entire length of the structure. The reader is referred to [16,17,18] for a more extensive discussion of the properties of perfectly periodic structures.

Now we consider the case when the structure is not perfectly periodic. Even relatively minor variations from bay to bay can drastically change the dynamic picture presented above. The mode shape amplitudes of the disordered structure are spatially localized and not extended as in the perfectly periodic case. Equivalently, waves are attenuated in all frequency bands including what had been the passbands of the perfectly periodic structure. It is this latter wave attenuation effect that is studied closely in the paper.

When a periodic structure is disordered, the transfer matrix for the entire system is not T^N , but rather a product of random transfer matrices:

$$\prod_{j=1}^N T_j = T_N \dots T_1 \quad (3)$$

The transfer matrices are assumed to be functions of a single random variable, like a mass or a spring constant. In addition, the random variables and in turn the random transfer matrices are independent and identically distributed. Thus the disorder is distributed equally among all the bays and not confined to just a few.

Unlike the case of Equations 1 and 2 for the periodic system, one cannot simultaneously diagonalize each transfer matrix of Equation 3 with the same similarity transformation. However, it is possible to put each of the random matrices forming the product into the following wave transmission form:

$$\begin{bmatrix} A_R \\ B_R \end{bmatrix} = \begin{bmatrix} \frac{1}{t_j} & -\frac{r_j}{t_j} \\ -\frac{r_j}{t_j} & \frac{1}{t_j} \end{bmatrix} \begin{bmatrix} A_L \\ B_L \end{bmatrix} \quad (4)$$

This is a wave transmission matrix for one random bay inserted in the middle of an otherwise perfectly periodic structure carrying a pair of traveling waves. Physically, $|t_j|^2$ represents the ratio of transmitted energy to incident energy, and $|r_j|^2$ the ratio of reflected energy to incident energy. Energy conservation implies that $|t_j|^2 + |r_j|^2 = 1$.

So the transfer matrix in wave transmission form for the entire structure is:

$$\prod_{j=1}^N W_j = \begin{bmatrix} \frac{1}{t_N} & -\frac{r_N}{t_N} \\ -\frac{r_N}{t_N} & \frac{1}{t_N} \end{bmatrix} \quad (5)$$

The wave transmission matrices in Equations 4 and 5 are matrices of the Cayley type written as:

$$C = \begin{bmatrix} a & b \\ b^* & a^* \end{bmatrix} \quad (6)$$

A random transfer matrix T_j can be put in Cayley form via a certain similarity transformation:

$$C_j = X^{-1} T_j X$$

We also require that the similarity transformation diagonalize the transfer matrix of the perfectly periodic structure. Hori [19] has given conditions that the transformation should satisfy to ensure that T_j can be transformed to a matrix of Cayley type. The Cayley form of the transfer matrix may not be precisely the wave transmission form of Equation 4; however, in Equation 6 a will be precisely $\frac{1}{t_j}$ while b may differ from $-\frac{r_j}{t_j}$ by at most a phase factor. The wave transmission or Cayley forms are convenient for understanding and calculating localization effects.

4 Calculation of Localization Factors

In the introduction the dynamic effect of localization was described as being an attenuation of waves and a spatial localization of modal amplitudes. We will see that the waves in the disordered periodic structure are attenuated as $e^{-\gamma N}$ where γ is the real localization factor. It has been argued that this same exponential, $e^{-\gamma N}$, describes the envelope of the localized modal amplitude [12,20].

As mentioned earlier, a long disordered periodic structure can be modeled as a product of random matrices. The question arises as how to measure the effect of this randomness. Does one examine the reflection coefficient for this disordered periodic structure and then show that it is very large for the disordered system indicating decaying wave propagation? This point is critical and even confused some solid state physicists in the late 1970's. Choosing the wrong variable to examine can lead to very misleading results. Anderson et. al. [6] argued somewhat heuristically that the appropriate variable to average when studying localization effects is the natural logarithm of the absolute value of the transmission coefficient of the system. Ironically, Matsuda and Ishii [12], relying on Furstenberg [8], much earlier had shown $\ln |t_N|$ to be the key variable to average. Here a much more straightforward argument than [12] is made to show the relevance of $\ln |t_N|$ to localization studies of systems described by 2×2 transfer matrices.

Furstenberg [8] showed that products of random matrices follow a law of large numbers. (This is most easily seen if this product acting on some input vector is viewed as a Markov chain [10]). One result of [8] was the following equation:

$$\gamma = \lim_{N \rightarrow \infty} \frac{1}{N} \ln \|T_N \dots T_1\| \quad (7)$$

or

$$\gamma = \lim_{N \rightarrow \infty} \frac{1}{N} \ln \|W_N \dots W_1\| \quad (8)$$

where $\gamma > 0$. The norm here is simply the 2-norm or the maximum singular value of the matrix product. Recall that the singular values of a matrix A are simply the positive square roots of $A^H A$ or $A A^H$. This norm is also defined as

$$\|A\| = \max_{x \neq 0} \frac{\|Ax\|}{\|x\|}$$

The most insight into the meaning of γ comes by examining the maximum singular value of the matrix product of 5 in wave transmission form. Recalling Equation 5 a little algebra shows that

$$\left\| \prod_{j=1}^N W_j \right\| = \frac{1 + |r_N|}{|t_N|}$$

so from Equation 8

$$\gamma = \lim_{N \rightarrow \infty} \frac{1}{N} (\ln(1 + |r_N|) - \ln |t_N|)$$

Because $0 < |r_N| < 1$, taking the limit means the first term will vanish and we are left with

$$\gamma = \lim_{N \rightarrow \infty} -\frac{1}{N} \ln |t_N|$$

Note that an average over an ensemble of $\ln |t_N|$ is not taken. Furstenberg's theorem tells us that by letting $N \rightarrow \infty$ we need not average over an ensemble. Variables like $\ln |t_N|$ behaving in this way are called self-averaging. This result indicates why $\ln |t_N|$ is relevant to the study of localization.

We are able to consider as well disordered periodic structures with finitely many bays. These can be simulated by a product of a finite number of random matrices. The final matrix product can be put in wave transmission form, after which the transmission coefficient can be extracted and the localization factor calculated as

$$\gamma = -\frac{\ln |t_N|}{N}$$

Because we have not allowed N to tend to infinity we must really average $\ln |t_N|$ over some ensemble. This is accomplished computationally via a Monte Carlo simulation. So for the case of finitely many bays:

$$\gamma = -\frac{\langle \ln |t_N| \rangle}{N}$$

The next goal is to show how the localization factor can be computed analytically for models described by 2×2 transfer matrices. In addition to Equation 7, the localization factor, γ , is the following limit:

$$\gamma = \lim_{n \rightarrow \infty} \frac{1}{n} \ln \|T_n \dots T_1 x\|$$

where again the matrices are independent and identically distributed.

Furstenberg found that this limit can be calculated from the following double integral:

$$\gamma = \int \int \ln \|T(\alpha)x\| p(\alpha) d\alpha p(x) dx \quad (9)$$

For this 2×2 case x represents a point on the unit circle. Equation 9 is valid subject to the probability density for x being invariant with respect to the probability density for the random variable inside the transfer matrix. In other words, for Equation 9 to be valid we must find a probability density for the direction of a vector, such that when it is multiplied by the random transfer matrix, $T(\alpha)$, the resulting vector will have probability density for its direction identical to that of the premultiplying vector.

This required condition of invariance is described mathematically in many ways including:

$$\int 1_A(x) p(x) dx = \int \int 1_A\left(\frac{T(\alpha)x}{\|T(\alpha)x\|}\right) p(\alpha) d\alpha p(x) dx \quad (10)$$

where A is some arc along the unit circle. This equation is known in the solid state physics literature as the Furstenberg-Schmidt self-consistency condition [21].

Unfortunately it is difficult, if not impossible, to find the invariant probability density for x . Therefore Equation 9 can rarely be solved.

One must then consider approximations to the localization factor. Because it is never quite certain over what frequency ranges these approximations are valid, Monte Carlo simulations are used to check those ranges.

Baluni and Willemsen [15] suggested a Taylor series expansion of terms inside the integral 9 as well as 10 except for the probability density of α . This leads to an approximation for the localization factor which is good to order in the variance of the disordered parameter in the transfer matrix. The motivated reader is encouraged to consult [15]. The answer is arrived at conveniently when the random transfer matrix is put in wave transmission form. The localization factor is then calculated as

$$\gamma = \frac{i}{2} \frac{\partial^2 (\ln \langle \frac{1}{t(\alpha)} \rangle)}{\partial \alpha^2} \sigma_\alpha^2 + o(\sigma_\alpha^2) \quad (11)$$

It is this equation that we will use to compute the wave attenuation effects present in disordered periodic structures. Note that only the (1,1) term of the wave transmission matrix (or Cayley matrix) is needed in Equation 11.

5 Localization Effects for a Mass-Spring System

In this section we will use a simple example to demonstrate the localization calculations. The structure is the infinite mass spring system shown in Figure 3. First consider the transfer equation for one bay of the system:

$$\begin{bmatrix} u_{j+1} \\ u_j \end{bmatrix} = \begin{bmatrix} 2 - \frac{\omega^2 m}{k_s} & -1 \\ 1 & 0 \end{bmatrix} \begin{bmatrix} u_j \\ u_{j-1} \end{bmatrix}$$

For the disordered system, m is replaced by m_j where



Figure 3. A chain of springs and masses.

$m = \langle m_j \rangle$. The terms are nondimensionalized as follows:

$$\begin{bmatrix} u_{j+1} \\ u_j \end{bmatrix} = \begin{bmatrix} 2 - \bar{\omega}^2 & -1 \\ 1 & 0 \end{bmatrix} \begin{bmatrix} u_j \\ u_{j-1} \end{bmatrix}$$

where

$$\bar{\omega} = \frac{\omega^2}{(\frac{k_s}{m})}$$

and

$$\mu_j = \frac{m_j}{m}$$

For the perfectly periodic system $\mu_j = 1$. From the condition that $|\text{trace}(\mathbf{T})| < 2$ in a passband we can see that a single passband exists for the perfectly periodic system when:

$$0 < \bar{\omega} < 2$$

All higher frequencies are in the stopband. A more extensive discussion of the perfectly periodic structure can be found in [16]. The wave number for the passband of the periodic mass-spring system is governed by this equation:

$$\cos k = 1 - \frac{\bar{\omega}^2}{2}$$

Using an appropriate eigenvector similarity transformation, the random transfer matrix is put in Cayley form. Here

$$\mathbf{X} = \begin{bmatrix} e^{ik} & 1 \\ 1 & e^{ik} \end{bmatrix}$$

and

$$\mathbf{X}^{-1} = \begin{bmatrix} (-i)/(2 \sin k) & (ie^{-ik})/(2 \sin k) \\ (ie^{-ik})/(\sin k) & (-i)/(2 \sin k) \end{bmatrix}$$

The transfer matrix in Cayley form is now:

$$\begin{bmatrix} e^{ik}(1 + i\delta_j) & i\delta_j \\ -i\delta_j & e^{-ik}(1 - i\delta_j) \end{bmatrix}$$

where $\delta_j = (\bar{\omega}^2(\mu_j - 1))/(2 \sin k)$

Note that the (1,1) term of this Cayley matrix is $(t(\mu_j))^{-1}$. Using Equation 11, the localization factor to order of the variance in the nondimensional mass is:

$$\gamma = \frac{\bar{\omega}^4 \sigma_\mu^2}{8 \sin^2 k}$$

with $\sin^2 k = \bar{\omega}^2 - \frac{\bar{\omega}^4}{4}$ then:

$$\gamma = \frac{\bar{\omega}^4 \sigma_\mu^2}{8(1 - \frac{\bar{\omega}^2}{4})} \quad (12)$$

If we allow $\bar{\omega} \rightarrow 0$, the localization factor is:

$$\gamma = \frac{\bar{\omega}^4 \sigma_\mu^2}{8}$$

and switching back to dimensional form, at low frequency:

$$\gamma = \frac{\omega^4 \sigma_m^2}{8k_s m}$$

which is the result usually found in the physics literature and is derived through much more torturous methods than are used here. The theoretical result of Equation 12 is plotted in Figure 4 for the passband of the underlying

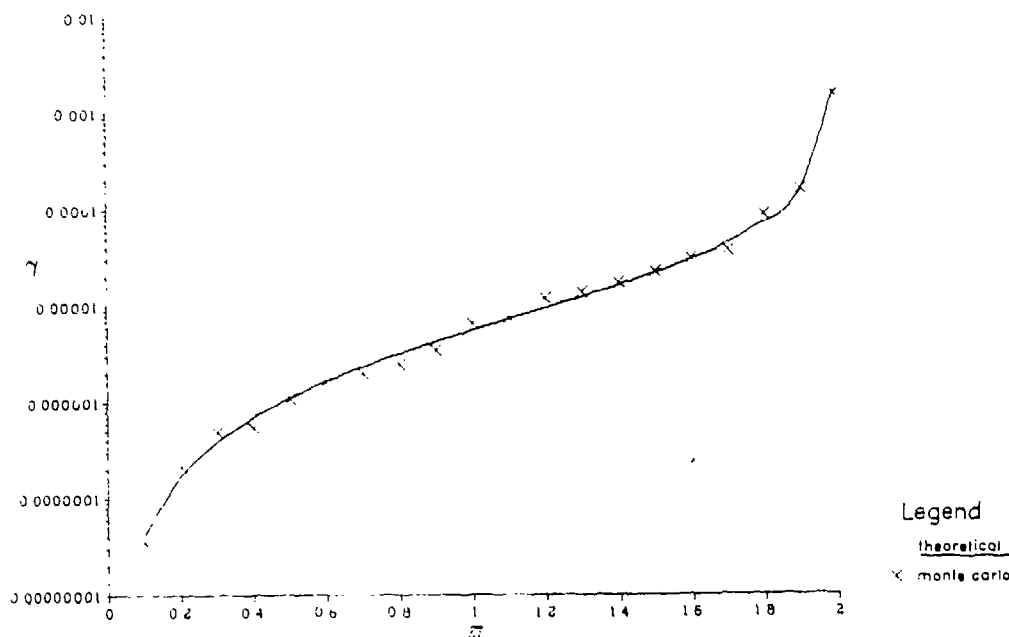


Figure 4. Localization factor for mass-spring system. Masses disordered, with $\langle \mu_j \rangle = 1$ and $\sigma_\mu^2 = .333 \times 10^{-4}$.

perfectly periodic structure. Localization would provide only a small amount of added attenuation to that already occurring in the stopband.

A Monte Carlo simulation was made of the disordered mass-spring system using 200 random transfer matrices. The random nondimensional mass, μ_j , had a uniform probability density function with width of .02 centered around $\langle \mu_j \rangle = 1$. As a result, $\sigma_\mu^2 = .333 \times 10^{-4}$. Monte Carlo results are also shown in Figure 4. Notice how well the Monte Carlo simulation tracks the theoretical result. The plot will be raised or lowered depending on whether the disorder is greater or smaller as reflected in the nondimensional mass variance.

Clearly the maximum attenuation occurs as we approach the nominal stopband. At $\bar{\omega} = 1.99$, for example, where $\gamma = .1654 \times 10^{-2}$ a wave will have decayed by a factor of .44 after 500 bays even though no damping is present. A modal amplitude for a normal mode at that frequency would be confined to an exponential envelope governed by $\gamma = .1654 \times 10^{-2}$. The localization effect is obviously less pronounced at lower frequencies, but is nonetheless present.

The attenuation caused by the disorder is unlike that of dissipation. Here localization prevents the wave from traveling along the structure, unlike the case for a perfectly periodic system, where the wave would travel without attenuation. Localization tends to confine the wave near its point of origin, where it is eventually dissipated by the damping that inevitably exists in all real structures.

6 Localization Effects for a Rod with Disordered Resonators

In this section we investigate localization factors for a model proposed by von Flotow [18] which mimics some of the important behavior of a truss structure. The model is a longitudinal wave carrying rod with attached resonators that represent the vibrating cross-members present in a real truss structure. The model and relevant properties are shown in Figure 5.

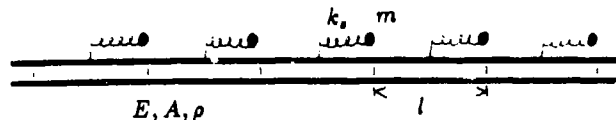


Figure 5. Rod carrying longitudinal waves with attached resonators.

The transfer equation for the perfectly periodic model is:

$$\begin{bmatrix} \bar{U}_{j+1} \\ \bar{N}_{j+1} \end{bmatrix} = \begin{bmatrix} c + \frac{\bar{H}_j}{2} & \frac{1}{2} - \frac{\bar{H}_j(1-c)}{2} \\ 3s + \frac{\bar{H}_j(1+c)}{2} & c + \frac{\bar{H}_j}{2} \end{bmatrix} \begin{bmatrix} \bar{U}_j \\ \bar{N}_j \end{bmatrix} \quad (13)$$

where

$$c = \cos \pi \bar{\omega}$$

$$s = i \sin \pi \bar{\omega}$$

$$\bar{s} = i \pi \bar{\omega}$$

where the nondimensional transfer function of the attached resonator is:

$$\bar{H} = \left(\frac{1}{\bar{k}_s} - \frac{1}{\bar{\omega}^2 \pi^2 \mu} \right)^{-1}$$

and where the nondimensional frequency, stiffness and mass are:

$$\bar{\omega} = \frac{\omega l \left(\frac{\rho}{E} \right)^{1/2}}{\pi}$$

$$\bar{k}_s = \frac{k_s l}{EA}$$

$$\mu = \frac{m}{(\rho A l)}$$

The transfer matrix models a bay extending across a length of rod, across a resonator, and then across another length of rod.

Here the attached mass is randomized so that μ_j becomes a nondimensional random variable and $\mu = \langle \mu_j \rangle$. A discussion of the dynamic characteristics of the perfectly periodic structure can be found in [18]. The wave number k for the passbands of the perfectly periodic structure is determined by

$$\cos k = c + \frac{\bar{H}s}{2\bar{s}}$$

By applying the transformation:

$$X = \begin{bmatrix} i \sin k & -i \sin k \\ 3s + (\bar{H}(1+c))/(2) & 3s + (\bar{H}(1+c))/(2) \end{bmatrix}$$

and

$$X^{-1} = \begin{bmatrix} (-i)/(2 \sin k) & (23s + \bar{H}(1+c))^{-1} \\ (i)/(2 \sin k) & (23s + \bar{H}(1+c))^{-1} \end{bmatrix}$$

the transfer matrix in Cayley form is obtained:

$$\begin{bmatrix} e^{ik}(1 - i\delta_j) & i\delta_j \\ -i\delta_j & e^{-ik}(1 + i\delta_j) \end{bmatrix}$$

where

$$\delta_j = \frac{(\sin \pi \bar{\omega}) \Delta \bar{H}_j}{2(\sin k) \pi \bar{\omega}}$$

and

$$\Delta \bar{H}_j = \left(\frac{1}{\bar{k}_s} - \frac{1}{\bar{\omega}^2 \pi^2 \mu_j} \right)^{-1} - \left(\frac{1}{\bar{k}_s} - \frac{1}{\bar{\omega}^2 \pi^2 \mu} \right)^{-1}$$

Again our attention focuses on the (1,1) term, which is the reciprocal of the transmission coefficient for one bay. Applying Equation 11, the localization factor for a rod with attached resonators having disordered masses is:

$$\gamma = \frac{(\sin^2 \pi \bar{\omega}) \sigma_\mu^2}{8(\sin^2 k) (\pi \bar{\omega})^6 \mu^4 ((1/\bar{k}_s) - (1/\bar{\omega}^2 \pi^2 \mu))^4}$$

This localization factor is plotted for the first four passbands of the system in Figure 6. For this plot $\bar{k}_z = .5$ and μ_j is random with a uniform probability density function of width .02 centered around $\langle \mu_j \rangle = .2$. This implies that $\sigma_\mu^2 = .333 \times 10^{-4}$. A little thought reveals that at low frequency the localization factor will go as ω^2 .

These results were confirmed with a Monte Carlo simulation of 200 bays with probability density mentioned above. The Monte Carlo results are also shown in Figure 6 and these results track the theoretical calculations quite well.

Clearly the maximum attenuation exists around the first stopband. This stopband occurs around $\bar{\omega} = (\frac{k_z}{\mu})^{1/2}/\pi$, the frequency at which the average attached resonator vibrates. Note that a wave near the first stopband at $\bar{\omega} = .45$ will have decayed by a factor of .25 after 200 bays even no though damping is present. The localization effects diminish substantially in the higher passbands.

7 Localization in Multiwave Systems

When a periodic structure is modeled with a transfer matrix of size $2n \times 2n$ with $n > 1$, the structure will carry n pairs of waves. Fewer results are available on localization effects in such multiwave disordered periodic structures.

Recent work by Pichard [22] on multiwave solid state systems has used the theorem of Oseledets [9,11]. To use Oseledets' theorem, we assume that the transfer matrices are independent and identically distributed and that they are symplectic. A matrix T is symplectic if $T^T J T = J$ where:

$$J = \begin{bmatrix} 0 & I \\ -I & 0 \end{bmatrix}$$

The symplectic property also implies that the eigenvalues of T will occur in reciprocal pairs.

The theorem of Oseledets tells us that

$$\lim_{n \rightarrow \infty} [(T_n \dots T_1)^T (T_n \dots T_1)]^{1/n} = B$$

where B is a random matrix, whose eigenvalues are non-random. The spectrum of B is:

$$\begin{bmatrix} e^{+\gamma_1} & & & \\ & \ddots & & \\ & & e^{+\gamma_n} & \\ & & & e^{-\gamma_n} \\ & & & & \ddots \\ & & & & & e^{-\gamma_1} \end{bmatrix}$$

where $\gamma_1 > \dots > \gamma_n$.

The eigenvalues physically represent n pairs of waves traveling in both directions. The theorem of Furstenberg allows us to calculate γ_1 . However, in this multiwave case with $\gamma_n < \gamma_1$, γ_n represents the wave with the

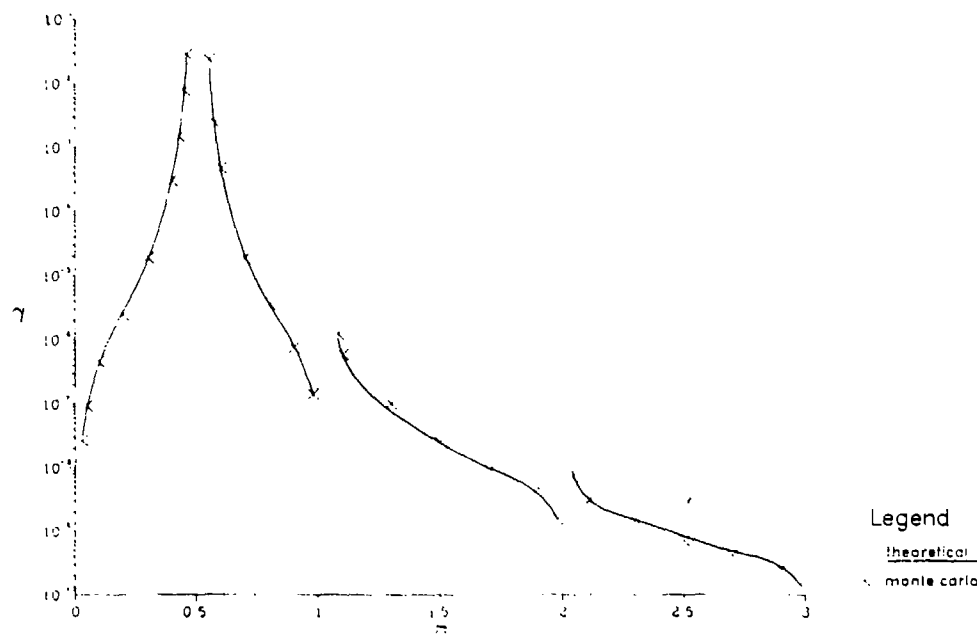


Figure 6. Localization factor for rod with attached resonators. Masses disordered, with $\langle \mu_j \rangle = .2$, $\sigma_\mu^2 = .333 \times 10^{-4}$ and $\bar{k}_z = .5$.

least amount of decay and thus it carries energy along the structure farther than the wave represented by γ_1 . Thus γ_n is the quantity of interest when calculating multiwave localization effects. What analog to $\frac{\ln |t_N|}{N}$ is represented by γ_n is not clear, though Anderson [23] has speculated about this point.

Clearly the study of localization effects in multiwave systems is a fruitful area of research. The best guidance for such work will probably come from [23,22,10].

8 Conclusions

Disruption in the regularity of periodic structures can have some dramatic structural dynamic consequences. Normal mode shapes will be spatially localized and traveling waves will be attenuated in all frequency bands, even in the passbands of the perfectly periodic counterpart. In this paper we have seen how these localization effects for disordered periodic structures carrying a single pair of waves can be calculated.

We have reviewed some of the work of physicists and engineers on the localization phenomenon. Only a few researchers have taken advantage of limit theorems for products of random matrices to calculate localization effects as has been done here.

We used the underlying wave mechanics of these systems to facilitate localization calculations. In particular, a random matrix product modeling a disordered periodic system can be transformed to a wave transmission matrix after which it is easy to show that the localization factor $\gamma = \lim_{N \rightarrow \infty} \frac{\ln |t_N|}{N}$. Furstenberg's limit theorem for random matrix products was exploited to state a formula for the localization factor good to order of the variance of the disordered parameter.

Localization calculations were then demonstrated on a mass-spring system with disordered masses and on a rod in longitudinal compression with disordered resonators. In both cases the theoretical results were confirmed with Monte Carlo simulations.

The multiwave localization problem was briefly mentioned with some lines of research pointed out.

Future papers will examine beams with randomized lengths between supports for which localization effects tend to be quite pronounced at high frequency. Periodic structures with several parameters simultaneously disordered will also be discussed.

Acknowledgements

This research was in part supported under a grant by

the Air Force Office of Scientific Research, with Dr. Tony Amos serving as technical monitor. The author would like to thank Professor Andy von Flotow for his continuing encouragement and interest in this research.

References

- [1] Covault, C., "Launch Capacity, EVA Concerns Force Space Station Redesign," *Aviation Week and Space Technology*, Vol. 125, No. 3, July 21, 1986.
- [2] Hodges, C. H., "Confinement of Vibration by Structural Irregularity," *Journal of Sound and Vibration*, Vol. 82, No. 3, 1982.
- [3] Hodges, C. H. and Woodhouse, J., "Vibration Isolation from Irregularity in a Nearly Periodic Structure: Theory and Measurements," *Journal of the Acoustical Society of America*, Vol. 74, No. 3, September 1983.
- [4] Dean, P. and Bacon, M. D., "The Nature of Vibrational Modes in Disordered Systems," *Proceedings of the Physical Society*, Vol. 81, 1963.
- [5] Anderson, P. W., "Absence of Diffusion in Certain Random Lattices," *Physical Review*, Vol. 109, 1958.
- [6] Anderson, P. W., Thouless, D. J., Abrahams, E. and Fisher, D. S., "New Method for a Scaling Theory of Localization," *Physical Review B*, Vol. 22, No. 8, October 15, 1980.
- [7] Stone, A. D., Joannopoulos, J. D. and Chadi, D. J., "Scaling Studies of the Resistance of the One-Dimensional Anderson Model with General Disorder," *Physical Review B*, Vol. 24, No. 10, Nov. 15, 1981.
- [8] Furstenberg, H., "Noncommuting Random Products," *Transactions of the American Mathematical Society*, Vol. 108, No. 3, September 1963.
- [9] Oseledets, V. I., "A Multiplicative Ergodic Theorem," *Transactions of the Moscow Mathematical Society*, Vol. 19, 1968.
- [10] Bougerol, P. and Larroix, J., *Products of Random Matrices with Applications to Schrödinger Operators*, Birkhäuser, Boston, 1985.
- [11] Cohen, J. F., Kesten, H. and Newman, C. M., eds., *Random Matrices and Their Applications*, Contemporary Mathematics, Vol. 50, American Mathematical Society, Providence, 1986.
- [12] Matsuda, H. and Ishii, K., "Localization of Normal Modes and Energy Transport in the Disordered Harmonic Chain," *Supplement of the Progress of Theoretical Physics*, No. 45, 1970.

- [13] Bendiksen, O. O. "Mode Localization Phenomena in Large Space Structures," Proceedings, AIAA Structures, Structural Dynamics and Materials Conference, San Antonio, TX, May 19-21, 1986.
- [14] Pierre, C., Tang, D. M. and Dowell, E. H., "Localized Vibrations of Disordered Multi-Span Beams: Theory and Experiment," AIAA Structures, Structural Dynamics and Materials Conference, San Antonio, TX, May 19-21, 1986.
- [15] Baluni, V. and Willemsen, J., "Transmission of Acoustic Waves in a Random Layered Medium," Physical Review A, Vol. 31, No. 5, May 1985.
- [16] Faulkner, M. G. and Hong, D. P., "Free Vibrations of a Mono-Coupled Periodic System," Journal of Sound and Vibration, Vol. 99, No. 1, 1985.
- [17] Mead, D. J., "Wave Propagation and Natural Modes in Periodic Systems: I. Mono-Coupled Systems," Journal of Sound and Vibration, Vol. 40, No. 1, 1975.
- [18] von Flotow, A., "Traveling Wave Effects in Large Space Structures," NASA Workshop on Applications of Distributed System Theory to the Control of Large Space Structures, Jet Propulsion Laboratory, July 14-16, 1982.
- [19] Hori, J., *Spectral Properties of Disordered Chains and Lattices*, Pergamon Press, Oxford, 1968.
- [20] Ishii, K., "Localization of Eigenvalues and Transport Phenomena in the One-Dimensional Disordered System," Supplement of the Progress of Theoretical Physics, No. 53, 1973.
- [21] Ziman, J. M., *Models of Disorder*, Cambridge University Press, Cambridge, England, 1979.
- [22] Pichard, J. L. and Sarma, G., "Finite Size Scaling Approach to Anderson Localisation," Journal of Physics C, Vol. 14, 1981, L127-L132.
- [23] Anderson, P. W., "New Method for Scaling Theory of Localization. II. Multichannel Theory of a "Wire" and Possible Extension to Higher Dimensionality," Physical Review B, Vol. 23 No. 10, May 15, 1981.

LOCALIZATION IN DISORDERED PERIODIC STRUCTURES

by

GLEN JAMES KISSEL

B.S., Oklahoma State University (1979)

S.M., Massachusetts Institute of Technology (1982)

SUBMITTED IN PARTIAL FULFILLMENT OF THE REQUIREMENTS FOR
THE DEGREE OF
DOCTOR OF PHILOSOPHY

at the

MASSACHUSETTS INSTITUTE OF TECHNOLOGY

FEBRUARY 1988

©Massachusetts Institute of Technology, 1988

Signature of Author

Glen J. Kissel
Department of Aeronautics and Astronautics September 24, 1987

Certified by

A. von Flotow
Professor Andreas H. von Flotow
Thesis Supervisor, Assistant Professor of Aeronautics and Astronautics

Certified by

Richard H. Battin
Dr. Richard H. Battin
Adjunct Professor of Aeronautics and Astronautics

Certified by

Wallace E. Vander Velde
Professor Wallace E. Vander Velde
Professor of Aeronautics and Astronautics

Certified by

George C. Verghese
Professor George C. Verghese
Associate Professor of Electrical Engineering

Accepted by

Professor Harold Y. Wachman
Chairman, Department Graduate Committee

LOCALIZATION IN DISORDERED PERIODIC STRUCTURES

by

GLEN JAMES KISSEL

Submitted to the Department of Aeronautics and Astronautics
on September 24, 1987 in partial fulfillment of the
requirements for the Degree of Doctor of Philosophy

ABSTRACT

Disorder in periodic structures is known to cause spatial localization of normal modes and attenuation of waves in all frequency bands. This thesis uses a traveling wave perspective to investigate these effects on one-dimensional periodic structures of interest to the engineer. Relevant work in the fields of solid state physics, mathematics and engineering is reviewed. A transfer matrix formalism including wave transfer matrices is used to model disordered periodic structures. A limit theorem of Furstenberg for products of random matrices is exploited to calculate localization effects as a function of frequency. The approach presented is applicable to virtually any disordered periodic system carrying a single pair of waves. Localization is studied on three disordered periodic systems using both theoretical calculations and Monte Carlo simulations. Localization is found to be quite pronounced at frequencies near the stopbands of the perfectly periodic counterparts. The problem of localization in one-dimensional systems carrying a multiplicity of wave types is examined using the theorem of Osleedets on products of random matrices. A new result is presented - the multiwave localization factor as a function of the transmission properties of the system.

Thesis Supervisor: Dr. Andreas H. von Flotow

Title: Assistant Professor of Aeronautics and Astronautics

Acknowledgement

I have had a lot of fun studying the localization phenomenon during the past two years. I have been fortunate to share that fun with my thesis supervisor, Professor Andy von Flotow. He has been kind enough to listen to me talk about my evolving understanding of localization week after week, and I have seen his creativity and energy at work as he helped me with this fascinating subject.

Dr. Richard Battin is the professor at MIT I have known the longest. From him I took some very enjoyable classes, and from him I first learned about symplectic matrices which have played such an important part in this thesis. I wish him all the best in his semi-retirement.

I learned a lot of what I know about stochastic processes from Professor Wallace Vander Velde. It is appropriate that he should be on my committee because of our common interests in flexible space structures and probability theory.

Professor George Verghese has had an interest in random matrices for quite a while, and it was through him that I learned of one of my most important references. I am grateful for his many useful suggestions on a draft of this thesis, and I am glad that I could share my insights with him.

I have received assistance in my work from other quarters as well. Professor Dick Dudley of the Mathematics Department helped me in my interpretation of some of the esoteric aspects of Furstenberg's theorem. Professor Patrick Lee of the Physics Department gave me a suggestion that led to the simplification of the derivation of the multiwave localization factor in Chapter 5.

During my sojourn in Cambridge there are many people that have helped me in many ways. One of those people is Eugene Gath. Eugene not only led me through the intricacies of Irish politics, but also guided me through the mysteries of Green's functions, p-forms and much more that I encountered in this research.

This research was supported in part by the Air Force Office of Scientific Research with Dr. Tony Amos as contract monitor.

Having been localized in Cambridge, it is time to propagate, but before I go, I must dedicate this thesis to Mom, Dad and Deb.

Contents

1	Introduction	16
1.1	Introduction to Localization	16
1.2	History of Localization Studies	21
1.2.1	Solid State Physics, Mathematics and the Localization Phenomenon	21
1.2.2	Structural Dynamic and Acoustical Applications of Localization Theory	24
1.3	Goals, Approach and Contribution of Thesis	26
1.4	Preview of Thesis	28
2	Transfer Matrix Models of Periodic and Disordered Periodic Structures	30
2.1	Introduction	30
2.2	Perfectly Periodic Structures	31
2.2.1	One-Dimensional Periodic Structures	31

2.2.2	Modeling of Perfectly Periodic Structures	31
2.2.3	Properties of Perfectly Periodic Structures	32
2.3	Disordered Periodic Structures	35
2.3.1	Nature of the Disorder	35
2.3.2	Modeling of Disordered Periodic Structures	36
2.3.2.1	Wave Transfer Matrix	36
2.3.2.2	Properties of the Wave Transfer Matrix	38
3	Furstenberg's Theorem and Calculation of Localization Factors for Mono-Coupled Disordered Periodic Structures	39
3.1	Introduction	39
3.2	Furstenberg's Theorem	40
3.3	Localization Factor as a Function of the Transmission Coefficient	44
3.4	Calculation of Localization Factors via an Approximation to Fursten- berg's Theorem	45
4	Calculation of Localization Factors for Three Mono-Coupled Disor- dered Periodic Structures	50
4.1	Introduction	50
4.2	Localization in a Mass-Spring Chain	51

4.2.1	Only Masses Disordered	52
4.2.2	Only Springs Disordered	61
4.2.3	Masses and Springs Disordered	62
4.3	Localization in a Rod with Attached Resonators	64
4.3.1	Only Masses Disordered	64
4.3.2	Only Springs Disordered	70
4.3.3	Only Lengths Between Resonators Disordered	75
4.3.4	All Three Parameters Disordered	76
4.4	Localization in a Beam on Simple Supports	80
4.5	Observations	87
5	Localization in Multiwave Systems	89
5.1	Wave Transfer Matrix Assumptions	92
5.2	Theorem of Oseledets	92
5.2.1	Eigenvalues of Limiting Matrix	93
5.2.2	Vector Propagation Interpretation of Oseledets' Theorem	94
5.3	Localization Factor for Multiwave Systems as a Function of the Transmission Matrix	96
5.4	Calculation of the Multiwave Localization Factor Via p-Forms	104

5.5 Summary	106
6 Conclusions and Recommendations	108
6.1 Conclusions	108
6.2 Recommendations	109
A Matrix and Group Properties	127
B Derivation of Mono-Coupled Wave Transfer Matrices	130
C Models of Three Periodic and Disordered Periodic Structures	133
C.1 Mass-Spring Chain	134
C.1.1 Only Masses Disordered	136
C.1.2 Only Springs Disordered	136
C.1.3 Masses and Springs Disordered	137
C.2 Rod with Attached Resonators	137
C.2.1 Only Masses Disordered	139
C.2.2 Only Springs Disordered	140
C.2.3 Only Lengths Disordered	140
C.2.4 All Three Parameters Disordered	141

C.3 Bernoulli-Euler Beam on Simple Supports	141
D A Simple Method to Calculate Localization Factors	144
E Properties of the Scattering and Wave Transfer Matrices	147

List of Figures

1.1	Periodic truss structure along the length of the space station from [Covault 86]	17
1.2	Alternating pass and stopbands of a perfectly periodic structure. The attenuation coefficient, α , represents the decay per bay	17
1.3	Mode of a perfectly periodic structure from [Hodges and Woodhouse 83]	18
1.4	Attenuation in all frequency bands of a disordered periodic structure	19
1.5	Mode of a disordered periodic structure from [Dean and Bacon 63]	19
4.1	Localization factor for mass-spring chain with masses disordered $\pm 1\%$ from their average value.	55
4.2	Localization factor for mass-spring chain with masses disordered $\pm 1\%$ from their average value.	59
4.3	Localization factor for mass-spring chain with masses disordered $\pm 10\%$ from their average value.	60
4.4	Localization factor for mass-spring chain with masses and springs disordered $\pm 1\%$ from their average values.	63

4.5	Localization factor for rod and attached resonators with masses disordered $\pm 1\%$ from their average value with $\bar{\mu} = 0.2$ and $\bar{k}_s = 0.5$	66
4.6	Localization factor for rod and attached resonators with masses disordered $\pm 1\%$ from their average value with $\bar{\mu} = 0.2$ and $\bar{k}_s = 0.5$	68
4.7	Localization factor for rod and attached resonators with masses disordered $\pm 10\%$ from their average value with $\bar{\mu} = 0.2$ and $\bar{k}_s = 0.5$	69
4.8	Localization factor for rod and attached resonators with springs disordered $\pm 1\%$ from their average value with $\bar{\mu} = 0.2$ and $\bar{k}_s = 0.5$	72
4.9	Localization factor for rod and attached resonators with springs disordered $\pm 1\%$ from their average value with $\bar{\mu} = 0.2$ and $\bar{k}_s = 0.5$	73
4.10	Localization factor for rod and attached resonators with springs disordered $\pm 10\%$ from their average value with $\bar{\mu} = 0.2$ and $\bar{k}_s = 0.5$	74
4.11	Localization factor for rod and attached resonators with lengths between resonators disordered $\pm 1\%$ from their average value with $\bar{\mu} = 0.2$ and $\bar{k}_s = 0.5$	77
4.12	Localization factor for rod and attached resonators with lengths between resonators disordered $\pm 1\%$ from their average value with $\bar{\mu} = 0.2$ and $\bar{k}_s = 0.5$	78
4.13	Localization factor for rod and attached resonators with lengths between resonators disordered $\pm 10\%$ from their average value with $\bar{\mu} = 0.2$ and $\bar{k}_s = 0.5$	79

4.14	Localization factor for rod and attached resonators with masses, springs and lengths between resonators disordered $\pm 1\%$, $\pm 1\%$ and $\pm 1\%$, respectively, from their average values with $\bar{\mu} = 0.2$ and $\bar{k}_s = 0.5$	81
4.15	Localization factor for beam on simple supports with lengths between supports disordered $\pm 1\%$ from their average value.	84
4.16	Localization factor for beam on simple supports with lengths between supports disordered $\pm 10\%$ from their average value.	86
C.1	Mass-spring chain.	134
C.2	One bay of mass-spring chain used to form its transfer matrix.	135
C.3	Rod with attached resonators	138
C.4	Beam on simple supports.	142

Nomenclature

a	element of Cayley matrix
A	cross-sectional area of rod
\bar{A}	amplitude of left traveling wave
b	element of Cayley matrix
\bar{B}	amplitude of right traveling wave
C	Cayley matrix
C^{2d}	complex Euclidean vector space of dimension $2d$
$diag\{*\}$	diagonal matrix
E	Young's modulus
H	(superscript) hermitian transpose
\bar{H}	nondimensional transfer function
i	$i^2 = -1$
I	area moment of inertia
k	wave number
k_s	spring constant
\bar{k}_s, \tilde{k}_s	nondimensional spring constant
l	length of a bay
\bar{l}, \tilde{l}	nondimensional length of a bay
m_j	random mass of j th bay

m	average mass, mass of perfectly periodic structure
n	number of bays
\bar{N}_j	nondimensional internal force, jth point
$o(*)$	terms of order greater than the argument
$p(*)$	probability density function of the indicated argument
r_j	reflection coefficient of jth bay
r	reflection matrix of a bay
\hat{r}	reflection matrix of a bay
R^{2d}	real Euclidean vector space
\sup	supremum
t_j	transmission coefficient of jth bay
t	transmission matrix of a bay
\hat{t}	transmission matrix of a bay
tr	trace of a matrix
T	(superscript) matrix transpose
T	transfer matrix
T_j	random transfer matrix, jth bay
$T(\alpha)$	transfer matrix, function of random variable α
u_j	displacement of jth mass
\bar{U}_j	nondimensional longitudinal displacement, jth point

$w.p. 1$	with probability one
W_j	wave transfer matrix, jth bay
x	a real state vector
\bar{x}	normalized real state vector or direction of state vector
X	eigenvector matrix
z	a complex state vector
\bar{z}	normalized complex state vector
α	random variable or vector
γ	localization factor
γ_j	jth Lyapunov exponent
λ	eigenvalue
Δ^p	p-form operator
$\mu_j, \bar{\mu}_j$	nondimensional jth mass
ρ	reflection matrix of n bays or mass density per unit volume
ρ_n	reflection coefficient of n bays
σ	singular value of a matrix
σ_α^2	variance of random variable or vector α
τ	transmission matrix of n bays
τ_n	transmission coefficient of n bays
ω	radian frequency

ω	nondimensional radian frequency
*	(superscript) complex conjugate
$\langle \alpha \rangle$	average of a random variable or vector α
$1_A(*)$	indicator function, its value is 1 when the argument lies on A and 0 otherwise
$ \langle \alpha \rangle$	evaluate at $\langle \alpha \rangle$.
$ \langle \alpha_j \rangle$	evaluated at $\langle \alpha_j \rangle$
\subset	subset of
\in	an element of

Chapter 1

Introduction

1.1 Introduction to Localization

This thesis describes some of the dynamic consequences of disorder in what are normally spatially periodic structures. Periodic structures are frequently encountered in many fields of engineering and physics. Periodic electromagnetic waveguides, crystalline structures and periodic truss structures are some examples that come to mind.

The periodic structures examined here are systems having repetitive bays along one linear dimension. Those of interest to the structural dynamicist include beams on evenly spaced supports, the skin-stringer panels found in airplane fuselages and truss beams that will form the support structure of the space station. See Figure 1.1.

The dynamics of perfectly periodic systems have special characteristics. Most notably they are characterized by frequency bands that alternately pass and stop traveling waves (assuming no damping) with the natural frequencies of the structure lying within the passbands. See Figure 1.2 In addition, the normal mode shapes of periodic structures are themselves periodic. See Figure 1.3.

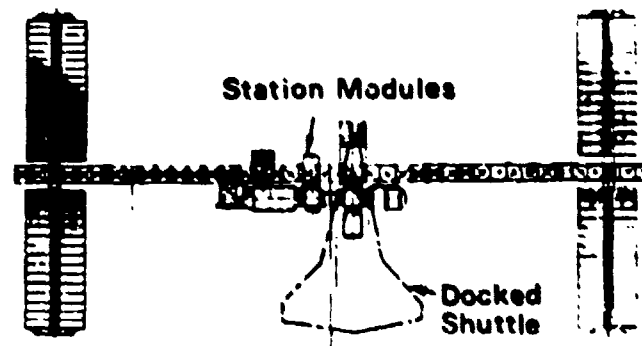


Figure 1.1: Periodic truss structure along the length of the space station from [Covault 86]



Figure 1.2: Alternating pass and stopbands of a perfectly periodic structure. The attenuation coefficient, α , represents the decay per bay

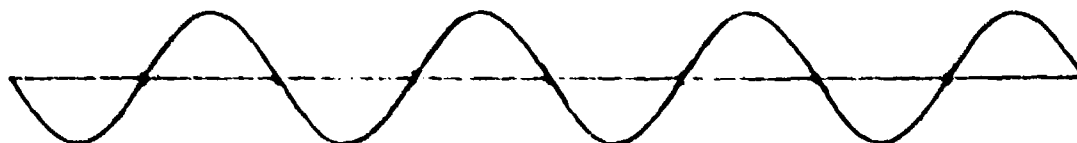


Figure 1.3: Mode of a perfectly periodic structure from [Hodges and Woodhouse 83]

Because of manufacturing or assembly defects, no structure will be perfectly periodic. Disorder can occur in the length of bays and in the material and mass properties of the structure. The disorder is assumed to be distributed among all the bays and not confined to just a few. Recently, [Hodges 82, Hodges and Woodhouse 83] demonstrated with simple examples that this disorder in periodicity can have some amazing consequences. Disruption in the periodicity will lead to attenuation of waves in all frequency bands independent of any dissipation in the system! See Figure 1.4 This is a result of the multiple scattering effects from the randomized bays. Equivalently, each normal mode, whose amplitude is periodic along the length of a perfectly periodic structure, will have its amplitude spatially localized in the disordered counterpart. See Figure 1.5.

This localized behavior of the mode shapes, or equivalently the attenuation of all the traveling waves, means that energy injected into one end of a disordered structure

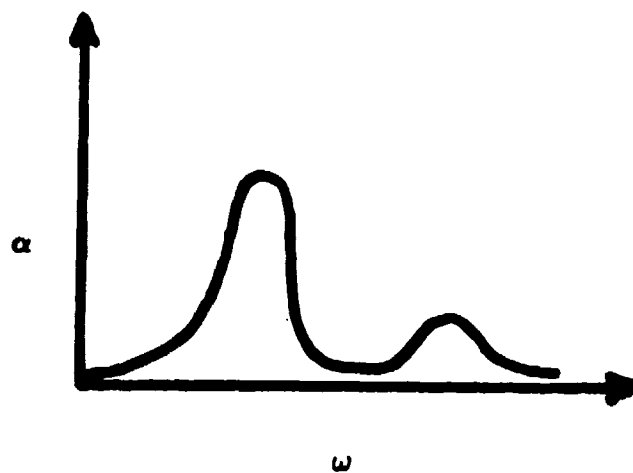


Figure 1.4: Attenuation in all frequency bands of a disordered periodic structure



Figure 1.5: Mode of a disordered periodic structure from [Dean and Bacon 63]

will not be able to propagate arbitrarily far, but will be confined to the region near the input. Because such behavior can impact disturbance propagation in and control of structures, as well as complicate schemes to identify the dynamic characteristics of a system, engineers should be aware of the localization phenomenon.

A simple example from [Hodges 82] will intuitively illustrate the localization phenomenon. Consider an infinite chain of equivalent pendula with nearest neighbors connected by identical springs. This is an example of a perfectly periodic structure and so its mode shapes will be periodic. Now consider disordering this system by replacing each pendulum by one with a random length. In this way the natural frequency of each pendulum is random, and so we no longer have a perfectly periodic system. First assume that the spring constant between each pendulum is zero, so that each pendulum vibrates independently. This is a trivial example of mode localization. Now consider adding a tiny amount of the same spring constant between each pendulum. In this case each pendulum will vibrate at a frequency different from its neighbor, and, with the spring stiffness being so small, its amplitude will not couple significantly with its neighbor. Indeed, if there is only a small probability of encountering within a short distance a pendulum with the same natural frequency as the one under consideration, we can understand how the vibrational amplitude of this pendulum will be localized.

Though the appellation "localization" comes from the fact that normal modes are spatially localized, we will be studying the phenomenon from a traveling wave perspective. Very few analytical results are available dealing directly with normal modes in disordered systems. Our approach is consistent with that in the field of solid state physics, where the phenomenon was originally discovered.

The localization phenomenon makes for a particularly attractive field of study. From the perspective of structural dynamics this is true because it seems to manifest itself as a damping mechanism even though vanishingly small damping may be present. The study of localization is frequently referred to as one of great mathematical richness

and subtlety and this has made for a challenging course of research, especially as we have made use of the mathematics for products of random matrices. The fact that the localization phenomenon has been studied for many years by solid state physicists allows us to borrow the insights and avoid the mistakes from their analogous work. In addition, any new results generated by this research have immediate applicability to virtually any disordered periodic system, even outside the structural dynamics field. Finally, connections between localization theory and the rapidly developing fields of fractals [Rubin 84], chaos [Ikeda and Matsumoto 86] and superconductivity [Lee and Ramakrishnan 85] have been noted.

1.2 History of Localization Studies

The study of the localization phenomenon has a colorful history spanning three decades, with major contributions from researchers in the United States, United Kingdom, Japan, France and the Soviet Union in the fields of solid state physics, mathematics and only lately in engineering. In this section we review some of that history in order that we can place the contribution of this thesis in proper context.

1.2.1 Solid State Physics, Mathematics and the Localization Phenomenon

Two notable papers in the 1950's [Dyson 53, Schmidt 57] explored the effects of disorder on the eigenvalues of an infinite mass-spring chain in one linear dimension. Though they did not examine the effects of disorder on the eigenvectors or on wave propagation, some of their results help explain the mathematics of wave transmission in such randomized systems.

The scientist to first describe eigenstate localization was solid state physicist Philip W. Anderson, whose 1958 paper [Anderson 58] showed that an electron in a three-dimensional disordered lattice of infinite extent had a finite probability of not being transported from its original site as time tended to infinity. In honor of his original contribution, the phenomenon is sometimes called Anderson localization. Localization was at first not well understood or even believed by many people. But through the efforts of researchers like [Mott and Twose 61] it gained acceptance in the solid state physics community. Meanwhile [Borland 63] examined the one-dimensional localization problem from a nonrigorous probabilistic perspective and [Dean and Bacon 63] did numerical simulations of disordered mass-spring chains of finite length showing that eigenmode localization was much more pronounced at high frequency than at low frequency. The solid state physics literature on localization has become quite extensive over the years and much of it is not relevant to this thesis. The reader is referred to [Ziman 79, Erdős and Herndon 82, Lee and Ramakrishnan 85] for extensive bibliographies relevant to that field. The remainder of this review will encompass those physics, mathematics and engineering papers that have had some impact on the thesis.

The pioneering work of [Furstenberg 63] on products of random matrices has provided rigorous results that have immediate applicability to the one-dimensional localization problem. This is so because each bay of a disordered periodic structure can be modeled with a random transfer matrix, and, as a result, the entire structure can be modeled with a product of random matrices. The researchers [McCoy and Wu 68] were apparently the first to recognize the importance of Furstenberg's theorem to disordered physical systems when they studied random Ising models of ferromagnetic systems. However, [Matsuda and Ishii 70] and [Ishii 73] were the first to bring Furstenberg's work to bear on the localization problem. They carefully related Furstenberg's results to eigenmode localization and wave propagation in disordered chains and some simple quantum mechanical models.

In [Oseledets 68] a Russian mathematician proved a multiplicative ergodic theorem

that has enhanced our understanding of the asymptotic behavior of products of random matrices. This theorem has important applications to the study of the localization phenomenon in systems carrying a multiplicity of wave types at a given frequency. Lately, [Pichard and Sarma 81-1], [Pichard and Sarma 81-2] and [Pichard and André 86] have examined localization in solid state multiwave systems. In analyzing these systems they have exploited the work of Oseledets on products of random matrices. Mathematicians have taken renewed interest in the theory of products of random matrices as indicated by two recent publications, [Bougerol and Lacroix 85,AMS 86].

The work of [Herbert and Jones 71,Thouless 72] provides another perspective as far as the calculation of localization effects are concerned. They derived a formula for the localization factor (defined below) which is a function of the spectrum of the disordered system. Their approach is nearly as rigorous as that using products of random matrices.

In 1977 when Anderson and Mott (and Van Vleck) were awarded the Nobel Prize in physics, they were cited in part for their work on localization. In his speech in Stockholm, Anderson [Anderson 78] made the following comment:

Localization ...has yet to receive adequate mathematical treatment, and one has to resort to the indignity of numerical simulations to settle even the simplest questions about it.

While it is still true that we must use numerical simulations to confirm our analytical insights about localization, we will argue in this thesis that mathematical tools are available which allow us to answer some very important questions about localization in one-dimensional systems.

Despite a Nobel Prize, [Czycholl and Kramer 79] raised serious questions with their numerical work about even the existence of localization in one-dimensional systems. This prompted [Anderson et al 80] to do some fundamental work on the localization

problem in one dimension. They derived what they called a scaling variable for one-dimensional disordered systems carrying a single pair of waves. This variable, involving $\ln |t|^2$ where t is the transmission coefficient for a bay, was argued to be the statistically meaningful quantity to average when examining one-dimensional random systems. They also argued that the variable satisfied a central limit theorem. Earlier [O'Connor 75] had made an important contribution toward establishing a central limit theorem for disordered periodic systems. Subsequently [Abrahams and Stephen 80], [Andereck and Abrahams 80] and [Stone 83] provided numerical evidence to support the central limit theorem ideas of [Anderson et al 80]. Apparently [Le Page 82] has provided the definitive mathematical work supporting a central limit theorem contention.

1.2.2 Structural Dynamic and Acoustical Applications of Localization Theory

Solid state physicist C. H. Hodges [Hodges 82] was the first to recognize the relevance of localization theory to disordered periodic systems of interest to the structural dynamicist. He used wave arguments to calculate localization effects at high frequency for a beam on randomly spaced supports. His work raised the possibility that disorder could have a dramatic impact on the dynamics of what are normally spatially periodic structures. Unfortunately, his analysis provided little indication of how localization effects varied with frequency, and his techniques were not applicable to a broad range of periodic structures. Both the insights and shortcomings of his work motivated research leading to this thesis.

¹The precise scaling variable they used was $\ln \frac{1}{|t|^2}$, which is simply $-2 \ln |t|$. They use the term scaling variable in the sense that the mean value of the variable for two bays is the sum of the mean values of the variable for each bay individually. Also the variance of this variable scales at least according to a weak law of large numbers.

In a later paper [Hodges and Woodhouse 83] attempted to apply the work of [Herbert and Jones 71, Thouless 72] to estimate localization effects in two passbands for a taut wire with unevenly spaced masses. They also conducted an experiment on the wire-mass system which qualitatively confirmed the localization effects.

More recently [Bendiksen 86, Bendiksen and Valero 87, Cornwell and Bendiksen 87] have examined mode localization in closed disordered periodic structures, like compressor rotors and dish antennas. These closed systems are not mathematically equivalent to the linear one-dimensional structures under consideration here. [Pierre et al 86] and [Pierre 87, Pierre and Dowell 87] have also examined localization, but only with the aid of deterministically disordered systems with as few as three bays. None of the engineering papers so far provided analytical calculations for localization effects over any significant frequency range. This thesis and [Kissel 87] are the first publications to calculate frequency dependent localization factors for disordered periodic systems of interest to the structural dynamicist.

The most rigorous examination of localization in an acoustical setting has been that by [Baluni and Willemsen 85]. They effectively used Furstenberg's work to calculate frequency dependent localization effects; however, their application was for layers of sandstone and shale with random thicknesses. The paper [Sheng et al 86] also examined localization with geophysical applications in mind.

Recently, more solid state physicists [Anderson 85, Flesia et al 87] have recognized that localization manifests itself in acoustical and optical systems. They append the term "classical localization" to the phenomenon when it occurs outside the context of quantum mechanics.

1.3 Goals, Approach and Contribution of Thesis

The ultimate goal of this research is to provide the analyst and experimentalist with the tools to decide (given some engineering judgement of the disorder) how significant the dynamic effects of disorder will be on a periodic structure as a function of frequency and the properties of the structure. This thesis is a major step toward the goal of providing tools to rigorously examine the localization phenomenon in one-dimensional disordered periodic structures. We present the tools for mono-coupled disordered periodic structures (structures in which one bay is connected to its neighboring bays through one coupling coordinate) to calculate, analytically and numerically, localization effects over a wide frequency range at moderate levels of disorder. In addition, an important new tool is presented here to guide localization work on multiwave systems.

The approach of the thesis is probabilistic, as opposed to the deterministic analysis of [Bansal 80, Pierre and Dowell 87]. The methods of probability theory allow us to model our uncertainty in a way that yields meaningful answers. This is particularly true when we make use of theory on products of random matrices, which puts us on a firm mathematical footing.

What had the most profound impact on the direction of the research was the observation of confusion about localization in the late 1970's in one-dimensional disordered systems. In this instance the confusion could have been avoided had more researchers availed themselves of the appropriate mathematical tools. The very important observation about the $\ln |t|$ being the key statistical variable in the study of localization can be easily deduced in a few algebraic steps by making use of wave transfer matrices and Furstenberg's theorem. This is explained in Chapter 3.

It is the philosophy of this thesis that the transfer matrix formalism accompanied by the appropriate theories on products of random matrices can lead to a better understanding of the localization phenomenon. This philosophy has been needlessly neglected

in most of the theoretical localization literature to date. The reason that theorems on products of random matrices have generally received scant attention from physicists working on localization is that they have relied on their own heuristic techniques, and that they have been more interested in two- and three-dimensional systems, which cannot be as easily handled with transfer matrices.

The first principal contribution of the thesis is the explanation of how random transfer matrix techniques can be used to model disordered systems, deduce transmission properties and calculate localization effects. This includes a discussion of the important transformation to wave transfer matrix form and the relevance of the theorems of Furstenberg and Oseledets to the one-dimensional localization problem.

The second principal contribution is the calculation of localization effects as a function of frequency for three disordered periodic models of interest to the structural dynamicist. In most instances the localization effects are found to be strongest at frequencies near the stopbands of the normally perfectly periodic structures. Localization effects are also pronounced when the length of a bay is disordered.

The third principal contribution is the derivation of the localization factor for multiwave one-dimensional systems as a function of the transmission matrix. This at last allows a rigorous treatment of localization in multiwave systems. Because transfer matrix methods can be used to model almost any disordered periodic system in one dimension, including systems of interest to the solid state physicist, the results here will be of interest outside the engineering field as well.

In addition to these principal contributions, we will note in the body of the thesis instances where previously published results are extended and where mistaken approaches and conclusions exist in the literature.

1.4 Preview of Thesis

Before studying the effects of disorder on periodic structures, Chapter 2 presents a brief discussion of the modeling and dynamics of perfectly periodic structures. Here the transfer matrix formalism is introduced and the important passband and stopband property is discussed. The modeling of disordered periodic structures is next presented and the very important wave transfer form of the transfer matrix is introduced.

This serves as a prelude to Chapter 3 in which we discuss Furstenberg's theorem on products of random matrices. This is the tool used to study localization for mono-coupled periodic structures. With Furstenberg's theorem in hand, we are able to deduce the asymptotic behavior of the transmission coefficient, τ_n , of the n bay disordered periodic structure. We will show that the wave intensity, $|\tau_n|$, decays as $e^{-\gamma n}$, where γ is the localization factor. We are also able, using the same theorem, to estimate the localization factor as a function of the level of disorder, frequency and physical properties of the system.

This theory is demonstrated on three examples in Chapter 4. The first and simplest example is a linear chain of springs and masses. Initially only the masses are disordered and then only the springs, followed by masses and springs disordered simultaneously. All calculations are confirmed by Monte Carlo simulations. Similarly, a rod with attached resonators is studied. First the masses, springs and lengths are disordered individually, after which all three variables are disordered. The last mono-coupled example is a Bernoulli-Euler beam on simple supports with random lengths between the supports.

Most real structures carry more than a single pair of wave types at a given frequency, so localization in these multiwave systems should be investigated. Unfortunately, Furstenberg's theorem will be of little use for investigating localization effects in multiwave structures; however, the theorem of Oseledets is precisely suited to mul-

tiwave analysis. In Chapter 5, after discussing Oseledets' theorem, we present a new result – the localization factor for multiwave systems in terms of the transmission matrix, τ . The significance of the result is discussed, and an analytical technique for calculating the localization factor for multiwave systems is suggested.

Concluding remarks and suggestions for future research are made in Chapter 6.

Several appendices are included and are referred to frequently in the body of the thesis. Appendix A discusses some definitions and properties from matrix theory and group theory used in the thesis. The derivation of the wave transfer matrix for mono-coupled systems is discussed in Appendix B. In Appendix C the modeling of a mass-spring chain, a rod with attached resonators and a beam on simple supports is discussed, both when they are periodic and when they are disordered. A simple method to calculate localization factors, not depending on theories for products of random matrices, is discussed in Appendix D. In the final appendix, Appendix E, we examine some properties of scattering and wave transfer matrices that will be useful in Chapter 5. The reader should at least scan these appendices before proceeding with the rest of the thesis.

Chapter 2

Transfer Matrix Models of Periodic and Disordered Periodic Structures

2.1 Introduction

In this chapter we will describe the nature of periodic structures of interest in the thesis and show how transfer matrices are used to model these structures. Some of the properties of periodic structures are mentioned, including the important passband and stopband characteristic. The modeling of disordered periodic structures via a product of random transfer matrices is then discussed, along with the very important transformation of these matrices to wave transfer form.

2.2 Perfectly Periodic Structures

2.2.1 One-Dimensional Periodic Structures

In Chapter 1 we described the kinds of periodic structures of interest in the thesis as those with repetitive bays in one linear dimension. These identical bays are connected in identical ways to form what is intended to be a perfectly periodic structure. Because we are looking at structures in a *linear* dimension, our discussion excludes closed periodic structures like a compressor rotor or a dish antenna which can be modeled as one-dimensional periodic structures [Bendiksen 86]. We will not be examining periodic structures in two or three dimensions as they are much more difficult to model with transfer matrices, and, in addition, the localization effects are understood to be much less pronounced in these higher dimensions than in the one-dimensional case.

2.2.2 Modeling of Perfectly Periodic Structures

The key modeling tool used throughout the thesis is the transfer matrix. Each bay of the periodic structure is modeled with a linear transformation, T , which relates a state vector of one cross-section to the state vector of the succeeding cross-section, namely:

$$\mathbf{x}_j = T\mathbf{x}_{j-1}$$

This is a difference equation, where the matrix T can be thought of as a spatial state transition matrix evaluated between the points j and $j - 1$. One transfer matrix is associated with each bay in the structure. The state vector may consist of generalized displacements and forces, for example, or it might consist of the generalized displacements of neighboring bays. The transfer matrix can be found by manipulating the dynamic equations of motion of a bay, possibly derived with the finite element method. The derivation of transfer matrices is discussed at length in [Pestel and Leckie 63]. The

formulation of the transfer matrix assumes a sinusoidal time dependence ($e^{i\omega t}$) in the equations of motion. No damping¹ is included in the models so that the effects of disorder can later be highlighted.

The transfer matrix will always be of even dimension, as will the state vector. For most of the thesis we will confine our discussion to bays modeled with 2×2 transfer matrices, which in turn means each state vector is 2×1 . These structures are called mono-coupled periodic structures because each bay is connected to its neighboring bays through one coupling coordinate. Mono-coupled periodic structures carry only a single pair of waves.

Because each bay is identical, the state vector after n bays is simply related [Faulkner and Hong 85] to the state vector at the beginning by

$$\mathbf{x}_n = \mathbf{T}^n \mathbf{x}_0$$

Because we are raising a transfer matrix to the n th power, we need only examine the transfer matrix \mathbf{T} to understand the dynamic properties of the periodic structure.

The three transfer matrices describing the three example periodic structures in this thesis can be found in Appendix C. These structures comprise a chain of springs and masses, a rod in longitudinal compression with attached resonators and a Bernoulli-Euler beam on simple supports.

2.2.3 Properties of Perfectly Periodic Structures

To appreciate the consequences of disorder in periodic structures we must first examine the modal and wave properties of periodic structures without disorder. There is extensive literature on perfectly periodic systems and the reader is referred to

¹The analogous assumption in the solid state localisation problem is to neglect inelastic scattering mechanisms.

[Brillouin 46, Miles 56, Mead 70, Cremer et al 73, Mead 75-1, Elachi 76, Engels 80] and [Faulkner and Hong 85, Mead 86]. The literature specifically examining periodic systems carrying a multiplicity of wave types is much less abundant, [Mead 73], [Mead 75-2], [Signorelli 87], [Bernelli et al 87]. The properties we are examining below are for structures with transfer matrices of dimension 2×2 .

In a periodic structure the vibrational mode shapes are themselves periodic, i.e., have amplitude equally strong along any section of the structure. As we will see shortly, the natural frequencies at which these modes vibrate tend to occur in clumps along the frequency axis.

Dual to the modal properties of the structure are the wave properties. Two types of waves, traveling waves and attenuating waves, occur in alternating frequency bands known as passbands and stopbands, respectively. In the passbands waves travel according to $e^{\pm ik}$, where k is the real wave number and the positive sign indicates negative-going waves and the negative sign positive-going waves. The wave number $k = \frac{2\pi}{\lambda}$ is a spatial frequency which refers to the phase difference of motions in adjacent bays. Here λ is the wavelength and k varies in magnitude from 0 to π or some multiple thereof. In the stopbands, waves propagate according to $e^{\pm \alpha}$ or $e^{\pm(\alpha + i\pi)}$. The real exponent α implies nontraveling or attenuating waves. The $\alpha + i\pi$ exponent implies adjacent bays vibrating out of phase with each other, in addition to wave attenuation. Both k and α are functions of frequency. Only in the passbands of the perfectly periodic mono-coupled structure can energy be transmitted along the structure [Mead 75-1]. Another type of wave - a complex traveling wave - can occur, but only for systems modeled by transfer matrices of dimension 4×4 or greater [Mead 75-2, Signorelli 87, Bernelli et al 87].

The frequency ranges of passbands for mono-coupled periodic structures can be found by determining those frequencies at which the eigenvalues of its transfer matrix are complex, $e^{\pm ik}$. By examining the characteristic equation of the 2×2 transfer matrix T , where $\det(T) = 1$ because we have assumed no damping, we readily deduce that

passbands occur at frequencies where $|\text{tr}(T)| < 2$. Otherwise, the eigenvalues are real, $e^{\pm\alpha}$ or $e^{\pm\alpha+i\pi}$, and we are in a stopband.

This passband and stopband property is characteristic of any periodic system, whether it be an electrical network, a periodic truss structure, a layered acoustic medium or a periodic potential along which electrons might propagate. It is important to remember that in the frequency ranges of the passbands of the perfectly periodic system there is perfect transmission of waves and energy.

The connection between the wave description and modal description for a finite structure is formally made with the phase closure principle [Cremer et al 73, Mead 75-1] and [Signorelli 87]. This principle says that at a natural frequency, the total phase change of a wave as it travels backwards and forwards once through the entire structure, including the phase changes at the boundaries, is an integral multiple of 2π . The connection between this wave description of a periodic system and a modal description becomes more apparent by noting that the natural frequencies of the periodic structure lie within the passbands. For a periodic structure of infinite extent an infinite number of natural frequencies lie densely in each passband. For an n bay periodic structure, n natural frequencies lie within each passband. (This result is strictly true only when each bay can be modeled as having symmetry of mass and stiffness about its midpoint. If the bay is unsymmetric, one frequency will occur in the stopband [Mead 75-1]).

Another property of mono-coupled periodic systems to note is the order in which the passbands and stopbands occur. For periodic systems connected to the ground, a stopband will occur first as a function of frequency followed by a passband after which the pattern is repeated. This makes sense because clearly the low frequency motion is constrained by the connection to the ground. For periodic systems not connected to the ground, this pattern is reversed, with a passband occurring first followed by a stopband and so on.

No real structure will have an infinite number of bays, but frequently a structure with a finite number of bays can mimic quite well the properties of an infinite structure, especially if it is long. But surprisingly, [Roy and Plunkett 86] note good agreement between passband/stopband properties of a theoretically infinite dissipationless beam with attached cantilevers and their experimental results for such a system with only 15 cantilevers.

2.3 Disordered Periodic Structures

Now that we have described the kinds of periodic structures of interest, and some properties they possess, we turn our attention to disordered periodic structures.

2.3.1 Nature of the Disorder

The term disorder refers to each bay of the structure having one or more of its properties departing in a random fashion from the average. We assume here that the disorder is distributed equally among all the bays and not scattered in a few. (In some literature [Toda 66] the term localization refers to the effect of disordering two well separated bays out of an otherwise perfectly periodic system. We are taking a more general definition of localization which encompasses a finite to an infinite number of disordered bays without any intervening perfectly periodic section of bays.) With this kind of disorder, the properties of the bay being disordered, whether masses, springs or lengths, can be modeled as independent identically distributed random variables. Note here that we do not model continuously disordered systems like a turbulent atmosphere [Wenzel 83] or a beam with mass that is a random function of length [Howe 72]. Rather, our disorder is discrete in that it occurs from bay to bay.

When several variables of a bay are disordered we assume that the random variables

are mutually independent. Because the randomness for any variable will not be considered too large, we will make use of "narrow" uniform probability density functions from which to draw the random variables. This is also in conformity with the practice in the solid state localization literature.

2.3.2 Modeling of Disordered Periodic Structures

For the disordered periodic structure we will continue to use the transfer matrix formalism established in Section 2.2.2. For each bay now the transfer matrix, T_j , is simply a function of one or more random variables, $T_j(\alpha_1, \dots, \alpha_q)$. See Appendix C for the random transfer matrices of our three periodic structures. Because the random variables are independent and identically distributed, so also are the random transfer matrices.

The disordered periodic structure with n bays cannot be modeled as T^n , but is modeled as a product of random transfer matrices:

$$\prod_{j=1}^n T_j = T_n \cdots T_1$$

This is the key modeling assumption of the entire thesis. We will examine one important asymptotic property of products of random matrices and deduce from that the nature of the localization phenomenon.

2.3.2.1 Wave Transfer Matrix

Because strong wave attenuation already occurs in the stopbands, our focus is on the effects of disorder in the passbands of the normally perfectly periodic structure. Unlike the case for the perfectly periodic structure, we cannot simultaneously diagonalize each T_j with the same eigenvector similarity transformation. However, we can transform

each random transfer matrix, T_j , forming the product into a *wave transfer matrix*, W_j , seen in the following equation (see Appendix B):

$$\begin{bmatrix} \vec{A}_j \\ \vec{B}_j \end{bmatrix} = \begin{bmatrix} \frac{1}{t_j} & -\frac{r_j}{t_j} \\ -\frac{r_j}{t_j} & \frac{1}{t_j} \end{bmatrix} \begin{bmatrix} \vec{A}_{j-1} \\ \vec{B}_{j-1} \end{bmatrix} \quad (2.1)$$

where \vec{A} is the amplitude of the left traveling wave and \vec{B} is the amplitude of the right traveling wave.

This is a wave transfer matrix for one random bay inserted in the middle of an otherwise perfectly periodic structure carrying a pair of traveling waves. The wave amplitudes in Equation 2.1 are those supported by the periodic system surrounding the disordered bay. The transmission coefficient, t_j , is the complex amplitude of a wave emerging from the right of this random bay when a wave of amplitude 1 is incident at the left. The reflection coefficient, r_j , is the complex amplitude of the reflected wave when a wave of amplitude 1 is incident from the left. Physically, $|t_j|^2$ represents the ratio of transmitted energy to incident energy, and $|r_j|^2$ the ratio of reflected energy to incident energy. Energy conservation implies that $|t_j|^2 + |r_j|^2 = 1$.

Some readers may be more familiar with r_j and t_j appearing in a *scattering matrix*. The scattering matrix corresponding to Equation 2.1 appears in the following equation:

$$\begin{bmatrix} \vec{A}_{j-1} \\ \vec{B}_j \end{bmatrix} = \begin{bmatrix} r_j & t_j \\ t_j & r_j \end{bmatrix} \begin{bmatrix} \vec{B}_{j-1} \\ \vec{A}_j \end{bmatrix}$$

The scattering matrix relates wave amplitudes leaving a bay (which are on the left of the equation) to those entering the bay (which premultiply the scattering matrix). The disadvantage in using the scattering matrix to analyze a disordered periodic system is that it is not a transfer matrix. This means that the scattering matrix for two or more bays cannot be realized by simple multiplication of the respective scattering matrices. The scattering matrix for two or more bays is realized through a complicated "star product" described in [Redheffer 61].

We will use the wave transfer matrix precisely because it is a transfer matrix and because it allows us to model disordered periodic structures by pure matrix multiplication. So the wave transfer matrix for the n disordered bays is:

$$\prod_{j=1}^n \mathbf{W}_j = \begin{bmatrix} \frac{1}{\tau_n} & -\frac{\rho_n}{\tau_n} \\ -\frac{\rho_n^*}{\tau_n^*} & \frac{1}{\tau_n^*} \end{bmatrix}$$

where τ_n is the transmission coefficient of the n bay disordered system, and ρ_n is the reflection coefficient of the n bay disordered system. Here $|\tau_n|^2$ is the ratio of transmitted energy to incident energy for the disordered structure.

2.3.2.2 Properties of the Wave Transfer Matrix

The wave transfer matrix has some special properties that will be exploited to simplify our analysis of the localization phenomenon. First, because we will always use transfer matrices of determinant one to model our disordered bays (this is true because no dissipation is included in the models), the corresponding wave transfer matrix will have unit determinant. Thus the wave transfer matrix is an element of (see Appendix A) $SU(1, 1)$ and $Sp(1, C)$.

Recall that the original transfer matrix, \mathbf{T} , was real and of unit determinant, and so was an element of the group $SL(2, R)$. What has happened in going from \mathbf{T} to \mathbf{W} is that we have taken advantage of an isomorphism between $SL(2, R)$ and $SU(1, 1)$.

Chapter 3

Furstenberg's Theorem and Calculation of Localization Factors for Mono-Coupled Disordered Periodic Structures

3.1 Introduction

As has been discussed earlier, disordered periodic structures can be modeled via a product of random transfer matrices. In this section we will exploit the mathematical theory of products of random matrices to reveal an important transmission property of disordered periodic systems. It is precisely this transmission property that we associate with the localization phenomenon. In the chapter we will formally state Furstenberg's theorem, then restate it in more familiar terms. We then relate the localization factor to the transmission coefficient of the long disordered system, after which we will find an approximate analytical expression to calculate the localization factor.

3.2 Furstenberg's Theorem

A rigorous statement about the properties of a product of a finite number of random matrices is difficult to make; however, we can come to some rigorous conclusions on properties when the number of matrices in the product becomes very large. We will focus on one property that was originally proved in [Furstenberg 63] and which we specialize to 2×2 matrices. One formal statement of this limiting behavior of products of random matrices is as follows:

Theorem 1 (Furstenberg's Theorem, original form) *Let T_1, T_2, \dots, T_n be independent identically distributed 2×2 random matrices with distribution μ . Let G be the smallest closed subgroup of $SL(2, R)$ containing the support of μ . If G is a noncompact subgroup of $SL(2, R)$ such that no subgroup of G of finite index is irreducible and if*

$$E[\max(\ln \|T_j\|, 0)] < +\infty$$

then there exists $\gamma > 0$ such that for each $x_0 \neq 0$

$$\lim_{n \rightarrow \infty} \frac{1}{n} \ln \|T_n \cdots T_1 x_0\| = \gamma \quad w.p. 1$$

and

$$\lim_{n \rightarrow \infty} \frac{1}{n} \ln \|T_n \cdots T_1\| = \gamma \quad w.p. 1.$$

and if ν is a μ -invariant distribution on $P(R^2)$ ($P(R^2)$ is the projective space of R^2 , namely half of the unit circle), then

$$\gamma = \iint \ln \|T\bar{x}\| d\mu(T) d\nu(\bar{x}) \quad (3.1)$$

where \bar{x} is in $P(R^2)$.

The condition of invariance for ν is stated mathematically in many ways including:

$$\int 1_A(\bar{x}) d\nu(\bar{x}) = \iint 1_A\left(\frac{T\bar{x}}{\|T\bar{x}\|}\right) d\mu(T) d\nu(\bar{x})$$

where $1_A(*)$ is the indicator function; its value is one when the argument lies on A and 0 otherwise.

There is one special direction for the initial vector x_0 for which the Furstenberg result will not hold for a given realization of $T_n \cdots T_1$. Namely if x_0 is along this special direction, then

$$\lim_{n \rightarrow \infty} \frac{1}{n} \ln \|T_n \cdots T_1 x_0\| = -\gamma$$

This is a consequence of the theorem of Oseledets which will be discussed in Chapter 5.

The above theorem can be modified and restated in more familiar terms with just a few assumptions and some explanation.

As stated in Chapter 2 we are considering our random matrices to be functions of one or more random variables, where the random variables are drawn from some probability density function (Dirac delta functions are permissible in our definition of probability density functions, so probability mass functions are possible in the above). We exclude Bernoulli random variables (random variables having probability density functions with mass at only two points) in our transfer matrices because they can result in the distribution ν having neither mass nor density. The distribution for ν would be a so-called continuous singular probability measure. So now probability measures μ and ν become $p(\alpha)$ and $p(\bar{x})$, respectively.

The subgroup G can now be interpreted as the set of all matrices generated by the probability density functions of the random variables plus the inverses of those matrices, plus the identity matrix, plus any products of the above matrices. The conditions concerning noncompactness and irreducibility of G have been shown by [Matsuda and Ishii 70] to be equivalent to requiring that G contain two elements in $SL(2, R)$ with no common eigenvectors. In addition, [Goda 82] has shown that the Furstenberg result will hold for matrices in $GL(2, R)$ as long as

$$\lim_{n \rightarrow \infty} \frac{1}{n} \ln \left(\prod_{j=1}^n |\det T_j| \right) = 0 \quad (3.2)$$

Finally, the theorem will also hold for matrices with complex entries [Bougerol and Lacroix 85].

Now that we have clarified some of the conditions under which Furstenberg's theorem holds, let us examine why the Furstenberg result, Equation 3.1, is reasonable. As the deterministic vector \mathbf{x}_0 is propagated by the random matrices, its direction, $\bar{\mathbf{x}}$, begins to take on a probability density of its own. In fact as $n \rightarrow \infty$, the probability density of this direction becomes invariant with respect to the probability density for the random transfer matrices. Specifically, the invariance condition means if

$$\mathbf{x}_n = \mathbf{T}_n \mathbf{x}_{n-1}$$

then as $n \rightarrow \infty$

$$p(\bar{\mathbf{x}}_n) = p(\bar{\mathbf{x}}_{n-1})$$

This condition of invariance is frequently called the Dyson-Schmidt self-consistency condition in the solid state physics literature [Ziman 79]. This condition of invariance does not hold for systems in two or three dimensions or for closed periodic structures in one dimension [Ziman 79, page 309]. Therefore, as $n \rightarrow \infty$ the two relevant probability distributions are those for \mathbf{T} and $\bar{\mathbf{x}}$, and the double integral of $\ln \|\mathbf{T}\bar{\mathbf{x}}\|$ over these two distributions seems reasonable.

With these points in mind, we can restate Furstenberg's theorem as follows:

Theorem 2 (Furstenberg's Theorem, modified form) *Let $\mathbf{W}_1, \mathbf{W}_2, \dots, \mathbf{W}_n$ be complex valued, invertible, independent identically distributed 2×2 matrices where $\mathbf{W}_j = \mathbf{W}_j(\alpha)$ is a function of the random vector α with probability density $p(\alpha)$. If at least two of the random transfer matrices do not have common eigenvectors, and if*

$$\lim_{n \rightarrow \infty} \frac{1}{n} \ln \left(\prod_{j=1}^n |\det \mathbf{W}_j| \right) = 0$$

and if

$$E[\max(\ln \|\mathbf{W}_j\|, 0)] < +\infty$$

then there exists $\gamma > 0$ such that for each $z_0 \neq 0$

$$\lim_{n \rightarrow \infty} \frac{1}{n} \ln \|W_n \cdots W_1 z_0\| = \gamma \quad w.p. 1$$

and

$$\lim_{n \rightarrow \infty} \frac{1}{n} \ln \|W_n \cdots W_1\| = \gamma \quad w.p. 1$$

where

$$\gamma = \iint \ln \|W(\alpha)z\| p(\alpha) d\alpha p(z) dz \quad (3.3)$$

where $p(z)$ is invariant with respect to the probability density function $p(\alpha)$ for the random transfer matrices, i.e.

$$\int 1_A(z) p(z) dz = \iint 1_A\left(\frac{W(\alpha)z}{\|W(\alpha)z\|}\right) p(\alpha) d\alpha p(z) dz$$

where A is any arc along the half unit circle.

A number of other properties for products of random matrices can be shown [Bougerol and Lacroix 85]; however, Furstenberg's theorem gives the one property which, as we will see, is relevant to localization in a disordered periodic system.

Furstenberg's theorem is a law of large numbers for products of random matrices. More recently a central limit theorem [Le Page 82, Bougerol and Lacroix 85] has been proved for products of random matrices. The central limit theorem tells us that

$$\frac{1}{\sqrt{n}} (\ln \|W_n \cdots W_1\| - n\gamma) \xrightarrow{\text{distribution}} N(0, \sigma^2)$$

The conditions on the random matrices are a little more restrictive than the ones for Furstenberg's theorem, but determining whether they apply to the transfer matrices considered here is left for future research.

3.3 Localization Factor as a Function of the Transmission Coefficient

Now we will relate the Furstenberg limit theorem for products of random matrices to a transmission property of disordered periodic systems. From Furstenberg's theorem we know

$$\gamma = \lim_{n \rightarrow \infty} \frac{1}{n} \ln \|W_n \cdots W_1\| \quad w.p. 1 \quad (3.4)$$

Recall that a product of n wave transfer matrices is of the form:

$$\prod_{j=1}^n W_j = \begin{bmatrix} \frac{1}{r_n} & -\frac{\rho_n}{r_n} \\ -\frac{\rho_n}{r_n} & \frac{1}{r_n} \end{bmatrix} \quad (3.5)$$

To apply Equation 3.4 we first take a matrix norm of Equation 3.5. Here we choose the maximum singular value (see Appendix A); so a little algebra gives:

$$\gamma = \lim_{n \rightarrow \infty} \frac{1}{n} \ln \left(\frac{1 + |\rho_n|}{|r_n|} \right)$$

or

$$\gamma = \lim_{n \rightarrow \infty} \frac{1}{n} \ln(1 + |\rho_n|) - \frac{1}{n} \ln |r_n|$$

Knowing that $0 \leq |\rho_n| < 1$, the first term vanishes, and we are left with

$$\gamma = - \lim_{n \rightarrow \infty} \frac{1}{n} \ln |r_n| \quad (3.6)$$

Now we can understand the relevance of γ to the dynamic properties of a disordered periodic structure. Asymptotically, Equation 3.6 says that the absolute value of the transmission coefficient decays exponentially with n , the number of bays. The rate of decay per bay is governed by γ which will be called the localization factor. Thus traveling waves will no longer be propagated perfectly, but will tend to be confined near their point of origin according to the localization factor γ . This result says that $|r_n|^2 \sim e^{-2\gamma n}$, the transmitted energy decays exponentially with n . It has been argued

[Matsuda and Ishii 70, Pastawski et al 85] that the now spatially localized modes are governed by an exponential envelope of the form $e^{-\gamma n}$.

We observe that $\ln |\tau_n|$ is a statistically well behaved variable, namely we have derived an asymptotic relation for it based on a law of large numbers for products of random matrices. Notice also that we are not taking an expectation of $\ln |\tau_n|$ to find γ ; the result holds as $n \rightarrow \infty$. Random variables with this property are called self-averaging [Pastur 80, van Hemmen 82].

The notion that the $\ln |\tau_n|$ is statistically well-behaved is further strengthened if one applies these same manipulations to the central limit theorem for products of random matrices. Thus using the available mathematical tools, we confirm in just a few steps the conjecture about the statistical behavior of $\ln |\tau_n|$ by [Anderson et al 80] and [Stone et al 81].

3.4 Calculation of Localization Factors via an Approximation to Furstenberg's Theorem

In this section we will simplify Equation 3.3 of Furstenberg's Theorem; this will lead to an approximation for the localization factor, γ . First recall Equation 3.3

$$\gamma = \iint \ln \|\mathbf{W}(\alpha)\mathbf{z}\| p(\alpha) d\alpha p(\mathbf{z}) d\mathbf{z}$$

then without loss of generality we have:

$$\mathbf{z} = \frac{1}{\sqrt{2}} \begin{bmatrix} e^{i\theta} \\ e^{-i\theta} \end{bmatrix}$$

$$\mathbf{W}(\alpha) = \begin{bmatrix} \frac{1}{i} & -\frac{r}{i} \\ -\frac{r^*}{i} & \frac{1}{i} \end{bmatrix}$$

where for the moment we suppress the dependence of t and r on α . So,

$$\mathbf{W}(\alpha)\mathbf{z} = \frac{1}{\sqrt{2}} \begin{bmatrix} \frac{e^{i\theta}}{t} - \frac{re^{-i\theta}}{t} \\ -\frac{r^*e^{i\theta}}{t^*} + \frac{e^{-i\theta}}{t^*} \end{bmatrix}$$

After some complex algebra we find:

$$\|\mathbf{W}(\alpha)\mathbf{z}\| = \left| \frac{1}{t} - \frac{r}{t} e^{-i2\theta} \right|$$

Now the equation for γ is

$$\gamma = \iint \ln \left| \frac{1}{t} - \frac{r}{t} e^{-i2\theta} \right| p(\alpha) d\alpha p(\theta) d\theta \quad (3.7)$$

where $p(\theta)d\theta$ must satisfy the invariance condition:

$$\int 1_A(\theta) p(\theta) d\theta = \iint 1_A \left(\frac{\mathbf{W}(\alpha)\mathbf{z}(\theta)}{\|\mathbf{W}(\alpha)\mathbf{z}(\theta)\|} \right) p(\alpha) d\alpha p(\theta) d\theta \quad (3.8)$$

Because $p(\theta)$ can only be found in rare instances [Pincus 80], we will find an approximation to γ by taking a Taylor series expansion about $\langle \alpha \rangle$, recalling that α is a vector, of the terms in Equations 3.7 and 3.8 and retaining terms to first order in σ_α^2 . This approach has been discussed in [Baluni and Willemsen 85]. Let us first recall the form of the Taylor series expansion for a multivariable function. The first three terms are:

$$\begin{aligned} f(\alpha) &= f(\alpha)|_{\langle \alpha \rangle} + \sum_{l=1}^q (\alpha_l - \langle \alpha_l \rangle) \frac{\partial f(\alpha)}{\partial \alpha_l} |_{\langle \alpha \rangle} + \\ &\quad \frac{1}{2} \sum_{l=1}^q \sum_{l'=1}^q (\alpha_l - \langle \alpha_l \rangle) (\alpha_{l'} - \langle \alpha_{l'} \rangle) \frac{\partial^2 f(\alpha)}{\partial \alpha_l \partial \alpha_{l'}} |_{\langle \alpha \rangle} + \dots \end{aligned}$$

We now examine the expansion of $\ln \left| \frac{1}{t(\alpha)} - \frac{r(\alpha)}{t(\alpha)} e^{-i2\theta} \right|$. The first term in the expansion is simply that for the undistorted or perfectly periodic system. Recall that

$$\begin{bmatrix} \frac{1}{t} & -\frac{r}{t} \\ -\frac{r^*}{t^*} & \frac{1}{t^*} \end{bmatrix} = \begin{bmatrix} e^{ik} & 0 \\ 0 & e^{-ik} \end{bmatrix}$$

for the perfectly periodic system in the passband. Therefore the first term is:

$$\ln |e^{ik}| = 0$$

The second term in the expansion will not be needed because the terms $(\alpha_i - \langle \alpha_i \rangle)$ vanish when integrated over $p(\alpha)$.

Finally, the third term is examined. Because the terms in the random vector are mutually independent, we know that $(\alpha_i - \langle \alpha_i \rangle)(\alpha_j - \langle \alpha_j \rangle)$ $i \neq j$ will vanish after integrating over $p(\alpha)$. We are left with

$$\frac{1}{2} \sum_{i=1}^q (\alpha_i - \langle \alpha_i \rangle)^2 \frac{\partial^2 \ln \left| \frac{1}{t(\alpha)} - \frac{r(\alpha)}{t(\alpha)} e^{-i2\theta} \right|}{\partial \alpha_i^2} \Big|_{\langle \alpha \rangle}$$

So γ to first order in the variance of the α_i s is:

$$\gamma = \frac{1}{2} \sum_{i=1}^q \sigma_{\alpha_i}^2 \int \frac{\partial^2 \ln \left| \frac{1}{t(\alpha)} - \frac{r(\alpha)}{t(\alpha)} e^{-i2\theta} \right|}{\partial \alpha_i^2} \Big|_{\langle \alpha \rangle} p^0(\theta) d\theta \quad (3.9)$$

where we now must find $p^0(\theta)$ which is $p(\theta)$ to the zeroth order in the variance of α .

To find $p^0(\theta)$ we examine Equation 3.8 where we only look at terms to zeroth order in σ_{α}^2 , namely:

$$\int 1_A(\theta) p^0(\theta) d\theta = \iint 1_A \left(\frac{W(\alpha) Z(\theta)}{\|W(\alpha) Z(\theta)\|} \Big|_{\langle \alpha \rangle} \right) p(\alpha) d\alpha p^0(\theta) d\theta$$

but

$$W(\alpha) Z \Big|_{\langle \alpha \rangle} = \begin{bmatrix} e^{ik} & 0 \\ 0 & e^{-ik} \end{bmatrix} \frac{1}{\sqrt{2}} \begin{bmatrix} e^{i\theta} \\ e^{-i\theta} \end{bmatrix} = \frac{1}{\sqrt{2}} \begin{bmatrix} e^{i(k+\theta)} \\ e^{-i(k+\theta)} \end{bmatrix}$$

We therefore require $p^0(\theta)$ to satisfy

$$\int 1_A(\theta) p^0(\theta) d\theta = \int 1_A(k + \theta) p^0(\theta) d\theta$$

Because k can take on any value between 0 and π , or some multiple thereof, we must have that $p^0(\theta) = \frac{1}{\pi}$, which is a uniform probability density function.

To further simplify Equation 3.9 we note that

$$\ln \left| \frac{1}{t(\alpha)} - \frac{r(\alpha)}{t(\alpha)} e^{-i2\theta} \right| = \ln \left| \frac{1}{t(\alpha)} \right| + \ln |1 - r(\alpha) e^{-i2\theta}|$$

The term $\ln |1 - r(\alpha) e^{-i2\theta}|$ can be expanded in a series, and recalling $e^{-i2\theta} = \cos 2\theta - i \sin 2\theta$, the term vanishes after integrating.

Therefore we are left with

$$\gamma = \frac{1}{2} \sum_{i=1}^q \sigma_{\alpha_i}^2 \frac{\partial^2 \ln |t(\alpha)|}{\partial \alpha_i^2} |_{\langle \alpha \rangle} + o(\sigma_{\alpha}^2)$$

or

$$\gamma = -\frac{1}{2} \sum_{i=1}^q \sigma_{\alpha_i}^2 \frac{\partial^2 \ln |t(\alpha)|}{\partial \alpha_i^2} |_{\langle \alpha \rangle} + o(\sigma_{\alpha}^2)$$

This is also equivalent to

$$\gamma = \frac{1}{2} \sum_{i=1}^q \sigma_{\alpha_i}^2 \frac{\partial^2 \ln |t(\alpha)|}{\partial \alpha_i^2} |_{\langle \alpha \rangle} + o(\sigma_{\alpha}^2) \quad (3.10)$$

where

$$\langle \alpha \rangle = \begin{bmatrix} \langle \alpha_1 \rangle \\ \vdots \\ \langle \alpha_{l-1} \rangle \\ \alpha_l \\ \langle \alpha_{l+1} \rangle \\ \vdots \\ \langle \alpha_q \rangle \end{bmatrix}$$

The prime indicates that all but the l th term is evaluated at the mean value. This latter result says we can calculate localization effects by disordering one variable at a time in a transfer matrix.

Notice that the localization factor to first order in the variance is simply a sum of the localization factors for each variable randomized individually. We suspect that as the variance of the disordered variables increases the estimate of γ will be poorer because we have retained terms only to first order in the variances.

We also note that Furstenberg's theorem has been shown to be robust to uncertainty in the probability law of the random transfer matrices. The paper [Slud 86] shows that if the postulated probability measure for the transfer matrices is "close" to the actual one then the asymptotic behaviors will be arbitrarily close.

A technique to approximately calculate localization factors without resorting to theories on products of random matrices is presented in Appendix D.

Chapter 4

Calculation of Localization Factors for Three Mono-Coupled Disordered Periodic Structures

4.1 Introduction

This chapter will illustrate localization calculations for three periodic structures that can be modeled with 2×2 transfer matrices. The results will show dramatically how localization effects can vary with frequency. The analytical results are compared to Monte Carlo simulations of these systems. We provide, where possible, a physical explanation for the observed localization effects.

The first system examined is a chain of spring and masses. This simplest possible system provides a convenient vehicle to illustrate the calculation of localization effects. Indeed, this thesis provides the first comprehensive examination of the localization effects of a disordered mass-spring chain.

The second example is a rod in longitudinal compression with attached resonators which mimics some of the important dynamic behavior of a real truss structure. Unlike the mass-spring system which has only a single passband, the rod with resonators has an infinite number of passbands. We examine localization effects over several of these passbands.

The final example is a Bernoulli-Euler beam on simple supports. When we disorder the distances between the supports we will see a very pronounced effect near the stopbands of the underlying periodic structure.

In our analysis we will consider the random variables, α_i disordered $\pm p\%$ from the average value $\langle \alpha_i \rangle$. A disorder of $\pm p\%$ from the average value $\langle \alpha_i \rangle$ translates into a uniform probability density function with width of $\frac{2p\langle \alpha_i \rangle}{100}$ and height of $\frac{100}{2p\langle \alpha_i \rangle}$. The uniform probability density function will be centered around $\langle \alpha_i \rangle$. Note that the variance of any random variable with a uniform probability density function is always $\frac{\text{width}^2}{12}$.

4.2 Localization in a Mass-Spring Chain

We will examine at length the localization effects in a chain of springs and masses. The mass-spring chain is an excellent example to begin our discussion of localization, not only because of its simplicity, but also because this system and its analogs have been studied over the years, giving us the opportunity to directly compare our results with those already published. Even though the mass-spring chain and its equivalents have received a lot of attention in the literature, amazingly it has not received exhaustive treatment. For example, in the literature the chain is examined with only the mass disordered and the localization factor calculated is generally valid over only the first half of the passband. In this thesis we will study localization in this chain where masses and springs are disordered and the equation we present for the localization factor will

be valid over virtually the entire passband.

In the next sections we will first examine the chain with only masses disordered and present our analytical approximation of the localization factor based on Equation 3.10. These results will be confirmed by a Monte Carlo simulation. We will also compare this analytical result with the one usually found in the literature. The localization factor will be studied for three levels of disorder: masses with a .1%, 1% and 10% variation above or below the nominal value. We will see that the localization factor depends only on frequency and the level of disorder. Throughout the thesis any such dependencies are suppressed when writing the localization factor, γ .

Next we examine the chain with only springs disordered and show that this disorder is dual to the mass disorder. Finally both masses and springs are disordered and we again confirm the analytical results with a Monte Carlo simulation.

4.2.1 Only Masses Disordered

We first examine a chain with disordered masses, which in the physics literature is identified as isotopic disorder, referring to atomic systems with various isotopes. This chain with masses disordered has been examined in [Matsuda and Ishii 70, Rubin 84]; its electrical circuit analog was studied in [Akkermans and Maynard 84], and the solid state analog in [Stone et al 81] and elsewhere.

The mass-spring model and its transfer matrix are presented in Appendix C.1. We make use of a nondimensional frequency, $\bar{\omega}$, in the transfer matrix and our analysis :

$$\bar{\omega} = \frac{\omega}{2\sqrt{\frac{k_s}{m}}}$$

The condition for the existence of a passband (see Chapter 2) tells us that only one passband exists and occurs for

$$0 < \bar{\omega} < 1$$

In the passband waves and energy travel with perfect transmission. However when the system is disordered, the transmission is disrupted; and the resulting disruption in the passband is what we are examining.

In our analysis we will first consider masses disordered from their average value on the chain. We make use of nondimensional quantities wherever possible. Here the nondimensional mass is μ_j , where

$$\mu_j = \frac{m_j}{m} \quad \text{and} \quad m = \langle m_j \rangle$$

and m is the mass for the perfectly periodic system. The transfer matrix for one bay of this chain with a disordered mass is shown in Appendix C.1 and the (1,1) term of that transfer matrix is $\frac{1}{t(\mu_j)}$, Equation C.1, which can be used in Equation 3.10 to calculate the localization factor, γ_μ . For this mass-spring system with masses disordered we will go through the calculation of the localization factor; this will serve as an example of the steps necessary to do the calculation for any disordered system. Equation 3.10 now becomes

$$\gamma_\mu \doteq \frac{1}{2} \sigma_\mu^2 \frac{\partial^2 (\ln |\frac{1}{t(\mu_j)}|)}{\partial \mu_j^2} |_{\langle \mu_j \rangle}$$

where \doteq indicates we are neglecting terms of order greater than the variance. From Appendix C.1.1 we have

$$\frac{1}{t(\mu_j)} = e^{ik} (1 - i\delta_j)$$

where

$$\delta_j = \frac{2\bar{\omega}^2(1 - \mu_j)}{\sin k}$$

and where

$$\cos k = 1 - 2\bar{\omega}^2$$

Suppressing the subscript j , we now have

$$\gamma_\mu \doteq \frac{1}{4} \sigma_\mu^2 \frac{\partial^2 \ln(1 + \delta^2)}{\partial \mu^2} |_{\langle \mu \rangle}$$

Letting

$$\delta' = \frac{\partial \delta}{\partial \mu} = \frac{-2\bar{\omega}^2}{\sin k}$$

we have the first partial derivative

$$\frac{\partial \ln(1 + \delta^2)}{\partial \mu} = \frac{2\delta\delta'}{1 + \delta^2}$$

Taking a partial derivative again we have

$$\frac{\partial^2 \ln(1 + \delta^2)}{\partial \mu^2} = -\frac{2\delta\delta'}{(1 + \delta^2)^2} + \frac{2\delta'}{1 + \delta^2} + \frac{2\delta\delta''}{1 + \delta^2}$$

We have to evaluate the above terms at $\langle \mu \rangle$. Note that δ evaluated at $\langle \mu \rangle$ is zero, so now we have

$$\gamma_\mu \doteq \frac{1}{4} \sigma_\mu^2 2\delta''|_{\langle \mu \rangle}$$

or

$$\gamma_\mu \doteq \frac{2\bar{\omega}^4 \sigma_\mu^2}{\sin^2 k}$$

Knowing $\cos k$ from above, we can calculate $\sin^2 k$ and so finally for the mass-spring system in the passband, $0 < \bar{\omega} < 1$:

$$\gamma_\mu \doteq \frac{\bar{\omega}^2 \sigma_\mu^2}{2[1 - \bar{\omega}^2]} \quad (4.1)$$

We observe that the localization factor is a function of the nondimensional frequency $\bar{\omega}$ and the variance of the nondimensional mass. Clearly the localization effects increase with frequency and also with the amount of disorder. At low frequency

$$\gamma_\mu \doteq \frac{\bar{\omega}^2 \sigma_\mu^2}{2} \quad (\bar{\omega} \rightarrow 0) \quad (4.2)$$

indicating that γ_μ is proportional to $\bar{\omega}^2$ at low frequency. The low frequency estimate of the localization factor for a chain with disordered masses is the one usually seen in the literature [Matsuda and Ishii 70], but in the following dimensional form (and derived through much more torturous methods than are used here):

$$\gamma_m \doteq \frac{\omega^2 \sigma_m^2}{8k_m} \quad (\omega \rightarrow 0)$$

The nondimensional analytical results of Equation 4.1 and Equation 4.2 for masses disordered $\pm 1\%$ from the average value are plotted in Figure 4.1 with the nondimensional frequency as the abscissa and $\log_{10}(\gamma_\mu)$ as the ordinate.

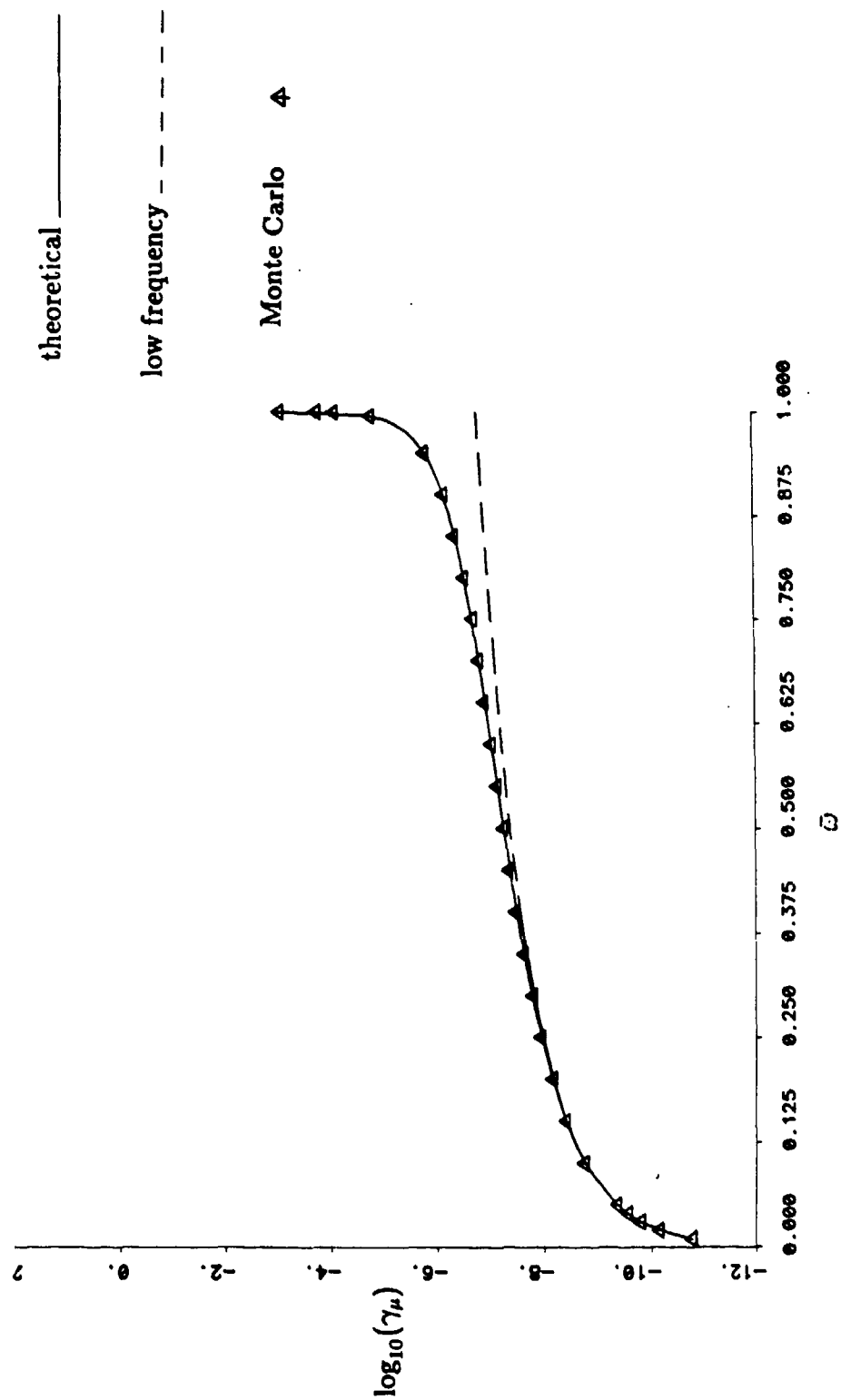


Figure 4.1: Localization factor for mass-spring chain with masses disordered $\pm 1\%$ from their average value.

The frequency dependence of γ can now be seen explicitly. Note the rising value of γ as it approaches the stopband near $\bar{\omega} = 1$. This makes physical sense, because the masses are vibrating at higher frequencies as we approach the end of the passband, so we expect that disorder will have a greater impact than it would for masses vibrating at lower frequencies. The dashed line represents the nondimensional low frequency estimate of γ_μ . Clearly it provides an adequate estimate of γ_μ for about half the passband, while it grossly underestimates the localization effects at the highest frequencies of the passband.

As an example, let us consider the effects of localization at $\bar{\omega} = .9995$, where $\gamma_\mu = .1665 \times 10^{-3}$. This result tells us that on average the transmitted energy, $|\tau_n|^2$, after 1000 bays will be $e^{-2.1665 \times 10^{-3} 1000} = .72$ of the incident energy even though no damping is present. A modal amplitude for a normal mode at that frequency would be confined to an exponential envelope governed by $e^{-\gamma n}$ with $\gamma = .1665 \times 10^{-3}$. The localization will be less pronounced at lower frequencies, but is nonetheless present. The attenuation caused by the disorder is unlike that of dissipation. Here localization prevents the wave from traveling along the structure, unlike the case for a perfectly periodic system, where the wave would travel without attenuation. Localization tends to confine the wave near its point of origin, where it is eventually dissipated by the damping that inevitably exists in all real structures.

Our localization result in Equation 4.2 is one-half the result¹ presented by [Chow and Keller 72]. In their work they calculated the effects of randomness on the coherent portion of waves traveling through a random chain. We can reproduce their results with the aid of Appendix D. If in Appendix D we proceed to find the mean value of τ_n and then take the natural log, instead of averaging $\ln |\tau_n|$ directly, we will get twice the result of Equation 4.2. Clearly, they are averaging the wrong variable, τ_n . In addition to making the statistical arguments about averaging of proper variables, we can

¹Note that the relevant result in [Chow and Keller 72] has a typographical error on the bottom of page 1412. It should read $Imk(\omega, \epsilon^2) = \frac{\epsilon^2 \omega^2 \langle \mu^2 \rangle}{d\omega_0}$.

make the following physical argument to explain their results. By examining only the coherent or mean wave, as was also done by [Eatwell 83], they really neglect the incoherent portion of the wave which can also carry energy. When we average over $\ln |\tau_n|$ we are taking into account all the energy transmitted, because by definition $|\tau_n|$ is the ratio of transmitted energy to incident energy. Other authors have pointed out the invalidity of averaging other quantities like $|\tau_n|$ [Hodges 82], ρ_n [Baluni and Willemsen 85] and $\frac{|\rho_n|^2}{|\tau_n|^2}$ [Stone et al 81].

The validity of the analytical result should be verified by some numerical simulation. Specifically, we want to see whether the analytical result is valid for the entire frequency range of interest and for increasing levels of disorder. The obvious simulation is to multiply a huge number of random transfer matrices at a given frequency to see if indeed

$$\gamma = - \lim_{n \rightarrow \infty} \frac{1}{n} \ln |\tau_n|$$

Because we cannot really take an infinite number of products, we must resort to averaging $\ln |\tau_n|$ over an ensemble of realizations of the chain. The question arises whether to use a large number of matrices per ensemble or a large number of ensembles and a few matrices. Upon examining this issue numerically, we found that we did not even have to take a product of random matrices to get Monte Carlo results that matched our analytical results. Rather, averaging $\ln |t_j|$ from an individual matrix over a sufficient number of realizations (in our case 1001) gave excellent agreement with the analytical results over large frequency ranges. A similar observation was made by [Pastawski et al 85]. The agreement was good in the sense that the mean value of the Monte Carlo simulation tracked our analytical results well (as can be seen in the numerous figures), but also in the sense that the standard error was consistently one to two orders of magnitude smaller than the mean value.

Recall that in a Monte Carlo simulation [Hammersley and Handscomb 64] the un-

biased estimator of the mean value is

$$\langle \ln |t_j| \rangle = \frac{1}{r} \sum_{j=1}^r \ln |t_j|$$

where r is the number of realizations in the simulation. We estimate the standard error as:

$$\text{standard error} = \frac{s}{\sqrt{r}}$$

where s^2 is the unbiased estimator of the variance:

$$s^2 = \frac{1}{r-1} \sum_{j=1}^r (\ln |t_j| - \langle \ln |t_j| \rangle)^2$$

Again the standard error was one to two orders of magnitude smaller than the mean value for the simulations of all three structures. The results of the Monte Carlo simulation are indicated with the small triangles in Figure 4.1. They confirm the validity of the analytical result over the entire passband.

Now we choose to increase the disorder in the masses so that they vary $\pm 1\%$ from some nominal value, which means that the uniform probability density function has width of .02. Examining Equation 4.1, we would simply expect our localization factor to be scaled by the new σ_μ^2 compared to the previous result. Indeed this is what we confirm with our simulation illustrated in Figure 4.2.

Finally we examine the chain with a 10% variation in the masses. Such a highly disordered state would probably not occur through unintentional assembly or manufacturing error, but rather we look at this highly disordered situation to see if the theory accurately predicts the localization effect. Because of the increased disorder we will clearly have greater localization, as is pictured in Figure 4.3.

Notice, however, at high frequency that our theoretical result overpredicts the localization factor. For example, at $\bar{\omega} = .9999$, at the very edge of the passband, $\gamma_{\text{Monte Carlo}} = .1178$ and $\gamma_{\text{theoretical}} = 8.332$. This discrepancy can probably be attributed to the neglecting of higher order terms in our Taylor series expansion performed in

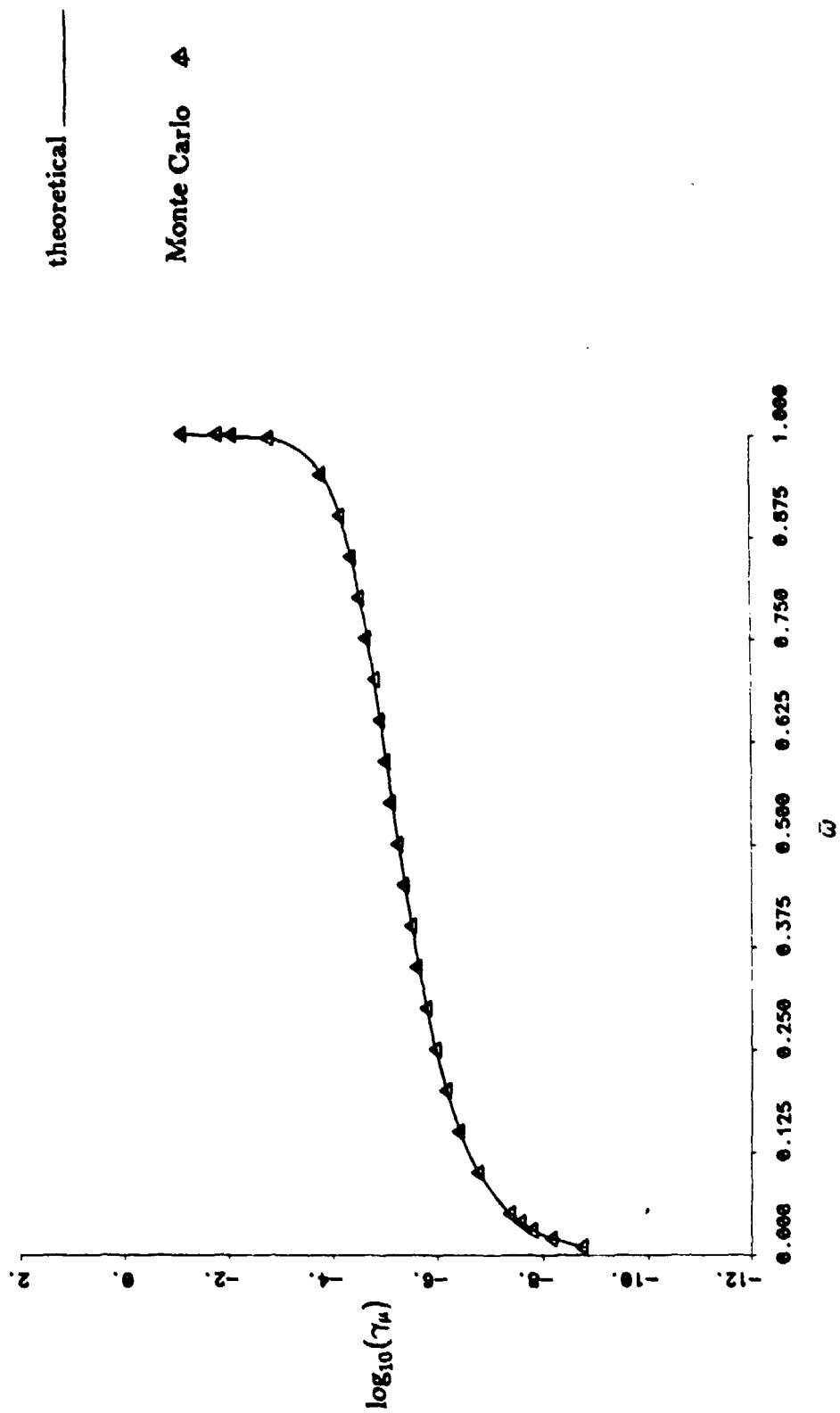


Figure 4.2: Localization factor for mass-spring chain with masses disordered $\pm 1\%$ from their average value.

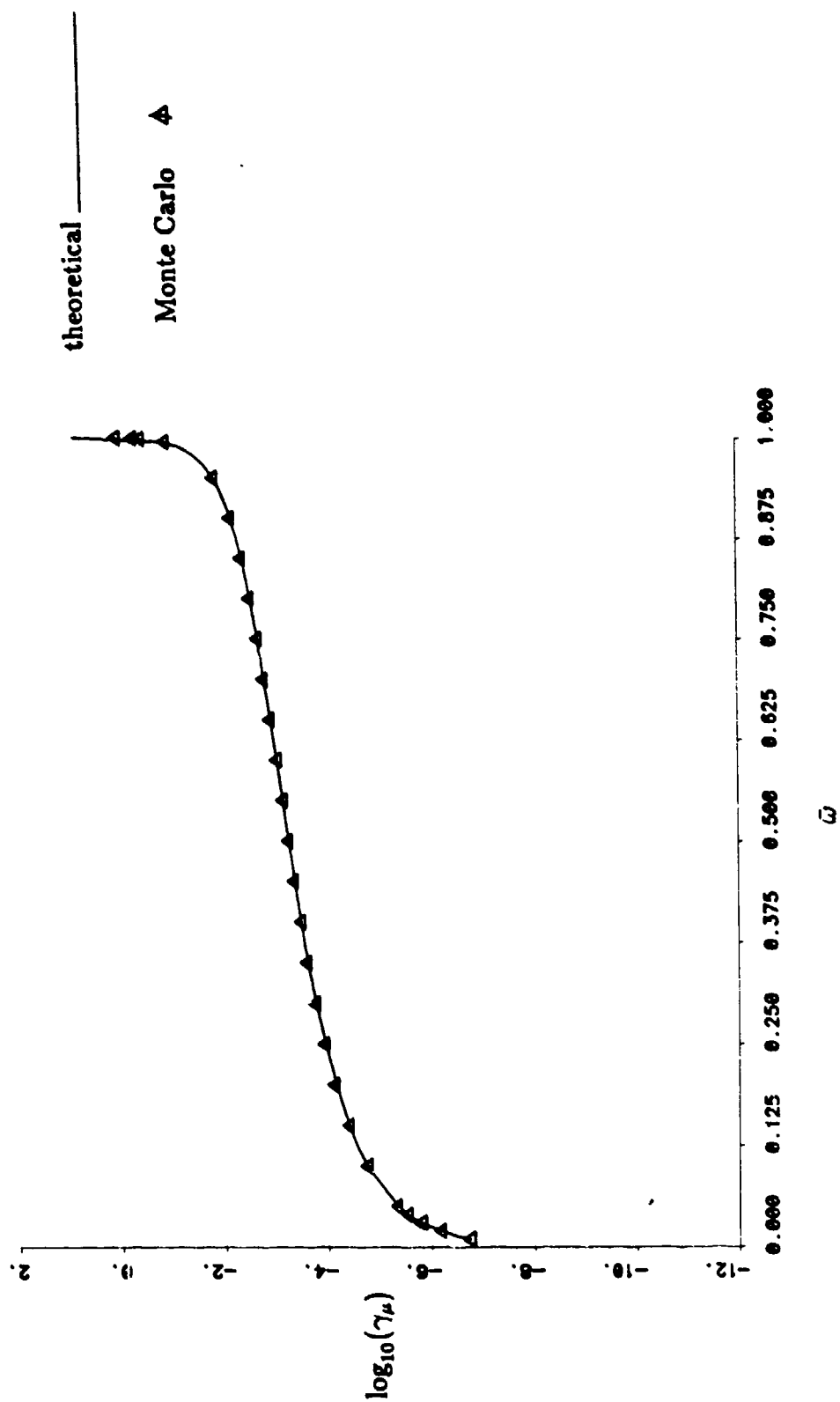


Figure 4.3: Localization factor for mass-spring chain with masses disordered $\pm 10\%$ from their average value.

Chapter 3. These higher order terms could become significant as we approach the edge of the passband ($\bar{\omega} = 1$), just as the term to first order in σ_μ^2 in Equation 4.1 becomes significant as $\bar{\omega} \rightarrow 1$.

4.2.2 Only Springs Disordered

Consider a chain in which every mass is exactly the same, but each spring, k_s , varies in a random fashion from some average value. This localization problem for the mass-spring system has been rarely discussed in the literature. One researcher, [Goda 82] (citing [Toda 66]) argues that the localization problem with only springs disordered is exactly dual to the localization problem with only masses disordered. Our calculations support this contention. Duality [Toda 66] here means that each mass of a mass-spring system can be replaced by a certain spring and each spring can be replaced by a certain mass such that the new system behaves in the same way as the old and in particular has the same natural frequency.

To examine the problem, we begin with the transfer matrix for the chain with only springs disordered, which is in Appendix C.1. Here $\tilde{k}_{s,j}$ is the nondimensional spring constant. Identifying $\frac{1}{i(k_{s,j})}$ in Appendix C.1, we again use Equation 3.10 to calculate $\gamma_{\tilde{k}_s}$ and find:

$$\gamma_{\tilde{k}_s} = \frac{\bar{\omega}^2 \sigma_{\tilde{k}_s}^2}{2[1 - \bar{\omega}^2]}$$

So indeed this is the same as Equation 4.1 with σ_μ^2 replaced by $\sigma_{\tilde{k}_s}^2$, and confirms Goda's contention that the localization problem with masses disordered is dual to that with springs disordered. This means that all the localization results displayed in Figures 4.1-4.3 will apply to the problem of springs disordered by simply replacing the word mass by the word spring.

4.2.3 Masses and Springs Disordered

Finally we consider the situation where both masses and springs are disordered. As was stated in Chapter 3 the localization factor for this situation is simply the sum of the individual localization factors when a single variable is randomized. So

$$\gamma_{\mu\bar{k}_s} = \gamma_\mu + \gamma_{\bar{k}_s} \doteq \frac{\omega^2(\sigma_\mu^2 + \sigma_{\bar{k}_s}^2)}{2[1 - \omega^2]}$$

We check this result with a Monte Carlo simulation in which both masses and springs are randomly varied from their average values by $\pm 1\%$. The Monte Carlo results again track the analytical results. See Figure 4.4.

Before closing this section, one final note is in order. When [Goda 82] originally considered the localization problem of masses and springs disordered (without solving for $\gamma_{\mu\bar{k}_s}$), his transfer matrix did not have unit determinant, so he knew he could not use Furstenberg's original theorem which requires unit determinant for the random matrix. As a consequence he spent most of the paper proving that the Furstenberg result will hold even if the determinant is not unity, so long as Equation 3.2 is satisfied. Apparently Goda was not aware that the transfer matrix could be reformulated so that even when both masses and springs were disordered the transfer matrix would still have unit determinant. The transfer matrix Goda used had the state vector containing two adjacent generalized displacements:

$$\begin{bmatrix} d_n \\ d_{n-1} \end{bmatrix}.$$

while the state vector we use contains a generalized displacement and a generalized nondimensional force at the same point.

$$\begin{bmatrix} d_{n-1} \\ f_{n-1} \end{bmatrix}$$

resulting in a unit determinant transfer matrix.

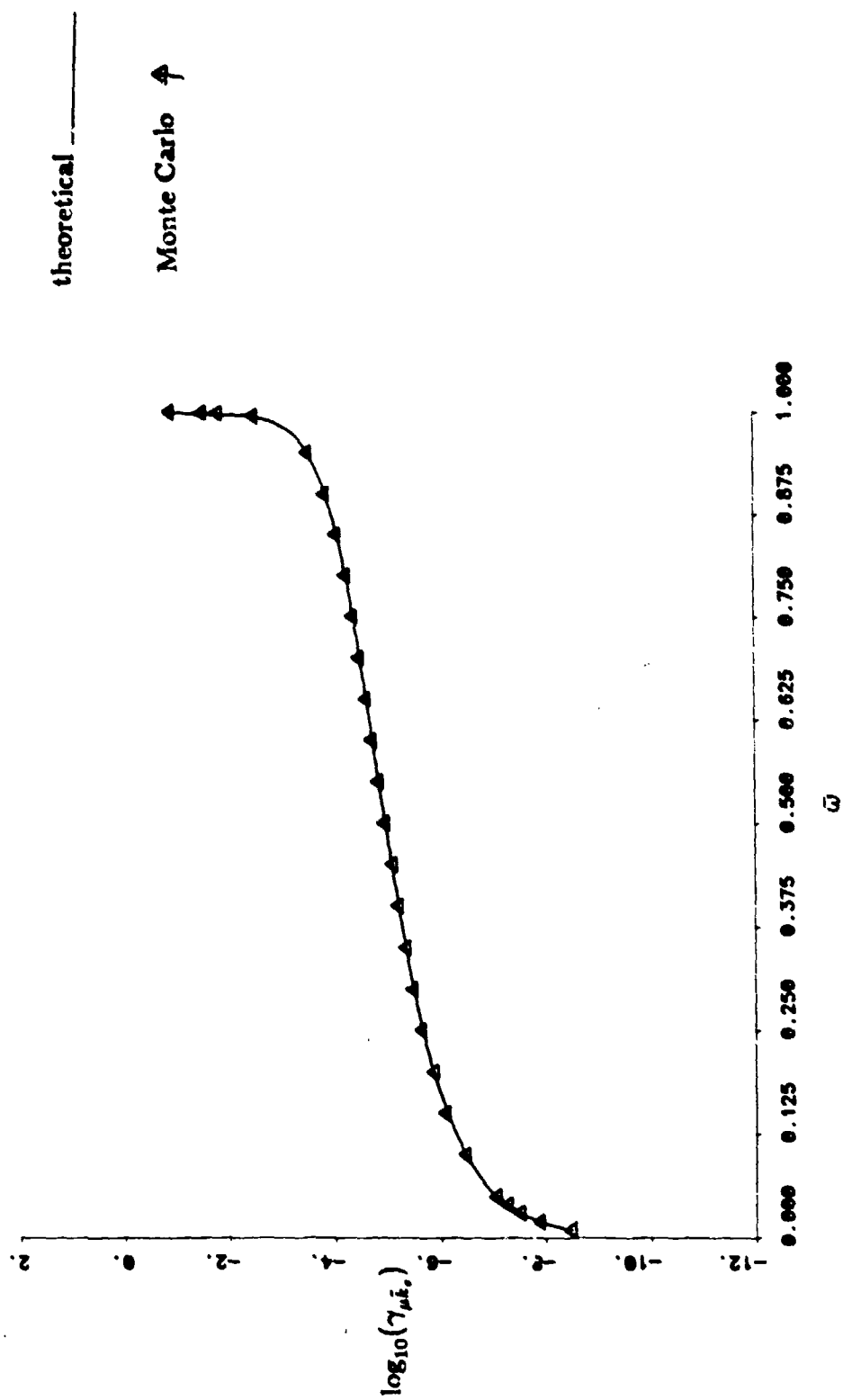


Figure 4.4: Localization factor for mass-spring chain with masses and springs disordered

$\pm 1\%$ from their average values.

4.3 Localization in a Rod with Attached Resonators

In this section we investigate localization factors for a model proposed by [von Flotow 82] which mimics some of the important behavior of a periodic truss structure. The model is a longitudinal wave carrying rod with attached resonators, where the attached resonators represent the vibrating cross-members present in a real truss structure and the continuous rod models compression, bending, shear or any continuous deformation of the truss member. This simple model allows us to gain some insight into the dynamic behavior of truss structures without having to deal with models of real truss members involving transfer matrices of dimensions possibly 12×12 or greater. The model and relevant properties are discussed in Appendix C.2.

We will explore the localization phenomenon when the attached masses, the attached springs and the distances between the attached resonators are individually disordered. Finally we examine the system when all three variables are disordered. Our results will indicate that the most pronounced localization effects will occur at frequencies near the stopbands.

4.3.1 Only Masses Disordered

We first consider disordering only the masses on the attached resonators and evaluate the effects on the transmission properties of the system. The transfer matrix and wave transfer matrix when the attached masses are disordered are presented in Appendix C.2. Note our use of the nondimensional mass, $\bar{\mu}_j$, where $\langle \bar{\mu}_j \rangle = \bar{\mu}$. In all of our examples for the rod with attached resonators $\bar{\mu} = 0.2$ and $\bar{k}_s = 0.5$. These values allow for the ease of presentation of results and are consistent with [von Flotow 82].

Now we use the equation for $\frac{1}{t(\bar{\mu}_j)}$, appearing in Appendix C.2, in Equation 3.10 and

find that

$$\gamma_{\mu} = \frac{(\sin^2 \pi \bar{\omega}) \sigma_{\mu}^2}{8(\sin^2 k)(\pi \bar{\omega})^6 \bar{\mu}^4 ((1/\bar{k}_s) - (1/\bar{\omega}^2 \pi^2 \bar{\mu}))^4} \quad (4.3)$$

Clearly the dependence of γ_{μ} on frequency is much more complicated than we found for the simple mass-spring system. An analysis of the localization factor shows that it is proportional to $\bar{\omega}^2$ at very low frequency, as was the case for the mass-spring chain.

We now examine the localization factor over the frequencies of the passbands of the periodic system. Our first analytical and numerical results are for the masses disordered $\pm 1\%$ from the average value of $\bar{\mu} = .2$. As can be seen in Figure 4.5 we have excellent agreement between the analytical and Monte Carlo results even when the localization factor varies by seven orders of magnitude over one passband.

Some distinguishing features are noticeable for this type of disorder. First, the localization factor is largest in the vicinity of the first stopband. This first stopband occurs around $\bar{\omega} = (\frac{E}{\mu})^{1/2}/\pi = .5033$, the natural frequency at which the average attached resonator vibrates. Adding even more resonators would compound this effect. Second, we notice that the localization effects generally decrease with increasing frequency. This result seems reasonable because we suspect that at higher frequency, the attached mass vibrates less and less because of its inertia.

Notice that near the second and higher stopbands (each of which begins at integer values of $\bar{\omega}$) the localization factor decreases with frequency approaching the beginning of the stopband, while on the other side of the passband the localization factor is clearly amplified near the stopband. One explanation for this behavior is that the frequency at the beginning of the second and higher stopbands ($\bar{\omega} = 1, 2, \dots$) coincides with the frequencies in the perfectly periodic system at which the rod of length l between the resonators vibrates as if it had fixed-fixed boundary conditions [Mead 75-1]. Some calculations confirm this effect. Therefore, at these integral frequencies, the rod does not vibrate at the points of attachment of the resonator, thus the fact that the mass on the resonator is disordered would have little impact on the dynamic behavior. On

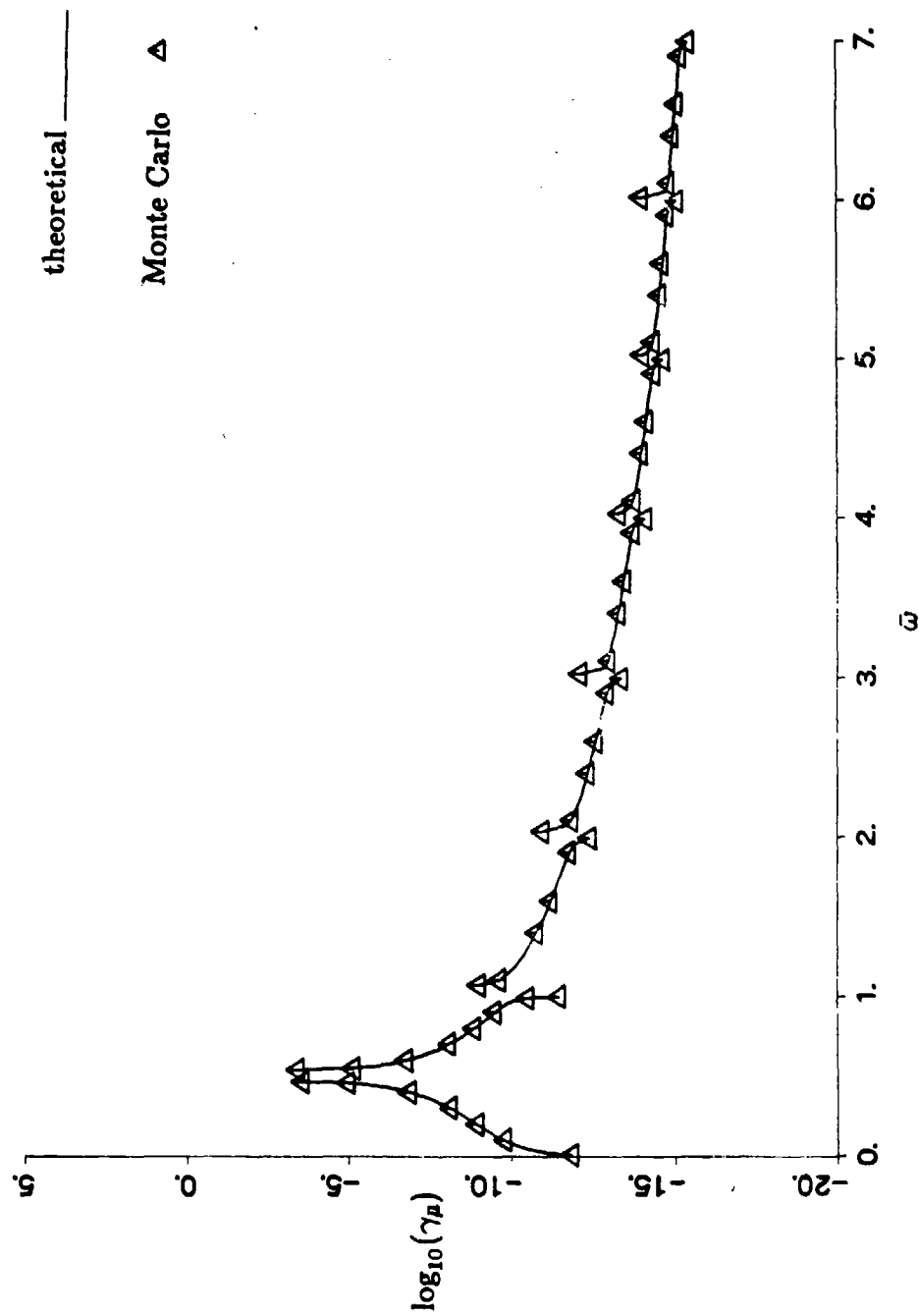


Figure 4.5: Localization factor for rod and attached resonators with masses disordered

$\pm 1\%$ from their average value with $\bar{\mu} = 0.2$ and $\bar{k}_r = 0.5$.

the upper end of each stopband each segment of rod no longer vibrates in a fixed-fixed condition and so the disordered mass can now influence the transmission properties.

To give us some idea what the nondimensional frequencies might correspond to in reality, we have substituted some values for the physical parameters. From Appendix C.2 we have

$$\bar{\omega} = \frac{\omega l (\frac{\rho}{E})^{\frac{1}{2}}}{\pi}$$

We choose a length l of 9 feet (2.74 m), E of 45×10^6 lb/in² (3.103×10^8 kN/m²) and ρ of .063 lb/in³ (1.7×10^3 kg/m³). This corresponds to a graphite epoxy rod, and the bay length was suggested at one time for the space station. With these values we find that $\bar{\omega} = 1$, the beginning of the second stopband, corresponds to $\omega = 15,491$ rad/s or a frequency of 2465.5 Hz.

We next consider the attached masses disordered with a 1% variation from the average value. In this case the localization effects are increased proportionately through σ_μ^2 in Equation 4.3. We show the localization factor as a function of frequency in four passbands for this level of disorder in Figure 4.6. We essentially see the same pattern we saw for the lower level of disorder.

Finally we increase the disorder of the mass to $\pm 10\%$ of the average value of the nondimensional mass. The results are presented in Figure 4.7. Again we see the familiar behavior of the localization factor as a function of frequency. As we did in the previous section on the mass-spring chain, we notice that the theoretical prediction diverges from our Monte Carlo simulation when the localization factor has a value of .1 or greater. Again this must be a result of only calculating γ_μ to first order in σ_μ^2 .

In summary, we conclude that the localization effects are strongest in the vicinity of the stopband associated with the natural frequency of the average attached resonator, while the effects become less and less significant at higher frequencies.

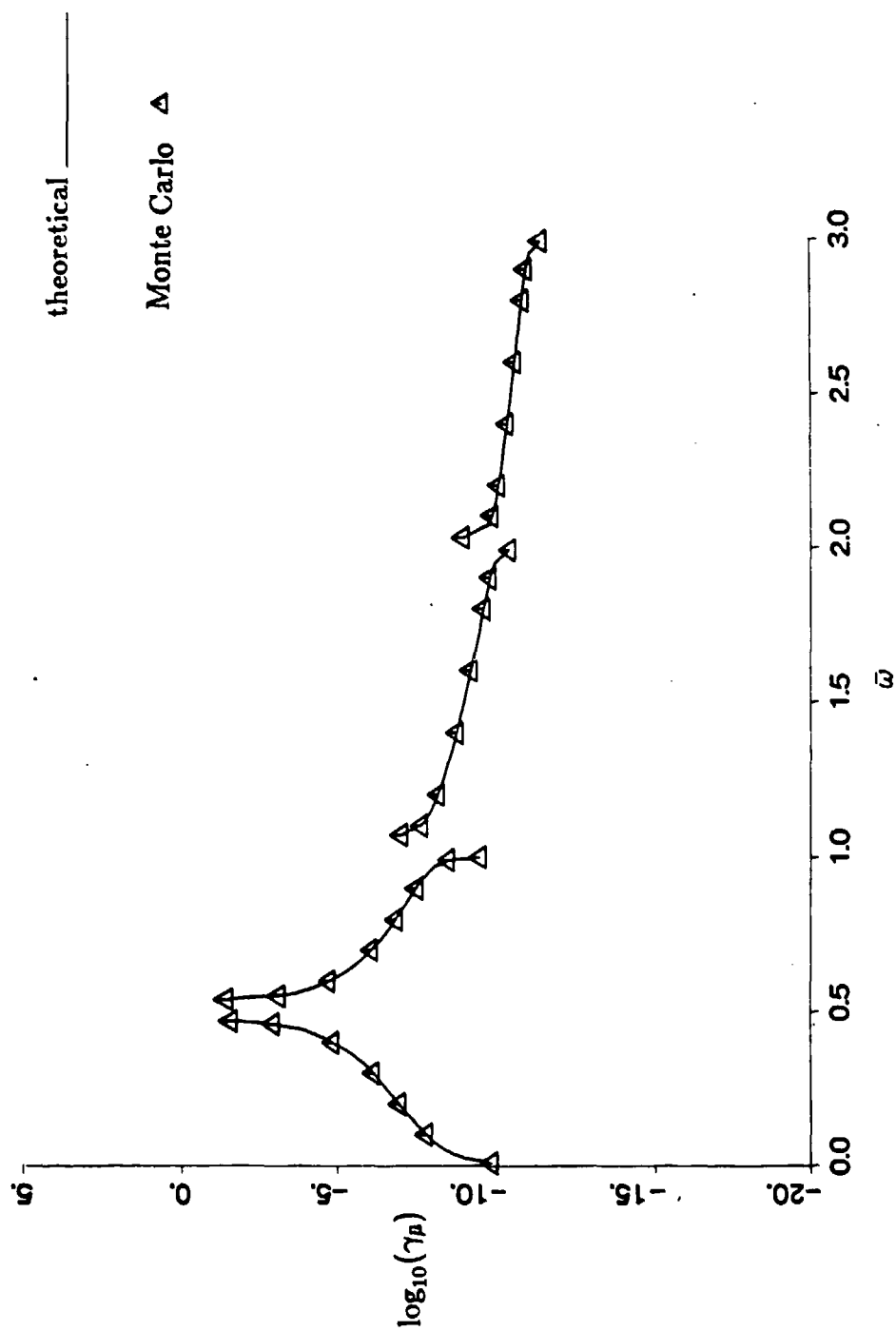


Figure 4.6: Localization factor for rod and attached resonators with masses disordered $\pm 1\%$ from their average value with $\bar{\mu} = 0.2$ and $\bar{k} = 0.5$.

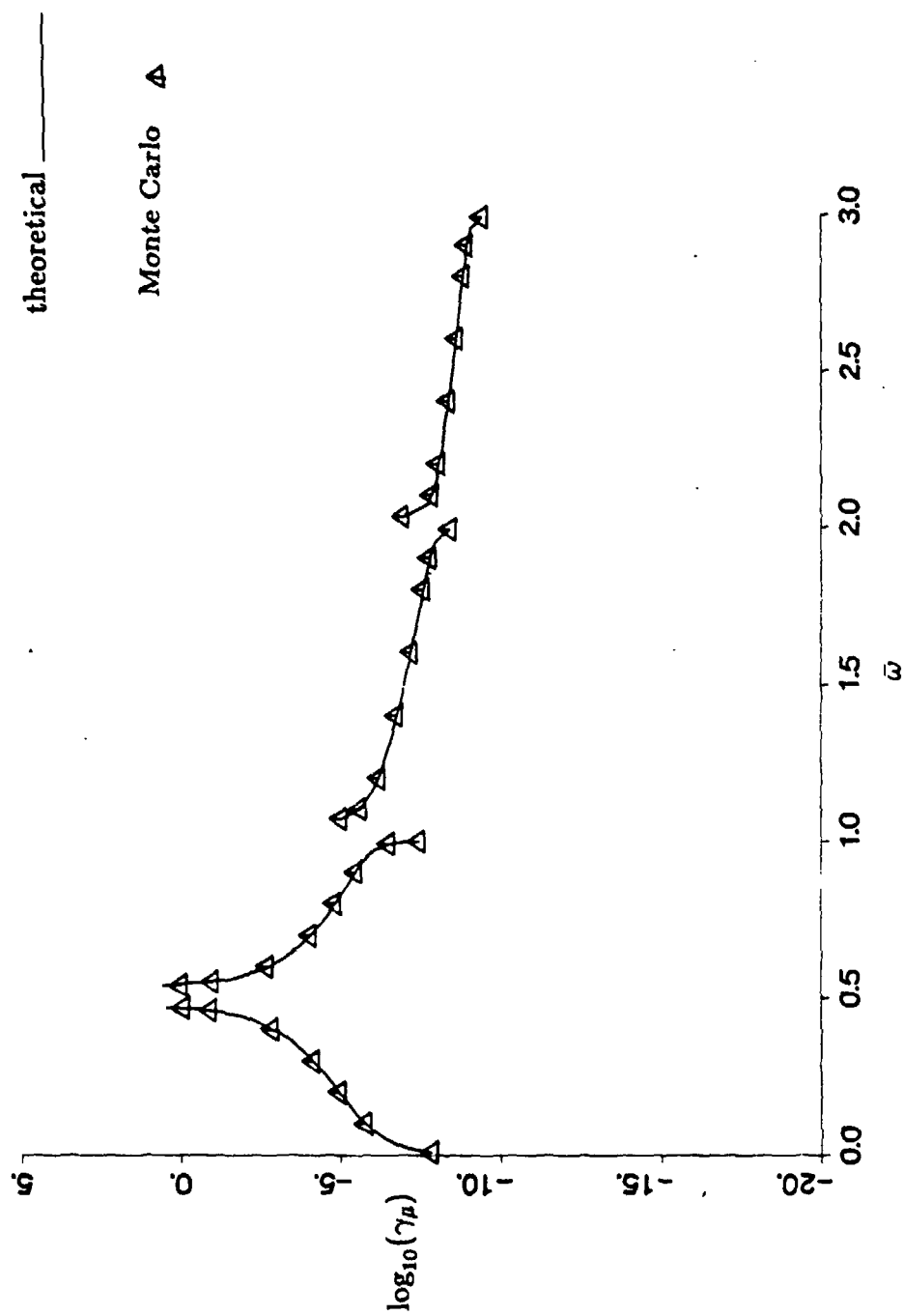


Figure 4.7: Localization factor for rod and attached resonators with masses disordered $\pm 10\%$ from their average value with $\bar{\mu} = 0.2$ and $\bar{k}_s = 0.5$.

4.3.2 Only Springs Disordered

We next disorder only the springs of the attached resonators, where the average nondimensional spring constant, $\langle \bar{k}_s \rangle = \bar{k}_s = .5$. We will examine springs disordered $\pm 1\%$, $\pm 1\%$ and $\pm 10\%$ from the average value. In all instances the localization effects follow, as a function of frequency, a pattern very similar to that seen for only masses disordered. One difference we will note though is that at the same levels of disorder, the localization effects that are due to the mass disorder are greater than those due to the spring disorder in the first passband. In the second and higher passbands the trend is reversed and we find that disorder in the springs has greater localizing effects than does the comparable disorder in the masses.

The transfer matrix and wave transfer matrix with the springs disordered is discussed in Appendix C.2. By using Equation 3.10 we find the localization factor for only springs disordered:

$$\gamma_{k_s} = \frac{(\sin^2 \pi \bar{\omega}) \sigma_{k_s}^2}{8(\sin^2 k)(\pi \bar{\omega})^2 \bar{k}_s^4 ((1/\bar{k}_s^4) - (1/\bar{\omega}^2 \pi^2 \bar{\mu}))^4} \quad (4.4)$$

Note that γ_{k_s} is very similar to γ_{μ} , though they are not dual to each other.

This localization factor is plotted in Figure 4.8 for $\pm 1\%$ variation in the springs. The results of the Monte Carlo simulation are also plotted at several frequencies and follow very closely the analytical results. One discrepancy between analytical and Monte Carlo results occurs at the lowest frequency shown. This is a consequence of working with numbers that are too low even for double precision simulations. Note the frequency dependent pattern is very similar to that for the case when the masses were disordered. Again we see the most pronounced localization effects occurring around the first stopband. In addition the localization effects become less pronounced with increasing frequency. We again see that on the immediate left hand side of the second and higher passbands the localization factor is diminished while on the immediate right

hand sides it is amplified.

Comparing this localization factor with the one for masses only disordered we find that γ_p is consistently larger than γ_k in the first passband. This difference can be as much as one or two orders of magnitude at the very lowest frequencies plotted. The lower the frequency the greater the difference. On the other hand, for the second and higher passbands the localization effects due to spring disorder are consistently greater than those due to mass disorder. These differences can be as great as four orders of magnitude at the highest frequencies seen in Figure 4.8. The effect is more pronounced with increasing frequency. Similar effects are noted for the higher levels of disorder. These effects seem reasonable if one considers the effect of wiggling the end of a spring with a mass on the other end of it (this is essentially what the rod is doing to the attached resonator). At low frequency, most of the motion is associated with the movement of the mass, while the spring stretches and compresses very little. Therefore we expect that disorder in the mass will have a greater impact at low frequency than will disorder in the spring. This is indeed what we observe. At higher frequencies, as we move past resonance, $\omega = .5033$, the inertia of the mass will cause it to move little while the spring will see a lot of motion. So disorder in the springs should give a much larger contribution to localization effects at high frequency than should disorder in the masses. This too was observed.

Finally, the localization factor is plotted for variations of $\pm 1\%$ and $\pm 10\%$ in the nondimensional spring constant in Figures 4.9 and 4.10, respectively. With increasing disorder the localization effects are amplified, and we again see that our theoretical results mispredict the localization factor near the first stopband for the highest level of disorder.

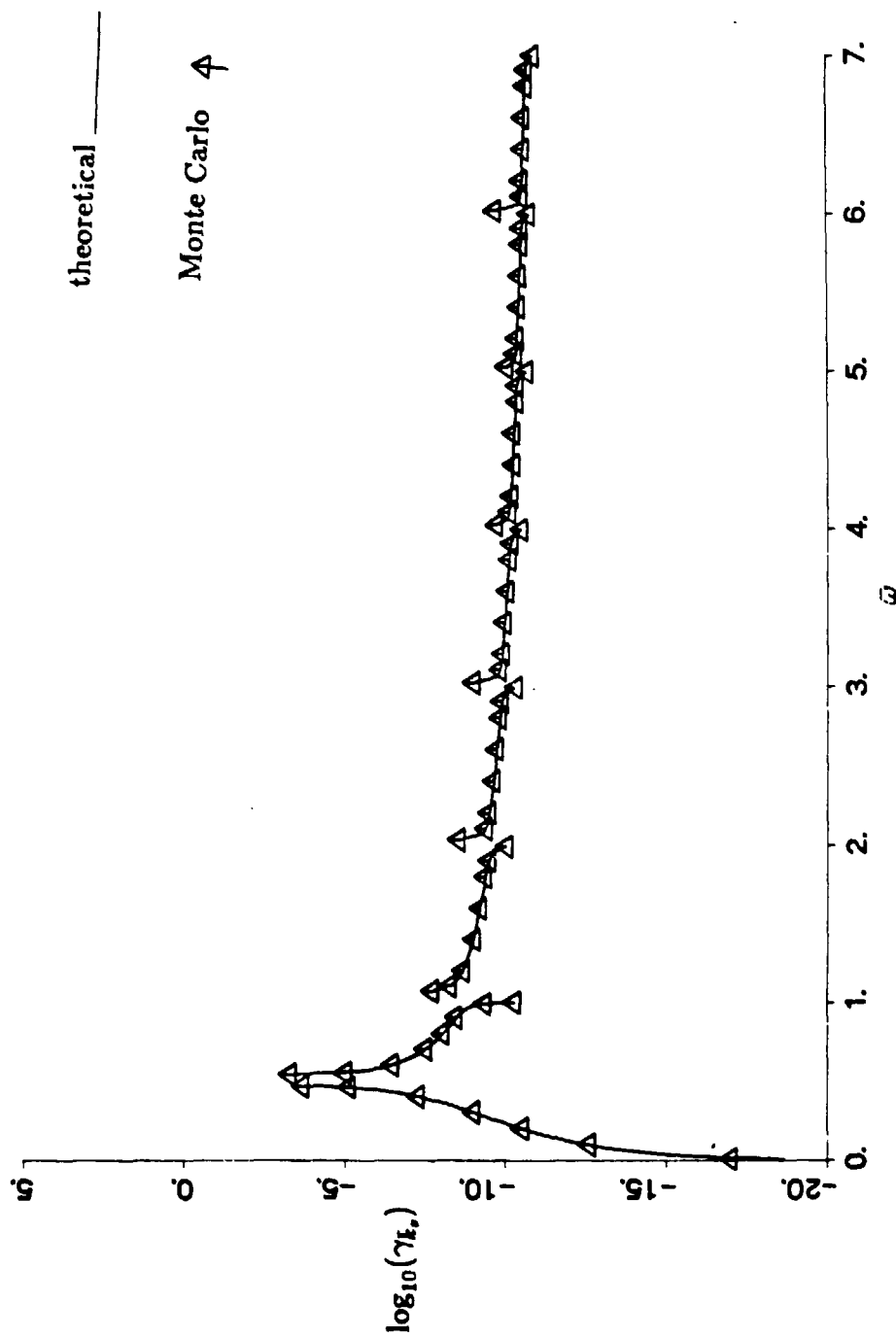


Figure 4.8: Localization factor for rod and attached resonators with springs disordered $\pm 1\%$ from their average value with $\bar{\mu} = 0.2$ and $\bar{k}_s = 0.5$.

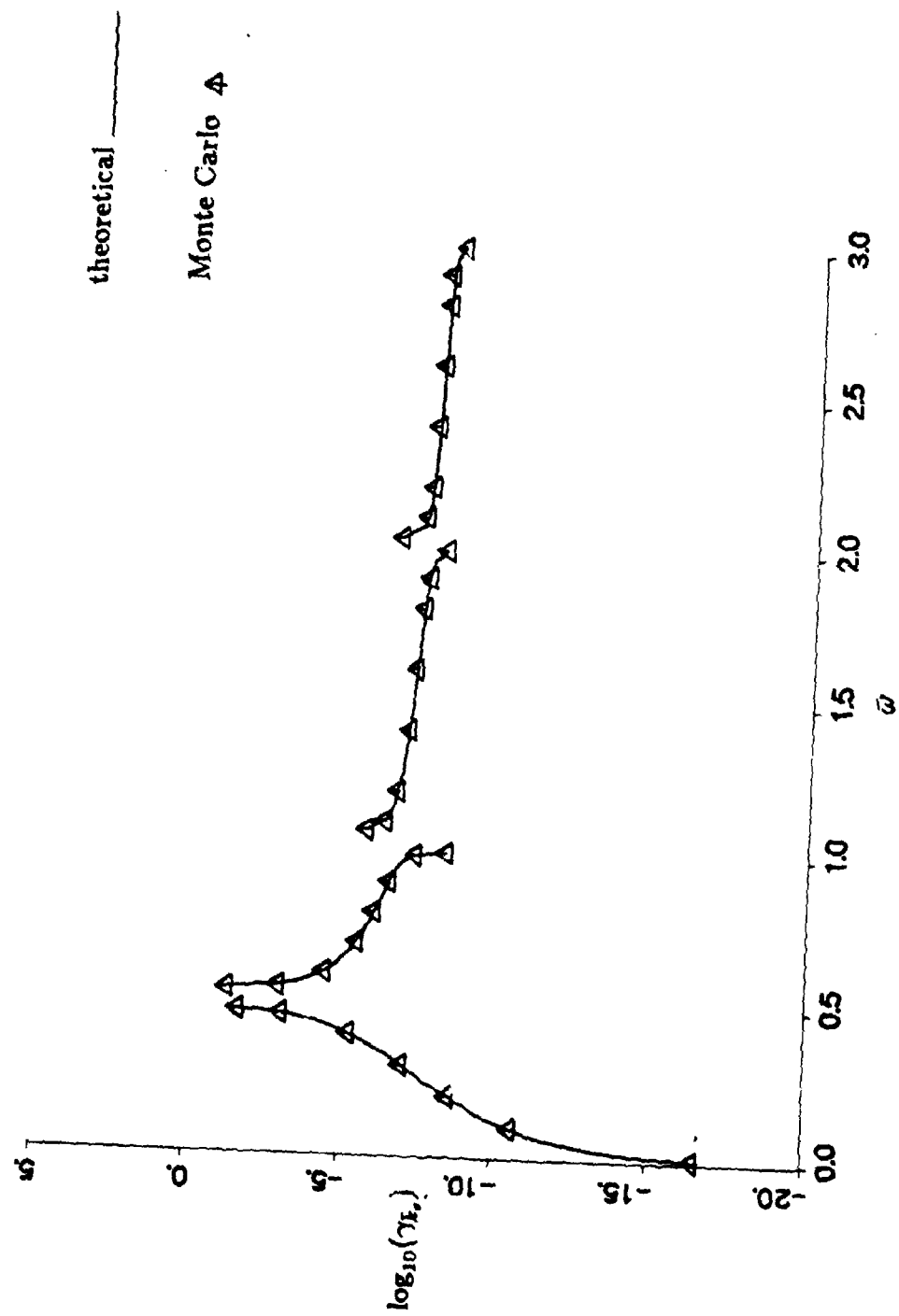


Figure 4.9: Localization factor for rod and attached resonators with springs disordered $\pm 1\%$ from their average value with $\bar{\mu} = 0.2$ and $\bar{k}_s = 0.5$.

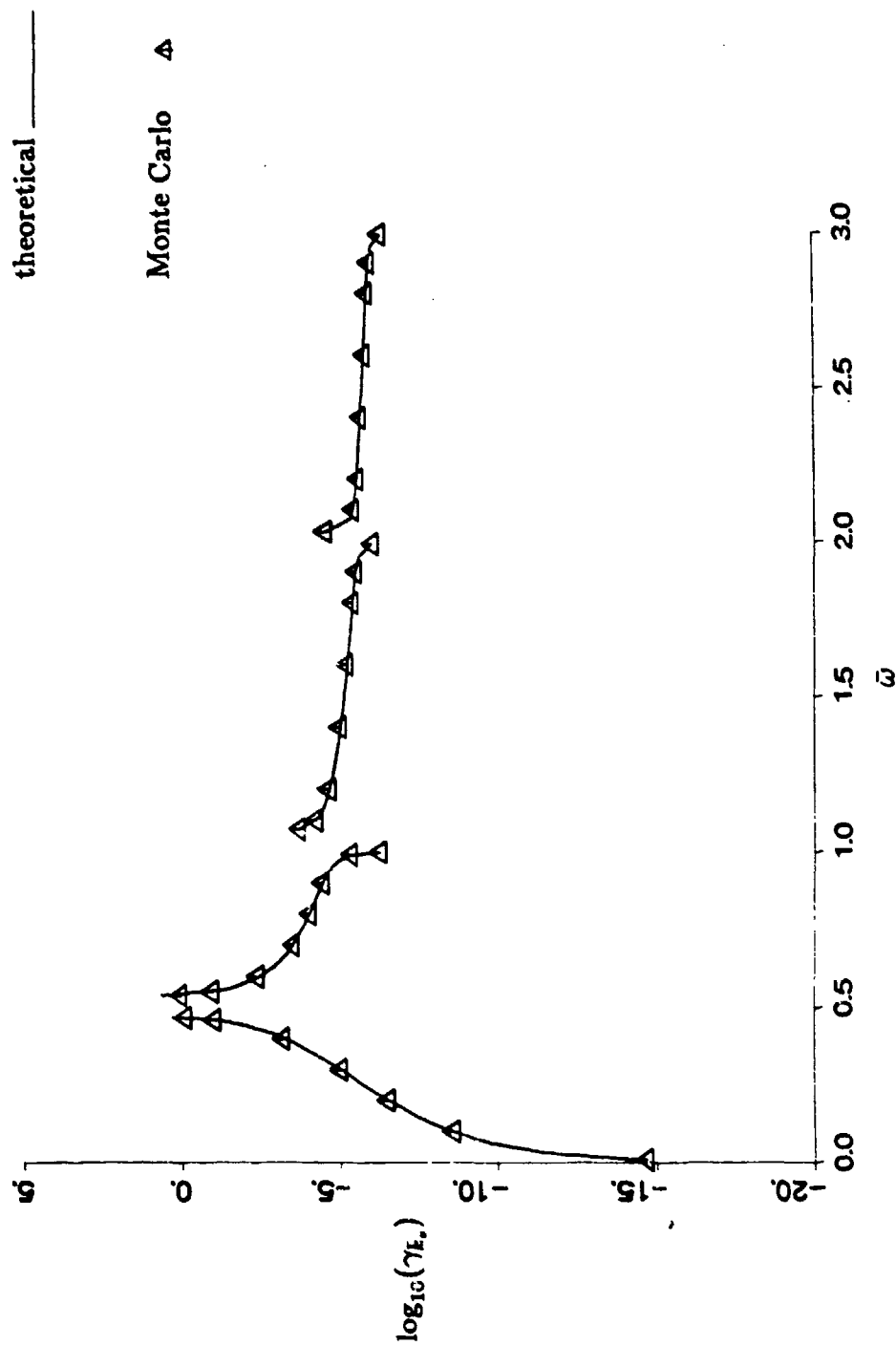


Figure 4.10: Localization factor for rod and attached resonators with springs disordered $\pm 10\%$ from their average value with $\bar{\mu} = 0.2$ and $\bar{k}_s = 0.5$.

4.3.3 Only Lengths Between Resonators Disordered

Now we allow all the resonators to be the same with $\bar{\mu} = .2$ and $\bar{k}_s = .5$, while we will disorder the lengths between the attached resonators by $\pm 1\%$, $\pm 1\%$ and $\pm 10\%$ from the nominal value. The transfer matrix and wave transfer matrix for lengths disordered are discussed in Appendix C.2. Note that we use the nondimensional variable $\bar{l}_j = \frac{l_j}{\langle l_j \rangle}$, so that $\langle \bar{l}_j \rangle = 1$. With the lengths only disordered we will find a startling change in behavior of the localization factor as a function of frequency compared to the cases where only the masses or springs were disordered.

The calculation of the localization factor for lengths only disordered, γ_l , is much more complicated than that for the previous two cases. Applying Equation 3.10 we find:

$$\begin{aligned} \gamma_l = & \frac{\sigma_l^2}{4} \left[-\pi\bar{\omega} \sin(\pi\bar{\omega}) \bar{H} \cos(\pi\bar{\omega}) \right. \\ & - (\pi\bar{\omega})^2 \cos^2(\pi\bar{\omega}) - \frac{\bar{H}^2 \sin^2(\pi\bar{\omega})}{4} \\ & + \frac{\cos^2 k}{2 \sin^2 k} \{ 2(\pi\bar{\omega})^2 \sin^2(\pi\bar{\omega}) - 2(\pi\bar{\omega}) \bar{H} \cos(\pi\bar{\omega}) \\ & \left. + \frac{\bar{H}^2}{2} + \frac{\bar{H}^2 \cos^2(\pi\bar{\omega})}{2} \} \right] \end{aligned} \quad (4.5)$$

At low frequency γ_l behaves as $\bar{\omega}^2$, as was the case for γ_μ and γ_{k_s} .

This localization factor is plotted in the first eight passbands of the underlying perfectly periodic system in Figure 4.11. Here we immediately notice some striking differences from our previous localization plots for the rod with attached resonators. We notice that the localization effects are amplified on either side of all stopbands. We also notice that for a narrow band of frequencies in each passband, the localization factor is greatly diminished. Note that it was difficult for the Monte Carlo simulation to reproduce the extremely small localization factors seen in the plot in the middle

of the passbands. We do not believe that this is a result of numerical problems at these low values, but rather is a result of our neglecting higher order terms in our Taylor series expansion that apparently make a significant enough contribution at those frequencies. At higher disorders the effect is even more pronounced. The fact that these discrepancies do not show up in the fifth and eighth passbands is because we have not found that frequency where the localization factor takes its smallest values in those passbands.

These effects seem reasonable because the wavelength of the traveling wave at the end and beginning of each stopband is some multiple of the length between the resonators. Thus we would expect that disorder in the length between resonators would have its greatest effect at those frequencies as opposed to other frequencies where the wavelengths are not so correlated with the bay length. Why γ_l becomes so extremely small in the middle of the passbands is not clear.

Similar effects are noted when the disorder in length is increased to $\pm 1\%$ and $\pm 10\%$ from the nominal value. The corresponding localization factors as a function of frequency are shown in Figures 4.12 and 4.13.

4.3.4 All Three Parameters Disordered

Finally we examine what might be the most realistic situation in which the masses, springs and lengths between the resonators are disordered. The transfer matrix as a function of $\bar{\mu}_j$, $\bar{k}_{j,j}$ and \bar{l}_j is presented in Appendix C.2. Again we assume that $\langle \bar{\mu}_j \rangle = .2$, $\langle \bar{k}_{j,j} \rangle = .5$ and $\langle \bar{l}_j \rangle = 1$. Here we will disorder both the masses and springs $\pm 1\%$ from their average values, while we will only disorder the lengths by $\pm .1\%$ from its average value. As was explained in Chapter 3, the localization factor with several variables disordered is simply the sum of the localization factors when each

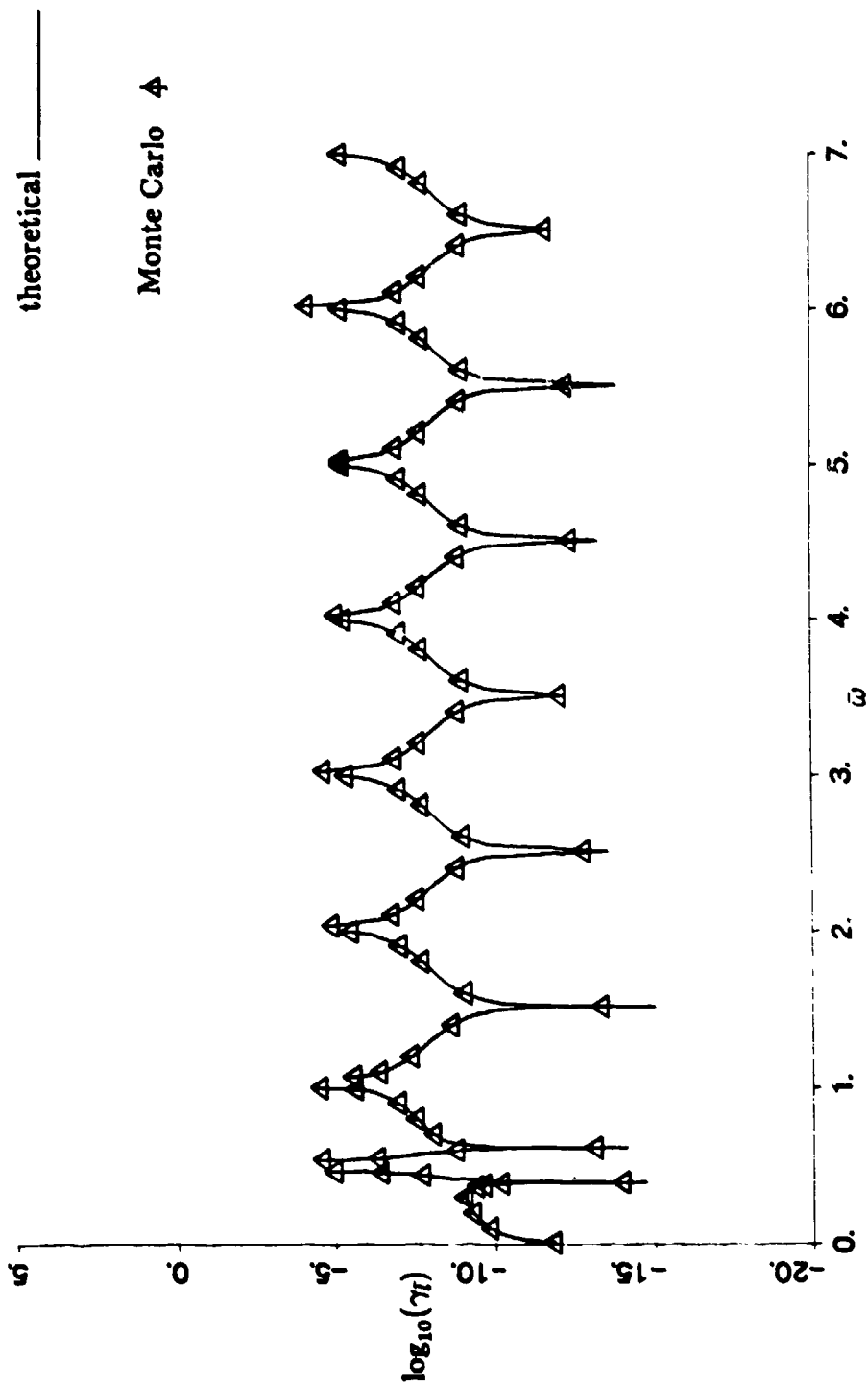


Figure 4.11: Localization factor for rod and attached resonators with lengths between resonators disordered $\pm 1\%$ from their average value with $\bar{\mu} = 0.2$ and $\bar{k}_r = 0.5$.

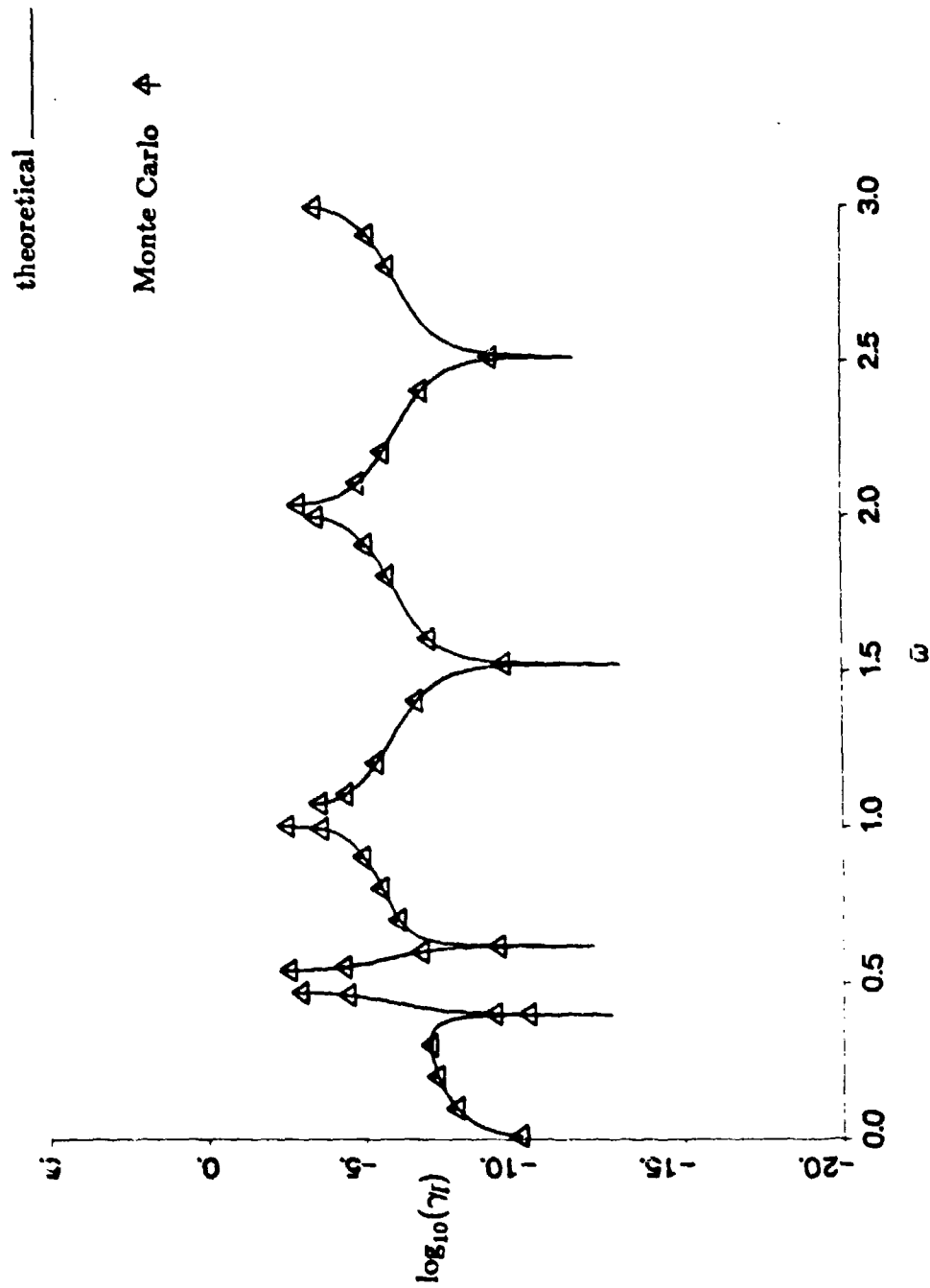


Figure 4.12: Localization factor for rod and attached resonators with lengths between resonators disordered $\pm 1\%$ from their average value with $\bar{\mu} = 0.2$ and $\bar{k}_s = 0.5$.

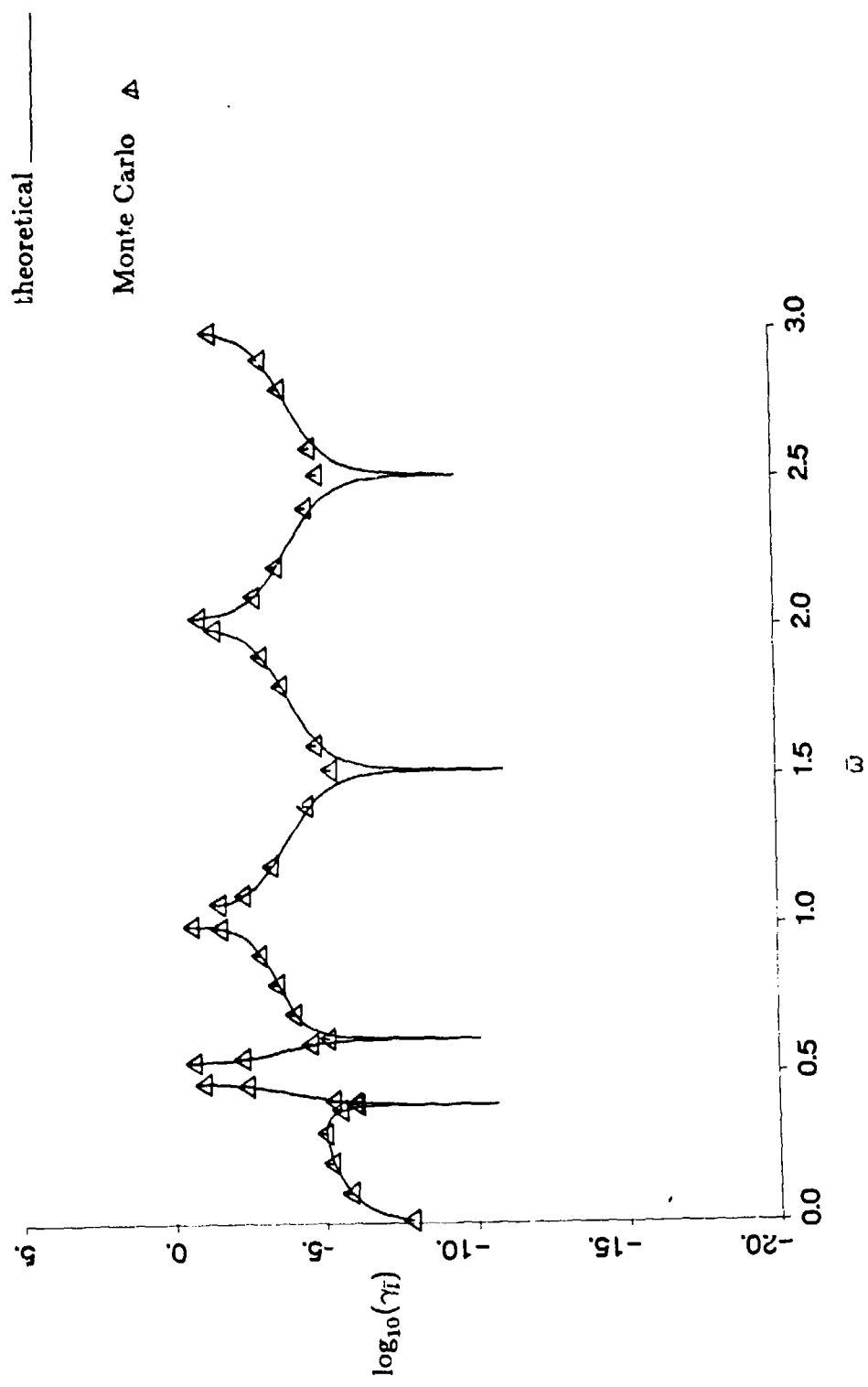


Figure 4.13: Localization factor for rod and attached resonators with lengths between resonators disordered $\pm 10\%$ from their average value with $\bar{\mu} = 0.2$ and $\bar{k}_r = 0.5$.

variable is disordered individually,

$$\gamma_{pk,l} = \gamma_p + \gamma_k + \gamma_l$$

In Figure 4.14 we see that our analytical results and Monte Carlo simulation agree very well over eight passbands for these levels of disorder. In this case the localization factor is greatly amplified around all the stopbands, particularly the first one which is associated with the natural frequency of the average attached resonator. The localization effects tend to diminish with increasing frequency. For these levels of disorder, we find that the localization effects are predominately caused by the mass disorder in most of the first passband, while in most of the second passband and in the middle of the subsequent passbands the disorder in the springs has the greatest contribution to $\gamma_{pk,l}$. Only near the second and subsequent stopbands does the disorder in the length predominate in the localization factor. The physical reasoning given earlier when each parameter was disordered individually helps to explain these effects.

4.4 Localization in a Beam on Simple Supports

The final example concerns a Bernoulli-Euler beam on evenly spaced simple supports in the perfectly periodic case, and on randomly spaced simple supports in the disordered case. The perfectly periodic system is presented in Appendix C.3 and its dynamics have been discussed extensively by [Miles 56, Mead 70].

The beam on randomly spaced supports has been discussed in [Yang and Lin 75] and [Lin 76]. There they considered a beam on up to six supports and numerically averaged frequency response functions when the beam was under point loading or convected loading. Their results were consistent with what one would expect from localized dynamics. Unfortunately this approach gives very little insight into the underlying mechanisms associated with disruption of periodicity. Our approach is analytically rig-

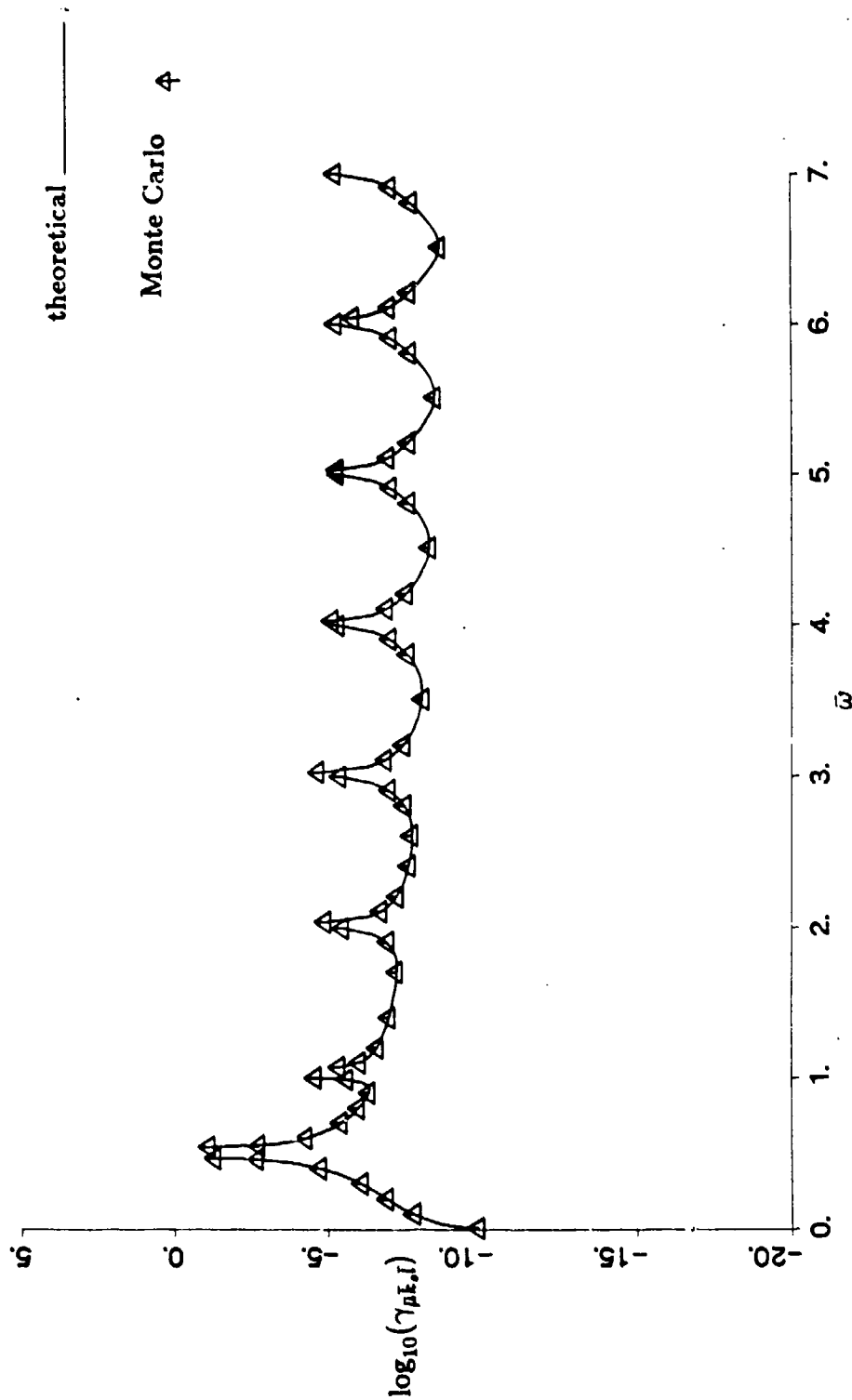


Figure 4.14: Localization factor for rod and attached resonators with masses, springs and lengths between resonators disordered $\pm 1\%$, $\pm 1\%$ and $\pm 1\%$, respectively, from their average values with $\bar{\mu} = 0.2$ and $\bar{k}_s = 0.5$.

orous and centers on a variable which is known to be statistically well-behaved and has physical meaning. In [Bansal 80] a situation similar to ours was considered in which a disordered segment of beam was inserted between perfectly periodic beams on supports. However, the analysis was for deterministically disordered segments.

The transfer matrices for the perfectly periodic system, as well as for the disordered system are presented in Appendix C.3. The random length is nondimensionalized so that $\hat{l}_j = \frac{l_j}{\langle l_j \rangle}$ and $\langle \hat{l}_j \rangle = 1$. From the equation for $\frac{1}{\hat{l}_j}$ and Equation 3.10 we can calculate the localization factor. The calculation is quite involved and many of the terms needed in the calculation are presented in [Yang and Lin 75, Lin 76]² After extensive calculation we find

$$\gamma_i = \frac{1}{4} \sigma_i^2 [2g_r'^2 + 2g_r g_r'' + 2g_i'^2 + 2g_i g_i'' - (2g_r g_r' + 2g_i g_i')^2]$$

where

$$g_r = \cos k$$

$$g_r' = -\sqrt{\bar{\omega}} [s_4 + \cos k c_2] / s_3$$

$$g_r'' = -\bar{\omega} \cos k [2c_4 + s_1 s_3] / s_3^2$$

$$g_i = \sin k$$

$$g_i' = \frac{\sin k}{2\alpha} \sqrt{\bar{\omega}} [\cos k - \frac{c_4 c_2}{s_3^2}] + \frac{\alpha \sqrt{\bar{\omega}}}{4 \sin k} [\sinh^2 \sqrt{\bar{\omega}} \cos \sqrt{\bar{\omega}} - \cosh \sqrt{\bar{\omega}} \sin^2 \sqrt{\bar{\omega}}] / s_3^2$$

²We believe one term in Appendix A of [Lin 76] and Appendix I of [Yang and Lin 75] should read

$$b_{12}'' = -(\xi/ET) \{ [s_4(l) + 2 \cos \theta c_2(l)] / s_3(l) - c_4(l) [2c_2^2(l) - s_1(l) s_3(l)] / s_3^3 \}$$

$$\begin{aligned}
g_i'' = & -\frac{\bar{\omega} \sin k}{2\alpha} [(s_4 + 2c_2 \cos k)/s_3 \\
& - c_4(2c_2^2 - s_1 s_3)/s_3^3] \\
& + \frac{\bar{\omega} \alpha}{2 \sin k} [2s_3 \cos^2 k - s_1 s_4]/s_3^2
\end{aligned}$$

Clearly, we will have to look at a plot of γ_f in the passbands to make some sense of the above equation. This has been done in Figure 4.15 where we have disordered the nondimensional length by $\pm 1\%$ from the average value.

In the eight passbands we clearly see that the maximum localization effects occur in the immediate vicinity of the stopbands, while in the middle of the nominal passbands the localization factor is greatly diminished. These results seem reasonable because in the perfectly periodic system at the beginning of the stopbands it is well known [Mead 70] that each span of the beam vibrates as if it were clamped on both ends, while at the end of each stopband it vibrates as if it were pinned on both ends. Indeed, the traveling waves become standing waves at the edges of the stopbands. Thus, the dynamics of the system are very sensitive to the distances between supports at frequencies near the beginning and ends of the stopbands. This explains the large localization factors at those frequencies. At all other frequencies the wave motion is not so physically correlated with the span lengths.

To give some meaning to our nondimensional frequency, we choose some properties for our physical parameters corresponding to those given in [Yang and Lin 75]. From Appendix C.3 we have

$$\bar{\omega} = \omega \sqrt{\frac{\mu l^4}{EI}}$$

If we let the thickness of the beam be .05 inches and the width be 1 inch, E be 10.5×10^6 lb/in² and μ be 2.616×10^{-4} lbs²/in², we find that for $\bar{\omega} = 100$, we have $\omega = 1530.5$ rad/s or 243 Hz.

Finally, we examine the case of extreme disorder where the distances between the

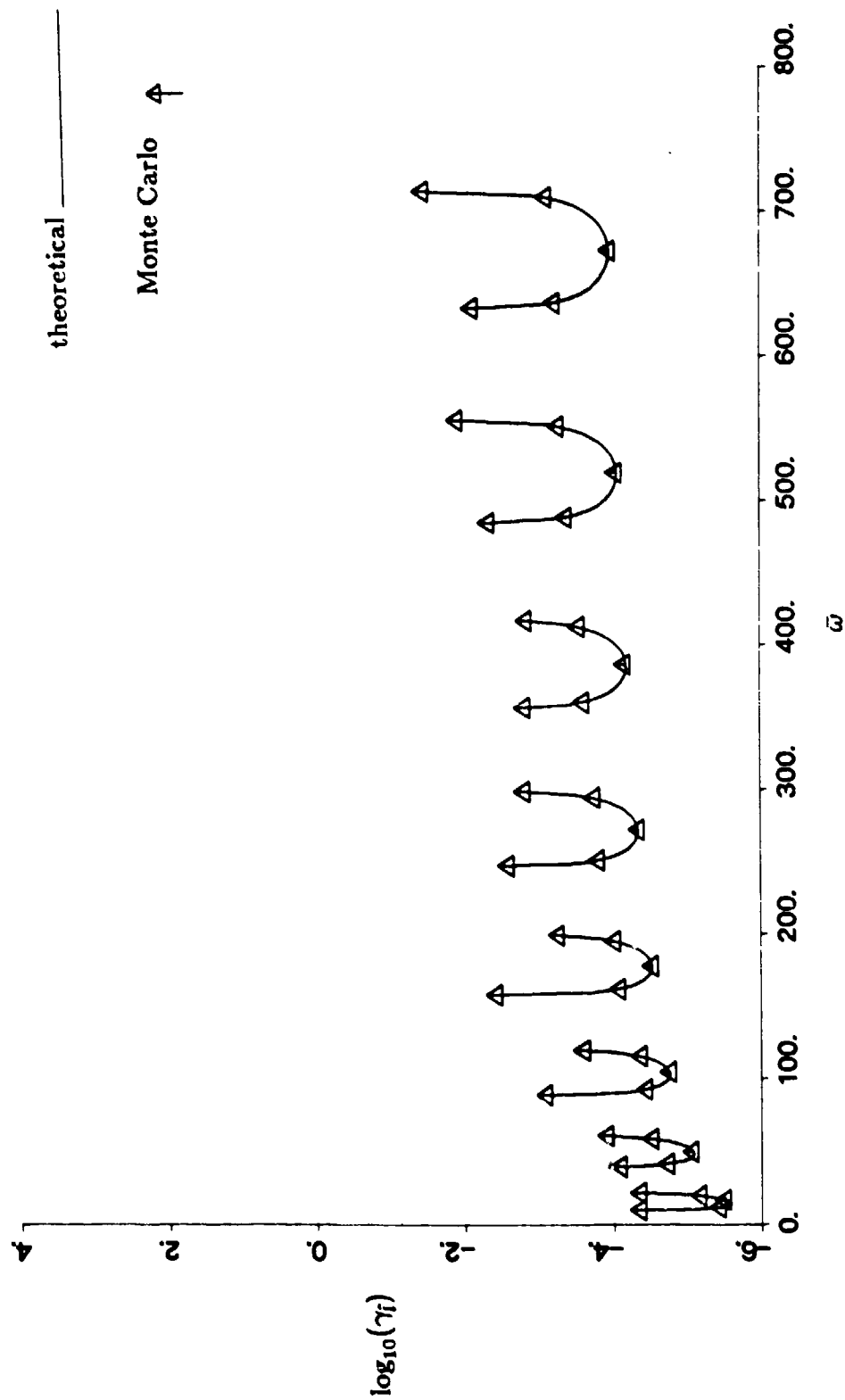


Figure 4.15: Localization factor for beam on simple supports with lengths between supports disordered $\pm 1\%$ from their average value.

supports are randomized by $\pm 10\%$ from their average value. The localization results are plotted in Figure 4.16. Our localization factors take on very high values and we see that the theoretical result overpredicts the Monte Carlo simulation. Yet, the simulation clearly shows the same pattern observed at the lower disorder. The localization effects are most pronounced near the stopbands.

We also notice that the localization effects seem to become stationary with increasing frequency in that the pattern of the localization factor as a function of frequency does not change substantially. This may be a function of the phase randomness ideas discussed by [Hodges 82, Lambert and Thorpe 82, Lambert and Thorpe 83] and [Baluni and Willemsen 85]. The argument here is that at high enough frequency complete phase uncertainty in the wave sets in leading to a particularly simple calculation of the localization factor. The calculation leads to the conclusion that the localization factor will be a constant as a function of frequency. In [Hodges 82] it is found that

$$\gamma_f = \ln |t_{\text{support}}|$$

where t_{support} is the transmission coefficient for one support on an infinitely long beam. From [Cremer et al 73, page 321] we find that $|t_{\text{support}}|^2 = .5$. This gives a value of the localization factor that is .347. Clearly, though, we do not observe the localization factor becoming a constant as a function of frequency. Instead it is noticeably amplified in the vicinity of the stopbands. Therefore the notion that the localization factor becomes a constant with frequency must be considered misleading for this kind of system. However, the fact that the localization factor behaves in the same manner from passband to passband at high frequency could be a consequence of these phase randomness ideas.

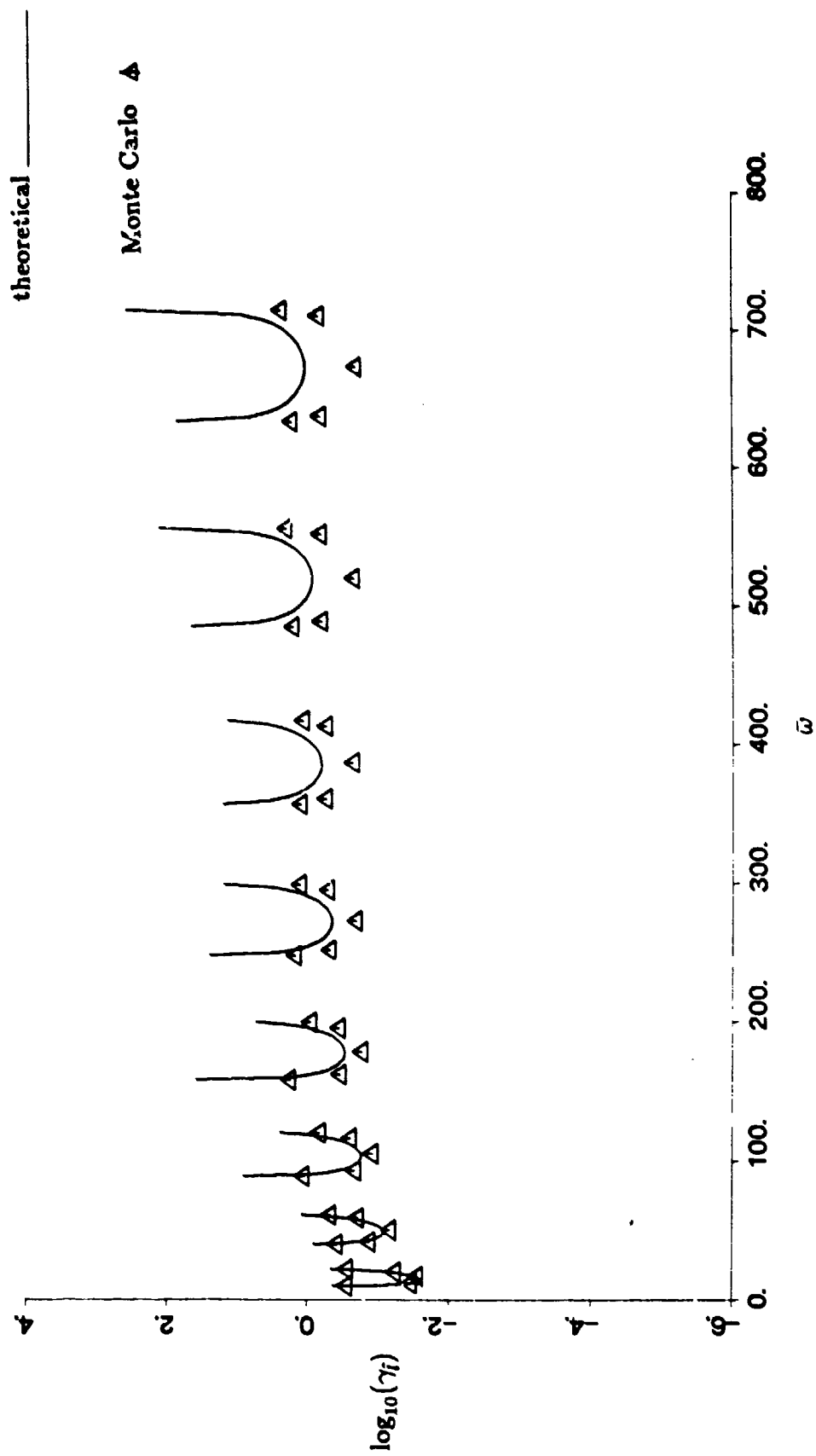


Figure 4.16: Localization factor for beam on simple supports with lengths between supports disordered $\pm 10\%$ from their average value.

4.5 Observations

We have collected a lot of results in this chapter on localization effects in some useful structural dynamic examples, so we need to reflect on some of the insights we have gained.

Clearly the localization effects increase with greater amounts of disorder, though our theoretical results have difficulty tracking the localization factor when it becomes greater than $\gamma = .1$. More importantly, localization effects are strongly varying functions of frequency. Whenever the first frequency band is a passband, we notice that the localization factor is proportional to frequency squared. The most dramatic frequency effect we see is that the localization effects can be quite pronounced around the stopbands. The localization factor was particularly high in the vicinity of the stopband associated with the natural frequency of the attached resonator on the rod. This result indicates that localization effects could be quite important on periodic truss structures which have a number of cross-members. Real periodic truss structures are really multiwave systems which will be investigated in Chapter 5; however, we suspect that the insights we have generated with the mono-coupled systems should generalize to the multiwave systems. We also notice that disorder in the lengths of bays result in quite pronounced localization effects in the vicinity of stopbands as well. Specifically, we see that the localization factor when lengths are disordered consistently take on high values at the edges of the passbands, while they are consistently small in the middles of the passbands. This is in contrast to disorder in masses and springs where the localization factor does not vary so dramatically over any but the first passband. Because localization can become quite pronounced in the vicinity of stopbands, experimental measurements on real periodic structures in those frequency regimes could be susceptible to the effects of disorder.

In addition, our analytical and numerical work has clarified some of the few, yet misleading, results that have appeared in the literature. Most published results up to

this point have simply indicated that the localization effects increase with frequency and take on constant values at high frequency. Clearly these results are mistaken. Our work indicates that the importance of localization effects can vary greatly over even a single passband and generally become quite pronounced near the stopbands.

Chapter 5

Localization in Multiwave Systems

For the bulk of this thesis we have considered the localization phenomenon in mono-coupled disordered periodic structures, i.e., systems modeled with 2×2 random transfer matrices. However, most real structures are better modeled with transfer matrices that are of dimension 4×4 or greater. This implies the structures can carry a multiplicity of wave types at a single frequency as opposed to the one wave type in the mono-coupled case. Periodic structures of this kind are called multiwave or multichannel systems. Frequently in the solid state physics literature the term "wire" is used to describe these systems in contrast to the term "chain" used to describe mono-coupled systems. Just as there are many complications in going from single-input single-output to multiple-input multiple-output control system design and analysis, there are analogous complications in going from disordered one-dimensional systems carrying a single pair of waves to disordered one-dimensional systems carrying a multiplicity of waves.

Before embarking on our analysis of multiwave systems, let us review the territory we have covered for mono-coupled disordered systems. After briefly summarizing some relevant properties of periodic systems, we demonstrated that disordered periodic structures can be modeled via a product of random transfer matrices. That product of

random matrices was then transformed to a wave transfer matrix involving transmission and reflection coefficients. By employing Furstenberg's theorem on products of random matrices, we were able to show that the transmission coefficient, τ_n , is well-behaved in the sense that

$$\gamma = - \lim_{n \rightarrow \infty} \frac{1}{n} \ln |\tau_n|, \quad \gamma > 0$$

Furstenberg's theorem also provides us with a closed-form solution for γ involving a double integral over two probability density functions. Because one of the probability density functions is virtually impossible to find, we were forced to approximate the double integral to first order in the variances of the disordered variables.

We then examined the localization factor for three one-dimensional disordered mono-coupled periodic structures. For reasonable levels of disorder our analytical solution to γ provided a good approximation to the Monte Carlo calculations of the localization factor. We noticed that the localization factor was a strongly varying function of frequency taking on its greatest values at frequencies near the stopbands of the underlying perfectly periodic system.

We believe the approach followed in the study of mono-coupled disordered periodic systems should be followed in the study of multiwave systems to yield the best results. Indeed, as we will see below, this approach has already been successful in giving us the multiwave localization factor as a function of the transmission matrix.

Perfectly periodic multiwave structures have been examined by [Mead 73, Mead 75-1] and [Roy and Plunkett 86, Signorelli 87, Signorelli and von Flotow 87, Bernelli et al 87]. Just as mono-coupled periodic structures have passbands and stopbands, so do multiwave periodic systems. However, in the passbands of multiwave systems, both traveling and attenuating waves, frequently called evanescent waves, can exist simultaneously. Indeed, even complex waves, those which propagate according to e^{ik+a} , are known to exist, yet these act as if they were evanescent waves. Because evanescent waves are already strongly localized, our focus in this chapter will be on the effects of disorder

on the traveling waves [Büttiker et al 85].

The localization phenomenon in multiwave systems has received much less attention than its single wave counterpart. Anderson [Anderson 81] derived a scaling variable for multiwave systems from an analysis of the scattering matrix. Several researchers [Pichard and Sarma 81-1, Pichard and Sarma 81-2, Pichard 86, Pichard and André 86] and [Imry 86] have used the transfer matrix formalism and theory on products of random matrices to study multiwave systems, though mainly with the intention of extending the results to two- and three-dimensional systems. In [Johnston and Kunz 83-1] and [Johnston and Kunz 83-2] the localization problem of multiwave systems is examined in its own right.

In our analysis of the problem, we state our assumptions about the wave transfer matrix, which follows from certain properties of the scattering matrix. As we shall see, Furstenberg's theorem will not be of use in analyzing multiwave localization. As in [Pichard and Sarma 81-1], we will use the theorem of Oseledets to guide our work. Two subsections are devoted to discussing this important theorem. Our goal is to find the multiwave analog to our mono-coupled result:

$$\gamma = - \lim_{n \rightarrow \infty} \frac{1}{n} \ln |\tau_n|$$

We will indeed derive a multiwave analog to this and compare our result with three others that have appeared in the literature. Physically, our goal is to find that wave in the multiplicity of attenuated waves, which is attenuated the least by the disorder. This least attenuated wave carries energy the farthest and so is the one of interest when thinking about localization in multiwave systems.

5.1 Wave Transfer Matrix Assumptions

Our wave transfer matrix assumptions will follow from two properties of the scattering matrix usually found in the solid state literature [Anderson 81] and [Johnston and Kunz 83-1, Büttiker et al 85]. We assume the scattering matrix of one disordered bay sitting in an otherwise perfectly periodic system is both symmetric and unitary.¹ The symmetry of the scattering matrix follows from the symmetry of the impedance (or admittance matrix) describing the bay [Carlin and Giordano 64] and unitarity follows from assuming no dissipation and excluding any evanescent waves [Büttiker et al 85]. See Appendix E.

Our two assumptions about the scattering matrix, S , translate into two properties of the wave transfer matrix, W . First

$$S \text{ symmetric} \iff W \text{ symplectic}$$

and second

$$S \text{ unitary} \iff W \in SU(d, d)$$

These properties are discussed in Appendix E. Both properties will be important in the derivation of the multiwave localization factor in what follows. The wave transfer matrix W can be derived from the corresponding real transfer matrix, T , by premultiplying T by the transposes of the left eigenvectors and postmultiplying by the right eigenvectors corresponding to the traveling waves.

5.2 Theorem of Oseledets

As we did for mono-coupled systems, we will in the case of multiwave systems rely on a theory for products of random matrices to guide our work. We use the theorem

¹This corresponds to the physical assumptions of time reversal symmetry and current conservation in the solid state localization problem.

of Oseledets [Oseledets 68] specialized to symplectic matrices; however, the reader is referred to [Bougerol and Lacroix 85] and [AMS 86] to better understand its relevance to the problem at hand. We divide the relevant portions of Oseledets' theorem into several parts. First we will state a result concerning the eigenvalues of an asymptotic matrix product, then we will discuss a vector propagation interpretation of the same theorem. In the final section we will see how the Lyapunov exponents (defined below) might be calculated analytically.

5.2.1 Eigenvalues of Limiting Matrix

Let W_1, W_2, \dots, W_n form a sequence of independent identically distributed random symplectic matrices of size $2d \times 2d$. Suppose also that

$$E(\sup\{\ln \sigma_{\max}(W_1), 0\}) < +\infty$$

If we set $V_n = W_n \cdots W_1$ then the sequence of matrices $(V_n^H V_n)^{\frac{1}{2n}}$ converges *w.p.1* as $n \rightarrow \infty$ to a random matrix B with $2d$ nonrandom eigenvalues $e^{\gamma_1}, \dots, e^{\gamma_d}, e^{-\gamma_d}, \dots, e^{-\gamma_1}$ where $\gamma_1 \geq \dots \geq \gamma_d > 0$ [Johnston and Kunz 83-1]. These γ_i s are the Lyapunov exponents of the random matrix product $W_n \cdots W_1$. In random dynamical systems, Lyapunov exponents are considered a measure of stochasticity [Benettin and Galgani 79].

The eigenvalues physically represent d pairs of waves traveling in both directions. The theorem of Furstenberg applied to $2d \times 2d$ matrices allows us to calculate γ_1 , which is the uppermost Lyapunov exponent. However, in this multiwave case with $\gamma_d \leq \gamma_1$, γ_d represents the wave with potentially the least amount of decay, and so it carries energy along the structure farther than the wave represented by γ_1 . As a result, γ_d is the quantity of interest when calculating multiwave localization effects.

Note that we can also express the Lyapunov exponents of this random symplectic matrix product in terms of its singular values (see Appendix A), $\sigma_j = \sigma_j(V_n)$. If

we recall that the singular values of a symplectic matrix occur in reciprocal pairs: $\sigma_1, \dots, \sigma_d, \sigma_d^{-1}, \dots, \sigma_1^{-1}$ where $\sigma_1 \geq \dots \geq \sigma_d \geq 1$. Then w.p. 1

$$\gamma_j = \lim_{n \rightarrow \infty} \frac{1}{n} \ln \sigma_j(V_j) \quad 1 \leq j \leq d$$

This result [Bougerol and Lacroix 85] will be very useful in the section in which we derive γ_d as a function of the transmission properties of the system.

5.2.2 Vector Propagation Interpretation of Oseledets' Theorem

Another aspect of Oseledets' theorem involves the limiting behavior of a random matrix product premultiplied by a nonrandom vector. This aspect will help explain one of the properties mentioned in connection with Furstenberg's theorem in Chapter 3.

Given the assumptions and results of the previous section, let $\psi_1 > \psi_2 > \dots > \psi_r$ (with $r \leq 2d$) be the strictly decreasing sequence of distinct elements of $(\gamma_1, \dots, \gamma_d, -\gamma_d, \dots, -\gamma_1)$. Then there exists a strictly increasing sequence of subspaces

$$\{0\} = S_{r+1} \subset S_r \subset \dots \subset S_1 = C^{2d}$$

(known as a filtration of C^{2d}) such that if

$$z_0 \in S_j \setminus S_{j+1}$$

then

$$\lim_{n \rightarrow \infty} \frac{1}{n} \ln \|W_n \dots W_1 z_0\| = \psi_j \quad j \leq r$$

Here $z_0 \in S_j \setminus S_{j+1}$ says that z_0 is an element of the subspace S_j but not an element of S_{j+1} . Also we have

$$\dim S_{j+1} - \dim S_j =$$

number of elements of the sequence $(\gamma_1, \dots, \gamma_d, -\gamma_d, \dots, -\gamma_1)$

which are equal to ψ_j

This vector propagation property is best understood by examining the example of 2×2 real transfer matrices. In this case our sequence of Lyapunov exponents is $(\gamma_1, -\gamma_1)$ where $\gamma_1 > 0$, so $r = 2$ and $\psi_1 = \gamma_1$ and $\psi_2 = -\gamma_1$. We have the sequence of subspaces

$$\{0\} = S_3 \subset S_2 \subset S_1 = R^2$$

If

$$\dot{x}_0 \in S_2 \setminus S_3$$

i.e.,

$$\dot{x}_0 \in S_2 \setminus \{0\}$$

where S_2 is a particular line in R^2 , then

$$\lim_{n \rightarrow \infty} \frac{1}{n} \ln \|T_n \cdots T_1 \dot{x}_0\| = -\gamma_1$$

What direction \dot{x}_0 takes in R^2 will depend on the particular realization of the infinite matrix product. Likewise if $x_0 \in S_1 \setminus S_2$, i.e., $x_0 \in R^2 \setminus S_2$ then

$$\lim_{n \rightarrow \infty} \frac{1}{n} \ln \|T_n \cdots T_1 x_0\| = \gamma_1$$

These vector propagation ideas are the basis for numerical methods to calculate Lyapunov exponents of various dynamical systems [Benettin and Galgani 79] and [Pichard and Sarma 81-2, Ikeda and Matsumoto 86].

This propagation behavior is very analogous to what happens when a vector is propagated by a product of deterministic matrices, T , whose eigenvalues are λ and $\frac{1}{\lambda}$ with $\lambda > 1$. If we choose any vector v , so long as it has some piece along the eigenvector associated with λ , then as n becomes large the direction of $T^n v$ will become aligned with the eigenvector associated with the λ . If, on the other hand, the vector v is aligned with the eigenvector associated with $\frac{1}{\lambda}$ then $T^n v$ will always be aligned with that eigenvector no matter how large n is.

5.3 Localization Factor for Multiwave Systems as a Function of the Transmission Matrix

In the previous sections we have identified the d th Lyapunov exponent, γ_d , of the matrix product $W_n \cdots W_1$ as the localization factor for a multiwave disordered periodic system. Much as we did for mono-coupled systems, in which we showed

$$\gamma = - \lim_{n \rightarrow \infty} \frac{1}{n} \ln |\tau_n|$$

we want to find γ_d as a function of the transmission properties of the system. Work relevant to this issue has been done by [Anderson 81], [Johnston and Kunz 83-1] and [Imry 86].

Here we assume the $2d \times 2d$ wave transfer matrix is symplectic and is an element of $SU(d, d)$, so

$$V_n = \prod_{j=1}^n W_j = \begin{bmatrix} \tau_n^{-1} & -\tau_n^{-1} \rho_n \\ -\tau_n^{-1*} \rho_n^* & \tau_n^{-1*} \end{bmatrix} \quad (5.1)$$

The form and properties of the wave transfer matrix were established in Appendix E. The two assumptions about the wave transfer matrix are those made by [Anderson 81], [Johnston and Kunz 83-1], [Imry 86], though [Anderson 81] adds more restrictive assumptions. For the rest of the discussion we will suppress the subscript n on the transmission and reflection matrices, τ and ρ , respectively.

We will show that the localization factor (or the d th Lyapunov exponent of V_n) is

$$\gamma_d = - \lim_{n \rightarrow \infty} \frac{1}{n} \ln \sigma_{\max}(\tau)$$

or

$$\gamma_d = - \lim_{n \rightarrow \infty} \frac{1}{n} \ln [tr(\tau \tau^H)]^{\frac{1}{2}}$$

or

$$\gamma_d = - \lim_{n \rightarrow \infty} \frac{1}{n} \ln |\tau_{ij}|_{\max}$$

where τ is $d \times d$ and τ_{ij} is the ij th element of τ and all the results hold w.p. 1.

The derivation of these results begins by recalling

$$\gamma_d = \lim_{n \rightarrow \infty} \frac{1}{n} \ln \sigma_d(V_n)$$

Recalling that the d th singular value of V_n is the positive square root of the d th eigenvalue of $V_n^H V_n$ we have

$$\gamma_d = \lim_{n \rightarrow \infty} \frac{1}{2n} \ln \lambda_d(V_n^H V_n)$$

Consider the matrix

$$V_n^H V_n = \begin{bmatrix} 2(\tau\tau^H)^{-1} - \mathbf{I} & -\rho^T(\tau^*\tau^T)^{-1} - (\tau\tau^H)^{-1}\rho \\ -\rho^H(\tau\tau^H)^{-1} - (\tau^*\tau^T)^{-1}\rho^* & 2(\tau^*\tau^T)^{-1} - \mathbf{I} \end{bmatrix} \quad (5.2)$$

Here $V_n^H V_n$ is symplectic, so its eigenvalues will occur in reciprocal pairs $\lambda_1, \dots, \lambda_d, \frac{1}{\lambda_d}, \dots, \frac{1}{\lambda_1}$ where $\lambda_1 \geq \dots \geq \lambda_d \geq 1$.

Our analysis will be simplified by recognizing the following ²:

$$(V_n^H V_n) + (V_n^H V_n)^{-1} = \begin{bmatrix} 4(\tau\tau^H)^{-1} - 2\mathbf{I} & \mathbf{0} \\ \mathbf{0} & 4(\tau^*\tau^T)^{-1} - 2\mathbf{I} \end{bmatrix} \quad (5.3)$$

where each block in the matrix is $d \times d$. The matrix has repeated eigenvalues $\lambda_1 + \frac{1}{\lambda_1}, \dots, \lambda_d + \frac{1}{\lambda_d}$ for a total of $2d$ eigenvalues. However, we notice that these eigenvalues are the eigenvalues of the two diagonal blocks of this block diagonal matrix. The eigenvalues of each block are clearly real because both blocks are Hermitian. In addition, each block is the complex conjugate of each other, and real eigenvalues being invariant with respect to complex conjugation, both blocks must have the same eigenvalues.

So the eigenvalues, μ_j , of $4(\tau\tau^H)^{-1} - 2\mathbf{I}$ are

$$\mu_1 = \lambda_1 + \frac{1}{\lambda_1}, \dots, \mu_d = \lambda_d + \frac{1}{\lambda_d}$$

²[Engels 80, Pichard and André 86] recognised a similar result, though [Engels 80], working in a different context, never realised he was dealing with symplectic matrices.

where

$$\mu_1 \geq \dots \geq \mu_d$$

Now let $\mu_j[*]$ be the j th eigenvalue of the indicated argument. So

$$\begin{aligned}\lambda_d + \frac{1}{\lambda_d} &= \mu_d[4(\tau\tau^H)^{-1} - 2\mathbf{I}] \\ &= \mu_{\min}[4(\tau\tau^H)^{-1} - 2\mathbf{I}] \\ &= 4\mu_{\min}[(\tau\tau^H)^{-1}] - 2\end{aligned}$$

where we have used a couple of determinant identities in the last equation. Now taking the same limit on both sides:

$$\lim_{n \rightarrow \infty} \frac{1}{2n} \ln(\lambda_d + \frac{1}{\lambda_d}) = \lim_{n \rightarrow \infty} \frac{1}{2n} \ln\{4\mu_{\min}[(\tau\tau^H)^{-1}] - 2\}$$

We notice that

$$\begin{aligned}\lim_{n \rightarrow \infty} \frac{1}{2n} \ln(\lambda_d + \frac{1}{\lambda_d}) &= \lim_{n \rightarrow \infty} \frac{1}{2n} \ln(\lambda_d)(1 + \frac{1}{\lambda_d^2}) \\ &= \lim_{n \rightarrow \infty} \frac{1}{2n} \ln(\lambda_d) + \lim_{n \rightarrow \infty} \frac{1}{2n} \ln(1 + \frac{1}{\lambda_d^2})\end{aligned}$$

Recalling that $\lambda_d \geq 1$, the second term above must vanish in the limit. So we are left with (recalling the definition of γ_d)

$$\begin{aligned}\gamma_d &= \lim_{n \rightarrow \infty} \frac{1}{2n} \ln(\lambda_d) \\ &= \lim_{n \rightarrow \infty} \frac{1}{2n} \ln\{4\mu_{\min}[(\tau\tau^H)^{-1}] - 2\}\end{aligned}$$

Note that

$$\mu_{\min}[(\tau\tau^H)^{-1}] = \frac{1}{\mu_{\max}[\tau\tau^H]}$$

So we can write

$$\gamma_d = \lim_{n \rightarrow \infty} \frac{1}{2n} \ln\left(\frac{4}{\mu_{\max}[\tau\tau^H]} - 2\right)$$

or

$$\gamma_d = \lim_{n \rightarrow \infty} \frac{1}{2n} \ln\left(\frac{1}{\mu_{\max}[\tau\tau^H]}\right)(4 - 2\mu_{\max}[\tau\tau^H])$$

or

$$\begin{aligned}\gamma_d &= \lim_{n \rightarrow \infty} \frac{1}{2n} \ln \left(\frac{1}{\mu_{\max}[\tau\tau^H]} \right) \\ &\quad + \lim_{n \rightarrow \infty} \frac{1}{2n} \ln(4 - 2\mu_{\max}[\tau\tau^H])\end{aligned}$$

In Appendix E we show that $0 < \mu_{\max}[\tau\tau^H] \leq 1$, so that the second term above must vanish in the limit.

We are left with:

$$\gamma_d = - \lim_{n \rightarrow \infty} \frac{1}{2n} \ln \mu_{\max}[\tau\tau^H]$$

or recalling the definition of singular values

$$\gamma_d = - \lim_{n \rightarrow \infty} \frac{1}{n} \ln \sigma_{\max}(\tau) \quad (5.4)$$

As a byproduct of this analysis we can find all d of the Lyapunov exponents of V_n in terms of the transmission matrix τ . First recall from Section 5.2.1

$$\gamma_j = \lim_{n \rightarrow \infty} \frac{1}{2n} \ln(\lambda_j) \quad 1 \leq j \leq d$$

and from earlier in this section

$$\begin{aligned}\lambda_j + \frac{1}{\lambda_j} &= \mu_j[4(\tau\tau^H)^{-1} - 2\mathbf{I}] \\ &= 4\mu_j[(\tau\tau^H)^{-1}] - 2\end{aligned}$$

Note here that

$$\mu_j[(\tau\tau^H)^{-1}] = \frac{1}{\mu_{d-j+1}[\tau\tau^H]} \quad 1 \leq j \leq d$$

So taking limits on both sides and discarding vanishing terms we find:

$$\gamma_j = - \lim_{n \rightarrow \infty} \frac{1}{n} \ln \sigma_{d-j+1}(\tau)$$

This reproduces our result for γ_d , and also tells us that

$$\begin{aligned}\gamma_1 &= - \lim_{n \rightarrow \infty} \frac{1}{n} \ln \sigma_d(\tau) \\ &= - \lim_{n \rightarrow \infty} \frac{1}{n} \ln \sigma_{\min}(\tau)\end{aligned}$$

Now we return to examining γ_d and proceed to show that in addition to Equation 5.4

$$\gamma_d = - \lim_{n \rightarrow \infty} \frac{1}{n} \ln[tr(rr^H)]^{\frac{1}{d}}$$

First examine

$$- \lim_{n \rightarrow \infty} \frac{1}{2n} \ln tr(rr^H)$$

Take an eigenvector decomposition of the Hermitian matrix rr^H , and rewrite this as:

$$- \lim_{n \rightarrow \infty} \frac{1}{2n} \ln tr(U \text{diag}\{\mu_i\} U^H)$$

where U is a unitary matrix. Recalling that $tr(ABC) = tr(BCA)$ for compatible matrices we see that the above limit equals

$$- \lim_{n \rightarrow \infty} \frac{1}{2n} \ln tr(\text{diag}\{\mu_i\})$$

or

$$- \lim_{n \rightarrow \infty} \frac{1}{2n} \ln(\mu_1 + \dots + \mu_d)$$

or

$$- \lim_{n \rightarrow \infty} \frac{1}{2n} \ln(\mu_1 [1 + \frac{\mu_2}{\mu_1} + \dots + \frac{\mu_d}{\mu_1}])$$

Recalling that $\mu_1 \geq \dots \geq \mu_d > 0$, we have that the term in brackets is finite and bounded below by 1 and above by d , so when taking the limit, we are left with

$$- \lim_{n \rightarrow \infty} \frac{1}{2n} \ln \mu_1 [rr^H]$$

which is precisely equal to

$$- \lim_{n \rightarrow \infty} \frac{1}{n} \ln \sigma_{\max}(r) = \gamma_d$$

Thus we have indeed shown that

$$\gamma_d = - \lim_{n \rightarrow \infty} \frac{1}{n} \ln[tr(rr^H)]^{\frac{1}{d}} \quad (5.5)$$

One final simplification in our result is now possible. Starting with

$$\gamma_d = - \lim_{n \rightarrow \infty} \frac{1}{2n} \ln[tr(rr^H)]$$

let r_{ij} be the ij th element of the matrix r . Now (this is the square of the Frobenius norm of r)

$$\begin{aligned} \text{tr}(rr^H) &= \sum_{i=1}^d \sum_{j=1}^d |r_{ij}|^2 \\ &= |r_{11}|^2 + |r_{12}|^2 + \cdots + |r_{dd}|^2 \end{aligned}$$

We have that for one element of r , $|r_{ij}| \geq |r_{kl}|$, $k \neq i, l \neq j$, and we will denote it $|r_{ij}|_{\max}$. So

$$\text{tr}(rr^H) = |r_{ij}|_{\max}^2 \left(\sum_{i=1}^d \sum_{j=1}^d \frac{|r_{ij}|^2}{|r_{ij}|_{\max}^2} \right)$$

So

$$\gamma_d = - \lim_{n \rightarrow \infty} \frac{1}{2n} \ln \left\{ |r_{ij}|_{\max}^2 \left(\sum_i \sum_j \frac{|r_{ij}|^2}{|r_{ij}|_{\max}^2} \right) \right\}$$

and because the term in parentheses is finite and bounded below by 1 and above by d^2 , it vanishes after taking the limit, so we are left with

$$\gamma_d = - \lim_{n \rightarrow \infty} \frac{1}{2n} \ln |r_{ij}|_{\max}^2$$

or

$$\gamma_d = - \lim_{n \rightarrow \infty} \frac{1}{n} \ln |r_{ij}|_{\max} \quad (5.6)$$

This result tells us that the wave that propagates the farthest is governed by the transmission coefficient with the largest absolute value, which makes perfect sense. Notice that our result agrees with our localization result in the mono-coupled case where the matrix r is a scalar.

Now we are in a position to compare our result with three others that have appeared in the literature. In [Anderson 81], a scaling variable, mentioned in Chapter 1, is derived for multiwave systems in which Anderson tried to mimic the techniques which accurately gave him the scaling variable for mono-coupled disordered periodic systems [Anderson et al 80]. In addition to assuming that the scattering matrix was symmetric and unitary, he also assumed, in order to make the problem tractable from his point of

view, that certain channels in what he called a back reflection matrix were independent. In the paper he acknowledged that this latter assumption was not correct, but guessed it would have little impact on the final result. The scaling variable he arrived at was

$$\rho_c \ln(1 + \frac{1}{\rho_c \text{tr}[\tau\tau^H]})$$

with

$$\rho_c = 2, \frac{1}{\text{tr}[\tau\tau^H]} \rightarrow 0$$

$$\rho_c = 1.764, \frac{1}{\text{tr}[\tau\tau^H]} \rightarrow +\infty$$

For us $\frac{1}{\text{tr}[\tau\tau^H]} \rightarrow +\infty$ is the relevant limit. An analysis of our results indicates that we would expect the scaling variable to be

$$\ln(\frac{1}{\text{tr}[\tau\tau^H]})$$

Apparently the difference between the results is a consequence of Anderson's extra assumptions on channel independence. Note also that Anderson's result does not reduce down to the scaling variable in the mono-coupled case.

A much more direct comparison of results can be made with [Imry 86]. Imry made exactly the same assumptions about the wave transfer matrix as we have, and, through the work of Pichard, was aware of Oseledets' theorem. In his paper, Imry makes some heuristic arguments concerning $\text{tr}(\tau\tau^H)$ leading to the inverse localization length, $\frac{1}{\xi}$, (the same thing as our multiwave localization factor) being

$$\frac{1}{\xi} = - \lim_{n \rightarrow \infty} \frac{1}{n} \ln \text{tr}(\tau\tau^H)$$

The problem with this result is the missing square root over $\text{tr}(\tau\tau^H)$.

Finally we compare our result with [Johnston and Kunz 83-1] who relied rigorously on theories of products of random matrices. In their paper, Johnston and Kunz used the work of [Tutubalin 68, Virster 70], though they were aware of Pichard's work. Arguing

as we have, that the smallest Lyapunov exponent of a random symplectic matrix product is the localization factor for long multiwave systems, they derived the localization factor as:

$$\gamma_d = - \lim_{n \rightarrow \infty} \frac{1}{n} \ln |r_{ij}| \quad \text{for any } r_{ij}$$

This result differs from the one presented in Equation 5.6 in that our γ_d involves only the limit of $|r_{ij}|_{\max}$. To evaluate whether the result of [Johnston and Kunz 83-1] makes sense, we see if it gives us the correct answer for the undisordered or perfectly periodic system. For a perfectly periodic system with n bays, the transmission matrix, r , would look like:

$$r = \begin{bmatrix} e^{-ik_1 n} & & \\ & \ddots & \\ & & e^{-ik_d n} \end{bmatrix}$$

with all the off-diagonal terms zero. In [Johnston and Kunz 83-1] the claim is that we can take any element of r and get the proper localization factor. Yet if we choose any off-diagonal term we get the following absurd result:

$$\begin{aligned} \gamma_d &= - \lim_{n \rightarrow \infty} \frac{1}{n} \ln(0) \\ &= - \lim_{n \rightarrow \infty} \frac{-\infty}{n} \end{aligned}$$

This is in contrast to Equation 5.6 which takes the element of r with the maximum absolute value, namely, $|e^{-ik_j}| = 1$, from which we find

$$\gamma_d = - \lim_{n \rightarrow \infty} \frac{1}{n} \ln(1) = 0$$

This is precisely the result for perfectly periodic systems, i.e., there is no localization.

Note that all three of our localization results, Equations 5.4, 5.5 and 5.6 only hold as $n \rightarrow \infty$. Indeed all three must give equivalent answers in the limit. However, if we were to evaluate each of the three expressions for finite n we would likely find three different answers. This is a consequence of

$$|r_{ij}|_{\max} \leq \sigma_{\max}(r) < \sqrt{\text{tr}(rr^H)}$$

Clearly, when we are averaging one or a finite number of bays over an ensemble, $|r_{ij}|_{\max}$ appears to be the variable to average, otherwise we would mispredict the value for γ_d . Indeed, we conjecture that by averaging $-\ln|r_{ij}|_{\max}$ over a large ensemble of wave transfer matrices we could compute an accurate estimate of γ_d . This observation could lead to a method which would bypass the necessity of multiplying as many as 10,000, 50,000 or even 60,000 matrices together as has been done in [Pichard and Sarma 81-1, Johnston and Kunz 83-2, García et al 86].

However, before pursuing some complicated numerical analysis, we should first try to discover an analytical solution for γ_d with which to compare any numerical result. This is the subject of the next section.

5.4 Calculation of the Multiwave Localization Factor Via p-Forms

Similar to our approach in Chapter 3, we need to examine the analytical tools to actually calculate γ_d , the multiwave localization factor. For mono-coupled systems we had Equation 3.3 that gave a closed form solution for γ . We will discuss the analogous equation for γ_d in this section.

The mathematics for calculating Lyapunov exponents for products of random $2d \times 2d$ matrices becomes increasingly complex compared to the case of 2×2 matrices. In particular, we will be making use of p-forms. The recent book, [Bougerol and Lacroix 85] is an excellent reference on the mathematics necessary to handle multiwave disordered systems. For completeness the relevant theorem is as follows and is adapted from [Bougerol and Lacroix 85, page 89]

Theorem 3 (Calculation of Lyapunov Exponents) *Let W_1, W_2, \dots, W_n be in-*

dependent identically distributed $2d \times 2d$ random symplectic matrices with distribution μ and let p be an integer in $\{1, \dots, d\}$. Suppose that \mathcal{W}_μ , the smallest closed semigroup in $Gl(d, C)$ containing the support of μ , is p -contracting and L_p -strongly irreducible and that $E[\ln \|\mathbf{W}_1\|]$ is finite. Then the following hold

$$\gamma_p > \gamma_{p+1}$$

For any nonzero \mathbf{z}_0 in L_p ,

$$\lim_{n \rightarrow \infty} \frac{1}{n} \ln \|\Lambda^p \mathbf{W}_n \cdots \mathbf{W}_1 \mathbf{z}_0\| = \sum_{j=1}^p \gamma_j$$

and

$$\lim_{n \rightarrow \infty} \frac{1}{n} \ln \|\Lambda^p \mathbf{W}_n \cdots \mathbf{W}_1\| = \sum_{j=1}^p \gamma_j$$

There exists a unique μ -invariant probability distribution ν_p on

$$P(L_p) = \{\bar{\mathbf{z}} \in P(\Lambda^p R^{2d}); \mathbf{z} \in L_p\}$$

then

$$\sum_{j=1}^p \gamma_j = \int \int \ln \|\Lambda^p \mathbf{W} \bar{\mathbf{z}}\| d\mu(\mathbf{W}) d\nu_p(\bar{\mathbf{z}}) \quad (5.7)$$

Clearly to calculate γ_d we do it inductively. Namely, we have to calculate from Equation 5.7

$$\gamma_1 + \cdots + \gamma_d$$

then

$$\gamma_1 + \cdots + \gamma_{d-1}$$

from which we can obtain γ_d .

To illustrate the increased complexity of this multiwave localization problem we note that for a 4×4 matrix, \mathbf{W} , we have that $\Lambda^1 \mathbf{W}$ is just the matrix \mathbf{W} while $\Lambda^2 \mathbf{W}$ is a 6×6 matrix in an appropriate basis. This also means, when $p = 2$ in the above,

that \mathbf{z} will be a 6×1 vector. We should also note that the norms of these p-forms take a particularly simple form:

$$\|\Lambda^p \mathbf{W}\| = \sigma_1 \sigma_2 \cdots \sigma_p$$

where σ_i is the i th singular value of the matrix \mathbf{W} .

The path of the research seems clear. First the conditions of Theorem 3 need to be clarified to show that they clearly apply to transfer matrices that would occur in practice. Then an approach similar to that in Chapter 3 could be taken. Namely, we could perform a Taylor series expansion on the relevant terms of Equation 5.7 in order to get some analytical approximation for γ_d to first order in the variance of the disordered parameter. Then we would be in position to calculate localization factors numerically and have some analytical results with which to compare them.

5.5 Summary

In this chapter we have tackled the very difficult problem of localization in one-dimensional multiwave disordered periodic systems. The multiwave nature increases the complexity of analysis considerably compared to the localization problem in mono-coupled periodic structures. Our first task was to clarify the assumptions on our wave transfer matrices, after which we appealed to the theorem of Oseledets to understand the asymptotic behavior of products of random multiwave matrices. We noted that the theorem of Furstenberg was of little use here. The principal contribution of the chapter was the derivation of the multiwave localization factor (the d th Lyapunov exponent) as a function of the transmission matrix, for the disordered system. This issue has been addressed, but in our view unsatisfactorily, by a number of solid state physicists. Thus our results and insights should have some impact in the solid state field where traditionally most of the localization work has been done. In addition, the recent work of [Pichard and Sarma 81-1, Pichard and Sarma 81-2] indicates that

our result may have some impact in clarifying the localization mechanism in two- and three-dimensional disordered systems. Finally, we pointed out the tools that can be used to analytically calculate the localization factor.

Chapter 6

Conclusions and Recommendations

6.1 Conclusions

In this thesis we have explored the effects disorder has on the transmission properties of normally perfect periodic structures. Disorder is known to spatially localize the mode shapes of disordered periodic systems, so the term localization is used to describe the various dynamic manifestations of disorder. The localization phenomenon has been most extensively studied in the context of solid state physics and only recently with disordered systems of interest to the engineer in mind.

This thesis has provided the tools with which engineers can decide the importance of the dynamic effects of disorder on mono-coupled periodic structures. The first principal contribution was the elucidation of random transfer matrix techniques to model disordered systems and calculate transmission properties. This included a discussion of the important transformation to wave transfer matrix form and the relevance of the theorems of Furstenberg and Oseledec to the one-dimensional localization problem.

The second principal contribution was the calculation of localization effects as a

function of frequency for three periodic models of interest to the structural dynamicist. In most instances the localization effects were found to be strongest near the stopbands of the normally perfectly periodic structures. This result indicates that care must be taken when doing experimental work at frequencies near the stopbands of what are ostensibly periodic structures. Effects of length disorder in the bays were quite pronounced, even at high frequency.

The third principal contribution was the derivation of the localization factor for multiwave one-dimensional systems as a function of the transmission matrix.

6.2 Recommendations

The localization phenomenon is a fascinating and difficult problem to tackle. This thesis has presented some very useful tools that have allowed us to make some important progress in understanding localization effects. The primary recommendation is to continue work with random transfer matrices and theories on products of random matrices to gain further insights about the phenomenon. The tools we have discussed in this thesis have immediate applicability to many other fields of engineering that involve disordered periodic systems, as well as the field of solid state physics where localization work is traditionally done.

The analytical formula for calculating the localization factor to first order in the variance could be extended to include higher order effects. This would allow us to predict analytically the transmission behavior for highly disordered systems at frequencies where the localization phenomenon is most strongly felt. Possibly some asymptotic analysis near the stopbands would be another alternative to pinning down the transmission behavior there analytically. The issue of localization in one-dimensional systems which include damping should be addressed as well as the manifestation of the phenomenon in finitely long structures with fixed boundary conditions.

The localization phenomenon in multiwave systems with the evanescent waves included should be studied more rigorously. This, however, will require a better understanding of the wave transfer matrices in these situations, for which there is a dearth of information in the literature. Indeed, we observe that there is a need for a comprehensive study of the interrelationship of admittance, impedance, real transfer, scattering and wave transfer matrices for both periodic and disordered periodic multiwave systems.

In Chapter 5 we have presented the background that could lead to an analytical formula, analogous to the single wave case, for localization effects in multiwave systems. This is a very important area of research needed to understand localization effects in multiwave systems. Also, as [Pichard and André 86] have pointed out, the one-dimensional multiwave analysis could prove to be the key to understanding the localization phenomenon in two- and three-dimensional systems. Localization of classical waves in two-dimensional systems has recently been studied by [Flesia et al 87]. Only after the analytical issues have been explored should we proceed to examine the numerical issues in multiwave one-dimensional analysis and possible extensions to higher dimensions. The results in Chapter 5 could potentially simplify the numerical computations considerably by eliminating the need to multiply huge chains of matrices.

While we think that the transfer matrix formalism is a powerful tool to study the localization phenomenon, we also feel that the Herbert-Jones-Thouless formula should be explored to see if it can be easily applied to structural dynamic systems. Some efforts in this direction have already been made by [Hodges and Woodhouse 83]. Also [Johnston and Kunz 83-2] have developed the corresponding formula for multiwave systems.

Other important issues continue to be explored in the literature. Systems with correlated disorder among the bays, as opposed to the usual case of independent identically distributed random variables, have been studied by [Johnston and Kramer 86].

The impact of system nonlinearities on localization effects has been addressed by [Doucot and Rammal 87].¹ In the nonlinear case the transfer matrix formalism will be of little use.

An intentionally disordered periodic system could be valuable for the attenuation of propagating disturbances. However, if active control is performed on the same structure, the fact that the mode shapes are spatially localized may complicate the control effectiveness of actuators that are placed at locations where mode shapes have little amplitude.

Some experimental structural dynamic/acoustical verification of localization has been reported by [Hodges and Woodhouse 83, Pierre et al 86, Dépollier et al 86] and by [Hyde and Sybert 87], where the latter work was inconclusive. Further experimental work would clarify our analytical and numerical thinking. These experiments would have to be done with care. Initially, the dynamic characteristics of the perfectly periodic system should be understood experimentally. Clearly, the effects of damping and boundary conditions need to be taken into account when comparisons are made with our analytical results. In an actual experiment on a disordered system, the measurements would have to be done over many realizations in order that the results could be compared with the theoretical prediction. The experimental techniques of [Hodges and Woodhouse 83, Roy and Plunkett 86] seem particularly attractive. In these cases a disturbance was inserted into one end of the system and the effects were measured at the other end. The beam with cantilevers of [Roy and Plunkett 86] was a perfectly periodic system but could be easily randomized and would provide an excellent structure to verify multiwave localization effects.

The study of the literature has provided invaluable insights into the localization phenomenon. Future researchers should continue to avail themselves of the work done on localization in many fields in order that maximum progress can be achieved in

¹In solid state physics this is equivalent to considering electron-electron interactions.

understanding the effects of disorder.

Bibliography

- [Abrahams and Stephen 80] Abrahams, E. and Stephen, M. J., "Resistance Fluctuations in Disordered One-Dimensional Conductors," *Journal of Physics C: Solid State Physics*, Vol. 13, 1980, pp. L377-L389.
- [Akkermans and Maynard 84] Akkermans, E. and Maynard, R., "Chains of Random Impedances," *Journal de Physique*, Vol. 45, No. 9, September 1984, pp. 1549-1557.
- [AMS 86] Cohen, J. E., Kesten, H. and Newman, C. M., eds., *Random Matrices and Their Applications*, Contemporary Mathematics, Vol. 50, American Mathematical Society, Providence, 1986.
- [Andereck and Abrahams 80] Andereck, B. S. and Abrahams, E., "Numerical Studies of Inverse Localization Length in One Dimension," *Journal of Physics C: Solid State Physics*, Vol. 13, 1980, pp. L383-L389.
- [Anderson 58] Anderson, P. W., "Absence of Diffusion in Certain Random Lattices," *Physical Review*, Vol. 109, 1958.
- [Anderson 78] Anderson, P. W., "Localized Moments and Localized States," *Review of Modern Physics*, Vol. 50, No. 2, April

1978, pp. 191-201.

- [Anderson 81] Anderson, P. W., "New Method for Scaling Theory of Localization. II. Multichannel Theory of a "Wire" and Possible Extension to Higher Dimensionality," *Physical Review B*, Vol. 23 No. 10, May 15, 1981.
- [Anderson 85] Anderson, P. W., "The Question of Classical Localization. Theory of White Paint?," *Philosophical Magazine B*, Vol. 52, No. 3, 1985, pp. 505-509.
- [Anderson et al 80] Anderson, P. W., Thouless, D. J., Abrahams, E. and Fisher, D. S., "New Method for a Scaling Theory of Localization," *Physical Review B*, Vol. 22, No. 8, October 15, 1980.
- [Baluni and Willemsen 85] Baluni, V. and Willemsen, J., "Transmission of Acoustic Waves in a Random Layered Medium," *Physical Review A*, Vol. 31, No. 5, May 1985.
- [Bansal 80] Bansal, A. S., "Free-wave Propagation Through Combinations of Periodic and Disordered Systems," *Journal of the Acoustical Society of America*, Vol. 67, No. 2, February, 1980, pp. 377-389.
- [Bendiksen 86] Bendiksen, O. O., "Mode Localization Phenomena in Large Space Structures," *Proceedings, 27th AIAA/ASME/ASCE/AHS Structures, Structural Dynamics and Materials Conference*, San Antonio, TX, May 19-21, 1986.
- [Bendiksen and Valero 87] Bendiksen, O. O. and Valero, N., "Localization of Natural Modes of Vibration in Bladed Disks," *Proceedings,*

ASME Gas Turbine Conferences and Exhibition, Anaheim, CA, May 31 - June 4, 1987.

- [Benettin and Galgani 79] Benettin, G. and Galgani, L., "Ljapunov Characteristic Exponents and Stochasticity," *Intrinsic Stochasticity in Plasmas*, Laval, G. and Gresillon, D., editors, Editions de Physique, Orsay, 1979.
- [Bernelli et al 87] Bernelli Zazzera, F., Ercoli Finzi, A. and Mantegazza, P., "Modular Large Space Structures Dynamic Modeling with Nonperfect Junctions," Proceedings, Sixth VPI&SU/AIAA Symposium on Dynamics and Control of Large Space Structures, Blacksburg, VA, June 29 - July 1, 1987.
- [Borland 63] Borland, R. E., "The Nature of Electronic States in Disordered One-Dimensional Systems," Proceedings of the Royal Society, Vol. A274, 1963, pp. 529-545.
- [Bouchaud and Daoud 86] Bouchaud, E. and Daoud, M., "Reflection of Light by a Random Layered System," *Journal de Physique*, Vol. 47, No. 9, September 1986, pp. 1467-1475.
- [Bougerol and Lacroix 85] Bougerol, P. and Lacroix, J., *Products of Random Matrices with Applications to Schrödinger Operators*, Birkhäuser, Boston, 1985.
- [Brillouin 46] Brillouin, L., *Wave Propagation in Periodic Structures*, Dover Publications, Inc., New York, 1946.
- [Büttiker et al 85] Büttiker, M., Imry, Y., Landauer, R. and Pinhas, S., "Generalized Many-Channel Conductance Formula with Application to Small Rings," *Physical Review B*, Vol. 31, No. 10, May 15, 1985, pp. 6207-6215.

- [Carlin and Giordano 64] Carlin, H. J. and Giordano, A. B., *Network Theory: An Introduction to Reciprocal and Nonreciprocal Circuits*, Prentice-Hall Inc., Englewood Cliffs, NJ, 1964.
- [Chow and Keller 72] Chow, P.-L. and Keller, J. B., "Wave Propagation in a Random Lattice. I," *Journal of Mathematical Physics* Vol. 13, No. 9, September 1972. pp. 1404-1411.
- [Cornwell and Bendiksen 87] Cornwell, P. J. and Bendiksen, O. O., "Localization of Vibrations in Large Space Reflectors," *Proceedings, AIAA Dynamic Specialists Conference*, Monterey, CA, April 3-10, 1987.
- [Covault 86] Covault, C., "Launch Capacity, EVA Concerns Force Space Station Redesign," *Aviation Week and Space Technology*, Vol. 125, No. 3, July 21, 1986.
- [Cremer et al 73] Cremer, L., Heckl, M. and Ungar, E. E., *Structure Borne Sound*, Springer-Verlag, New York, 1973.
- [Czycholl and Kramer 79] Czycholl, G. and Kramer, B., "Nonvanishing Zero Temperature Static Conductivity in One Dimensional Disordered Systems," *Solid State Communications*, Vol. 32, 1979, pp. 945-951.
- [Dean and Bacon 63] Dean, P. and Bacon, M. D., "The Nature of Vibrational Modes in Disordered Systems," *Proceedings of the Physical Society*, Vol. 81, 1963.
- [Dépollier et al 86] Dépollier, C., Kergomard, J. and Laloe, F., "Localisation d'Anderson des ondes dans les réseaux acoustiques unidimensionnels aléatoires," *Annales de Physiques*, Vol. 11, No. 5, October 1986, pp. 457-492.

- [Doucot and Rammal 87] Doucot, B. and Rammal, R., "Invariant-imbedding Approach to Localization. II. Non-linear Random Media," *Journal de Physique*, Vol. 48, No. 4, April 1987, pp. 527-546.
- [Dyson 53] Dyson, F. J., "The Dynamics of a Disordered Linear Chain," *The Physical Review*, Vol. 92, No. 6, Dec. 15, 1953, pp. 1331-1338.
- [Eatwell 83] Eatwell, G. P., "Free-Wave Propagation in an Irregularly Stiffened, Fluid-Loaded Plate," *Journal of Sound and Vibration*, Vol. 88, No. 4, 1983, pp. 507-522.
- [Elachi 76] Elachi, C., "Waves in Active and Passive Periodic Structures: A Review," *Proceedings of the IEEE*, Vol. 64, No. 12, December 1976, pp. 1666-1698.
- [Engels 80] Engels, R. C., "Response of Infinite Periodic Structures," *Journal of Sound and Vibration*, Vol. 69, No. 2, 1980, pp. 181-197.
- [Erdős and Herndon 82] Erdős, P. and Herndon, R. C., "Theories of Electrons in One-Dimensional Disordered Systems," *Advances in Physics*, Vol. 31, No. 2, March/April 1982, pp. 65-163.
- [Faulkner and Hong 85] Faulkner, M. G. and Hong, D. P., "Free Vibrations of a Mono-Coupled Periodic System," *Journal of Sound and Vibration*, Vol. 99, No. 1, 1985.
- [Flesia et al 87] Flesia, C., Johnston, R. and Kunz, H., "Strong Localisation of Classical Waves: A Numerical Study," *Europhysics Letters*, Vol. 3, No. 4, February 15, 1987, pp. 497-502.

- [von Flotow 82] von Flotow, A., "Traveling Wave Effects in Large Space Structures," NASA Workshop on Applications of Distributed System Theory to the Control of Large Space Structures, Jet Propulsion Laboratory, July 14-16, 1982.
- [Furstenberg 63] Furstenberg, H., "Noncommuting Random Products," Transactions of the American Mathematical Society, Vol. 108, No. 3, September 1963.
- [García et al 86] García, M. E., Llois, A. M., Balseiro, C. A. and Weissmann, M., "Transport Properties of One-Dimensional, Disordered Two-Band Systems," Journal of Physics C: Solid State Physics, Vol. 19, 1986, pp. 6053-6061.
- [Goda 82] Goda, M., "Localization of Eigenstates in One-Dimensional Disordered Systems," Supplement of the Progress of Theoretical Physics, No. 72, 1982, pp. 232-246.
- [Hammersley and Handscomb 64] Hammersley, J. M. and Handscomb, D. C., *Monte Carlo Methods*, Methuen & Co., 1964.
- [van Hemmen 82] van Hemmen, J. L., "On Thermodynamic Observables and the Anderson Model," Journal of Physics A: Mathematical and General, Vol. 15, 1982, pp. 3891-3897.
- [Herbert and Jones 71] Herbert, D. C. and Jones, R., "Localized States in Disordered Systems," Journal of Physics C: Solid State Physics, Vol. 4, 1971, pp. 1145-1161.
- [Hlawiczka 65] Hlawiczka, P., *Matrix Algebra for Electronic Engineers* Hayden Book Co., New York, 1965.

- [Hodges 82] Hodges, C. H., "Confinement of Vibration by Structural Irregularity," *Journal of Sound and Vibration*, Vol. 82, No. 3, 1982.
- [Hodges and Woodhouse 83] Hodges, C. H. and Woodhouse, J., "Vibration Isolation from Irregularity in a Nearly Periodic Structure: Theory and Measurements," *Journal of the Acoustical Society of America*, Vol. 74, No. 3, September 1983.
- [Hori 66] Hori, J., *Spectral Properties of Disordered Chains and Lattices*, Pergamon Press, Oxford, 1968.
- [Howe 72] Howe, M. S., "Multiple Scattering of Bending Waves By Random Inhomogeneities," *Journal of Sound and Vibration*, Vol. 23, No. 3, 1972, pp. 279-290.
- [Hyde and Sybert 87] Hyde, T. and Sybert, C., 16.622 projects course experiment, Department of Aeronautics and Astronautics, MIT, April, 1987.
- [Ikeda and Matsumoto 86] Ikeda, K. and Matsumoto, K., "Study of a High-Dimensional Chaotic Attractor," *Journal of Statistical Physics*, Vol. 44, Nos. 5/6, 1986, pp. 955-983.
- [Imry 86] Imry, Y., "Active Transmission Channels and Universal Conductance Fluctuations," *Europhysics Letters*, Vol. 1, No. 5, March 1, 1986, pp. 249-256.
- [Ishii 73] Ishii, K., "Localization of Eigenvalues and Transport Phenomena in the One-Dimensional Disordered System," *Supplement of the Progress of Theoretical Physics*, No. 53, 1973.

- [Johnston and Kramer 86] Johnston, R. and Kramer, B., "Localization in One Dimensional Correlated Random Potentials," *Zeitschrift Für Physics B - Condensed Matter*, Vol. 63, 1986, pp. 273-281.
- [Johnston and Kunz 83-1] Johnston, R. and Kunz, H., "The Conductance of a Disordered Wire," *Journal of Physics C: Solid State Physics*, Vol. 16, 1983, pp. 3895-3912.
- [Johnston and Kunz 83-2] Johnston, R. and Kunz, H., "A Method for Calculating the Localisation, with an Analysis of the Lloyd Model," *Journal of Physics C: Solid State Physics*, Vol. 16, 1983, pp. 4565-4580.
- [Kirkman and Pendry 84] Kirkman, P. P. and Pendry, J. B., "The Statistics of One-Dimensional Resistances," *Journal of Physics C: Solid State Physics*, Vol. 17, 1984, pp. 4327-4344.
- [Kissel 87] Kissel, G. J., "Localization in Disordered Periodic Structures," 28th AIAA/ASME/ASCE/AHS Structures, Structural Dynamics and Materials Conference, April 6-8, 1987, Monterey, CA.
- [Lambert and Thorpe 82] Lambert, C. J. and Thorpe, M. J., "Phase Averaging in One-Dimensional Random Systems," *Physical Review B*, Vol. 26, No. 8, October 15, 1982, pp. 4742-4744.
- [Lambert and Thorpe 83] Lambert, C. J. and Thorpe, M. J., "Random T-Matrix Approach to One-Dimensional Localization," *Physical Review B*, Vol. 27, No. 2, January 15, 1983, pp. 715-726.
- [Lee and Ramakrishnan 85] Lee, P. A. and Ramakrishnan, T. V., "Disordered Electronic Systems," *Reviews of Modern Physics*, Vol. 57, No. 2, April 1985, pp. 287-337.

- [Le Page 82] Le Page, E., Théorèmes Limites Pour les Produits de Matrices Aléatoires, *Probability Measures on Groups*, H. Heyer, editor, Lecture Notes in Mathematics, no. 928, 1982, Springer Verlag, Berlin, pp. 258-303.
- [Lin 76] Lin, Y. K., "Random Vibration of Periodic and Almost Periodic Structures," *Mechanics Today*, Vol. 3, 1976, pp. 93-124.
- [Matsuda and Ishii 70] Matsuda, H. and Ishii, K. "Localization of Normal Modes and Energy Transport in the Disordered Harmonic Chain," *Supplement of the Progress of Theoretical Physics*, No. 45, 1970.
- [McCoy and Wu 68] McCoy, B. M. and Wu, T. T., "Theory of a Two-Dimensional Ising Model with Random Impurities. I. Thermodynamics," *Physical Review*, Vol. 176, No. 2, 10 Dec. 1968.
- [Mead 70] Mead, D. J., "Free Wave Propagation in Periodically Supported, Infinite Beams," *Journal of Sound and Vibration*, Vol. 11, No. 2, 1970, pp. 181-197.
- [Mead 73] Mead, D. J., "A General Theory of Harmonic Wave Propagation in Linear Periodic Systems with Multiple Coupling," *Journal of Sound and Vibration*, Vol. 27, No. 2, 1973, pp. 235-260.
- [Mead 75-1] Mead, D. J., "Wave Propagation and Natural Modes in Periodic Systems: I. Mono-Coupled Systems," *Journal of Sound and Vibration*, Vol. 40, No. 1, 1975.
- [Mead 75-2] Mead, D. J., "Wave Propagation and Natural Modes in Periodic Systems: II. Multi-Coupled Systems With and

- Without Damping," *Journal of Sound Vibration*, Vol. 40, No. 1, 1975, pp. 19-39.
- [Mead 86] Mead, D. J., "A New Method of Analyzing Wave Propagation in Periodic Structures; Applications to Periodic Timoshenko Beams and Stiffened Plates," *Journal of Sound and Vibration*, Vol. 104, No. 1, 1986, pp. 9-27.
- [Miles 56] Miles, J., "Vibrations of Beams on Many Supports," *Journal Engineering Mechanics Division, Proceedings of the American Society of Civil Engineers*, January 1956, pp. 1-9.
- [Mott and Twose 61] Mott, N. F. and Twose, W. D., "The Theory of Impurity Conduction," *Advances in Physics*, Vol. 10, 1961, pp. 107-155.
- [Noble and Daniel 77] Noble, B. and Daniel, J. W., *Applied Linear Algebra*, second edition, Prentice Hall, Englewood Cliffs, NJ, 1977.
- [O'Connor 75] O'Connor, A. J., "A Central Limit Theorem for the Disordered Harmonic Chain," *Communications in Mathematical Physics*, Vol. 45, No. 1, 1975, pp. 63-77.
- [Omar and Schünemann 85] Omar, A. S. and Schünemann, K., "Transmission Matrix Representation of Finline Discontinuities," *IEEE Transactions on Microwave Theory and Techniques*, Vol. MTT-33, No. 9, September 1985, pp. 765-770.
- [Osawa and Kotera 66] Osawa, T. and Kotera, T., "The Scattering Matrix Method in the Linear Chain," *Supplement of the Progress of Theoretical Physics*, No. 36, 1966, pp. 120-137.

- [Oseledets 68] Oseledets, V. I., "A Multiplicative Ergodic Theorem," Transactions of the Moscow Mathematical Society, Vol. 19, 1968.
- [Pastawski et al 85] Pastawski, H. M., Slutzky, C. M. and Weisz, J. F., "Localization as a Breakdown of Extended States," Physical Review B, Vol. 32, No. 6, September 15, 1985, pp. 3642-3633.
- [Pastur 80] Pastur, L. A., "Spectral Properties of Disordered Systems in the One-Body Approximation," Communications in Mathematical Physics, Vol. 75, 1980, pp. 179-196.
- [Pestel and Leckie 63] Pestel, E. C. and Leckie, F. A., *Matrix Methods in Elastomechanics*, McGraw-Hill, 1963.
- [Pichard 86] Pichard, J. L., "The One-Dimensional Anderson Model: Scaling and Resonances Revisited," Journal of Physics C: Solid State Physics, Vol. 19, 1986, pp. 1519-1535.
- [Pichard and André 86] Pichard, J. L. and André, G., "Many-Channel Transmission: Large Volume Limit of the Distribution of Localization Lengths and One-Parameter Scaling," Europhysics Letters, Vol. 2, No. 6, September 15, 1986, pp. 477-486.
- [Pichard and Sarma 81-1] Pichard, J. L. and Sarma, G., "Finite Size Scaling Approach to Anderson Localisation," Journal of Physics C: Solid State Physics, Vol. 14, 1981, L127-L132.
- [Pichard and Sarma 81-2] Pichard, J. L. and Sarma, G., "Finite Size Scaling Approach to Anderson Localisation: II. Quantitative Analysis and New Results," Journal of Physics C: Solid State Physics, Vol. 14, 1981, L617-L625.

- [Pierre 87] Pierre, C., "Localized Free and Forced Vibrations of Nearly Periodic Disordered Structures," 28th AIAA/ASME/ASCE/AHS Structures, Structural Dynamics and Materials Conference, April 6-8, 1987, Monterey, CA.
- [Pierre and Dowell 87] Pierre, C. and Dowell, E. H., "Localization of Vibrations by Structural Irregularity," *Journal of Sound and Vibration*, Vol. 114, No. 3, May 8, 1987, pp. 549-564.
- [Pierre et al 86] Pierre, C., Tang, D. M. and Dowell, E. H., "Localized Vibrations of Disordered Multi-Span Beams: Theory and Experiment," 27th AIAA/ASME/ASCE/AHS Structures, Structural Dynamics and Materials Conference, May 19-21, 1986, San Antonio, TX.
- [Pincus 80] Pincus, M. J., "Strong Laws of Large Numbers for Products of Random Matrices," Department of Mathematics, MIT, Ph.D. Thesis, June 1980.
- [Redheffer 61] Redheffer, R., "Difference Equations and Functional Equations in Transmission-Line Theory," *Modern Mathematics for the Engineer*, second series, ed. Edwin F. Beckenbach, McGraw-Hill, New York, 1961, pp. 282-337.
- [Roy and Plunkett 86] Roy, A. K. and Plunkett, R., "Wave Attenuation in Periodic Structures," *Journal of Sound and Vibration*, Vol. 104, No. 3, 1986, pp. 395-410.
- [Rubin 84] Rubin, R. J., "Transport in a Disordered One-Dimensional System: A Fractal View," *Journal of Statistical Physics*, Vol. 36, Nos. 5/6, 1984, pp. 615-624.

- [Rubin 64] Rubin, S., "Transmission Matrices for Vibration and Their Relation to Admittance and Impedance," *Journal of Engineering for Industry* (Trans. of the ASME), February 1964, pp. 9-21.
- [Schmidt 57] Schmidt, H., "Disordered One-Dimensional Crystals," *Physical Review*, Vol. 105, no. 2, Jan. 15, 1957, pp. 425-441.
- [Sheng et al 86] Sheng, P., Zhang, Z.-Q., White, B. and Papanicolaou, G., "Multiple-Scattering Noise in One Dimension: Universality Through Localization-Length Scaling," *Physical Review Letters*, Vol. 57, No. 8, August 25, 1986, pp. 1000-1003.
- [Signorelli 87] Signorelli, J., "Wave Propagation in Periodic Truss Structures," S.M. Thesis, Department of Aeronautics and Astronautics, MIT, February, 1987.
- [Signorelli and von Flotow 87] Signorelli, J. and von Flotow, A. H., "Wave Propagation in Periodic Truss Structures," *Proceedings, AIAA Dynamics Specialists Conference*, Monterey, CA, April 9-10, 1987.
- [Slud 86] Slud, E., "Stability of Exponential Rate of Growth of Products of Random Matrices Under Local Random Perturbations," *Journal of the London Math. Society*, Vol. 33, No. 2, 1986, pp. 180-192.
- [Stone 83] Stone, A. D., "Localization and Low Temperature Transport in Disordered One-Dimensional Systems," Ph. D. Thesis, Department of Physics, MIT, January, 1983.

- [Stone et al 81] Stone, A. D., Joannopoulos, J. D. and Chadi, D. J., "Scaling Studies of the Resistance of the One-Dimensional Anderson Model with General Disorder," *Physical Review B*, Vol. 24, No. 10, Nov. 15, 1981, pp. 5583-5596.
- [Thouless 72] Thouless, D. J., "A Relation Between the Density of States and Range of Localization for One Dimensional Random Systems," *Journal of Physics C: Solid State Physics*, Vol. 5, 1972, pp. 77-81.
- [Toda 66] Toda, M., "One-Dimensional Dual Transformation," *Supplement of the Progress of Theoretical Physics*, No. 36, 1966, pp. 113-119.
- [Tutubalin 68] Tutubalin, V. N., "Approximation of Probability Measures in Variation and Products of Random Matrices," *Theory of Probability and Its Applications*, Vol. 13, No. 1, pp. 65-83, 1968.
- [Virster 70] Virster, A. D., "Central Limit Theorem for Semisimple Lie Groups," *Theory of Probability and Its Applications*, Vol. 15, No. 4, pp. 667-687, 1970.
- [Wenzel 83] Wenzel, A. R., "Supersaturation of Complex-Amplitude Fluctuations of Waves Propagating in a Random Medium," *Journal of the Acoustical Society of America*, Vol. 74, No. 3, September 1983, pp. 1021-1024.
- [Yang and Lin 75] Yang, J. N. and Lin, Y. K., "Frequency Response Functions of a Disordered Periodic Beam," *Journal of Sound and Vibration*, Vol. 38, No. 3, 1975, pp. 317-340.
- [Ziman 79] Ziman, J. M., *Models of Disorder*, Cambridge University Press, Cambridge, England, 1979.

Appendix A

Matrix and Group Properties

In this appendix we collect most of the matrix and group properties mentioned in the thesis. First we note that all of the matrices in the thesis will be of even dimension, $2d \times 2d$, where d ranges from 1 to some finite value. In addition, all matrices will be invertible and so they are elements of the group $GL(2d, C)$. Here the letter G stands for the word *general* which means that the matrix is invertible. The letter L stands for the word *linear*. The $2d$ inside the parentheses implies the matrix dimension is $2d \times 2d$, and C tells us that in general the matrix elements are complex. If we were restricting ourselves to matrices with only real entries, C would of course be replaced by R .

Frequently we will make use of matrices which have unit determinant; these matrices are elements of $SL(2d, C)$. The letter S stands for the word *special* which means that the matrix has determinant equal to one.

Some of the more familiar matrices we will use are unitary matrices, which satisfy

$$\mathbf{W}^H \mathbf{W} = \mathbf{W} \mathbf{W}^H = \mathbf{I}$$

Note that unitary matrices are elements of $SU(2d)$. Symmetric matrices satisfy

$$\mathbf{W}^T = \mathbf{W}$$

even if they have complex entries, while Hermitian matrices satisfy

$$W^H = W$$

The symplectic (Sp) matrix group will be frequently encountered in the thesis. Symplectic matrices are always of even dimension and their group is identified as $Sp(d, C)$.

A matrix W is symplectic if

$$W^T J W = J$$

where

$$J = \begin{bmatrix} 0 & I \\ -I & 0 \end{bmatrix}$$

where I is $d \times d$. Note that we take a transpose even though W is a complex matrix.

The inverse of a symplectic matrix is easy to find:

$$W^{-1} = -J W^T J$$

An important property of symplectic matrices is that their eigenvalues occur in reciprocal pairs, λ and $\frac{1}{\lambda}$ [Bougerol and Lacroix 85]. It is also not difficult to prove that any 2×2 matrix with unit determinant is automatically symplectic. This tells us that $SL(2, C) = Sp(1, C)$.

The special unitary group, $SU(d, d)$ will be met in the thesis. A matrix W is an element of $SU(d, d)$ if

$$W^H \Delta W = \Delta$$

where

$$\Delta = \begin{bmatrix} I & 0 \\ 0 & -I \end{bmatrix}$$

where again I is $d \times d$. The 2×2 matrices which are elements of $SU(1, 1)$ are of the form

$$\begin{bmatrix} a & b \\ b^* & a^* \end{bmatrix}$$

This matrix is in the so-called Cayley form [Hori 68].

We will make use of matrix singular values in the thesis. Any reader not already familiar with singular values and the singular value decomposition of a matrix is encouraged to consult [Noble and Daniel 77]. The singular values, σ_i , of a complex $2d \times 2d$ invertible matrix W are

$$\sigma_i(W) = \{\lambda_i(W^H W)\}^{\frac{1}{2}} \quad i = 1, \dots, 2d$$

where we assume that the σ_i are ordered such that $\sigma_i \geq \sigma_{i+1}$. Note that the singular values of a symplectic matrix will occur in reciprocal pairs σ and $\frac{1}{\sigma}$.

The maximum singular value, $\sigma_{\max}(W)$ coincides with the spectral norm of a matrix:

$$\sigma_{\max}(W) = \max_{z \neq 0} \frac{\|Wz\|_2}{\|z\|_2} = \|W\|_2$$

where $\|z\|_2$ is the usual Euclidean length of the vector z .

Another matrix norm that is useful is the Frobenius (sometimes called Euclidean) norm:

$$\begin{aligned} \|W\|_F &= \{tr(W^H W)\}^{\frac{1}{2}} \\ &= \left\{ \sum_{i=1}^d \sum_{j=1}^d |w_{ij}|^2 \right\}^{\frac{1}{2}} \end{aligned}$$

Appendix B

Derivation of Mono-Coupled Wave Transfer Matrices

In this appendix we show how the wave transfer matrix, W_j of a bay (ordered or disordered) is calculated for frequencies in the passbands of the normally periodic system. In terms of the left and right traveling wave amplitudes, \vec{A} and \vec{B} , we have:

$$\begin{bmatrix} \vec{A}_j \\ \vec{B}_j \end{bmatrix} = W_j \begin{bmatrix} \vec{A}_{j-1} \\ \vec{B}_{j-1} \end{bmatrix}$$

where

$$W_j = \begin{bmatrix} \frac{1}{t_j} & -\frac{r_j}{t_j} \\ -\frac{r_j}{t_j} & \frac{1}{t_j} \end{bmatrix}$$

The approach is to express our traveling wave amplitudes first in terms of a state vector involving generalized displacements, then to express the wave amplitudes in terms of a state vector which includes generalized displacements and generalized forces. This latter relationship is what we desire because all of our real transfer matrices involve

a state vector which includes generalized displacements and forces, namely,

$$\begin{bmatrix} u_j \\ f_j \end{bmatrix} = T_j \begin{bmatrix} u_{j-1} \\ f_{j-1} \end{bmatrix} \quad (\text{B.1})$$

where

$$T_j = \begin{bmatrix} T_{11} & T_{12} \\ T_{21} & T_{22} \end{bmatrix}$$

and where u_j is a generalized displacement and f_j is a generalized force. Note that u_j and f_j may be nondimensional. When u_j is nondimensional, then the wave amplitudes will be nondimensional as well. Again T_j is the transfer matrix for the periodic or disordered system.

The generalized displacements of the perfectly periodic system can be expressed in terms of the wave amplitudes via

$$\begin{bmatrix} u_j \\ u_{j-1} \end{bmatrix} = Q \begin{bmatrix} A_j \\ B_j \end{bmatrix}$$

where

$$Q = \begin{bmatrix} 1 & 1 \\ e^{-ik} & e^{ik} \end{bmatrix}$$

Note that k is the wave number of the perfectly periodic system.

Now from B.1 we find

$$\begin{bmatrix} u_j \\ f_j \end{bmatrix} = V \begin{bmatrix} u_j \\ u_{j-1} \end{bmatrix}$$

where

$$V = \begin{bmatrix} 1 & 0 \\ T_{22}T_{12}^{-1} & T_{21} - T_{22}T_{12}^{-1}T_{11} \end{bmatrix}$$

So now we find

$$\begin{bmatrix} u_j \\ f_j \end{bmatrix} = X \begin{bmatrix} A_j \\ B_j \end{bmatrix} \quad (\text{B.2})$$

where

$$X = VQ$$

Equations B.1 and B.2 imply

$$\begin{bmatrix} A_j \\ B_j \end{bmatrix} = \mathbf{X}^{-1} \mathbf{T}_j \mathbf{X} \begin{bmatrix} A_{j-1} \\ B_{j-1} \end{bmatrix}$$

So the wave transfer matrix for a single bay is

$$\mathbf{W}_j = \mathbf{X}^{-1} \mathbf{T}_j \mathbf{X} \quad (\text{B.3})$$

Note that we have used the perfectly periodic wave basis to derive our wave transfer matrix, whether the real transfer matrix is random or not. The columns of the matrix \mathbf{X} are the eigenvectors of the transfer matrix of the perfectly periodic system. When the transfer matrices are random, the eigenvector matrix will be that for the *average* transfer matrix. So for the perfectly periodic system in the passband the wave transfer matrix looks like

$$\mathbf{W}_j = \begin{bmatrix} e^{ik} & 0 \\ 0 & e^{-ik} \end{bmatrix}$$

while in general

$$\mathbf{W}_j = \begin{bmatrix} \frac{1}{t_j} & -\frac{r_j}{t_j} \\ -\frac{r_j^*}{t_j} & \frac{1}{t_j} \end{bmatrix}$$

Note that both matrices are elements of $SU(1,1)$.

Finally, we note that $\frac{1}{t_j}$ can be shown to be invariant with respect to the scaling of the eigenvector similarity transformation used in Equation B.3, while $\frac{r_j}{t_j}$ will be off by at most a magnitude and a phase factor. Using the eigenvector transformation \mathbf{X} defined above, though, we are guaranteed to get exactly the wave transfer matrix, \mathbf{W}_j .

Appendix C

Models of Three Periodic and Disordered Periodic Structures

In this appendix the three periodic structures examined in the thesis are described. The first system is a chain of springs and masses. The second structure is a rod in longitudinal compression with attached resonators. The final structure is a Bernoulli-Euler beam on simple supports. For each system the transfer matrix for a typical bay of the perfectly periodic structure is presented along with the associated state vector. Also shown are the eigenvector similarity transformations which induce a wave transfer matrix. Most variables are nondimensionalized in the transfer matrix descriptions. Then a single variable is randomized and the associated transfer matrix is presented, along with the relevant terms in the wave transfer matrix. Some general properties of transfer matrices are discussed in [Rubin 64].

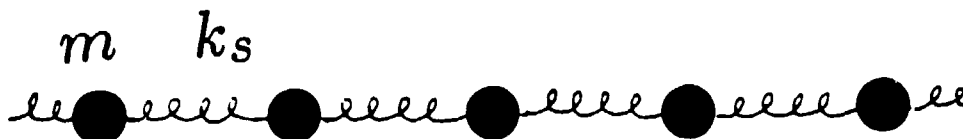


Figure C.1: Mass-spring chain.

C.1 Mass-Spring Chain

A chain of springs and masses is one of the simplest periodic structures we can examine. The system is pictured in Figure C.1 and a typical bay is shown in Figure C.2. This choice of bay (as opposed to one involving a spring and a half of two masses, for example) ensures that the $\det(\mathbf{T}) = 1$ whether m , k_s , or both are disordered. For this bay:

$$\begin{bmatrix} d_j \\ \frac{f}{k_{s,j}} \end{bmatrix} = \begin{bmatrix} 1 - \frac{m\omega^2}{k_s} & -1 \\ \frac{m\omega^2}{k_s} & 1 \end{bmatrix} \begin{bmatrix} d_{j-1} \\ \frac{f}{k_{s,j-1}} \end{bmatrix}$$

Here d_j is the displacement of the j th mass and f_j is the force on the j th mass. Note that $\frac{f}{k_{s,j}}$ has units of displacement as does d_j . Let $\bar{\omega}^2 = \frac{\omega^2}{4k_s/m}$, which is the frequency at which the passband ends, then

$$\mathbf{T} = \begin{bmatrix} 1 - 4\bar{\omega}^2 & -1 \\ 4\bar{\omega}^2 & 1 \end{bmatrix}$$



Figure C.2: One bay of mass-spring chain used to form its transfer matrix.

From the condition that $|tr(\mathbf{T})| < 2$ in a passband (see Chapter 2), we see that a single passband exists for the perfectly periodic system at $0 < \bar{\omega} < 1$. All higher frequencies are in the stopband. The wave number (the spatial frequency of the traveling waves) for the traveling waves in the passband of the mass-spring chain is governed by

$$\cos k = 1 - 2\bar{\omega}^2$$

A more extensive discussion of the mass-spring system can be found in [Faulkner and Hong 85].

The eigenvector similarity transformation used here, which will induce a wave transfer matrix (see Appendix B), is:

$$\mathbf{X} = \begin{bmatrix} 1 & 1 \\ e^{-ik} - 1 & e^{ik} - 1 \end{bmatrix}$$

and its inverse is

$$\mathbf{X}^{-1} = \begin{bmatrix} (e^{ik} - 1)/(2i \sin k) & -1/(2i \sin k) \\ (1 - e^{-ik})/(2i \sin k) & 1/(2i \sin k) \end{bmatrix}$$

C.1.1 Only Masses Disordered

Now consider disordering only the masses, i.e., let the mass be a random variable and let $\mu_j = \frac{m_j}{\langle m_j \rangle}$, where $\langle m_j \rangle = m$ so

$$\mathbf{T}(\mu_j) = \begin{bmatrix} 1 - \mu_j 4\bar{\omega}^2 & -1 \\ \mu_j 4\bar{\omega}^2 & 1 \end{bmatrix}$$

The corresponding wave transfer matrix is, where we suppress the subscript j on the transmission and reflection coefficients.

$$\mathbf{W}(\mu_j) = \mathbf{X}^{-1} \mathbf{T}(\mu_j) \mathbf{X} = \begin{bmatrix} \frac{1}{t} & -\frac{r}{t} \\ -\frac{r^*}{t^*} & \frac{1}{t^*} \end{bmatrix}$$

where

$$\frac{1}{t} = e^{ik}(1 - i\delta_j) \quad (\text{C.1})$$

and

$$-\frac{r}{t} = -e^{ik}i\delta_j$$

where

$$\delta_j = \frac{2\bar{\omega}^2(1 - \mu_j)}{\sin k}$$

C.1.2 Only Springs Disordered

Now consider disordering only the springs, i.e., let k_s be a random variable and let $\tilde{k}_{s,j} = \frac{k_{s,j}}{\langle k_{s,j} \rangle}$, where $\langle k_{s,j} \rangle = k_s$. The transfer matrix is:

$$\mathbf{T}(\tilde{k}_{s,j}) = \begin{bmatrix} 1 - \frac{4\bar{\omega}^2}{\tilde{k}_{s,j}} & -\frac{1}{\tilde{k}_{s,j}} \\ 4\bar{\omega}^2 & 1 \end{bmatrix}$$

In the corresponding wave transfer matrix

$$\frac{1}{t} = e^{ik}(1 - i\delta_j)$$

and

$$-\frac{r}{t} = i\delta_j$$

where now

$$\delta_j = \frac{2\bar{\omega}^2}{\sin k} \left(1 - \frac{1}{\tilde{k}_{s,j}}\right)$$

C.1.3 Masses and Springs Disordered

Finally with both the masses and springs disordered we have:

$$\mathbf{T}(\mu_j, \tilde{k}_{s,j}) = \begin{bmatrix} 1 - \frac{4\bar{\omega}^2\mu_j}{\tilde{k}_{s,j}} & -\frac{1}{\tilde{k}_{s,j}} \\ 4\bar{\omega}^2\mu_j & 1 \end{bmatrix}$$

Note that we have no need to compute the wave transfer matrix in the calculation of the localization factor when both the masses and springs are disordered, because of the additive nature of the localization factor discussed in Chapter 3.

C.2 Rod with Attached Resonators

The second model is a longitudinal wave carrying rod with attached resonators that represent the vibrating cross-members present in a real truss structure. The model and relevant properties are shown in Figure C.3.

The transfer equation for the perfectly periodic model is:

$$\begin{bmatrix} \bar{U}_{j+1} \\ \bar{N}_{j+1} \end{bmatrix} = \begin{bmatrix} c + \frac{R_s}{2l} & \frac{s}{l} - \frac{R(1-c)}{2l^2} \\ 3s + \frac{R(1+c)}{2} & c + \frac{R_s}{2l} \end{bmatrix} \begin{bmatrix} \bar{U}_j \\ \bar{N}_j \end{bmatrix} \quad (\text{C.2})$$

where

$$\bar{U}_j = \frac{U_j}{l}$$

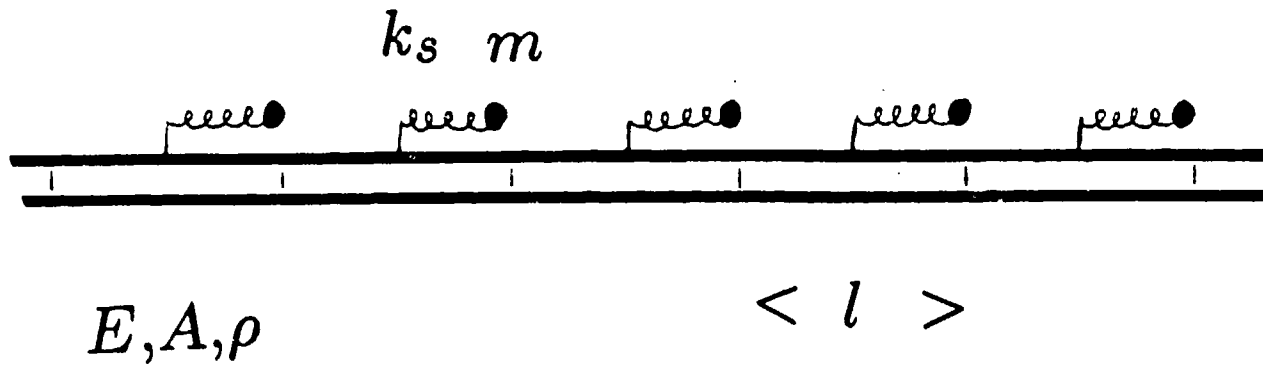


Figure C.3: Rod with attached resonators

is the nondimensional longitudinal displacement of the j th point and

$$\bar{N}_j = \frac{N_j}{EA}$$

is the nondimensional internal force at the j th point. Also

$$c = \cos \pi \bar{\omega}$$

$$s = i \sin \pi \bar{\omega}$$

$$\bar{s} = i \pi \bar{\omega}$$

where the nondimensional transfer function of the attached resonator is:

$$\bar{H} = \left(\frac{1}{\bar{k}_s} - \frac{1}{\bar{\omega}^2 \pi^2 \bar{\mu}} \right)^{-1}$$

and where the nondimensional frequency, stiffness and mass are:

$$\bar{\omega} = \frac{\omega l \left(\frac{\rho}{E} \right)^{\frac{1}{2}}}{\pi}$$

$$\bar{k}_s = \frac{k_s l}{EA}$$

$$\bar{\mu} = \frac{m}{(\rho A l)}$$

The transfer matrix models a bay extending across a length of rod, across a resonator, and then across another length of rod.

A discussion of the dynamic characteristics of the perfectly periodic structure can be found in [von Flotow 82]. For our work on the rod with attached resonators, we will use $\bar{\mu} = .2$ and $\bar{k}_s = .5$. These values put our first stopband around $\bar{\omega} = .5033$ which is the natural frequency of the attached resonator. This particular stopband frequency makes for ease of presentation of localization effects in the first passband. In real structures the stopband associated with the resonant frequency of a cross-member is likely to be much closer to $\bar{\omega} = 0$.

The wave number k for the passbands of the perfectly periodic structure is determined by

$$\cos k = c + \frac{\bar{H}s}{2\bar{s}}$$

The eigenvector similarity transformation that induces the wave transfer form is

$$\mathbf{X} = \begin{bmatrix} 1 & 1 \\ i \sin k / (\frac{s}{\bar{s}} - \frac{R(1-c)}{2\bar{s}^2}) & -i \sin k / (\frac{s}{\bar{s}} - \frac{R(1-c)}{2\bar{s}^2}) \end{bmatrix}$$

and

$$\mathbf{X}^{-1} = \begin{bmatrix} \frac{1}{2} & -i(\frac{s}{\bar{s}} - \frac{R(1-c)}{2\bar{s}^2}) / (2 \sin k) \\ \frac{1}{2} & i(\frac{s}{\bar{s}} - \frac{R(1-c)}{2\bar{s}^2}) / (2 \sin k) \end{bmatrix}$$

C.2.1 Only Masses Disordered

Now disorder the mass, m , of the attached resonator. So let

$$\bar{\mu}_j = \frac{m_j}{\rho A l}$$

be the nondimensional random variable, $\langle \bar{\mu}_j \rangle = \bar{\mu}$. Note that we do not feel compelled to divide by the average value of $\bar{\mu}$ because this variable is already nondimensional. Now the random transfer matrix $\mathbf{T}(\bar{\mu}_j)$ is found by replacing $\bar{\mu}$, which occurs in \bar{H} , in the nonrandom transfer matrix, \mathbf{T} , by $\bar{\mu}_j$. In the corresponding wave transfer matrix

$$\frac{1}{t} = e^{ik}(1 - i\delta_j)$$

and

$$-\frac{r}{t} = -i\delta_j$$

where

$$\delta_j = \frac{(\sin \pi \bar{\omega}) \Delta \bar{H}_j}{2(\sin k) \pi \bar{\omega}}$$

and

$$\Delta \bar{H}_j = \left(\frac{1}{\bar{k}_s} - \frac{1}{\bar{\omega}^2 \pi^2 \bar{\mu}_j} \right)^{-1} - \left(\frac{1}{\bar{k}_s} - \frac{1}{\bar{\omega}^2 \pi^2 \bar{\mu}} \right)^{-1}$$

C.2.2 Only Springs Disordered

Now consider disordering the springs of the attached resonators. Let

$$\bar{k}_{s,j} = \frac{k_{s,j} l}{EA} \text{ where } \langle \bar{k}_{s,j} \rangle = \bar{k}_s$$

be the nondimensional random variable. The transfer matrix $\mathbf{T}(\bar{k}_{s,j})$ is the nonrandom transfer matrix with \bar{k}_s replaced by $\bar{k}_{s,j}$. The wave transfer matrix is the same as for the disordered masses except that

$$\Delta \bar{H}_j = \left(\frac{1}{\bar{k}_{s,j}} - \frac{1}{\bar{\omega}^2 \pi^2 \bar{\mu}} \right)^{-1} - \left(\frac{1}{\bar{k}_s} - \frac{1}{\bar{\omega}^2 \pi^2 \bar{\mu}} \right)^{-1}$$

C.2.3 Only Lengths Disordered

Finally we examine the disordering of the bay length, i.e. the distance between the resonators. Let the nondimensional random variable be

$$\bar{l}_j = \frac{l_j}{\langle l_j \rangle}$$

where $\langle l_j \rangle = l$. The transfer matrix for the lengths disordered is

$$\mathbf{T}(\bar{l}_j) = \begin{bmatrix} \cos(\pi\bar{\omega}\bar{l}_j) + \frac{R \sin(\pi\bar{\omega}\bar{l}_j)}{2\pi\bar{\omega}} & \frac{\sin(\pi\bar{\omega}\bar{l}_j)}{\pi\bar{\omega}\bar{l}_j} + \frac{R[1-\cos(\pi\bar{\omega}\bar{l}_j)]}{2\pi^2\bar{\omega}^2\bar{l}_j} \\ -\pi\bar{\omega}\bar{l}_j \sin(\pi\bar{\omega}\bar{l}_j) + \frac{\bar{l}_j R [1+\cos(\pi\bar{\omega}\bar{l}_j)]}{2} & \cos(\pi\bar{\omega}\bar{l}_j) + \frac{R \sin(\pi\bar{\omega}\bar{l}_j)}{2\pi\bar{\omega}} \end{bmatrix}$$

In the corresponding wave transfer matrix

$$\frac{1}{t} = \alpha - \frac{i[\beta + \nu]}{2 \sin k}$$

and

$$-\frac{r}{t} = \frac{i[-\beta + \nu]}{2 \sin k}$$

where α is the (1,1) term of $\mathbf{T}(\bar{l}_j)$ and where

$$\beta = \left[-\pi\bar{\omega}\bar{l}_j \sin(\pi\bar{\omega}\bar{l}_j) + \frac{\bar{l}_j \bar{H} [1 + \cos(\pi\bar{\omega}\bar{l}_j)]}{2} \right] \left[\frac{s}{\bar{s}} - \frac{\bar{H}(1-c)}{2\bar{s}^2} \right]$$

and

$$\nu = \left[\frac{\sin(\pi\bar{\omega}\bar{l}_j)}{\pi\bar{\omega}\bar{l}_j} + \frac{\bar{H}[1 - \cos(\pi\bar{\omega}\bar{l}_j)]}{2\pi^2\bar{\omega}^2\bar{l}_j} \right] \left[\bar{s}s + \frac{\bar{H}(1+c)}{2} \right]$$

C.2.4 All Three Parameters Disordered

Finally the transfer matrix for masses, springs and lengths disordered, $\mathbf{T}(\bar{\mu}_j, \bar{k}_{sj}, \bar{l}_j)$ is simply $\mathbf{T}(\bar{l}_j)$ with \bar{H} replaced by

$$\bar{H}_j = \left(\frac{1}{\bar{k}_{sj}} - \frac{1}{\bar{\omega}^2 \pi^2 \bar{\mu}_j} \right)^{-1}$$

C.3 Bernoulli-Euler Beam on Simple Supports

The final system examined is a Bernoulli-Euler beam on simple supports shown in Figure C.4. In setting up the transfer matrix for the beam on supports we will use much of the terminology of [Yang and Lin 75, Lin 76], except we nondimensionalize

ρ, EI

$< l >$



Figure C.4: Beam on simple supports.

where possible. The transfer matrix for a bay relates the slope, ϕ , and nondimensional moment at adjacent supports

$$\begin{bmatrix} \phi_j \\ \frac{lM}{EI}_j \end{bmatrix} = \begin{bmatrix} \cos k & \frac{\alpha}{\sqrt{\bar{\omega}}} \\ -\frac{\sqrt{\bar{\omega}} \sin^2 k}{\alpha} & \cos k \end{bmatrix} \begin{bmatrix} \phi_{j-1} \\ \frac{lM}{EI}_{j-1} \end{bmatrix} \quad (C.3)$$

where

$$\cos k = \frac{\sinh \sqrt{\bar{\omega}} \cos \sqrt{\bar{\omega}} - \cosh \sqrt{\bar{\omega}} \sin \sqrt{\bar{\omega}}}{\sinh \sqrt{\bar{\omega}} - \sin \sqrt{\bar{\omega}}}$$

where

$$\bar{\omega} = \omega \sqrt{\frac{\mu l^4}{EI}}$$

$\mu = \text{mass of beam per unit length}$

and where (adopting the notation of [Yang and Lin 75, Lin 76])

$$\alpha = \frac{c_4}{s_3}$$

$$c_4 = (\cosh \sqrt{\bar{\omega}} \cos \sqrt{\bar{\omega}} - 1)/2$$

$$s_3 = (\sinh \sqrt{\omega} - \sin \sqrt{\omega})/2$$

$$s_4 = \sinh \sqrt{\omega} \sin \sqrt{\omega}$$

$$c_2 = (\cosh \sqrt{\omega} - \cos \sqrt{\omega})/2$$

The eigenvector similarity transformation which induces the wave transfer matrix is

$$\mathbf{X} = \begin{bmatrix} 1 & 1 \\ i\frac{\sqrt{\omega}}{\alpha} \sin k & -i\frac{\sqrt{\omega}}{\alpha} \sin k \end{bmatrix}$$

and

$$\mathbf{X}^{-1} = \begin{bmatrix} \frac{1}{2} & -\frac{i\alpha}{2\sqrt{\omega} \sin k} \\ \frac{1}{2} & \frac{i\alpha}{2\sqrt{\omega} \sin k} \end{bmatrix}$$

Now consider disordering the length l between each bay and let the nondimensional random length be

$$\hat{l}_j = \frac{l_j}{\langle l_j \rangle}$$

where $\langle l_j \rangle = l$. So the transfer matrix $\mathbf{T}(\hat{l}_j)$ can be written by simply replacing $\sqrt{\omega}$ whenever it appears as an argument of sin, sinh, cos and cosh by $\sqrt{\omega}\hat{l}_j$. Anywhere l appears it can be interpreted as $\langle l_j \rangle$.

In the wave transfer matrix for the beam on disordered supports

$$\frac{1}{t} = \cos k(\hat{l}_j) + i \left[\frac{\alpha(\hat{l}_j) \sin k}{2\alpha} + \frac{\alpha \sin^2 k(\hat{l}_j)}{2\alpha(\hat{l}_j) \sin k} \right]$$

and

$$-\frac{r}{t} = i \left[\frac{\alpha \sin^2 k(\hat{l}_j)}{2\alpha(\hat{l}_j) \sin k} - \frac{\alpha(\hat{l}_j) \sin k}{2\alpha} \right]$$

Once again, whenever the argument (\hat{l}_j) appears, it implies that the underlying circular and hyperbolic functions should have $\sqrt{\omega}$ replaced by $\sqrt{\omega}\hat{l}_j$.

Appendix D

A Simple Method to Calculate Localization Factors

This appendix describes the calculation of localization factors using a simple method which does not depend on theories involving products of random matrices. The method has given very good results for systems with sufficiently low randomness and over wide frequency ranges. The method is applied to systems that can be described with 2×2 transfer matrices and is a generalization of a result which appeared in [Akkermans and Maynard 84].

Briefly, the method involves taking a transfer matrix which is a function of a random variable and expanding it in terms of a Taylor series expansion about the average value of the random variable. Only the first two terms of the expansion are retained, after which they are converted to wave transfer form via the appropriate similarity transformation. Products of this low order form are taken, but only terms of order one are retained. From this low order representation of the matrix product, the transmission coefficient, τ_n , is extracted and the localization factor, γ , is calculated as

$$\gamma = -\frac{\langle \ln |\tau_n| \rangle}{n}$$

First consider the bay transfer matrix which is a function of the random variable α , $T(\alpha)$ or T for short. Now expand T in a Taylor series expansion about the mean value of α .

$$T = T|_{\langle \alpha \rangle} + \delta\alpha \frac{\partial T}{\partial \alpha}|_{\langle \alpha \rangle} + \frac{(\delta\alpha)^2}{2!} \frac{\partial^2 T}{\partial \alpha^2}|_{\langle \alpha \rangle} + \dots$$

Consider retaining only the first two terms:

$$T \doteq T|_{\langle \alpha \rangle} + \delta\alpha \frac{\partial T}{\partial \alpha}|_{\langle \alpha \rangle}$$

Now choose an eigenvector transformation that induces a wave transfer matrix, so

$$X^{-1}TX \doteq X^{-1}T|_{\langle \alpha \rangle}X + \delta\alpha X^{-1} \frac{\partial T}{\partial \alpha}|_{\langle \alpha \rangle}X = \begin{bmatrix} e^{+ik} & \\ & e^{-ik} \end{bmatrix} + \delta\alpha \begin{bmatrix} a & b \\ b^* & a^* \end{bmatrix}$$

So now we have approximated the j th wave transmission matrix as

$$W_j \doteq \begin{bmatrix} e^{ik} + (\delta\alpha_j)a & (\delta\alpha_j)b \\ (\delta\alpha_j)b^* & e^{ik} + (\delta\alpha_j)a^* \end{bmatrix}$$

Now let us calculate $\prod_{j=1}^n W_j$ by retaining terms only to first order in $\delta\alpha_j$. Note for example that terms like $\delta\alpha_i \delta\alpha_j$, $i \neq j$ will vanish by mutual independence when averaging. The final result gives:

$$\prod_{j=1}^n W_j \doteq \begin{bmatrix} e^{in k} + e^{(n-1)k} a (\sum_{j=1}^n \delta\alpha_j) & (2,1)^* \\ e^{-in k} [\sum_{j=1}^n \delta\alpha_j e^{i(2j-1)k}] & (1,1)^* \end{bmatrix}$$

The $(1,1)$ term of the above matrix product approximation is our approximation to $\frac{1}{r_n}$.

From this, one can calculate $|\tau_n|^2$:

$$|\tau_n|^2 \doteq 1/[1 + a^* e^{ik} (\sum_{j=1}^n \delta\alpha_j) + a e^{-ik} (\sum_{j=1}^n \delta\alpha_j) + |a|^2 (\sum_{j=1}^n \delta\alpha_j)^2]$$

Taking the natural log of $|\tau_n|^2$

$$\ln |\tau_n|^2 \doteq \ln(1) - \ln(1 + a^* e^{ik} (\sum_{j=1}^n \delta\alpha_j) + a e^{-ik} (\sum_{j=1}^n \delta\alpha_j) + |a|^2 (\sum_{j=1}^n \delta\alpha_j)^2)$$

Recalling the following expansion:

$$\ln(1+z) = z - \frac{z^2}{2} + \frac{z^3}{3} - \dots \quad |z| \leq 1, \quad z \neq -1$$

So retaining terms to first order in z :

$$\ln |r_n|^2 \doteq -a^* e^{ik} \left(\sum_{j=1}^n \delta \alpha_j \right) - a e^{-ik} \left(\sum_{j=1}^n \delta \alpha_j \right) - |a|^2 \left(\sum_{j=1}^n \delta \alpha_j \right)^2$$

Now taking the average of $\ln |r_n|^2$ and recalling that $\langle \delta \alpha_j \rangle = 0$ and invoking independence of $\delta \alpha_j$ s we arrive at:

$$\langle \ln |r_n|^2 \rangle \doteq -|a|^2 \left(\sum_{j=1}^n \langle (\delta \alpha_j)^2 \rangle \right) = -|a|^2 n \sigma_\alpha^2$$

Now

$$\gamma = - \frac{\langle \ln |r_n| \rangle}{n}$$

or

$$\gamma = - \frac{\langle \ln |r_n|^2 \rangle}{2n} \doteq \frac{|a|^2 \sigma_\alpha^2}{2}$$

which is the final result.

We find the result agrees with calculations from Equation 3.10 when $\frac{1}{t_j}$ has the forms $e^{ik}(1 + i\delta_j)$ or $(1 + i\delta_j)$. So this formula is valid for the mass-spring chain and the rod with disordered masses or springs on the attached resonators. The formula will not give accurate results for the rod with disordered lengths between resonators or for the beam with random lengths between supports.

Appendix E

Properties of the Scattering and Wave Transfer Matrices

In this appendix we discuss some of the properties of the scattering matrices and wave transfer matrices used in the thesis. These matrices will be used to describe the propagation of traveling waves in the passbands of periodic or disordered periodic structures. We will state the scattering and wave transfer matrices in their most general forms and then impose conditions on the scattering matrix and discuss what this implies for the wave transfer matrix. Note that we will suppress any subscripts on our transmission and reflection matrices. The scattering and wave transfer matrices are of dimension $2d \times 2d$. Scattering and wave transfer matrices are discussed in [Redheffer 61] and in [Carlini and Giordano 64, Hlawiczka 65] and for some specific disordered systems in [Osawa and Kotera 66, Omar and Schünemann 85].

The scattering matrix, S , in its most general form is

$$\begin{bmatrix} \vec{A}_{j-1} \\ \vec{B}_j \end{bmatrix} = \begin{bmatrix} r & t \\ \hat{t} & \hat{r} \end{bmatrix} \begin{bmatrix} \vec{B}_{j-1} \\ \vec{A}_j \end{bmatrix} \quad (\text{E.1})$$

where \vec{A} and \vec{B} represent vectors of traveling wave amplitudes in the indicated direc-

tions. The corresponding wave transfer matrix involves a rearrangement of the state vector, so that we relate waves on the right of a bay to those on the left of a bay:

$$\begin{bmatrix} \vec{\mathbf{A}}_j \\ \vec{\mathbf{B}}_j \end{bmatrix} = \begin{bmatrix} t^{-1} & -t^{-1}r \\ \hat{r}t^{-1} & \hat{t} - \hat{r}t^{-1}r \end{bmatrix} \begin{bmatrix} \vec{\mathbf{A}}_{j-1} \\ \vec{\mathbf{B}}_{j-1} \end{bmatrix} \quad (\text{E.2})$$

Now we require that the scattering matrix be symmetric. This means that

$$r = r^T$$

$$\hat{r} = \hat{r}^T$$

and

$$t = \hat{t}^T$$

These are exactly the same conditions needed for the symplecticity of the wave transfer matrix \mathbf{W} , namely that

$$\mathbf{W}^T \mathbf{J} \mathbf{W} = \mathbf{J}$$

be satisfied. Thus

$$S \text{ symmetric} \iff W \text{ symplectic}$$

Now we impose the requirement that \mathbf{S} be unitary, namely

$$\mathbf{S}^H \mathbf{S} = \mathbf{S} \mathbf{S}^H = \mathbf{I}$$

Now $\mathbf{S}^H \mathbf{S} = \mathbf{I}$ tells us that

$$\begin{aligned} \mathbf{r}^H \mathbf{r} + \hat{\mathbf{t}}^H \hat{\mathbf{t}} &= \mathbf{I} \\ \mathbf{t}^H \mathbf{t} + \hat{\mathbf{r}}^H \hat{\mathbf{r}} &= \mathbf{I} \\ \mathbf{r}^H \mathbf{t} + \hat{\mathbf{t}}^H \hat{\mathbf{r}} &= 0 \end{aligned} \quad (\text{E.3})$$

These are precisely the same conditions that must hold when \mathbf{W} is an element of $SU(d, d)$ or

$$\mathbf{W}^H \Delta \mathbf{W} = \Delta$$

We conclude that

$$S \text{ unitary} \iff W \in SU(d, d)$$

Now imposing both symmetry and unitarity on the scattering matrix we have

$$S = \begin{bmatrix} \mathbf{r} & \mathbf{t} \\ \mathbf{t}^T & -\mathbf{t}^{-1*} \mathbf{r}^* \mathbf{t} \end{bmatrix}$$

where $\mathbf{r} = \mathbf{r}^T$ and $-\mathbf{t}^{-1*} \mathbf{r}^* \mathbf{t} = -\mathbf{t}^T \mathbf{r}^* \mathbf{t}^{-H}$. Equivalently when the wave transfer matrix is symplectic and an element of $SU(d, d)$ we have

$$W = \begin{bmatrix} \mathbf{t}^{-1} & -\mathbf{t}^{-1} \mathbf{r} \\ -\mathbf{t}^{-1*} \mathbf{r}^* & \mathbf{t}^{-1*} \end{bmatrix}$$

From the condition $\mathbf{t}^H \mathbf{t} + \hat{\mathbf{r}}^H \hat{\mathbf{r}} = \mathbf{I}$ above, we can prove that

$$0 < \mu_i[\mathbf{t}^H \mathbf{t}] \leq 1$$

where $\mu_i[*]$ is the i th eigenvalue of the indicated argument. Also note that

$$\mu_i[\mathbf{t}^H \mathbf{t}] = \mu_i[\mathbf{t} \mathbf{t}^H]$$

so that all the results stated below hold for $\mathbf{t} \mathbf{t}^H$ as well as $\mathbf{t}^H \mathbf{t}$. First we assume that $\mathbf{t}^H \mathbf{t}$ is invertible so that it is positive definite:

$$\mathbf{t}^H \mathbf{t} > 0$$

We also have that $\hat{\mathbf{r}}^H \hat{\mathbf{r}}$ is at least positive semi-definite:

$$\hat{\mathbf{r}}^H \hat{\mathbf{r}} \geq 0$$

From Equation E.3 we have

$$\mathbf{t}^H \mathbf{t} = \mathbf{I} - \hat{\mathbf{r}}^H \hat{\mathbf{r}}$$

Doing an eigenvector decomposition on the above equation we get

$$\begin{aligned} \mathbf{t}^H \mathbf{t} &= \mathbf{I} - \hat{\mathbf{r}}^H \hat{\mathbf{r}} \\ &= \mathbf{U}(\mathbf{I} - \text{diag}\{\mu_i[\hat{\mathbf{r}}^H \hat{\mathbf{r}}]\})\mathbf{U}^H \end{aligned}$$

The positive definiteness of $\mathbf{t}^H \mathbf{t}$ and the positive semi-definiteness of $\hat{\mathbf{r}}^H \hat{\mathbf{r}}$ now imply

$$0 \leq \mu_i[\hat{\mathbf{r}}^H \hat{\mathbf{r}}] < 1$$

and

$$0 < \mu_i[\mathbf{t}^H \mathbf{t}] \leq 1$$

which is the desired result.

Biography

Glen J. Kissel was born January 5, 1957, in Evansville, Indiana, where he attended grade school and three semesters at F. J. Reitz High School. He graduated from Protection High School in Protection, Kansas in 1975. His undergraduate work was done at the Oklahoma State University in Stillwater, Oklahoma, where he graduated with a B.S. in Mechanical Engineering (Aerospace Major) in 1979. There he was named the Outstanding Student in the School of Mechanical and Aerospace Engineering. He then began graduate studies at the Massachusetts Institute of Technology in Cambridge, Massachusetts, on the Donald W. Douglas Fellowship. He received his S.M. in Aeronautics and Astronautics in 1982. His research has focused on the dynamics and control of flexible space structures. Glen is a member of the AIAA, IEEE and Sigma Xi. He has published in the *Journal of Aircraft* and the *IEEE Control Systems Magazine*. He has worked summers at the Federal Aviation Administration in Washington, D.C., the John F. Kennedy Space Center in Florida and the C. S. Draper Laboratory in Cambridge, Massachusetts. Glen has published a number of articles on the U.S. space program and has appeared on television to talk about space spinoffs. He is interested in national and international politics and has debated a primary congressional candidate on the Strategic Defense Initiative. Glen's parents, Marlin and Agnes Kissel, and a sister, Debbie, reside in Pratt, Kansas. He will shortly take up employment in southern California.

Mode/Wave Localization in Disordered Periodic Structures

16.622

Final Report

4:25pm

Author: Tristram Hyde

May 14, 1987

Massachusetts Institute of Technology

Advisor: Prof. A. VonFlotow

Partner: Cathy Sybert

ABSTRACT

Theories have been developed predicting wave and mode localization in disordered periodic structures, but only one experiment has been previously conducted to test the theory. Theory predicts attenuation of wave amplitudes at all frequencies, and spatial localization of mode shapes in a disordered periodic structure. Our experiment tests for amplitude localization in a truss model. The apparatus consisted of a steel ribbon under tension (modeling the truss) and spring-mass sub-structures (modeling cross members) spaced evenly along the ribbon length. The perfectly periodic structure had equal oscillator mass in each bay and the disordered structure had random mass in each bay. It was shaken at one end and ribbon amplitudes were measured at each bay. There was little or no difference between the disordered case and the control case in the amplitude versus position profiles. A single mode could not be identified in the control or disordered experiments due to non-zero damping. An alternate experiment using the same structures involved forcing the ribbon at one end with white noise and reading the ribbon amplitude near the other end. By taking the Fourier transform of the transfer function of output amplitude over input force, a localization factor can be deduced. The results again showed no localization.

TABLE OF CONTENTS

Introduction.....	1
Previous work.....	2
Overview of our experiment.....	2
 Theoretical Analysis.....	5
 The Experimental Apparatus.....	10
 Amplitude vs. Position Experiment.....	14
Procedure.....	14
Results.....	15
Discussion.....	17
 Transfer Function Experiment.....	19
Procedure.....	19
Results.....	21
Discussion.....	22
 Conclusions.....	23
 Recommendations.....	24

INTRODUCTION

Many engineering systems deal with vibrations of one form or another. An important engineering system that is getting a lot of attention is the space station. A major component of the space station will be large trusses. Theoretical and experimental research has been done on these periodic structures; however, it is assumed that the structure is perfectly periodic. Yet, there could be inconsistencies in the material properties or the exact length of the bays of the truss structure. These inconsistencies cause a certain disorder in the structure. Another example of a periodic structure is an aircraft skin stiffened with stringers located at intervals across the skin. In both the space truss and the skin-stringer systems, the main structure has sub-structures located across the main structure.

Disorder, whether designed or unintentional will change the oscillatory properties of any system. The disorder will disrupt the vibration propagation properties found in the perfectly periodic structure. The difference in the properties from one bay to the next causes reflections of travelling waves and tends to spatially localize amplitudes in one region. It is important to understand this localization phenomenon in order to exploit it and to be aware of possible problems it could cause. It can be useful in isolating vibrations to areas where the energy can be dissipated harmlessly and not propagate to more sensitive areas of the structure. The localization could be harmful if large amplitude vibrations localized in a sensitive area (especially important in the near-zero damping conditions of space). One can exploit this phenomenon in a space station design, where, for example, the vibrations caused by a meteor strike on a solar panel would not be transmitted down the

truss to more sensitive parts of the space station.

Previous work

Disorder in a periodic structure was first connected with solid state physics and the mathematics of random matrices. The localization phenomenon was first explained by P. W. Anderson in an article on electron transport in disordered crystal lattices.¹ In 1963, H. Furstenberg wrote on products of random matrices, which can be applied to the traveling wave properties of each bay in a disordered structure.² The only experiment on the structural dynamics application of this phenomenon was performed by Hodges and Woodhouse using an eight bay model and randomizing the length of the bays.³ They used seven beads on a string as their apparatus, plucked it at one end, and measured string amplitude near the other end. A localization factor was deduced from the Fourier transform of the string amplitude. The results of the Hodges and Woodhouse experiment showed a moderate amount of localization even for very weak disorder.

Overview of our experiment

Our study is centered on a disordered truss structure where the cross-member in each bay has a random oscillatory behavior (natural frequency). The disorder is distributed across the whole structure. In probability terms, this is called "independently and identically distributed," which means that the random property in a bay doesn't depend on that of any other bay. The disorder that is present in the system should cause an attenuation of traveling wave amplitude at all frequency bands. This is different from the perfectly periodic system, where waves are attenuated only in certain frequency ranges (stop bands) and travel without attenuation in

other frequency ranges (pass bands). This attenuation can be equivalently described as mode localization, where significant amplitudes are confined to a region in the disordered structure and are equally predominant along the perfectly periodic structure (see figure 1).

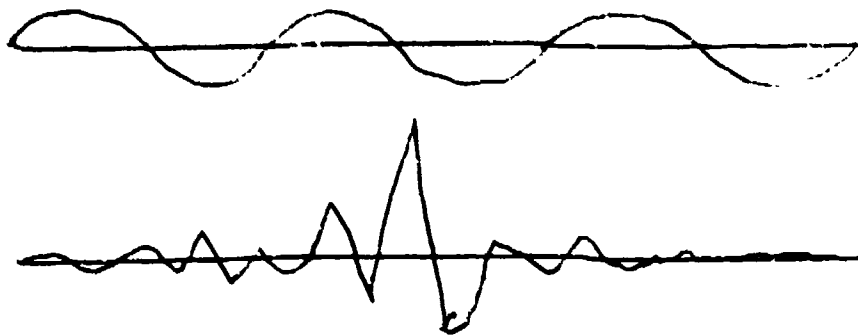


Figure 1: Typical mode shapes for a perfectly periodic structure (top) and a disordered periodic structure (bottom).

The experiment consists of an idealized truss structure made of a steel ribbon under tension and idealized sub-structures made of spring-mass oscillators (see figure 2). The disorder in the structure is realized by randomizing the mass of the spring-mass sub-structures. We attempted to keep the effective spring constant and bay length constant for all bays. A sine wave was input to a shaker at one end of the ribbon, and ribbon amplitudes were measured at each bay to get amplitude versus position graphs at varying frequencies above the stop band. A localization factor was to be taken from these graphs by fitting the amplitudes to an exponential decay envelope. Figure 3 shows this envelope, where the localization factor is one over the localization length. An alternative experiment, similar to that of Hodges and Woodhouse, was conducted on the same structure. We input a white noise force

to the ribbon at one end and measured ribbon amplitude near the other end. Using a digital signal processor, a transfer function of ribbon amplitude over forcing input was determined. Following the method of Hodges and Woodhouse, we tried to deduce a localization factor from the Fourier transforms of the transfer functions of the disorderd case compared to the perfectly periodic case. Due to some non-idealities in the experiment, there was no localization determined by either of the two methods attempted. In hindsight, we found that to see localiztion cleanly, a different experimental setup would have to be used.

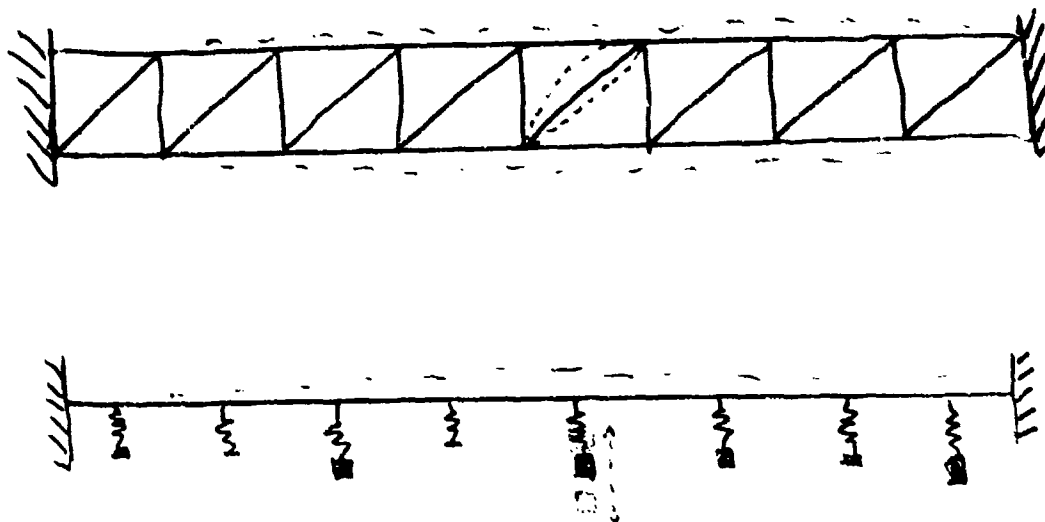


Figure 2: Our experimental structure models a vibrating truss with vibrating sub-structures.

Theoretical Analysis

Graduate work on this topic is currently being done at MIT by Mr. Glen Kissel, under the counseling of Professor Andrew von Flotow. In Kissel's paper "Localization in Disordered Periodic Structures," products of random matrices are used to develop a theory that predicts localization.⁴ The end result of these mathematical calculations is a frequency dependent localization factor for the disordered periodic structure. Kissel uses a mathematical model of an infinitely long, undamped periodic structure with traveling waves.

Kissel models each bay of this structure with a two by two transfer matrix, which implies a pair of waves traveling along the structure (one to the right and one to the left). No damping (dissipation) is modeled to make the effects of localization more pronounced. No end conditions are modeled to make the calculations easier. The transfer matrix of the j^{th} bay is denoted by T_j and relates wave transmission from the left side to the right side of the bay as shown:

$$\begin{bmatrix} A_R \\ B_R \end{bmatrix} = \begin{bmatrix} r_j & t_j \\ t_j^* & r_j \end{bmatrix} \begin{bmatrix} B_L \\ A_L \end{bmatrix} \quad (1)$$

The transmission coefficient of the j^{th} bay is t_j , and the reflection coefficient is r_j , and the superscript * denotes complex conjugate. Wave A is traveling from right to left and wave B is traveling from left to right. Conservation of energy considerations give $(t_j)^2 + (r_j)^2 = 1$.

A section of the structure can be modeled by multiplying the transfer matrices for the bays together. If the structure section of n bays is denoted with the subscript N , the wave transmission characteristics of that section can be described by:

$$\begin{bmatrix} A_R \\ B_R \end{bmatrix}_N = \prod_{j=1}^n T_j \begin{bmatrix} B_R \\ A_L \end{bmatrix}_N \quad (2)$$

Where the product is of the form:

$$\prod_{j=1}^n T_j = \begin{bmatrix} 1/t_N & -r_N/t_N \\ -r_N^*/t_N^* & 1/t_N^* \end{bmatrix} \quad (3)$$

Kissel randomizes the transmission and reflection coefficients of the model to introduce disorder. Through these calculations, a localization factor γ is determined. This factor is the average wave attenuation factor per bay, so is defined by

$$\gamma = \frac{-\langle \ln |t_N| \rangle}{n} \quad (4)$$

where $\langle \rangle$ denotes a statistical average. If γ is the attenuation factor per bay there will be an average decay envelope like $e^{\gamma x}$, where x is the number of bays away from the localization center.

A localization factor expression was developed by Mr. Kissel and depends on several non-dimensional parameters (frequency, stiffness ratio, and mass ratio):

$$\bar{\omega} = \frac{\omega}{L(fA/T)^{1/2}} \quad (5)$$

$$\bar{k} = \frac{kT}{L} \quad (6)$$

$$\mu = \frac{m}{\rho AL} \quad (7)$$

where ω is the frequency of oscillation, L is the length of the structure, ρ is the mass density of the structure, A is the cross sectional area of the structure, T is the tension, and m is the mass of the mass-spring substructure.

A Taylor series expansion of Furstenberg's formulas is used to arrive at:

$$\gamma(\bar{\omega}) = \frac{\sigma_{\mu}^2 \sin^2(\pi \bar{\omega})}{4 \sin^2 k_p (\pi \bar{\omega})^6 \langle \mu \rangle^4 \chi^4} \quad (8)$$

where σ_{μ}^2 is the variance of μ and $\langle \mu \rangle$ is the statistical average of μ . k_p represents a wave number for the perfectly periodic structure and is defined by:

$$\cos k_p = \cos(\pi \bar{\omega}) + \frac{\sin(\pi \bar{\omega})}{2\chi \pi \bar{\omega}} \quad (9)$$

$$\text{where } \chi = \frac{L}{k} - \frac{1}{(\pi \bar{\omega})^2 \langle \mu \rangle} \quad (10)$$

We adapted Mr. Kissels formulas to our experiment and the results of versus frequency are plotted in figure 3.

A more clear explanation of the difference between the modes expected in the perfectly periodic case and those expected in the disordered case was given by Prof. von Flotow. Figure 4 shows that the localized mode phenomenon is predicted only in the first pass band (at the natural frequency of the mass-spring sub-structures, ω_0). This modal theory predicts 30 closely spaced modes all in the vicinity of ω_0 . In the second and higher passbands, the sub-structures vibrate with a much smaller amplitude than the main structure, and there is little difference between the disordered and perfectly periodic structures.

Frequency vs gamma

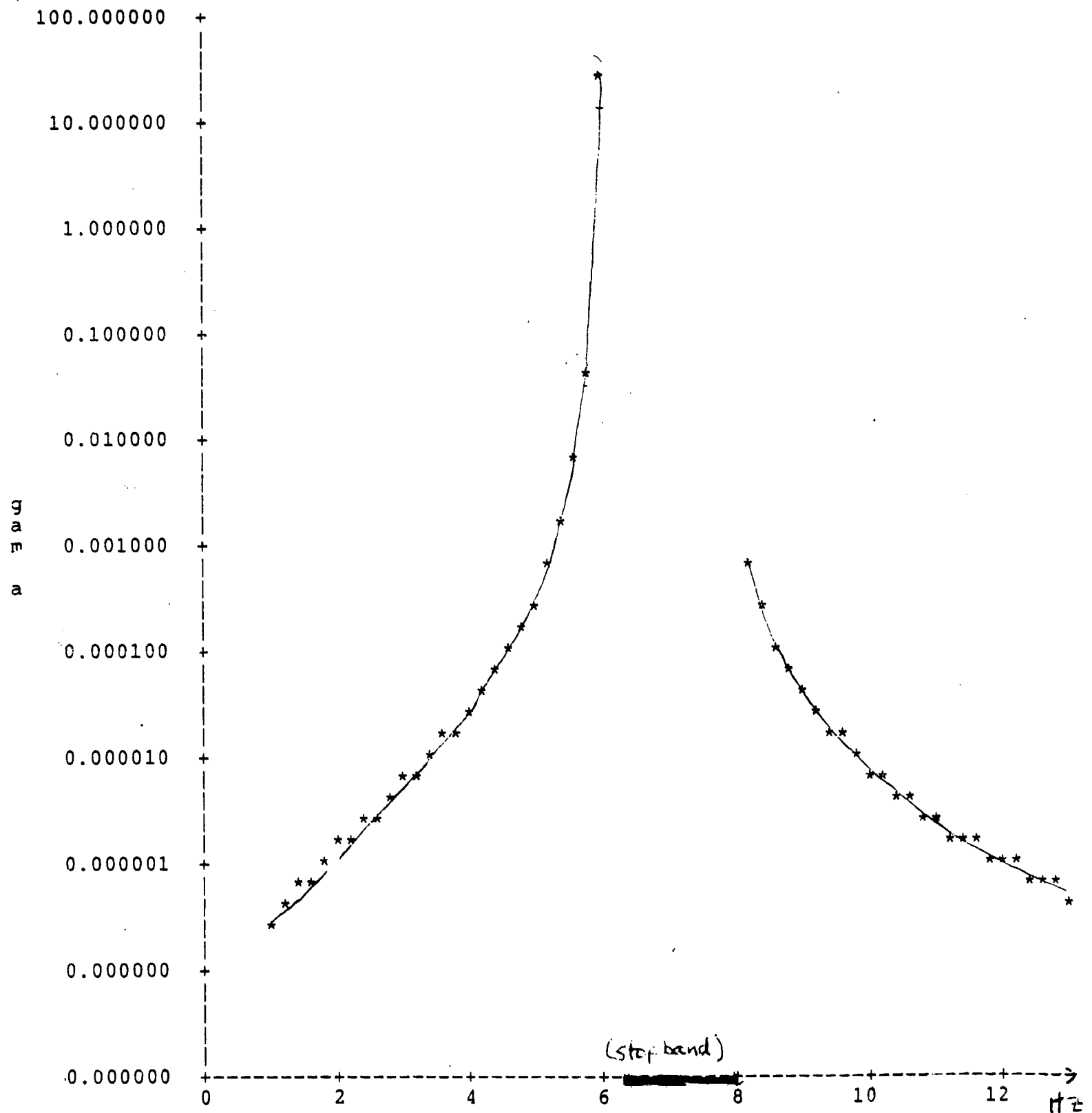


Figure 3: Localization factor versus frequency predicted for our experimental structure.

First passband

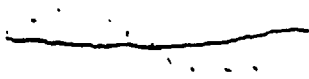
Perfectly Periodic

Disordered

~ 8 Hz



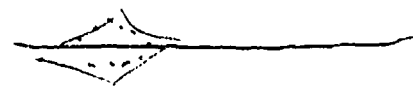
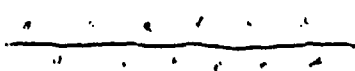
~ 8 Hz



...

...

~ 8 Hz

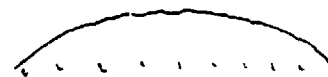
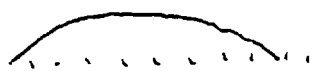


Second Passband

Perfectly Periodic

Disordered

~ 30 Hz



~ 60 Hz



...

...

~ 900 Hz



—

ribbon (main structure)

...

substructures

Figure 4: Predicted mode shapes for the first and second passbands, comparing the perfectly periodic and disordered cases.

Experimental Apparatus

The experimental structure consists of a steel ribbon that models a truss. 30 evenly spaced mass-spring resonators model the substructures of the truss (see figure 5). The ribbon is ten mil thick steel, six inches wide and eight feet long. It is clamped at both ends and tensioned to about one third of its ultimate stress. A shaker is attached near one end to input a force into the ribbon. The mass-spring substructures consist of "diving-board" cantilevered beams made of four mil thick shims. These diving board resonators have washers bolted to the tips and vibrate in the vertically through holes cut in the ribbon. The holes are one and three quarters inches in diameter (centered three inches apart), and the shim resonators are one half inch wide and one and a half inches long. The spring-mass properties are provided by the bending stiffness of the cantilevered shim and the washer mass at the beam tip. The washers are bolted to the tips of the shim resonators. In the perfectly periodic tests an equal number of washers were bolted to each of the 30 resonator tips. In the disordered case, the number of washers on the tip was changed to a random number (from zero to twelve). The number of washers for each bay of the disordered structure was generated by a pocket-calculator random number generator. Each washer weighed a little less than a gram, and the nut and bolt weighed approximately the equivalent of two washers. The effective spring constant of the cantilevered shim was such that under full loading (twelve washers), the tip sagged a half an inch at rest.

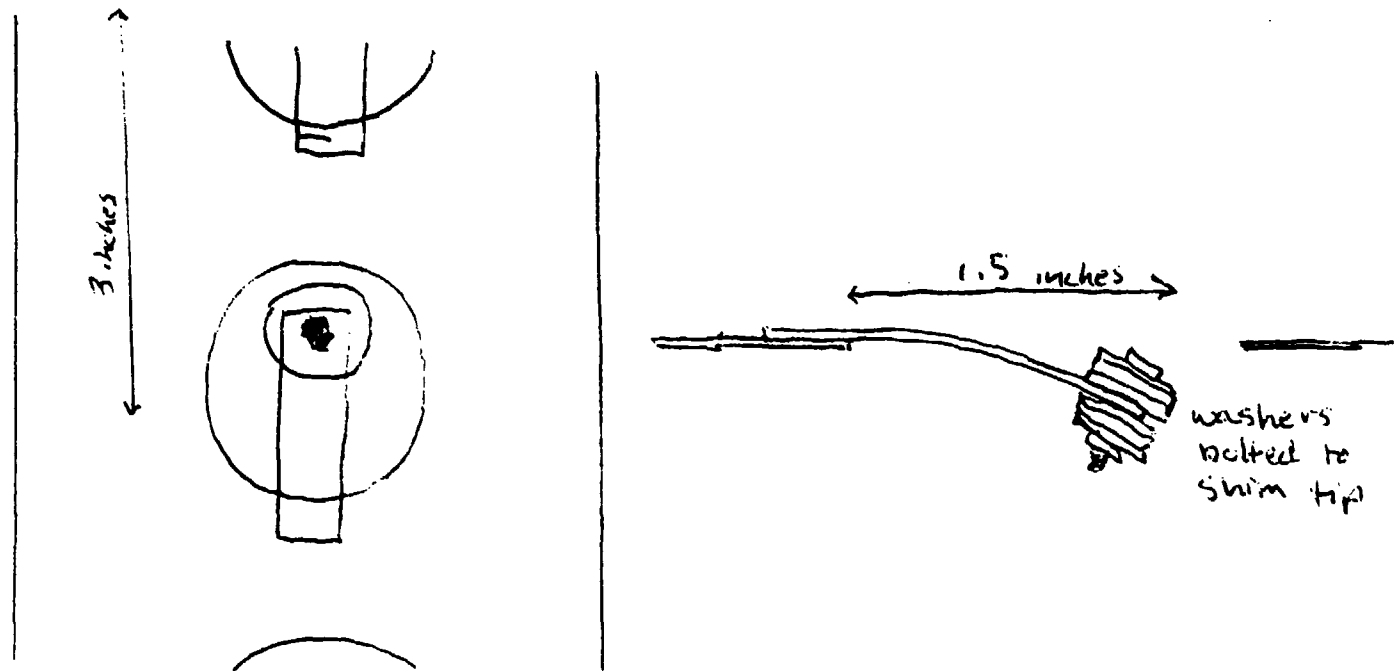
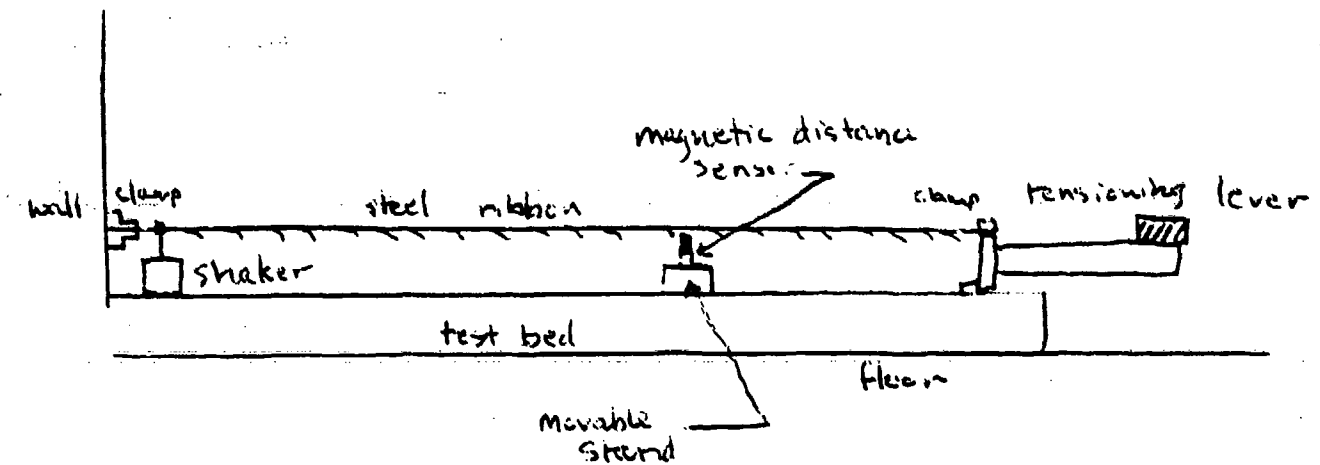


Figure 5: Experimental apparatus, and detail of one bay showing the "diving board" mass-spring sub-structure.

The choice of the cantilevered beam approach to the resonator was determined by a need to restrict freedom of movement to the vertical direction. At small amplitudes of tip oscillation the mass travels approximately only up and down. An attempt was made to keep tip oscillation

from being too great and thereby keep the oscillations linear. The thicknesses and tension and average tip mass considerations were made on two guidelines: (1) the average tip mass in a bay is approximately the same as the mass of the ribbon in a bay; (2) the pinned-pinned first mode of the overall structure is significantly higher in frequency than the natural frequency of the average resonator. Both the average tip mass and the ribbon mass per bay are about seven grams. The first global ribbon mode is at about 30 hertz and the average resonator has a natural frequency of about eight hertz. Since most testing occurred at frequencies less than 20 hertz, this kept us from exciting the global ribbon mode at 30 hertz.

The ribbon was supported by the railroad type I-beams of the test bed in the basement of building 33 at MIT. Angle iron clamps were used at the wall (and shaker) end of the ribbon and the other end was clamped to the tensioning lever. This lever consisted of a four foot long beam effectively hinged to the test bed on the end (see figure 6). The other end had iron and lead weights placed on it to transfer tension to the ribbon clamped to upper side of the lever base. This lever transferred weight of about 150 pounds into tension of about 700 pounds. This constant tension was used through all experiments and could not be affected by creep or temperature changes.

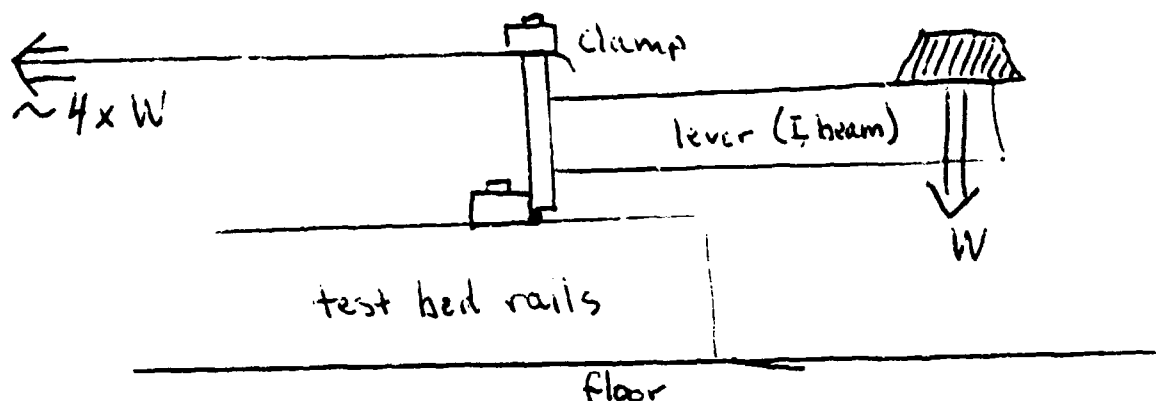


Figure 6: Tensioning lever scheme detail. The force of the weight placed on the end is magnified by the lever and applied as tension on the ribbon.

A magnetic distance sensor is used to measure the ribbon amplitude at any bay. This device outputs a voltage proportional to the distance between the ribbon and the tip of the sensor probe. A recording oscilloscope is used to measure the AC peak to peak amplitude of this voltage. In calibrating the sensor, we found it to operate linearly in the range needed with a DC voltage of about negative six volts. The sensor is held by a movable stand and the tip height can be adjusted so that the sensor is measuring AC amplitudes in its linear range. The stand can be moved to any bay and ribbon amplitudes measured from beneath the ribbon at a point in the center of the ribbon directly between the holes. A second identical sensor is placed to measure shaker amplitude so that output amplitude voltages could be normalized to input amplitude voltages, getting a non-dimensional ribbon amplitude at each bay.

A quick look at some errors inherent in the manufacture of our experimental structure reveal that even the "perfectly periodic" case is somewhat disordered. The location of the small hole through which the bolt passes is in error of about ten percent from to bay. The epoxy technique yields a fifteen percent error that affects the coefficient of end fixity and therefor the effective spring constant. These two major manufacturing inconsistencies yield a possible error in the natural frequency of any oscillator to 25 percent. This error in resonant frequency was seen in the initial testing of the perfectly periodic structure.

how determined?

Amplitude versus Position Experiment

From this experiment graphs of ribbon amplitude at each bay versus bay position were generated for sinusoidal inputs of several frequencies above the stop band. The nominal experimental plan was to identify a specific localized mode in the disordered structure and deduce its localization factor using an exponential curve fit to the amplitude versus position graphs as shown in figure 7. The perfectly periodic case was expected to exhibit no localization.

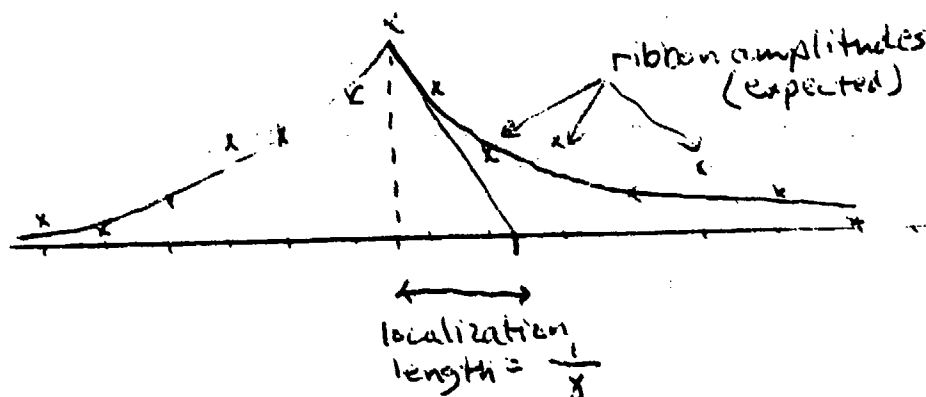


Figure 7: Original method of determining localization length with an exponential curve fit. This method could not be used because a single mode could not be identified.

Procedure

A signal generator is used to generate a sine wave of a frequency between 10 and 20 hertz. This sinusoidal input is amplified and sent to the shaker that forces the ribbon with the same sinusoid. The amplitude of the ribbon at the shaker is adjusted (by adjusting the volume of the amplifier) to be approximately a sixteenth of an inch (corresponding to five volts peak-to-peak from the distance sensor above the ribbon, next to the shaker). The other

non-linear
magnetic distance sensor was placed under the ribbon and its height adjusted so that it is operating in the linear range. The probe tip was positioned beneath the ribbon at a location directly between the holes of each bay. On our initial tests, we noticed a substantial 30 hertz component of the ribbon amplitude due to the first global mode of the entire ribbon. This should not be present in a linear system, if we are exciting it at frequencies less than 20 hertz, but our system is relatively non-linear. To avoid the effect of this component on our ribbon amplitude measurements, we low pass filtered the sensor output with a cutoff frequency of 27 hertz. The peak-to-peak amplitude of the filtered output of the sensor was measured from the oscilloscope and recorded for each bay. We did tests at 12, 14, and 16 hertz for both the perfectly periodic structure and the disordered structure.

Results

should have done more 8Hz
Amplitude versus position graphs were generated using the non-dimensional amplitude arrived at by dividing the measured peak-to-peak amplitude voltage by the five volt shaker amplitude. The position variable is the index of the bay where the amplitude was measured and numbers from 3 to 29 (sensor would not fit beneath bays 1, 2, and 30). Error in the amplitude measurement is estimated to be five percent due to the precision of reading the oscilloscope and the error of the sensor. Figure 8 shows the results from the 14 hertz tests of both the perfectly periodic and disordered cases. There is little or no difference between the amplitude versus position plots of the two cases. This is obviously not what we suspected, since it implies that there is no difference in the two cases determined by this method. The tests at 12 and 16 hertz were almost identical to the 14 hertz test shown. All three tests showed both the perfectly periodic and the disordered amplitude versus

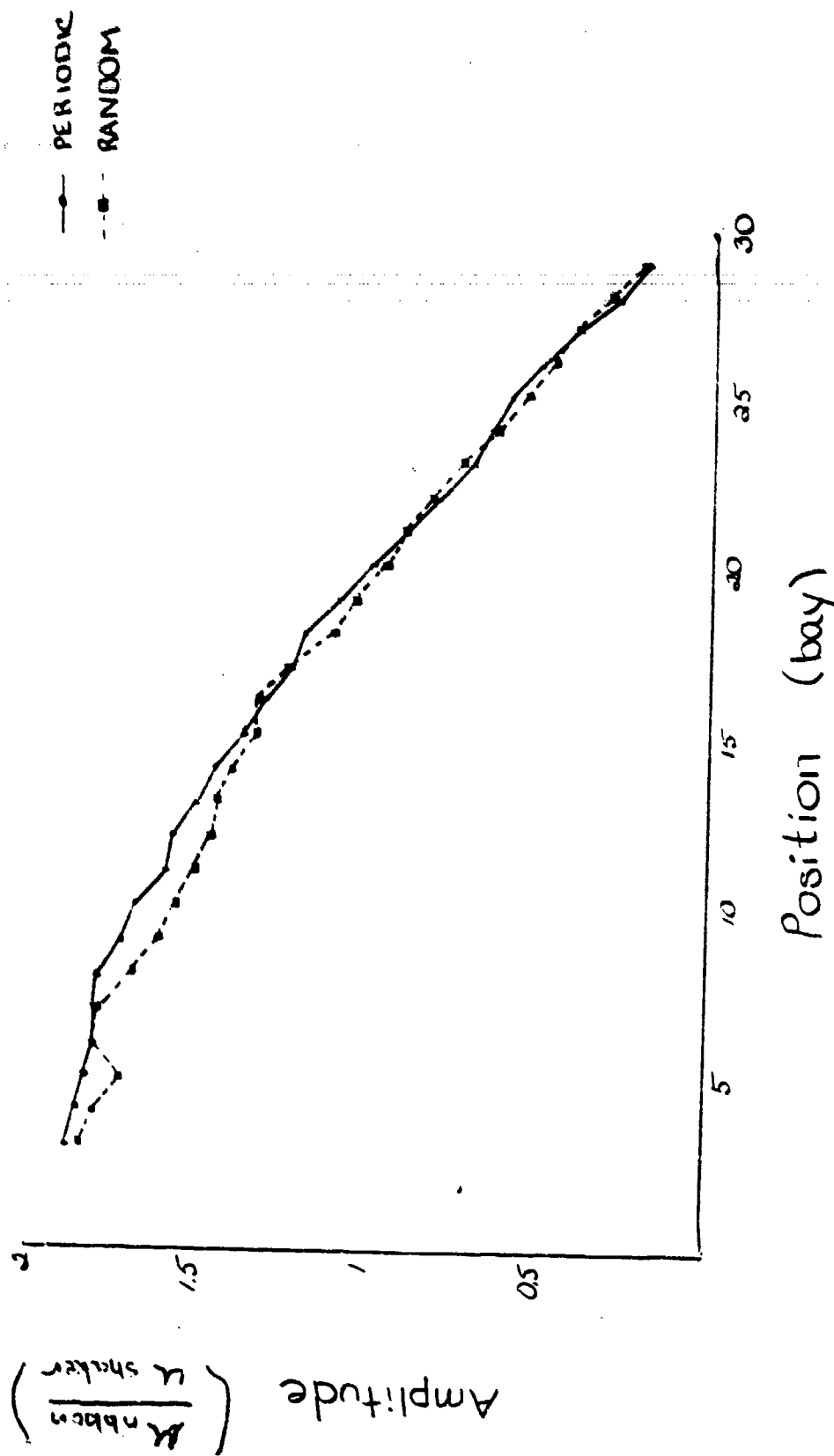


Figure 3: Ribbon amplitude versus bay position for the perfectly periodic case and the disordered case. This test was conducted at 14 hertz.

position graphs falling from about twice the input amplitude near the shaker end to near zero at the far (clamped) end. Since the first three tests showed no localization and indeed no difference in the two cases, we did not experiment further.

Discussion

The nominal experimental plan was to identify a single mode in the disordered structure. We were not able to do this due to non-zero damping which causes modal overlap. Theoretically, there are 30 modes in the structure, all near the average natural frequency of the resonators (8 hertz). If this were true, these modes would have to be spaced extremely close together in frequency. Since the damping due to air friction is not zero, we could not excite one specific mode without exciting the others. The problem is that the modes are closely spaced and lightly damped (rather than undamped, as theory assumes). Figure 9 shows the difference that the damping makes on the ability to isolate a single mode. Mode equations reveal that the modal spacing over the mode frequency has to be much greater than the damping in order to be able to excite a single mode. If $\Delta\omega$ is the frequency difference between two adjacent modes:

$$\xi \ll \frac{\Delta\omega}{\omega}$$

This condition is far from present in our experimental setup, so in 20-20 hindsight, we realize that we could not identify a single mode.

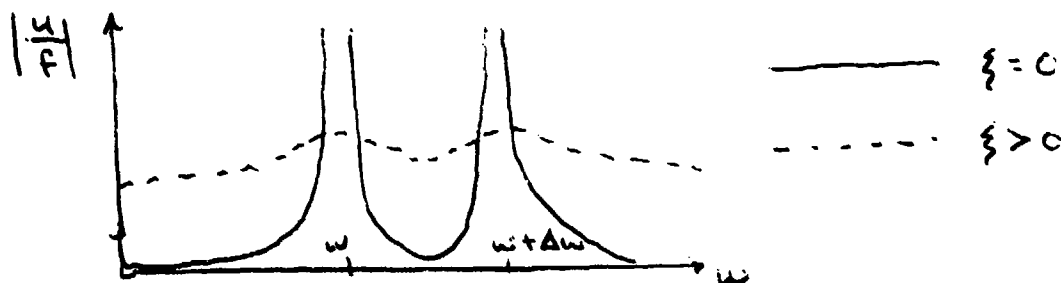


Figure 9: Magnitude of ribbon amplitude over frequency versus frequency. Only when there is infinitesimal damping can only one mode be excited.

Another non-ideal condition present in our setup is the relative disorder in the supposedly perfectly periodic structure. The 25 percent possible error in the natural frequency of the resonators makes the control case not valid as a control. The trend of ribbon amplitude decaying away from the shaker may be localization, but even if this is the case, the disordered structure is much more disordered than the perfectly periodic case, and should exhibit a greater localization. There is no way to determine if the small disorder in the perfectly periodic setup is causing localization without building a setup that is more strictly perfectly periodic. The decay toward the clamped end could also be just due to the fact that there is a clamped end; the theory that is being tested assumes an infinitely long structure (no end constraints). The inability to identify single modes in the disordered case and the relative disorder in our control case prevent this experiment from determining localization. Ignoring damping in the development of theories makes it difficult to test those theories in an experiment where damping is unavoidable.

Transfer Function Experiment

Since no conclusive results were obtained in the first experiment, we attempted to adapt our experiment to the experimental method used by Hodges and Woodhouse on their beaded string experiment. An alternate experimental using the same apparatus involved forcing the ribbon at one end with white noise and reading the ribbon amplitude near the other end. A localization can then be deduced from a comparison of the spectrums of the transfer functions of the disordered structure and the perfectly periodic structure.

Procedure

We used a PC based digital signal processor to generate our forcing waveform and to sample the ribbon amplitude. A white noise waveform was created by selecting the random output waveform from the signal processor (the ribbon was forced equally in all frequencies). The white noise forcing signal was also fed back into a channel of the signal processor for digital sampling. The magnetic distance sensor was placed and calibrated as in the first experiment, but was stationary at the 27th bay for this second experiment. The sensor output voltage was fed into a separate channel of the signal processor for digital sampling. A Hanning digital low pass filter was used to prevent sampling alias. Both signals were sampled so that frequencies up to 20 hertz could be determined, and a digital fast Fourier transform done to get their spectrum. These spectra were determined ten times and the results were then averaged. Using math software available with the signal processor, we divided the spectrum of the output amplitude by the input forcing to get the spectrum of the transfer function. This transfer function spectrum was integrated over frequency and the "step" near 8 hertz measured graphically.

The test was done on the perfectly periodic case (six washers in each bay) and the disordered case (same random configuration as was used in the amplitude versus position experiment), as well as a "semi-random" configuration (only five or six washers on each).

The significance of this step height is determined through some modal analysis. If we assume the transfer function of output ribbon amplitude to input forcing is given by

$$\frac{u(\omega)}{f(\omega)} = \sum_{j=1}^{\infty} \frac{\Gamma_j}{\omega_j^2 - \omega^2 - i 2 \zeta_j \omega_j \omega}$$

where Γ_j is the modal residue, given by the product of the modal amplitudes at the driving point and the response point. We expect the ratio of the modal residues for the two cases to be related to the localization factor:

$$\frac{\Gamma_j(\text{random})}{\Gamma_j(\text{perfect})} \approx e^{-\gamma(\omega_j)L}$$

where L is the number of bays between excitation and response. If one assumes as Hodges and Woodhouse did, that γ is constant over the frequency range examined then:

$$\frac{\text{step random}}{\text{step perfect}} = e^{-\gamma L}$$

which leads to:

$$\gamma(\bar{\omega}) = \left(\ln \frac{\text{step perfect}}{\text{step random}} \right) / L$$

Results

The spectrums of the transfer functions and their integrations are shown in figure 10 for both the perfectly periodic case and the disordered case.

Remembering

$$\gamma \propto \ln \frac{\text{step perfect}}{\text{step random}}$$

then the step height for the perfectly periodic case should be larger than that of the disordered case. The step heights determined by our experiment show the disordered case to be about five times greater than the perfectly periodic case. This result implies negative localization, which is a meaningless concept. The step height determined for the semi-random case was larger than that of the perfectly periodic case, and smaller than the fully random case, as might be expected.

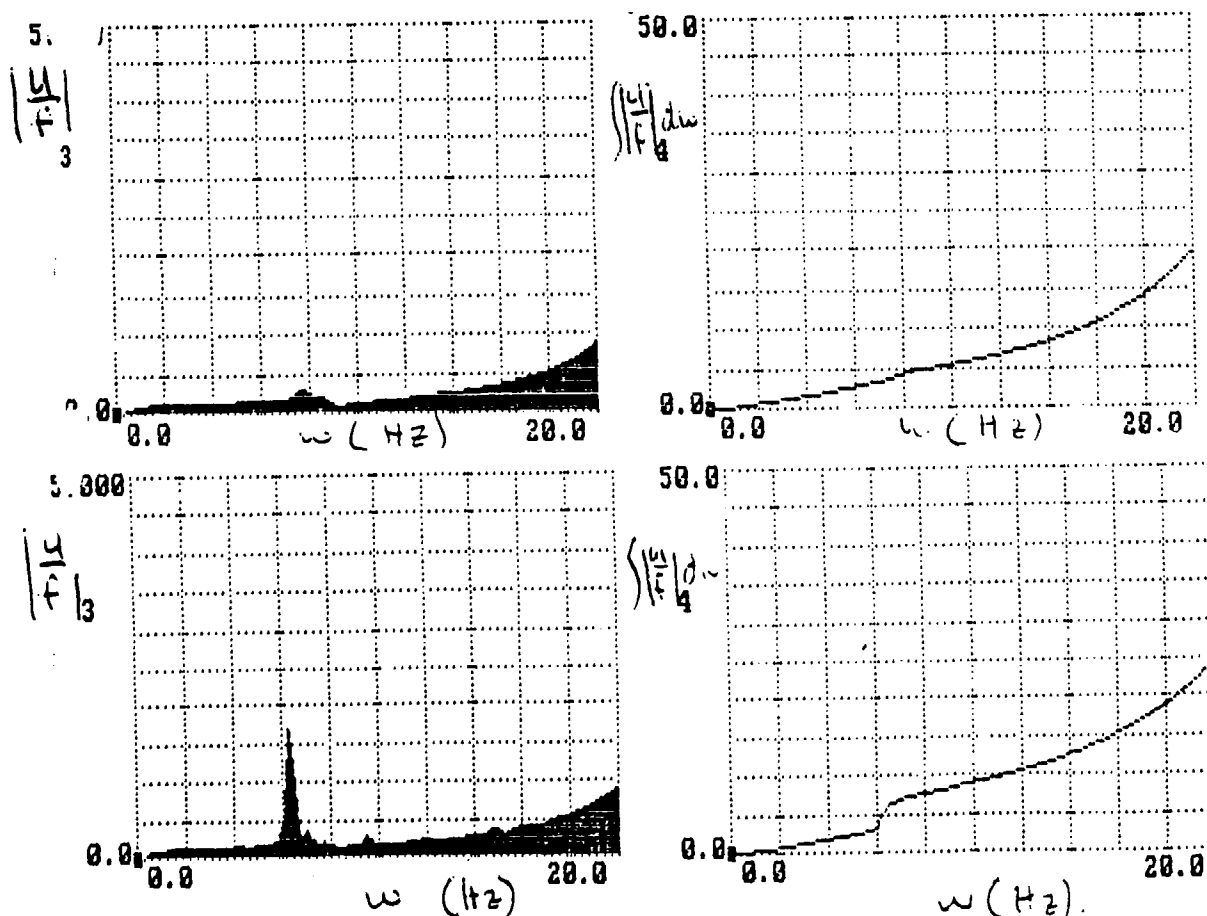


Figure 10: Spectra (left) and integrated spectra (right) for the transfer functions of the perfectly periodic case (top) and the disordered case (bottom). For localization to be observed, the step of the perfectly periodic case should be larger than the disordered case (doesn't happen).

Discussion

The result of no localization in this second experiment is due to the unexpectedly large step in the disordered case compared to the perfectly periodic case. The large step height of the disordered case is due to a large component in the frequency response near 8 hertz. This result could possibly be due to a local ~~peak~~^{mode} at the sensor location. This local peak could be due to mode localization or due to the resonator of the 27th being excited at its natural frequency. We could avoid this possible local peak phenomenon by averaging the response of many different configurations of the same randomness. This is done by generating more random numbers (still zero to twelve washers) and changing the washer placement configuration. Averaging the results of many configurations would reduce the effects of possible singularities at the sensor location. Furthermore, the relatively low step height in the perfectly periodic case could be due to the unintentional disorder or the modal overlap problem discovered in the amplitude versus position experiment. The modal theory predicts 30 closely spaced frequency response modes near 8 hertz, but the spectrum showed only a "lump" near 8 hertz. The lack of identifiable spikes is probably due to the modal overlap caused by non-zero damping.

Conclusions

Although we did not support nor disprove the wave/mode localization theory, this was a useful experiment. We suspected to observe localization in the disordered structure when we were designing it, and we expected to be able to produce a near perfectly periodic control structure. The fact that neither of these goals was achieved leads to two useful conclusions: all real world structures have some inherent disorder that cannot be totally eliminated, and this particular theory assumes some idealities that cannot be achieved in a real structure (i.e. zero damping or infinitely long). We did some additional research and found that the coupling of one bay to the next figures significantly into the localization prediction. In our case we were constrained to have very little coupling from one bay to the next. The small coupling was due to the high ribbon tension necessary to keep from exciting the full ribbon mode. There also seemed to be little coupling between the ribbon and the resonators; at most frequencies the resonators seemed to be just "going along for the ride" and not influencing the ribbon or the next resonator. We attempted to make up for this small coupling with a large degree of randomness in the disordered structure. A different experimental setup would perhaps be better for observing localization if it used large coupling between bays and only a small degree of disorder. Our only definite conclusion is that localization theory can be neither proved nor disproved with this particular experimental setup. The experiment must meet the constraints assumed by the theory if the theory is to be supported.

Recommendations

In subsequent experiments, the perfectly periodic system must be as perfectly periodic as possible to be a valid control. Also care must be taken to better fit the coupling/disorder constraints and the damping/end conditions constraints. Hodeges used a mathematical model of a coupled pendula system in his initial research; perhaps this system could form the basis of an experiment⁵. The coupled pendula apparatus could consist of many (more than 30) pendula connected together with relatively soft springs. The whole experiment could be conducted in a vacuum with an impedance matched far end; this would better approximate the zero damping and infinitely long constraints on the system. Another idea is a slinky type traveling wave experiment where reflected wave phenomena could be observed by eye. In both cases only weak disordering of the bays would be necessary to observe localization since the coupling would be stronger. This topic definitely warrants further study, and I would enjoy experimenting on a disordered system where the wave/mode effects would be slow enough in time and large enough in size to be observed by the naked eye. This condition would provide a better understanding of the reflection and transmission effects, on which the localization theory is based.

References

- 1 Anderson, P.W., "Absence of Diffusion in Certain Random Lattices," Physical Review, vol. 109, pp. 1492-1505, 1958
- 2 Furstenberg, H., "Non-commuting Random Products," Transactions of the American Mathematical Society, vol. 108, no. 3, September, 1963
- 3 Hodges, C.H., and Woodhouse, J., "Vibration Isolation from Irregularity in a nearly Periodic Structure: Theory and Measurements," Journal of Acoust. Soc. Am., vol. 74, pp. 894-905, 1983
- 4 Kissel, G.J., "Localization in Disordered Periodic Structures," extended abstract, MIT, 1986
- 5 Hodges, C.H., "Confinement of Vibration by Structural Irregularity," Journal of Sound

A HIERARCHIC CONTROL ARCHITECTURE FOR INTELLIGENT STRUCTURES

Kevin J. O'Donnell¹, Edward F. Crawley²,
Benjamin A. Ward³, Steven R. Hall⁴

The development of an echelon hierarchic feedback architecture applicable to intelligent flexible structures, i.e., structures with widely distributed sensors and actuators, is presented. The control functions are divided into global and regional control, which in turn are performed in one centralized global controller and many decentralized regional controllers, each of which is associated with a finite control element. The global processor calculates global control forces based on virtual measurements of the global nodal states of the finite control elements. Each regional processor reduces measurements from the sensors within its element to yield the virtual measurements of the nodal states, and likewise the regional processor distributes global control forces to the actuators in its element. Residual control, implemented by regional processors, acts on the difference between the global estimate of the motion of the structure and the actual regional measurements. Residual and distributed global control forces are combined to form the complete hierarchic control forces. A NIMO zero analysis provides a method for evaluating the effect of the global and residual controllers on the poles of the system for performance requirements.

¹ Research Assistant, Massachusetts Institute of Technology

² Associate Professor, Massachusetts Institute of Technology

³ Research Engineer, Tektronix Inc., Beaverton, OR

⁴ Assistant Professor, Massachusetts Institute of Technology

INTRODUCTION

The large dimensions and high performance requirements of envisioned space structures will result in close modal frequency spacing within the bandwidth of the control system. The control of structural vibrations will therefore be a critical part of the primary control system for many applications, including large communication satellites and precision optical structures. Control system design techniques which focus on modification of vibratory characteristics of flexible structures will be necessary in future system design procedures.

The goal of this research is to develop a hierarchic control methodology for flexible structures. This methodology is based on the assumption of an intelligent structure, i.e., a structure which incorporates widely distributed sensors and actuators possibly numbering in the hundreds or even thousands. Such high numbers are quite feasible with the projected technology for distributed components (Ref. 1). A feasible approach for such a highly distributed intelligent structure is to distribute the control functions into an echelon feedback architecture. The primary reason for developing this particular control methodology is to reduce the computational burden of structural control by dividing the control among many independent processors while limiting the input/output handling requirements of each processor to a smaller number of measurements and control commands. Further, it is proposed that this distribution be done in such a way as to complement the dynamic modeling of the structure.

The most conceptually simple traditional approach which might be considered for structural control is full state feedback, in which each control force is a function of every measurement. The computational requirements of such a scheme are quite demanding and can become a limiting factor in the real time application of control of a structure. In addition, the possible lack of access to the full state would make a full state feedback implementation unlikely. For these reasons, full state feedback control of large systems has generally been avoided.

Another approach to the control of flexible structures is to feed back the measurements from a small number of sensors to drive the available actuators. Such an approach can be based on optimal or suboptimal direct output feedback (Refs. 2,3). Alternatively, the measurements can be used to drive a "full" or reduced order estimator (Refs. 2,4,5). Such approaches have evolved by the extension of techniques originally developed for relatively modest dimensional systems (such as the six degree of freedom dynamics of an aircraft or spacecraft). They have in various ways been modified to take into account the high dimensional nature of the structural control task. Yet they are still conceptually focused on doing the most with a small number of sensors and actuators.

The above approaches call for a central processor to perform, at a minimum, a computation of the order of the number of sensors times the number of actuators, and at a frequency which is a multiple of the highest mode to be controlled. The estimator based systems must also perform additional calculations to update the dynamic estimate. But as

the number of sensors, actuators, and modeled modes increases, the number of computations required per second increases at a power between N^3 and N^4 even for output feedback systems. One must begin to consider systems which distribute the processing, preferably in a way which will also reflect the physical distribution of information flow in the structure, and therefore reduce the possibility of unwanted control spillover.

A division of control effort, suggested by Aubrun and Margulies (Ref. 6), is that there be two parallel control tasks, high authority control (HAC) and low authority control (LAC). The objective of LAC is to supplement the natural damping in the structure by providing simple state feedback at all colocated sensors and actuators, reducing the possibility of destabilization due to control spillover from the HAC. This colocated LAC feedback mechanism provides simple damping to the whole structure with good stability characteristics (Refs. 7,8). The HAC loop is then designed to meet performance specifications for the new plant which includes the supplemental feedback. There is no coordination between the control effort of the HAC and LAC loops. The input/output requirements of the HAC controller offer no improvement over single control approaches in that the HAC loop generally requires the processing of every measurement to determine every control force.

Another control architecture, which addresses the issues of dividing the control responsibility and computational and input/output burden, is hierarchic control (Ref. 9). The hierarchic feedback structure considered here is based on the assumption of widely distributed sensors and actuators and involves a two-level echelon feedback architecture (Fig. 1). Level 1 consists of many autonomous regional processors which interface with the sensors and actuators in separate finite control elements of the structure. The design of these finite control elements must also allow for the distribution of the processing among independent processors, i.e., the structural model and control must be regionally banded. The functions of the regional controllers are coordinated by a global processor, at level 2.

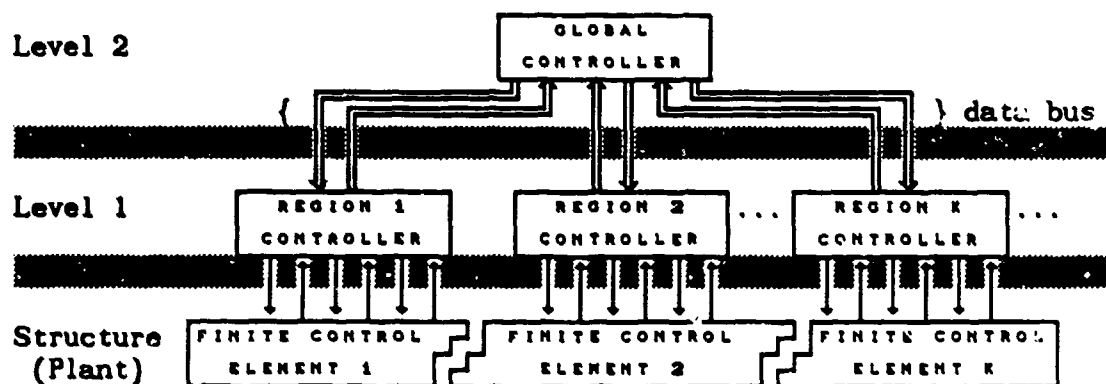


Fig. 1 Two-level hierarchic control structure.

In contrast to the HAC/LAC formulation, the information flow in this design does not require that any single controller be responsible for

coordinating all the measurements and control forces of the system. This greatly reduces the input/output burden of any single processor. In addition, with sufficiently simplified control tasks performed at the global and regional levels, computational requirements can theoretically be reduced by two or more orders of magnitude compared to a full state feedback design.

This paper details the development and evaluation of a two-level echelon hierarchic control methodology for implementation in flexible structure control. The methodology outlines the division of control between global and regional control and specifies the control functions performed at the two different levels. Methods of analyzing the control interaction between the two control functions is discussed in terms of pole-zero analysis. The procedure is then applied to the simple example of a rod in extension.

HIERARCHIC CONTROL SYNTHESIS

Architecture

The fundamental idea behind the hierarchic control formulation presented here is a parallelism between the division of an original large finite dimensional structural model into finite control elements and the division of control authority into regional controllers overseen by a global controller. Just as short wavelength disturbances are propagated in a structure locally (i.e., the stiffness matrices are banded), the control is distributed into local regions. And as it is possible for long wavelength modes to develop, there is also a global controller. Global control is based on nodal state information represented at the nodes of a finite control element reduction of the original large finite dimensional model of the structure (Fig. 2). The global model characterizes structural motion by virtual displacements q_i and velocities \dot{q}_i at these discrete node points. These global virtual states are related to the degrees of freedom of the original finite dimensional model by the element interpolation functions (e.g., T_{ij}), in a manner discussed below. Likewise, structural forces can be represented by equivalent virtual forces acting at those same node points. The regional control model is based on the original finite dimensional model of the structure. This is the level at which the location and influence of the physical sensors and actuators are important. This method of representing the structural behavior by boundary nodal values is conceptually similar to the component mode synthesis approach of structural dynamics (Ref. 10).

The corresponding division of control function in a two-level hierarchic controller is outlined in Fig. 3. The global controller is responsible for implementing control functions based on the global nodal states \hat{x}_g . As in finite element structural modeling techniques, the effectiveness of the global controller is based on the assumption that the global model accurately describes the structural motion. The regional controllers, when combined form the residual control block in Fig. 3, operate within the global element boundaries based on \hat{e} , the residual of the local measurements y and the estimates of the local measurements

interpolated from the global estimates \hat{x}_g . The specific objective of the regional controller is to perform inner loop compensation within each region to force the structure to track the behavior expected by the global model.

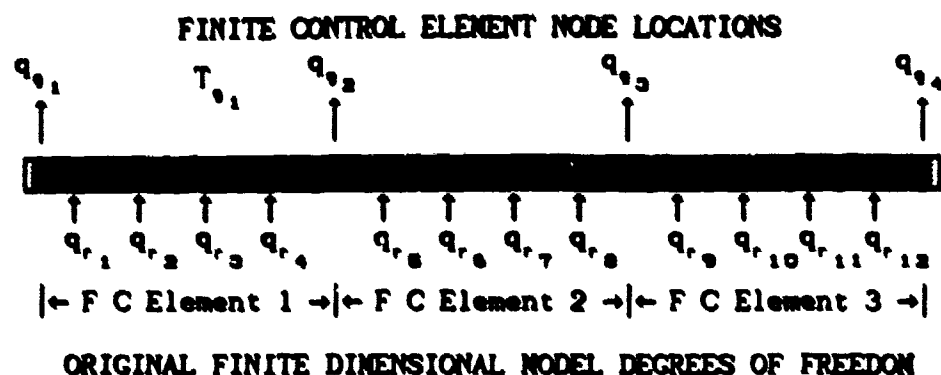


Fig. 2 Control domains based on finite dimensional model

Control Objectives

The objective of the global control is to control the overall behavior of the structure based on the global finite control element model. Three basic tasks are involved in implementing global feedback and are shown in Fig. 3: the measurement aggregation which reduces the system measurements y into an estimate of the states in the global model \hat{x}_g ; the computation of the virtual global control commands v_g from the estimates of the global states; and the distribution of the global control which calculates the physical control forces v_r to be applied to the system based on the global commands.

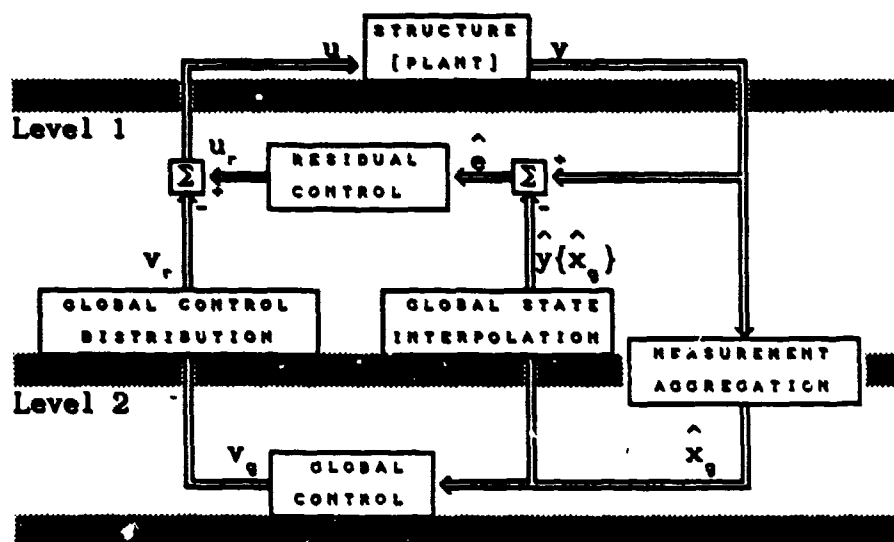


Fig. 3 Hierarchic Control Functional Block Diagram

The residual controller operates on the difference between the global finite element model and the original, higher dimensional model of the

structure. The estimated global states are interpolated to form a set of estimated measurements \hat{y} that are consistent with the nodal states \hat{q}_i . These measurements are differenced with the actual measurements of the system y to form an estimate of the residual error \hat{e} . The residual controller calculates control forces u_r to drive the residual error to zero. The combined global control forces v_r and residual control forces u_r are then commanded of the actuators.

In order to understand the steps involved in Fig. 3, consider first the original finite dimensional model of the structure. This model is derived using any appropriate finite element, finite difference, or other modeling technique. As with most structural models, the inherent damping is initially assumed to be zero. The second order dynamic equation describing the structure is then

$$M \ddot{q} + K q = \Psi u \quad (1)$$

where $q \in R^n$ is the vector of the generalized coordinates, $u \in R^m$ is the vector of control inputs, M is a symmetric, positive definite mass matrix, K is a symmetric, non-negative definite stiffness matrix, and Ψ is the control influence matrix.

For the following development of the two-level hierarchic control technique, two simplifying assumptions will be made. The first is that complete measurements of the full state of the original finite dimensional model (q , and \dot{q}) are available. This assumption is intentionally restrictive in order to simplify the presentation of the technique. In most systems, the full state must be estimated from partial state measurements. The second assumption is that the system has as many nonredundant actuators as generalized coordinates (i.e., Ψ is square and full rank). This assumption is also restrictive and further simplifies the analysis. Since the probable application of this technique is to systems with large numbers of distributed sensors and actuators, these restrictions are not as severe as might be thought. Currently, research is underway to analyze the implications of relaxing these constraints, but the remainder of this presentation will accept the restrictions.

Global Control Synthesis

The objective of the global control law is to control the long wavelength motion in the structure that is critical to the system performance. In the global model, the motion of each finite control element is defined in terms of the global nodal degrees of freedom as shown in Fig. 2. According to finite element theory, the motion of every point within the finite control element is specified in terms of exact interpolation functions (such as T_{i1} in Fig. 2) and the associated nodal degrees of freedom. In this formulation, the finite element interpolation is applied to an existing finite dimensional model, rather than the continuous structure. Thus, each finite control element contains a unique subset of the original finite dimensional model degrees of freedom and an associated subset of the sensors and actuators. In terms of the global degrees of freedom, the original degrees of freedom can be represented as

$$\mathbf{q}(\mathbf{q}_0) = \mathbf{T}_0 \mathbf{q}_0 \quad (2)$$

where $\mathbf{q}_0 \in \mathbb{R}^{n_0}$ is the vector of global nodal degrees of freedom of the global model and n_0 is the number of global degrees of freedom. \mathbf{T}_0 is an interpolation matrix constructed by combining the local transformation matrices from each finite control element into a single matrix. \mathbf{T}_0 is also used to consistently interpolate from the global to the original model velocity by differentiating Eqn. 2 with respect to time.

The consistent global equation of motion is obtained by substituting Eqn. 2 into Eqn. 1 and premultiplying by \mathbf{T}_0^T , transpose, yielding

$$\mathbf{M}_0 \ddot{\mathbf{q}}_0 + \mathbf{K}_0 \mathbf{q}_0 = \mathbf{T}_0^T \boldsymbol{\psi} \mathbf{v}_r \quad (3)$$

where $\mathbf{M}_0 = \mathbf{T}_0^T \mathbf{M} \mathbf{T}_0$ is the global mass matrix and $\mathbf{K}_0 = \mathbf{T}_0^T \mathbf{K} \mathbf{T}_0$ is the global stiffness matrix. Since n_0 is usually much smaller than n , this system has a far greater number of actuators than generalized coordinates. Since a full state feedback control of the global system will result in at most n_0 independent control forces, a transformation must be defined for distributing those n_0 global control forces over the entire set of n actuators. In this sense, a nodal force is spatially distributed over the discrete actuators within the element.

A global control vector, \mathbf{v}_0 , is defined so that the control vector consists of n_0 independent virtual global forces, each associated with one of the global degrees of freedom in the vector \mathbf{q}_0 . These virtual global forces must then be distributed into physical forces, \mathbf{v}_r , according to the general relation

$$\mathbf{v}_r = \mathbf{S}_0 \mathbf{v}_0 \quad (4)$$

where \mathbf{S}_0 is the global force distribution matrix. One way of specifying a complementary choice of \mathbf{S}_0 which is consistent with the measurement interpolation is to require

$$\mathbf{S}_0 = \boldsymbol{\psi}^{-1} \mathbf{M} \mathbf{T}_0 \quad (5)$$

This choice of \mathbf{S}_0 will provide that the control force distribution matrix is banded with respect to the regions in that the control commands can be divided among the regions for application to the structure by the actuators controlled by the regional processors. The effect of this choice of \mathbf{S}_0 can be seen by substituting Eqns. 4 and 5 back into the global dynamic model, Eqn. 3, yielding

$$\mathbf{M}_0 \ddot{\mathbf{q}}_0 + \mathbf{K}_0 \mathbf{q}_0 = \mathbf{M}_0 \mathbf{v}_0 \quad (6)$$

It is seen that the global control force distribution causes the virtual global controls to appear as global node acceleration commands and thus results in structural accelerations which are consistent with the global model. Each global control force is distributed by the global interpolation matrix, multiplied by the local mass to generate the appropriate force, and then multiplied by the inverse of the control influence matrix to obtain actual control commands (Eqn. 5).

Since the global nodal states required for global control are not directly measured, the virtual measurements must be estimated by spatially filtering the physical measurements within each control

element. The global finite control element formulation assumes that the interpolation functions (Eqn. 2) provide an exact description of the structural deformation for the subset of the degrees of freedom within the element. In reality, there is a difference, or residual, between the actual structural deflections, described by the original finite dimensional model, and the global description. The error based on the estimated global displacements is given by:

$$\hat{e} = q - T_e \hat{q}_e \quad (7)$$

where $\hat{e} \in R^n$ is the vector of the estimated residual degrees of freedom. The optimal estimate of the global state is defined in terms of minimizing a weighted quadratic of the estimate of the residual.

$$\hat{q}_e = (T_e^T M T_e)^{-1} T_e^T M q = T_e^{-L} q \quad (8)$$

The resulting matrix that relates q to \hat{q}_e is actually a pseudo left inverse of the transformation matrix T_e . In other words, \hat{q}_e is the weighted least squares estimate of the global states based on the interpolation functions. The mass was used as the weighting matrix due to the similarity of the pseudo inverse with the standard modal orthogonality condition. If the actual mode shapes are represented by the transformation matrix, T_e , then Eqn. 8 will yield an exact transformation from physical to modal coordinates. For consistency, the same transformation is used for both displacement and velocity.

Now that the measurement aggregation function (the transformation from q to \hat{q}_e) has been defined, the effect of the global control loop on the structure can be examined by substituting the reduced global control law back into the original equation of motion, which yields

$$M \ddot{q} + K q = M \dot{1}_e^T F_{e,v}^M T_e^{-L} \dot{q} + M T_e^T F_{e,d}^M T_e^{-L} \hat{q}_e \quad (9)$$

where F_e^M denotes the feedback gains and has been broken into velocity and displacement submatrices. Equation 9 can now be used to predict changes in system performance due to the global control loop.

Residual Control Synthesis

The residual control (inner loop) of the hierarchic control scheme generates control signals based on the residual error between the actual measurements of the states of the original finite dimensional model and the interpolation of the virtual global states. The objective of the residual control is to suppress the local structural motion that is inconsistent with the global model dynamics. One of the primary requirements of the residual control implementation is that it be performed within each of the regions based only upon local information and information received from the global controller. Also, the residual control should not excite the global motion of the structure. These two requirements will restrict the possible control implementations. In addition, it is desirable that the residual control be computationally simple.

In order to analyze the residual control, consider the estimate of the displacement residual error as

$$(8)$$

$$\hat{\mathbf{e}} = \mathbf{q} - \hat{\mathbf{q}} = (\mathbf{I} - \mathbf{T}_q \mathbf{T}_q^{-1}) \mathbf{q} \quad (10)$$

The general form of the feedback law that implements the residual control is

$$\mathbf{u}_r = -\mathbf{F}_{r_d} \hat{\mathbf{e}} - \mathbf{F}_{r_v} \dot{\hat{\mathbf{e}}} \quad (11)$$

Since the residual control is designed not to excite global motion, the component of the structural acceleration that results from residual control forces must be analyzed. This acceleration, which will be called the residual control acceleration, is

$$\ddot{\mathbf{q}}_r = \mathbf{M}^{-1} \Psi \mathbf{u}_r \quad (12)$$

An estimate of the global acceleration due to the residual control acceleration can be determined using the same estimation matrix that is used to determine the reduced order global state measurements from the full order measurements (Eqn. 8)

$$\hat{\ddot{\mathbf{q}}}_{r_g} = \mathbf{T}_q^{-1} \mathbf{M}^{-1} \Psi \mathbf{u}_r \quad (13)$$

The first requirement that the residual control only affect the residual motion is satisfied if Eqn. 13 is identically zero.

One restricted form for the residual feedback gain that meets this requirement, and the requirement that the feedback be applied based only on local information, is

$$\mathbf{F}_{r_d} = \alpha \Psi^{-1} \mathbf{M} \quad , \quad \mathbf{F}_{r_v} = \beta \Psi^{-1} \mathbf{M} \quad (14)$$

where α and β are nonnegative scalar constants. The residual control acceleration for these gains is

$$\ddot{\mathbf{q}}_r = -\alpha \hat{\mathbf{e}} - \beta \dot{\hat{\mathbf{e}}} \quad (15)$$

Here, the residual control acceleration is in direct proportion to the estimates of the residual states in the system and will be called direct proportional feedback. In addition, if α and β are negative, the control acceleration always acts against the residual displacement and velocity.

To analyze the effect of the direct proportional feedback on the dynamics of the system, consider the reduced model based only on the residual modes. Just as the global model describes the dynamics of a subset of modes in the system (Eqn. 3), there also exists a model of the subset of the residual modes of the system. This reduced model requires a transformation that relates a set of residual model states to the full order residual of the system. The transformation \mathbf{T}_q maps the n_q dimensional global displacement vector \mathbf{q}_q into the n dimension vector space of \mathbf{q} . Therefore, the residual must reside in the remaining subspace of \mathbf{q} that is orthogonal to the subspace of \mathbf{q}_q . The dimension of that subspace is $n_r = n - n_q$. Therefore, the complete vector \mathbf{q} can be expressed as

$$\mathbf{q} = \mathbf{T}_r \mathbf{q}_r + \mathbf{T}_q \mathbf{q}_q \quad (16)$$

where $\mathbf{q}_r \in \mathbb{R}^{n_r}$ is the vector of residual degrees of freedom and \mathbf{T}_r is the residual transformation matrix. The combination of the two mapping functions in Eqn. 16 must span all possible vectors \mathbf{q} (i.e., the matrix \mathbf{T}_r spans the null space of \mathbf{T}_q).

The exact choice of the residual transformation matrix is found by considering the estimated global degrees of freedom based on Eqn. 16 and premultiplying by T_g^{-L} (Eqn. 8) to obtain

$$\hat{q}_g = T_g^{-L} T_r q_r + q_g \quad (17)$$

To make the estimate of the global degrees of freedom equal the actual values, the first product in Eqn. 17 should always be zero. This product is identically zero only when $T_g^{-L} T_r$ is null. Examining the definition of T_g^{-L} in Eqn. 8, this requirement reduces to

$$T_g^T M T_r = 0 \quad (18)$$

(i.e., T_r is orthogonal to T_g with respect to M). The combined requirements of Eqn. 18 and that T_r span the null space of T_g fully specifies the space mapped by T_r .

The reduced order residual model can now be formed by assuming that the residual motion in the structure is orthogonal or decoupled from the global motion in the structure. Thus, there is a subset of structural motions for which $T_g q_g$ is zero and the remaining motions are described by the relation

$$q \{q_r\} = T_r q_r \quad (19)$$

Substituting this into the original equation of motion (Eqn. 1) and premultiplying by T_r transpose yields the reduced order residual model equation of motion

$$M_r \ddot{q}_r + K_r q_r = -\alpha \cdot M_r q_r - \beta \cdot M_r \dot{q}_r \quad (20)$$

where $M_r = T_r^T M T_r$ and $K_r = T_r^T K T_r$. While the reduced order global model characterizes the longer wavelength modes of the higher order dynamic model of the system, Eqn. 21 provides a reduced order characterization of the remaining modal dynamics.

The effects of the residual feedback on the reduced order residual model is best evaluated if Eqn. 20 is transformed into modal coordinates (Ref. 11) to obtain

$$\ddot{F}_r + \beta \cdot \dot{F}_r + (\alpha \cdot I + \Lambda_r) F_r = 0 \quad (21)$$

where $F_r \in R^{n_r}$ is the vector of the residual model modal coordinates and Λ is the diagonal matrix of the residual model squared natural frequencies. It is clear from the form of Eqn. 21 that the decay rate ($\beta/2$) for each of the residual model modes is the same. Likewise, the increase in the square of the natural frequency (α) is the same for all modes due to direct proportional feedback. Thus, it can be concluded that direct proportional feedback affects all residual model modes equally.

One possible selection of the residual control feedback gains α and β is to choose them as the averages of the closed loop gains of the full state optimal regulator solution applied to the entire structure. The residual modes' decay rates can be made to approximate the full order optimal regulator decay rates of the residual modes if β is selected as

$$\beta = 2/n_r \sum \sigma_i^* \quad (22)$$

(10)

where σ_i^* is the real part of the closed loop poles of mode i of the full order optimal regulator and the summation is made over all system modes in the residual model. A similar approach can be used in selecting the stiffness parameter α . The stiffness increase of the residual modes is chosen to equal the average stiffness increase of the associated modes in the full order control system by selecting α to be

$$\alpha = 2/n_r \sum (\omega_i^{*2} - \omega_i^2) \quad (23)$$

where ω_i^* is the closed loop natural frequency of mode i of the optimally controlled full order dynamic model and ω_i is the open loop natural frequency of mode i of the full order dynamic model. The hierarchic control that results from this selection of α and β and the global control of the previous section can now be combined to analyze the total system performance.

HIERARCHIC CONTROL ANALYSIS

Using standard techniques, the two-level hierarchic control scheme can be designed with stable controllers for each level of control. However, since the two controllers do not operate in isolation, the two control functions will interact with each other. Large levels of control interaction may result in system destabilization. Therefore, the ability to accurately predict the closed loop dynamics of the hierarchic control implementation is an important concern.

Control Coupling

In order to evaluate the effect of control interaction between the global and residual control, the mechanisms through which these functions interact must be established. The full closed loop dynamic equation can be written by combining Eqn. 9 and Eqn. 20 to obtain

$$\begin{aligned} \mathbf{M} \ddot{\mathbf{q}} + \mathbf{K} \mathbf{q} = & - (\mathbf{M} \mathbf{T}_g^T \mathbf{F}_{g,d}^* \mathbf{T}_g^{-L} + \alpha \mathbf{M} (\mathbf{I} - \mathbf{T}_g \mathbf{T}_g^{-L})) \mathbf{q} \\ & - (\mathbf{M} \mathbf{T}_g^T \mathbf{F}_{g,v}^* \mathbf{T}_g^{-L} + \beta \mathbf{M} (\mathbf{I} - \mathbf{T}_g \mathbf{T}_g^{-L})) \dot{\mathbf{q}} \end{aligned} \quad (24)$$

where the terms involving \mathbf{F}_g^* result from the global feedback implementation and the terms involving α and β result from the residual feedback implementation. The coupled dynamics of the two subsystems can be obtained by substituting Eqn. 16 into Eqn. 24 and premultiplying by suitable transformation matrices to obtain

$$\mathbf{M}_g \ddot{\mathbf{q}}_g + \mathbf{K}_g \mathbf{q}_g + \mathbf{K}_{g,r} \mathbf{q}_r = - \mathbf{M}_g \mathbf{F}_{g,d}^* \mathbf{q}_g - \mathbf{M}_g \mathbf{F}_{g,v}^* \dot{\mathbf{q}}_g \quad (25)$$

$$\mathbf{M}_r \ddot{\mathbf{q}}_r + \mathbf{K}_r \mathbf{q}_r + \mathbf{K}_{g,r}^T \mathbf{q}_g = - \alpha \mathbf{M}_r \mathbf{q}_r - \beta \mathbf{M}_r \dot{\mathbf{q}}_r \quad (26)$$

The two subsystems of Eqns. 25 and 26 are the global and residual models developed in the previous section with the addition of an elastic coupling term, $\mathbf{K}_{g,r} = \mathbf{T}_g^T \mathbf{K} \mathbf{T}_r$. When $\mathbf{K}_{g,r}$ is identically zero, \mathbf{T}_g exactly represents a linear combination of n_g natural modes of the original system, and \mathbf{T}_r exactly represents a linear combination of the other n_r natural modes. The coupling between the two systems will be light if \mathbf{T}_g closely approximates a subset of the normal modes and the control forces have been selected to not introduce any further coupling.

To guarantee that the full hierarchic feedback system is stable, one viable solution is that the control implemented in the global and residual design models (Eqns. 25 and 26) must duplicate the effects of passive components. With this restriction, both models will act as stable passive systems. This will guarantee system stability since the coupling of two passively stable systems cannot result in overall system instability (Ref. 9).

MIMO System Zero Analysis

The assurance of a stable control design is just one important aspect in evaluating the effect of control coupling in the hierarchic control design. The primary design goal is not just one of stability, but of meeting specific performance requirements. This means that the effect of the hierarchic control on the closed loop dynamics of the system must be understood.

The primary method of analysis used in this section is based on the relationship between the generalized zeros of MIMO system (Ref. 12) and feedback system response. With few exceptions, such as the work done by Taylor (Ref. 13), MIMO system zero analysis has not been applied to structural control design. MIMO system zeros are close counterparts to zeros of classical single-input/single-output (SISO) systems and their properties can be exploited in many of the same ways.

There are two important properties of MIMO system zeros that directly relate to output feedback control laws. The first is that system zeros remain invariant under output state feedback (Ref. 14). The second property is that if the MIMO system has j finite system zeros, then j of the $2n$ system poles will converge on the finite zeros and the remaining $(2n-j)$ poles will go to infinity as the output feedback gains are increased to $+\infty$ in a positive definite manner (Ref. 15). Both these properties are familiar to SISO feedback systems and are used explicitly in root locus analysis design. For the same reasons, the MIMO zeros are important to MIMO feedback system design. In particular, the evaluation of the MIMO zeros of the global and residual control functions will be important to the evaluation of the hierarchic control design.

Three topics will be discussed with respect to MIMO zero analysis of the complete hierarchic control structure. First, the mechanisms which cause system zeros in the global and residual control implementations will be established. Second, the relationship between global and residual system zeros and the closed loop dynamics of the full order structure will be examined. Finally, an exact method of determining the location of these zeros and the mechanisms that influence their locations is established. The culmination of these results will provide valuable guidelines for the hierarchic control design.

For the hierarchic development presented in the hierarchic control synthesis, the initial structure had full state measurement and complete independent control. Given these constraints, it can be shown that there are no zeros for the full system. However, MIMO zero analysis is useful for analyzing the subsystems defined by the global and residual

control functions. The global feedback gains perform output feedback around the residually controlled structure and, therefore, will not affect the location and number of possible zeros of the global control system. Since the global measurement and the global control influence matrices are designed to isolate motions in the structure that are consistent with the reduced order global model, there are many motions in the structure that cannot be represented or affected by this control system. These motions will be characterized by the global system zeros. The analysis of the residual control system zeros is nearly identical in that zeros arise in this system that correspond to structural motions that cannot be represented or affected by the residual control system.

The relationship between global and residual zeros and the closed loop dynamics of the structure will be examined through the evaluation of a particular example. This example is the unique case in which the reduced order global model exactly characterizes a subset (n_g) of the structural modes. Subsequently, the motions described by the residual model must exactly describe the remaining n_r modes of the structure. Thus, the global and residual subsystems are totally decoupled (i.e., $K_{gr} = 0$).

For this simple case, the subsystem decoupling can be described in terms of global and residual control system zeros. For complete decoupling of the two subsystems, it can be shown that the measurement matrices of the two subsystems are each orthogonal to the modes of the other. Therefore, the global controller must have decoupling zeros at each of the residual pole locations. Likewise, the residual controller will have system zeros at the global pole locations. Therefore, for completely decoupled subsystems, the zeros of the two subsystems will correspond exactly with the locations of the closed loop poles of the combined system.

The next step is then to consider the effect when T_g and T_r do not provide exact models of the global and residual system modes. The global and residual zeros will not disappear, but rather many (or all) of the decoupling zeros will become transmission zeros. If the new T_g is very close to the decoupling matrix just discussed, the zeros of the global or residual control systems should be close to their previous locations (i.e., the poles of opposite system). If this is the case, the zero locations offer an approximate description of the closed loop dynamics of the structure.

For selection of T_g that does not provide exact or near decoupling between the global and residual subsystem, the relationship between the respective system zeros and the system dynamics becomes less clear. It is clear that feedback of the residual system will affect the zeros of the global system and vice versa. The relationship between the controls and the closed loop zero locations can be determined through the results of two theorems (Ref. 9).

Theorem 1: In the limit, as the global displacement feedback gain, F_{ga} , becomes very large (in a positive definite sense) and $\|F_{ga}\| \gg \|F_{gv}\|$, $2n_r$ of the system poles converge to the closed loop poles of the residual control model (Eqn. 21) and the remaining $2n_g$ of the system

poles are the closed loop poles of the global model (Eqn. 9).

Theorem 2: In the limit, as $\alpha \gg 0$ and $|\alpha| \gg |\beta|$, $2n_r$ of the system poles converge to the closed loop poles of the global control model and the remaining $2n_g$ of the system poles are the closed loop poles of the residual model.

These theorems summarize the analysis of the closed loop poles of the coupled global and residual subsystems. Of these closed loop pole locations, $2n_r$ converge to the closed loop pole locations of the residual model and $2n_g$ converge to the closed loop pole locations of the global model. Since the residual model pole locations remain fixed as $F_{g,0}$ is increased and since these are converging points of the full order system poles, they must also be the zero locations of the global controller. Likewise, since the global model pole locations are fixed as α is increased, the remaining converging points are the zero locations of the residual controller.

From this analysis, it is clear that the proximity of the global and residual control system zeros to the poles of the actual system is a direct indicator of the decoupling between the global and residual controllers. For perfectly decoupled control systems, the zeros of the global control system correspond to $2n_r$ of the system poles and the zeros of the residual control system correspond to the remaining $2n_g$ poles of the system. Even with coupled subsystems, the poles of the complete system will tend to follow the poles of the uncoupled subsystems, depending on the amount of coupling and the relative magnitudes of the feedback gains.

As with all finite element applications, a more accurate model of the structural modes will produce more accurate predictions of the response. For the application to the control problem, accurate modeling of the structural modes is seen to reduce the control problem into decoupled subsystems which can be effectively controlled using the hierarchic control technique. The natural conclusion from this analysis is that the free model parameters should be selected to provide the lowest coupling between the global and residual controllers.

EXAMPLE

For the following example, the hierarchic control technique will be applied to the case of controlling a bar in extension using widely distributed sensors and actuators. A possible model for the full order control problem is shown in Fig. 4. This lumped parameter model is assumed to have seven degrees of freedom with a sensor and actuator on each mass. In addition, the value of each mass and stiffness is set to unity.

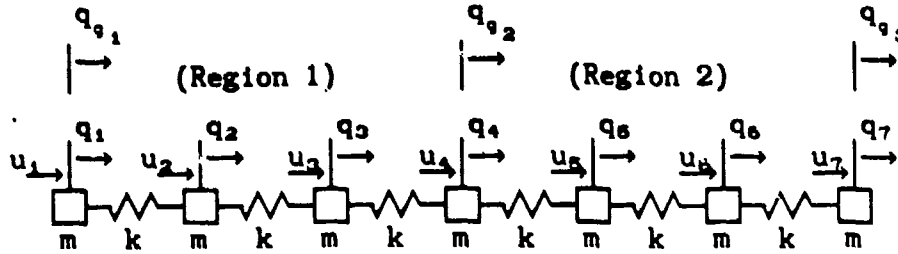


Fig. 4 A 7 Degree of Freedom Model of a Bar in Extension

The open loop pole locations of the full order system are shown in the first column of Table 1. This model will be used to demonstrate the various synthesis processes in the development of the complete two-level hierarchic controller.

Global Control

Assume that, due to performance requirements, the global control will nominally control the relative position of degrees of freedom q_1 , q_4 , and q_7 of the original model. These three degrees of freedom will be the locations of the global degrees of freedom q_{g1} , q_{g2} , and q_{g3} . The global finite control element model defined by these three nodes will have two finite control elements. The degree of freedom q_4 will be assigned to the first global element so that the full order degrees of freedom included in the first element are 1 through 4 and in the second element are 5 through 7. A linear interpolation between the global nodes is used to define the relationship between the global degrees of freedom and the regional degrees of freedom within each element. The interpolation between global and regional degrees of freedom is given by

$$q\{1\} = T_g\{1\} q_g\{1\} \quad \text{and} \quad q\{2\} = T_g\{2\} q_g\{2\}$$

where

$$q\{1\} = [q_1 \ q_2 \ q_3 \ q_4]^T, \quad q\{2\} = [q_5 \ q_6 \ q_7]^T$$

$$q_g\{1\} = [q_{g1} \ q_{g2}]^T, \quad q_g\{2\} = [q_{g2} \ q_{g3}]^T$$

$$T_g\{1\} = \frac{1}{3} \begin{bmatrix} 3 & 2 & 1 & 0 \\ 0 & 1 & 2 & 3 \end{bmatrix}^T, \quad T_g\{2\} = \frac{1}{3} \begin{bmatrix} 2 & 1 & 0 \\ 1 & 2 & 3 \end{bmatrix}^T$$

Combining these two regional relations results in the global interpolation relation (Eqn. 2), where

$$T_g = \frac{1}{3} \left[\begin{array}{ccc|ccc} 3 & 2 & 1 & 0 & 0 & 0 \\ 0 & 1 & 2 & 3 & 2 & 1 & 0 \\ 0 & 0 & 0 & 0 & 1 & 2 & 3 \end{array} \right]^T$$

The reduced order global model (Eqn. 3) can now be formed by using the interpolation matrix T_g for both displacement and velocity. The open loop pole locations of the global system are shown in the second column of Table 1. The modal frequencies of the global model are very close to the modal frequencies of the first three modes of the full order system. The rigid body mode is identically modeled in the global model and modes 2 and 3 are 10% and 4% higher than the full model.

As was stated previously, the main computational effort of the hierarchic control technique is distributed among the many regional processors, which are overseen by the global processor. Therefore, the global state aggregation (Eqn. 8) is divided into three sequential processes, one performed at the regional level and the remaining two at the global level.

$$\hat{q}_g = M_g^{-1} T_g^T M q = M_g^{-1} z_g = M_g^{-1} \sum y_g\{i\}$$

Working from right to left in the above equation, the first process, which is performed by the regional processors, creates regional estimates $y_g\{i\}$ of the global nodal states by multiplying the regional measurements by the regional mass and interpolation matrices. Since the mass matrix is unity, this becomes

$$y_g\{1\} = [y_{g1}^{(1)} \ y_{g2}^{(1)}]^T = T_g\{1\}^T q\{1\}$$

$$y_g\{2\} = [y_{g2}^{(2)} \ y_{g3}^{(2)}]^T = T_g\{2\}^T q\{2\}$$

The remaining two processes are performed at the global level. In the first, the regional estimates of the global nodal states are sent to the global processor to form a new intermediate estimate of the global nodal state z_g by averaging all of the regional estimates at that node.

$$z_g = [y_{g1}^{(1)} \ \frac{1}{2}(y_{g2}^{(1)} + y_{g2}^{(2)}) \ y_{g3}^{(2)}]^T$$

The second global process then correlates these intermediate virtual estimates into the final virtual displacement estimate q_g by premultiplying by the inverse of the global mass matrix defined in Eqn. 3. A simple check will verify that these steps reproduce the pseudo left inverse of the transformation matrix as defined in Eqn. 8. The formation of the estimated global velocity is identical.

Since the actual form of the global control is not critical to the hierarchic control formulation, a simple full order optimal regulator was derived with the state penalty placed uniformly on displacement, no velocity penalty, and a nondimensional control penalty of unity. The poles of the optimally controlled full order system are listed in the first column of Table 2 and shown in Fig. 5. The optimal regulator problem was then solved for the 3x3 global system using the known T_g and S_g from Eqn. 5. The closed loop poles of the global model are shown in the second column of Table 2 and also in Fig. 5. Comparing the closed loop pole locations of the global model with the closed loop pole locations of the lowest three modes of the full order system indicates that they are very similar. The global control synthesis has, therefore, resulted in implementation that effectively isolates the first three modes.

Residual Control

The functions of residual control consist of obtaining estimates of the residual error state and applying colocated feedback based on the estimate. The two steps to the estimation process are global state interpolation and differencing the interpolated state estimates with the actual measurements. From the regional interpolation functions $T_g\{i\}$, the residual states in each region can be independently calculated by

the associated regional processor using Eqn. 7 where the estimates of the global states are given to the regional processors from the global processor.

To demonstrate the synthesis of a reduced order residual model, the first step involves the formation of the residual transformation matrix, T_r . For the model of the bar in extension, the residual model had four remaining degrees of freedom (or modes) to be modeled. In addition, it must also be orthogonal to T_0 with respect to M (Eqn. 18). The resulting residual transformation matrix can be obtained as

$$T_r = \begin{bmatrix} .360 & -.270 & -.540 & 0 & .540 & .270 & -.360 \\ .362 & -.475 & -.135 & .497 & -.135 & -.475 & .362 \\ .217 & -.531 & .413 & 0 & -.413 & .531 & -.217 \\ .059 & -.347 & .515 & -.455 & .515 & -.347 & .059 \end{bmatrix}$$

The open loop poles of the residual model are shown in the last column of Table 1. These pole locations are very close to the open loop pole locations for the highest four modes of the full order system. In all cases, the residual model poles are slightly below the comparable poles of the full order system.

The process of constructing direct proportional residual feedback and its effect on the closed loop dynamics depends on the selection of the feedback parameters α and β . Using the four highest modes of the full state optimal regulator solution, Eqns. 22 and 23 were used to compute values of $\alpha = 0.193$ and $\beta = 0.613$. The closed loop pole locations of the reduced order residual model for these residual feedback parameters are shown in the fourth column of Table 2 and in Fig. 5. As was predicted from the analysis of the residual model, the poles of all four system modes have been affected equally.

The full hierarchic closed loop pole locations are shown in the last column of Table 2 and in Fig. 5. It can be seen from these pole locations that the residual control has caused the decay rates of the four higher modes to increase by approximately the same amount. The closed loop pole locations of the residually controlled system are also very close to the closed loop pole locations of the higher four modes of the full hierarchic implementation. The closed loop poles of the full state optimal regulator are also very close to those of the full hierarchic control implementation.

CONCLUSIONS

This paper has presented the initial development of a hierarchic control technique for flexible structures. A two-level architecture was outlined which consisted of many decentralized regional controllers and one centralized global controller. The hierarchic architecture was developed to both reduce the computational requirements and to reduce the input and output communication requirements compared to using a single centralized processor for a system with a large number of sensors and actuators.

The hierarchic control methodology is capable of yielding low interaction between the global and residual control functions. It was found that the interaction between the global and residual control operations is only due to elastic coupling between the global and residual control design models. For global feedback gains that meet certain requirements, it could also be guaranteed that the coupling would not destabilize the structure.

There are several issues that should be addressed in the future development of the hierarchic control design. First, the control synthesis was developed under the constraint of full state measurement and full actuation of the highest order control design model. A control synthesis which relaxed this constraint should be developed and evaluated through system zero analysis or some other technique. Also, analysis of the performance of the hierarchic control design through numerical simulation and laboratory experiment should be performed to verify the viability of the control design. Finally, the regional controller implementation was of the simplest proportional feedback design. Regional controllers based on traveling wave, distributed parameter or component mode concepts should also be investigated.

ACKNOWLEDGEMENTS

This research was sponsored under a grant by the Air Force Office of Scientific Research, with Dr. Tony Amos serving as technical monitor. The authors would also like to thank Dr. William Widnall for his advise and assistance in the research.

REFERENCES

1. E.F. Crawley and J. De Luis, "Use of Piezo-Ceramics as Distributed Actuators in Large Space Structures," Proceedings of AIAA/ASME/ASCE/AHS 26th Structures, Structural Dynamics, and Materials Conference, Part 2. Orlando, Fla., April 15-17, 1985 pp. 126-133.
2. W.S. Levine and M. Athens, "On the Determination of the Optimal Constant Output Feedback Gains for Linear Multivariable Systems," IEEE Transactions on Automatic Control, Vol. AC-15, No. 1, Feb. 1970, pp. 44-48.
3. R.L. Kosut, "Suboptimal Control of Linear Time Invariant Systems Subject to Control Structure Constraints," IEEE Transactions on Automatic Control, Vol. AC-15, No. 5, Oct. 1970, pp. 557-563.
4. D.S. Bernstein, L.D. Davis, and D.C. Hyland, "The Optimal Projection Equations for Reduced-Order, Discrete-Time Modeling, Estimation, and Control," AIAA Journal of Guidance, Control, and Dynamics, Vol. 9, No. 3, May-June 1986, pp. 288-93.
5. R.E. Skelton, P.C. Hughes, and H.B. Hablani, "Order Reduction for Models of Space Structures Using Modal Cost Analysis," AIAA Journal of Guidance, Control, and Dynamics, Vol. 5, No. 4, July-Aug 1982, pp. 351-7.

6. J.N. Aubrun and G. Marguiles, "Low-Authority Control Synthesis for Large Space Structures," Lockheed Palo Alto Research Laboratory, Contract Report on Contract NAS1-14887, May 1982.
7. M.J. Balis, "Feedback Control of Flexible Systems," IEEE Transactions on Automatic Control, Vol. AC-23, No. 5, Aug. 1978, pp. 673-679.
8. G.S. West-Vukovich, E.J. Davison, and P.C. Hughes, "The Decentralized Control of Large Flexible Structures," IEEE Transactions on Automatic Control, Vol. AC-29, No. 10, Oct. 1984
9. B.A. Ward and E.F. Crawley, "A Hierarchical Control Architecture for Large Flexible Structures," MIT Space Systems Lab Report #18-85, Aug. 1985.
10. R.R. Craig, Structural Dynamics: An Introduction to Computer Methods, John Wiley & Sons, New York, 1981.
11. L. Meirovitch, Elements of Vibration Analysis, McGraw-Hill, Inc., New York, 1975.
12. Rosenbrock, H.H., State Space and Multivariable Theory, Nelson, London, 1970.
13. Taylor, E.G., "Optimal Regulation Within Spatial Constraints - An Application to Flexible Structures," Ph.D. Thesis, Dept. of Aeronautics and Astronautics, M.I.T., Aug. 1980.
14. MacFarlane, A.G.J., Karcanas, N., "Poles and Zeros of Linear Multivariable Systems: A Survey of the Algebraic and Complex-Variable Theory," Int. J. of Control, Vol. 24, No. 1, 1976, pp. 33-74.
15. Kouvaritakis, B., Shaked, U., "Asymptotic Behavior of Root-Loci of Linear Multivariable Systems," Int. J. of Control, Vol. 23, No. 3, 1976, pp. 297-340.

Table 1
OPEN LOOP POLES OF THE FULL SYSTEM
COMPARED TO THE SUBSYSTEM POLES

Full 7 DOF	3 DOF Global	4 DOF Regional
0.0 ± 0.0001	0.0 ± 0.0001	
0.0 ± 0.4481	0.0 ± 0.4631	
0.0 ± 0.8681	0.0 ± 0.8991	
0.0 ± 1.2471		0.0 ± 1.2411
0.0 ± 1.5641		0.0 ± 1.5621
0.0 ± 1.8021		0.0 ± 1.8011
0.0 ± 1.9501		0.0 ± 1.9371

Table 2
CLOSED LOOP POLE COMPARISON OF THE FULL OPTIMAL REGULATOR
WITH THE SUBSYSTEM POLES AND FULL HIERARCHIC DESIGN

Full 7 DOF Optimal Reg	3 DOF Global Optimal Reg	4 DOF Residual State Feedback	Full Hierarchic Control Design
$-0.707 \pm 0.707i$	$-0.707 \pm 0.707i$		$-0.707 \pm 0.707i$
$-0.641 \pm 0.780i$	$-0.638 \pm 0.788i$		$-0.632 \pm 0.776i$
$-0.499 \pm 1.001i$	$-0.489 \pm 1.023i$		$-0.488 \pm 0.998i$
$-0.383 \pm 1.308i$		$-0.308 \pm 1.281i$	$-0.310 \pm 1.285i$
$-0.314 \pm 1.598i$		$-0.308 \pm 1.593i$	$-0.307 \pm 1.595i$
$-0.274 \pm 1.823i$		$-0.308 \pm 1.829i$	$-0.307 \pm 1.829i$
$-0.284 \pm 1.988i$		$-0.308 \pm 1.983i$	$-0.309 \pm 1.975i$

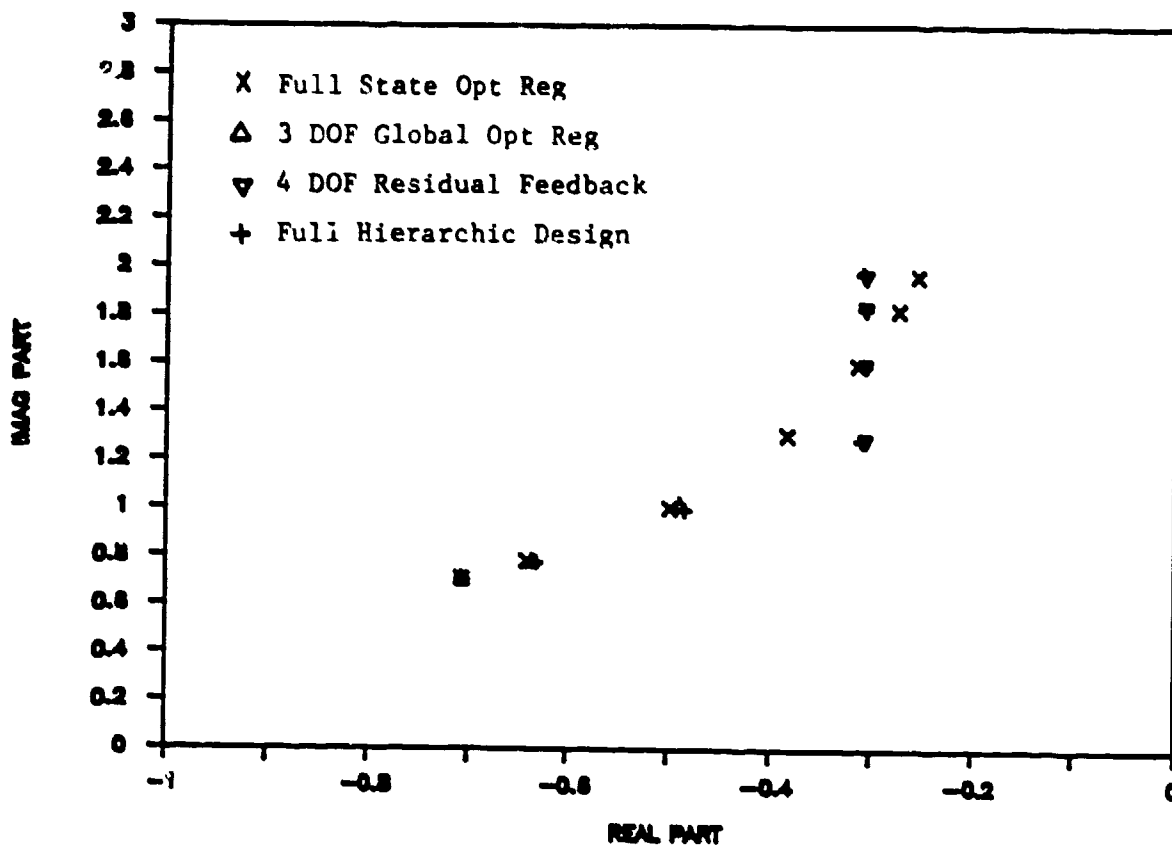


Fig. 5 Closed Loop Pole Comparison of the Full Optimal Regulator with the Subsystem Poles and Full Hierarchic Design

A. H. von Flotow*

Massachusetts Institute of Technology

ABSTRACT

This paper reviews past approaches to control-motivated dynamic tailoring and their impact upon the problem of active control of structural dynamics. The costs and benefits of passive damping augmentation are estimated; the conclusion is drawn that the optimum structural design will be in the "half α -plane". New results on dynamic tailoring of truss-work structures are presented. The proposed techniques exploit inherent characteristics of such structures to reduce the mass penalty associated with passive damping augmentation.

INTRODUCTION

The control of flexible structures is proving to be a serious challenge to the capabilities of control theory. Features of the structural dynamics which exacerbate the difficulties include:

- A structural response characterized by a dense spectrum of structural modes.
- The precise prediction of these modes is difficult, both with respect to their frequencies and especially their gains (mode shapes).
- Most aerospace structures are characterized by low natural damping.

It is clear that the structure can be redesigned to ease the control task. Many approaches to such redesign are possible. Perhaps the most important is passive damping augmentation.

Effect of Damping

A reliable stabilizing controller does not exist for infinite-dimensional models of undamped flexible structures[1,2]. "For successful application, every control scheme relies upon and presumes the existence of a finite amount of structural damping." [1] This statement becomes less absolute for large but finite dimensional mathematical models of structural response; nevertheless there can be no doubt that passive damping is very useful.

Although it has proven possible to design stabilizing controllers for quite large mathematical models of structural dynamics, these controllers are often unacceptably sensitive to modelling errors. Reference [1] separates these modelling errors into four contributions: ϵ_d due to parameter errors, ϵ_t due to truncation errors, ϵ_n due to incorrectly modelled disturbances, and ϵ_{nl} due to unmodelled non-linearities. A practical controller must be robust with respect to each of these errors.

One recent paper[3] reports the design of an eighteenth order compensator and the problems encountered when attempting to make the design robust with respect to truncation errors ϵ_t . In this case the "truth model" included 150 elastic modes, each with a damping ratio of $\zeta = 0.001$. Although a stabilizing controller was designed, stability was achieved only at considerable cost in performance, and robustness to other types of modelling errors (and to additional truncation errors) was not demonstrated. The authors state: "We have not achieved performance robustness with our designs and have suggested that a remedy must begin with the reexamination of the design model of the plant." One thesis of this paper is that a reexamination of the "truth model" would be equally productive. In particular, a structure with 150 elastic modes, each with a damping ratio of $\zeta = 0.001$, has never been built. Such behaviour is displayed only by idealised mathematical models of structural dynamics. As such, the utility of developing specialised techniques for such models is questionable.

Damping is one aspect of structural dynamics that is usually very poorly modelled, and, perversely, is important to control design. Even a relatively small amount of passive damping can be very helpful. A precise measure of how helpful is only available as one outcome of detailed study of individual cases. Nevertheless estimates are available for the general situation.

An argument due to Gran[2] is based upon conservative measures of gain margin in multi-variable loops; the singular values of the loop transfer matrix. Gran demonstrates that the high frequency behaviour of the singular values of an optimal regulator (a controller which minimises a quadratic cost function, using output feedback), is inversely proportional to frequency;

$$\sigma_R(\omega \rightarrow \infty) \propto \frac{1}{\omega} \quad (2)$$

If a Kalman filter is used to estimate the states, the high frequency limiting behaviour of the singular values of the compensator is

$$\sigma_C(\omega \rightarrow \infty) \propto \frac{1}{\omega^2} \quad (1)$$

Transfer functions describing structural response are often written as an infinite sum;

$$\sum_{i=1}^{\infty} \frac{A_i \omega_i^2}{s^2 + 2\zeta_i \omega_i s + \omega_i^2} \quad (3)$$

The maximum value of the structural response occurs at resonance, $\omega = \sqrt{1 - 2\zeta_i^2} \omega_i$ and has the value

$$\frac{A_i}{2\zeta_i \sqrt{1 - \zeta_i^2}} \approx \frac{A_i}{2\zeta_i} \quad (4)$$

A singular value decomposition of the loop transfer matrix would thus display a high frequency behaviour

$$\sigma_L(\omega \rightarrow \infty) \propto \begin{cases} 1/\omega \zeta_i & \text{(regulator)} \\ 1/\omega^2 \zeta_i & \text{(compensator)} \end{cases} \quad \begin{matrix} (5) \\ (6) \end{matrix}$$

If a given value (say unity) for the maximum singular value of the loop transfer matrix implies unconditional stability, then for a given controller and structure, the frequency above which the system will be unconditionally stable is related to the damping ratio by

$$\omega > \begin{cases} k_R/\zeta_i & \text{(regulator)} \\ k_C/\sqrt{\zeta_i} & \text{(compensator)} \end{cases} \quad \begin{matrix} (7) \\ (8) \end{matrix}$$

where k_R and k_C are constants.

An increase of the damping ratio ζ from say $\zeta = 0.001$ to $\zeta = 0.01$ would thus substantially reduce the bandwidth required of a "truth model". The implication is that the controller could then also be designed with reference to a lower order model and that the control implementation would be simplified.

Damping Augmentation

To augment the foregoing discussion on the approximate benefits of passive damping, it is useful to estimate the costs associated with passive damping augmentation. For space applications the prime cost driver appears to be total mass, thus it is appropriate to express these costs as a mass penalty. No unified theory or analysis can be called upon to provide these estimates, rather it seems appropriate to review past accomplishments and to evaluate them in terms of one figure of merit: the relative mass penalty incurred per damping ratio achieved. This figure might then become one entry in a gradient matrix used in an optimisation scheme.

A recently published book[4] has been a useful source of such data. This book reviews linear damping treatments as they have been applied to aerospace structures. Such damping treatments may be broadly classified into two groups; static and dynamic. Static damping treatments usually take the form of viscoelastic materials which, when applied to the structure, deform proportionally to instantaneous structural deformations, thus the term "static". The composite loss factor is then approximated by the weighted average of material loss factors, each

* Assistant Professor, Aeronautics and Astronautics, member AIAA

weighted according to the fraction of strain energy in that material. To obtain maximum damping per mass of viscoelastic material added to the structure, geometries must be devised which create large strains in the lossy material. Past practice has been to add thin surface layers of these materials to existing structures, as sketched in Figure 1a. Review of results reported in reference [4] suggests that the mass penalty associated with achieving a composite loss factor of η with such an approach is approximately

$$\frac{\Delta M}{M} = \frac{1.5 \text{ to } 3}{\eta_2} \eta \quad (9)$$

valid for small η , say $\eta < 0.10$ and negligible inherent structural damping, $\eta_1 \approx 0$. Note that the mass penalty incurred to achieve a given composite loss factor depends inversely on the loss factor, η_2 , of the viscoelastic material. These material loss factors are typically frequency and temperature dependent. Figure 2 shows this dependence for a material being marketed for space applications, indicating that loss factors greater than $\eta_2 = 0.6$ can be provided over a frequency range of one decade, or for a given frequency, over a temperature range of 50 Fahrenheit degrees. The frequency and temperature range of high damping

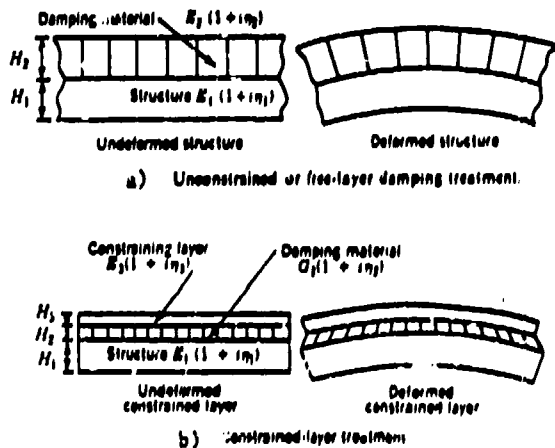


FIGURE 1 Surface damping treatments typically employ a thin layer of viscoelastic material, which may be constrained to deform strongly in shear by a stiff constraining layer. The mass penalties associated with this type of damping are given by expressions (9) and (10).

can be extended by using several viscoelastic materials or geometries, each active in a particular temperature/frequency range. The mass penalty associated with this technique will be approximately additive to that predicted by equation (9).

One approach used to enhance the effectiveness of such static damping treatments is to sandwich the viscoelastic material between the structure and a thin, extensionally stiff, constraining layer (see Figure 1b). The constraining layer induces large shear deformation of the viscoelastic material when the substructure deforms. Review of results reported in reference [4] suggests that the use of constraining layers reduces the mass penalty associated with achieving a composite loss factor of η to

$$\frac{\Delta M}{M} = \frac{.5 \text{ to } 1.5}{\eta_2} \eta \quad (10)$$

valid for small η , say $\eta < 0.10$ and negligible inherent structural damping, $\eta_1, \eta_2 \approx 0$. The tentative conclusion to be drawn from equations (9) and (10) is that static viscoelastic damping treatments will introduce a modest mass penalty, adding perhaps three percent in mass to achieve a loss factor of $\eta = 0.02$, ($\zeta = 0.01$).

Further geometric techniques are available to reduce the mass penalty of damping treatments. The basic idea is to locate (or create) areas of high strain for a given structural deformation, and to place lossy material into those locations. One such approach is the tuned vibration absorber. This device uses dynamic effects to create large local strains at a particular frequency. This frequency is then typically chosen such that the device is tuned to a particular structural resonance. The result is that the structure is strongly damped

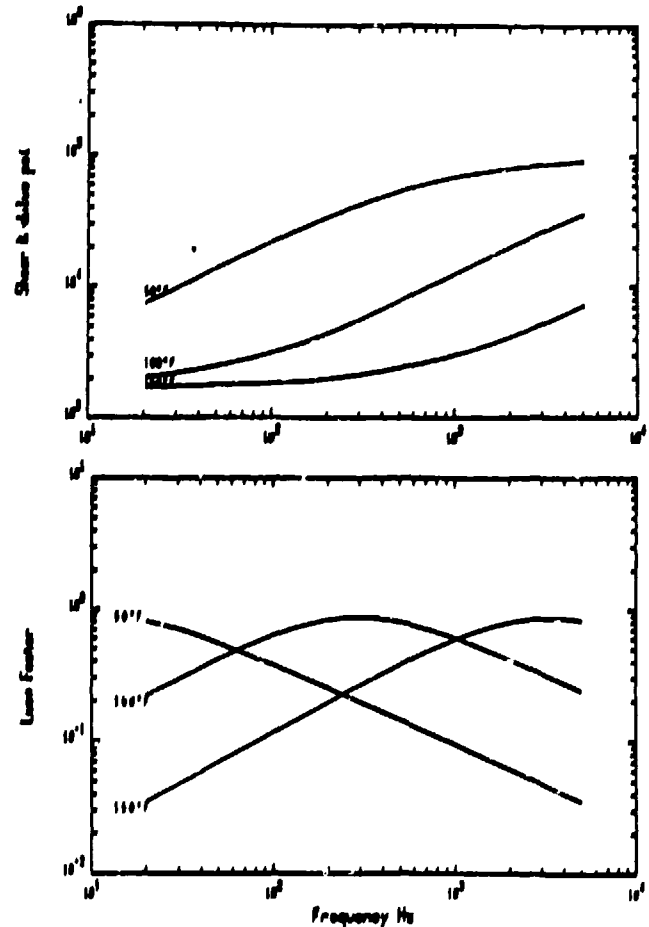


FIGURE 2 At least one viscoelastic material is being marketed for space applications; General Electric Corp.'s SMRD 100F90. These performance curves were taken from reference [4].

over a relatively narrow frequency range. The mass penalty associated with this approach is somewhat more difficult to evaluate, since it will depend upon many factors. Results reported in references [4] and [5], both based upon single tuned vibration absorbers applied to beams in bending, suggest that to achieve a modal damping ratio of ζ , a mass penalty of

$$\frac{\Delta M}{M} = 1/6 \zeta = 1/3 \eta, \quad (11)$$

will be incurred, using optimally tuned and damped absorbers. If this result can be extrapolated to arbitrary structures, the tentative conclusion is that modal damping ratios of $\zeta = 0.01$ can be obtained with a mass penalty of $\Delta M/M = 0.006$ per damped mode. Subsequent discussion suggests the possibility of using portions of the structure as tuned vibration absorbers; thus this mass penalty may be further reduced.

During vibration of truss structures, the largest strains are typically at or in the joints; thus these would be efficient locations to place damping treatments. An analysis of the effect of such joint damping [6] shows that damping is maximized when the joint stiffness is comparable to member stiffness. This seems to imply a reduction in global truss stiffness, with concomitant reduction in frequencies. Such a stiffness reduction may not be necessary; joints can be made stiff in extension and dissipative and compliant in rotation. Extensional joint stiffness contributes to global truss stiffness, rotational joint motion can be used for efficient damping. The mass penalty associated with such a technique is difficult to estimate; further discussion is postponed to a subsequent section.

Active Damping

Many early structural control experiments [7] were concerned only with active damping augmentation. As such, the results might be compared with passive damping techniques; in particular, the mass penalty associated with an active damping implementation might be estimated. When summing the component masses in an active damping system, the question arises what masses to assign to power supplies, filters, and assorted laboratory equipment. If all equipment used in the experiment is included, it is doubtful if an experiment has been performed in which the control system weighed less than the structure! Although flight hardware will doubtless be less massive than laboratory equipment, the mass penalty of an active damping augmentation system is likely to be quite high. It is not clear that the mass penalties estimated for passive damping treatments can be improved upon with an active damping system.

Active damping augmentation systems may actually destabilize high frequency modes. A minimum amount of passive damping must be present to prevent this destabilization, which occurs because the inevitable roll-off of the active system.[8] The level of active damping that can be achieved is proportional to the passive damping already present,[8] thus an active damping system is perhaps best thought of as a multiplicative approach; an undamped infinite-dimensional structure cannot be damped by purely active means. Damping inherent in many of the beams, plates and other laboratory structures used to date has often been insufficient to prevent such instability.

Spectrum Tailoring

Tailoring of the structural response spectrum has been a common approach for avoiding interactions between spacecraft attitude control systems and structural dynamics. The structure is simply stiffened to raise the structural eigen-frequencies beyond the control bandwidth. A frequency ratio of six to ten [9] between controller bandwidth and structural resonances is typically sufficient. Since structural frequencies scale inversely with dimension, this technique will not be practical for arbitrarily large structures. Extension of such spectral separation to the problem of active control of the first few modes of a structure is possible in principle; one would need to design the structure to provide a broad resonance-free range in the vicinity of the control roll-off. Figure 3 makes this point graphically. To be effective, this range would need to be quite broad, on the order of one decade.

It does not appear practical to achieve this goal with structural re-design. If "resonance free" is interpreted somewhat liberally to include well-damped resonances, the approach may become feasible. If damping is provided by passive tuned vibration absorbers, such considerations may be used to choose modes to tune to. Realization of this idea through minor modifications of existing truss-work structures appears feasible, and is discussed in a subsequent section.

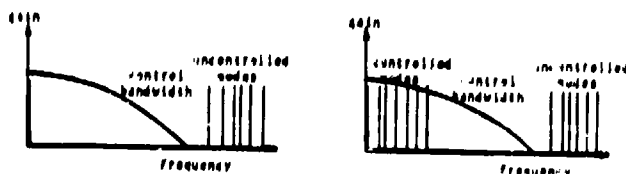


FIGURE 3 One approach to "spectrum tailoring" involves stiffening of the structure to raise the eigen-frequencies beyond the controller bandwidth. The analogue to this for extremely large structures would be to provide an intermediate resonance-free range.

Residue Tailoring

Much research has been performed on the strong effect of actuator and sensor positioning on the performance of active control systems.[10] Actuator and sensor positioning governs the residues and serves of structural transfer functions, but to first order, not the poles. Thus the pole-zero sequence along the $j\omega$ -axis is changed, potentially altering the interaction between modes and the control system to be stabilizing or destabilizing[2]. In the extreme case of dual sensing and actuation, all residues are positive, and all modes stably interacting.[11] Attempts to optimize actuator and sensor positions[10], tend to be computation intensive. Insight into the process is lost, and the optimization may converge to any of several local optima.

Residue tailoring can also be accomplished by modification of mode shapes by structural re-design. This need not modify the resonant frequencies[12], but in general will do so.

Optimization

The formalisation of residue and spectrum tailoring leads to structural optimisation. References [12,13] and [14] are representative of this approach. Although optimisation is beyond the scope of this paper, one observation will be made; it is unlikely that a globally optimum structural design will be achieved by shuffling transfer function poles and zeroes along the $j\omega$ -axis, particularly in view of the relatively modest mass penalties associated with passive damping treatments. The potential system benefits of passive damping in terms of reduction of complexity and size of the active control system are just too great. The optimum structural design will be in the "left-half s -plane".

TAILORING OF TRUSS STRUCTURES

Truss structures appear to offer opportunities for synergistic effects in dynamic tailoring. This is due to their relatively unique dynamic properties; the coexistence of very different "local" and "global" modes. Figure 4 shows a truss structure scheduled for on orbit vibration test in 1989.[15] The vibrations of this structure will be governed by member elongation (and joint compliance) up to approximately 10 Hz. This frequency range includes the first 8 flexible modes when the beam is fully deployed.[15] The pinned-pinned frequency of the diagonal members is at 12 Hz.[15,16] Thus, at or near 12 Hz, these 168 diagonals will participate strongly in the response, adding 336 "local" vibration modes. This will be repeated at higher frequencies, in the vicinity of each local resonance. To begin to model these local degrees of freedom with a finite element method would require approximately 1700 degrees of freedom. An alternative, based upon an input/output description of a single bay, is under development[17]. In the remainder of this paper this effect is examined using finite element models of a simpler truss structure.

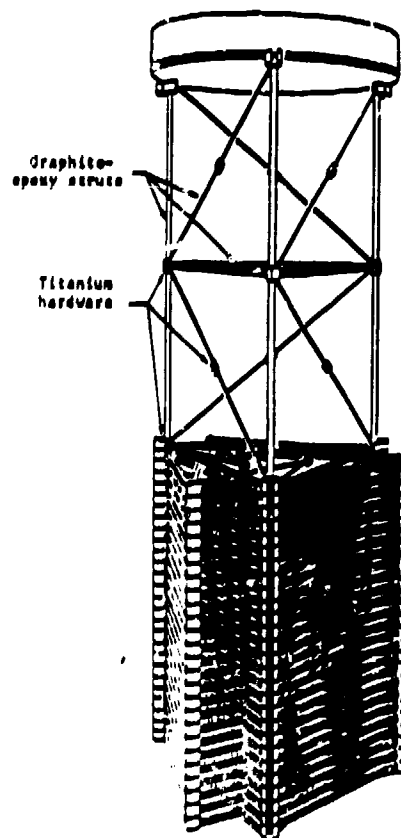


FIGURE 4 This deployable truss beam, scheduled for near term on-orbit vibration test, will display extreme modal degeneracy at approximately 12 Hz.

Figure 5 is a sketch of a planar model of an MIT experimental structure, the Structures Assembly Demonstration Experiment (SADE) truss. A three-dimensional version of this truss has been under consideration for a shuttle payload bay assembly and vibration experiment. The dynamics of this truss were the subject of a recent MIT thesis[18], in which the vibration mode shapes sketched in Figure 5 were reported. The dimensions used in the analysis were (for each member): bending

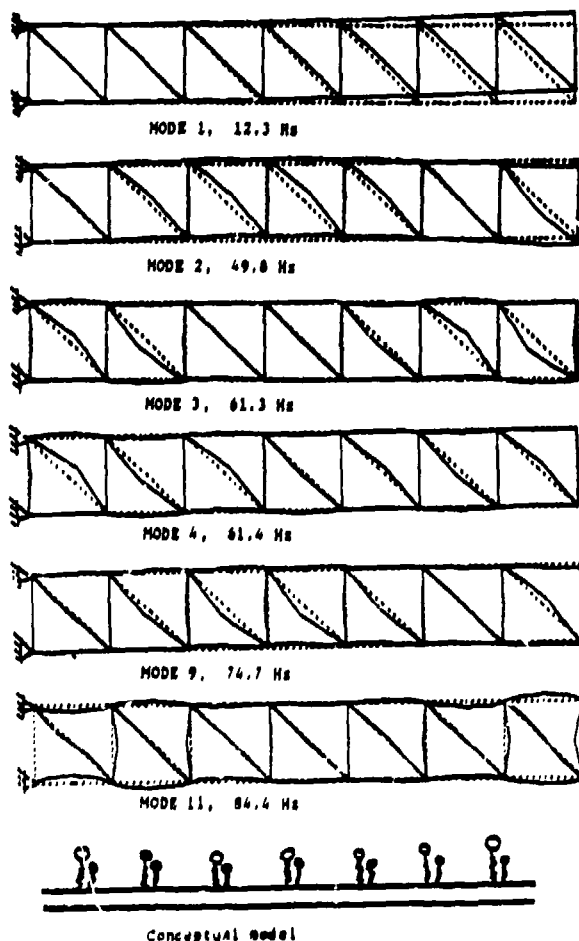


FIGURE 5 This planar truss was the subject of a recent MIT Masters thesis[18]. It is a planar model of a truss under consideration for experimental assembly on orbit.

stiffness $EI = 2.02 \times 10^6 \text{ lb-in}^2$; stretching stiffness $EA = 4.36 \times 10^6 \text{ lb}$; mass density $\mu = 1.01 \times 10^{-4} \text{ slug/inch}$; with member lengths of 55 and $55\sqrt{2}$ inches. The members are thus quite slender; if a solid section were used, the slenderness ratios would be 20 and 29 for the two member lengths. Note that in Figure 5 all modes beyond the first two are primarily member modes; member motion is much greater than joint motion. A conceptual model of such a truss is a continuum beam with periodically attached vibration absorbers. Member extensional stiffness governs the global modes, while member bending deformation has the global effect of a local vibration absorber. These "vibration absorbers" are strongly coupled (the joints are clamped), thus each local mode involves several members.

The frequencies of member modes are governed by the bending natural frequencies of the members. Member bending eigen-frequencies will potentially be very low, comparable to global frequencies, especially if the structure has been optimized with respect to static loading[19], or if deployment hardware (a hinge) is present on the member.[18] For this example, the diagonal members have pinned-pinned and clamped-clamped natural frequencies of 35 and 80 Hz respectively; the corresponding frequencies for the shorter members are 70 and 160 Hz. Thus there are several indistinct groups of member modes, each roughly associated with one of these local resonances. For this example, the first group of six member modes is associated with diagonal member bending and occurs in the range 60 to 65 Hz, between the pinned-pinned and

clamped-clamped frequencies of these members. This is followed by a mixed mode with both global and local response at 74 Hz, followed by many local modes beginning at 82 Hz. At these frequencies the system response is characterized by many similar and closely spaced modes. Many small non-linearities (joint backlash, member buckling, joint friction) are sure to be important, but are ignored in this analysis. Their expected effects will be briefly discussed in a subsequent section.

The member modes will be comparatively easy to damp; local strains are large and rotational joint motion is excited. A small amount of damping material, strategically placed, will have a large effect. Good locations would be member surfaces, even better would be internal to the joints. The mass penalty of this damping might be estimated by expressions (9) to (11), with the reference mass taken to be only the mass of those members participating in the response. The mass penalty would thus be correspondingly reduced.

Figure 6 gives a selected transfer function for this example. Damping is assumed to be present in two ways; Figure 6a assumes a uniform loss factor of unspecified origin and of level $\eta = 0.01$. Figure 6b is an attempt to illustrate the effect of local damping treatments; the modal loss factor is estimated to be the weighted average of two values, the bending loss factor $\eta_B = 0.05$, and the extensional loss factor of $\eta_S = 0.01$. Each is weighted according to the fraction of the modal strain energy attributable to that type of member deformation. The introduction of the large bending loss factor is an attempt to model the effect of joint and other local damping treatments.

Inspection of Figure 6b reveals that this member bending damping has little influence on the global modes, but that the member modes are all effectively damped with loss factors of $\eta = \eta_B = 0.05$ ($\zeta = 0.025$). This observation suggests the possibility of tuning the local modes,

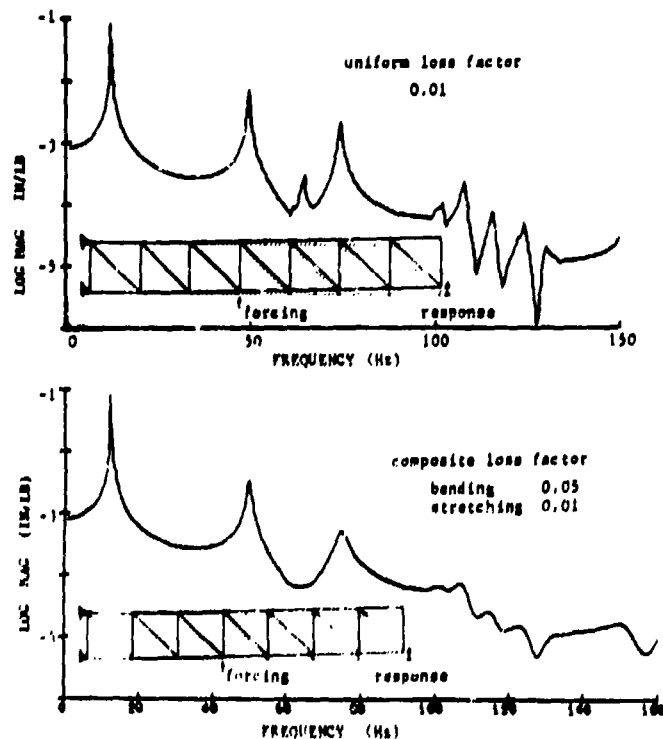


FIGURE 6 A representative transfer function for the truss of Figure 5 is depicted. The member modes near 63 Hz do not participate strongly in this response since both the driving and the response points are at joints. Very different transfer functions result from driving or observing at member midpoints. The effect of assuming large local damping is most strongly felt in the higher frequency "member" modes.

and using them to damp the global modes. This can be done with only minor influence upon the global frequencies. Figure 7 shows the results of two such attempts. The results of Figure 7a were calculated with the bending stiffness of the diagonal members reduced by a factor of $(43/63)^2$ in an attempt to tune these modes to the second bending frequency at 50 Hz. The result is a reduction of the amplitude of that mode, due to an increase of its loss factor from $\eta = 0.021$ to $\eta = 0.035$.

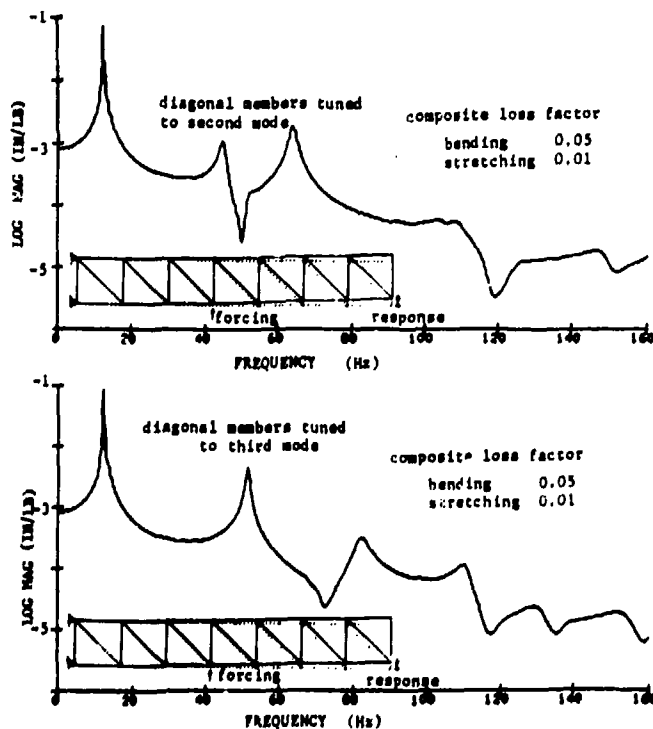


FIGURE 7 The diagonal members of the truss of Figure 5 can be tuned to resonate at selected frequencies. This figure shows two results; one with the diagonal members stiffened, the other softened, with respect to the reference truss.

The frequency decreased only slightly, to 44 Hz. This modal loss factor can only asymptotically approach $\eta_B = 0.05$, higher values of local loss factors, achieved with additional local damping treatment, would lead to further damping of this global mode. Figure 7b shows the effect of increasing the member bending stiffness by a ratio of $(74/60)^2$, in an attempt to tune to the mixed mode at 75 Hz. the effect in this case is less pronounced; this mode already involved significant member motion.

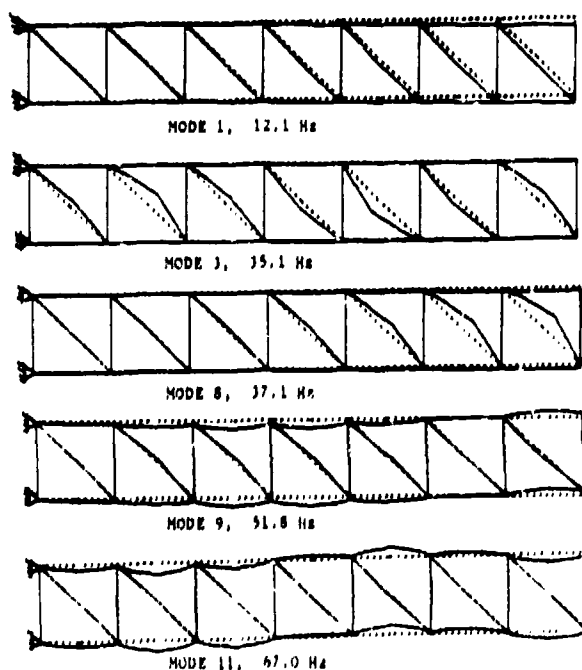


FIGURE 8 If the joints of the SADE truss were pinned, the pattern of mode shapes would be quite different.

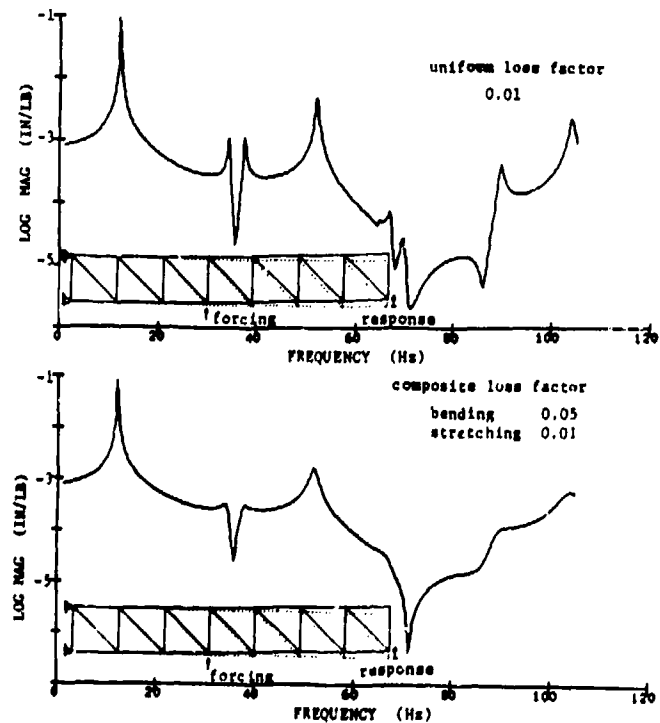


FIGURE 9 These transfer functions correspond to the mode shapes of Figure 8. Note that the member modes are much more tightly grouped than for the case with clamped joints, and that the global modes are effectively unchanged.

Greater tuning freedom is available if the joints are pinned rather than clamped. Figure 8 shows a few mode shapes for the SADE truss for the case of pinned joints. With these joints, there is less coupling of member motion, thus the first member modes come very tightly grouped about 35 Hz, in the range 33 to 37 Hz. The ninth mode,

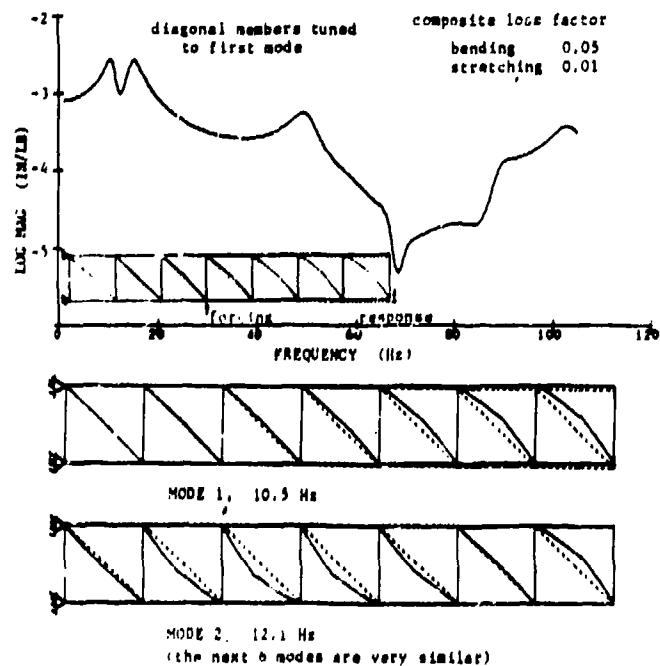


FIGURE 10 When the joints are pinned, the members may be much more precisely tuned. This transfer function shows the result of tuning the diagonal members to the first bending mode. Note that a factor 30 reduction of the response amplitude (compare with Figure 9b) has been achieved.

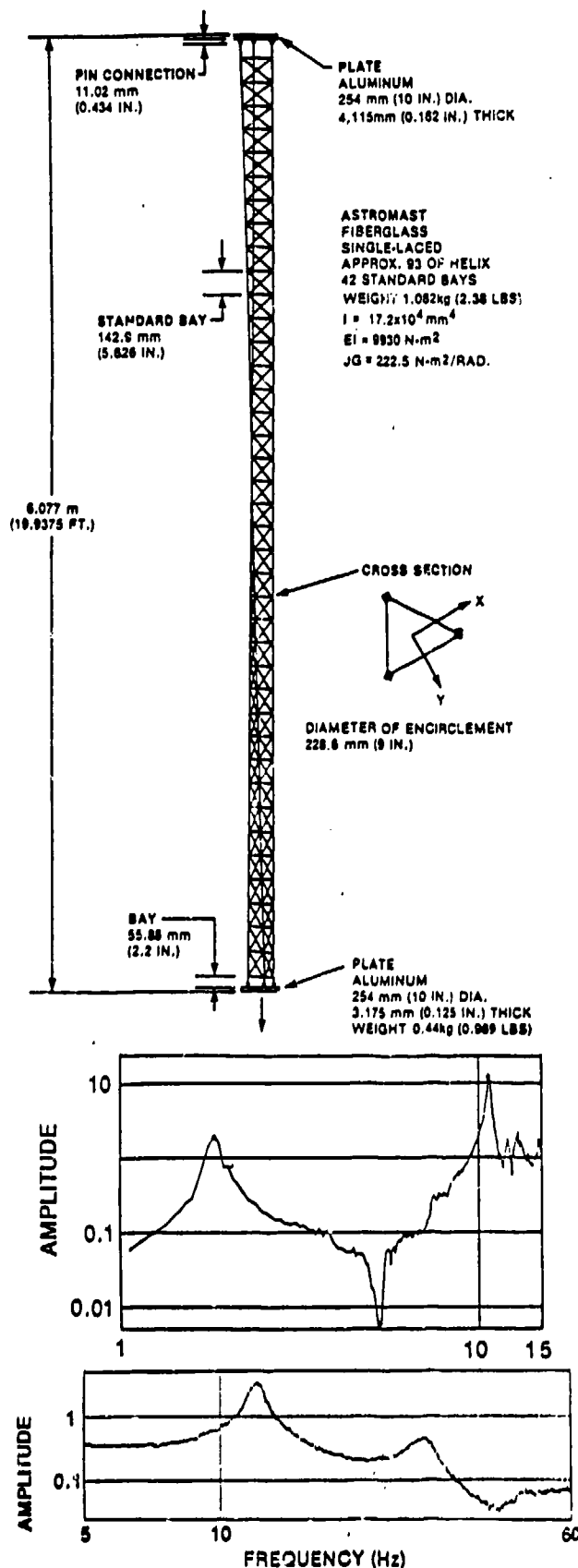


FIGURE 11 A relevant vibration test of a truss structure, reported in reference [20], is summarized in this figure. Note that high frequency resonances are indistinct, much like the computed results of Figures 6, 7, 9, and 10.

at 52 Hz, is essentially the second bending mode, as before. This is followed by many more tightly grouped member modes, each associated with either the diagonal or the short members. In more complex truss structures, such as the one sketched in Figure 4, one would expect such mode groups to be associated with a more complex form of local resonance. A representative transfer function for the SADE truss with pinned joints is given in Figure 9, both with a uniform loss factor of $\eta = 0.01$, and with the composite loss factor computed as before.

Tuning of this truss is relatively straight forward. Figure 9 suggests the possibility of tuning the diagonal members to the first bending mode (the second bending mode is already heavily damped.) Figure 10 shows the same transfer function as Figure 9, but with the bending stiffness of the diagonal members reduced by a factor $(12/35)^2$. For reference, selected mode shapes are also given. Note that bending of the diagonal members now participates strongly in the first mode. The large reduction in peak amplitude at 12 Hz is due to the damping introduced by this local vibration. The members are acting as effective vibration absorbers.

Experimental Verification

Experimental verification of the results of this paper is needed. The low mass penalties predicted for passive damping augmentation of structures in general and of tuned truss structures in particular, might be verified. Laboratory tests would be adequate, the relatively large damping levels of interest would not be difficult to measure. One relevant experiment has been performed. Figure 13, adapted from reference [20], describes a vibration experiment performed on a current spacecraft truss-work beam. The transfer function shown is similar in character to those of Figures 6, 7, 9, and 10; high frequency modes are indistinct and strongly damped. For this beam, the local member frequencies begin at approximately 30 Hz. Local damping in this beam is due to non-linear effects in the joints rather than to damping treatments.

Unmodelled Effects

The structural models used in this paper may not be valid for investigation of the effects described. It is well known that small coupling effects become important when the eigen-frequencies of a linear model are closely spaced in frequency. A truss-work structure will exhibit many non-linearities, most notably joint friction and backlash and member buckling. These non-linearities will couple the closely spaced modes, leading to beating and potential limit cycling of an active control system.

These modes will also be very sensitive to small parameter variations, particularly the mode shapes. Since the individual member bending motion is only weakly coupled to its neighbours, the phenomenon of mode localization [21,22,23] must be expected. Member modes will be spatially localised rather than extending through the entire structure.

The moderate frequency response of a real spacecraft truss-work structure may thus be characterised by a strongly damped local rattling motion which slowly exchanges energy with other such rattles. The impact of such dynamics on the performance of an active control system is unknown.

SUMMARY

The claim was made that a structure which is optimised for active control implementation will include significant passive damping. This claim was supported by estimates of mass penalties of passive damping treatments, and estimates of the benefits in terms of reduction in control system size and complexity. Subtle effects in the dynamics of truss-work structures were highlighted, and the possibility of their exploitation for control-motivated dynamic tailoring was investigated.

ACKNOWLEDGEMENTS

This paper has built upon the computational results presented in Ray Mills' 1985 MIT Masters thesis, performed under the direction of Professor John Dugundji. Additional computational work was performed by Richard Maurer under the auspices of MIT's Undergraduate Research Opportunities Program. Financial support was provided in part by the Air Force Office of Scientific Research, through Dr. Anthony Amos.

References

- 1 R. E. Skelton, "Algorithm Development for the Control Design of Flexible Structures", *Proceedings, Modelling, Analysis, and Optimisation Issues for Large Space Structures*, NASA CP 2258, Williamsburg, VA, May 13-14, 1982
- 2 R. Gran, "Finite Dimensional Controllers for Hyperbolic Systems", *Proceedings, Symposium on Dynamics and Control of Large Flexible Spacecraft*, Blacksburg, VA, June 15-17, 1981
- 3 G. J. Kissel, D. R. Hegg, "Stability Enhancement for Flexible Space Structure Control", *IEEE Control Systems Magazine*, in press, (June 1986?)
- 4 A. D. Nashif, D. I. G. Jones, J. P. Henderson, *Vibration Damping*, Wiley-Interscience, 1985
- 5 D. W. Miller, E. F. Crawley, B. A. Ward, "Inertial Actuator Design for Maximum Passive and Active Energy Dissipation in Flexible Space Structures", AIAA 85-0777-CP, *Proceedings, AIAA Structures Dynamics and Materials Conference*, Orlando, FL, April 1985
- 6 T. J. Herts, E. F. Crawley, "Damping in Space Structure Joints", AIAA 84-1039-CP, *Proceedings, AIAA Dynamics Specialists Conference*, Palm Springs, CA, May 1984
- 7 D. C. Fraser, "Large Space Structure Control: Early Experiments", *J. Guidance and Control*, Special Section, Vol. 7, No. 5, Sept.-Oct. 1984, pp. 513-562
- 8 J.-N. Aubrun, "Theory of the Control of Structures by Low-Authority Controllers", *J. Guidance and Control*, Vol. 3, No. 5, Sept.-Oct. 1980, pp. 444-451
- 9 A. E. Bryson, *Control of Spacecraft and Aircraft*, unpublished book draft, September 1985
- 10 G. Schuls, G. Heimbald, "Integrated Actuator/Sensor Positioning and Feedback Design for Large Flexible Structures", AIAA 82-1590-CP, *Proceedings, AIAA Guidance and Control Conference*, San Diego, CA, 1982
- 11 G. D. Martin, "On the Control of Flexible Mechanical Systems", Ph.D. Thesis, Dept. of Aeronautics and Astronautics, Stanford University, CA, May 1978
- 12 A. Messac, "Optimal Simultaneous Structural and Control Design of Large Space Structures", Ph.D. Thesis, Dept. of Aeronautics and Astronautics, Massachusetts Institute of Technology, November 1985
- 13 V. B. Venkayya, V. A. Tischler, "Frequency Control and the Effect on the Dynamic Response of Flexible Structures", AIAA 84-1044-CP, *Proceedings, AIAA Dynamics Specialists Conference*, Palm Springs, CA, May 1984
- 14 N. S. Khot, F. E. Eastep, V. B. Venkayya, "Optimal Structural Modifications to Enhance the Optimal Active Vibration Control of Large Flexible Structures", AIAA 85-0627-CP, *Proceedings, AIAA Structures Dynamics and Materials Conference*, Orlando, FL, April 1985
- 15 B. Hanks et. al., "Control of Flexible Structures," *Workshop Presentation Materials*, NASA Langley Research Center, Aug. 27-28, 1985.
- 16 J. Hedgepeth, personal communication, March 1986
- 17 J. Signorelli, "Local Models for Spacecraft Truss-Work Beams", in preparation
- 18 R. A. Mills, "Natural Vibrations of Beam-Like Trusses", MASC Thesis, Dept. of Aeronautics and Astronautics, Massachusetts Institute of Technology, June 1985.
- 19 M. S. Anderson, "Vibration of Prestressed Periodic Lattice Structures", *AIAA J.*, Vol. 20, No. 4, April 1982, pp. 551-555
- 20 Y. Soucy, F. Vigneron, "Modeling and Identification of the Structural Properties of an Astromast", *Canadian Communications Research Council Report*, Nov. 1983
- 21 O. O. Bendiksen, "Mode Localisation Phenomena in Large Space Structures", *Proceedings, AIAA Structures Dynamics and Materials Conference*, San Antonio, TX, May 1986
- 22 C. Pierre, D. M. Tang, E. H. Dowell, "Localised Vibrations of Disordered Multi-Span Beams: Theory and Experiment", *Proceedings, AIAA Structures Dynamics and Materials Conference*, Orlando, FL, April 1985
- 23 C. H. Hodges, J. Woodhouse, "Vibration Isolation from Irregularity in a Nearly Periodic Structure: Theory and Measurements", *Journal of the Acoustical Society of America*, Vol. 74, No. 3, 1983, pp. 894-905

Large Space Structures; Dynamics and Control
ed. S. Atluri, T. Amos, Springer Verlag, 1987

THE ACOUSTIC LIMIT OF CONTROL OF STRUCTURAL DYNAMICS

A. H. von Flotow
Department of Aeronautics and Astronautics
Massachusetts Institute of Technology
Cambridge, MA, 02139, USA

ABSTRACT

This paper investigates the acoustic limit of active control of structural dynamics; the limit as the control bandwidth includes a very large number of natural modes of the structure. The point is made that in this limit modal analysis cannot provide reasonably accurate models of the structural dynamics, and that control design with respect to modal models is then of questionable value. Alternative modeling approaches are reviewed. A particular wave propagation formalism, applicable to modeling the acoustic response of networks of slender structural members, is described in some detail. Control options designed with reference to this formalism are reviewed, and speculations as to future developments of such control are offered.

1. INTRODUCTION

Modal analysis is a powerful analysis technique, central to the discipline of structural dynamics since the publication of Rayleigh's[1] book. Nevertheless, practical limitations to the applicability of modal analysis do exist. This paper attempts a definition of one such limitation, the high-frequency acoustic limit, and points out the relevance of this limitation to the technology of active control of structural dynamics.

It is difficult to define the boundary between structural dynamics and structural acoustics, indeed, one might even insist that the former includes the latter. The boundary between analysis techniques is somewhat more clear; modal analysis relies upon a global description of an entire structure, while structural acoustic response is typically described in terms of the scattering properties of local components. Exceptions exist. It may be convenient to describe some portions of a structure in terms of acoustic parameters and other portions via modal analysis. Structures which are coupled to a fluid or elastic body[2] of infinite extent are examples of such exceptions, since it is then convenient to employ modal analysis for the structural response, and acoustic techniques to define the effect of the infinite medium.

The discussion of this paper will be confined to structures of finite extent. Even in such situations techniques of structural acoustics may be preferable to modal analysis. A structural component, though finite, may be effectively infinite. This limit is approached if the component is much larger than disturbance wavelengths or if damping levels are high enough to attenuate a disturbance before many reflections can occur. Both situations tend to occur when excitation frequencies include many of the structure's natural modes. The frequency boundary between structural acoustics and structural dynamics thus depends upon the structure under consideration. A reasonable division for aircraft might be a few tens of Hz. Ultrasonic devices are well described by modal analysis at frequencies of several hundred kHz. Large flexible spacecraft, with fundamental frequencies below one Hz, would enter the acoustic response regime at frequencies as low as a few Hz. Figure 1 attempts to provide a graphical version of these arguments.

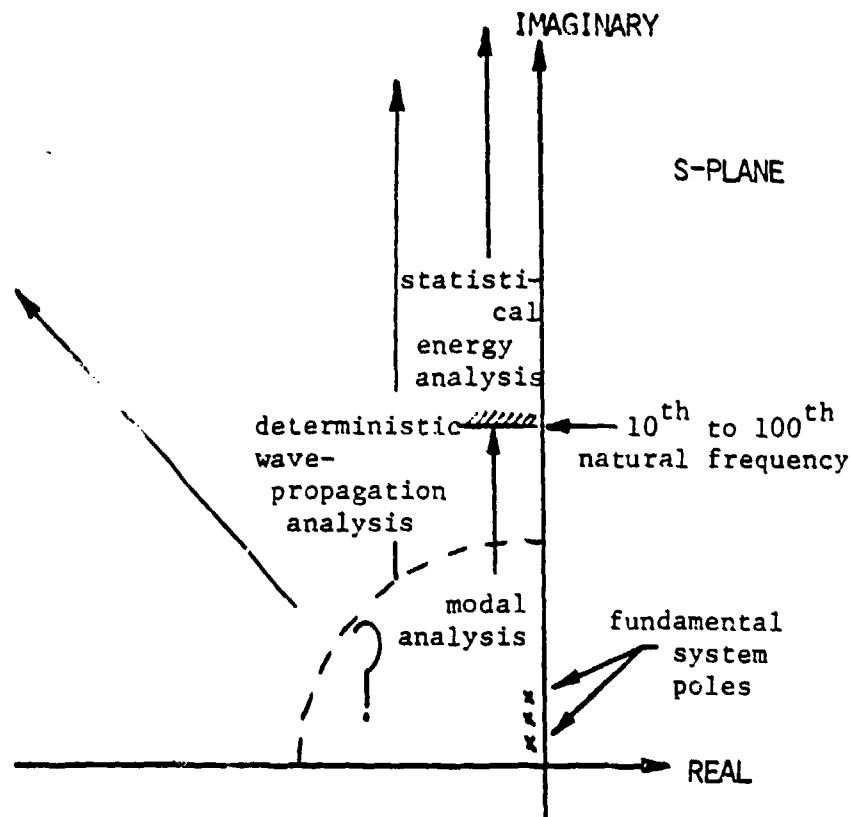


FIGURE 1 Approximate boundaries between the regions of applicability of modal analysis and local acoustic analysis are sketched in the *s* - plane. The high-frequency limit of modal analysis is due to sensitivity to parameter uncertainty. The low frequency limit of acoustic modeling is less well defined, and depends on geometrical complexity of the structure.

A relatively strong argument can be made for a high-frequency limit to the applicability of modal analysis. It is more difficult to define a low-frequency limit to the applicability of acoustic techniques. Local descriptions of component scattering behaviour can, in principle, be evaluated at any frequency, including zero, and can be linked into a global description, either in the frequency or the time domain. The convenience of such an approach will depend upon the geometric complexity of the structure, since this will govern the number of components and interconnections that must be independently modeled. The low-frequency limit of structural acoustic analysis is thus set by questions of convenience.

The advent of active control of flexible structures has underscored the limitations of structural modal analysis; high-performance active control depends upon a design model of high fidelity. Analyses of the response of proposed large flexible spacecraft suggest that hundreds of modes[3,4] will contribute significantly to the performance metric, often defined as a line-of-sight error or other measure of image quality. One is thus interested in the response at frequencies well within the acoustic regime. Unfortunately modal analysis is unable to predict details of such responses reliably, and control design with reference to such a model is then of questionable value.

An increase in the level of passive damping can make a major contribution towards an engineering solution of active control of structural dynamics and structural acoustics. Passive damping treatments tend to result in modal damping ratios which increase with mode number. Strongly damped modes can often be safely ignored, since they will not contribute strongly to degradation of the performance metric, nor couple with the control system. The virtues of passive damping can be quantified with respect to the impact on control design.[5] Mass penalties associated with passive damping treatments need not be enormous. Recent estimates[6] suggest that damping ratios of five percent can be obtained in the fundamental mode with a mass penalty of five percent. Higher modes can be damped passively with a much lower mass penalty, and the bandwidth of such damping can be effectively infinite.

If passive damping treatment is excluded or insufficient, and active control of structural dynamics to acoustic frequencies must be accomplished, then it is appropriate to base the control design upon acoustic models. Since these models are local, acoustic control will also be local. Such control theory is not well developed; only a few studies have recently been published[7,8,9,10].

2. THE ACOUSTIC LIMIT OF STRUCTURAL DYNAMIC MODELING

Mathematical modeling of an elastic structure invariably introduces a sequence of mathematical idealisations. One of these is the constitutive law assumed to apply, others are the introduction of simplifying kinematic assumptions leading to beam, plate, shell, membrane and other idealized

models of components and boundary conditions for their connection. Assumptions of linear elasticity and infinitesimal deformations lead to a linear model of the structural dynamics of each component. If the components are linked by linear boundary conditions, they can be assembled into a global linear model which describes the dynamics of the entire structure.

2.1 A LIMITATION OF MODAL ANALYSIS

Modal analysis is a further manipulation of this global model. For relatively simple structural idealisations, spatial discretisation may be avoided and the modal parameters (natural frequencies and mode shapes) may be calculated as exact solutions of the global model. For most structures of practical interest, discretisation must be introduced and the calculated modal parameters are then only approximate solutions of the global model. The difference is perhaps only of academic interest, since any level of the model is merely an approximate description of the structure. Although one alternative produces modal parameters which are exact solutions of the lowest level of the model, neither approach yields the exact modal parameters of the structure. These exact modal parameters may not even exist, since even the slightest non-linearity or temporal variation of parameters excludes rigorous modal analysis.

It is often stated that a structure is infinite dimensional, and that discretisation of the mathematical model obscures this property by the enforcement of a finite number of degrees of freedom. Several analysts have questioned the validity of this claim,[11] pointing out that the origin of the infinite dimensionality of the structural model can be traced to the introduction of the idealisation of continuum constitutive laws, and that the infinite-dimensional viewpoint certainly fails when the model dimension exceeds the number of atoms in the structure. This paper refrains from contributing to this debate, and rather points out that a practical limit of modal analysis is reached long before the number of modeled natural modes approaches the number of atoms in the structure. The origin of this limit is the extreme sensitivity of modal analysis to modeling errors.

Several perturbation analyses have been published which define this sensitivity analytically. These analyses depend upon assumptions of linearity and time invariance of the model and its perturbation. Courant and Hilbert[12] offer an analysis in terms of operator notation, specific to self-adjoint operators:

Let the eigenvalue problem be defined by

$$L(u_n) + \lambda_n u_n = 0 \tag{1}$$

where L is a linear self-adjoint operator assumed to describe the structural dynamics and λ_n , u_n , $n = 1, 2, 3, \dots$, are pairs of eigenvalues and eigen-functions of L . If the structure is actually described by another linear operator, slightly perturbed from L ;

$$L(\bar{u}_n) - \epsilon r \bar{u}_n + \bar{\lambda}_n \bar{u}_n = 0 \quad (2)$$

where the function r defines this perturbation and ϵ is a small parameter, then the eigenvalues $\bar{\lambda}_n$ and eigen-functions \bar{u}_n of this perturbed operator can be related to those of L by a classic perturbation analysis. For the case of non-repeated eigenvalues λ_n the analysis goes as follows:

Expand the perturbed eigenvalues and eigen-functions in terms of the small parameter ϵ ;

$$\begin{aligned} \bar{u}_n &= u_n + \epsilon v_n + \epsilon^2 w_n + \dots \\ \bar{\lambda}_n &= \lambda_n + \epsilon \mu_n + \epsilon^2 \nu_n + \dots \end{aligned} \quad (3)$$

The first-order perturbation of the n^{th} eigenvalue is then the inner product $\mu_n = \langle r u_n, u_n \rangle$, and the first order perturbation of the n^{th} eigen-function, v_n , is given by a sum of the contributions of the other unperturbed eigen-functions u_j , $j \neq n$;

$$v_n = \sum_{j \neq n} \frac{\langle r u_n, u_j \rangle}{\langle L(u_n), u_n \rangle} \frac{\lambda_n}{\lambda_n - \lambda_j} u_j \quad (4)$$

A similar argument in terms of matrix notation, valid for non-self-adjoint systems, has been presented in reference [13].

Modal density is invariably an increasing function of frequency; natural frequencies become ever more closely spaced as the mode number increases. Inspection of equation (4) reveals that this results in high-frequency eigen-functions with extreme sensitivity to small modeling errors. Modal analysis is thus limited to frequency regimes where relative spacing of natural frequencies remains large compared to the relative parameter uncertainty;

$$\frac{\langle r u_n, u_j \rangle}{\langle L(u_n), u_n \rangle} \ll \frac{\lambda_n - \lambda_j}{\lambda_n} \quad (5)$$

Experience suggests that this limitation will not include hundreds or even tens of modes of any structure. Many modes can be calculated, but the information, though detailed, will be useless.

Alternatives to modal analysis of linear structural dynamics, applicable to the high-frequency regime, have been developed by acousticians. These analysis techniques can be classified according to whether a stochastic or deterministic approach is taken. Hodges and Woodhouse[14] recent review paper is a reasonable starting point for study of the stochastic approaches. These approaches include asymptotic modal analysis and statistical energy analysis, and predict mean levels of response to broadband excitation. Response to narrow band excitation is not available, nor is deterministic response to any form of deterministic excitation. Such stochastic approaches

are not useful for the design of active control, but can be used for performance analyses of open or closed-loop systems of very high order.

2.2 WAVE PROPAGATION ANALYSIS

A wave propagation analysis of structural acoustic response yields a deterministic model upon which active control can be based. A complex structure is modeled by an assemblage of local component models. Each component is described in the frequency domain by frequency-dependent scattering or propagation coefficients and by the equivalent impulse responses in the time domain.

Only a few books[2,15,16,17,18] have treated the subject of structural acoustics. The focus of these books has varied, this variation reflecting the wide variation of approaches to the problem. Lyon's[15] book on statistical energy analysis does not contribute to deterministic solution techniques. Junger and Feit[2] are primarily concerned with the coupling of structural response to the acoustic response of a surrounding fluid. Auld[16] treats problems arising in ultrasonics and response of crystals and di-electric materials. Cremer and Heckl[17] and Graff[18] treat situations relevant to this paper; wave propagation and scattering in structural components which can be idealized as beams, plates, shells, membranes and rods.

The treatments of both references [17] and [18] tend to be very example-oriented; indeed it is difficult to develop a generic treatment of wave propagation in arbitrary structures. Too often each new example considered introduces new types of behaviour. If the scope of the analysis is restricted to structural components consisting of slender one-dimensional members and their interconnections, quite a general treatment is possible. Such a formalism was developed in a recent dissertation[19] and in two derivative publications[20,21].

2.2.1 WAVE PROPAGATION ON SLENDER ONE-DIMENSIONAL MEMBERS

Modeling of a slender one-dimensional member begins with the introduction of kinematic assumptions. Each cross section is assumed to deform from its reference condition according to a number of deflection variables. These variables are a function of only one spatial coordinate, the axial location of the section, hence the member is termed "one-dimensional". If the measures of cross-sectional deformation are continuous functions of the axial coordinate, introduction of a constitutive relation leads to a set of partial differential equations in time and in one spatial dimension. If the member is spatially periodic (an important subset, since this includes periodic truss beams), the cross-sectional deflections are defined at a set of discrete locations.

2.2.1.1 DISPERSION AND WAVE MODES IN CONTINUUM MODELS

A continuum model of a structural member is traditionally formulated as a system of coupled partial differential equations. Fourier transformation yields a system of coupled ordinary differ-

ential equations. For the purpose of this analysis, it is convenient to transform into a system of first-order, ordinary differential equations;

$$\frac{dy}{dx} = A(\omega) y \quad (6)$$

in terms of the "cross-sectional state vector" y of physical cross-sectional variables. The dimension of y is equal to twice the number of deflection variables assigned to the cross section. The choice of the additional variables in y is not unique; they may represent internal forces, or spatial derivatives of the deflection variables.

Diagonalization of (6) may be interpreted in terms of wave propagation along the member. The eigenvalues of matrix $A(\omega)$ are "propagation coefficients" $\gamma_j(\omega) = \alpha_j(\omega) + ik_j(\omega)$, ($i = \sqrt{-1}$), of traveling wave modes. The wave modes appear in forward and backward traveling pairs, thus the eigenvalues of $A(\omega)$ appear in pairs $(\gamma_j, -\gamma_j)$. For non-dissipative models, $A(\omega)$ is real. Its eigenvalues are not arbitrary complex pairs, but are restricted by the principle of conservation of energy to the first and third quadrants of the complex γ -plane. Thus they are either real (near fields), or pure imaginary conjugate pairs (traveling wave trains). For dissipative models $A(\omega)$ becomes complex; the eigenvalues now appear anywhere in the first and third quadrants of the complex γ -plane.

The cross-sectional state vector w of the diagonalized system

$$\Gamma(\omega) = \text{diag}(-\gamma_1 \dots -\gamma_n, \gamma_1 \dots \gamma_n)$$

$$\frac{dw}{dx} = \Gamma(\omega) w \quad (7)$$

is related to y by a frequency dependent matrix of eigenvectors

$$y = Y(\omega) w \quad (8)$$

Each element of w represents the amplitude of a wave mode, with the corresponding eigenvector occupying a column of $Y(\omega)$. These wave modes travel independently of one another within the member; each has the form $w_j(\omega) y_j(\omega) e^{-\gamma_j(\omega) x}$.

The polynomial equation $\det[A(\omega) - \gamma_j I] = 0$ defines the dispersion relation between frequency and propagation coefficient. The phase speed c_p is defined by $c_p = \frac{\omega}{k}$. The group velocity c_g is defined by $c_g = \frac{\partial \omega}{\partial k}$. A medium for which these speeds are frequency dependent is called dispersive. In such media, the signal distorts as it propagates. Most structural models of interest, with the exception of the simple wave equation describing torsion and compression of a rod, and lateral deflection of a cable, are strongly dispersive.

The Timoshenko Beam Continuum Model

Bending and shear deformation of symmetric, solid section, slender beams is well described by the Timoshenko beam model, even to frequencies where the wavelength approaches the beam thickness. This model is also often used as an equivalent continuum description of truss-work beams in bending since the shear flexibility of such beams becomes important at much lower wave numbers than for solid sections. The governing partial differential equations of this model are typically given as a second order pair in terms of the deflection variables ψ (face rotation), and w (face translation)[18];

$$GA_s \left(\frac{\partial \psi}{\partial x} + \frac{\partial^2 w}{\partial x^2} \right) - \rho A \frac{\partial^2 w}{\partial t^2} = 0 \quad (9)$$

$$GA_s \left(\psi + \frac{\partial w}{\partial x} \right) - EI \frac{\partial^2 \psi}{\partial x^2} + \rho I \frac{\partial^2 \psi}{\partial t^2} = 0 \quad (10)$$

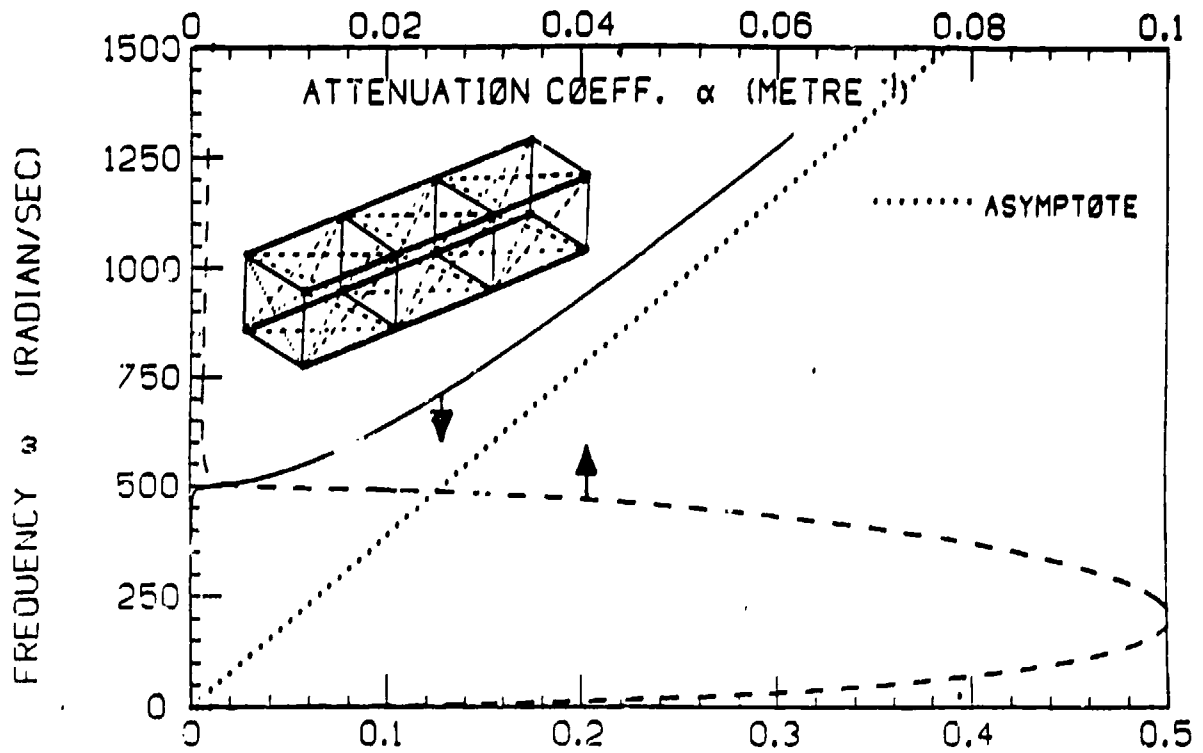
The cross-sectional state vector can be chosen to contain only deflections and the associated internal forces; $y = (-w, \psi, M, V)^T$, where the additional variables $M = EI \frac{\partial \psi}{\partial x}$ (bending moment), and $V = GA_s \left(\frac{\partial w}{\partial x} + \psi \right)$ (shear force), have been used. With this choice, the equivalent system of ordinary differential equations is

$$\frac{dy}{dx} = \begin{bmatrix} 0 & 1 & 0 & \frac{-1}{GA_s} \\ 0 & 0 & \frac{1}{EI} & 0 \\ 0 & -\rho I \omega^2 & 0 & 1 \\ \rho A \omega^2 & 0 & 0 & 0 \end{bmatrix} y \quad (11)$$

To make this example specific, four beam parameters of a continuum model[22] of a lattice beam were chosen. These correspond to a proposed space lattice beam with very slender members, overall width and thickness of 5 m, and bay length of 7.5 m. The values are; $\rho A = 2.39 \text{ kg/m}$, $\rho I = 11.8 \text{ kg-m}$, $EI = 1.77 \times 10^8 \text{ N-m}^2$, $GA_s = 2.94 \times 10^6 \text{ N}$. Structural damping of $\eta = 0.01$ is assumed.

The resulting dispersion curves are displayed in Figures 2a and 2b. This member supports two wave modes in each direction; traditionally they have been termed bending and shear modes[18], according to the dominant entry of the corresponding eigenvector. A key point to note in these dispersion curves is that both the attenuation coefficient $\alpha(\omega)$, and the wave number $k(\omega)$ become proportional to the frequency ω for large frequencies. Both modes are dispersive, but have non-dispersive asymptotes. This non-dispersive high-frequency asymptotic behaviour can be exploited in calculating transient response by wave propagation.[21]

DISPERSION CURVE OF THE TIMOSHENKO SHEAR MODE OF A LATTICE BEAM



DISPERSION CURVE OF THE TIMOSHENKO BENDING MODE OF A LATTICE BEAM

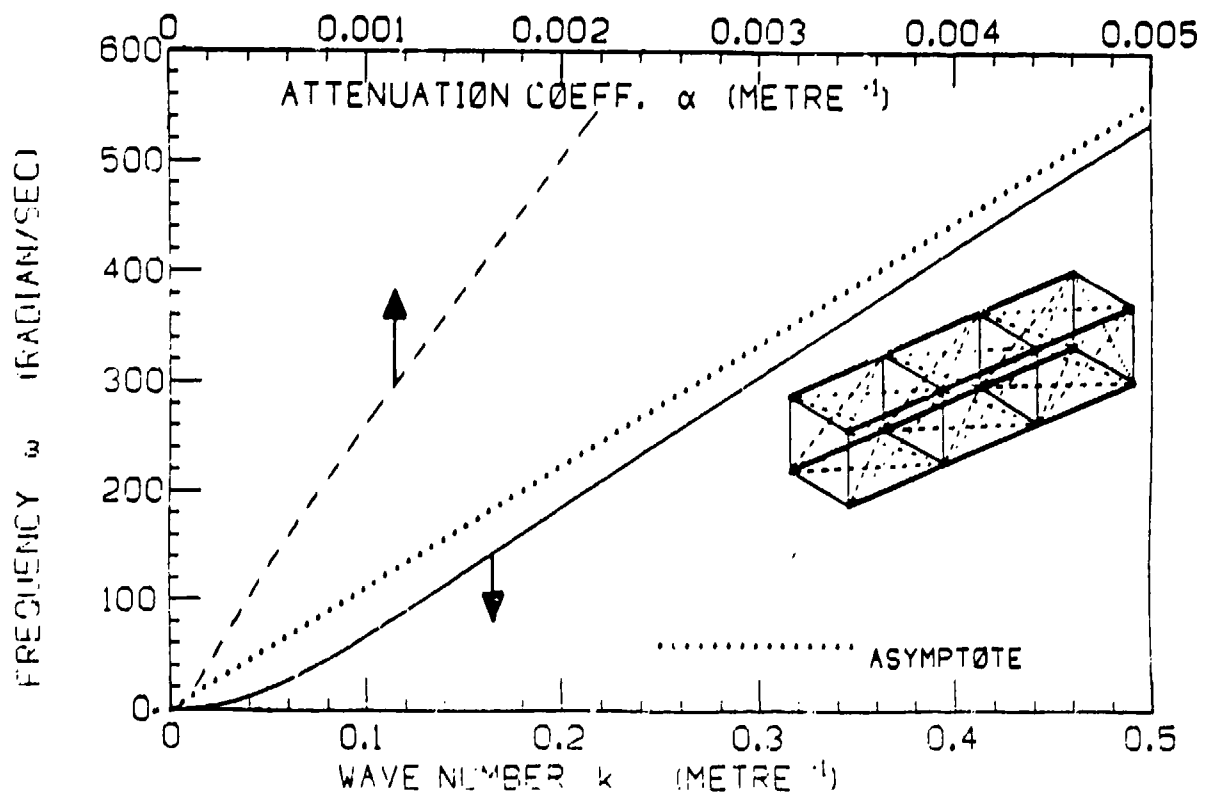


FIGURE 2 Dispersion curves for the two wave modes of the Timoshenko beam model. The beam parameters were taken from reference [22] where they were derived as an equivalent continuum model for the pictured lattice beam.

2.2.1.2 DISPERSION AND WAVE MODES IN PERIODIC MODELS

In the previous example the Timoshenko beam model was assumed to apply to the lattice beam sketched in Figures 2a and 2b. It has long been known that periodic structures in general[23], and lattice beams in particular[24,25], display somewhat different dispersive behaviour. This difference becomes significant when the wavelength becomes comparable to the length of a single bay, and at frequencies at which degrees of freedom internal to a single bay resonate. The corresponding dispersion curves display discontinuities and branching behaviour not exhibited by the dispersion curves of the "equivalent" continuum model.

Both these limitations can be overcome by the application of methods which explicitly exploit the periodicity of the structure. A convenient approach is based upon the transfer matrix of a basic cell. This matrix relates the cross-sectional state vector of coupling deflections and forces on one side of a cell to its counterpart on the other side;

$$y_{i+1} = T_y(\omega) y_i \quad (12)$$

One method of calculating the transfer matrix, $T_y(\omega)$, of a single bay employs finite-element derived mass and stiffness matrices[25].

The defining characteristic of a wave mode propagating along a periodic member is the fact that the entire cross-sectional state vector is multiplied by a complex factor, say ξ , as the wave passes through each cell;

$$y_{i+1} = \xi y_i \quad (13)$$

Equations (12) and (13) form an eigenvalue problem for ξ . These eigenvalues appear in pairs $(\xi_j, \frac{1}{\xi_j})$, corresponding to similar waves traveling in opposite directions. Equivalent propagation coefficients $\gamma_j(\omega)$ can be obtained from solution of the equation $\xi_j(\omega) = e^{\pm \gamma_j(\omega) l_{cell}}$ (where l_{cell} is the cell length). Care must be exercised to choose the correct branch of the complex logarithm. The corresponding eigenvectors of $T_y(\omega)$ have an interpretation identical to that of the wave-mode eigenvectors of continuum members (equation(8)), but are meaningful only at cell interfaces.

The important effect of periodicity, from the point of view of wave propagation, is to introduce discontinuities into the dispersion curves. Two types of discontinuity may appear. Excitation of an internal degree of freedom results in an additional branch in the dispersion curves, at the resonant frequency of the internal degree of freedom. Other discontinuities occur when $k = \frac{n\pi}{l_{cell}}$ (when the cell length is an integral multiple of the spatial half-wavelength). This is well beyond the range where an equivalent continuum model may be expected to be valid.

A Periodic Member in Torsion

Perhaps the simplest model of a periodic truss-work member is an equivalent continuum model which has been made periodic by the addition (at regular intervals) of masses, springs, or arbitrary dynamic systems. Torsion represents the simplest of this class of problems. We choose Noor's [22] equivalent continuum model for torsion of the member treated in the previous example. Periodicity is introduced by mounting five percent of the inertia of the rod on torsional springs, fastened to the rod at intervals equal to the bay length of 7.5 m. These springs are chosen to resonate at $\omega_R = 40 \text{ rad/sec}$, and are meant to represent an arbitrary internal degree of freedom. A structural loss factor of $\eta = 0.01$ is assumed for this internal degree of freedom, and for the continuum model. The continuum model has the parameter values $GJ = 3.67 \times 10^7 \text{ N} \cdot \text{m}^2$, $\rho J = 23.6 \text{ kg} \cdot \text{m}$.

The cell transfer matrix for such a model may be calculated exactly. The transfer matrix of a single cell is given by the product $T_{CELL} = T_{FIELD} T_{POINT} T_{FIELD}$ where the "field" transfer matrix, T_{FIELD} , is an exact solution of the governing partial differential equation, and relates the cross-sectional state vector at two points of a continuous rod, separated by a distance $\frac{l_{CELL}}{2}$;

$$\begin{pmatrix} \theta \\ GJ \frac{d\theta}{dz} \end{pmatrix}_{z=\frac{l_{CELL}}{2}} = \begin{bmatrix} \cos(\bar{\omega}) & \frac{l_{CELL}}{2GJ} \sin(\bar{\omega}) \\ -\frac{2GJ}{l_{CELL}} \sin(\bar{\omega}) & \cos(\bar{\omega}) \end{bmatrix} \begin{pmatrix} \theta \\ GJ \frac{d\theta}{dz} \end{pmatrix}_{z=0} \quad (14)$$

where $\bar{\omega} = \frac{l_{CELL}}{2} \omega \sqrt{\frac{\rho J}{GJ}}$. The "point" transfer matrix of a locally applied external torque $\Pi_{EXT} =$

$H(\omega)\theta$ is

$$\begin{pmatrix} \theta \\ GJ \frac{d\theta}{dz} \end{pmatrix}_{RIGHT} = \begin{bmatrix} 1 & 0 \\ H(\omega) & 1 \end{bmatrix} \begin{pmatrix} \theta \\ GJ \frac{d\theta}{dz} \end{pmatrix}_{LEFT} \quad (15)$$

The local degree of freedom is modeled as a simple oscillator, $H(\omega) = -\omega^2 I_R / (1 - (\frac{\omega}{\omega_R})^2)$.

The dispersion curves of this model are given in Figure 3. The internal degree of freedom introduces the discontinuity and the additional branch at its resonant frequency, $\omega_R = 40 \text{ rad/sec}$. Figure 3 shows that the resonant frequency of the internal degree of freedom becomes an upper limit for the applicability of an equivalent continuum model.

A real truss-work member will have many such internal resonances. Each of these resonances creates its own discontinuity, and its own additional branch in the dispersion curves. Reference [25] reports a computational investigation into the wave propagation behaviour of a particular truss beam, with each bay modeled via finite elements. Each of the wave modes supported by this model exhibits many discontinuities in its dispersion curve. A new type of traveling wave mode is reported in this work; a "complex wave mode" which both travels and is spatially attenuated.

DISPERSION CURVE OF A PERIODIC TORSION MODEL OF A LATTICE BEAM

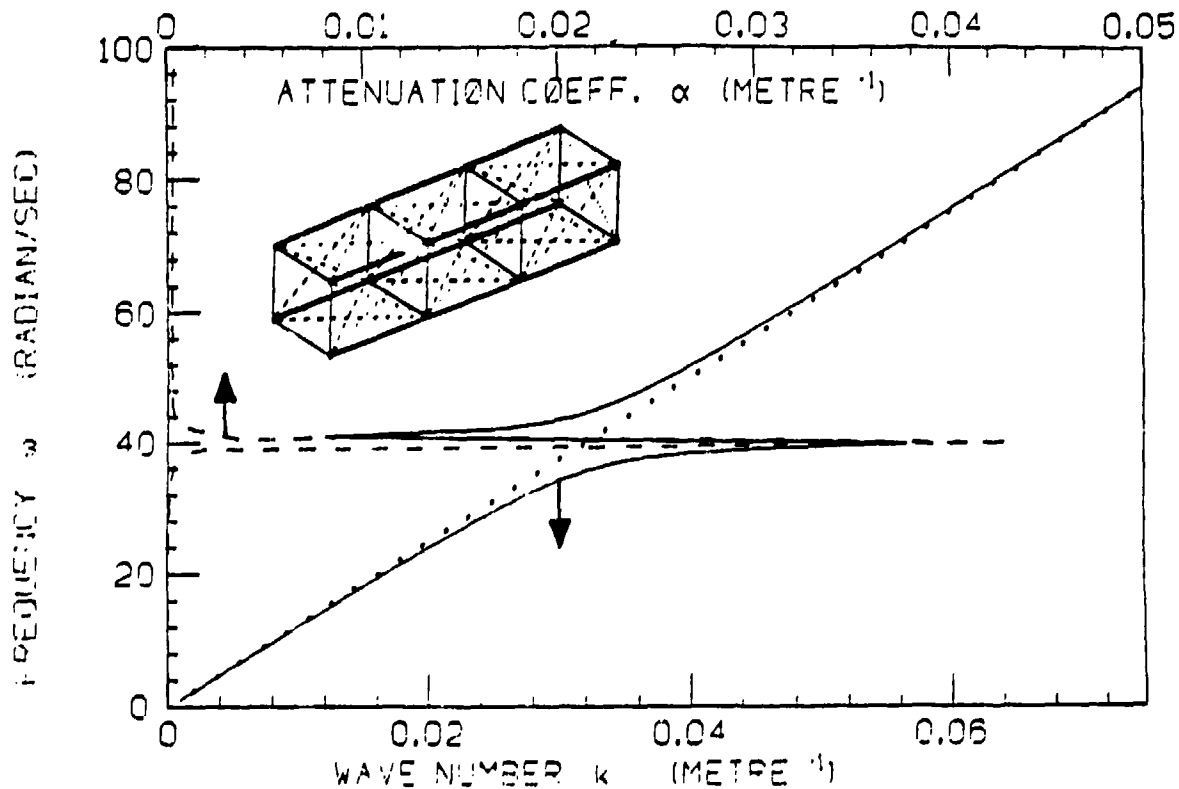


FIGURE 3 Dispersion curves of a periodic torsion model based upon an equivalent continuum model of the pictured lattice beam. The continuum model was developed in reference [22]. The discontinuity at $\omega = 40 \text{ rad/sec}$ is due to resonance of local degrees of freedom.

2.2.2 WAVE-MODE TRANSIENTS ON MEMBER SEGMENTS

The transient response of disturbance propagation along elastic members is conveniently calculated in terms of the traveling wave modes. Indeed, it is this convenience which prompted their introduction in the frequency domain description of the previous section. This transient calculation has historically been the focus of much work[18]. A computational approach based on extensive use of the discrete Fourier transform is reported in reference [21]. These calculations are not central to the remainder of this paper, particularly to the control design of section 3; their description is omitted here in the interest of brevity.

2.2.3 SCATTERING AT JUNCTIONS AND DISCONTINUITIES

The following discussion is based upon the "generic" junction of Figure 4. This sketch, and the notation (with the exception of the external forces, $p f$) can be found in most basic texts on microwave circuits.[26]

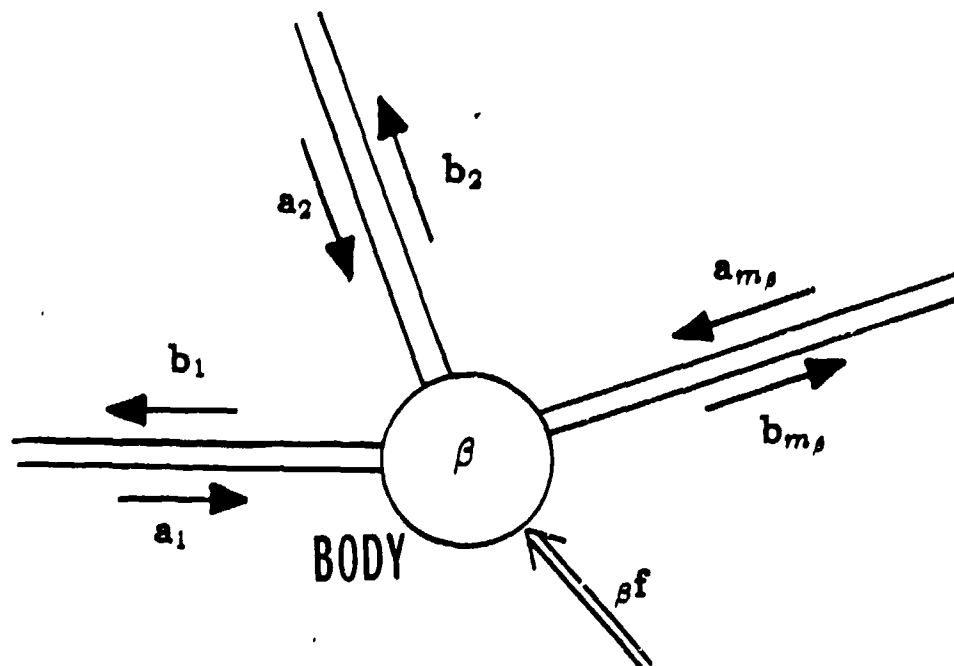


FIGURE 4 The generic junction. The junction can include a flexible body and can be connected to many members. Each member, j , transmits incoming wave modes, a_j , and outgoing wave modes, b_j . External forces are grouped in the vector f_β . The notation is standard in microwave circuit analysis[26].

Associated with each member j , is a cross-sectional state vector y_j , of size n_j , defined at the (arbitrary) interface between the junction and the member. This state vector may be transformed into wave-mode coordinates according to the transformation derived in the previous section. Each wave-mode state vector w_j can be grouped into incoming a_j and outgoing b_j wave modes.

The junction boundary conditions are conveniently defined in terms of the composite junction state vector, $y = (y_1^T, y_2^T \cdots y_{m_\beta}^T)^T$, having dimension $n = \sum_{j=1}^{m_\beta} n_j$. The boundary conditions can be expressed

$$B(\omega) y = f(\omega) \quad (16)$$

where $B(\omega)$ is a (possibly lively) function of frequency and has n columns and $\frac{n}{2}$ rows, and $f(\omega)$ is a vector of size $\frac{n}{2}$, of externally applied forces and deflections. If the junction contains a flexible body, and is described by a system of ordinary differential equations, its description may be reduced to the form of equation (16). Such reduction is described in reference [19] and is a relatively standard procedure in structural dynamics.

The junction boundary conditions can be transformed into wave-mode coordinates by use of a block-diagonal matrix of member transformation matrices;

$$\rho y = \rho Y(\omega) \rho w = \begin{bmatrix} Y_1 & & & \\ & Y_2 & & \\ & & \ddots & \\ & & & Y_{m_\rho} \end{bmatrix} \begin{pmatrix} w_1 \\ w_2 \\ \vdots \\ w_{m_\rho} \end{pmatrix} \quad (17)$$

After partitioning into incoming and outgoing wave modes, $\rho w = (\rho a^T, \rho b^T)^T$, and re-ordering, the junction boundary condition becomes;

$$[\rho B_a(\omega) \quad \rho B_b(\omega)] \begin{pmatrix} \rho a \\ \rho b \end{pmatrix} = \rho f(\omega) \quad (18)$$

If the sub-matrix ρB_b can be inverted, then the boundary equation (18) can be written in "causal" form;

$$\rho b(\omega) = \rho S(\omega) \rho a(\omega) + \rho \Psi(\omega) \rho f(\omega) \quad (19)$$

where the scattering matrix, $\rho S(\omega) = -\rho B_b^{-1}(\omega) \rho B_a(\omega)$, is a matrix of frequency-dependent transmission and reflection coefficients and $\rho \Psi(\omega) = \rho B^{-1}(\omega)$ is a matrix describing the generation of outgoing wave modes, ρb , by the external forcing ρf .

Junction of the Timoshenko Beam and Periodic Torsion Models

Numerous examples illustrating the application of the above derivation have been presented in reference [19]. The example presented here describes the perpendicular junction of the two members treated above. For this junction, the boundary conditions are;

$$\begin{bmatrix} 1 & 0 & 0 & -1 & 0 & 0 & 0 & 0 \\ 1 & 0 & 0 & 0 & 0 & 0 & -1 & 0 \\ 0 & 0 & 0 & 0 & 0 & 1 & 0 & 0 \\ 0 & -1 & 0 & 0 & 1 & 0 & 0 & 1 \end{bmatrix} \begin{pmatrix} y_{ROD_A} \\ y_{BEAM} \\ y_{ROD_B} \end{pmatrix} = 0 \quad (20)$$

Transformation into wave-mode coordinates and derivation of the scattering matrix is done numerically. The scattering matrix is presented in Figure 5, over the frequency range $0 \leq \omega \leq 1200 \text{ rad/sec}$. Periodicity of the rod member has been suppressed by setting $H(\omega) = 0$ in equation (15). Most of the activity in the frequency dependence of these scattering coefficients is due to the very dispersive nature of the Timoshenko shear mode. This mode exhibits a cut-off frequency at $\omega \approx 500 \text{ rad/sec}$ (see Figure 2).

2.2.4 TRANSIENTS IN JUNCTIONS

The calculation of transient wave scattering through a junction described by equation (19) has been the topic of published work[21]. This transient behaviour is not relevant to the control design techniques proposed in the next section, and so is omitted here for brevity.

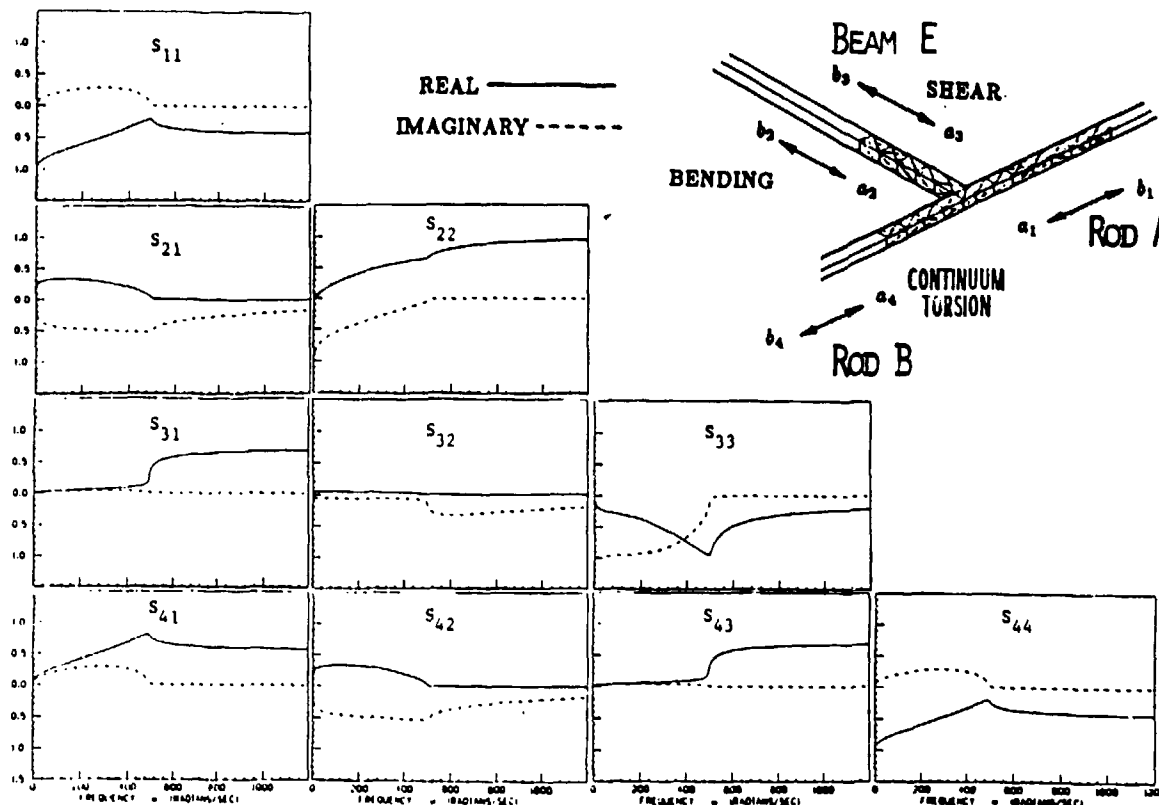


FIGURE 5 The scattering behaviour of the junction of a beam in bending modeled with Timoshenko beam theory and two rods in torsion. The periodicity of the torsion model has been suppressed by choice of $H(\omega) = 0$ in equation (15). The cut-off behaviour of the Timoshenko shear mode (at $\omega \approx 500 \text{ rad/sec}$) has a strong effect on these curves.

3. ACTIVE CONTROL OF STRUCTURAL ACOUSTICS

Active control of structural acoustic response, with reference to an explicit structural acoustic model, is an almost untouched field of investigation with only four known publications[7,8,9,10]. Conversely, control design for structural dynamics is the subject of a large literature[27]. Control design techniques developed for systems of low order are being extended to models with many (tens or even hundreds) of the structure's natural modes of vibration. Such extension is a de facto attempt to achieve active control of structural acoustics. Unfortunately a modal description of structural dynamics to these frequencies is essentially useless, as has been discussed in a previous section.

Since high fidelity deterministic models of structural acoustics are spatially local, control based upon such models will share this property. Each local controller will be based upon the local dynamics of a component. Supervisory coordination between these local controllers is possible, but the theory for such an architecture has not yet been developed. This section reviews approaches to component control design based upon wave propagation models, and draws upon previously published work for specific examples.

3.1 ACTIVE MODIFICATION OF WAVE PROPAGATION ON MEMBERS

Theory for the active control of disturbance propagation in structural members has not been developed. One could visualize many possibilities for such a spatially distributed control; design objectives might be to distort the symmetry of the wave propagation properties of the member. A member might be actively modified, perhaps in selected frequency ranges, to propagate disturbances in only one direction. Such member control might be spatially discretized for implementation with discrete actuators, or might be designed for a spatially discrete member such as a truss beam. Many possibilities exist, all have yet to be investigated.

3.2 ACTIVE MODIFICATION OF JUNCTION SCATTERING BEHAVIOUR

Equation (19) is the frequency domain description of reflection, transmission and wave generation at a junction of one or several structural members. Two approaches to control of such scattering have been developed, both build upon equation(19).

3.2.1 SPECIFICATION OF CLOSED-LOOP SCATTERING BEHAVIOUR

One might, based upon intuitive reasoning or analysis, wish to specify values for selected reflection and transmission coefficients of the closed-loop junction behaviour. Obvious choices for such a specification would be zero for some coefficients, although the specification might be more general, perhaps frequency dependent. This would result in selective absorption of incoming wave modes, or shunting of some incoming disturbances into selected outgoing directions.

If the controller exerts influences (forces and relative deflections) upon the junction which are grouped in the vector βf , and this control effort depends linearly upon the incoming wave modes a_β , then the control law

$$\beta f(\omega) = \beta \Psi^{-1}(\omega) [\beta S_{CL}(\omega) - \beta S(\omega)] \beta a(\omega) = C_a(\omega) \beta a(\omega) \quad (21)$$

leads to the desired closed-loop behaviour;

$$\beta b(\omega) = S_{CL}(\omega) \beta a(\omega) \quad (22)$$

Measurement of the incoming wave modes $\beta a(\omega)$ may not be practical since they are related to physical variables through a frequency-dependent transformation (equation (17)). Use of this transformation permits manipulation of equation (21) into the form

$$\beta f(\omega) = \beta S_{CL}(\omega) \beta a(\omega) = C_y(\omega) \beta y(\omega) \quad (23)$$

where the control forces are now given in terms of the physical variables βy .

The preceeding discussion has not considered the possibility that only a few actuators are available at a given junction to effect control. In this situation, the number of independent entries

in ${}_{\rho}f(\omega)$ would be less than the dimension of ${}_{\rho}a(\omega)$; more wave modes depart the junction than one has actuators available. Several options have been developed for this situation[9,19]. One might attempt to minimize a sum of squares of departing wave-mode amplitudes. One might set selected departing wave modes to zero, while letting the others behave as they will, or one might influence only subsets of the scattering coefficients. Each approach leads to a control of the form of equation (23).

Examples of Wave-Shunting Control Design

Two examples, taken from prior published work, are offered here to clarify the above discussion. Figure (5), from reference [9], gives the open-loop scattering behaviour of the junction of three members. One is modeled in bending with Timoshenko beam theory, the other two are modeled in torsion with simple rod theory. The member models thus support four incoming and four outgoing wave modes. As an arbitrary design exercise, a compensator has been calculated which prevents waves from departing the junction along one of the members, that is, with reference to Figure (5), $b_1 = 0$. The control force to accomplish this was (arbitrarily) chosen to be an external moment applied to the junction.

An external torque, M_{EXT} can be included in the boundary conditions of equation (20) by introduction of an external forcing vector ${}_{\rho}f = (0001)^T M_{EXT}$. The boundary conditions are then readily manipulated into the form of equation (19), where ${}_{\rho}S(\omega)$ is given in Figure 5. A bit of algebra, done numerically at each frequency, yields a compensator of the form

$$\begin{aligned} M_{EXT} = & C_{\theta_A} \theta_A + C_{\tau_A} \tau_A + C_{w_B} w_B + C_{\psi_B} \psi_B \\ & + C_{M_B} M_B + C_{V_B} V_B + C_{\theta_B} \theta_B + C_{\tau_B} \tau_B \end{aligned} \quad (24)$$

where θ (rotation) and τ (torque) are the cross-sectional state variables of the two torsion members at the junction, and w (lateral deflection), ψ (face rotation), M (bending moment) and V (shear force) are the four cross-sectional state variables of the bending member at the junction. Subscripts denote which member the variable corresponds to. Note that all eight local cross-sectional state variables are used by this compensator. The open loop scattering matrix of this junction (Figure 5) shows that all arriving wave modes must be countered. One of the eight compensators of equation (24) is displayed in Figure 6 (the other seven are available in reference [19]). Note that this compensator is both infinite dimensional and infinite in bandwidth.

Reference [9] takes this computational example somewhat further. The junction is imbedded into a structure, and transcendental transfer functions are calculated with and without this wave-absorbing control. The change in the structural response is dramatic.

A second example is taken from reference [10] and treats reflection cancellation for the free end of a beam in bending. A beam, if modeled with Bernoulli-Euler beam theory, supports one

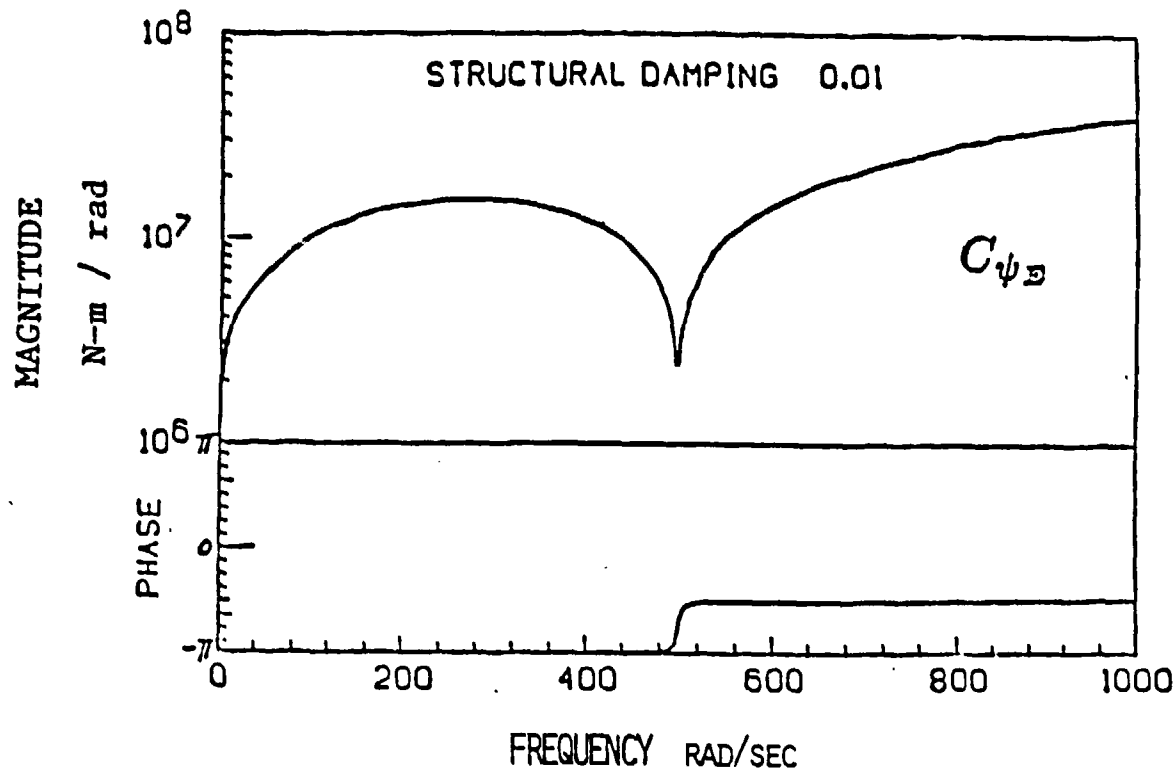


FIGURE 6 Frequency dependence of one of the eight compensators of equation (24). This compensator feeds local rotation at the junction depicted in Figure 5 back to a co-located external torque. The control task is to set $b_1 = 0$.

traveling wave mode in each direction. The governing differential equation permits another type of response; near fields which decay exponentially with axial distance and have a simple harmonic temporal behaviour. With reference to Figure 7 the deflection field can be written

$$v = a_t e^{ikz+i\omega t} + a_n e^{kz+i\omega t} + b_t e^{-ikz+i\omega t} + b_n e^{-kz+i\omega t} \quad (25)$$

where $k = \sqrt{\omega \sqrt{\rho A / EI}}$ is known as the wave number, EI is the bending stiffness, ρA is the mass per length of the beam and a_t , a_n , b_t and b_n are wave mode amplitudes at the left end of the beam, defined in Figure 7. If an external control torque, M_{EXT} , can be applied to the beam at the left end, the corresponding boundary conditions can be expressed in the form of equation (19) as

$$\begin{pmatrix} b_t \\ b_n \end{pmatrix} = \begin{pmatrix} -i & 1+i \\ 1-i & i \end{pmatrix} \begin{pmatrix} a_t \\ a_n \end{pmatrix} + \frac{1+i}{2\omega \sqrt{\rho A EI}} \begin{pmatrix} -1 \\ -i \end{pmatrix} M_{EXT} \quad (26)$$

The important entry of the scattering matrix is $S(1,1)$ since this term governs the creation of outgoing traveling wave modes as a function of incoming traveling wave modes. One choice for the compensation that achieves $S(1,1) = 0$ is

$$M_{EXT}(\omega) = -i \sqrt{\rho A EI} \omega v(x=0, \omega) \quad (27)$$

since for this choice the closed-loop reflection matrix becomes

$$S_{CL} = \begin{pmatrix} 0 & i \\ -i & 0 \end{pmatrix} \quad (28)$$

The compensation of equation (27) can be seen to be velocity feedback of local deflection to applied torque. The effect of finite actuator dynamics and other sources of gain roll-off yet needs to be investigated. The question is important to this example since experimental verification is planned.

3.2.2 OPTIMAL WAVE ABSORPTION

A recent development[10] in the theory of traveling wave control is the proposal of a meaningful cost function associated with the actively controlled junction. Minimization of this cost function then leads to a control design, which since a reasonable quantity is being minimized, is termed optimal. The proposed cost function is a weighted integral over frequency of the wave power flowing out of the junction along the members and the power exerted by the control forces;

$$J = \int_{-\infty}^{\infty} (\beta \mathbf{w}^H \mathbf{P} \beta \mathbf{w} + \beta \mathbf{f}^H \mathbf{R} \beta \mathbf{f}) d\omega \quad (29)$$

where the superscript H (Hermitian) denotes complex conjugate transpose. The first term in the above integrand is the power flow, as a function of frequency, being carried out of the junction by wave motion. The matrix \mathbf{P} depends upon the characteristics of the members attached to the junction under consideration, but is always Hermitian.[10] The second term in the integrand is a quadratic penalty on control effort. The matrix \mathbf{R} can be chosen by the control designer. It can be a function of frequency but must be Hermitian.

Since outgoing wave modes depend upon the control effort, this cost function can be further expanded using the substitution

$$\beta \mathbf{w} = \begin{pmatrix} \beta \mathbf{a} \\ \beta \mathbf{b} \end{pmatrix} = \begin{pmatrix} \beta \mathbf{a} \\ \beta \mathbf{S} \beta \mathbf{a} + \beta \mathbf{\Psi} \beta \mathbf{f} \end{pmatrix} \quad (30)$$

The cost functional is minimized with respect to the control, $\beta \mathbf{f}$ by

$$\beta \mathbf{f} = -[\beta \mathbf{\Psi}^H \mathbf{P}_{bb} \beta \mathbf{\Psi} + \mathbf{R}]^{-1} \beta \mathbf{\Psi}^H [\mathbf{P}_{ba} + \mathbf{P}_{bb} \beta \mathbf{S}] \beta \mathbf{a} \quad (31)$$

where the power flow matrix has been partitioned in an obvious way into square submatrices. The optimal control, given by equation (31), differs from the control which achieves zero outgoing disturbance, $S_{CL} = 0$, derivable from equation (21) as

$$\beta \mathbf{f} = -\beta \mathbf{\Psi}^{-1} \beta \mathbf{S} \beta \mathbf{a} \quad (32)$$

In part, this difference is due to the penalty associated with control effort. If the control penalty,

R , is set to zero in equation (31), then the P_{ba} term still creates a difference between the two control laws of equations (31) and (32). The presence of the term P_{ba} in equation (31) is due to another effect. This term attempts to exploit power flow coupling between wave modes to draw the elastic energy into the junction more effectively than merely waiting for it to arrive. The off-diagonal entries of the P matrix are often zero, however, and it is not yet clear if this type of "energy vacuuming" will be useful in application. The following example is intended to clarify the situation.

Optimal Wave Cancellation at a Free Beam End

This example is a continuation of the beam example begun in the preceding section. The junction is the termination of a single beam, so that the power flow matrix will correspond only to the four wave modes supported by the Bernoulli-Euler beam model;

$$P = 2\omega^2 k \sqrt{\rho A E I} \begin{bmatrix} -1 & 0 & 0 & 0 \\ 0 & 0 & 0 & i \\ 0 & 0 & 1 & 0 \\ 0 & -i & 0 & 0 \end{bmatrix} \quad (33)$$

The wave modes are ordered ${}_P w = (a_t a_n b_t b_n)^T$. From inspection of equation (33) one can deduce that the incoming traveling wave mode causes power to flow into the junction, the outgoing traveling wave mode cause power to flow out of the junction, while the two near fields can cause

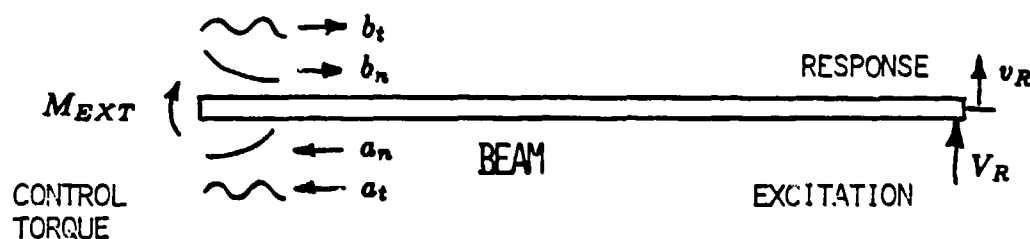


FIGURE 7 Schematic of a free-free beam in bending. The left end of beam is actively terminated by a wave absorbing controller, applying external torques, M_{EXT} , in response to local deflection or slope. The right end is excited by a lateral force.

power to flow in either direction but only through interaction with another. The in-phase portion of one near field interacts with the out-of-phase portion of the other near field to cause a net power flow. One near field is created at the junction. Equation (31) suggests that one exploit this interaction between near fields to increase the power flow into the actively controlled junction beyond that which is carried by the incoming traveling wave a_t .

When the requisite values of P , ${}_P \Psi$, and a value of $R = 0$ (no control penalty) are inserted into equation (31), and the boundary conditions are used to convert to physical variables, the optimal control becomes

$$M_{EXT} = \sqrt{EI/2\sqrt{\rho AEI}\sqrt{-i\omega}} \frac{dv}{dx}(x=0, \omega) \quad (34)$$

which involves feedback of the beam slope to the applied torque through a temporal "half differentiation".

Leaving aside, for the moment, questions of realizability, it is instructive to investigate the performance of such wave controllers in simulation. Figure 8 is a simulated transfer function of a finite length of the beam. It is clear that the effect of compensation of the form of either equation (27) or (34) would have a profound effect upon the behaviour of the beam segment. Seen from the driven (right) end, the controlled beam behaves essentially as if it extended to infinity.

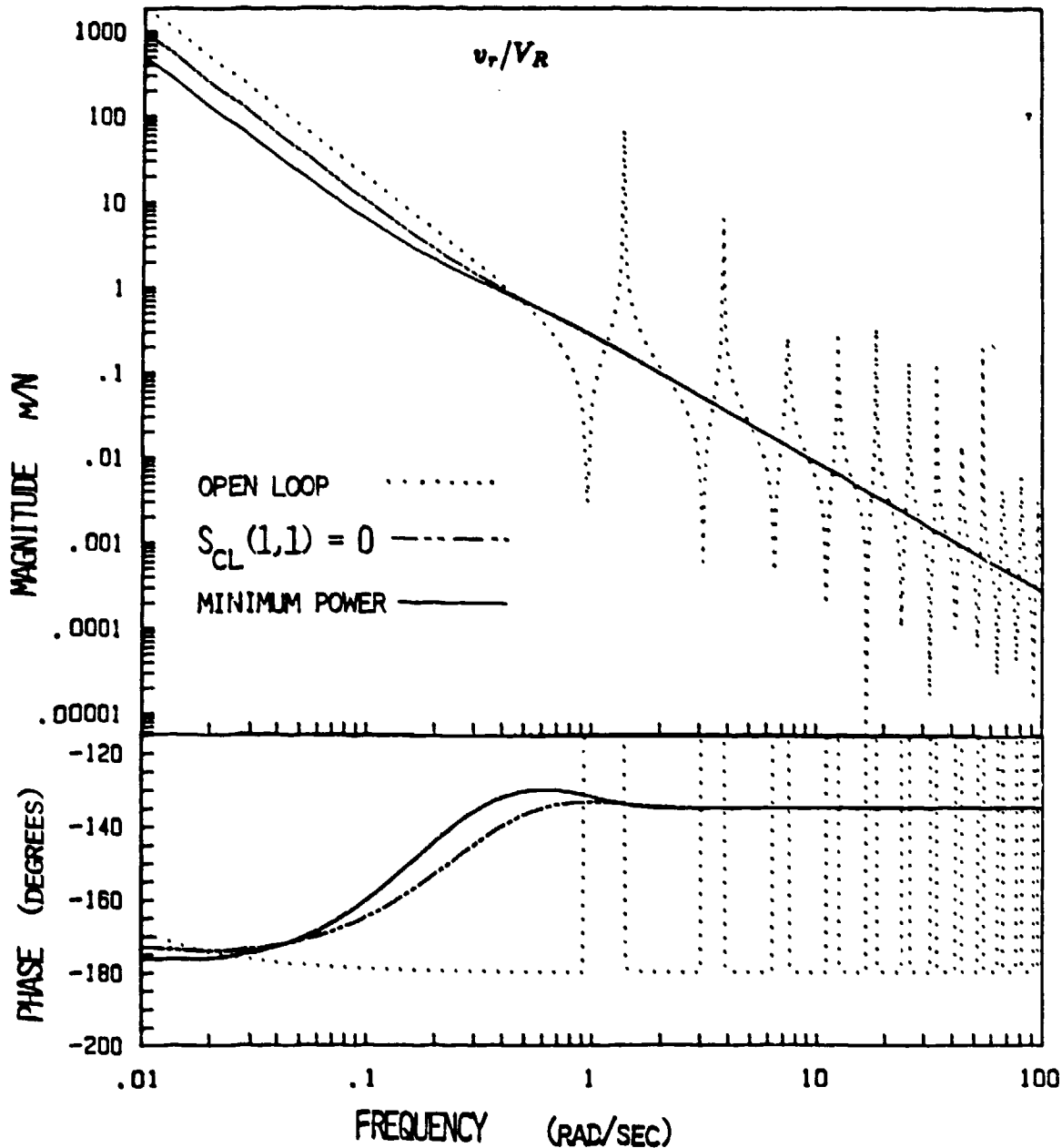


FIGURE 8 Magnitude and phase of the lateral deflection of the right end of the beam of Figure 7 to a lateral force also applied to the right end. The left end is controlled by a wave absorbing controller which either sets $S_{CL}(1,1) = 0$, or minimizes wave power departing the left end. Open-loop behaviour is shown for reference.

3.3 EXPERIMENTAL VERIFICATION OF TRAVELING WAVE CONTROL

The computational examples presented above have used very ideal assumptions in the derivations. In particular, no attempts were made to account for actuator or sensor limitations. Without exception, every compensator derived was of infinite bandwidth. The compensation is specified in the frequency domain, and is in general infinite-dimensional.

Wave absorbing compensation with finite bandwidth will always be derivable; one must simply trade performance against bandwidth. Several possibilities for doing this in a rational way come to mind. One might use a frequency-dependent control penalty matrix $R(\omega)$ in the optimal control derivation with the frequency dependence chosen such that the compensation gain rolls off as desired. One might specify a closed-loop scattering matrix S_{CL} in equation (21) in such a way as to create the same effect. As a last resort, one might simply roll-off the compensation with low-pass filtering. The trade-offs of these techniques have yet to be thoroughly studied.

Whichever technique is used to make the bandwidth of the wave absorbing compensators finite, their infinite-dimensionality will, in general, remain. Simplified and realizable approximations of such infinite-dimensional compensation can always be derived. A rational approach for deriving such approximations has not been developed. Since the compensation is specified in the frequency domain, a frequency domain fit with a realizable transfer function seems reasonable. Such techniques, and their laboratory application to this problem, have yet to be developed.

To date, only one experiment in active control of traveling wave in structures seems to have been reported[8]. This experiment attempted the cancellation of the reflection of bending waves on a thin(1 mm) sheet of stainless steel in the frequency range from zero to 25 Hz. The tip deflection could be sensed; actuation of lateral force was possible. The ideal compensation involved feedback of the tip deflection to the lateral force through a temporal "half differentiation", as in equation (34). Several analog circuits were used to crudely approximate this ideal actuation. The compensation actually achieved was finally very similar to a previously calculated optimal velocity feedback.

The performance achieved by the approximate wave-absorbing compensation in this experiment was very comparable to that achieved by the optimized velocity feedback. Although the two concepts represent alternative approaches to the problem of active damping of structural vibrations, this experiment did not permit a solid conclusion of their relative merits.

3.4 POTENTIAL EXTENSIONS OF TRAVELING WAVE CONTROL

The active control of traveling waves in structures is a very recent development. Only relatively crude theory has been developed, and an even cruder experiment has been conducted. Many extensions to this work can be considered:

- 1 The sensitivity of traveling wave controllers to errors in the local acoustical models should be investigated. A first order sensitivity to first order perturbations in the model is expected.
- 2 Explicit account might be taken of actuator and sensor dynamics during the design of wave controllers. It is anticipated that the specified wave control compensator will then include an inversion of these dynamics.
- 3 The approximation of specified wave control compensators with analog circuitry or digital filters should be studied. It seems likely that realizability of these compensators will be improved by measuring the approaching wave disturbance some distance "upstream" of the point of actuation. With such precognitive sensing, the inversion of actuator and sensor dynamics may even be possible.
- 4 Adaptation of wave controllers is possible. A signal upon which to base the adaptation might be the level of the outgoing wave mode which the control is designed to cancel.
- 5 Development of controllers based upon the propagation behaviour of members rather than scattering behaviour of junctions is a possibility. Such work would have to face the problem of non-existence of distributed actuators and sensors, and should perhaps focus on periodic truss beams.
- 6 Cooperative behaviour among several wave controllers and/or a global controller based upon a low-order modal model might be studied.
- 7 All the control schemes proposed must be realised in hardware to be useful. Such experimental work is perhaps the most important missing aspect of the work performed to date in active control of structural acoustics.

4. SUMMARY

This paper makes the point that high performance active control of structural dynamics over a bandwidth including many lightly damped modes is impractical if the control design is based upon a model derived via modal analysis. The fidelity demanded of the model is simply beyond that achievable with modal analysis. The analysis technique is too sensitive to small perturbations and uncertainties in the model parameters.

Alternatives exist. An important possibility is passive damping in conjunction with active control of a small subset of the lower modes. Active damping through direct velocity feedback can also be used. If active control of a lightly damped structure over a bandwidth including many modes of vibration must be accomplished, then local, structural acoustic models of the response are suitable for the control design. This leads to local traveling wave control.

The paper presents a formalism for the synthesis of traveling wave models of a particular class of structures; networks of slender elastic members. A review of control design techniques

applicable to the control of disturbance propagation in such structural networks is presented. The conclusion is drawn that the theory is very incomplete, and speculations are offered as to future developments.

ACKNOWLEDGEMENTS

Many of the ideas summarized in this paper are a direct development of a dissertation written at Stanford University in 1984 under the direction of Professor Holt Ashley, and with financial support from the Canadian Natural Sciences and Engineering Research Council and from the United States Air Force Office of Scientific Research (AFOSR). The ideas were developed further with the support of the German Aerospace Research Establishment (DFVLR), and the Alexander von Humboldt Foundation, and most recently, at the Massachusetts Institute of Technology with further support of the AFOSR.

REFERENCES

1. J. W. Strutt Lord Rayleigh, *Theory of Sound*, 1894, Dover 1945
2. M. C. Junger, D. Feit, *Sound, Structures and Their Interaction*, Massachusetts Institute of Technology Press, 1986
3. D. S. Bernstein, S. W. Greeley, "Robust Controller Synthesis Using the Maximum Entropy Design Equations," *IEEE Transactions Automatic Control*, Vol. AC-31, 1986, pp. 362-364
4. G. J. Kissel, D. R. Hegg, "Stability Enhancement for Control of Flexible Space Structures," *IEEE Control Systems Magazine*, Vol. 6, No. 3, June 1986, pp. 19-26
5. R. Gran, "Finite-Dimensional Controllers for Hyperbolic Systems," *Proceedings, Third VPI/SU/AIAA Symposium*, Blacksburg, VA, June 15-17, 1981
6. A. H. von Flotow, "Control Motivated Dynamic Tailoring of Spacecraft Truss Structures," *Proceedings, AIAA Guidance, Dynamics and Control Conference*, Williamsburg, VA, August 1986
7. D. R. Vaughan, "Applications of Distributed Parameter Concepts to Dynamic Analysis and Control of Bending Vibrations," *J. Basic Engng*, June 1968, pp. 157-166
8. A. H. von Flotow, B. Schäfer, "Wave-Absorbing Controllers for a Flexible Beam," *J. Guidance, Control and Dynamics*, Vol. 9, No. 6, Nov-Dec 1986, pp. 673-680
9. A. H. von Flotow, "Traveling Wave Control for Large Spacecraft Structures," *J. Guidance, Control and Dynamics*, Vol. 9, No. 4, July-August 1986, pp. 462-468
10. D. W. Miller, A. H. von Flotow, S. R. Hall, "Active Modification of Wave Reflection and Transmission in Flexible Structures," *Proceedings, American Control Conference*, June 10-12, 1987, Minneapolis, Minnesota
11. P. C. Hughes, presentation comments, NASA Workshop on Applications of Distributed System Theory to the Control of Large Space Structures, JPL, Pasadena, CA, July 14-16, 1982
12. R. Courant, D. Hilbert, *Methods of Mathematical Physics*, Vol. 1, Interscience, 1953
13. R. H. Plaut, K. Huseyin, "Derivatives of Eigenvalues and Eigenvectors in Non-Self-Adjoint Systems," *AIAA Journal*, Vol. 11, No. 2, Feb 1973

14. C. H. Hodges, J. Woodhouse, "Theories of Noise and Vibration Transmission in Complex Structures," *Reports on Progress in Physics*, 1986, 49, 107-170
15. R. H. Lyon, *Statistical Energy Analysis of Vibrating Systems*, Massachusetts Institute of Technology Press, 1975
16. B. A. Auld, *Acoustic Fields and Waves in Solids* (two volumes), John Wiley and Sons, 1973
17. L. Cremer, M. Heckl, E. E. Ungar, *Structure Borne Sound*, Springer-Verlag, 1973
18. K. F. Graff, *Wave Motion in Elastic Solids*, Ohio State University Press, 1975
19. A. H. von Flotow, "Disturbance Propagation in Structural Networks; Control of Large Space Structures," *Ph.D. Dissertation*, Department of Aeronautics and Astronautics, Stanford University, June 1984
20. A. H. von Flotow, "A Traveling Wave Approach to the Dynamic Analysis of Large Space Structures," *Proceedings AIAA/ASME/ASCE/AHS 24th Structures, Structural Dynamics and Materials Conference*, South Lake Tahoe, California, May 2-4, 1983
21. A. H. von Flotow, "Disturbance Propagation in Structural Networks," *J. Sound Vibration*, (1986), 106(3), 433-450
22. A. K. Noor, C. M. Andersen, "Analysis of Beam-Like Lattice Trusses," *Computer Methods in Applied Mechanics and Engineering*, 20, 1979, 53-70
23. L. Brillouin, *Wave Propagation in Periodic Structures*, Dover Publications, 1946
24. S. Sgubini, F. Graziani, A. Agneni, "Elastic Waves Propagation in Bounded Periodic Structures," *Proceedings, 35th Congress of the International Astronautical Federation*, October 8-13, 1984, Lausanne, Switzerland
25. J. Signorelli, A. H. von Flotow, "Wave Propagation in a Periodic Truss Beam," *Proceedings, AIAA Dynamics Specialists Conference*, April 9-10, 1987, Monterey, CA
26. R. H. Ghose, *Microwave Circuit Theory and Analysis*, McGraw-Hill, 1963
27. M. J. Balas, "Trends in Large Space Structure Control Theory: Fondest Hopes, Wildest Dreams," *IEEE Transactions Automatic Control*, Vol. Ac-27, June 1982